

A model study of strong correlations in Hund metals

The Numerical Renormalization Group as efficient multi-band impurity solver for Dynamical Mean-Field Theory

Katharina Maria Stadler



Munich 2019

A model study of strong correlations in Hund metals

The Numerical Renormalization Group as efficient multi-band impurity
solver for Dynamical Mean-Field Theory

Katharina Maria Stadler

A dissertation submitted
to the Faculty of Physics at the
Ludwig–Maximilians–Universität München
for the degree of
DOCTOR RERUM NATURALIUM



Munich, January 17, 2019

First referee: Prof. Dr. Jan von Delft
Second referee: Prof. Dr. Ulrich Schollwöck
Day of submission: January 17, 2019
Day of the oral examination: February 28, 2019

Summary

(Summary in English)

For a long time strong electronic correlations in metals have mainly been associated with Mottness, the proximity to a Mott metal-insulator transition (MIT), where large Coulomb interactions induce the localization of charges. However, triggered by the discovery of the iron-based superconductors about ten years ago, it was realized that multi-orbital materials with only moderate Coulomb but sizeable Hund’s rule interactions – so-called Hund metals – allow for a distinct screening mechanism towards strong correlations: Hundness. Here, Hund’s rule constrains the spin rather than the charge dynamics. This discovery led to a vividly debated fundamental issue in the field of strongly correlated condensed matter systems, which is the main topic of the present thesis: what is the origin of strong correlations in the normal phase of Hund metals, Mottness or Hundness? And what are their decisive fingerprints?

The goal of this dissertation is twofold. First, we present and advance our method: the numerical renormalization group (NRG) as viable real-frequency multi-band impurity solver for dynamical mean-field theory (DMFT), a common approach to tackle strongly correlated systems. Second, we apply DMFT+NRG to shed light on the Hund-metal problem raised above.

In the first part of this thesis we present our state-of-the-art NRG solver, which offers direct access to data with unprecedented real-frequency spectral resolution at arbitrarily low energies and temperatures in contrast to commonly used Quantum Monte Carlo solvers. It is based on matrix product states and exploits non-abelian symmetries to reduce numerical costs. In the case of orbital symmetry, this allows us to treat multi-band models with more than two bands, and thus to tackle the Hund-metal problem for the first time with NRG. For multi-band models without orbital symmetry, an “interleaved” scheme of NRG (iNRG) was recently developed, dramatically increasing the numerical efficiency. Remarkably, the accuracy of iNRG is comparable to standard NRG, as we reveal in a detailed study. This finding establishes iNRG as a promising DMFT solver for material-specific model simulations.

In the second part of this thesis we study a minimal toy model for Hund metals with DMFT+NRG, the orbital-symmetric three-band Hubbard-Hund model (3HHM) close to a lattice filling of $1/3$. Our major insight is “spin-orbital separation” (SOS), a Hund’s-rule-induced two-stage Kondo-type screening process, in which orbital screening occurs at much higher energies than spin screening. In Hund metals, i.e. far from a MIT phase boundary, SOS thus causes large electron masses by strongly reducing the coherence scale below which a Fermi liquid is formed. Further, it opens up a broad incoherent and strongly particle-hole asymmetric intermediate energy regime that reaches up to bare excitation scales. This SOS regime shows fractional power-law behavior and is characterized by resilient “Hund quasiparticles” with itinerant orbital degrees of freedom coupled non-trivially to quasi-free large spins. At zero temperature, the local density of states exhibits a two-tier quasiparticle peak on top of a broad incoherent background. In contrast, in Mott-correlated metals, i.e. close to the MIT phase boundary, the SOS regime becomes negligibly small and the Hubbard bands are well separated. These findings lead to distinct signatures of Hundness and Mottness in the temperature dependence of ARPES spectra, static local susceptibilities, resistivity, thermopower and entropy, many of which were also found in realistic simulations of the archetypal Hund- and Mott-correlated materials, Sr_2RuO_4 and V_2O_3 . In summary, we provide evidence that and elucidate how Hundness evokes strong correlation effects in Hund metals. This might help to better interpret experimental results and guide superconducting theories.

Zusammenfassung

(Summary in German)

Starke elektronische Korrelation in Metallen wurden lange Zeit überwiegend mit Mottness assoziiert, der Nähe zu einem Mott-Metall-Isolator-Übergang (MIT), bei dem große Coulombwechselwirkungsstärken zu einer Ladungslokalisierung führen. Mit der Entdeckung der eisenbasierten Supraleiter vor etwa zehn Jahren aber wurde erkannt, dass Multibandmaterialien mit nur moderater Coulombwechselwirkungs- aber erheblicher Hundscher Kopplungsstärke – sogenannte Hundsche Metalle – einen neuartigen Abschirmungsmechanismus zur Erzeugung starker Korrelationen ermöglichen: Hundness. Hierbei beeinträchtigt die Hundsche Regel eher die Spin- als die Ladungsdynamik. Diese Entdeckung führte zu einer intensiv diskutierten grundlegenden Fragestellung auf dem Forschungsfeld stark korrelierter Festkörpersysteme, deren Beantwortung das Hauptanliegen der vorliegenden Arbeit ist: Welcher Mechanismus verursacht das stark korrelierte Verhalten in der normalleitenden Phase von Hundschen Metallen, Mottness oder Hundness? Und was sind deren ausschlaggebende Merkmale?

Diese Dissertation verfolgt zwei Zielsetzungen. Zum einen stellen wir unsere Methode vor und entwickeln sie weiter: die Numerische Renormalisierungsgruppe (NRG) als zukunftsfähiger Mehrbandstörstellensolver für die Dynamische Molekularfeldtheorie (DMFT), eine weitverbreitete Methode zur Simulation stark korrelierter Systeme. Zum anderen gewinnen wir durch die Anwendung von DMFT+NRG grundlegende Erkenntnisse über Hundsche Metalle und tragen damit zur Beantwortung oben formulierter Problemstellung bei.

Im ersten Teil dieser Arbeit stellen wir unseren hoch kompetitiven NRG Solver vor, welcher im Unterschied zu herkömmlichen Quantum Monte Carlo Solvern direkten Zugang zu hochaufgelösten Spektraldaten bei niedrigen Energien und Temperaturen bietet. Er arbeitet im Rahmen von Matrixproduktzuständen und nutzt dabei nichtabelsche Symmetrien aus, um numerische Kosten zu senken. Bei vorliegender Orbitalsymmetrie ermöglicht uns dies Multibandmodelle mit mehr als zwei Bändern zu behandeln und damit die obige Problemstellung zu Hundschen Metallen erstmals mit NRG zu lösen. Für Multibandmodelle ohne Orbitalsymmetrie wurde kürzlich ein „verzahntes“ („interleaved“) NRG (iNRG) Schema entwickelt, welches die numerische Effizienz deutlich erhöht. Bemerkenswerterweise können wir in einer detaillierten Studie zeigen, dass die Genauigkeit der iNRG vergleichbar ist mit der herkömmlichen NRG. Diese Erkenntnis positioniert iNRG als vielversprechenden DMFT Solver für materialspezifische Modellsimulationen.

Im zweiten Teil dieser Arbeit untersuchen wir mittels DMFT+NRG ein Minimalmodell für Hundsche Metalle, das orbitalsymmetrische Dreiband-Hubbard-Hund-Modell (3HHM) bei einer Füllung nahe $1/3$. Unser Hauptresultat ist die Dissoziation des Verhaltens von orbitalen und Spinfreiheitsgraden („spin-orbital separation“, SOS), ein zweistufiger Kondo-Abschirmungsmechanismus von Elektronen, welcher durch die Hundsche Regel induziert wird und die orbitalen Freiheitsgrade bei weitaus höheren Energien abschirmt als die Spinfreiheitsgrade. In Hundschen Metallen, also weit von einer MIT Phasengrenze entfernt, führt SOS durch die Verminderung der Kohärenzskala, unterhalb derer eine Fermiflüssigkeit auftritt, zu schweren Elektronenmassen. Des Weiteren wird dadurch ein großer, inkohärenter und stark Teilchen-Loch-asymmetrischer, intermediärer Energiebereich geöffnet, welcher bis zu atomaren Energieskalen reicht. Dieser SOS-Bereich weist fraktionale Potenzgesetze auf und wird von robusten „Hundschen Quasiteilchen“ bestimmt, welche aus leitenden orbitalen Freiheitsgraden bestehen, die nicht trivial an langsam fluktuierende große lokale Spins gekoppelt sind. Bei

Nulltemperatur besteht die lokale Zustandsdichte aus einer zweistufigen Quasiteilchenspitze auf einem breiten, inkohärenten Untergrund. Im Gegensatz dazu wird in Mott-korrelierten Metallen, also nahe der MIT Phasengrenze, der SOS-Bereich vernachlässigbar klein und die Hubbard-Bänder sind gut voneinander getrennt. Diese Eigenschaften führen zu unterschiedlichen Hund- und Mottmerkmalen in der Temperaturabhängigkeit von ARPES Spektren, statischer lokaler Suszeptibilitäten, des Widerstands, des thermoelektrischen Effekts und der Entropie, von denen einige auch in realistischen Simulationen der archetypischen Hund- und Mott-korrelierten Materialien, Sr_2RuO_4 und V_2O_3 , gefunden wurden. Zusammengefasst weisen wir nach, dass Hundness stark korreliertes Verhalten in Hundschen Metallen hervorruft und erläutern den zugrundeliegenden Mechanismus. Dies könnte zu einer besseren Interpretation experimenteller Befunde beitragen sowie Orientierungshilfe für Theorien zur Supraleitung bieten.

Publications

This dissertation is based on the following journal articles, listed in chronological order:

- P1** *Dynamical Mean-Field Theory Plus Numerical Renormalization-Group Study of Spin-Orbital Separation in a Three-Band Hund Metal*
K. M. Stadler, Z. P. Yin, J. von Delft, G. Kotliar, and A. Weichselbaum
 Sec. 4.2 / [arXiv:1503.06467](#) *Phys. Rev. Lett.* 115, 136401 (2015)
- P2** *Interleaved numerical renormalization group as an efficient multiband impurity solver*
K. M. Stadler, A. K. Mitchell, J. von Delft, and A. Weichselbaum
 Sec. 2.3.2 / [arXiv:1602.02182](#) *Phys. Rev. B* 93, 235101 (2016)
- P3** *Open Wilson chains for quantum impurity models: Keeping track of all bath modes*
 B. Bruognolo, N.-O. Linden, F. Schwarz, S.-S. B. Lee, **K. Stadler**, A. Weichselbaum,
 M. Vojta, F. B. Anders, and J. von Delft
 Sec. 2.4.2 / [arXiv:1611.05291](#) *Phys. Rev. B* 95, 121115(R) (2017)
- P4** *Signatures of Mottness and Hundness in archetypal correlated metals*
 X. Deng, **K. M. Stadler**, K. Haule, A. Weichselbaum, J. von Delft, and G. Kotliar
 Sec. 6.2 / [arXiv:1708.05752](#) submitted to Nat. Commun.
- P5** *Hundness versus Mottness in a three-band Hubbard-Hund model: On the origin of strong correlations in Hund metals*
K. M. Stadler, G. Kotliar, A. Weichselbaum, J. von Delft
 Sec. 5.2 / [arXiv:1808.09936](#) accepted by Ann. Phys. (NY)

*Dank dieser Menschen bin ich nicht “vor die Hunde gegangen”.
Vielen, vielen Dank für die Unterstützung!*

Acknowledgements

I am very grateful to my supervisor Jan von Delft for giving me the opportunity and his confidence to establish DMFT+NRG as a new topic area in his group. I am thankful for his continuous support and guidance, for his always very helpful professional and also personal advice, for his critical eye in polishing publications, and for making it possible to participate in numerous conferences, summer schools, and research trips. I really enjoyed various collaborations that Jan initiated.

In particular, this work is deeply shaped by the fruitful collaboration with Gabriel Kotliar. In many ways he was more a mentor than a collaborator. Thanks to him and Robert Konik I had a very inspiring time at BNL on Long Island and in New York working for the Comscope project. In that regard my thanks goes also to the BNL crew, especially to Laura Classen with whom I changed the first flat car tire of my life in the middle of nowhere near Woodstock.

This project would not have been possible without Andreas Weichselbaum. He created an amazing toolbox for NRG/DMRG/tensor network states over many years which I could use for my research. Further, he provided invaluable input, was always reachable for questions and discussions, and helped to polish our publications.

I would like to thank Zhiping Yin for providing DMFT+CTQMC benchmark results.

I also thank Markus Hanl who introduced me very patiently to NRG at the very beginning.

My gratitude goes as well to Ulrich Schollwöck for refereeing this thesis.

My PhD was not only characterized by the work I did but also very much by the people around me. Therefore, I would like to thank all my colleagues, in particular my former and present room mates (in chronological order) Flo and Jan (with Anna on the couch), Frauke and Bene, Elias, Bin-Bin and Florian, the Punk colleagues Sebastian and Dima, and the Schollwöck colleagues Alex and Nils. Many of them became good friends. Without our coffee breaks on the balcony, my PhD time would have only been half as funny and productive. I am very happy that Seung-Sup, Fabian, and Elias are continuing the DMFT+NRG project in our group. Further, I thank our secretary Stéphane Schoonover for kindly taking care of much of the administrative processes.

A very important factor for the success of my PhD thesis was also the life outside the office. I am deeply grateful to my family and to Sims, my Munich family. They continuously accompanied, supported and carried me, especially during the last few years. Sims, thank you for all the deep conversations and funny activities, and for having me as your flatmate since more than eleven crazy years. I would also like to thank 4Gewinnt, the erstwhile Holzapfel11 Gang, the LMU Crew, the Geisen Crew, my Berlin connection, Hannah and Andrea, and Philip Böhm and the biophysicists for spending various lunchbreaks in the Eisbach or with listening to stories from Greek and Roman mythology. Last but not least, I deeply thank Max for his support and the balance he gave to my life during the last year.

Contents

Summary (Summary in English)	i
Zusammenfassung (Summary in German)	iii
Publications	v
Acknowledgements	vii
1 Introduction	1
1.1 Motivation	1
1.1.1 Iron-based high-temperature superconductors	1
1.1.2 Mott systems	2
1.1.3 Hund metals	3
1.2 Scope	5
1.2.1 Hund models	5
1.2.2 Dynamical mean-field theory plus numerical renormalization group	8
1.2.3 Hund-metal regime in the phase diagram of a three-band Hubbard-Hund model	10
1.2.4 Puzzling properties of the Hund-metal regime	10
1.3 Aim	16
2 Method	19
2.1 Single-site dynamical-mean field theory (DMFT) in a nutshell	19
2.2 Standard numerical renormalization group (NRG) as impurity solver for DMFT	22
2.2.1 A brief history.	22
2.2.2 NRG in a nutshell	22
2.2.3 Discretization in NRG+DMFT: stable implementation of Zitko’s discretization scheme	24
2.2.4 State-of-the-art fdmNRG impurity solver for DMFT	26
2.3 Interleaved numerical renormalization group (iNRG)	29
2.3.1 Overview	29
2.3.2 Publication: <i>Interleaved numerical renormalization group as an efficient multiband impurity solver</i>	32
2.4 Open Wilson chains	49
2.4.1 Overview	49
2.4.2 Publication: <i>Open Wilson chains for quantum impurity models: Keeping track of all bath modes</i>	50
3 Overview of computed physical quantities	69
3.1 Local orbital and spin susceptibilities and Kondo scales	69
3.2 Real-frequency self-energy	70
3.3 Real-frequency spectral function and local occupation	72
3.4 Matsubara Green’s function and self-energy	72
3.5 ARPES structure factor and band dispersion relation	73

3.6	Optical conductivity, kinetic energy, resistivity and the Mott-Ioffe-Regel (MIR) limit	73
3.7	Thermopower	74
3.8	Entropy	75
3.8.1	Impurity contribution to the entropy	75
3.8.2	Lattice entropy	75
3.9	Physical quantities in Landau's Fermi-liquid (FL) theory	79
3.10	Benchmarks	81
3.10.1	Friedel sum rule for NRG	82
3.10.2	Luttinger theorem and Luttinger pinning for DMFT	82
3.10.3	Hartree-Fock limit of Matsubara self-energy for DMFT	83
4	Spin-orbital separation (SOS)	85
4.1	Overview	85
4.2	Publication: <i>Dynamical Mean-Field Theory Plus Numerical Renormalization-Group Study of Spin-Orbital Separation in a Three-Band Hund Metal</i>	89
4.A	Results for a two-band Hund metal	99
4.B	Unveiling the FL phase from NRG eigenenergy spectra	99
5	Hundness versus Motttness: on the origin of strong correlations in Hund metals	103
5.1	Overview	103
5.2	Publication: <i>Hundness versus Motttness in a three-band Hubbard-Hund model: On the origin of strong correlations in Hund metals</i>	106
5.A	Power-law behavior	152
5.B	The search for a negative compressibility	153
6	Signatures of Motttness and Hundness in archetypal correlated metals	155
6.1	Overview	155
6.2	Publication: <i>Signatures of Motttness and Hundness in archetypal correlated metals</i>	158
7	SOS revisited: frequency and temperature dependence	175
7.1	Asymmetry of frequency-dependent quantities at zero temperature	177
7.2	Temperature dependence: ARPES and the optical conductivity	179
7.3	Temperature dependence of various physical quantities	188
7.4	Summary of main insights	196
8	Conclusion and outlook	199
	Bibliography	211

*We have a mammoth and an elephant in our refrigerator
– do we care much if there is also a mouse?*
— P. W. Anderson [And07]

1 Introduction

1.1 Motivation

1.1.1 Iron-based high-temperature superconductors

The iron age of superconductivity. Mind-boggling discoveries in science are often made by serendipity. In search of a new transparent semiconductor for flat screens in 2006, the research group of Hideo Hosono at the Tokyo Institute of Technology found a new class of high-temperature superconductors (HTSCs) [KHH⁺06, KWHH08], the iron-based HTSCs. These metallic compounds consist of conducting layers of iron and pnictogen (like arsenic or phosphorus) or chalcogen (like selenium or tellurium), and have critical temperatures up to 56K below which electricity is conducted without resistance [RCD⁺08, RYL⁺08, WXC⁺09]. This discovery brought a breath of fresh air in the decade-long research on high-temperature superconductivity, which, so far, focused mainly on the superconducting copper-oxides (cuprates) discovered in 1986 [BM86].

Understanding the superconducting mechanism of HTSCs is still one of the greatest challenges in condensed matter physics, with huge technological potential. In the 1980s, the dream of a sustainable powered future with loss-free production, distribution, and storage of energy at room temperature released a wave of euphoria with both technological utopias and ideas for commercial use.

The discovery of the iron-based HTSCs has now heralded the transition from the copper to the iron age in the research on superconductivity. It revived partly the euphoria of the 1980s, but also showed how little is really known about the phenomenon of high-temperature superconductivity.

Meanwhile, a broad consensus has been reached that some kind of pairing mechanism, as originally introduced in the context of BCS theory for conventional superconductivity [BCS57], is also involved in high-temperature superconductivity. But the conventional superconducting mechanism based on electron-phonon coupling is argued not to be strong enough to generate the high critical temperatures. Therefore, the pairing mechanism is assumed to be a genuine electronic one, as outlined, for instance, for cuprates by P. W. Anderson in 2007 [And07]. However, the precise mechanism remains unresolved both for the cuprates and the iron-based HTSCs. Moreover, even the nature of the non-superconducting normal phase is still debated highly controversially, especially in the case of the iron-based HTSCs.

We remark that the following introduction is adapted in parts from Ref. [SKWvD18].

Bad-metal superconductors. In fact, the mystery of high-temperature superconductivity in iron-based HTSCs begins in their paramagnetic normal phase. There, iron-based HTSCs are “bad metals”, i.e. they conduct surprisingly badly and show highly anomalous transport properties compared to conventional conductors. For instance, conventional Fermi-liquid (FL) behavior is only found below an unusually low coherence scale [HK09, YHK12, YLY⁺13, HBA⁺13, HBdM⁺16]. Above the FL scale puzzling non-Fermi-liquid (NFL) behavior [HSK08, HK09, LI10, IL10, ABM⁺10, YHK12, WCM⁺12, SMP⁺12, YLY⁺13, HBA⁺13, FCR⁺15, YLZ⁺15, HBdM⁺16] occurs in a large intermediate energy window, typically at or slightly

below room temperature, together with poorly screened large fluctuating local moments on the Fe sites, as observed in X-ray emission spectroscopy measurements [GLK⁺11, PHI⁺17, LGH⁺17]. At higher temperatures, the resistivity reaches unusually large values that exceed the Mott-Ioffe-Regel limit [HK09, HBA⁺13] (cf. Sec. 3.6 for a definition). Especially the latter phenomenon has led to the categorization of HTSCs as “bad metals” in the literature [EK95, HTT04]. Importantly, all these effects are accompanied by large electronic mass enhancements, as revealed in various experiments [QHB⁺09, TKK⁺10, TKS⁺10, TGR⁺10, YMI⁺10, BZE⁺10, TKK⁺13, YLY⁺13, HBA⁺13, YIN⁺14, FCR⁺15, YLZ⁺15, HBdM⁺16].

There is thus firm evidence that strong electronic correlations play a key role in iron-based HTSCs – similar to the strongly correlated unconventional cuprate HTSCs, but in stark contrast to conventional BCS-like superconductors. On the one hand, this explains why both the superconducting and the bad-metal normal state are still poorly understood in the iron-based HTSCs: the “standard model” of a FL description in condensed matter theory breaks down in the presence of strong correlations. On the other hand, a thorough investigation of the nature of strong correlations in the normal state of iron-based HTSCs may give hints to unveil the superconducting mechanism. In particular, one widely but controversially debated fundamental question pertains to the origin of strong correlations: is it “Mottness” or “Hundness”?

1.1.2 Mott systems

Mottness. For a long time strong electronic correlations in materials have mainly been associated with “Mottness”: the proximity to a Mott metal-insulator transition (MIT), i.e. (in its most common description) a transition at a critical interaction strength U_c from an increasingly correlated metal to a paramagnetic Mott insulator, which is driven by a large Coulomb repulsion, U . Originally suggested by N. F. Mott in 1949 to characterize the insulating state of nickel oxide [Mot49], this effect has been studied in great detail in the famous one-band Hubbard model (1HM) [Mot68, RKK⁺95, Kot99, KMR02, icvHP⁺13, DMicv⁺13], introduced by J. Hubbard in 1963 [Hub63]. This lattice model is defined via the tight-binding Hamiltonian

$$\hat{H}_{\text{1HM}} = -\mu \sum_{i\sigma} \hat{n}_{i\sigma} + \sum_{\langle ij \rangle \sigma} t \hat{c}_{i\sigma}^\dagger \hat{c}_{j\sigma} + U \sum_i \hat{n}_{i\uparrow} \hat{n}_{i\downarrow}, \quad (1.1)$$

where $\hat{n}_i \equiv \sum_{\sigma} \hat{c}_{i\sigma}^\dagger \hat{c}_{i\sigma}$ is the particle number operator of site i . $\hat{c}_{i\sigma}^{(\dagger)}$ denotes the corresponding annihilation (creation) operators for the conduction electrons with spin $\sigma = \uparrow, \downarrow$. $\sum_{\langle ij \rangle}$ is a sum over nearest neighbors i and j only. μ is the chemical potential and t the hopping amplitude between neighboring sites. The Coulomb interaction, U , acts only locally between electrons in one orbital per lattice site.

At half-filling, the MIT occurs as consequence of the competition between the repulsive Coulomb interaction and the kinetic energy associated with the electron hopping. For small U/t the system is in a metallic FL state. The electrons can move rather freely between the lattice sites only accounting for the Pauli exclusion principle. However, for large U/t , the Coulomb repulsion fully blocks the charge conduction and the system is insulating: at half-filling, charge fluctuations, i.e. the hopping of electrons in the lattice, lead to doubly occupied lattice sites, which become too costly for $U > U_c$. In this respect, a Mott insulator differs fundamentally from a conventional band insulator, where the highest occupied band is fully filled and the Pauli exclusion principle blocks charge fluctuations.

The local density of states of a Mott insulator is characterized by a lower and an upper Hubbard band, which are separated by a pronounced energy gap at the Fermi level. These bands are associated with the dispersion of an additional hole or an additional electron with excitation energies $-U/2$ or $+U/2$, respectively. In the metallic phase for sufficiently small

U , the Hubbard bands overlap, and the charge excitation gap is replaced by a quasiparticle (QP) band.

In summary, a half-filled Mott system is weakly correlated for small U and insulating for large U . For $U > U_c$, the itineracy of a Mott insulator can be restored by doping. Importantly, in proximity to the MIT, i.e. for U smaller but close to U_c or in the case of slight doping for $U > U_c$, a Mott system is strongly correlated: the charge fluctuations are considerably reduced and the effective electron mass is strongly enhanced.

Strong correlations in cuprates. The MIT as a fundamental mechanism towards strong correlations gained considerable interest in the context of the cuprate HTSCs. Nowadays, these ceramic compounds are widely considered as doped charge-transfer Mott insulators with strong correlations arising from Mottness [OM00, LNW06]. Indeed, in theoretical descriptions, the original multi-band electronic structure of cuprates is usually reduced to a low-energy effective (two-dimensional) one-band Hubbard model for which a Coulomb-interaction-induced MIT occurs for undoped cuprates at half-filling.

1.1.3 Hund metals

Hundness. This suggests that iron-based HTSCs might be governed by the proximity to a MIT, as well. Indeed, striking qualitative analogies in the (doping versus temperature) phase diagrams of cuprate and iron-based HTSCs hint towards a common framework. For instance, in both cases superconductivity emerges in the vicinity of an incoherent metallic regime with NFL properties and unconventional spin dynamics.

However, in contrast to the insulating parent cuprate compounds, undoped (and doped) iron-based HTSCs are *metallic* materials with an effective *multi*-band description. While, in principle, a MIT also occurs at any integer filling of multi-orbital materials (examples are various 3d and 4d transition metal oxides [dMMG11] with the prototypical Mott material V_2O_3 [MRR69, MMR⁺73, MRM⁺73, HTS⁺13, DSH⁺18]), the intrinsic metallicity together with the lack of Mott insulators in the iron-based family challenges the idea of Mottness in the context of the iron-based HTSCs.

The special multi-orbital character of these HTSCs (and most other strongly correlated materials) allows for a distinct route towards strong correlations: Hundness. It is based on an additional intra-atomic interaction only arising in multi-orbital systems: Hund's rule coupling, J , which favors the alignment of spins in different orbitals on the same (iron) atom. More precisely, J reduces the repulsive Coulomb interaction of two electrons with parallel spins placed in different orbitals as compared to two electrons with opposite spins in the same orbital.

Hund's rules. Originally, the effect of Hund's rule coupling was formulated by F. Hund in 1925 as a set of heuristic rules, the Hund's rules, to specify the electronic ground-state configuration of an atom [Hun25]. It is based on an atomic description, where the electrons can occupy different atomic shells, each consisting of a number of different orbitals. The ground state is characterized by its total spin, \mathbf{S} , its total orbital angular momentum, \mathbf{L} , and its total angular momentum, $\mathbf{J} = \mathbf{L} + \mathbf{S}$. First, the lower shells of an atom are filled with electrons, leading, due to the Pauli exclusion principle, to both a total spin and a total orbital angular momentum of zero. Thus, full shells and subshells do not contribute to the effective quantum numbers of the ground state. The occupation of the remaining shell is determined by the following Hund's rules, which minimize the ground state energy:

1. The total spin quantum number (multiplicity $2S + 1$) is maximized first, favoring the alignment of spins in different orbitals. This first rule is the most important one and therefore often referred to as simply the Hund's rule.
2. Hund's second rule states that, for given multiplicity, the total orbital angular momentum quantum number, L , is maximized.
3. Finally, Hund's third rule takes into account spin-orbit coupling, which only slightly affects the energies of the orbitals within a shell. The lowest total angular momentum quantum number, $\mathcal{J} = |L - S|$, is adopted for a subshell, which is less than half-filled or half-filled, while otherwise the largest total angular momentum quantum number, $\mathcal{J} = L + S$, is selected.

For atoms embedded in a solid-state environment, Hund's rules still hold and contribute to the regulation, i.e. correlation, of electron hopping in the system. Therefore, Hundness can be understood as the solid-state manifestation of sizeable Hund's rule coupling just as Mottness is the solid-state manifestation of large Coulomb repulsion. However, for a long time, the importance of Hund's coupling for strong correlations was overlooked, since its strength is much smaller than the Coulomb interaction or the bandwidth of multi-orbital systems (from a materials point of view one typically encounters $J/U \lesssim 0.2$ [GMM13]).

Hundness in iron-based HTSCs. The role of Hund's coupling, J , was first pointed out by K. Haule and G. Kotliar in 2009 in a pioneering material simulation of the only recently discovered iron oxypnictides ($\text{LaO}_{1-x}\text{F}_x\text{FeAs}$) [HK09]. They predicted a coherence-incoherence crossover with increasing temperature in these effective five-band materials [HSK08] with a coherence scale that is strongly suppressed by Hund's coupling. The bands are mainly of d character with a bandwidth in the order of 3eV. Only two orbitals (xz and yz) are degenerate, but the crystal-field splitting between other orbitals is one order of magnitude smaller than the bandwidth and thus quite weak. The Coulomb interaction of about 4eV is comparable to the bandwidth while the Hund's coupling is much smaller, $J \approx 0.35\text{-}0.4\text{eV}$. The parent compound LaOFeAs has an average occupancy of six d electrons for each iron atom. The normal state at high temperatures was shown to be highly anomalous with an enhanced magnetic susceptibility and a linear temperature dependence of the resistivity. A crossover to a Pauli-like susceptibility and a sharp drop in the resistivity at rather low temperatures were seen as hints for a FL ground state. Further, large mass enhancements were deduced from specific heat measurements, placing the iron pnictides in the broad category of strongly correlated bad-metal superconductors, though, one would naively have expected a perfect metal due to the large orbital degeneracy of the iron pnictides. Strong correlations induced by Hundness were argued to not only promote the highly incoherent normal state of iron-based HTSCs but to also enable their large critical temperatures by effectively reducing the kinetic energy of these systems [HSK08, YHK11a].

A few years later, resistivity, heat-capacity, thermal-expansion, and susceptibility measurements of the 122-iron pnictides [HBA⁺13, HBdM⁺16] confirmed the predictions of Ref. [HK09]. The coherence-incoherence crossover was observed in the electrical resistivity. The Sommerfeld coefficient and the Pauli susceptibility were found to be strongly enhanced with respect to their bare values, revealing a significant mass enhancement. In 2017, an (orbital-selective) coherent-incoherent crossover was also observed in optical conductivity measurements of KFe_2As_2 [YYW⁺17], with clear FL scaling of the scattering rate below 75K, and associated with Hund's-rule-driven Kondo-type screening rather than (orbital-selective) Mottness, due to the lack of a Mott gap.

This corroborates the idea of strong correlations playing a key role in iron-based HTSCs, and also suggests that Hundness rather than Mottness governs the physics of these systems.

Hund metals. The insights of Refs. [HSK08, HK09] and subsequent studies on iron pnictides and iron chalcogenides [YHK11a, YHK11b, YHK12, GMM13] led to the categorization of a new class of materials, which was dubbed “Hund metals” [YHK11a]. It includes multi-orbital materials like iron pnictides and chalcogenides [HK09, YHK11a, YHK12, WCM⁺12, SMP⁺12, GMM13, LSG⁺13, BVC16, dMC17], as well as various transition metal oxides of the 3d and 4d series, such as ruthenates [WGTM08, MAM⁺11, dMMG11, YHK12, GMM13, SMB⁺14, MG16]. Hund metals are strongly correlated but, at the same time, itinerant systems. They are characterized by rather broad bands leading to sizeable Hund’s coupling strengths compared to only moderate Coulomb interactions, which are strongly screened in these materials due to the large spatial extension of the correlated orbitals [KBK⁺08, MAM⁺11]. In principle, strong correlation effects in Hund metals may thus be caused by either Hundness, or Mottness, or a combination of both.

Although the importance of Hund’s coupling in realistic materials is increasingly being appreciated, there is still an ongoing debate whether Hundness or Mottness is the key player in renormalizing the electron mass of Hund metals. This is caused by the fact that the nature of the incoherent transport regime in Hund metals is hardly understood, and the MIT in multi-orbital systems has not been investigated much. Clear signatures to distinguish a Hund metal from a metal of Mott type are thus sparse. Therefore, the following questions have been raised [YHK12, FB15]:

What is the origin of strong correlations in the normal phase of Hund metals, Mottness or Hundness? And what are the decisive fingerprints of a Hund metal as opposed to a Mott-correlated metal?

In the present thesis, we address these questions from a fundamental model-based point of view: we investigate the zero- and finite-temperature normal-state properties of a toy model, the degenerate three-band Hubbard-Hund model Hamiltonian (3HHM) [YHK12, AK15, SYvD⁺15], based on the single-site dynamical mean-field theory (DMFT) and a powerful multi-band numerical renormalization group (NRG) impurity solver [WvD07, Wei12a, Wei12b, SYvD⁺15, DSH⁺18, SKWvD18] to tackle the correlated many-body problem.

1.2 Scope

In this section, we summarize the state of research on multi-band Hund models and elaborate on the scope of this thesis.

We first present Hund models, in particular the 3HHM. We then give a short overview of our method (DMFT+NRG). After this we turn to the phase diagram of the 3HHM and identify an intriguing region, the Hund-metal regime, which shows strongly correlated physics though being far from an MIT. We present insights of previous research on that regime and identify open and controversially debated questions, which will be the subject of our investigations.

1.2.1 Hund models

Hubbard-Kanamori model. A very basic approach to address the issue of “Hundness versus Mottness” in Hund metals is to study the paramagnetic phase diagram of Hubbard-Kanamori-like model Hamiltonians (for a review, cf. Ref. [GMM13]). These take into account

two spin and *multiple* (N_c) orbital degrees of freedom, a Coulomb interaction, U , and, most importantly, a finite ferromagnetic Hund's coupling, J . Hund-metal physics is then captured by these models for a filling, n_d , close to one charge away from half-filling: $n_d \approx N_c \pm 1$. This is motivated by the particle-hole asymmetry of real Hund materials. For instance, the average occupancy of the five Fe $3d$ orbitals is $d6$ for the undoped stoichiometric parent compounds of almost all iron-based HTSC families [dMC17]. Small to moderate crystal-field splittings, as well as hole or electron doping lead to variations in the occupancy, such that the electron densities can range between 5.5 and 6.3 electrons per iron atom [YHK11a, dMC17]. Assuming a fully filled e_g duplet, this leaves $n_d \sim 2$ electrons for three active t_{2g} orbitals. Similarly, ruthenates have an average filling of approximately four electrons in t_{2g} orbitals.

Three-band Hubbard-Hund model (3HHM). In this thesis, we study the minimal model [YHK12, AK15] with relevance for Hund metals, the 3HHM with three degenerate orbitals:

$$\hat{H}_{\text{HHM}} = \sum_i \left(-\mu \hat{n}_i + \hat{H}_{\text{int}}[\hat{d}_{i\nu}^\dagger] \right) + \sum_{\langle ij \rangle \nu} t \hat{d}_{i\nu}^\dagger \hat{d}_{j\nu}, \quad (1.2a)$$

$$\begin{aligned} \hat{H}_{\text{int}}[\hat{d}_{i\nu}^\dagger] &= U \sum_m \hat{n}_{im\uparrow}^\dagger \hat{n}_{im\downarrow} + (U - J) \sum_{m \neq m'} \hat{n}_{im\uparrow}^\dagger \hat{n}_{im'\downarrow} \\ &+ (U - 2J) \sum_{m < m', \sigma} \hat{n}_{im\sigma}^\dagger \hat{n}_{im'\sigma} - J \sum_{m \neq m'} \hat{d}_{im\uparrow}^\dagger \hat{d}_{im\downarrow} \hat{d}_{im'\downarrow}^\dagger \hat{d}_{im'\uparrow} \end{aligned} \quad (1.2b)$$

$$= \frac{1}{2} \left(U - \frac{3}{2} J \right) \hat{n}_i (\hat{n}_i - 1) - J \hat{\mathbf{S}}_i^2 + \frac{3}{4} J \hat{n}_i. \quad (1.2c)$$

The 3HHM is a minimal version of the generalized Hubbard-Kanamori Hamiltonian of Ref. [GMM13] with $U(1)_{\text{ch}} \times \text{SU}(2)_{\text{sp}} \times \text{SU}(3)_{\text{orb}}$ symmetry for its charge (ch), spin (sp) and orbital (orb) degrees of freedom. $\hat{d}_{i\nu}^\dagger$ creates an electron on site i of flavor (fl) $\nu = (m\sigma)$, which is composed of a spin ($\sigma = \uparrow, \downarrow$) and an orbital ($m = 1, 2, 3$) index. $\hat{n}_{i\nu} \equiv \hat{d}_{i\nu}^\dagger \hat{d}_{i\nu}$ counts the electrons of flavor ν on site i . $\hat{n}_i \equiv \sum_\nu \hat{n}_{i\nu}$ is the total number operator for site i with $n_d \equiv \langle \hat{n}_i \rangle$, and $\hat{\mathbf{S}}_i$ its total spin, with components $\hat{S}_i^\alpha = \sum_{m\sigma\sigma'} \hat{d}_{im\sigma}^\dagger \frac{1}{2} \sigma_{\sigma\sigma'}^\alpha \hat{d}_{im\sigma'}$, where σ^α are Pauli matrices. We study the artificial but simple Bethe lattice (cf. Sec. 2.1 for details) with degenerate bands, each of bandwidth $W = 4t$, i.e we assume negligible crystal-field splitting and a uniform hopping amplitude t restricted to nearest-neighbor hopping between the same kind of orbital and spin degrees of freedom. Both the chemical potential μ and the hopping amplitude t are then equal for all flavors, leading to a locally $\text{SU}(6)_{\text{fl}}$ symmetric kinetic term in Eq. (1.2a). $t = 1$ serves as energy unit.

The onsite interaction term, \hat{H}_{int} , incorporates Hund and Mott physics in its most basic form and reduces the symmetry to $\text{SU}(2)_{\text{sp}} \times \text{SU}(3)_{\text{orb}}$ for $J > 0$. It was first introduced by Dworin and Narath in a generalization of the Anderson impurity model to study magnetic impurities [DN70]. The first three terms of Eq. (1.2b) are density-density interactions. U is the intra-orbital Coulomb interaction between electrons with opposite spins in the same orbital, $U - J < U$ the inter-orbital Coulomb interaction between electrons with opposite spins in different orbitals, and $U - 2J$ the Coulomb interaction between electrons with parallel spins in different orbitals, where the inter-orbital Coulomb interaction is further reduced by the ferromagnetic exchange coupling J due to Hund's first rule favoring the alignment of spins. The last term of Eq. (1.2b) is a spin exchange term.

The generalized Hubbard-Kanamori Hamiltonian of Ref. [GMM13] involves some additional terms (also taking into account Hund's second rule) not present in Eq. (1.2), which reduce the $\text{SU}(3)_{\text{orb}}$ symmetry in the orbital sector to $\text{SO}(3)_{\text{orb}}$. However, these additional

terms do not affect the low-energy physics, since they are irrelevant in a renormalization group sense [HicvM16].

Eq. (1.2c) is a more compact notation of Eq. (1.2b) and summarizes the two main aspects of our model. The first term is known to trigger Mott physics, whereby U penalizes double occupancy of orbitals. The second term directly reflects Hund's first rule: it favors a large spin per site for $J > 0$. Note that the third term only shifts the chemical potential, μ .

The physical behavior of the system depends in a crucial manner on the multiplet structure of the local Hamiltonian, and can change in dramatic ways when parameters are tuned such that level crossings occur [APV⁺09, GMM13].

We choose μ such that we obtain a total filling per lattice site, $n_d = \langle \hat{n}_i \rangle$, of $1 \leq n_d \leq 3$ with particular emphasis on $n_d = 2$. (By the particle-hole symmetry of the model with respect to half-filling, this also describes the fillings $3 \leq n_d \leq 5$.) In multi-orbital systems Hund's first rule is only effective for a site occupation that is larger than one electron (and smaller than one hole), because only then a finite J changes the local multiplet structure (e.g. it reduces the atomic ground state degeneracy) and has a qualitative influence on the physics of the system (cf. Sec. 2.6.1 and Sec. 2.6.2 of Ref. [SKWvD18] reprinted in Sec. 5.2).

We remark that Eq. (1.2) can be equivalently used to describe a degenerate two-band model with orbital index, $m = 1, 2$. Then the system has $U(1)_{\text{ch}} \times SU(2)_{\text{sp}} \times SU(2)_{\text{orb}}$ symmetry. We will refer to this two-band Hubbard-Hund model as 2HHM. However, our main focus lies on the degenerate 3HHM (also referred to as SCAHM in Ref. [SYvD⁺15] in Sec. 4.2).

Note that we fully neglect any material-specific details like crystal-field splitting or realistic band structures, although undoubtedly present in real materials. On the one hand, this is important as we can thus explicitly exploit the $U(1)_{\text{ch}} \times SU(2)_{\text{sp}} \times SU(3)_{\text{orb}}$ symmetry of the 3HHM within NRG (cf. Sec. 2.2.4 for details), reducing numerical costs. On the other hand, the aim of this thesis is to focus attention on the most generic aspects of Hundness and Mottness in the maximally simple context of full orbital degeneracy, in order to reveal which many-body effects can be understood on this simple model level and which ones require full information of the electronic structure. With this strategy we intend to contribute to a general phenomenology of Hund metals. In this regard, we point out that, indeed, many of our results for the 3HHM are found in realistic simulations of Hund metals, which are based on ab-initio electronic structure methods, like the Kohn Sham density functional theory (DFT) [KS65, Koh99, vB04] or the GW method [HL85, KHSK12, KOK17] (for a review on low-energy microscopic models for iron-based superconductors, cf. Ref. [FC17]). An example for Sr_2RuO_4 and V_2O_3 is given in Ref. [DSH⁺18] in Sec. 6.2.

Three-band Anderson-Hund model (3AHM). Within DMFT (cf. Sec. 1.2.2 and Sec. 2.1) the 3HHM of Eq. (1.2) is iteratively mapped onto a three-band Anderson-Hund model (3AHM) of the form

$$\hat{H}_{\text{AHM}} = \hat{H}_{\text{imp}} + \hat{H}_{\text{bath+hyb}}, \quad (1.3a)$$

$$\hat{H}_{\text{imp}} = \varepsilon_d \hat{N} + \hat{H}_{\text{int}}[\hat{d}_\nu^\dagger] \quad (1.3b)$$

with the same local interaction term, \hat{H}_{int} , as in Eq. (1.2b), and with total number and spin operators, \hat{N} and \hat{S} , defined analogously to \hat{N}_i and \hat{S}_i . [Similarly, the 2HHM is mapped onto a two-band version of Eq. (1.3), the 2AHM.] Within this mapping process, the hybridization function, $\Gamma(\varepsilon) = \pi \sum_k |V_k|^2 \delta(\varepsilon - \varepsilon_k)$, which fully characterizes the interplay of the impurity

and the noninteracting three-band spinful bath,

$$H_{\text{bath+hyb}} = \sum_{k\nu} \left(\varepsilon_k c_{k\nu}^\dagger \hat{c}_{k\nu} + V_k [\hat{d}_\nu^\dagger \hat{c}_{k\nu} + \hat{c}_{k\nu}^\dagger \hat{d}_\nu] \right), \quad (1.4)$$

is determined self-consistently. Here \hat{d}_ν^\dagger creates a local (“impurity”) electron of flavor ν with energy $\varepsilon_d = -\mu$. The average local site occupation number of the impurity model, $n_d \equiv \langle \hat{n}_i \rangle$, is a measure of the lattice filling per site.

In this thesis, we study both the 3HHM and also, for comparison, the pure impurity 3AHM (dubbed IAHM in Ref. [SYvD⁺15] in Sec. 4.2), without DMFT self-consistency, using a flat hybridization function, $\Gamma(\varepsilon) = \Gamma\Theta(D_{\text{NRG}} - |\varepsilon|)$, with half-bandwidth $D_{\text{NRG}} = 1$.

Three-orbital Kondo model. Further, we compare our results for the 3HHM and 3AHM with the insights gained from a three-orbital Kondo model [YHK12, AK15, WSL⁺19], which was derived from the 3AHM by a Schrieffer-Wolff transformation in Refs. [YHK12, AK15]. In particular, the analytic RG analysis in Ref. [AK15] and the conformal field theory and NRG study in Ref. [WSL⁺19] help to unveil the route of screening from the atomic degrees of freedom towards the emerging QPs in Hund metals – under the assumption that a picture in terms of an effective broad-bandwidth metallic bath applies to these systems.

1.2.2 Dynamical mean-field theory plus numerical renormalization group

In this thesis, we treat the 3HHM of Eq. (1.2) with single-site DMFT and use full-density-matrix (fdm)NRG [WvD07] as real-frequency impurity solver.

Single-site DMFT. In general, the description of strong correlation effects (like the MIT) is highly challenging for most analytical and numerical methods, since competing mechanisms dominate the physics in a wide range of energy scales and lead to an intrinsic non-perturbative nature of the many-body problem. DMFT [GKKR96] is currently the most powerful theoretical non-perturbative many-body approach to strongly correlated systems.

The basic idea of single-site DMFT is to map a lattice model self-consistently onto an effective single-site quantum impurity model, whereby the full non-local self-energy of the correlated lattice model is approximated by the purely local but still frequency-dependent self-energy of the corresponding effective quantum impurity model. Spatial fluctuations are frozen out by this process, but local quantum fluctuations are retained. Thus, both the itinerant and localized nature of electrons and, therefore, both weak and strong correlations can be handled on equal footing.

This is considered to be of utmost importance for the description of iron-based HTSCs and other Hund metals, as neither a purely local picture nor pure band theory applies. In these bad-metallic multi-orbital systems, the existence and interplay of itinerant but strongly renormalized electrons and strongly but not fully localized large spins have to be analyzed without any method-induced bias [YHK11a, Man14, BVC16, PHI⁺17].

We remark that the approximation of a purely local self-energy in single-site DMFT is strictly valid only in the artificial limit of infinite lattice coordination number. Therefore cluster extensions of DMFT [MJPH05], such as the dynamical cluster approximation (DCA), should be applied to account for short-range spatial correlations of three-dimensional systems. However, if interactions act only locally in a lattice system with finite coordination number, as in the case of Hund’s rule coupling (which is adopted from local atomic physics), single-site DMFT is assumed to be an appropriate method to reproduce the correct physics. This assumption is supported by recent cluster-DMFT calculations for iron pnictides and chalcogenides [SHK17] and recent photoemission spectroscopy results for Sr₂RuO₄ [TZR⁺18],

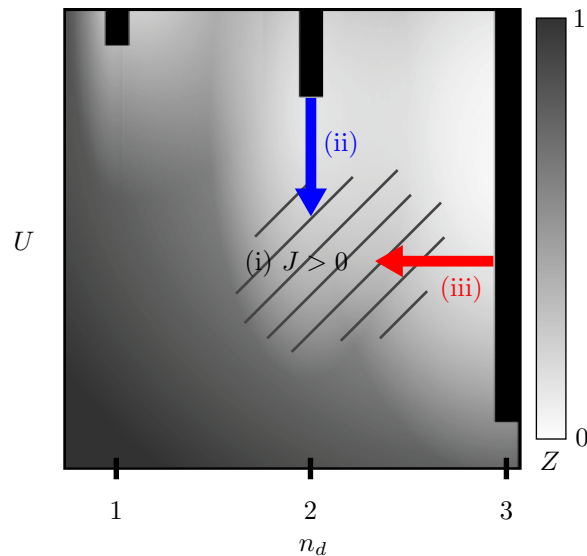


Figure 1.1 Schematic sketch of the n_d - U phase diagram for the 3HHM at finite J . We only show half of the phase diagram, as it is symmetric with respect to half-filling. The shading reflects the quasiparticle weight Z . Darker regions (large Z) indicate good metallic, lighter regions (small Z) bad-metallic behavior. The black bars mark Mott insulating phases. At all integer fillings, a MIT occurs above a (different) critical interaction strength, U_c . Interestingly, an extended light region exists also at moderate $U \ll U_c^{(2)}$ around $n_d = 2$ (and reaches to $n_d = 3$). In this “Hund-metal regime” (hatched area), where most Hund metals can be placed [dMMG11], strong electronic correlations might either be induced by Hundness, (i) the presence of sizeable J , or Mottness, (ii) the influence of the MIT at $n_d = 2$ (blue arrow), and (iii) the influence of the MIT at $n_d = 3$ (red arrow), or a combination of these scenarios. This figure is taken from Ref. [SKWvD18].

justifying the single-site DMFT approach used in this thesis. We remark, however, that others [NSA15] argue that Hund’s coupling significantly affects the non-local correlations, too.

The self-consistently determined quantum impurity model is solved by a so-called quantum impurity solver – the engine of the DMFT approach. For quantum impurity models several powerful non-perturbative methods have been known (some for many years), such as Quantum Monte Carlo (QMC) approaches, exact diagonalization, the Density Matrix Renormalization Group, or NRG, just to name a few, but also iterative perturbation theory, diagrammatic and interpolation schemes are used.

fdmNRG as DMFT impurity solver. In this thesis we employ fdmNRG [WvD07, Wei12a] and establish it as an efficient *real*-frequency *multi*-band impurity solver within single-site DMFT. NRG [Wil75, BCP08, Wei12a] is the gold standard for impurity models since many decades and has been successfully applied as DMFT impurity solver before – however only for lattice models with at most two bands [BHP98, Bul99, BCv01, PB05, DMicv⁺13, OPicv15], since the numerical costs of NRG increase exponentially with the number of flavors, drastically limiting its use compared to common solvers such as QMC. Recent significant technical progress has now made three-band calculations feasible due to various algorithmic NRG advances by us and others (cf. Sec. 2.2.4). This thesis is the first to harness the combined power of these technical advances in the context of three-band DMFT+NRG (cf. Chapter 2 for a more detailed presentation of DMFT+NRG).

1.2.3 Hund-metal regime in the phase diagram of a three-band Hubbard-Hund model

Hund-metal regime. Our work is motivated by the results of various single-site DMFT [WGTM08, dMMG11, dM11, GMM13] and slave-boson [FB15, dM17, dMC17] studies of degenerate three-band Hubbard-Kanamori-type models that investigated basic Hund metal physics. In the n_d - U phase diagram at finite J , they found strongly correlated (i.e. bad-metallic) behavior in an extended region around a filling of $n_d = 2$, which we dub ‘‘Hund-metal regime’’ (hatched area in Fig. 1.1 at moderate $U \ll U_c^{(2)}$). Naturally, bad-metallic behavior (light regions in Fig. 1.1) occurs close to the MIT at $n_d = 2$, i.e. for U close to $U_c^{(2)}$, but, interestingly, it also ranges down to rather small Coulomb interaction strengths $U \ll U_c^{(2)}$, provided that Hund’s coupling J is sizable (in a sense defined at the end of Sec. 2.6.1 of Ref. [SKWvD18], which is reprinted in Sec. 5.2). Most Hund metals can be placed there, around one charge away from half-filling and at moderate U . Further, the bad-metallic regime (light area) also reaches out to the insulating state at half-filling, $n_d = 3$, where the MIT develops already at a very low critical interaction strength, $U_c^{(3)}$, due to Hund’s coupling [dMMG11, GMM13].

Quasiparticle weight as a measure of strong correlations. Bad-metal behavior manifests itself by a small quasiparticle (QP) weight Z . Based on a coherent FL QP picture (cf. Sec. 3.9 for details), Z quantifies the weight of the coherent quasiparticle peak (QPP) of the local spectral function (correlated density of states). Within DMFT and slave-boson methods, the inverse QP weight is equivalent to the electronic mass enhancement, $Z^{-1} = m^*/m$ with the enhanced (bare) electronic mass m^* (m), and thus serves as measure for strong electronic correlations. For Hund models with $N_c > 3$ bands, equivalent regions of low Z (hatched area) were revealed around all integer fillings $1 < n_d < N_c$ [GMM13, FB15, dM17], but they are most prominent at $n_d = N_c \pm 1$ (see supplement of Ref. [FB15]).

Crystal-field effects. We note that in the presence of crystal-field splitting, Z and the filling can acquire an orbital dependence: various simulations [dMHCD09, LI10, IL10, YHK11a, YHK12, YS12, MNI12, BVC12, HDD12, LSG⁺13, YS13, dMGC14, FB15, HW16, YS17, KLK⁺19] and measurements [YLY⁺13, HBA⁺13, TKK⁺13, YIN⁺14, YLZ⁺15, HBdM⁺16, YYW⁺17] suggest the occurrence of orbital differentiation and even orbital-selective Mott phases (OSMP), depending on the type and strength of the splitting [HDD12, KLK⁺19]. In the phase diagram, both effects seem to intensify with increasing J , increasing U , and decreasing distance to half-filling. A thorough understanding of the physics of degenerate multi-orbital models, which we provide in this thesis, is a prerequisite for exploring these effects of orbital selectivity. However, pronounced orbital differentiation is considered to be relevant only for some Hund metals, e.g. for ruthenates. In contrast, for iron pnictides, it might be less important. In the class of the iron-based HTSCs, only iron chalcogenides are widely expected to be at the verge of an orbital-selective MIT [YHK11a, YS13]. Interestingly, many materials with large orbital differentiation are either no superconductors or exhibit only low transition temperatures: indeed, large orbital differentiation is argued to be harmful for superconductivity [YHK11a].

1.2.4 Puzzling properties of the Hund-metal regime

In the Hund-metal regime of a three-band Hund model one encounters various of the puzzling anomalous effects that have been found in real Hund metals, such as very low FL coherence scales, an intriguing incoherent transport regime, and large mass enhancements, just to name

a few. In the following paragraphs we give an overview of the state of research regarding the physics of the Hund-metal regime and point out a number of unresolved or ambiguous issues, which will be the subject of this thesis.

The origin of strong correlations in the Hund-metal regime. As motivated in Sec. 1.1 in the context of real Hund metals, a controversially debated primary issue pertains the origin of strong correlations. In principle, three scenarios seem possible to induce strong correlation effects and to lead to the bad-metallic behavior (low Z) in the Hund-metal regime (hatched area in Fig. 1.1) of a 3HHM, which lies sufficiently far away from any Mott insulating state (black bars in Fig. 1.1):

- (i) Hundness: sizeable J is the key player to induce strong correlations with considerable electronic mass enhancements.
- (ii) Mottness at $n_d = 2$: the interaction-induced MIT at one charge away from half-filling, $n_d = 2$, triggers the strong correlations (blue arrow in Fig. 1.1).
- (iii) Mottness at $n_d = 3$: the strong correlations are emanated by the half-filled Mott insulator (red arrow in Fig. 1.1).

Scenario (i) suggests a new Kondo-type screening mechanism towards strong correlations: Hundness. Sizeable Hund’s rule coupling, J , leads to the formation of high-spin states at intermediate energies and to the suppression of Z at low energies. It goes back to Ref. [HK09] and is supported in various publications [YHK11a, YHK11b, MAM⁺11, dMMG11, YHK12, SMP⁺12, GMM13, MG16].

Scenario (ii) is not much discussed in the literature, as $U_c^{(N_c-1)}$ is large while U has moderate values for Hund metals. However, a thorough investigation is needed to define clear signatures that distinguish the physics of the 3HHM in the Hund-metal regime far from and the Mott regime close to the MIT.

Scenario (iii) is motivated by the cuprate picture of doped half-filled Mott insulators and advocated by several authors [IL10, FB15, dM17, dMC17]. In this scenario the existence of finite J would have a subordinate role in correlating the electrons by lowering $U_c^{(3)}$.

Although all the model calculations listed above confirmed that strong correlation effects dominate the Hund-metal regime of the phase diagram, their origin and nature have been under debate even for this toy model until today, either based on different physical interpretations or just on inconsistent terminology. In particular, scenarios (i)-(iii) have been discussed in the context of

- (D1) the existence of a spin-freezing phase [WGTM08],
- (D2) the “Janus-faced” influence of Hund’s rule coupling on the MIT at $n_d = 2$ [dMMG11, dM11, GMM13], and
- (D3) proximity effects of the half-filled MIT [FB15, dM17, dMC17], such as Hund’s-coupling-induced FL instabilities [dM17].

In this thesis, we will elucidate the role of another very fundamental effect and its connection to the phenomena of (D1), (D2), and (D3):

- (D4) “spin-orbital separation” (SOS) [YHK12, AK15, SYvD⁺15, SKWvD18, DSH⁺18].

(D1) Spin-freezing phase. The so-called spin-freezing phase characterizes the Hund-metal regime in terms of a spin-spin correlation function with an unusually slow (imaginary-time) decay, which does not approach zero but a constant at finite temperature. In this picture, scattering off Hund’s-coupling-induced large composite and very long-lived (or even frozen) static magnetic moments leads to the incoherent transport behavior – a picture which is consistent with the persistence of spin excitations in non-magnetically ordered phases of Hund metals.

The spin-freezing scenario was introduced in 2008 in a first (finite-temperature) DMFT study [WGTM08] of the n_d - U phase diagram of a degenerate three-band Hubbard-Kanamori model using a QMC impurity solver. Later it was extended to (realistic) five-band calculations for iron pnictides [LI10, IL10, WCM⁺12, PHI⁺17] (demonstrating the importance of Hund’s rule coupling and electronic correlations for the formation of local moments in the paramagnetic phase [PHI⁺17]) and to models with crystal-field splitting [HW16] and spin-orbit coupling [KJWV17]. In 2015 it led to the proposal of a fluctuating-moment-induced spin-triplet superconducting mechanism for strontium ruthenates and uranium compounds [HW15].

The transition into the Hund-metal regime was first interpreted as a quantum phase transition from a paramagnetic metallic FL phase (at small n_d and/or small U) to an incoherent metallic NFL phase with frozen local moments (at larger n_d and/or larger U) [WGTM08]. Since 2011 the existence of a FL ground state (with fully screened local moments) has been anticipated in the Hund-metal regime and has led to the picture of a spin-freezing crossover at finite temperatures – although the complete decay of the imaginary-time spin-spin correlation function to zero has not been explicitly demonstrated with DMFT+QMC until very recently [KHW⁺18], because, in general, QMC solvers do not have access to low enough temperatures [dMMG11, WCM⁺12]. However, a new QMC technique using (super) state-sampling [KHW⁺18] was able to show the FL ground state in the spin-freezing phase for fillings up to $n_d = 2.63$.

Spin freezing has been assumed to originate, in principle, from (i) Hundness. However, similar to Z , the spin-freezing phenomenon is considered to be strongly doping dependent and is very pronounced in the vicinity of the half-filled Mott insulator [WGTM08, HW15]. Interestingly, the crossover towards spin freezing near $n_d = N_c - 1$ is characterized by a steep drop of Z as a function of n_d . A detailed quantitative analysis if and how the spin-freezing phenomenon is connected to Z , induced by (i) Hundness and/or influenced by Mottness of kind (ii) or (iii) has not yet been performed. One reason for this is that the mass enhancement could only be computed in an approximate manner because the QMC solver did not reach the FL regime [HW15]. Further, data was only available on the imaginary Matsubara frequency axis.

(D2) Janus-faced influence of Hund’s rule coupling on the MIT. The “Janus-faced” influence of Hund’s rule coupling was a major result of a first more detailed DMFT+QMC study of the phase diagram of the degenerate three-band Hubbard-Kanamori model [dMMG11, dM11, GMM13] (including a realistic classification of various 3d and 4d transition metal oxides via their mass enhancements). A detailed exploration in terms of the QP weight, Z , revealed that Hund’s coupling induces apparent conflicting tendencies at $n_d = 2$. On the one hand, increasing J promotes metallicity by shifting the critical interaction strength, $U_c^{(2)}$, of the MIT at $n_d = 2$ to higher values. On the other hand, at moderate U , increasing J reduces Z , supporting scenario (i) that Hund’s-coupling-induced strong correlations lead to strongly-correlated behavior far from a Mott phase. Together, this Janus-faced behavior results in an interesting MIT for sizeable J upon increasing U that is qualitatively different from the MIT of one-band and multi-band Hubbard models without Hund’s coupling: starting from a weakly correlated metal at small U , the system first evolves into a strongly correlated

metal, which is stable for an extended range of U values and characterized by very small Z , before it eventually reaches the Mott insulating phase at large $U_c^{(2)}$.

The degenerate three-band study of Refs. [dMMG11, dM11] was followed by similar analyses for up to five bands, both with [GMM13, FB15, dM17] and without [BCV10, YS12, BVC12, dM17] orbital degeneracy, revealing qualitatively similar behavior as in the three-band case. For degenerate models, Janus-faced behavior emerges for any integer filling away from single and half-filling.

But even for the degenerate three-band Hund model the origin of the Janus-faced behavior has not been fully revealed. Obviously both the QPP itself and the opening of the insulating Mott gap are affected at the same time by changing J . Previous studies [dMMG11, dM11, GMM13, dMC17] quantified these changes by performing a Hubbard-I-type analysis for the gap dependence and by calculating Z to characterize the QPP. However, without access to (reliable) real-frequency spectral data, the Hubbard-I predictions could never be explicitly verified and the physical origin of the low Z could only be speculated about. A connection to the low coherence scale in Hund metals was assumed but never proven, and the nature of the incoherent regime remained unclear. Although considered, a clear connection between spin freezing and the Janus-faced behavior has not yet been demonstrated. Moreover, we note that the value of Z can have an error of up to 10% in these DMFT+QMC simulations (see supplement of Ref. [dMMG11]), also strongly affecting the values of U_c .

(D3) Proximity to the half-filled MIT. At half-filling, $n_d = 3$, $U_c^{(3)}$ is strongly reduced. The region of low Z in Fig. 1.1 directly starts at the border of the MIT at $n_d = 3$ and extends, even at moderate U , from there to $n_d = 2$ with Z slightly increasing when passing from $n_d = 3$ to $n_d = 2$. Such a filling dependence is observed in simulations and experiments of iron-based superconductors: their correlations are enhanced with hole-doping (i.e. approaching half-filling) [SWM⁺11, TKK⁺13, dMGC14, HBdM⁺16, PHI⁺17]. Furthermore, also the spin-freezing phenomenon [WGTMO8] is strongly doping dependent: the spin-freezing phase occurs in the vicinity of the half-filled MIT.

Motivated by this behavior, it has been argued in Refs. [FB15, dM17, dMC17] that the suppression of Z around $n_d = 2$ at moderate U is connected to the MIT at half-filling, $n_d = 3$. In particular, the effect of suppressing intra-orbital double occupancy by J has been regarded as a direct link to the MIT at $n_d = 3$ [FB15]. However, it has been noted that in contrast to the one-band Hubbard model, the reduction of Z in Hund metals does not imply the general suppression of charge fluctuations (far from the MIT) [FB15, DSH⁺18], and Z is thus not a good measure of Mottness: the origin of low Z and its filling dependence is subtle. Again, DMFT+NRG real-frequency data can help to further investigate this issue by complementing the slave-boson approaches of Refs. [FB15, dMC17] and quantitatively revealing the connection between spin freezing and Z .

We note that for non-degenerate models, low Z is argued to be induced by the “proximity to a half-filled MIT”, as well, but here, the half-filled MIT denotes an orbital selective Mott transition: when an orbital is individually half-filled it can become insulating, independently of the other orbitals [dMGC14]. This orbital decoupling effect is enhanced by Hund’s coupling, but will not be discussed further in this thesis.

In a slave-boson study [dM17] of degenerate and non-degenerate multi-band Hund models, a zone of negative compressibility, $\kappa_{\text{el}} = \frac{\partial n_d}{\partial \mu} < 0$, is observed at zero temperature for nonzero J in the n_d - U phase diagram, above $U \geq U_c$, reaching (depending on N_c) from half-filling towards $n_d = N_c + 1$. The transition from $\kappa_{\text{el}} > 0$ to $\kappa_{\text{el}} < 0$ is realized through a divergence of the compressibility, which occurs in the phase diagram together with a strong reduction in Z . In the absence of symmetry breaking in the model, this divergence is interpreted as a genuine thermodynamic Hund’s-coupling-induced instability towards a phase separation.

The enhancement of κ_{el} has been argued to be directly connected to the enhanced critical temperature of HTSCs [dMHCD09, dM11, HDD12, dM17]. This statement of a negative compressibility is solely based on slave-boson approaches (rotationally invariant form of the Kotliar-Ruckenstein slave-bosons for the full Hubbard-Kanamori model involving two bands, and slave-spin mean-field approximation for the Hubbard-Kanamori model without spin-flip and pair-hopping term involving up to five bands). It has so far not been validated by another (zero-temperature) method.

(D4) Spin-orbital separation (SOS). As a central result of this thesis, we will unambiguously establish “spin-orbital separation” (SOS) as a new screening route towards heavy masses in the Hund-metal regime. SOS is a complex intertwined two-stage screening process, in which orbital screening occurs at much higher energies than spin screening, while both degrees of freedom are still coupled. It is based on several previous findings.

Besides the phenomena (D1), (D2), and (D3), also the Hund’s-coupling-induced coherence-incoherence crossover with increasing temperature has been discussed as a new and generic normal-state property of Hund metals in the literature [HK09, MAM⁺11, YHK12]. As described in Sec. 1.1.3, DFT+DMFT+QMC simulations [HSK08, HK09] of $\text{LaO}_{1-x}\text{F}_x\text{FeAs}$ have revealed a low coherence temperature for this system, opening a large incoherent transport regime, characterized by an enhanced magnetic susceptibility and a linear temperature dependence of the resistivity. Similarly, DFT+DMFT+QMC simulations [MAM⁺11] have found a coherence-incoherence crossover and low Z in Sr_2RuO_4 .

Further, at low temperatures, (DFT+)-DMFT+QMC simulations [YHK12] for iron-chalcogenide and ruthenate superconductors and the 3HHM have revealed an incoherent frequency regime with anomalous fractional power-law exponents in the Matsubara self-energy for fillings, $1.5 \lesssim n_d \lesssim 2.5$, which is most pronounced at $n_d = 2$. Similar power-law behavior had been found before in the spin-freezing context for the Hubbard-Kanamori model [WGMT08]. In Ref. [YHK12] it has been speculated, solely based on imaginary-frequency data, that this apparent fractional power law on the imaginary frequency axis does imply a generic fractional power law in the self-energy on the real frequency axis and is related to experimentally observed fractional power-law behavior in the optical conductivity of ruthenates and FeTe systems.

The incoherent temperature and frequency regime has been proposed [YHK12] to be induced by two degrees of freedom that behave in different ways: the orbital degrees of freedom of Hund systems are quenched and fluctuate very rapidly while the spin degrees of freedom are unquenched and fluctuate albeit slowly (accordingly the local spin susceptibility has Curie-Weiss form and a large static value). This “separation” of spin and orbital degrees of freedom, which we have dubbed “spin-orbital separation” in Ref. [SYvD⁺15], had already been anticipated in 1973 in the context of a generalized Kondo-type model [OY73]. There, I. Okada and K. Yosida had deduced on qualitative grounds that the Kondo scale associated with orbital screening is much larger than the Kondo scale for spin screening: $T_{\text{K}}^{\text{orb}} > T_{\text{K}}^{\text{sp}}$. However, they had not been able to give explicit expressions for $T_{\text{K}}^{\text{orb}}$ and T_{K}^{sp} .

Much more recently, an analytic RG analysis (poor man’s scaling RG) in the Kondo regime of the 3HHM [AK15] has provided a simple understanding of the origin of the incoherent regime and established how the Kondo scales depend on the representations of the spin and orbital operators. Interestingly, in this complex multi-orbital Kondo model, spin and orbital degrees of freedom are explicitly coupled, resulting in a non-trivial protracted RG flow of a subtle spin-orbital Kondo effect: first, at higher energies, the intermediate-coupling NFL fixed point of an underlying effective 2 (spin)-channel $\text{SU}(3)$ Coqblin-Schrieffer model is reached, where the ferromagnetic spin coupling is quenched. Then, at much lower energies, the spin coupling renormalizes to an anti-ferromagnetic value and the RG flow results in a

strong-coupling FL fixed point. For $J = 0$, the Kondo model reduces to the single-channel antiferromagnetic $SU(3 \times 2)$ Coqblin-Schrieffer model.

Experimentally, possible signatures of such a two-stage screening of electrons have meanwhile been observed, for instance, in infrared spectroscopy [SMP⁺12], in resistivity, heat-capacity, thermal-expansion, and susceptibility measurements of the 122-iron pnictides [HBA⁺13, HBdM⁺16], in the optical response of Sr_2RuO_4 in terms of unusual excess spectral weight [SMB⁺14], in ARPES spectra of iron-based superconductors [MWR⁺14], in the thermopower of ruthenates [MG16], and in optical conductivity measurements [YYW⁺17] of KFe_2As_2 .

However, still, several issues have needed clarification. In particular, the DMFT+QMC calculations can not reach sufficiently low temperatures to fully reveal the FL phase of the 3HHM. An unambiguous quantitative confirmation of SOS has been missing, especially in frequency space at low enough temperatures, including a thorough investigation of the Kondo scales. Neither the weak-coupling nor the strong-coupling approach of Ref. [AK15] and Ref. [OY73], respectively, have provided direct access to the incoherent regime to analyze its transport nature. Here, a method is needed that can access all energy scales equally reliably. Further, there has been no clear evidence that the Kondo picture is really applicable to Hund lattice models. Importantly, real-frequency data has been needed to clarify the existence of power laws in the self-energy on the real-frequency axis. Moreover, signatures of SOS in the temperature dependence of the 3HHM have not yet been thoroughly studied previous to this thesis.

The need for real-frequency impurity solvers for DMFT. Many of the open questions about the physics of the 3HHM, which we have presented in this section, have remained unresolved due to the lack of appropriate *real*-frequency *multi*-band DMFT impurity solvers.

The scope and quality of DMFT results depends crucially on that of the impurity solver used to self-consistently solve its underlying quantum impurity model. In this respect, Hund models are particularly challenging. They involve at least three spinful bands and they are particle-hole asymmetric. The coherence scale is unusually low in these systems and the incoherent intermediate regime is the result of a complex Kondo-type screening process. At the same time, the 3HHM can undergo a MIT at integer filling at very large U , i.e. also atomic excitations need to be captured accurately by the impurity solver.

At the moment, (continuous-time) QMC solvers [RSL05, WCdM⁺06, Hau07b, GWPT08, GML⁺11] are often favored among impurity solvers in terms of versatility and performance, especially for models with multiple bands or cluster sites. However, numerically exact QMC results are only obtained on the imaginary frequency axis. Access to real-frequency spectra, as relevant, for instance, for ARPES or conductivity experiments, requires analytic continuation of imaginary (Matsubara) frequency QMC data, which is notoriously difficult. Furthermore, sign problems that occur for some models and extensive numerical costs at low temperatures limit their use in many cases. These shortcomings explain why QMC solvers experience difficulties in grasping the full picture of Hund-metal physics, which is extended over many energy scales.

Similarly, other solvers face severe problems. For instance, in exact diagonalization (ED) the numerical costs increase exponentially with the number of bands. Thus, for standard implementations of ED [CK94] methods three-band models are extremely challenging and even out of reach if one needs a very refined spectral resolution at the Fermi level due to the limited number of bath sites.

In a nutshell, there is a continued need for *real*-frequency impurity solvers suitable for *multi*-band DMFT applications, which work reliable at arbitrary temperatures and yield high

resolution at the Fermi level. In this thesis, we establish NRG as such a powerful tool.

We remark that during the last few years also several other promising real-frequency impurity solvers appeared on the stage. Especially, DMRG [WMPS14, WMS14, BWM⁺15, WGM⁺15, NnFH17, NnFKH18, NnFH18] strongly advanced and is now broadly applicable to various DMFT setups, including cluster DMFT [WMPS14, WGM⁺15] and nonequilibrium DMFT [WMS14, BWM⁺15]. Furthermore, an efficient ED-based real-frequency solver [LHGH14] using a restricted optimized active basis set can now handle several hundred uncorrelated bath sites, reaching spectral resolutions better than 1% of the bandwidth. This solver is part of Quany [Hav16], a tool for core level spectroscopy. In 2017, a new tensor network approach, called fork tensor-product states (FTPS), was presented in Ref. [BZT⁺17], which is able to reliably treat three-orbital lattice models, including the resolution of fine structures in the spectral function at higher energies by using more than 100 bath sites.

1.3 Aim

In his article “Is There Glue in Cuprate Superconductors?” [And07] P. W. Anderson argued for an electronic pairing mechanism in cuprates based on strong correlations instead of a “bosonic glue”:

“The crucial point is that there are two very strong interactions, U (> 2 eV) and J (~ 0.12 eV), that we know are present in the cuprates [...]. Whether any additional ‘glue’ exists is of lesser interest. We have a mammoth and an elephant in our refrigerator – do we care much if there is also a mouse?” [And07]

In this thesis we study the importance of Coulomb repulsion U (the “mammoth”) and ferromagnetic Hund’s coupling J (the “elephant”) in a minimal multi-band model with relevance for Hund’s metals, including the iron-based HTSCs. We especially focus on the role of orbital and spin degrees of freedom. While our results are obtained for the normal phase, our insights might provide guidance for theories of high-temperature superconductivity.

In particular, the aim of this dissertation is twofold:

- (i) We extend the scope of NRG as viable *real-frequency multi-band* impurity solver for DMFT.
- (ii) We apply DMFT+NRG to a degenerate three-band Hubbard-Hund model. Thereby, we unveil the nature and origin of strong correlations in Hund metals, and establish clear signatures distinguishing between Hund metals and metals of Mott type.

As a result of (i) and (ii) we revive DMFT+NRG as a competitive and distinguished tool in the DMFT community, and lay the foundation for various follow-up projects, like applications of DMFT+NRG to other multi-band lattice models [LvDW17, LvDW18] and realistic materials [KLK⁺19] or cluster DMFT+NRG [Gle19].

The present thesis is structured as follows. In Chapter 2 we present our DMFT+NRG method. In Sec. 2.1 we first give a compact introduction to single-site DMFT in the context of NRG as a real-frequency impurity solver, and then, in Sec. 2.2, focus on the standard NRG method. There, we provide an overview of K. G. Wilson’s basic NRG ideas in Sec. 2.2.2. We further introduce a stable implementation of Zitko’s discretization scheme [vP09, Ž09] in Sec. 2.2.3 to deal with the frequency-dependent hybridization functions arising in DMFT+NRG. We summarize recent technical advances for NRG in Sec. 2.2.4, such as the

use of matrix product states and complete many-body basis sets or the explicit exploitation of non-abelian symmetries for high-symmetry models, which led to the powerful state-of-the-art fdmNRG implementation employed in this thesis. We also discuss the advantages of fdmNRG as impurity solver. Moreover, in Sec. 2.3 (Ref. [SMvDW16]) we implement a recently developed “interleaved” scheme of NRG (iNRG) [MGWF⁺14], which dramatically increases the numerical efficiency of NRG for low-symmetry impurity models. We demonstrate in an extensive study that the accuracy of iNRG is comparable to standard NRG, and thus establish iNRG as a promising DMFT solver for material-specific model simulations. We complete Chapter 2 with a discussion of so-called “open Wilson chains” in Sec. 2.4 (Ref. [BLS⁺17]). Within NRG the bath of the impurity model is discretized and then mapped onto a Wilson chain, a one-dimensional tight-binding chain. Thereby, in the standard Wilson chain setup, bath modes are truncated. In contrast, we construct open Wilson chains which keep track of all bath modes.

In Chapter 3 we give an overview over the computation of important physical quantities, investigated in this thesis.

In Chapter 4 (Ref. [SYvD⁺15]) we demonstrate the power of our real-frequency multi-band (standard) fdmNRG impurity solver, for the first time, in the context of an orbital-symmetric three-band Hubbard-Hund model with relevance for Hund metals. As a main result of this thesis, we unambiguously establish SOS as a new Hund’s-rule-induced two-stage Kondo screening mechanism towards heavy masses, and thus also prove the existence of a FL ground state in these systems.

In Chapter 5 (Ref. [SKWvD18]) we show that the phenomena of (D1), (D2), and (D3) are directly connected to SOS and analyze, based on this insight, the origin of strong correlations, Hundness versus Mottness [scenarios (i)-(iii) of Sec. 1.2.4], from the perspective of SOS using real-frequency DMFT+NRG data. To this end, we investigate the 3HHM phase diagram at zero temperature including a detailed study of the MIT at $n_d = 2$ and the dependence of SOS on system parameters. We elaborate on the consequences of SOS for the nature of the incoherent transport regime, discuss anomalous power-law behavior, and establish a basic definition of strongly correlated Hund metals and metals of Mott type at 1/3 filling.

In Chapter 6 (Ref. [DSH⁺18]) we reveal distinct signatures of Mottness and Hundness in the temperature dependence of local spectra and the local susceptibilities describing the charge, spin and orbital degrees of freedom. These signatures are qualitatively similar for realistic material simulations of two archetypal Mott- and Hund-correlated materials, V_2O_3 and Sr_2RuO_4 , respectively, and model calculations of the 3HHM. We thus contribute to a general phenomenology of Mott and Hund physics, applicable to real materials but independently of material-dependent details.

In Chapter 7 we discuss in detail the consequences of particle-hole asymmetry in the 3HHM. In order to establish more features to distinguish between Hund metals and metals of Mott type, we also (re)investigate the evolution of the QPP with increasing temperature, and the temperature dependence of various quantities, like static local susceptibilities, the QP weight, scattering rate, resistivity, thermopower, or entropy. We suggest the existence of resilient “Hund quasiparticles” governing the SOS-induced incoherent state in the normal phase of Hund metals. These can be described in terms of itinerant orbital degrees of freedom coupled non-trivially to quasi-free large spins.

We summarize the main insights of this thesis in Chapter 8 and shortly present related current and future DMFT+NRG projects.

2 Method

In this Chapter, we give a compact and generic introduction to DMFT+NRG based on an extensive presentation of this method in Ref. [Sta13]. Note that we will omit any flavour indices in Sec. 2.1 and Sec. 2.2, for simplicity. Further, we use the short notation $\int \equiv \int_{-\infty}^{\infty}$ within this thesis. In Sec. 2.3, we present interleaved NRG [MGWF⁺14, SMvDW16], and in Sec. 2.4, a new Wilson chain setup for quantum impurity models, so-called open Wilson chains.

2.1 Single-site dynamical-mean field theory (DMFT) in a nutshell

DMFT key insights. DMFT is currently the most successful non-perturbative method to treat interacting lattice models (for a review, cf. [GKKR96]). The foundation of single-site DMFT was laid by W. Metzner and D. Vollhardt in 1989 [MV89] and by A. Georges and G. Kotliar in 1992 [GK92], studying the Hubbard model in infinite dimensions. It is based on two key insights:

- (i) In the limit of infinite dimensions or lattice connectivity, i.e. coordination number z , the self-energy of the lattice problem becomes purely local in real space,

$$\Sigma_{ij}(\omega) \xrightarrow{z \rightarrow \infty} \Sigma(\omega)\delta_{ij}, \quad (2.1a)$$

or momentum-independent in Fourier space,

$$\Sigma_{\mathbf{k}}(\omega) \xrightarrow{z \rightarrow \infty} \Sigma(\omega), \quad (2.1b)$$

with the same $\Sigma(\omega)$, simply referred to as “the self-energy”, since $\Sigma_{ij}(\omega) = \Sigma(\omega, \mathbf{r}_j - \mathbf{r}_i) = \frac{1}{N_B} \sum_{\mathbf{k}} \Sigma_{\mathbf{k}}(\omega) e^{i\mathbf{k}(\mathbf{r}_j - \mathbf{r}_i)} = \Sigma(\omega) \frac{1}{N_B} \sum_{\mathbf{k}} e^{i\mathbf{k}(\mathbf{r}_j - \mathbf{r}_i)} = \Sigma(\omega)\delta_{ij}$, where i, j denote lattice sites, and N_B the number of \mathbf{k} -points of the Brillouin zone.

Spatial fluctuations are thus neglected in this “mean-field” approach, similar to its classical counterparts. However, temporal quantum fluctuations are retained in the energy dependence of the “dynamical” self-energy. This explicit energy dependence of DMFT allows to capture effects based on competing energy scales, thus both atomic-like and band-like properties, and characterizes DMFT as an inherently non-perturbative method, bridging the gap between the earlier Hubbard-I and Gutzwiller-Brinkman-Rice approaches to the Mott-Hubbard problem.

- (ii) Based on the purely local lattice self-energy, $\Sigma(\omega)$, an interacting lattice site can be treated in “dynamical mean-field fashion” as an interacting impurity, where a single site with same local interactions as in the lattice model is embedded in an effective mean-field bath, which represents the “rest” of the lattice (including all its hopping processes) in a self-consistent manner. This means that, within the DMFT framework, techniques developed for impurity models can be directly used to solve lattice models.

DMFT self-consistency condition. Let us elaborate on (ii). In more technical terms, the lattice model [e.g. the 3HHM of Eq. (1.2)] is mapped [cf. Fig. 2.1(a)] iteratively onto a quantum impurity model [e.g. the 3AHM of Eq. (1.3)], which is described by the local (lattice) self-energy, $\Sigma(\omega)$, and by a self-consistently determined hybridization function (the “Weiss mean field” of DMFT), $\Delta(\omega) = \sum_k \frac{V_k^2}{\omega - \varepsilon_k}$, which is fully specified by its imaginary part,

$$\Gamma(\omega) = -\text{Im} \Delta(\omega) = \pi \sum_k |V_k|^2 \delta(\omega - \varepsilon_k), \quad (2.2)$$

with $\omega \equiv \omega^+$. For the purely local lattice self-energy, $\Sigma(\omega)$, in Eq. (2.1), the lattice dynamics is completely captured by the local retarded lattice Green’s function [which is chosen to be at site $\mathbf{r} = 0$ for convenience, i.e. $G_{\text{latt}}(\omega) \equiv G_{\text{latt}}(\omega, \mathbf{r} = 0)$],

$$G_{\text{latt}}(\omega) = \frac{1}{N_B} \sum_{\mathbf{k}} G_{\text{latt},\mathbf{k}}(\omega) e^{i\mathbf{k}(\mathbf{r}=0)} = \frac{1}{N_B} \sum_{\mathbf{k}} \frac{1}{\omega + \mu - \varepsilon_{\mathbf{k}} - \Sigma(\omega)} = \int d\varepsilon \frac{\rho_0(\varepsilon)}{\omega + \mu - \varepsilon - \Sigma(\omega)}. \quad (2.3)$$

$\rho_0(\varepsilon)$ is the non-interacting density of states of a given lattice [cf. Eq. (2.8) for the Bethe lattice], and

$$G_{\text{latt},\mathbf{k}} \equiv \langle \hat{d}_{\mathbf{k}} \| \hat{d}_{\mathbf{k}}^\dagger \rangle_\omega = \frac{1}{\omega + \mu - \varepsilon_{\mathbf{k}} - \Sigma(\omega)} \quad (2.4)$$

is the retarded lattice Green’s function in momentum space with the chemical potential μ of the lattice. After the self-consistent mapping, the local lattice Green’s function is equal to the retarded impurity Green’s function,

$$G_{\text{imp}}(\omega) \equiv \langle \hat{d} \| \hat{d}^\dagger \rangle_\omega = \frac{1}{\omega - \varepsilon_d - \Delta(\omega) - \Sigma(\omega)}, \quad (2.5)$$

with $\varepsilon_d = -\mu$, imposing the self-consistency condition:

$$G_{\text{latt}}(\omega) \stackrel{!}{=} G_{\text{imp}}(\omega) \equiv G(\omega). \quad (2.6)$$

Inserting Eq. (2.5) into Eq. (2.6) leads to a simple relation for the imaginary part of the self-consistency condition,

$$\Gamma(\omega) = \text{Im} (G_{\text{latt}}(\omega)^{-1} + \Sigma(\omega)), \quad (2.7)$$

which constitutes a closed set of DMFT equations that can be solved iteratively using a quantum impurity solver. In this thesis, we employ fdmNRG for the latter purpose (cf. Sec. 2.2).

DMFT self-consistency loop. The iterative DMFT self-consistency procedure [cf. triangle in Fig. 2.1(b)] is initialized by an arbitrary input hybridization function, $\Gamma(\omega)$, for instance a constant box distribution, $\Gamma(\omega) = \Gamma \Theta(D_{\text{NRG}} - |\omega|)$, with half-bandwidth $D_{\text{NRG}} = 1$. This fully defines a quantum impurity model, which is solved with NRG [cf. black box in Fig. 2.1(b)]. The NRG impurity solver returns a local self-energy, $\Sigma(\omega)$, which is computed with the “self-energy trick” [BHP98] (cf. Sec. 3.2). $\Sigma(\omega)$ can be used to calculate a new lattice Green’s function via Eq. (2.3). In a final step, the self-consistency condition, Eq. (2.7), yields a new version of $\Gamma(\omega)$, and the procedure starts all over again, until we arrive at a converged result for the effective environment in terms of the hybridization function $\Gamma(\omega)$ and hence for the self-energy $\Sigma(\omega)$ (in practice, we may stop at a maximum relative error between two subsequent hybridization functions of 0.2% in the case of the 3HHM).

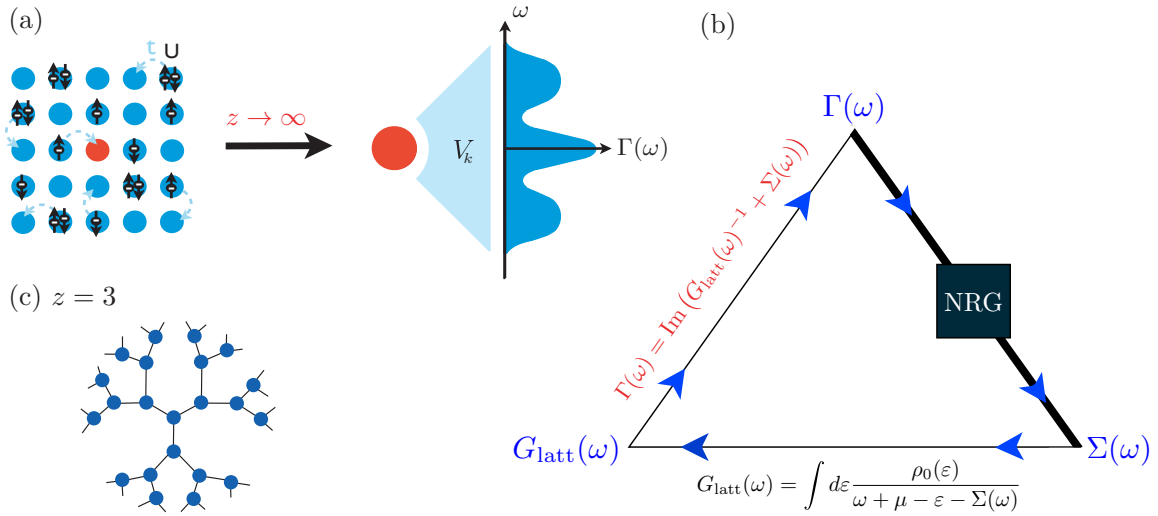


Figure 2.1 (a) Within DMFT an interacting lattice model is mapped self-consistently onto a quantum impurity model (here, illustrated for a one-band model). (b) DMFT self-consistency loop with NRG as impurity solver (black box). Solving the impurity model is computationally the most costly step of the iterative mapping process, which is indicated by a thick line in the triangle. (c) Caley tree for $z = 3$. The Caley tree for $z \rightarrow \infty$ is the Bethe lattice with semi-circular density of states. This figure is adapted from Ref. [Sta13].

Bethe lattice. In this thesis, we study the 3HHM solely on the infinite Caley tree [cf. Fig. 2.1(c)], also called Bethe lattice, i.e. we use the non-interacting semi-circular density of states,

$$\rho_0^B(\varepsilon) = \frac{1}{\pi t} \sqrt{1 - \left(\frac{\varepsilon}{2t}\right)^2}, \quad \varepsilon \in [-2t, 2t], \quad (2.8)$$

that occurs in this limit of infinite lattice coordination. t is the hopping matrix between lattice sites [cf. Eq. (1.2)]. The Bethe lattice is an artificial but convenient lattice type within DMFT. For the Bethe lattice, the integral in Eq. (2.3) can be straightforwardly evaluated, resulting in the simple self-consistency condition

$$\Gamma(\omega) = -t^2 \text{Im} G(\omega), \quad (2.9)$$

and the local lattice Green's function,

$$G_{\text{latt}}(\omega) = \frac{1}{2t^2} \left(\xi - \sqrt{\xi^2 - (2t)^2} \right), \quad (2.10)$$

with $\xi \equiv \omega + \mu - \Sigma(\omega)$.

The core part of the DMFT self-consistency procedure is the solution of the quantum impurity model. Therefore, the numerical efficiency and accuracy of DMFT solely depend on the impurity solver. In the next section, we present (fdm)NRG and its merits for DMFT.

2.2 Standard numerical renormalization group (NRG) as impurity solver for DMFT

2.2.1 A brief history.

NRG [Wil75, Wei12a] has a longstanding and successful history as the standard tool to deal with impurity models (cf. [BCP08] for a review). Its basic idea goes back to K. G. Wilson who developed this method to solve the Kondo problem in a fully non-perturbative way in 1975 [Wil75]. Together with H. R. Krishna-murthy and J. W. Wilkins, they applied it successfully to the single impurity Anderson model (SIAM) in 1980 [KmWW80]. About ten years later DMFT was invented [GK92, GK96]. In 1998, R. Bulla *et al.* introduced an elegant and accurate way to employ the NRG as impurity solver for DMFT to investigate the symmetric 1HM [BHP98, Bul99]. Applications of DMFT+NRG to two-band lattice models followed several years later [PB05, PP10, PKP11]. However, the computational cost of NRG scales exponentially with the number of fermionic bands. And so, for a long time, NRG was extremely limited to go beyond two bands. In this thesis, we show that recent significant technical advances – which not only improved the performance of the codes but also the quality of NRG results – have now made applications of DMFT+NRG to three-band models routinely feasible [SYvD⁺15, DSH⁺18, SKWvD18]. Even four-band calculations seem within reach in the presence of large orbital symmetries, yet also in the absence of non-abelian symmetries with the invention of interleaved NRG [MGWF⁺14, SMvDW16] (cf. Sec. 2.3).

In the following three sections, we first give a short introduction to Wilson’s NRG idea, introduce a stable implementation of R. Zitko’s discretization scheme for DMFT+NRG [vP09, Ž09], and then present our cutting-edge `fdmNRG` code.

2.2.2 NRG in a nutshell

Energy-scale separation. The key idea of K. G. Wilson’s NRG [Wil75] is to construct an iterative renormalization group flow that results in a systematic energy-scale separation, which can be exploited in the description of a quantum-many-body impurity problem in order to handle its huge Fock space: high-energy eigenstates do not severely affect the low-energy physics and are therefore less accurately resolved.

Logarithmic discretization. To realize this concept, the noninteracting continuous bath [cf. Eq. (1.4)] of an impurity model Hamiltonian [cf. Fig. 2.2(a)] is discretized by the introduction of bath intervals with logarithmically decreasing widths, $I_n \propto \Lambda^{-n}$, where $\Lambda > 1$ is the NRG discretization parameter, resulting in an exponentially high resolution at the Fermi level. In the coarse grained Hamiltonian each interval is represented by only one single bath state [cf. blue circles in Fig. 2.2(b)], instead of infinitely many, while the overall coupling of the impurity and the bath is preserved. In short, the open system is approximated by a closed system (cf. Sec. 2.4 for an alternative discretization scheme that systematically keeps track of neglected bath modes). Each single bath mode is characterized by its “representative” energy, ξ_n , and its coupling strength, $\gamma_n = \int_{I_n} d\omega \Gamma(\omega)/\pi$, to the impurity, given in terms of the weight of the hybridization function in interval n . In this thesis, we use a stable implementation of R. Zitko’s discretization scheme to compute ξ_n in a manner which accurately deals with the frequency dependence of DMFT hybridization functions.

Wilson chain. In a next step, the discretized Hamiltonian is mapped exactly onto a one-dimensional semi-infinite tight-binding chain, a “Wilson chain”, with the interacting impurity

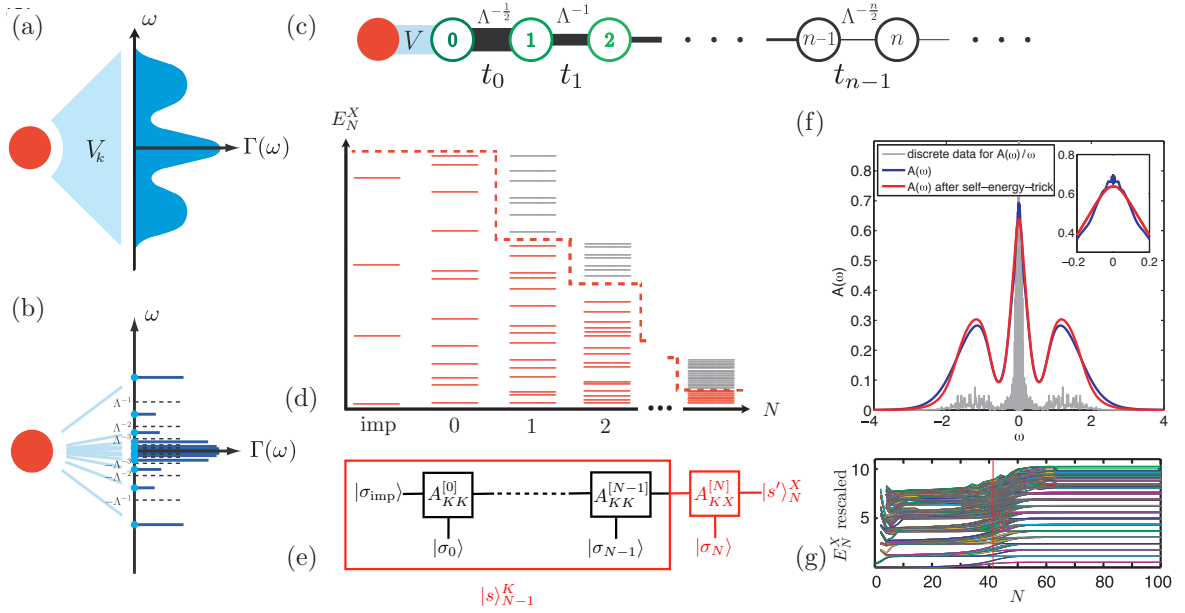


Figure 2.2 NRG in a nutshell. (a) Sketch of a self-consistently determined (one-band) quantum impurity model with the impurity (red) coupled (bright blue) to a non-interacting continuous bath (dark blue). (b) Within NRG the bath is discretized logarithmically with discretization parameter, $\Lambda > 1$. Each bath interval is represented by one bath state (blue circles). (c) The discretized model is mapped onto a one-dimensional semi-infinite “Wilson chain”, with the interacting impurity site coupled to one end, and nearest-neighbor hopping matrix elements, t_n , decaying logarithmically down the chain. (d) An iterative RG procedure is applied, in which the Wilson chain Hamiltonian is successively diagonalized. At each iteration, N , high energy eigenstates (grey) are discarded and low energy states (red) are kept. (e) The resulting eigenstates can be formulated in matrix-product-state (MPS) language. (f) full-density-matrix (fdm)NRG allows to compute highly accurate spectral functions, here exemplified for the symmetric 1HM, Eq. (1.1), with $U/D = 2$, $T = 0$, $\Lambda = 2$, and $N_z = 4$ ($D = 2t$). Raw spectral data, $A_{\text{raw}}/|\omega|$ is plotted in grey, the smoothed spectral function in blue, and an improved spectral function [cf. Sec. 3.3] in red. (g) Renormalization group flow diagram for the symmetric SIAM ($U = 0.8$, $\Gamma = 0.02$, $\Lambda = 2$, $D_{\text{NRG}} = 1$) plotted for even iterations. The red bar marks the spin Kondo scale $N(T_K)$. This figure is adapted from Ref. [Sta13].

site coupled to one end [cf. Fig. 2.2(c)]. This unitary mapping is usually achieved by a standard Lanczos tridiagonalization procedure. The Wilson chain Hamiltonian is characterized by hopping matrix elements between neighboring sites, which decay exponentially down the Wilson chain and reflect the desired energy-scale separation of the system. This Hamiltonian can be written in terms of a recursion relation of the form $\hat{H}_N = R(\hat{H}_{N-1})$ for Wilson chain site N , and interpreted as a renormalization group (RG) transformation.

Iterative renormalization group procedure. Now an iterative RG procedure can be applied to compute the eigenenergies and eigenstates of the Wilson chain Hamiltonian. It is based on successive diagonalization and truncation of high-energy states [cf. Fig. 2.2(d)]. Starting at the impurity site, at each iteration, first \hat{H}_N is constructed from \hat{H}_{N-1} with given eigenstates, $|s\rangle_{N-1}^K$, and eigenenergies, E_{N-1}^K , by adding a new Wilson chain site N , which is represented in terms of the local basis set $|\sigma_N\rangle$ of dimension d_{loc} (e.g. $d_{\text{loc}} = 2^2 = 4$ for a single spinful band). The new state space of site N is then given by the enlarged non-diagonal state space, $|s, \sigma\rangle_N = |\sigma_N\rangle \otimes |s\rangle_{N-1}$. Next, \hat{H}_N is diagonalized, resulting in a new set of refined eigenstates, $|s'\rangle_N^X$, with eigenenergies, E_N^X , for site N , which are connected to the

previous states, $|s\rangle_{N-1}^K$, via a unitary transformation:

$$|s'\rangle_N^X = \sum_{\sigma_N^s} [A_{KX}^{[\sigma_N]}]_{ss'} |\sigma_N\rangle |s\rangle_{N-1}^K. \quad (2.11)$$

In a last step, high-energy states, $|s\rangle_N^D$, with energies, E_N^D , exceeding a given truncation energy, are discarded [cf. grey lines in Fig. 2.2(d)], while the lower lying eigenstates, $|s\rangle_N^K$, are kept [cf. red lines in Fig. 2.2(d)]. Note that X labels kept, K , or discarded, D , states after truncation, and both types of states, $X = K, D$, before truncation. The size of the Fock state space can thus be kept fixed with increasing chain length, while still obtaining an exponentially increased resolution of the low-energy part of the spectrum. The resolution at high energies is, however, more coarse-grained, since discarded states remain degenerate. Nevertheless, our approach captures all essential high-energy features [WvD07, SKWvD18, LW16, LvDW17]. The iterative RG procedure is stopped by discarding all states at iteration N_T as soon as the required energy resolution is reached. From the resulting spectrum, one can then compute spectral functions directly on the real-frequency axes (cf. Sec. 2.2.4 for details).

Renormalization group flow. The RG scheme of NRG allows to investigate the physics of an impurity model from an RG perspective. The lowest-lying kept eigenenergies of each iteration can be plotted in a rescaled fashion, i.e. in terms of the characteristic energy scale (\propto energy level spacing) of each Wilson chain site, which is given in units of $\omega_N \propto \Lambda^{-N/2}$ (in the convention of Ref. [Wei12b]; cf. supplement of Ref. [SYvD⁺15]). This results in a RG energy flow diagram [cf. Fig. 2.2(d)], which reveals the relevant physics at all energy scales. Conceptually, the rescaled energy levels represent the finite-size spectrum of the impurity+bath put in a spherical box of radius $R_N \propto \Lambda^{N/2}$, centered on the impurity [Wil75, vDZF98]: as N increases, the finite-size level spacing $\omega_N \propto 1/R_N$ decreases exponentially. The corresponding flow of the finite-size spectrum is stationary (N -independent) while ω_N lies within an energy regime governed by one of the fixed points, but changes when ω_N traverses a crossover between two fixed points [SYvD⁺15, SKWvD18]. For instance, for a SIAM with constant hybridization function, three different regimes exist: the free orbital regime for very small N , the local moment regime for intermediate N and the strong coupling regime below the Kondo scale $N(T_K)$, which is also called FL fixed point (cf. Ref. [KmWW80] for a detailed discussion). In the case of a FL fixed point the fixed-point spectrum can be easily understood in a non-interacting QP picture (cf. Sec. 3.9 and Sec. 4.B). Otherwise, it can be interpreted using conformal field theory arguments [BHZ97, vDZF98, WSL⁺19].

While this section contains a qualitative description of NRG, equations and further details are provided in Sec. 2.3. All computational parameters and details of our DMFT+NRG calculations are listed in the Supplementary material of Ref. [SYvD⁺15].

2.2.3 Discretization in NRG+DMFT: stable implementation of Zitko's discretization scheme

For pure quantum impurity models usually a box distribution, $\Gamma(\omega) = \Gamma\Theta(D_{\text{NRG}} - |\omega|)$, is used to describe the hybridization function. In contrast, within DMFT, the NRG discretization scheme has to be adapted to optimally discretize the non-trivial frequency-dependent hybridization functions, $\Gamma(\omega)$, that emerge in every step of the self-consistency loop. In this section, we present a numerically stable implementation of the scheme in Refs. [vP09, Ž09] to accurately represent the frequency-dependent continuous baths in terms of discrete bath modes.

In Refs. [vP09, Ž09] R. Zitko and T. Pruschke derived a discretization scheme based on the requirement to correctly reproduce the original continuous hybridization function after “z-averaging” in the limit of infinitely many z-shifts, $N_z \rightarrow \infty$,

$$\Gamma(\omega) \stackrel{!}{\underset{N_z \rightarrow \infty}{=}} \int_0^1 dz \Gamma^{\text{disc}}(\omega, z). \quad (2.12)$$

$\Gamma^{\text{disc}}(z, \omega) = \pi \sum_n \gamma_n^z \delta(\omega - \xi_n^z)$ is the hybridization function after discretization. $z \in]0, 1[$ is a z-shift [vP09, OO94], which uniformly shifts the logarithmic discretization grid, i.e. $I_n \propto \Lambda^{-(n+z)}$ (cf. also Sec. 2.2.4).

In his derivation, Zitko introduced a continuous grid parameter $x = n + z \in [1, \infty[$ for the (in principle arbitrary but usually strictly logarithmically defined) discretization grid $\epsilon(x)$. For simplicity, we restrict our discussion to positive frequencies. In practice, we use $\epsilon(x) = \tilde{\omega} \Lambda^{2-x}$ for $x \geq 2$, with $\tilde{\omega}$ chosen slightly smaller than the overall (half) width of the frequency-dependent hybridization function, $\Gamma(\omega)$, and $\epsilon(x) = \omega_{\text{max}}$ for $x < 2$, with the maximal value of the numerical frequency grid, ω_{max} , a choice that always ensures a finite weight in the outermost interval. The continuous grid function, $\epsilon(x)$, for $x \leq 2$, and accordingly also the continuous function describing the representative energies, $\xi(x)$, are strictly monotonically decreasing functions, and fulfill the following (boundary) conditions:

$$\epsilon(x = 2) = \tilde{\omega} \quad \text{and} \quad \lim_{x \rightarrow \infty} \epsilon(x) = 0, \quad (2.13)$$

$$\xi(x = 1) = \tilde{\omega} \quad \text{and} \quad \lim_{x \rightarrow \infty} \xi(x) = 0. \quad (2.14)$$

The ansatz, Eq. (2.12), leads to a differential equation for the representative energies, $\xi(x)$, of the form

$$-\frac{d\xi(x)}{dx} = \frac{\int_{\epsilon(x+1)}^{\epsilon(x)} d\omega \Gamma(\omega)}{\Gamma[\xi(x)]}, \quad (2.15)$$

which can be solved for given $\epsilon(x)$ using a differential equation solver, for instance based on the fourth-order Runge-Kutta method (as used in Ref. [Ž09]).

However, Eq. (2.15) is highly nonlinear. Small errors in the solution of Eq. (2.15) accumulate in an exponential manner and the error in $\xi(x)$ tends to diverge with increasing x . Increasing the accuracy of the outcome conversely dramatically slows down the solver. Moreover, for hybridization functions, $\Gamma(\omega)$, with frequency regimes of essentially zero (or very small) weight as in the case of a gap in the density of states, Eq. (2.15) is not well defined (or at least very unstable in its solution).

We therefore introduce a new stable implementation of Eq. (2.15) based on the simple insight that this differential equation can be reformulated by using the chain rule for derivatives, $\Gamma[\xi(x)](d/dx)\xi(x) = (d/dx)\tilde{\Gamma}(\xi(x))$ with $(d/d\omega)\tilde{\Gamma}(\omega) = \Gamma(\omega)$. Multiplying Eq. (2.15) by Γ , it can be integrated over an interval $x + 1$ to x , resulting in the recursion relation

$$\int_{\xi(x+1)}^{\xi(x)} d\omega \Gamma(\omega) = - \int_{x+1}^x dx f(x) \quad \text{with} \quad f(x) = \int_{\epsilon(x+1)}^{\epsilon(x)} d\omega \Gamma(\omega). \quad (2.16)$$

For given $\epsilon(x)$, the function $f(x)$ is known. For a given discretization, and hence a given z-shift, one only needs to determine the discrete set $\xi(x = n + z)$ for the fixed grid $\epsilon(x = n + z)$, which is more naturally and easily done in the above integral formulation. Eq. (2.16) can be solved iteratively, starting at a maximal value $x + 1 = x_{\text{max}}$ and using the approximation $\xi(x_{\text{max}}) \approx \epsilon(x_{\text{max}})$. Relative errors of $\mathcal{O}(1)$ in the first few iterations with large x (induced by the slightly wrong start values) reduce exponentially fast with linearly decreasing x , since we

go from exponentially small to large orders of magnitude in the numerical calculation. If the spectral function has a gap, it is convenient to start from a value x_{\max} with small but finite $\Gamma[\epsilon(x_{\max} - 1)]$. We remark that, in principle, one would also assume a more stable numerical behavior in solving Eq. (2.15) by starting at x_{\max} .

In summary, we conclude that Eq. (2.16) is easy to implement and works reliably for arbitrarily shaped hybridization functions.

2.2.4 State-of-the-art fdmNRG impurity solver for DMFT

In recent years, significant technical progress has been made in transforming NRG into an efficient high-quality multi-band DMFT impurity solver. In particular, A. Weichselbaum has developed a flexible high-performance toolbox, the QSpace tensor library [Wei12a], for implementing NRG computations in terms of matrix product states (MPS) [WvD07, WVS⁺09, Wei11, Sch11, Wei12b]. Our full-density-matrix (fdm)NRG [WvD07] impurity solver is based on the following advances.

Matrix product states. fdmNRG is implemented in the transparent language and framework of matrix product states (MPS) [Wei12b] (cf. Ref. [Sch11] for a review on MPS). These are directly generated in NRG. For instance, the eigenstates, $|s'\rangle_N^X$, can be written as MPS of the form,

$$|s'\rangle_N^X = \sum_{\sigma_N \dots \sigma_0 \sigma_{\text{imp}}} \text{Tr} \left(A_{KK}^{[\sigma_0]} \dots A_{KK}^{[\sigma_{N-1}]} A_{KX}^{[\sigma_N]} \right) |\sigma_N\rangle \otimes |\sigma_{N-1}\rangle \otimes \dots \otimes |\sigma_0\rangle \otimes |\sigma_{\text{imp}}\rangle, \quad (2.17)$$

by iterative insertions of Eq. (2.11). $|\sigma_{\text{imp}}\rangle$ represents the impurity basis. The A-matrices of the basis transformations in the iterative RG procedure, written as $A_{KX}^{[\sigma_N]}$, are three-dimensional tensors in the space spanned by $|s\rangle_{N-1}^K$, $|\sigma_N\rangle$ and $|s'\rangle_N^X$. In a diagrammatical tensor network representation, each A-matrix [cf. e.g. the red matrix in Fig. 2.2(e)] thus has three legs, one for each index: $|s\rangle_{N-1}^K$ to the left, $|\sigma_N\rangle$ at the bottom, and $|s'\rangle_N^X$ to the right. Connected legs in Fig. 2.2(e) symbolize contractions, leading to the trace in Eq. (2.17).

Abelian and non-abelian symmetries. In the QSpace tensor library, abelian and non-abelian symmetries are implemented on a generic level: the state space is organized into symmetry multiplets, and tensors “factorize” into two parts, acting in the reduced multiplet space and the Clebsch Gordon coefficient space, respectively (cf. Ref. [Wei12a] for details). Diagonalization of the NRG Hamiltonian at each RG iteration can then be performed in multiplet space rather than state space, significantly reducing the matrix sizes and hence computational cost. NRG calculations with three and even more *degenerate* bands have thus become feasible, also in the DMFT context [SYvD⁺15, DSH⁺18, SKWvD18, LvDW18]. For solving our 3HHM of Eq. (1.2), we explicitly exploit its $U(1)_{\text{ch}} \times SU(2)_{\text{sp}} \times SU(3)_{\text{orb}}$ symmetry for its charge (ch), spin (sp) and orbital (orb) degrees of freedom.

Full-density-matrix (fdm)NRG. The fdmNRG solver is established on a complete approximate basis set [AS05, AS06] of the full Hamiltonian, constructed from the discarded states of all NRG iterations by appending to each discarded state, $|s\rangle_N^D$, a degenerate “environmental” state, $|e_N\rangle \equiv |\sigma_{N_T}\rangle \otimes \dots \otimes |\sigma_{N+1}\rangle$, i.e. a tensor product constructed from the local basis states of all later iterations. The many-body basis set is thus of the form $\{|se\rangle_N^D = |s\rangle_N^D \otimes |e_N\rangle\}$.

Importantly, the full thermal density matrix, $\hat{\rho} = e^{-\beta \hat{H}} / Z$ with $\beta = 1/k_B T$, as used for the calculation of spectral functions, can be expressed as a weighted sum, $\hat{\rho} \approx \sum_N w_N \hat{\rho}_{DD}^{[N]}$, of

normalized thermal density matrices, $\hat{\rho}_{DD}^{[N]}$, over all Wilson shells N , build from the discarded states at each iteration (cf. Ref. [WvD07] for details).

Spectral functions are given by the Lehmann representation as a sum of poles,

$$\mathcal{A}(\omega) = \sum_{a,b} \langle b | \hat{C} | a \rangle \frac{e^{-\beta E_a}}{Z} \langle a | \hat{B} | b \rangle \delta(\omega - E_{ab}) \stackrel{\text{fdmNRG}}{=} \sum_N w_N \mathcal{A}_N^{BC}(\omega), \quad (2.18)$$

with $Z = \sum_a e^{-\beta E_a}$ and $E_{ab} = E_b - E_a$, and can be calculated accurately directly on the real-frequency axis in sum-rule conserving fashion [PPA06, WvD07] at zero or arbitrary finite temperature. In fdmNRG, $\mathcal{A}(\omega)$ is expressed in terms of discarded states only. Finally, fdmNRG yields Eq. (2.18) in the form

$$A_{\text{raw}}(\omega) = \sum_j a_j \delta(\omega - \omega_j), \quad (2.19)$$

a sum over discrete delta-peaks of weights a_j located at real frequencies, ω_j , with $\sum_j a_j = 1$. Continuous spectra are obtained by broadening the discrete data with a standard log-gaussian Kernel of frequency-dependent width [WvD07, BCP08].

To improve the resolution of spectral data, we “ z -average” over the results obtained from several, differing NRG runs, for which the logarithmic discretization of the bath has been uniformly shifted with respect to each other [vP09, OO94]. Within the DMFT+NRG approach, the resolution of spectral data can be further improved by applying the so-called self-energy trick [BHP98] (cf. Sec. 3.3).

The real parts of the smoothened spectral functions are obtained via a Kramers-Kronig transformation,

$$\text{Re } \mathcal{G}(\omega) = \frac{1}{\pi} \mathcal{P} \int_{-\infty}^{\infty} dx \frac{\text{Im } \mathcal{G}(x)}{x - \omega}, \quad (2.20)$$

considering that spectral functions are of the form $\mathcal{A} = -\frac{1}{\pi} \text{Im } \mathcal{G}$.

Discarded weight. In the iterative RG procedure of NRG high energy states are discarded, introducing an error in the treatment of the low-energy spectrum. The convergence of fdmNRG with a given truncation threshold and discretization parameter, Λ , can be analyzed in terms of the estimated discarded weight, $\delta\rho_{\text{disc}}$: as with DMRG, the decay of the eigenspectrum of site-specific reduced density matrices, built from the ground state space of later iterations, can be used as a quantitative (a posteriori) measure of the convergence (cf. Ref. [Wei11] for details). In Sec. 2.3, we show that a modified approach to the discarded weight, which quantifies the contributions of high-lying energy eigenstates to reduced density matrices, rather than analyzing the eigenspectrum of the reduced density matrices, is more flexible and allows a direct comparison of $\delta\rho_{\text{disc}}$ for distinct Λ and between different models.

Very recently, an adaptive broadening scheme was developed [LW16], increasing the resolution of spectral data at large frequencies, thus allowing high-resolution DMFT+NRG [LvDW17]. Further, also non-diagonal hybridization functions can be handled now. However, these advancements have not yet been employed within this thesis.

Merits of fdmNRG as DMFT impurity solver. Being the gold standard for quantum impurity models, (fdm)NRG has developed to a state-of-the art *real*-frequency impurity solver for *multi*-band DMFT applications, which offers a number of advantages over other solvers such as QMC or ED.

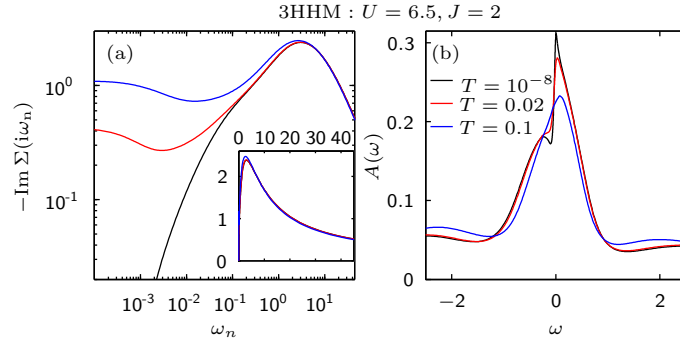


Figure 2.3 (a) Matsubara self-energy, $\text{Im} \Sigma(i\omega_n)$, plotted on a logarithmic imaginary-frequency scale for different temperatures for the 3HHM with $U = 6.5$, and $J = 2$. The inset shows the same data on a linear scale. (b) Corresponding spectral functions, $A(\omega)$, plotted versus linearly scaled *real* frequencies.

- (i) (fdm)NRG has an exponentially enhanced resolution around the Fermi level. Thus, spectral features are resolved down to the lowest relevant energy scale of the system. The Friedel sum rule and Luttinger pinning within DMFT are fulfilled to very high accuracies (cf. Sec. 3.10).
- (ii) fdmNRG works equally reliable with comparable computational costs at zero and arbitrary finite temperatures, and also for arbitrary impurity fillings, arbitrary interaction strengths, etc.
- (iii) fdmNRG provides high-quality correlation functions directly on the real-frequency axis without analytical continuation. The availability of numerically exact real-frequency data considerably facilitates the physical interpretation of DMFT results as compared to results on the imaginary Matsubara frequency axis. This is illustrated in Fig. 2.3: while the zero-temperature result of $A(\omega)$ (black) [cf. Eq. (3.7)] of the 3HHM exhibits a tiny shoulder in the QPP [cf. Fig. 2.3(b)], which dissolves with increasing temperature, the Matsubara self-energy, $\text{Im} \Sigma(i\omega_n)$ [cf. Eq. (3.13)] is rather unstructured [cf. Fig. 2.3(a)], especially when plotted on a linear scale [cf. inset of Fig. 2.3(a)].
- (iv) Renormalization group flow diagrams unambiguously reveal the relevant physics at all energy scales.
- (v) A stable implementation of Zitko's discretization scheme [vP09, Ž09] ensures a reliable approximation of the frequency-dependent bath of the self-consistent impurity model in DMFT+NRG applications.

For inherent limitations of NRG (computational costs increase exponentially with the number of particle flavors; NRG has a poor spectral resolution at high energies) remedies were provided recently, reducing these problems:

- (vi) fdmNRG is implemented in the QSpace tensor library [Wei12a] which allows to exploit all abelian and non-abelian symmetries of the impurity system, considerably reducing numerical costs in the case of high-symmetry models.
- (vii) For low-symmetry models, iNRG [MGWF⁺14, SMvDW16] can be used (cf. Sec. 2.3 for details).
- (viii) The high-energy spectral resolution is improved by an adaptive broadening scheme [LW16].

We remark that besides fdmNRG also DMRG [WMPs14, WMS14, BWM⁺15, WGM⁺15, NnFH17, NnFKH18, NnFH18] is a viable real-frequency multi-band impurity solver. Most importantly, in contrast to NRG, DMRG shows no exponential growth of the local Hilbert space with the number of flavors. In particular, DMFT+DMRG is very powerful for studying ground state properties. However, with a focus on both frequency and temperature dependence, we want to put fdmNRG as DMFT impurity solver to the proof within this thesis.

2.3 Interleaved numerical renormalization group (iNRG)

2.3.1 Overview

The major bottleneck of NRG (and also other methods that need to deal with the fully interacting quantum many-body state space) is the exponential scaling of its numerical costs with the number of flavors. This strongly limits a broad application of NRG to multi-band impurity setups. The underlying reason for the exponential scaling is easily identified.

Let us consider a multi-flavor impurity model with m different flavors, for instance $m = 2N_c$ for N_c spinful bands. In the standard NRG (sNRG) procedure (cf. Sec. 2.2.2), each of the m conduction bands is discretized equally and then mapped onto a Wilson chain, that consequently consists of m identical subchains. One “supersite” of the full Wilson chain is thus composed of m subsites corresponding to different flavors, respectively. Within the iterative RG process of solving the full Wilson chain, in principle, at each step an A-matrix of size $N_{\text{tot}} = N_K \times d_{\text{loc}}$ has to be diagonalized, when N_K states are kept along the chain and d_{loc} additional local quantum degrees of freedom couple into the system. N_K determines the accuracy and N_{tot} the numerical costs of NRG (the time and memory for matrix diagonalization scale as $\propto N_{\text{tot}}^3$ and $\propto N_{\text{tot}}^2$, respectively). In sNRG, $d_{\text{loc}}^{\text{sNRG}} = d_f^m$ with $d_f = 2$ for fermionic flavors. This obviously leads to an exponential increase of the numerical costs with m (together with the fact that also $N_K = N_K^{(m)}$ scales exponentially with the complexity of the many-body problem, cf. below), limiting brute-force NRG implementations to maximally two spinful channels.

For highly symmetric multi-band models, effective matrix sizes and thus numerical costs can be dramatically lowered by using fdmNRG based on the QSpace tensor library (cf. Sec. 2.2.4), which allows to exploit all abelian and, importantly, non-abelian symmetries of a given system. Matrix diagonalization, for example, is then only performed in the reduced multiplet space. This has made multi-band calculations feasible, as demonstrated for the 3HHM in this thesis. However, if symmetries are broken, the numerical expense of sNRG increases rapidly, making sNRG for settings, that are accessible in the presence of symmetries, essentially out of reach for broken symmetries.

In this section we present a recently developed new NRG scheme, called “interleaved” NRG (iNRG) [MGWF⁺14], which enables an efficient treatment of both low-symmetry and high-symmetry multi-band models, and map out its potential as an alternative to sNRG in our article entitled “Interleaved numerical renormalization group as an efficient multiband impurity solver” [SMvDW16].

The key idea of iNRG is to introduce an additional energy-scale separation between all subsites associated with the same supersite, i.e. to “interleave” the Wilson subchains of different flavors to form a m times longer “generalized” Wilson chain with a reduced local state space dimension $d_{\text{loc}}^{\text{iNRG}} = d_f$. This is achieved by modifying the discretization scheme: the logarithmic grid is slightly shifted between conduction bands of different electronic flavors, artificially breaking the flavour symmetry if present. Diagonalization and truncation in iNRG is then performed separately after addition of each electron flavor. In summary, this more fine-

grained RG scheme dramatically reduces numerical costs. For instance, computation times are smaller by a factor of order $(N_{\text{tot}}^{\text{sNRG}}/N_{\text{tot}}^{\text{iNRG}})^3 = d_f^{3(m-1)}$ (for $N_K^{\text{sNRG}} = N_K^{\text{iNRG}} = N_K$).

However, in Ref. [MGWF⁺14], it was originally assumed that the additional truncation steps in iNRG reduce its accuracy. In this article, we demonstrate that, remarkably, *iNRG yields results of comparable accuracy to sNRG, but at dramatically reduced numerical costs if symmetries are broken.*

We systematically examine and compare the accuracy and efficiency of iNRG and sNRG in the context of the single impurity Anderson model, the two-channel Kondo model, and a three-channel Anderson-Hund model. We explore different ways of interleaving the electronic flavors in iNRG, and test different symmetry settings in iNRG and sNRG. We perform iNRG and sNRG calculations for equivalent settings, i.e. we use a comparable discretization, parametrized by Λ , to achieve the same energy-scale separation between supersites in iNRG and sNRG; we keep (on average) the same number of kept states, $N_K^{\text{iNRG}} \approx N_K^{\text{sNRG}} \equiv N_K$; and exploit the same symmetries. In addition, we also run sNRG calculations with full model symmetries.

To be able to perform a reliable comparison between iNRG and sNRG,

- we define the truncation energy in iNRG, such that, on average, iNRG and sNRG calculations with the “same” truncation energy lead to similar N_K ;
- we introduce a more reliable definition of the discarded weight, $\delta\rho_{\text{disc}}$ (cf. Sec. 2.2.4), which quantifies the contributions of high-lying energy eigenstates to reduced density matrices, rather than analyzing the eigenspectrum of the reduced density matrices as in Ref. [Wei11] (this allows to compare the convergence properties for different Λ and between different models);
- we present an efficient tuning protocol to restore channel symmetries, which are broken artificially in iNRG, which is important in the vicinity of a quantum critical point, such as in the case of the symmetric two-channel Kondo model.

Our main results are summarized in the following.

1. Using equivalent settings, we obtain, for a given model,
 - the *same NRG convergence for iNRG and sNRG*, which is estimated in terms of the discarded weight, $\delta\rho_{\text{disc}}$,
 - the *same accuracy for iNRG and sNRG*, which is monitored by the deviation of calculated physical quantities from certain exact results (such as the Friedel sum rule), but
 - *much lower computational costs for iNRG than sNRG*, which are tracked in terms of CPU times. This is achieved by removing the exponential scaling with m in the local state space, as present for sNRG, in iNRG: $d_{\text{loc}}^{\text{sNRG}} = d_f^m$ whereas $d_{\text{loc}}^{\text{iNRG}} = d_f$.
2. However, we show that *the kept states $N_K = N_K^{(m)}$ scale roughly exponentially with m for both iNRG and sNRG*, reflecting the inherent complexity of the many-body problem.
3. When comparing the best sNRG calculation, exploiting full model symmetries, to the most efficient iNRG calculation, where certain flavor symmetries are broken, we observe a similar performance.

We therefore conclude that, for low-symmetry models iNRG clearly outperforms sNRG in terms of efficiency. Moreover, iNRG can be used to solve a range of lower-symmetry

multi-band models that are inaccessible to sNRG. But also for high-symmetry models, iNRG is a viable and technically simple alternative to sNRG. In practice, optimal efficiency is often reached by a hybrid method, i.e. by interleaving the Wilson chains of some flavors while exploiting the symmetries of the remaining ones.

Importantly, iNRG can now be employed as impurity solver for DMFT, considerably extending the scope of DMFT+NRG for multi-band applications, including models with crystal-field splitting, realistic material simulations using DFT+DMFT+iNRG [KLK⁺19], or cluster extensions of DMFT [Gle19]. Even four-band impurity models are within reach. We remark however that, within this thesis, we only applied sNRG as impurity solver for DMFT.

Interleaved numerical renormalization group as an efficient multiband impurity solver

by

K. M. Stadler,¹ A. K. Mitchell,² J. von Delft,¹ and A. Weichselbaum¹

¹Physics Department, Arnold Sommerfeld Center for Theoretical Physics and Center for NanoScience, Ludwig-Maximilians-Universität München, 80333 München, Germany

²Institute for Theoretical Physics, Utrecht University, Leuvenlaan 4, 3584 CE Utrecht, The Netherlands

reprinted on pages [33–48](#)

with permission from

Phys. Rev. B **93**(4), 235101 (2016),

DOI: [10.1103/PhysRevB.93.235101](https://doi.org/10.1103/PhysRevB.93.235101).

© 2016 American Physical Society

Interleaved numerical renormalization group as an efficient multiband impurity solverK. M. Stadler,¹ A. K. Mitchell,² J. von Delft,^{1,*} and A. Weichselbaum¹¹*Physics Department, Arnold Sommerfeld Center for Theoretical Physics and Center for NanoScience, Ludwig-Maximilians-Universität München, 80333 München, Germany*²*Institute for Theoretical Physics, Utrecht University, Leuvenlaan 4, 3584 CE Utrecht, The Netherlands*

(Received 12 February 2016; revised manuscript received 24 March 2016; published 1 June 2016)

Quantum impurity problems can be solved using the numerical renormalization group (NRG), which involves discretizing the free conduction electron system and mapping to a “Wilson chain.” It was shown recently that Wilson chains for different electronic species can be interleaved by use of a modified discretization, dramatically increasing the numerical efficiency of the RG scheme [Phys. Rev. B **89**, 121105(R) (2014)]. Here we systematically examine the accuracy and efficiency of the “interleaved” NRG (iNRG) method in the context of the single impurity Anderson model, the two-channel Kondo model, and a three-channel Anderson-Hund model. The performance of iNRG is explicitly compared with “standard” NRG (sNRG): when the average number of states kept per iteration is the same in both calculations, the accuracy of iNRG is equivalent to that of sNRG but the computational costs are significantly lower in iNRG when the same symmetries are exploited. Although iNRG weakly breaks $SU(N)$ channel symmetry (if present), both accuracy and numerical cost are entirely competitive with sNRG exploiting full symmetries. iNRG is therefore shown to be a viable and technically simple alternative to sNRG for high-symmetry models. Moreover, iNRG can be used to solve a range of lower-symmetry multiband problems that are inaccessible to sNRG.

DOI: [10.1103/PhysRevB.93.235101](https://doi.org/10.1103/PhysRevB.93.235101)**I. INTRODUCTION AND MOTIVATION**

Quantum impurity problems are relevant to a range of physical phenomena in which strong electron correlations play a key role [1]. They describe a generic class of systems comprising a few interacting degrees of freedom coupled to a continuum bath of noninteracting conduction electrons. The Kondo model [2] is the simplest exemplar, featuring a single spin- $\frac{1}{2}$ “impurity” coupled to a single spinful conduction electron channel. The basic physics can be understood within the renormalization group (RG) framework: the effective impurity-bath coupling grows as the temperature/energy scale is reduced. The RG flow from weak to strong coupling is characterized by the Kondo temperature T_K , which sets the scale for onset of strong coupling physics and the dynamical screening of the impurity spin by conduction electrons [1].

A detailed understanding of this problem was first obtained using Wilson’s numerical renormalization group (NRG) [3–5]. The method involves discretization of the conduction electron Hamiltonian, and mapping to a 1D tight-binding Wilson chain. The transformation is defined so that the interacting impurity subsystem couples to one end of the noninteracting Wilson chain. A special form of the discretization is used that ensures exponential decay of hopping matrix elements down the chain [3]. This energy-scale separation justifies an RG scheme based on successive diagonalization and truncation, starting at the impurity subsystem and working down the chain. At each step, a Wilson shell with d_{loc} additional local quantum degrees of freedom couples into the system, but only the lowest N_K eigenstates of the enlarged state space are kept after diagonalization. This scheme ensures that the Fock space of kept states does not increase exponentially with chain length,

and allows the physics to be investigated at successively lower energies.

The computational costs of using NRG scale *exponentially* with the number of fermionic bands (distinct flavors), m , involved in the quantum impurity model. The power and applicability of NRG would be greatly improved if these numerical costs could be reduced, since *multiflavor* quantum impurity problems appear in a wide range of contexts. For example, iron impurities in gold are described by a spin- $\frac{3}{2}$ three-channel Kondo model [6,7]; multiple impurities separated in real space [8,9] or manipulated by STM [10] necessitate a multichannel description, as do magnetic nanostructures [11]; single carbon nanotube quantum dots display entangled spin-orbital $SU(4)$ Kondo physics [12], while certain nanotube double dot [13] and multilead semiconductor coupled dot devices [14–16] are described by generalized two-channel models; and nanowire/superconductor heterostructures hosting lead-coupled Majorana fermions give rise to effective multichannel topological Kondo models [17,18]. Furthermore, quantum impurity problems appear as effective local models within dynamical mean-field theory (DMFT) for correlated materials. Multiorbital/band lattice models map to generalized multichannel impurity problems [19–21], and in cluster extensions of DMFT, the number of bands of the effective impurity model scales with the number of cluster sites [22].

There is thus much incentive to improve the efficiency of NRG when dealing with multiflavor models. The present paper aims to make a contribution towards this goal, by offering a detailed analysis of a recently-proposed scheme of “interleaving” the Wilson chains for different fermion flavors [23]. Having a purely methodological focus, it is based on well-studied physical models and is particularly addressed at a readership of NRG practitioners. New physical applications of iNRG are left for follow-up projects.

To set the scene, we first briefly summarize why the numerical costs of NRG scale exponentially with m . For a

*Corresponding author: vondelft@lmu.de

given conduction electron discretization, the *accuracy* of the calculation is controlled by the number of states *retained* or *kept* at each step of the iterative RG scheme, N_K . On the other hand, the computational *cost* of an NRG run is controlled by the *total size* of the Hilbert space to be diagonalized at each step, $N_{\text{tot}} = N_K \times d_{\text{loc}}$, which is the tensor product of the space of states retained from the previous iteration (of dimension N_K), and the state space of a newly added Wilson shell (of dimension d_{loc}). The computational time for matrix diagonalization scales as N_{tot}^3 , while the memory required scales as N_{tot}^2 . In Wilson's original "standard" NRG formulation [3] (sNRG), the local dimension for a system with m distinct fermionic flavors scales exponentially in m , $d_{\text{loc}}^{\text{sNRG}} = d_f^m$, with d_f the state space dimension of a single flavor. For a single fermionic level, it follows that $d_f = 2$, since it can be either occupied or unoccupied. Commonly, quantum impurity models involve N_c channels of *spinful* conduction electrons. In this case, $m = 2N_c$, such that $d_{\text{loc}}^{\text{sNRG}} = 4^{N_c}$.

In fact, as the number m of flavors increases, the number N_K of states kept at each step of an NRG calculation must also be increased to maintain the same accuracy (i.e., the same degree of numerical convergence). We find that for converged sNRG calculations, N_K scales roughly exponentially with the number of flavors, which we will indicate by writing $N_K \equiv N_K^{(m)}$. This scaling property is demonstrated explicitly in this paper.

Overall then, N_{tot} depends exponentially on m through both N_K and d_{loc} in sNRG:

$$N_{\text{tot}}^{\text{sNRG}} = N_K^{(m)} \times d_f^m. \quad (1)$$

This exponential scaling imposes severe limitations on the applicability of sNRG to treat quantum impurity problems with several conduction electron channels. In practice, unless large symmetries can be exploited, sNRG cannot be used for problems with more than two spinful channels.

Two approaches have been developed to improve the efficiency of NRG applied to multichannel quantum impurity models. One approach exploits non-Abelian symmetries if present: diagonalization of the NRG Hamiltonian at each step can then be done in *multiplet* space rather than state space, significantly reducing the matrix sizes and hence computational cost.

From the very first sNRG studies of the Anderson impurity model [4], it was essential to exploit the SU(2) spin symmetry so that the calculations could be performed with the limited computational resources available at that time. In Ref. [24], the use of SU(2) symmetries was incorporated into the framework of the density-matrix (DM) NRG [25] to obtain dynamical results for a symmetric two-channel model. Finally, a generalized and flexible framework was pioneered in Ref. [26], which now allows much larger symmetries to be handled, including arbitrary non-Abelian symmetries. The precise gain in computational efficiency with this scheme naturally depends on the specific model and its symmetries; its scope of application is of course limited when symmetry-breaking perturbations (such as a magnetic field) are present.

A second, very different strategy has recently been proposed in Ref. [23]. This "interleaved" NRG (iNRG) method, described in detail in Sec. II, introduces slightly different discretization schemes for conduction bands of different

electronic flavors, leading to inequivalent Wilson chains (even for flavors related by symmetries of the bare model). For m electronic flavors, the m Wilson chains are interleaved to form a single generalized Wilson chain [23], which still has the required property of exponential energy-scale separation down the chain. The diagonalization and truncation step in iNRG is then done *separately* after addition of *each* electron flavor, rather than after addition of the entire "shell" of m flavors, as in sNRG. In practice, we specify the truncation threshold not by fixing the number of states to be kept, but by fixing a truncation energy: all states with higher energies are discarded at every step.

Full interleaving leads to a reduction of the local state space from $d_{\text{loc}}^{\text{sNRG}} = d_f^m$ in sNRG to $d_{\text{loc}}^{\text{iNRG}} = d_f$ in iNRG, independent of m . However, it also raises the question as to whether the truncation energy required to reach accurate, well-converged results needs to be changed when switching from sNRG to iNRG. One of the main conclusions of the present paper is that it essentially does not change: an extensive comparison of iNRG and sNRG results, obtained using comparable discretization settings and exploiting the same symmetries for both methods, shows that results of comparable accuracy are obtained if on average the "same" truncation energy is used (see Sec. IIC for a detailed discussion). Moreover, this implies that the number of states kept at a given step is the same, on average, for both methods:

$$N_K^{\text{iNRG}} \simeq N_K^{\text{sNRG}} \equiv N_K^{(m)}. \quad (2)$$

We find that $N_K^{(m)}$ still depends exponentially on m , as for sNRG. Thus, for iNRG, the computational costs are governed by

$$N_{\text{tot}}^{\text{iNRG}} = N_K^{(m)} \times d_f, \quad (3)$$

where the first factor $N_K^{(m)}$ is essentially the same as that in Eq. (1) for $N_{\text{tot}}^{\text{sNRG}}$. However, the exponential dependence of d_{loc} on m in the second factor is entirely eliminated in iNRG.

As a result, when equivalent settings are used for both methods, iNRG yields results of comparable accuracy as sNRG at dramatically reduced numerical cost: computation times are smaller by a factor of order $(N_{\text{tot}}^{\text{sNRG}}/N_{\text{tot}}^{\text{iNRG}})^3 = d_f^{3(m-1)}$, and the required storage resources are smaller by a factor of order $d_f^{2(m-1)}$.

Although d_{loc} is smaller in iNRG than sNRG, an additional minor cost is incurred in iNRG because the interleaved Wilson chain is m times longer than the standard Wilson chain (resulting in an additional *linear* increase in overall computation time with m). Furthermore, fine tuning of bare parameters is also necessary for effective restoration of broken symmetries in cases where flavor symmetry-breaking is a relevant perturbation, requiring multiple iNRG runs (the exponentially rapid convergence in the number of runs is discussed in Sec. IVE).

The conclusions summarized above are established in this paper by a direct comparison of iNRG and sNRG for several symmetric quantum impurity problems (specified in Sec. III) with $N_c = 1, 2, \text{ and } 3$ spinful conduction electron channels. Within iNRG, we explore different ways of interleaving the electronic flavors, and exploit all symmetries that remain after interleaving. For each such iNRG calculation, we perform a

corresponding sNRG calculation using the same symmetries, a comparable discretization choice, and the same average truncation energies, i.e., we adopt “equivalent settings.” Moreover, for each model, we also perform a set of benchmark calculations exploiting the *full* symmetries of the bare model, serving as an absolute reference.

Our iNRG-sNRG comparison for equivalent settings focuses particularly on comparing their *efficiency* (Sec. IV C) and their *accuracy* (Sec. IV D). We determine efficiency by tracking representative CPU times. We gauge accuracy in two ways: (i) deviations of numerically computed physical quantities from certain exact results yield an absolute measure of the accuracy of both methods; (ii) the discarded weight [27] estimates the degree of numerical convergence of a given NRG run (see also Sec. II D).

It may be surprising at first that the accuracy of iNRG and sNRG are equivalent when using equivalent settings, since iNRG involves significantly more truncation steps. This result can, however, be rationalized by noting that the truncation at each step of iNRG is less severe than in sNRG (fewer states are discarded at any given step), producing a more fine-grained RG description. For equivalent settings, iNRG clearly outperforms sNRG in terms of efficiency because the state space diagonalized at each step is much smaller in iNRG. In fact, for the high-symmetry multiband models studied here, iNRG is absolutely competitive even when compared to sNRG calculations that exploit the *full* symmetry of the model.

This finding greatly increases the scope of possibilities available for NRG treatments of multiband impurity models. For models with high symmetries, *both* sNRG and iNRG can be highly efficient methods. In such cases, iNRG is a viable and technically simple alternative to sNRG. For models having lower symmetries (for example, when a magnetic field is applied, particle-hole symmetry is broken, or other channel anisotropies are present), iNRG has a clear advantage over sNRG.

In a pure renormalization group (RG) sense, the artificial symmetry breaking, of course, is clearly also visible in the resulting energy flow diagrams derived from finite-size spectra [3–5]. There, a full RG step, which in sNRG requires two iterations (e.g., to get from one even site to the next even site), now requires $2m$ iNRG steps. Nevertheless, aside from possible fine-tuning as discussed in Sec. IV E, this does not affect the energy scales of different phases (fixed points) [23] nor does it affect thermodynamical physical quantities of the model of interest.

II. METHODS

The Hamiltonian of quantum impurity models has the form

$$\hat{H} = \hat{H}_{\text{imp}} + \hat{H}_{\text{cpl}}(\{\hat{f}_{0\nu}\}) + \hat{H}_{\text{bath}}. \quad (4)$$

It describes an interacting “impurity” subsystem, \hat{H}_{imp} , coupled by $\hat{H}_{\text{cpl}}(\{\hat{f}_{0\nu}\})$ to a bath of noninteracting conduction electrons,

$$\hat{H}_{\text{bath}} = \sum_{\nu=1}^m \sum_k \varepsilon_{k\nu} \hat{c}_{k\nu}^\dagger \hat{c}_{k\nu}, \quad (5)$$

where $\nu = 1, \dots, m$ labels the m distinct electron flavors, and $\hat{c}_{k\nu}^\dagger$ creates an electron with a given flavor ν and momentum k at energy $\varepsilon_{k\nu} \in [-D_\nu, D_\nu]$. The impurity is taken to be located at real-space site $\mathbf{r} = 0$, and coupled to local bath sites $\hat{f}_{0\nu} = V_\nu^{-1} \sum_k V_{k\nu} \hat{c}_{k\nu}$, with the normalization factor $|V_\nu|^2 = \sum_k |V_{k\nu}|^2$. The density of bath states with flavor ν at the impurity position is then given by $\rho_\nu(\omega) = \sum_k |V_{k\nu}/V_\nu|^2 \delta(\omega - \varepsilon_{k\nu})$, defined inside a band of half-width D_ν . We assume constant (momentum-independent) couplings for which the density of bath states simplifies to a box function, $\rho_\nu(\omega) = \Theta(\omega - |\varepsilon|)/(2D_\nu)$. When N_c channels of spinful conduction electrons are involved, $\nu \equiv (\alpha, \sigma)$, where $\alpha \in \{1, \dots, N_c\}$ labels channels and $\sigma \in \{\uparrow, \downarrow\}$ labels spins.

A. Standard Wilson chains

Within sNRG, \hat{H}_{bath} is discretized and mapped onto a 1D tight-binding Wilson chain [3], consisting of m identical “subchains,” one for each flavor. The subchains are constructed as follows: first, each band $\rho_\nu(\omega)$ is divided up into energy intervals with exponentially reducing width. The discretization points are given by

$$\varepsilon_{n\nu}^\pm(z) = \begin{cases} \pm D_\nu & n = 0, \\ \pm D_\nu \Lambda^{-n+z_\nu} & n = 1, 2, \dots, \end{cases} \quad (6)$$

where $\Lambda > 1$ is a dimensionless discretization parameter, and $z_\nu \in [0, 1[$ (defined modulo 1) is a continuous “twist” parameter that shifts the discretization points. Conventionally, the twist parameter is applied symmetrically to all electronic flavors by choosing $z_\nu \equiv z$. If desired, results of N_c separate NRG runs with uniformly distributed z can be averaged to remove certain discretization artifacts [28,29].

A discretized version of the continuous spectrum $\rho_\nu(\omega)$ is obtained by replacing the electron density in each interval by a single pole of the same total weight,

$$\rho_\nu^{\text{disc}}(\omega, z) = \sum_{n=0}^{\infty} \sum_{\lambda=\pm} \gamma_{n\nu}^\lambda(z) \delta(\omega - \xi_{n\nu}^\lambda(z)), \quad (7)$$

where $\gamma_{n\nu}^\lambda(z) = \int_{\varepsilon_{n+1,\nu}^\lambda(z)}^{\varepsilon_{n\nu}^\lambda(z)} d\omega \rho_\nu(\omega)$ gives the pole weights. The pole positions, $\xi_{n\nu}^\lambda(z)$, are determined from a differential equation introduced in Ref. [30], which is based on the condition that the original (continuous) bath density of states is reproduced exactly in the limit $N_c \rightarrow \infty$ after z averaging, $\rho_\nu(\omega) = \int_0^1 dz \rho_\nu^{\text{disc}}(\omega, z)$. For constant density of states, we use

$$\gamma_{n\nu}^\lambda(z) = D_\nu \begin{cases} 1 - \Lambda^{z-1} & n = 0 \\ \left(1 - \frac{1}{\Lambda}\right) \Lambda^{-n+z} & n = 1, 2, \dots \end{cases}, \quad (8a)$$

$$\xi_{n\nu}^\lambda(z) = \lambda \frac{\gamma_{n\nu}^\lambda(z)}{\ln \Lambda} \begin{cases} +z & n = 0 \\ 1 & n = 1, 2, \dots \end{cases}. \quad (8b)$$

The Wilson subchain for flavor ν is defined uniquely [3] as the semi-infinite 1D tight-binding chain that reproduces the discretized density of states $\rho_\nu^{\text{disc}}(\omega)$ at the terminal site. The discretized bath is represented by the sum of all m Wilson subchains, which together form the “full” Wilson chain, with Hamiltonian

$$\hat{H}_{\text{bath}}^{\text{disc}} = \sum_{\nu=1}^m \sum_{n=0}^{\infty} [(t_{n\nu} f_{n,\nu}^\dagger f_{n+1,\nu} + \text{H.c.}) + \varepsilon_{n\nu} f_{n,\nu}^\dagger f_{n,\nu}], \quad (9)$$

The Wilson chain coefficients t_{nv} and ε_{nv} are obtained in practice by Lanczos tridiagonalization [5] [in contrast to the index k in Eq. (5), n refers to sites of the Wilson chain].

Importantly, due to the logarithmic discretization, the hopping matrix elements decay exponentially along each subchain [3],

$$t_{nv}/D_\nu \sim \Lambda^{z_\nu - n/2}, \quad (10)$$

for $n \gg 1$, and as such depend on NRG discretization parameters Λ and z_ν . For equal bandwidths $D_\nu \equiv D$ and constant $z_\nu \equiv z$, there is an energy-scale separation between sites with different n ,

$$t_{n+1,\nu}/t_{nv} \stackrel{\text{sNRG}}{\sim} \Lambda^{-1/2}. \quad (11)$$

However, since the subchains are identical for sNRG, there is no scale separation between different flavors with the same site index n . Together, these flavors form “supersite” n of the full Wilson chain: they all have the *same* characteristic energy scale

$$\omega_n = a\Lambda^{-n/2}, \quad (12)$$

(the constant a is chosen such that the rescaled hoppings $t_{n-1}/\omega_n \rightarrow 1$ as $n \rightarrow \infty$). As a consequence, all m subsites of supersite n must be treated equivalently in a single step in sNRG.

The discretized model Hamiltonian in Eqs. (4) and (9) is diagonalized iteratively [3], starting at the impurity and working down the chain in sNRG by adding an entire supersite at each iteration n . The energy-scale separation embodied by Eq. (11) justifies truncation at each step: the lowest N_K states are kept, forming a Wilson “supershell,” and the remaining $N_K \times (d_f^m - 1)$ states are discarded. If the eigenenergies E_n of supershell n are given in units of ω_n (“rescaled units”), the typical level spacing of the lowest-lying levels is of order 1.

B. Interleaved Wilson chains

We now turn to the iNRG method, introduced in Ref. [23]. Its key idea is to modify the discretization scheme in such a way that energy-scale separation is achieved between all subsites associated with the same supersite, as well as between different supersites. The subsites from different subchains can then be interleaved in a linear sequence, labeled by $\tilde{n} \equiv (n, \nu) = mn + (\nu - 1) = 0, 1, 2, \dots$ to form a single interleaved Wilson chain, m times longer than the corresponding standard Wilson chain [compare Figs. 1(a) and 1(b)]. The hopping matrix element $\tilde{t}_{\tilde{n}} = \tilde{t}_{(n,\nu)}$ describes hopping between subsites of the same flavor ν in adjacent supersites n and $n+1$. For $m > 1$, there is thus no “nearest-neighbor” hopping on the Wilson chain as in sNRG. Importantly, $\tilde{t}_{\tilde{n}}$ progressively decreases as \tilde{n} increases. To ensure a net rate of decrease equivalent to that of a standard Wilson chain going from one supersite to the next [see Eq. (11)], we have $\tilde{t}_{\tilde{n}+m}/\tilde{t}_{\tilde{n}} \propto \Lambda^{-1/2}$. Moreover, to achieve *uniform* energy-scale separation along the interleaved chain, this decrease should occur uniformly from one subsite to the next [see Fig. 1(d)], with $\tilde{t}_{\tilde{n}+1}/\tilde{t}_{\tilde{n}} \propto \Lambda^{-1/(2m)}$. By contrast, sNRG amounts to keeping $\tilde{t}_{\tilde{n}}$ constant for all m subsites associated with the same supersite [see Fig. 1(c)]. The above behavior of $\tilde{t}_{\tilde{n}}$ can be achieved by choosing the twist parameter z_ν differently for each conduction electron flavor ν , namely

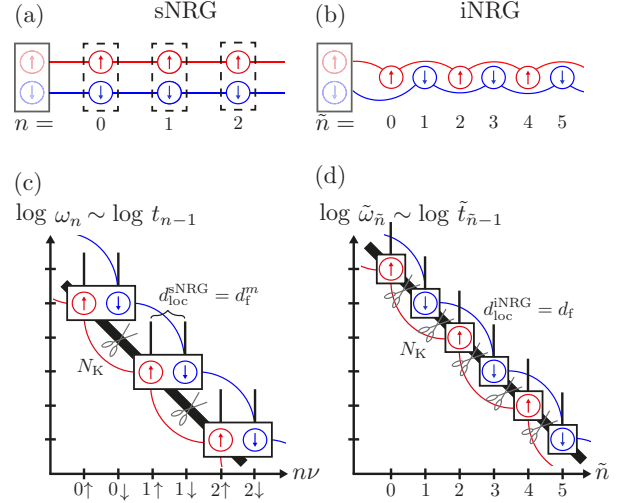


FIG. 1. Schematic illustration of standard (left) and interleaved (right) Wilson chains, for a spinful single-channel model ($m = 2$). (a) In sNRG, subsites for spin up (red) and spin down (blue) are grouped into supersites (indicated by dashed boxes), which are connected by nearest-neighbor hopping (thin lines). (b) In iNRG, subsites are interleaved in linear fashion and hopping occurs between next-nearest neighbors. n labels sNRG supersites, while \tilde{n} labels iNRG subsites. (c) and (d) Depictions of the MPS-structure used for sNRG and iNRG: boxes represent MPS tensors, vertical thin legs represent local state spaces of dimension d_f , and thick diagonal lines represent the state spaces obtained after diagonalizing a Wilson shell and discarding all but the lowest N_K states (the truncation process is indicated by scissors). The matrix size to be diagonalized is reduced from $N_{\text{tot}}^{\text{sNRG}} = N_K \times d_f^m$ in sNRG to $N_{\text{tot}}^{\text{iNRG}} = N_K \times d_f$ in iNRG. The vertical positions of the boxes reflect, on a logarithmic scale, the characteristic energies ω_n (sNRG) and $\tilde{\omega}_{\tilde{n}}$ (iNRG) of each shell. The additional energy-scale separation within each supershell justifies the additional truncations in iNRG.

$z_{\nu+1} = z_\nu - 1/(2m)$. This leads to

$$\frac{\tilde{t}_{\tilde{n}+1}}{\tilde{t}_{\tilde{n}}} = \frac{\tilde{t}_{n,\nu+1}}{\tilde{t}_{nv}} \stackrel{\text{iNRG}}{\sim} \Lambda^{-1/(2m)} \equiv \tilde{\Lambda}^{-1/2}, \quad (13)$$

with $\tilde{t}_{n,m+1} = \tilde{t}_{n+1,1}$. Evidently, the effective discretization parameter for iNRG is smaller than for sNRG, namely $\tilde{\Lambda} \equiv \Lambda^{1/m}$, thus generating scale separation from subsite to subsite within a supersite. We choose $z_m = z$, such that $\tilde{t}_{(n,m)} = t_n$, i.e., the iNRG hopping matrix element of the last ($\nu = m$) subsite of supersite n is identical to the sNRG hopping matrix element for that supersite. Correspondingly, the characteristic energy scale for subsite \tilde{n} of the interleaved Wilson chain is now

$$\tilde{\omega}_{\tilde{n}} = \tilde{a} \tilde{\Lambda}^{-\tilde{n}/2} = a \tilde{\Lambda}^{-(m(n-1)+\nu)/2}, \quad (14)$$

where the requirement $\tilde{\omega}_{(n,m)} = \omega_n$ (which follows from $\tilde{t}_{(n,m)} = t_n$) fixes the prefactor as $\tilde{a} = a \tilde{\Lambda}^{(m-1)/2}$.

Scale separation *within* a given Wilson shell n is exploited in iNRG by performing a truncation after the addition of each new subsite (rather than only after an entire supersite of m subsites has been added, as in sNRG). With a local state space of $d_{\text{loc}}^{\text{iNRG}} = d_f$, at each step N_K states are kept (forming a

Wilson subshell), and $N_K \times (d_f - 1)$ ($= N_K$ for $d_f = 2$) states are discarded.

If the eigenenergies $\tilde{E}_{\tilde{n}}$ of iNRG subshell \tilde{n} are measured in rescaled units of $\tilde{\omega}_{\tilde{n}}$, the spacing of the lowest-lying levels is again of order 1. In absolute units, however, the level spacing in iNRG scales as the m th root compared with sNRG, because the m subsites are added asymmetrically (one by one with different hopping matrix elements) in iNRG, implying m times more iteration steps that lift level degeneracies. iNRG therefore constitutes a more fine-grained RG scheme, as illustrated in Fig. 7 (compare the faint red and blue lines).

C. Truncation energy

In practice, the value of N_K needed to reach a specified degree of accuracy depends sensitively on the specific physical model Hamiltonian, discretization scheme, and energy regime. This type of dependence of the accuracy on various details can be circumvented by using an *energy-based* truncation strategy [27], which we also adopt in this paper: for a given NRG calculation, we specify a fixed, dimensionless truncation energy, to be called $E_{\text{trunc}}^{\text{sNRG}}$ or $E_{\text{trunc}}^{\text{iNRG}}$, and keep only those states whose absolute (not rescaled) energies lie below $E_{\text{abs-trunc}}^{\text{sNRG}} = E_{\text{trunc}}^{\text{sNRG}} \times \omega_n$ at iteration n of an sNRG calculation, or below $E_{\text{abs-trunc}}^{\text{iNRG}} = E_{\text{trunc}}^{\text{iNRG}} \times \tilde{\omega}_{\tilde{n}}$ at iteration \tilde{n} of an iNRG calculation. Using this energy-based truncation scheme, N_K becomes a *dynamical* parameter that changes from iteration to iteration in a given NRG run, in a way that depends on E_{trunc} , Λ , and details of the particular model under consideration (Fig. 3 below shows an example of the resulting N_K values as a function of iteration number n).

When, in our numerical analysis below, we cite sNRG values for the number of states N_K and N_{tot} (or for the corresponding number of symmetry multiplets, N_K^* and N_{tot}^*), these will refer to the geometric average over adjacent even and odd sNRG supershells chosen around a specified energy E_{ref} deep in the low-energy regime, where $E_{\text{ref}} \ll T_K$. Similarly, the corresponding iNRG values refer to a geometric average over all iNRG subshells associated with both even and odd supershells near E_{ref} .

In general, sNRG calculations performed for the same choice of $E_{\text{trunc}}^{\text{sNRG}}$ yield results of comparable accuracy and degree of convergence, which are to a large extent independent of the specific model and discretization settings being considered. We have confirmed this expectation for the models studied in this paper, as discussed in detail in Sec. IV below. For sNRG, the truncation energy is therefore the key quantity controlling accuracy and convergence.

In fact, we find that this is true also for iNRG. Moreover, we find that sNRG and iNRG calculations yield results with comparable accuracy and convergence properties, provided that their truncation energies are related in such a manner that the resulting N_K^{iNRG} and N_K^{sNRG} values are equal “on average,” i.e., after geometrically averaging over all subsites in a neighboring pair of even and odd supersites. We find empirically that this is achieved by choosing

$$E_{\text{trunc}}^{\text{iNRG}} = E_{\text{trunc}}^{\text{sNRG}} \Lambda^{\frac{m-1}{4m}}, \quad (15)$$

which implies that the parameter $E_{\text{trunc}}^{\text{iNRG}}$ is larger than the parameter $E_{\text{trunc}}^{\text{sNRG}}$. Nevertheless, the phrase “equivalent set-

tings” includes this choice. By contrast, the simpler choice $E_{\text{trunc}}^{\text{iNRG}} = E_{\text{trunc}}^{\text{sNRG}}$ leads to a smaller average N_K^{iNRG} than N_K^{sNRG} .

In Appendix A, we present a heuristic justification for Eq. (15). In Sec. IV, sNRG and iNRG results demonstrate explicitly that the choice of Eq. (15) leads to the desired equivalence of the number of kept states, accuracy, and convergence. In the rest of this paper, we will specify truncation energies in relation to the usual sNRG value $E_{\text{trunc}} \equiv E_{\text{trunc}}^{\text{sNRG}}$, taking it to be understood that the corresponding $E_{\text{trunc}}^{\text{iNRG}}$ is given by Eq. (15).

D. Discarded weight

The convergence of sNRG and iNRG calculations, with a given truncation threshold E_{trunc} and discretization parameter Λ , can be analyzed for each model in terms of the estimated discarded weight [27] $\delta\rho_{\text{disc}}$. As with the density matrix renormalization group (DMRG), the decay of the eigenspectrum of site-specific reduced density matrices, built from the ground state space of later iterations, can be used as a quantitative (*a posteriori*) measure of the convergence as proposed in Ref. [27]. However, in contrast to Ref. [27], where only the SIAM with $\Lambda = 2$ was investigated, we wish to compare NRG calculations performed using a range of different (effective) discretization parameters Λ (or $\tilde{\Lambda}$) in different models. Since the truncation in NRG is decided on the basis of an *energy* threshold, in this context it is more natural to quantify the contributions of high-lying *energy eigenstates* to reduced density matrices, rather than analyzing the eigenspectrum of the reduced density matrices as in Ref. [27]. The details of our modified approach are presented in Appendix B.

By examining the decay of the discarded weight $\delta\rho_{\text{disc}}$ with increasing E_{trunc} , and observing the corresponding convergence of physical quantities, we have found that calculations can be considered converged when $\delta\rho_{\text{disc}} < 10^{-6}$. An important advantage of defining the discarded weight in terms of the energy eigenbasis is that $\delta\rho_{\text{disc}}$, evaluated at fixed E_{trunc} , is rather insensitive to changing the discretization parameter Λ .

The discarded weight analysis is particularly important in benchmarking the iNRG, because the interleaving approach appears to weaken the energy scale separation ($\tilde{\Lambda} < \Lambda$). One might then expect [23] that a larger bare Λ would be required in iNRG compared with sNRG to achieve convergence with the same discarded weight. However, our detailed study of discarded weights in Sec. IV in fact reveals the *same* degree of convergence for iNRG and sNRG when the same Λ and E_{trunc} are used.

E. Numerical implementation

Both sNRG and iNRG can be formulated within the framework of matrix product states (MPS), which allows for a systematic and efficient numerical implementation. Here we employ the unified tensor representation of the QSpace approach introduced in Ref. [26], in which Abelian and non-Abelian symmetries can be implemented on a generic level. The state space is labeled in terms of the symmetry eigenbasis, and the Wigner-Eckart theorem is used to determine the matrix representation of irreducible operator sets. Based on this, every (rank-3) tensor object relevant to NRG calculations splits into a

tensor product of two objects that have identical data structures within the QSpace approach, operating respectively on the reduced multiplet space and the Clebsch-Gordan coefficient space. Matrix diagonalization, for example, is then only performed in the reduced multiplet space, resulting in an enormous gain of numerical efficiency.

All correlation functions presented in Sec. IV are calculated with the full-density-matrix (fdm-)NRG approach of Ref. [31]. It is established on a complete basis set [32], constructed from the discarded states of all NRG iterations. Since iNRG also produces a matrix-product-state similar to sNRG, from the point of view of fdm-NRG, iNRG cannot be distinguished from sNRG. Therefore the intrinsic multishell approach of fdm-NRG to finite temperature has the major advantage here that the subshell structure of iNRG poses no complications and is automatically taken care of. Spectral functions for the discretized model then are given from the Lehmann representation as a sum of poles, and can be calculated accurately at zero or arbitrary finite temperature. Continuous spectra are obtained by broadening the discrete data with a standard log-Gaussian kernel of frequency-dependent width [5,31].

III. MODELS

In this paper, we study three representative models with $N_c = 1, 2$, and 3 spinful conduction electron channels. In Sec. IV, iNRG and sNRG are used to solve these models; the accuracy and efficiency of the two methods are then compared. Here we study models with rather high symmetries; sNRG calculations can exploit either the full symmetries of the model, or lower symmetries if desired for comparison with iNRG. We therefore assume symmetry between the bands in the following, with half-bandwidth $D_\nu \equiv D = 1$ independent of ν . This also sets the half-bandwidth as the unit of energy.

A. Single-impurity Anderson model ($N_c = 1$)

The single impurity Anderson model [1] (SIAM) describes a single correlated quantum level,

$$\hat{H}_{\text{imp}}^{\text{SIAM}} = \sum_\nu \varepsilon_{d\nu} \hat{d}_\nu^\dagger \hat{d}_\nu + U \hat{d}_\uparrow^\dagger \hat{d}_\uparrow \hat{d}_\downarrow^\dagger \hat{d}_\downarrow, \quad (16)$$

tunnel-coupled to a single spinful channel of conduction electrons \hat{H}_{bath} [Eq. (5) with $m = 2$] via

$$\hat{H}_{\text{cpl}}(\{\hat{f}_{0\nu}\}) = \sum_{k\nu} (V_{k\nu} \hat{d}_\nu^\dagger \hat{c}_{k\nu} + \text{H.c.}) \quad (17)$$

$$\equiv \sqrt{\frac{2D\Gamma}{\pi}} \sum_\nu (\hat{d}_\nu^\dagger \hat{f}_{0\nu} + \text{H.c.}), \quad (18)$$

where $\nu \equiv \sigma \in \{\uparrow, \downarrow\} = \{+, -\}$. Here, \hat{d}_ν^\dagger creates an electron of flavor ν on the impurity, with energy $\varepsilon_{d\sigma} = \varepsilon_d + \sigma h/2$ in a Zeeman field h . For constant, flavor-independent couplings, $V_{k\nu}$, the hybridization strength is given by $\Gamma_\nu(\varepsilon) = \pi |V_\nu|^2 \rho_\nu(\varepsilon) \equiv \Gamma \Theta(D - |\varepsilon|)$ within a band of half-width $D \equiv 1$.

The SIAM possesses an $SU(2)$ spin symmetry for $h = 0$, to be denoted by $SU(2)_{\text{spin}}$, which reduces to $U(1)_{\text{spin}}$ for $h \neq 0$. Moreover, at particle-hole symmetry, $\varepsilon_d = -U/2$, the SIAM possesses an $SU(2)$ symmetry involving transformations be-

tween particles and holes, to be called $SU(2)_{\text{charge}}$. This reduces to $U(1)_{\text{charge}}$ for $\varepsilon_d \neq -U/2$. Depending on the symmetries allowed by the choice of model parameters, sNRG can exploit any combination of these spin and charge symmetries. In this paper, we set $h = 0$ and $\varepsilon_d = -U/2$, and employ either $U(1)_{\text{spin}} \times U(1)_{\text{charge}}$ or $SU(2)_{\text{spin}} \times SU(2)_{\text{charge}}$ symmetries.

Within iNRG, we can interleave Wilson chains for the $\nu = \uparrow$ and \downarrow conduction electrons species, discretizing these separately for a given Λ using two different z shifts, $z_\uparrow = z + \frac{1}{4}$ and $z_\downarrow = z$. Since this ‘‘spin-interleaved’’ scheme (spin-iNRG) artificially breaks the bare symmetry between spin up and down, it reduces the $SU(2)_{\text{spin}}$ symmetry to $U(1)_{\text{spin}}$. Furthermore, $SU(2)_{\text{charge}}$ is reduced to $U(1)_{\text{charge}}$ in spin-iNRG, as the irreducible operator set for $SU(2)_{\text{charge}}$ mixes spin components, and therefore cannot be defined within the state space of a single fixed-spin subsite. Consequently, spin-iNRG studies of the SIAM can employ $U(1)_{\text{spin}} \times U(1)_{\text{charge}}$ symmetries only.

B. Two-channel Kondo model ($N_c = 2$)

The two-channel Kondo model (2CKM) [33] features a single spin- $\frac{1}{2}$ impurity with spin $\hat{S}_\frac{1}{2}$ coupled by antiferromagnetic Heisenberg exchange to two spinful conduction electron channels [Eq. (5) with $m = 4$]

$$\hat{H}_0^{2\text{CKM}} = \sum_\alpha J_\alpha \hat{S}_\frac{1}{2} \cdot \hat{s}_\alpha + h S_\frac{1}{2}^z, \quad (19)$$

where $\hat{s}_\alpha = \sum_{\sigma\sigma'} \hat{f}_{0\alpha\sigma}^\dagger \frac{\vec{\sigma}_{\alpha\sigma'}}{2} \hat{f}_{0\alpha\sigma'}$ is the conduction electron spin density at the impurity in channel $\alpha = 1, 2$ (and $\vec{\sigma}$ is a vector of Pauli matrices).

In the spin sector, the 2CKM possesses an $SU(2)_{\text{spin}}$ symmetry for $h = 0$, and an $U(1)_{\text{spin}}$ symmetry for $h \neq 0$. In the case of particle-hole and channel symmetry ($J_1 = J_2$), the $m = 4$ flavors possess the enlarged symplectic symmetry $\text{Sp}(4)_{\text{charge,channel}}$. This reduces to $[\text{SU}(2)_{\text{charge}}]^2$ if channel symmetry is broken ($J_1 \neq J_2$), and further to $[\text{U}(1)_{\text{charge}}]^2$ if particle-hole symmetry is broken (not considered here). Depending on the symmetries allowed by the choice of model parameters, sNRG can exploit any combination of these spin and charge symmetries. We will here set $h = 0$ and employ either the $U(1)_{\text{spin}} \times [\text{U}(1)_{\text{charge}}]^2$, $SU(2)_{\text{spin}} \times [\text{SU}(2)_{\text{charge}}]^2$, or $SU(2)_{\text{spin}} \times \text{Sp}(4)_{\text{charge,channel}}$ symmetries.

Within iNRG, the four electron flavors can be interleaved in several different ways. For example, using spin-iNRG (as described above, with $z_{\alpha,\uparrow} = z + \frac{1}{4}$ and $z_{\alpha,\downarrow} = z$), the spin symmetry is reduced to $U(1)_{\text{spin}}$. Although $z_{1,\sigma} = z_{2,\sigma}$, this can only be combined with $U(1)_{\text{charge}}$ symmetries in the particle sector.

Alternatively, one can interleave the spinful $\alpha = 1, 2$ channels, discretizing them separately using $z_{\alpha=1,\sigma} = z + \frac{1}{4}$ and $z_{\alpha=2,\sigma} = z$ (but $z_{\alpha,\uparrow} = z_{\alpha,\downarrow}$). This ‘‘channel-interleaved’’ scheme (channel-iNRG) breaks the symmetry between channel 1 and 2 (even if $J_1 = J_2$) and hence the full $\text{Sp}(4)_{\text{charge,channel}}$ symmetry is broken. However, $[\text{SU}(2)_{\text{charge}}]^2$ symmetry can still be exploited, in combination with either $SU(2)_{\text{spin}}$ or $U(1)_{\text{spin}}$.

In the most asymmetric case, all four electron flavors of the 2CKM are interleaved, using $z_{1\uparrow} = z + \frac{3}{8}$, $z_{1\downarrow} = z +$

$\frac{2}{8}, z_{2,\uparrow} = z + \frac{1}{8}, z_{2,\downarrow} = z$. The maximum symmetry consistent with this “flavor-interleaved” scheme (flavor-iNRG) is $U(1)_{\text{spin}} \times [U(1)_{\text{charge}}]^2$. In this paper, our iNRG studies of the 2CKM will employ the latter flavor-iNRG scheme, and also channel-iNRG with $SU(2)_{\text{spin}} \times [SU(2)_{\text{charge}}]^2$ symmetry.

The point $J_1 \rho_1(0) = J_2 \rho_2(0)$ is a critical point of the 2CKM, characterized by a frustration of screening that gives rise to fragile non-Fermi liquid physics [33,34]. Any finite channel anisotropy $J_1 \rho_1(0) \neq J_2 \rho_2(0)$ produces a crossover [34,35] to a Fermi liquid ground state, corresponding to Kondo strong coupling between the impurity and channel $\alpha = 1$ (or 2) for $(J_1 \rho_1(0))/(J_2 \rho_2(0)) > 1$ (or < 1). Because the interleaving in iNRG spoils the channel symmetry [$\rho_1^{\text{disc}}(0) \neq \rho_2^{\text{disc}}(0)$] even in the isotropic case $J_1 = J_2$, the critical point of the 2CKM is spuriously destabilized. Fine-tuning of the ratio $J_1/J_2 \approx 1$ must then be carried out to access the critical physics [23]. This is discussed further in Sec. IV E.

C. Anderson-Hund model ($N_c = 3$)

Finally, we consider the particle-hole symmetric three-channel Anderson-Hund model (3CAHM) of Refs. [7,26,36]. The isolated ‘impurity’, comprising $\alpha = 1, 2, 3$ orbitals, each with spin $\sigma = \uparrow, \downarrow$, is described by

$$\hat{H}_{\text{imp}}^{\text{3CAHM}} = -J_H \hat{S}^2, \quad (20)$$

where $\hat{S} = \sum_{\alpha} \sum_{\sigma, \sigma'} d_{\alpha\sigma}^{\dagger} \frac{\vec{\sigma}_{\alpha\sigma'}}{2} d_{\alpha\sigma'}$ is the *total* impurity spin. Electrons of different impurity orbitals interact through the Hund coupling, J_H , in Eq. (20).

Each impurity orbital with flavor $\nu = (\alpha, \sigma)$ is tunnel-coupled to a conduction electron band of the same flavor, via Eq. (18); overall there are $m = 6$ electronic flavors. The large local state space $d_{\text{loc}}^{\text{sNRG}} = 64$ for the 3CAHM means that iterative diagonalization in *state* space (rather than multiplet space) is practically intractable for sNRG. However, this 3CAHM possesses large symmetries that can be optimally exploited in sNRG: $SU(2)_{\text{spin}}$ symmetry in the spin sector, and $Sp(6)_{\text{charge, channel}}$ symmetry in the particle-hole/channel sector. The 64 states describing a single Wilson supersite reduce to a mere four multiplets in this case.

The $Sp(6)_{\text{charge, channel}}$ symmetry reduces to $U(1)_{\text{charge}} \times SU(3)_{\text{channel}}$ if particle-hole symmetry is broken, or to $[SU(2)_{\text{charge}}]^3$ if channel symmetry is broken. Exploiting one of these three large symmetries is essential when using sNRG. For iNRG, one again has several options for interleaving. We will consider channel-iNRG with $SU(2)_{\text{spin}} \times [SU(2)_{\text{charge}}]^3$ symmetry, and full flavor-iNRG with $U(1)_{\text{spin}} \times [U(1)_{\text{charge}}]^3$ symmetry. A major advantage of iNRG is that such models can be solved even when no large symmetries are available [cf. yellow dashed curve in Fig. 5(b) that shows the spectral function of the 3CAHM calculated with iNRG and $U(1)_{\text{spin}} \times [U(1)_{\text{charge}}]^3$ symmetry].

IV. RESULTS

In the following, we present a comprehensive comparison of iNRG and sNRG for the three models introduced in Sec. III. We begin in Sec. IV A by summarizing our main conclusions, referring only briefly to the relevant figures. We then offer a detailed analysis of the figures to substantiate our main results

in the subsequent sections. In particular, we compare iNRG and sNRG by examining the number of kept multiplets in Sec. IV B, the efficiency of the calculations in Sec. IV C, and the accuracy/convergence of the results in Sec. IV D. The take-home message is that iNRG offers significant improvements in efficiency without compromising accuracy and convergence properties.

A. Overview

We perform calculations in which, for a given model, discretization parameter Λ , and choice of exploited symmetries, the truncation energies of iNRG and sNRG are related by Eq. (15). This use of *equivalent settings* allows for optimal comparability, because it ensures that, on average, the same number of states are kept at each iteration in both methods. The number of kept *multiplets*, N_{K}^* , is therefore also the same on average—as demonstrated explicitly in Figs. 2(a)–2(c) and 3.

Number of multiplets. N_{K}^* , and thus also N_{K} , is found to increase roughly exponentially with E_{trunc} and also with the number of conduction electron channels N_c [Figs. 2(a)–2(c) and 4]. This scaling is common to both iNRG and sNRG. It simply reflects the fact that the number of many-body eigenstates of a gapless system grows exponentially with energy, with an exponent that increases linearly with N_c . Since we exploit symmetries and conserved quantities in the calculations, the number of kept *multiplets* N_{K}^* is far smaller than the number of kept *states* N_{K} in both iNRG and sNRG. When iNRG and sNRG use the same symmetry setting, the total number of multiplets to be diagonalized at each iteration, N_{tot}^* , is far smaller for iNRG than sNRG [Figs. 2(d)–2(f)], due to the intermediate truncations in iNRG. However, iNRG cannot always exploit the full model symmetries due to the interleaving process. As a consequence there can be an efficiency tradeoff in iNRG: the advantage of a reduced local state space comes at the cost of fewer symmetries being available to exploit. This is shown by Figs. 2(d)–2(f), where N_{tot}^* for the most efficient iNRG calculation is essentially the same as that of the best sNRG calculation (exploiting all symmetries) in each case [in fact, N_{tot}^* is actually lower in sNRG for the SIAM in panel (d)].

Efficiency. The total CPU time for a given iNRG calculation is smaller than that of the corresponding sNRG calculation with equivalent settings [Figs. 2(g)–2(i)]. In fact, with $\Lambda = 4$, spin-iNRG for the SIAM, spin and channel-iNRG for the 2CKM and channel-iNRG calculations for the 3CAHM are also more efficient than the *best* sNRG calculations exploiting full symmetries. Even though N_{tot}^* is typically similar or even lower for the best sNRG compared to the best iNRG calculations, the book-keeping overheads involved in exploiting symmetries can outweigh the potential gains of doing so (this is especially pronounced for smaller E_{trunc}). In general, the gain in iNRG efficiency becomes more significant as the number of flavors increases. Importantly, some low-symmetry, many-band models that are prohibitively expensive for sNRG can still be tackled with iNRG.

Accuracy and convergence. Remarkably, these gains in efficiency do not compromise accuracy and convergence properties. To establish this, we performed extensive comparisons

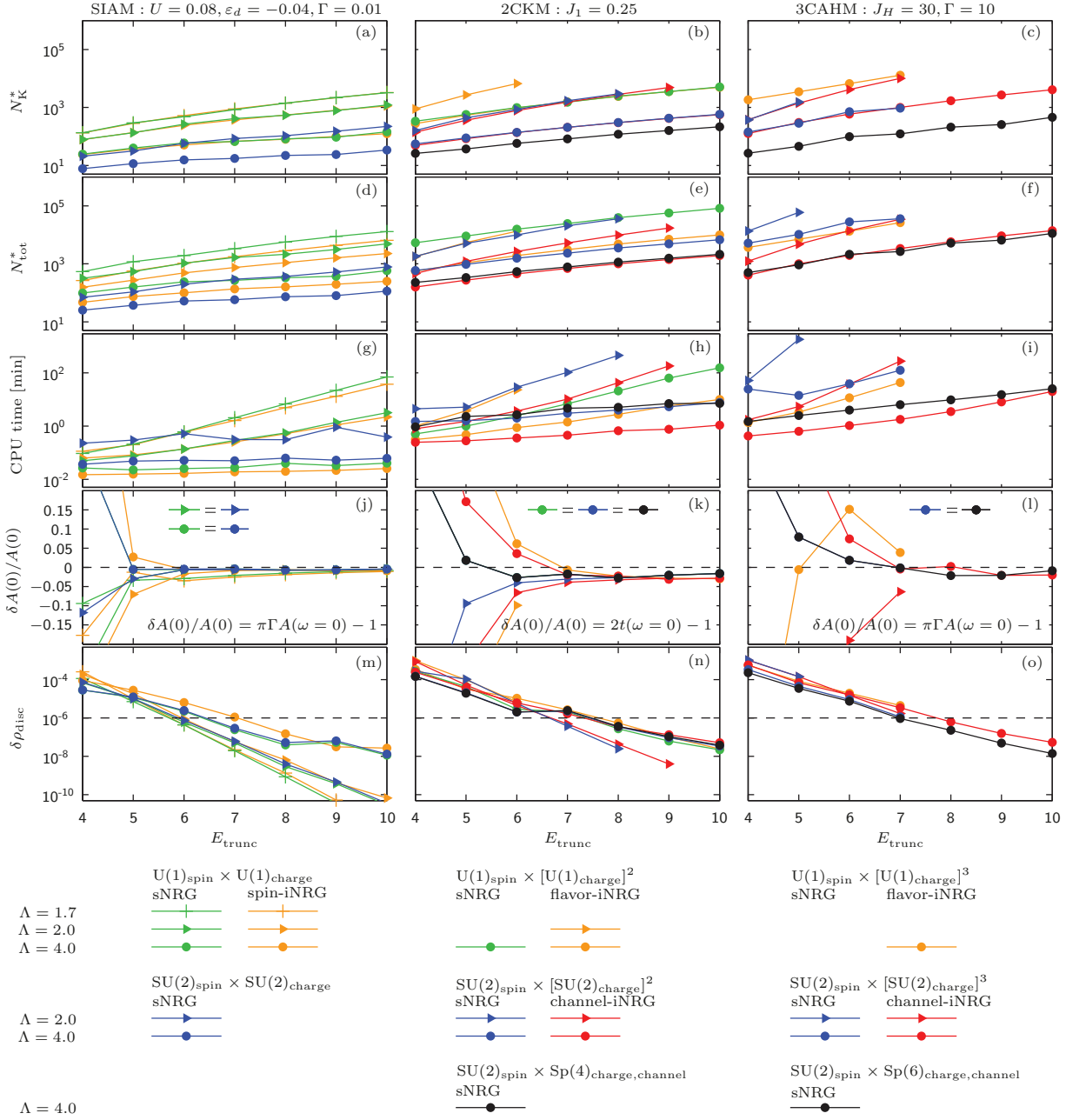


FIG. 2. Comparison of sNRG and iNRG for three models: SIAM (left column), 2CKM (middle column), and 3CAHM (right column). (a)–(c) The number of kept multiplets, N_K^* ; (d)–(f) the total number of multiplets generated during an NRG step, N_{tot}^* ; (g)–(i) the total CPU time for one NRG run; (j)–(l) the relative deviations $\delta A(0)/A(0)$ of correlation functions at the Fermi energy $\omega = 0$ from their exact values [cf. Eqs. (21)]; and (m)–(o) the discarded weight $\delta \rho_{\text{disc}}$ (the horizontal dashed lines indicate the convergence threshold). All quantities (computable with a maximum memory of 128 GB) are plotted versus E_{trunc} ($\equiv E_{\text{trunc}}^{\text{sNRG}}$), for $\Lambda = 1.7$ (crosses), 2.0 (triangles), and 4.0 (circles). Each symmetry setting is identified by a particular color in iNRG and sNRG. iNRG results have been geometrically averaged over all interleaved flavors. Data for N_K^* and N_{tot}^* have been geometrically averaged over even and odd Wilson shells at an energy scale $E_{\text{ref}} = 5 \times 10^{-8} D \ll T_K$. We used $z = 0$ in all cases except for (j)–(l), where data for $z = 0$ and 0.5 have been averaged. An exception is the flavor-iNRG data point at $E_{\text{trunc}} = 7$ in (l), which was obtained for $z = 0$ without z averaging ($z = 0.5$ exceeded memory resources). In (j)–(l), sNRG results with the same Λ but different symmetry settings coincide.

between iNRG and sNRG using equivalent settings [see Figs. 2(j)–2(l), 2(m)–2(o), and 5].

The accuracy of iNRG was established directly, by monitoring the deviation of calculated physical quantities from certain exact results. In particular, we studied the value of the impurity spectral function (or t matrix) at the Fermi level, relative to known analytic results [Figs. 2(j)–2(l)]. The quality of the results improves with increasing E_{trunc} as expected, and exact results are reproduced to within a few percent for $E_{\text{trunc}} > 7$ in both sNRG and iNRG. This conclusion is further supported by comparisons of the full frequency dependence of impurity spectral functions in Fig. 5.

Furthermore, our analysis of the discarded weight shows that both iNRG and sNRG calculations are effectively converged for $E_{\text{trunc}} > 7$ [Figs. 2(m)–2(o)]. This demonstrates explicitly that the states discarded at intermediate steps in iNRG do not contribute appreciably to low-energy eigenstates at later iterations, thus validating the more fine-grained RG scheme employed by iNRG.

Artificially broken symmetries. Finally, we examined the tuning protocol employed in iNRG to restore channel symmetries that are broken artificially by the interleaved discretization (see Fig. 6). Such channel symmetries are of course not always relevant perturbations (an example is the 3CAHM, where the same basic low-energy physics arises even in the channel-anisotropic case). The worst-case scenario for iNRG emerges in the vicinity of a quantum critical point, where channel asymmetries generate a relevant RG flow to a different fixed point [33,34]. The classic exemplar is the 2CKM, whose frustrated critical point occurs precisely at $J_1\rho_1(0) = J_2\rho_2(0)$. In iNRG, where $\rho_1^{\text{disc}}(0) \neq \rho_2^{\text{disc}}(0)$, the ratio J_1/J_2 must be tuned to access this physics, but is found in practice to deviate from its exact value by only $\sim 1\%$. We also show that the critical point can be located exponentially rapidly in the number of iNRG runs, keeping calculation overheads to a minimum.

B. Number of kept multiplets

The key difference between sNRG and iNRG is the size of the local state space, i.e., $d_{\text{loc}}^{\text{sNRG}} = d_f^m$ versus $d_{\text{loc}}^{\text{iNRG}} = d_f$. However, to compare fairly the relative efficiency, we must ensure that both calculations are of comparable accuracy. By choosing the “same” truncation energies in iNRG and sNRG [via Eq. (15)], a comparable number of multiplets is kept in both calculations, as argued in Sec. II C. Here we present data to substantiate this. Moreover, the consequence of this choice is that sNRG and iNRG calculations are of equivalent accuracy, as demonstrated explicitly below in Sec. IV D.

Figures 2(a) and 2(c) show N_K^* obtained for the SIAM, 2CKM, and 3CAHM, with several different choices of Λ , and employing various symmetry settings. In all cases, we find that $N_K^{*,\text{iNRG}}$ and $N_K^{*,\text{sNRG}}$ are comparable when the same symmetry setting is used. However, note that the different iNRG subshells contribute unequally to their geometric average, because the absolute truncation energy changes from subshell to subshell in iNRG, as explained in Sec. II C. This is illustrated in Fig. 3, which shows N_K^* as function of Wilson shell index n for the 2CKM. For iNRG, the number of multiplets kept after adding the first channel (red dashed line) is smaller than the number of multiplets kept after adding the second channel (red dash-

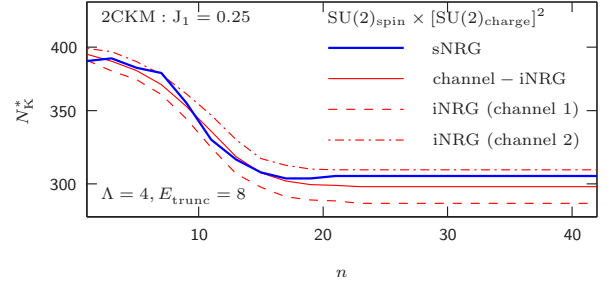


FIG. 3. Number of kept multiplets N_K^* vs Wilson shell index n for the 2CKM within the $SU(2)_{\text{spin}} \times [SU(2)_{\text{charge}}]^2$ symmetry setting. For iNRG (red), the number of multiplets kept after adding channel 1 (dashed) or channel 2 (dash-dotted) are shown separately, as well as their geometric average (solid). sNRG results are shown in blue for comparison. All results are geometrically averaged over even and odd iterations.

dotted), but their geometric average (red solid) is rather similar to the number of kept multiplets in the corresponding sNRG calculation (blue solid line) for all n .

Furthermore, Figs. 2(a) and 2(c) confirm that the total number of kept multiplets N_K^* depends exponentially on E_{trunc} , with a growth exponent that increases with N_c [the slope of the line increases from Figs. 2(a) to 2(c)]. This behavior is expected for the many-body eigenstates of a gapless system, whose number increases exponentially with energy.

Naturally, exploiting larger symmetries means that fewer multiplets are kept for a given E_{trunc} . [For example, in Fig. 2(c) for $\Lambda = 4$, the black circles lie well below the red and blue circles.] This reduction of the multiplet space arises by splitting off large Clebsch-Gordan spaces. We also note that smaller Λ , which reduces energy-scale separation between iterations, leads to larger N_K^* , and to a faster increase of N_K^* with E_{trunc} . [For example, in Fig. 2(b), the blue and red triangles for $\Lambda = 2$ lie above the blue and red circles for $\Lambda = 4$, and rise with a greater slope.]

Furthermore, the number of kept states, N_K (which is independent of the symmetry settings used), increases roughly exponentially with the number of conduction electron channels, m . This is confirmed in Fig. 4, which shows N_K for the multichannel Kondo model (N_c -CKM) and the multichannel Anderson-Hund model (N_c -CAHM), with $N_c = 1, 2, 3$ spinful channels [these models are the generalizations of Eqs. (19) and (20) to the case of N_c channels]. Figure 4 also shows that the description of certain multichannel fixed points requires a greater number of kept states than others, reflecting their relative complexity. For example, the frustrated non-Fermi liquid fixed points of the N_c -CKM (with $N_c \geq 2$) require a larger N_K than the corresponding Fermi liquid fixed points of the N_c -CAHM at $E_{\text{trunc}} = 7$.

These results confirm that the exponential scaling of required computational resources with m in both sNRG and iNRG cannot be avoided—it simply reflects elementary state-counting properties for gapless multichannel systems. However, the efficiency of the calculation for a given model can be substantially improved by exploiting symmetries in sNRG, or by interleaving flavors in iNRG, as now discussed.

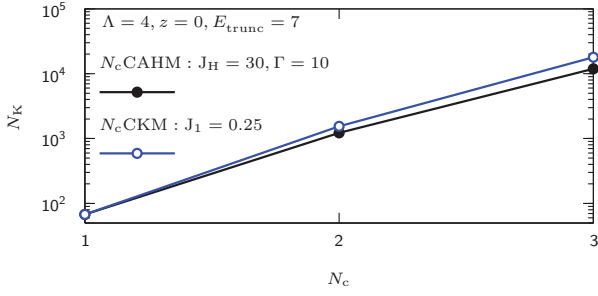


FIG. 4. Number of kept *states* N_K at the low-energy fixed point of the N_c CAHM (black) and N_c CKM (blue), showing a roughly exponential increase with the number of channels, N_c . Results were obtained with sNRG and have been geometrically averaged over even and odd Wilson shells at energy scale $E_{\text{ref}} = 5 \times 10^{-8} D \ll T_K$.

C. Efficiency

The *total* number of multiplets, N_{tot}^* , generated in NRG near the low-energy fixed point of the three models, is plotted as a function of E_{trunc} in Figs. 2(d)–2(f). As with N_K^* , the size of N_{tot}^* depends on the particular model under consideration, Λ , E_{trunc} , and the symmetry setting used. Additionally, we now also see a dramatic difference between iNRG and sNRG. When the same symmetry setting is used, $N_{\text{tot}}^{*,\text{iNRG}}$ is far smaller than $N_{\text{tot}}^{*,\text{sNRG}}$, because $d_{\text{loc}}^{\text{iNRG}}$ is smaller than $d_{\text{loc}}^{\text{sNRG}}$. [For example, the red data points lie clearly below the blue data points in Fig. 2(f) for the 3CAHM and in Fig. 2(e) for the 2CKM.] Moreover, then also the ratio $N_{\text{tot}}^{*,\text{sNRG}}/N_{\text{tot}}^{*,\text{iNRG}}$ grows exponentially with the number of interleaved flavors. For a given model and symmetry, $N_{\text{tot}}^{*,\text{sNRG}}/N_{\text{tot}}^{*,\text{iNRG}}$ would therefore be larger for full flavor-iNRG than channel-iNRG. However, note that in general N_{tot}^* itself might be smallest for channel-iNRG, meaning that the optimal strategy might involve keeping some symmetries at the expense of interleaving fewer flavors. An example of this is seen clearly for the 2CKM in Figs. 2(e) and 2(f), where red dots lie below orange dots.

These trends in N_{tot}^* are reflected in the CPU time plotted in Figs. 2(g)–2(i), which is the ultimate measure of calculation efficiency. The total CPU time for an NRG calculation is generally dominated by matrix diagonalizations (especially for large E_{trunc}), and therefore scales as $\sim (N_{\text{tot}}^*)^3$. Since N_K^* and N_{tot}^* grow with E_{trunc} , so too does the CPU time – the faster so with smaller Λ . For small E_{trunc} , however, numerical overheads can also have a noticeable influence. [For example, in Fig. 2(e) for N_{tot}^* , the green and orange circle points for $\Lambda = 4$ show a separation that is quite large and approximately constant; by contrast, Fig. 2(h) shows an increasing difference in the CPU time with increasing E_{trunc} . At large E_{trunc} , the difference is essentially attributable to the difference in N_{tot}^* alone. At small E_{trunc} , the numerical overhead in iNRG can presumably be attributed to larger Wilson chain lengths.]

The maximum efficiency gain of iNRG over sNRG in terms of CPU time occurs if no symmetries are used in either iNRG or sNRG. This gain is then of order $\sim d_f^{3(m-1)}/m$, where the factor of $1/m$ arises because the interleaved Wilson chain is m times longer than the standard Wilson chain. Similarly, the corresponding gain in terms of memory resources is given by

$\sim d_f^{2(m-1)}$, here without the factor of $1/m$, since memory is required on the level of a specific NRG iteration rather than for the whole calculation. The following table summarizes the theoretical maximum gain relative to sNRG (in the absence of symmetries) obtained with channel-iNRG and flavor-iNRG for models with $N_c = 1, 2, 3$:

No. spinful channels	No. channels interleaved	Max. speedup factor (CPU)	Max. gain in memory
$N_c = 1$	$N_{v=\sigma} = 2$	4	4
$N_c = 2$	$N_{v=\alpha} = 2$	32	16
	$N_{v=\alpha\sigma} = 4$	128	64
$N_c = 3$	$N_{v=\alpha} = 3$	1365	256
	$N_{v=\alpha\sigma} = 6$	5461	1024

When symmetries are exploited in the calculations, the efficiency gain for iNRG over sNRG is reduced, relative to the value cited in the above table, because the local Hilbert space of each supersite in sNRG (or subsite in iNRG) is organized into *multiplets* instead of states. The factor $d_f^{3(m-1)}/m$, which was based on a *state*-counting argument, is then effectively reduced. Note, however, that handling and bookkeeping of Clebsch-Gordan coefficient spaces also introduces a numerical overhead. For very small E_{trunc} , this can even outweigh the efficiency gains of exploiting symmetries. However, the symmetry gains grow with increasing E_{trunc} (which leads to increasingly large block sizes for reduced matrix elements), and eventually always dominate compared to book-keeping overheads. [For example, in Fig. 2(h) for $\Lambda = 4$, the green circles lie below the blue circles for small E_{trunc} , but cross at $E_{\text{trunc}} \simeq 6$. For large E_{trunc} , the most efficient sNRG calculations are those that exploit the largest symmetries (the black circles start crossing the blue circles at $E_{\text{trunc}} = 10$.)]

Ultimately, when the same symmetries are used for both calculations, iNRG clearly requires far smaller CPU time than sNRG for a given Λ and E_{trunc} , see Figs. 2(h) and 2(i). This effect becomes more pronounced with increasing E_{trunc} .

The models considered here have high intrinsic symmetries, which can be more fully exploited in sNRG than iNRG. The “best case” scenario for sNRG, in which the *full* model symmetries are exploited, are shown as the blue data points in the first column of Fig. 2 and as black points in the second and third columns of Fig. 2. For $N_c = 1$ [panel (d)], this optimal sNRG generates a slightly smaller N_{tot}^* than the best corresponding iNRG calculation (for a given Λ and E_{trunc}). However, when the number of channels is increased to $N_c = 2$ or 3 [panels (e) and (f)], we find similar N_{tot}^* for the best iNRG calculations (red dots) and the best sNRG calculations (black dots). Nevertheless, for the range of E_{trunc} values used here, the total CPU times [panels (h) and (i)] for $\Lambda = 4$ calculations employing channel-iNRG (red dots) are still lower than for sNRG (black dots), even when full symmetries are exploited in sNRG (the difference is attributable to additional bookkeeping costs incurred when handling large symmetries in sNRG).

The benefits of exploiting symmetries increase for larger N_{tot}^* and hence E_{trunc} . As a consequence, we find that the CPU time increases with E_{trunc} slower for full-symmetry sNRG than for iNRG. For example, for $N_c = 3$ and $\Lambda = 4$, in panel (f) for N_{tot}^* the black (sNRG) and red (iNRG) dots are approximately

equivalent, while in panel (i) for the CPU times, the black dots lie well above the red dots for small E_{trunc} , but then rise more slowly with E_{trunc} , so that both roughly coincide for $E_{\text{trunc}} = 10$. Similarly, for $N_c = 1$ and $\Lambda = 2$, in panel (g) for N_{tot}^* the blue triangles (sNRG) start above the orange triangles (iNRG) for small E_{trunc} , but rise more slowly and end up below the latter for $E_{\text{trunc}} \gtrsim 7$, showing that full-symmetry sNRG can sometimes be the most efficient method. We also anticipate that full-symmetry sNRG for $N_c = 3$ [panel (i)] would be more efficient than iNRG for $E_{\text{trunc}} \gtrsim 10$.

Finally, we note that the optimal iNRG calculation does not necessarily involve interleaving all possible flavors, due to the tradeoff in lowered symmetries. Indeed, making partial use of interleaving and partial use of symmetries can yield the best results, as seen, for example in panels (h) and (i) for the CPU times of $N_c = 2$ and 3, respectively, where the red symbols (channel-iNRG) lie below the corresponding orange symbols (flavor-iNRG).

D. Accuracy

As highlighted above, the iNRG scheme is more efficient due to the intermediate truncations along the interleaved Wilson chain, which results in the smaller local state space $d_{\text{loc}} = d_f$ at each step (if all flavors are interleaved). A key question is whether these intermediate truncations adversely affect the accuracy of iNRG results. In the following, we show that, for the same model and same Λ , with truncation energies set equal as in Eq. (15), we obtain results with similar accuracy and convergence properties for both iNRG and sNRG.

The absolute accuracy of both iNRG and sNRG can be directly assessed from calculated physical quantities. In particular, we focus on $T = 0$ correlation functions. For the particle-hole symmetric SIAM and 3CAHM, the impurity spectral function $A(\omega) = -\frac{1}{\pi} \text{Im} \langle \hat{d}_v; \hat{d}_v^\dagger \rangle_\omega$ is pinned by the Friedel sum rule at the Fermi level, $\omega = 0$. The exact analytic result [1] is $\pi \Gamma A(0) = 1$. As a measure of the accuracy in NRG, we therefore consider the relative deviation at the Fermi energy,

$$\delta A(0)/A(0) = \pi \Gamma A(0) - 1, \quad (21a)$$

shown in Figs. 2(j) and 2(l). For the 2CKM, we consider the spectrum $t(\omega) = -\pi \rho(\omega) \text{Im} T(\omega)$, where $T(\omega)$ is the scattering t matrix. Again, the spectrum is pinned at the low-energy non-Fermi liquid fixed point; the exact analytic result [37] is $t(0) = \frac{1}{2}$. In Fig. 2(k), we therefore consider the relative NRG deviation at the Fermi energy,

$$\delta A(0)/A(0) = 2t(0) - 1. \quad (21b)$$

We find that iNRG and sNRG perform similarly, recovering exact results to within a few percent for $E_{\text{trunc}} > 7$. For each case studied, iNRG appears to deviate somewhat stronger from $\delta A(0)/A(0) = 0$ for $E_{\text{trunc}} < 7$ than sNRG; but approximately equivalent results are obtained for $E_{\text{trunc}} > 7$. Even when interleaving all 6 flavors in the 3CAHM, using Abelian symmetries only, we similarly anticipate that $\delta A(0)/A(0)$ will converge to 0 for sufficiently large E_{trunc} . [This is supported in Fig. 2(l) by the orange data point at $E_{\text{trunc}} = 7$, which was calculated for $z = 0$ only.]

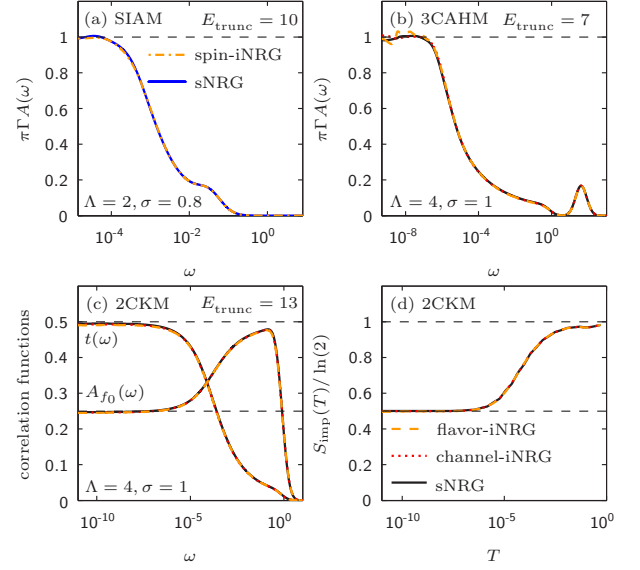


FIG. 5. Comparison of physical quantities calculated with iNRG and sNRG. (a) Impurity spectral function $\pi \Gamma A(\omega)$ at $T = 0$ for the SIAM; (b) impurity spectral function $\pi \Gamma A(\omega)$ at $T = 0$ for the 3CAHM; (c) spectrum of the t matrix $t(\omega)$ and the correlator $A_{f_0}(\omega)$ at $T = 0$ for the 2CKM; (d) impurity contribution to the entropy, $S_{\text{imp}}(T)$, for the 2CKM. For the dynamical correlators shown in (a)–(c), the protocol of Ref. [31] was used to broaden discrete data, using a broadening parameter of $\sigma_{\text{broad}} = 0.8$ or 1 for $\Lambda = 2.0$ or 4.0, respectively. All quantities were z -averaged over $z = 0$ and 0.5, except for the flavor-interleaved 3CAHM spectral function in (b), which was only calculated for $z = 0$ ($z = 0.5$ exceeded memory resources). The observed low-frequency oscillations are therefore an artifact of underbroadening, and would be removed by additional z averaging or use of a larger σ_{broad} .

This conclusion is further substantiated by Fig. 5, which shows the full frequency dependence of dynamical correlation functions at $T = 0$ in panels (a)–(c), and the temperature dependence of the impurity entropy in panel (d). For the SIAM in panel (a), the iNRG and sNRG impurity spectral functions are essentially indistinguishable for $E_{\text{trunc}} = 10$ and $\Lambda = 2$, at all frequencies. For the 3CAHM in panel (b), channel-iNRG and sNRG results for the impurity spectral function are again indistinguishable for $E_{\text{trunc}} = 7$ and $\Lambda = 4$. Flavor-iNRG shows some oscillations on the lowest energy scales due to underbroadening: the iNRG calculation was performed only for $z = 0$. Obtaining a completely smooth curve would either require additional z averaging (but $z = 0.5$ exceeded memory resources) or the use of a larger broadening, σ_{broad} . Panel (c) shows the spectrum of the t matrix $t(\omega)$, and the local bath spectral function $A_{f_0}(\omega) = -\frac{1}{\pi} \text{Im} \langle \hat{f}_{0v}; \hat{f}_{0v}^\dagger \rangle_\omega$ for the 2CKM. At $E_{\text{trunc}} = 13$ for $\Lambda = 4$, both iNRG and sNRG yield equivalent and highly accurate results. Finally, panel (d) confirms that thermodynamic quantities (here illustrated for the impurity contribution to the total entropy) are accurately reproduced using both iNRG and sNRG for the 2CKM. In particular, the nontrivial residual entropy [37] $S_{\text{imp}}(T = 0) = \frac{1}{2} \ln(2)$ is correctly reproduced.

In Figs. 2(m)–2(o), we examine the convergence of both iNRG and sNRG calculations, analyzed quantitatively in terms of the NRG discarded weight $\delta\rho_{\text{disc}}$ (see Sec. II D). As expected, the discarded weight decays exponentially with increasing E_{trunc} . The calculations are considered fully converged when $\delta\rho_{\text{disc}} < 10^{-6}$, which is reached in all cases at around $E_{\text{trunc}} \approx 7$. No qualitative changes occur in physical results on further increasing E_{trunc} [panels (j)–(l)]. Figures 2(m)–2(o) show clearly that the convergence behavior of iNRG is equivalent to that of sNRG, implying that the states additionally discarded by iNRG at intermediate steps do *not* have appreciable weight in the eigenstates of later iterations. Indeed, the discarded weights for iNRG (orange and red symbols) and sNRG (green, blue and black symbols) for the same Λ are approximately equal. [The only exception is seen in panel (m), for $N_c = 1$ and $\Lambda = 4$, where the discarded weight differences between sNRG (green circles) and iNRG (orange circles) are apparently somewhat larger. We attribute this to inaccuracies in the estimation of the discarded weight, since, by far, the smallest number of data points (diagonal weights ρ_s) were available for the extrapolation in this case.]

For $\delta\rho_{\text{disc}} \gtrsim 10^{-6}$, i.e., above the convergence threshold, the discarded weights behave similarly for *all* NRG calculations irrespective of the choice of Λ ; below this threshold, the behavior becomes somewhat dependent on Λ : for a given E_{trunc} , larger Λ yields a larger discarded weight both for iNRG and sNRG [panels (m) and (n)]. The reason for this is that the spectrum of *rescaled* eigenenergies in NRG shows a Λ dependence for higher energies: while rescaling is designed to ensure that the low-energy regime (dominated by single-particle excitations) of the rescaled eigenspectrum is almost Λ -independent, it stretches apart the high-energy regime (dominated by many-particle excitations). High-energy states are therefore shifted up more for larger Λ . The consequence is that, on increasing E_{trunc} and Λ , the weight of the reduced density matrices is shifted to higher rescaled energies. This means that the slope κ of the dashed red line in Fig. 8 would decrease, causing an increase in the total integrated discarded weight $\delta\rho_{\text{disc}}$.

E. Fine tuning in iNRG

If a given model possesses an exact flavor symmetry—and furthermore, if the breaking of this flavor symmetry is an RG *relevant* perturbation—iNRG must be combined with parameter fine tuning. This is because the asymmetric discretization required to interleave different Wilson chains in iNRG artificially breaks bare flavor symmetries, albeit rather weakly. However, effective channel symmetry in the discretized model can be restored through the fine-tuning of couplings [23].

A prime example is the 2CKM, for which channel symmetry-breaking is relevant [33,34]. The critical point of the 2CKM is realized at precisely $\rho_1(0)J_1 = \rho_2(0)J_2$, embodying the frustration responsible for its non-Fermi liquid properties. In sNRG, channel symmetry is exactly preserved: $\rho_1^{\text{disc}}(\varepsilon) = \rho_2^{\text{disc}}(\varepsilon)$, and so the critical physics is accessible along the line $J_1 = J_2$ (only the Kondo temperature T_K^{2CK} is affected by the actual value chosen for $J_1 = J_2$). However, we note that even in sNRG, the precise value of $\rho_\alpha^{\text{disc}}(0)J_\alpha$

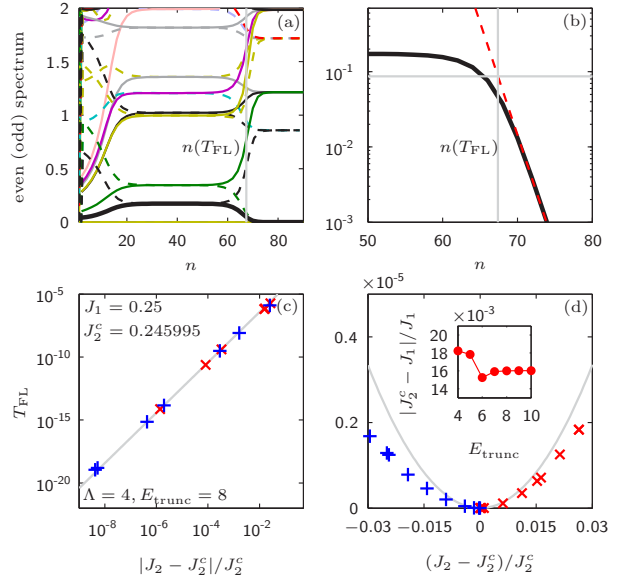


FIG. 6. Fine tuning in iNRG for the 2CKM (a) Flow of iNRG many-particle energies with Wilson shell index n [solid (dashed) lines for even (odd) n] for the 2CKM. Different colors correspond to states with different quantum numbers. (b) The Fermi liquid crossover scale T_{FL} can be extracted from the flow of the first excited state (thick black line): we fit its large- n behavior with a power law (dashed red line), take $n(T_{\text{FL}})$ to be the iteration number [vertical grey line in (a) and (b)] at which this power law reaches half of the fixed-point value of this state (horizontal grey line), and define the Fermi liquid scale as $T_{\text{FL}} = \omega_{n(T_{\text{FL}})}$. In (c) and (d), the resulting values of T_{FL} are plotted as function of $J_2 - J_2^c$ on a log-log or linear plot, respectively, using red (blue) symbols for $J_2 > J_2^c$ ($< J_2^c$). Grey lines give the asymptotic form $T_{\text{FL}} \sim (J_2 - J_2^c)^2$. By using an extrapolative protocol, the critical coupling J_2^c can be located exponentially rapidly in the number of separate iNRG runs. [Inset to (d)] The difference between the critical coupling J_2^c and J_1 , plotted as a function of the truncation energy.

can deviate very slightly from the bare value $\rho_\alpha(0)J_\alpha$, due to the discretization. Although the T_K^{2CK} obtained in sNRG might therefore also be slightly different from the true value, it should be emphasized that the *universal* low-energy physics is identical.

Likewise, $\rho_\alpha^{\text{disc}}(0)J_\alpha$ deviates from $\rho_\alpha(0)J_\alpha$ in iNRG. However, the important difference is that $\rho_1^{\text{disc}}(0)J_1 \neq \rho_2^{\text{disc}}(0)J_2$, even when $\rho_1(0)J_1 = \rho_2(0)J_2$. In the presence of this small channel asymmetry perturbation, the critical point is destabilized, leading to a flow *away* from the non-Fermi liquid fixed point, and toward a stable Fermi liquid fixed point [34,35,37]. The temperature/energy scale characterizing this Fermi liquid crossover is denoted T_{FL} . To access the critical physics for a given J_1 , one must therefore fine tune the value of $J_2 \rightarrow J_2^c$ such that $T_{\text{FL}} \rightarrow 0$. In principle, T_{FL} can be extracted from any physical quantity; it can also be extracted directly from the flow of NRG many-particle energies, as shown in Figs. 6(a) and 6(b) (see caption for details).

A very efficient extrapolative tuning protocol can be employed if the functional dependence of T_{FL} on $J_2 - J_2^c$ is

known analytically. In the case of the 2CKM, it is known [37] that $T_{\text{FL}} \sim (J_2 - J_2^c)^2$ when $T_{\text{FL}} \ll T_{\text{K}}^{2\text{CK}}$. This can be exploited by adopting the following protocol (somewhat similar to Newton's method for finding roots from a linear fit): the lowest two values of T_{FL} extracted from previous iNRG runs are used to fit a parabola; the trial value of J_2 for the next iNRG run is then given by the minimum of the parabola. This protocol is illustrated in Figs. 6(c) and 6(d). J_2 converges to the critical value J_2^c exponentially rapidly in the number of separate iNRG runs. In Fig. 6(c), T_{FL} decreases by roughly one order of magnitude per iNRG run.

When the dependence of T_{FL} on the model parameters is not known analytically, a more general bisection method can instead be used to locate the critical point, provided the two phases separated by it can be distinguished in different iNRG runs. For example, in the 2CKM, the critical point J_2^c separates Kondo strong coupling phases where the impurity spin is ultimately fully screened by either lead $\alpha = 1$ or 2 (depending on the sign of $J_2 - J_2^c$). These phases can be distinguished by physical observables, e.g., the t matrix for channel α , since $t_{\alpha=2}(0) = 1$ and $t_{\alpha=1}(0) = 0$ when $J_2 > J_2^c$. In practice, a simpler and more direct way to distinguish the two phases involves comparing their NRG fixed point energy level structures, which are indexed differently.

The bisection method also involves multiple iNRG runs: each new run uses a value J_2 that is an average of two previous J_2 values (one in each phase) lying closest to each other. T_{FL} does not need to be calculated explicitly here. This protocol also locates the critical point exponentially rapidly (although utilizing information about the functional dependence of T_{FL} , where available, is the optimal strategy).

Finally, we note that the precise value of J_2^c in iNRG depends on the discretization details. However, the critical ratio J_2^c/J_1 is generally found to deviate from its exact (undiscretized) value of 1 by about 1% [see the inset of Fig. 6(d)]. We also find that J_2^c/J_1 converges to a specific value on increasing E_{trunc} , and is essentially invariant for $E_{\text{trunc}} > 7$. This indicates that the critical value of J_2^c determined by the above tuning protocol in iNRG is the true (converged) value for the asymmetrically discretized model.

V. CONCLUSION

In this paper, we compared two methods for treating multiband quantum impurity problems with NRG: sNRG exploiting model symmetries [26], and iNRG exploiting symmetry-breaking [23]. Our analysis of the NRG discarded weight [27] and the error in certain calculated physical quantities demonstrates that sNRG and iNRG are of comparable accuracy when the same discretization parameter Λ is used, and when the same number of states are kept on average at each iteration. iNRG therefore constitutes a more fine-grained RG scheme, in which intermediate state-space truncations do not adversely affect convergence or accuracy.

For models that possess high intrinsic symmetries, sNRG is a highly efficient tool for treating multiband quantum impurity problems, because full use can be made of the symmetries. But in models with lower symmetries, sNRG quickly becomes inefficient, and in practice unusable, when more than two spinful conduction electron channels are involved.

We find that iNRG is much more efficient than sNRG for treating a given model with equivalent settings. This is the appropriate comparison for systems where bare model flavor symmetries are already broken. Such a scenario naturally arises on inclusion of a magnetic field, potential scattering, channel anisotropies, and in the vicinity of high-symmetry critical points. In these cases, iNRG has the clear advantage.

For high-symmetry models where sNRG can exploit larger symmetries than iNRG, the ‘‘best’’ sNRG and iNRG calculations are found to be of roughly comparable efficiency. In this case, iNRG can be regarded as a viable and technically simple alternative to sNRG. However, *optimal* efficiency can often be obtained by *combining* features of sNRG and iNRG to interleave the Wilson chains for some electronic flavors, while retaining and exploiting other symmetries.

The results of this paper suggest that iNRG could find powerful application as an impurity solver for multiband DMFT. For example, Hubbard models of transition metal oxides with partially filled d orbitals, ruthenates, or iron pnictide and chalcogenide high-temperature superconductors map within DMFT to effective multichannel impurity problems that could be solved accurately using iNRG. In the context of simulating real strongly correlated materials, channel symmetries are generally broken (for example, due to crystal field splitting). Our analysis indicates the feasibility of studying such channel-asymmetric models for three effective channels, and further suggests that 4- and even 5-channel problems could be tackled using iNRG in the future.

We conclude that iNRG is a competitive and versatile alternative to sNRG, even for high-symmetry models. When large symmetries are not available, iNRG is far more efficient than sNRG. Moreover, iNRG provides a way forward for complex models with lower symmetries that are beyond the reach of sNRG, opening up possibilities for new applications of NRG as an impurity solver.

ACKNOWLEDGMENTS

K.M.S., A.W., and J.v.D. were supported by the DFG through SFB-TR12, SFB631, WE4819/1-1, WE4819/2-1, and the Cluster of Excellence *NanoSystems Initiative Munich*. AKM acknowledges funding from the D-ITP consortium, a program of the Netherlands Organisation for Scientific Research (NWO) that is funded by the Dutch Ministry of Education, Culture and Science (OCW).

APPENDIX A: CHOICE OF TRUNCATION ENERGY IN iNRG

In this Appendix, we provide a heuristic justification of the choice of truncation energy $E_{\text{trunc}}^{\text{iNRG}}$ proposed in Eq. (15). In iNRG, the subsites $\tilde{n} = (n, \nu)$ of supersite n are added one by one, each followed by a truncation with a different absolute truncation energy, $E_{\text{abs-trunc}}^{\text{iNRG}} = E_{\text{trunc}}^{\text{iNRG}} \tilde{\omega}_{(n,\nu)}$. The geometric average of these truncation energies over the supershell is

$$\langle E_{\text{abs-trunc}/n}^{\text{iNRG}} \rangle^{\text{geom}} = E_{\text{trunc}}^{\text{iNRG}} \left(\prod_{\nu=1}^m \tilde{\omega}_{(n,\nu)} \right)^{1/m}. \quad (\text{A1})$$

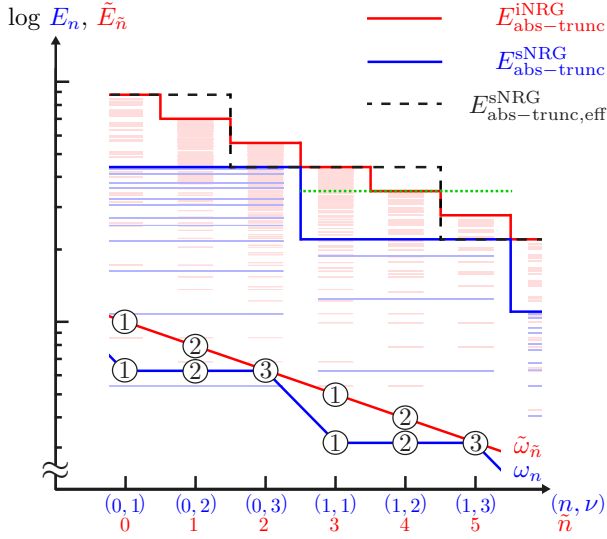


FIG. 7. Schematic depiction of the sNRG (blue) and iNRG (red) truncation schemes used here, illustrated for a model with $m = 3$ flavors. The vertical axis corresponds to absolute energies on a logarithmic scale, while the Wilson (sub)shell index is given on the horizontal axis. The lower part of the sketch depicts the evolution of the characteristic energies ω_n and $\tilde{\omega}_n$ for sNRG and iNRG. Thin faint blue and red lines depict the excitation eigenenergies (relative to the ground state energy) of sNRG supershells or iNRG subshells. In sNRG, all three subsites comprising the supersite for that iteration are added at once (there is no intermediate truncation), while in iNRG the subsites are added separately, and truncation occurs at each step. The absolute truncation energies $E_{\text{abs-trunc}}^{\text{sNRG}}$ and $E_{\text{abs-trunc}}^{\text{iNRG}}$ therefore form two different staircases, depicted as the thick blue and red lines, respectively (the step width for sNRG is m times longer than that of iNRG). States with higher energies are discarded. The truncation pattern of sNRG, when viewed from the perspective of iNRG, amounts to employing the effective truncation energy $E_{\text{abs-trunc,eff}}^{\text{sNRG}}$, shown as the black dashed line: by using a high truncation threshold (that of the previous iteration, $E_{\text{trunc}}^{\text{sNRG}} \times \omega_{n-1}$) for the first $m - 1$ subsites, and then dropping to $E_{\text{trunc}}^{\text{sNRG}} \times \omega_n$ only for the last subsite, all states are effectively kept until the supersite is complete. Viewed from this iNRG perspective, the truncation energies of iNRG and sNRG are the same on average (green dotted line for supersite $n = 1$) and the areas under the red solid, black dashed, and green dotted lines are the same, provided $E_{\text{trunc}}^{\text{sNRG}}$ and $E_{\text{trunc}}^{\text{iNRG}}$ are related via Eq. (15).

In sNRG, by contrast, all m subsites of supersite n are added as one unit, followed by truncation at the absolute truncation energy $E_{\text{abs-trunc}}^{\text{sNRG}} = E_{\text{trunc}}^{\text{sNRG}} \omega_n$. The thick red and blue lines in Fig. 7 show the resulting evolution of the absolute truncation energies in iNRG and sNRG with NRG iteration number, respectively. The characteristic energies $\tilde{\omega}_n$ and ω_n are shown as the circles in the lower part of the figure.

To meaningfully compare sNRG and iNRG, it is instructive to view the truncation profile of sNRG within the framework of iNRG. One can think of sNRG as an effective iNRG calculation, in which subsites are added separately, but the effective truncation threshold $E_{\text{abs-trunc,eff}}^{\text{sNRG}}$ for the first $m - 1$ subsites is high enough so that all states are kept. This is

guaranteed by using the absolute truncation energy of the previous iteration, $E_{\text{trunc}}^{\text{sNRG}} \times \omega_{n-1}$. Only when the supersite is complete after adding the last subsite with $\nu = m$, the effective absolute truncation energy is reduced to induce the necessary truncation $E_{\text{trunc}}^{\text{sNRG}} \times \omega_n$. Overall, the effective truncation energy in sNRG is subsite-dependent: specifically, within supersite n , we have $E_{\text{abs-trunc,eff}}^{\text{sNRG}} = E_{\text{trunc}}^{\text{sNRG}} \times \omega_{n-1+\delta_{\nu m}}$. This is shown as the black dashed line in Fig. 7. The geometric average of the effective sNRG truncation energies is

$$\langle E_{\text{abs-trunc,eff}}^{\text{sNRG}} \rangle_n^{\text{geom}} = E_{\text{trunc}}^{\text{sNRG}} \left(\omega_n \prod_{\nu=1}^{m-1} \omega_{n-1} \right)^{1/m}. \quad (\text{A2})$$

By demanding that the average truncation energies Eqs. (A1) and (A2) are the same (illustrated by the green dotted line in Fig. 7 for iteration $n = 1$), we obtain the relation between $E_{\text{trunc}}^{\text{iNRG}}$ and $E_{\text{trunc}}^{\text{sNRG}}$ announced in Eq. (15).

Finally, we comment that, given a specific number of flavors m , the choice of Eq. (15) implies that the area under the lines $E_{\text{abs-trunc}}^{\text{iNRG}}$ (red) and $E_{\text{abs-trunc,eff}}^{\text{sNRG}}$ (black dashed) is the same for each supersite n and (as exemplified for $n = 1$ in Fig. 7) corresponds to the area under the green dotted line.

The important consequence of effectively using ‘same’ absolute truncation energies on average is that the number of kept states turns out to be the same on average for iNRG and sNRG. Nevertheless, similar to even-odd effects in the number of states of sNRG, subshell-dependent variations of N_K occur in iNRG (see Fig. 3).

APPENDIX B: DISCARDED WEIGHT BASED ON ENERGY EIGENSTATES

In this Appendix, we describe how to quantify the contributions of highly energetic *energy eigenstates* to reduced density matrices, rather than evaluating the eigenspectrum of the reduced density matrices as in Ref. [27]. We do this by analyzing the diagonal weights of $\hat{\rho}$, i.e., the diagonal elements of the reduced density matrix in the *energy* eigenbasis $|s\rangle_K$ within the kept sector, $\rho_s = \langle s | \hat{\rho} | s \rangle_K$. Hence we employ a strategy analogous to that of Ref. [27], but here we use the energy eigenbasis (cf. Fig. 3 of Ref. [27] and Fig. 8) rather than the eigenbasis of the reduced density matrices (cf. Fig. 4 of Ref. [27]) to estimate the discarded weight. This leads to a slightly different definition of the discarded weight, as described below.

Due to the energy scale separation in NRG, the diagonal weights of the reduced density matrices decrease exponentially when plotted versus their corresponding rescaled eigenenergies (cf. colored dots in Fig. 8). The same is true for the integrated weight distribution [cf. Eq. (18) of Ref. [27] and black solid line in Fig. 8], which as such constitutes an upper bound for the weights, and scales as $\rho(E) \approx \kappa e^{-\kappa E}$ (normalized such that $\int_0^\infty \rho(E) dE = 1$). This exponential decay shows that the contribution of an NRG state with rescaled energy E to the properties of subsequent shells decreases exponentially with E . This justifies the strategy in NRG to keep track of these contributions only up to a threshold energy of E_{trunc} . Moreover, by extrapolating the exponential form to energies beyond E_{trunc} , the sum of weights associated with all discarded high energy states with $E > E_{\text{trunc}}$ can be estimated. We therefore define the total discarded weight by

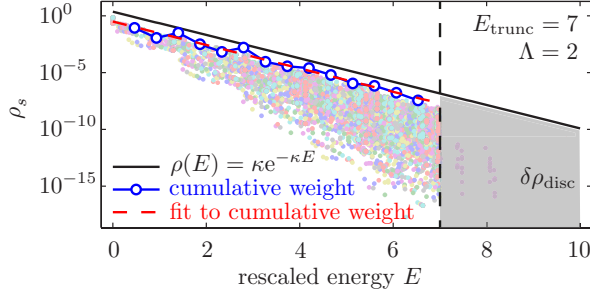


FIG. 8. Estimating the discarded weight, $\delta\rho_{\text{disc}}$, of a single NRG run. Colored dots show the diagonal weights of the reduced density matrices in the energy eigenbasis of NRG. Different colors represent the weights for different NRG iterations. We calculate and plot the cumulative weights (blue open circles) using 16 bins in the energy window $[0, E_{\text{trunc}}]$. The truncation energy $E_{\text{trunc}} = 7$ is indicated by the vertical black dashed line. The red dashed line is an exponential fit to the cumulative weights; its slope gives κ as defined in Eq. (B1). The black line shows the normalized integrated weight distribution $\rho(E) = \kappa e^{-\kappa E}$, extrapolated to energies $E > E_{\text{trunc}}$. The shaded grey area under this black line then serves as estimate for the discarded weight: $\delta\rho_{\text{disc}} = e^{-\kappa E_{\text{trunc}}}$. This example is well-converged, with $\kappa = 2.37$ yielding $\delta\rho_{\text{disc}} = 6.23 \times 10^{-8}$.

the following integral (represented by the shaded grey area in Fig. 8):

$$\delta\rho_{\text{disc}} = \int_{E_{\text{trunc}}}^{\infty} \rho(E) dE = e^{-\kappa E_{\text{trunc}}}. \quad (\text{B1})$$

In practice, we obtain $\delta\rho_{\text{disc}}$ numerically as follows. First, a cumulative histogram is constructed of the discrete weights ρ_s for $E < E_{\text{trunc}}$ over all NRG iterations, using coarse-grained energy bins (e.g., keeping 16 bins in the energy window $[0, E_{\text{trunc}}]$). This histogram represents $\rho(E)$. A linear fit to its shape on a semilogarithmic scale then yields κ , which in turn gives $\delta\rho_{\text{disc}}$, via Eq. (B1). Since $\delta\rho_{\text{disc}}$ depends only on the dimensionless quantity κE_{trunc} , the result is independent of the choice of energy unit for E_{trunc} .

By examining the decay of the discarded weight $\delta\rho_{\text{disc}}$ with increasing E_{trunc} , and observing the corresponding convergence of physical quantities, we have found that calculations can be considered converged when $\delta\rho_{\text{disc}} < 10^{-6}$. This convergence criterion has been determined to ensure that further increasing E_{trunc} does not qualitatively change the results [see, e.g., Figs. 2(j)–2(o)]. We note that the numerical value of this threshold is about the square-root of and thus considerably larger than that reported in Ref. [27], which was obtained using the alternative definition of discarded weight in terms of the eigenspectrum of reduced density matrices.

An important advantage of defining the discarded weight in terms of the energy eigenbasis is that $\delta\rho_{\text{disc}}$, evaluated at fixed E_{trunc} , is rather insensitive to changing the discretization parameter Λ (we verified this explicitly over a range of Λ typically used in NRG, $1.7 \lesssim \Lambda \lesssim 7$). We found that $E_{\text{trunc}} \gtrsim 7$ generally suffices to obtain well-converged results for physical quantities. In contrast, the discarded weight defined in terms of density matrix eigenvalues [27] turns out to show a much more pronounced dependence on Λ at fixed E_{trunc} , which would be inconvenient for the present purposes.

-
- [1] A. C. Hewson, *The Kondo Problem to Heavy Fermions* (Cambridge University Press, Cambridge, 1993).
- [2] J. Kondo, *Prog. Theor. Phys.* **32**, 37 (1964).
- [3] K. G. Wilson, *Rev. Mod. Phys.* **47**, 773 (1975).
- [4] H. R. Krishnamurthy, J. W. Wilkins, and K. G. Wilson, *Phys. Rev. B* **21**, 1003 (1980).
- [5] R. Bulla, T. Costi, and T. Pruschke, *Rev. Mod. Phys.* **80**, 395 (2008).
- [6] T. A. Costi, L. Bergqvist, A. Weichselbaum, J. von Delft, T. Micklitz, A. Rosch, P. Mavropoulos, P. H. Dederichs, F. Mallet, L. Saminadayar, and C. Bäuerle, *Phys. Rev. Lett.* **102**, 056802 (2009).
- [7] M. Hanl, A. Weichselbaum, T. A. Costi, F. Mallet, L. Saminadayar, C. Bäuerle, and J. von Delft, *Phys. Rev. B* **88**, 075146 (2013).
- [8] B. A. Jones, C. M. Varma, and J. W. Wilkins, *Phys. Rev. Lett.* **61**, 125 (1988); B. A. Jones, *Physica B: Condens. Matter* **171**, 53 (1991).
- [9] A. K. Mitchell, P. G. Dery, and D. E. Logan, *Phys. Rev. B* **91**, 235127 (2015).
- [10] J. Bork, Y. hui Zhang, L. Diekhöner, L. Borda, P. Simon, J. Kroha, P. Wahl, and K. Kern, *Nat. Phys.* **7**, 901 (2011).
- [11] A. Schwabe, M. Hänsel, M. Potthoff, and A. K. Mitchell, *Phys. Rev. B* **92**, 155104 (2015).
- [12] P. Jarillo-Herrero, J. Kong, H. S. J. van der Zant, C. Dekker, L. P. Kouwenhoven, and S. D. Franceschi, *Nature* **434**, 484 (2005).
- [13] S. J. Chorley, M. R. Galpin, F. W. Jayatilaka, C. G. Smith, D. E. Logan, and M. R. Buitelaar, *Phys. Rev. Lett.* **109**, 156804 (2012).
- [14] M. Pustilnik, L. Borda, L. I. Glazman, and J. von Delft, *Phys. Rev. B* **69**, 115316 (2004).
- [15] A. K. Mitchell and D. E. Logan, *Phys. Rev. B* **81**, 075126 (2010).
- [16] A. K. Mitchell, D. E. Logan, and H. R. Krishnamurthy, *Phys. Rev. B* **84**, 035119 (2011).
- [17] B. Béni and N. R. Cooper, *Phys. Rev. Lett.* **109**, 156803 (2012).
- [18] M. R. Galpin, A. K. Mitchell, J. Temaismithi, D. E. Logan, B. Beri, and N. R. Cooper, *Phys. Rev. B* **89**, 045143 (2014).
- [19] A. Georges, G. Kotliar, W. Krauth, and M. J. Rozenberg, *Rev. Mod. Phys.* **68**, 13 (1996).
- [20] T. Pruschke and R. Bulla, *Eur. Phys. J. B* **44**, 217 (2005).
- [21] K. M. Stadler, Z. P. Yin, J. von Delft, G. Kotliar, and A. Weichselbaum, *Phys. Rev. Lett.* **115**, 136401 (2015).
- [22] M. H. Hettler, M. Mukherjee, M. Jarrell, and H. R. Krishnamurthy, *Phys. Rev. B* **61**, 12739 (2000).
- [23] A. K. Mitchell, M. R. Galpin, S. Wilson-Fletcher, D. E. Logan, and R. Bulla, *Phys. Rev. B* **89**, 121105(R) (2014).
- [24] A. I. Tóth and G. Zaránd, *Phys. Rev. B* **78**, 165130 (2008).
- [25] W. Hofstetter, *Phys. Rev. Lett.* **85**, 1508 (2000).

- [26] A. Weichselbaum, *Ann. Phys.* **327**, 2972 (2012).
- [27] A. Weichselbaum, *Phys. Rev. B* **84**, 125130 (2011).
- [28] L. N. Oliveira, V. L. Libero, H. O. Frota, and M. Yoshida, *Physica B: Condensed Matter* **171**, 61 (1991).
- [29] W. C. Oliveira and L. N. Oliveira, *Phys. Rev. B* **49**, 11986 (1994).
- [30] R. Zitko and T. Pruschke, *Phys. Rev. B* **79**, 085106 (2009).
- [31] A. Weichselbaum and J. von Delft, *Phys. Rev. Lett.* **99**, 076402 (2007).
- [32] F. B. Anders and A. Schiller, *Phys. Rev. Lett.* **95**, 196801 (2005); *Phys. Rev. B* **74**, 245113 (2006).
- [33] P. Nozières and A. Blandin, *J. Phys. (Paris)* **41**, 193 (1980).
- [34] I. Affleck, A. W. W. Ludwig, H.-B. Pang, and D. L. Cox, *Phys. Rev. B* **45**, 7918 (1992).
- [35] E. Sela, A. K. Mitchell, and L. Fritz, *Phys. Rev. Lett.* **106**, 147202 (2011); A. K. Mitchell and E. Sela, *Phys. Rev. B* **85**, 235127 (2012).
- [36] M. Hanl, A. Weichselbaum, J. von Delft, and M. Kiselev, *Phys. Rev. B* **89**, 195131 (2014).
- [37] I. Affleck and A. W. W. Ludwig, *Phys. Rev. B* **48**, 7297 (1993).

2.4 Open Wilson chains

2.4.1 Overview

In this section we present a side project of this dissertation, which is based on the following background. In SWCs bath modes are neglected within the discretization process by keeping only a single mode per interval (cf. Sec. 2.2.2) and by cutting the Wilson chain at site N_T . These approximations essentially replace an open by a closed system and introduce finite size effects, leading to errors in the renormalization of impurity properties and in bath induced dissipative effects, as required for the correct description of nonequilibrium situations. Already K. G. Wilson himself has pointed out the importance of these neglected bath modes when he introduced NRG in Ref. [Wil75].

In our article entitled “Open Wilson chains for quantum impurity models: Keeping track of all bath modes” [BLS⁺17], we introduce a new Wilson chain construction, leading to so-called open Wilson chains (OWCs), which *systematically and fully keep track of bath modes neglected in the standard Wilson chain (SWC) setup*, thus solving a longstanding fundamental problem.

OWCs are iteratively constructed by a continued fraction expansion of the free retarded bath correlator, introducing energy-scale separation by splitting the emerging retarded self-energies in each step into high-energy and low-energy parts. This results in a SWC, where each Wilson site is coupled to a bath of its own (“fast” bath) and the last chain site additionally to a “slow” bath, representing the rest of the infinite chain. This retains the open character of the many-body impurity problem.

In this article we concentrate on impurity models with asymmetric bath spectral functions, namely a dissipative harmonic oscillator (DHO) and the sub-Ohmic spin-boson model (SBM) at quantum criticality, for which the neglect of the slow bath introduces the so-called “mass-flow problem”, a qualitatively wrong renormalization of system parameters at finite temperature. To cure the mass-flow problem in practice, we define a renormalized Wilson chain (RWC) – a SWC with shifted on-site energies – taking into account the energy shifts induced by each of the baths in terms of the real parts of their retarded self-energies at zero frequency. We solve the DHO and SBM using the variational matrix-product-state (VMPS) approach of Refs. [GWvDV12, BWG⁺14] (instead of NRG) to reliably deal with the bosonic baths. We demonstrate the value of RWCs by reproducing exactly known results for the susceptibility in the DHO, which are not captured correctly in the framework of SWCs. Furthermore, we reach the Gaussian critical fixed point of the SBM at quantum criticality with full RWCs, which is inaccessible for SWCs. We are even able, for the first time, to directly investigate the energy RG flow towards this fixed point, quantitatively reproducing analytic predictions from a controlled perturbative RG.

Besides solving the mass-flow problem, we stress that the framework of OWCs is broadly applicable to a variety of physical problems. In particular, OWCs allow to include dissipative effects, as required for the description of nonequilibrium physics, by taking into account the imaginary parts of the retarded bath self-energies. But OWCs can also be used, for instance, in the context of DMFT to construct the Wilson chains for effective multi-channel impurity models with off-diagonal couplings.

As a final remark, we acknowledge that VMPS calculations were carried out by the first and second author, B. Bruognolo and N.-O. Linden. The author of this thesis contributed to this project by codeveloping and testing the OWC scheme, by helping the former master student N.-O. Linden with NRG-related issues and by supervising a bachelor thesis on using an OWC approach to broaden discrete spectral functions (Lorenz Mayer, [Broadening of spectral functions in the discretized single impurity Anderson model](#), 2015).

Open Wilson chains for quantum impurity models: Keeping track of all bath modes

by

B. Bruognolo,^{1,2} N.-O. Linden,¹ F. Schwarz,¹ S.-S. B. Lee,¹ K. Stadler,¹ A. Weichselbaum,¹ M. Vojta,³ F. B. Anders,⁴ and J. von Delft¹

¹Physics Department, Arnold Sommerfeld Center for Theoretical Physics and Center for NanoScience, Ludwig-Maximilians-Universität München, D-80333 München, Germany

²Max-Planck-Institut für Quantenoptik, Hans-Kopfermann-Strasse 1, D-85748 Garching, Germany

³Institut für Theoretische Physik, Technische Universität Dresden, D-01062 Dresden, Germany

⁴Lehrstuhl für Theoretische Physik II, Technische Universität Dortmund, D-44221 Dortmund, Germany

reprinted on pages **51–55**

with permission from

***Phys. Rev. B* 95, 121115(R) (2017),**

DOI: [10.1103/PhysRevB.95.121115](https://doi.org/10.1103/PhysRevB.95.121115).

© 2017 American Physical Society

Supplemental Material reprinted on pages **56–67**.

Open Wilson chains for quantum impurity models: Keeping track of all bath modesB. Bruognolo,^{1,2} N.-O. Linden,¹ F. Schwarz,¹ S.-S. B. Lee,¹ K. Stadler,¹ A. Weichselbaum,¹ M. Vojta,³ F. B. Anders,⁴ and J. von Delft¹¹*Physics Department, Arnold Sommerfeld Center for Theoretical Physics and Center for NanoScience, Ludwig-Maximilians-Universität München, D-80333 München, Germany*²*Max-Planck-Institut für Quantenoptik, Hans-Kopfermann-Strasse 1, D-85748 Garching, Germany*³*Institut für Theoretische Physik, Technische Universität Dresden, D-01062 Dresden, Germany*⁴*Lehrstuhl für Theoretische Physik II, Technische Universität Dortmund, D-44221 Dortmund, Germany*

(Received 22 November 2016; published 31 March 2017)

When constructing a Wilson chain to represent a quantum impurity model, the effects of truncated bath modes are neglected. We show that their influence can be kept track of systematically by constructing an “open Wilson chain” in which each site is coupled to a separate effective bath of its own. As a first application, we use the method to cure the so-called mass-flow problem that can arise when using standard Wilson chains to treat impurity models with asymmetric bath spectral functions at finite temperature. We demonstrate this for the strongly sub-Ohmic spin-boson model at quantum criticality where we directly observe the flow towards a Gaussian critical fixed point.

DOI: [10.1103/PhysRevB.95.121115](https://doi.org/10.1103/PhysRevB.95.121115)

A quantum impurity model describes a discrete set of degrees of freedom, the “impurity”, coupled to a bath of excitations. For an infinite bath this is effectively an *open* system. However, the most powerful numerical methods for solving such models, Wilson’s numerical renormalization group (NRG) [1,2] and variational matrix-product-state (VMPS) generalizations thereof [3–6], actually treat it as *closed*: The continuous bath is replaced by a so-called Wilson chain, a finite-length tight-binding chain whose hopping matrix elements t_n decrease exponentially with site number n , ensuring energy-scale separation along the chain. This works well for numerous applications, ranging from transport through nanostructures [7,8] to impurity solvers for dynamical mean-field theory [9–11]. However, replacing an open by a closed system brings about finite-size effects. Wilson himself had anticipated that the effect of bath modes neglected during discretization might need to be included perturbatively “to achieve reasonable accuracy”, but concluded that “this has proven to be unnecessary” for his purposes (see p. 813 of Ref. [1]). By now, it is understood that finite-size effects often do matter. They hamper the treatment of dissipative effects [12], e.g., in the context of nonequilibrium transport [13] and equilibration after a local quench [14]. Moreover, even in equilibrium, they may cause errors when computing the bath-induced renormalization of impurity properties [15–17]. Indeed, finite-size issues constitute arguably the most serious conceptual limitation of approaches based on Wilson chains.

Here, we set the stage for controlling finite-size effects by constructing “open Wilson chains” (OWCs) in which each site is coupled to a bath of its own. The resulting open system implements energy-scale separation in a way that, in contrast to standard Wilson chains (SWCs), fully keeps track of all bath-induced dissipative and renormalization effects. The key step involved in any renormalization group (RG) approach, namely, integrating out degrees of freedom at one energy scale to obtain a renormalized description at a lower scale, can then be performed more carefully than for SWCs. We illustrate this by focusing on renormalization effects, leaving a systematic treatment of dissipative effects on OWCs for the future.

A SWC is constructed by logarithmically discretizing the bath and tridiagonalizing the resulting discrete bath Hamiltonian to obtain a tight-binding chain, with the impurity coupled to site $n = 0$ [1,2]. Properties at temperature T are calculated using a chain of finite length N_T , chosen such that its smallest energy scale matches the temperature $t_{N_T} \simeq T$ ($k_B = 1$). However, since sites $n > N_T$ are neglected, the contribution of the corresponding truncated bath modes (TBMs) to the renormalization of impurity properties is missing [17]. For example, for a local level linearly coupled to a bath with an asymmetric bath spectrum, this coupling generates a physical shift in the level energy. When this shift is computed using a SWC of length N_T , the result contains a temperature-dependent error. Hence, the use of SWCs generically leads to qualitative errors in the temperature dependence of renormalized model parameters, called the “mass-flow problem” [16,17]. Quantitative errors persist even for $T \rightarrow 0$, when $N_T \rightarrow \infty$, because constructing a SWC actually involves neglecting TBMs at *every* site.

The mass-flow problem is particularly serious when targeting a quantum critical point, where it causes errors for critical exponents describing finite-temperature properties at the critical point. This has been studied in some detail for the dissipative harmonic oscillator (DHO) and the sub-Ohmic spin-boson model (SBM). For both, SWCs are unable to even qualitatively describe the temperature dependence of the local susceptibility $\chi(T)$ at criticality [15–17]. Both involve Gaussian criticality of ϕ^4 type and hence a bosonic mode whose excitation energy vanishes at the critical fixed point. The finite-temperature RG flow in its vicinity cannot be correctly described using finite-length SWCs because the erroneous mass dominates over physical interaction effects. Summarizing, methods based on SWCs produce systematic quantitative errors for all impurity problems with asymmetric baths, and they fail even qualitatively in addressing Gaussian criticality and other phenomena with zero modes.

Here, we show that these issues *can* be addressed using OWCs: The bath coupled to each site of the OWC induces an energy shift for that site that can be computed *exactly* and

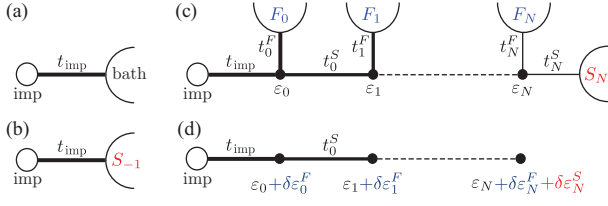


FIG. 1. (a) Impurity model. (b) Initialization. (c) Open Wilson chain (OWC). (d) Renormalized Wilson chain (RWC).

used to define a “renormalized Wilson chain” (RWC). The ground-state properties of a RWC of length N_T mimic the finite- T properties of the original model in a way that is free from mass-flow problems. We demonstrate this explicitly by using VMPS techniques [6] on RWCs to compute $\chi(T)$ for the DHO and SBM. We also compute the energy-level flow of the SBM; it unambiguously reveals flow towards a Gaussian fixed point with a dangerously irrelevant interaction term.

Model. We consider a generic single-band impurity model with Hamiltonian $\mathcal{H} = \mathcal{H}^{\text{imp}}[b^\dagger t_{\text{imp}}] + \mathcal{H}^{\text{bath}}$, where $\mathcal{H}^{\text{bath}}$ describes the bath, and \mathcal{H}^{imp} the impurity and its coupling to the bath via normalized bath operators b^\dagger and b , with coupling constant t_{imp} [Fig. 1(a)]. The free ($t_{\text{imp}} = 0$) dynamics of b^\dagger , generated by $\mathcal{H}^{\text{bath}}$, is encoded in the free retarded correlator $\mathcal{G}^{\text{bath}}(\omega) = \langle\langle b|b^\dagger \rangle\rangle_\omega$, which is uniquely characterized by its spectral function $\mathcal{A}^{\text{bath}}(\omega) = -\frac{1}{\pi} \text{Im} \mathcal{G}^{\text{bath}}(\omega)$. The impurity dynamics is therefore fully determined once \mathcal{H}^{imp} and the “bath spectrum”, $\Gamma^{\text{bath}}(\omega) = |t_{\text{imp}}|^2 \mathcal{A}^{\text{bath}}(\omega)$, have been specified.

Continued-fraction expansion. One well-known way of mapping an impurity model to a chain is to iteratively construct a continued-fraction expansion (CFE) for $\mathcal{G}^{\text{bath}}$ [18]. Our main idea is to do this in a way that *zooms in on low energies* without discarding high-energy information. Our construction involves a sequence of retarded correlators $\mathcal{G}_n^X(\omega)$, with $X = S$ or F , describing the effective “slow” (low-energy) or “fast” (high-energy) bath modes of iteration step n , with spectral functions $\mathcal{A}_n^X(\omega) = -\frac{1}{\pi} \text{Im} \mathcal{G}_n^X(\omega)$ having unit weight $\int d\omega \mathcal{A}_n^X(\omega) = 1$. We initialize our CFE construction with $\mathcal{G}_{-1}^S = \mathcal{G}^{\text{bath}}$ [Fig. 1(b)]. Starting with $n = 0$, we iteratively use \mathcal{G}_{n-1}^S , describing the low-energy modes of the previous iteration, as input to define a new retarded correlator \mathcal{G}_n and its retarded self-energy Σ_n ,

$$\mathcal{G}_n(\omega) = \mathcal{G}_{n-1}^S(\omega) = 1/[\omega - \varepsilon_n - \Sigma_n(\omega)], \quad (1)$$

with $\varepsilon_n = \int d\omega \omega \mathcal{A}_n(\omega)$ [19]. Then we split this self-energy into low- and high-energy parts by writing it as

$$\Sigma_n(\omega) = \Sigma_n^S(\omega) + \Sigma_n^F(\omega), \quad \Sigma_n^X(\omega) = |t_n^X|^2 \mathcal{G}_n^X(\omega). \quad (2)$$

Here, the corresponding retarded correlators $\mathcal{G}_n^{S/F}$ are defined by choosing their rescaled spectral functions $|t_n^{S/F}|^2 \mathcal{A}_n^{S/F}(\omega)$ to represent the low- and high-energy parts of $\Gamma_n(\omega) = -\frac{1}{\pi} \text{Im} \Sigma_n$, with t_n^X chosen such that \mathcal{A}_n^X has unit weight (see Sec. S-1 A of Ref. [19] for details). To be explicit, we write $\Gamma_n = \Gamma_n^S + \Gamma_n^F$, with $\Gamma_n^X(\omega) = w_n^X(\omega) \Gamma_n(\omega)$. The splitting functions $w_n^{S/F}(\omega)$ are defined on the support of Γ_n , take values in the interval $[0, 1]$, satisfy $w_n^S(\omega) + w_n^F(\omega) = 1$, and have weight predominantly at low/high energies. Then

we write the split bath spectra as $\Gamma_n^X(\omega) = |t_n^X|^2 \mathcal{A}_n^X(\omega)$, with “couplings” t_n^X chosen as $|t_n^X|^2 = \int d\omega \Gamma_n^X(\omega)$, and define new retarded correlators via $\mathcal{G}_n^X(\omega) = \int d\tilde{\omega} \frac{\mathcal{A}_n^X(\tilde{\omega})}{\omega - \tilde{\omega} + i0^+}$, also fixing $\Sigma_n^X(\omega)$ via Eq. (2).

Iterating, using \mathcal{G}_n^S as input to compute new correlators \mathcal{G}_{n+1}^X while retaining the self-energy Σ_n^F , we obtain a sequence of exact CFE representations for $\mathcal{G}^{\text{bath}}$. That of depth 2, e.g., reads

$$\mathcal{G}^{\text{bath}}(\omega) = \frac{1}{\omega - \varepsilon_0 - \Sigma_0^F(\omega) - \frac{|t_0^S|^2}{\omega - \varepsilon_1 - \Sigma_1^F(\omega) - \frac{|t_1^S|^2}{\omega - \varepsilon_2 - \Sigma_2^F(\omega)}}}.$$

To ensure energy-scale separation, we choose $\mathcal{A}_n^X(\omega)$ such that the CFE parameters decrease monotonically, $\max\{|\varepsilon_n|, |t_n^S|\} \leq \max\{|\varepsilon_{n-1}|, |t_{n-1}^S|\}/\Lambda$, with $\Lambda > 1$ [20].

Open Wilson chain. We now use the CFE data $(\varepsilon_n, t_n^X, \mathcal{G}_n^X)$ to represent the original bath in terms of a chain with $N + 1$ sites, each coupled to a bath of its own, and site 0 coupled to the impurity (site -1) [Fig. 1(c)]. This OWC is constructed such that the free ($t_{\text{imp}} = 0$) correlator of site 0 is exactly equal to the depth- N CFE found above, i.e., $\mathcal{G}_0 = \mathcal{G}^{\text{bath}}$, implying that the chain and original bath have the same effect on the impurity.

The key point is that each CFE step of writing $\mathcal{G}_{n-1}^S(\omega)$ in the form $\mathcal{G}_n(\omega) = 1/[\omega - \varepsilon_n - \Sigma_n(\omega)]$ can be implemented on the level of the Hamiltonian: It corresponds to replacing the bath represented by \mathcal{G}_{n-1}^S , say, S_{n-1} , by a new site n , with energy ε_n and normalized site operators f_n^\dagger and f_n , which is linearly coupled to a new bath that generates the self-energy Σ_n . In the present case, the latter is split into low- and high-energy contributions, $\Sigma_n^S + \Sigma_n^F$. We can generate these by linearly coupling the new site with couplings t_n^S and t_n^F to two new baths, say, S_n and F_n , via normalized bath operators $b_{S_n}^\dagger, b_{S_n}$ and $b_{F_n}^\dagger, b_{F_n}$, that are governed by bath Hamiltonians \mathcal{H}_n^X chosen such that $\langle\langle b_{Xn}|b_{Xn}^\dagger \rangle\rangle_\omega$ equals the $\mathcal{G}_n^X(\omega)$ found above (see Sec. S-1 A of Ref. [19] for details). For the next iteration, we retain the fast bath F_n , but replace the slow bath S_n by a new site $n + 1$ coupled to new baths S_{n+1} and F_{n+1} , etc. This leads to replacing \mathcal{H} by $\mathcal{H}_N^{\text{OWC}} = \mathcal{H}_N^{\text{SWC}} + \mathcal{H}_N^{\text{TBM}}$, with

$$\begin{aligned} \mathcal{H}_N^{\text{SWC}} &= \mathcal{H}_f^{\text{imp}} + \sum_{n=0}^N \varepsilon_n f_n^\dagger f_n + \sum_{n=0}^{N-1} (f_{n+1}^\dagger t_n^S f_n + \text{H.c.}), \\ \mathcal{H}_N^{\text{TBM}} &= \sum_{n=0}^N (b_{F_n}^\dagger t_n^F f_n + \text{H.c.}) + \sum_{n=0}^N \mathcal{H}_n^F \\ &\quad + (b_{S_N}^\dagger t_N^S f_N + \text{H.c.}) + \mathcal{H}_N^S, \end{aligned} \quad (3)$$

and $\mathcal{H}_f^{\text{imp}} = \mathcal{H}^{\text{imp}}[f_0^\dagger t_{\text{imp}}]$. This chain Hamiltonian is depicted schematically in Fig. 1(c). $\mathcal{H}_N^{\text{SWC}}$ has the structure of a SWC, while $\mathcal{H}_N^{\text{TBM}}$ describes the couplings to all fast baths $F_{n \leq N}$, and of the last site N to its slow bath S_N . These “fast and last slow” baths F_n and S_N constitute TBMs, since a SWC neglects them. By instead using an OWC, we can keep track of their influence, namely, to shift, mix, and broaden the eigenstates of those subchains to which they couple. Equation (3), which represents an impurity model in terms of a Wilson chain that

still is a fully open system, is the first main result of this Rapid Communication.

Renormalized Wilson chain. For concrete numerical calculations, we need to approximate an OWC by a RWC that can be treated using standard NRG or VMPS methods, while still including information about the TBMs. To this end, we replace \mathcal{H}^{OWC} by \mathcal{H}^{RWC} [Fig. 1(d)], a Hamiltonian of the same form as \mathcal{H}^{SWC} (without fast or last baths), but with each on-site energy ε_n shifted to

$$\tilde{\varepsilon}_n = \varepsilon_n + \delta\varepsilon_n^F + \delta_{nN} \delta\varepsilon_N^S, \quad \delta\varepsilon_n^X = \text{Re}[\Sigma_n^X(0)]. \quad (4)$$

For the CFE of $\mathcal{G}^{\text{bath}} = \mathcal{G}_{-1}^S = \mathcal{G}_0$, this amounts to replacing the slow and fast self-energies by the real parts of their zero-frequency values [21]. Therefore, $\text{Re}[\Sigma^{\text{bath}}(0)]$, the real part of the zero-frequency self-energy of $\mathcal{G}^{\text{bath}}$, is reproduced correctly [22], irrespective of the length N of the RWC used to calculate $\mathcal{G}^{\text{bath}}$. (Since the imaginary parts of all self-energies are neglected, dissipative effects are not included.) If the original bath spectrum is symmetric, $\Gamma^{\text{bath}}(\omega) = \Gamma^{\text{bath}}(-\omega)$, as often happens for fermionic models, then $\delta\varepsilon_n^{S/F} = 0$. However, for an asymmetric bath function [e.g., $\Gamma^{\text{bath}}(\omega < 0) = 0$, as is the case for bosonic baths], these shifts are in general nonzero.

We will henceforth consider two types of RWCs, labeled by C1 or C2 [23]. A C1 chain includes only fast shifts ($\delta\varepsilon_N^S = 0$); this turns out to lead to results qualitatively similar to those obtained using a SWC constructed by discretizing the original bath logarithmically, as done by Wilson, and tridiagonalizing the bath Hamiltonian $\mathcal{H}^{\text{bath}}$. A C2 chain includes both the fast and slow shifts from Eq. (4), thus correctly reproducing $\text{Re}[\Sigma^{\text{bath}}(0)]$.

Dissipative harmonic oscillator. As a first example, consider a DHO with Hamiltonian $\mathcal{H}_{\text{DHO}}^{\text{imp}} + \mathcal{H}^{\text{bath}}$, where

$$\mathcal{H}_{\text{DHO}}^{\text{imp}} = \Omega a^\dagger a + \frac{1}{2}(a + a^\dagger)[\epsilon + t_{\text{imp}}(b + b^\dagger)] \quad (5)$$

describes an “impurity” oscillator with bare frequency Ω and displacement force ϵ , linearly coupled to a bosonic bath. The bath spectral function has the form

$$\Gamma^{\text{bath}}(\omega) = 2\alpha\omega_c^{1-s}\omega^s, \quad 0 < \omega < \omega_c, \quad (6)$$

where $s > -1$, α characterizes the dissipation strength, and ω_c is a cutoff frequency, henceforth set to unity. This model is exactly solvable. The static impurity susceptibility at temperature T , defined by $\chi(T) = \frac{d\langle a + a^\dagger \rangle_T}{d\epsilon}|_{\epsilon=0}$, turns out to be temperature independent and given by [17] $\chi_{\text{exact}}(T) = 1/\Omega_r$, where $\Omega_r = \Omega + \text{Re}[\mathcal{G}^{\text{bath}}(\omega = 0)]$ can be interpreted as the renormalized impurity frequency, reduced relative to the bare one by the coupling to the bath. It vanishes at the critical coupling $\alpha_c = s\Omega/(2\omega_c)$, beyond which the model becomes unstable.

When $\chi(T)$ is computed numerically for $\alpha < \alpha_c$ using NRG to perform thermal averages on SWCs of length N_T , one does not obtain a constant but a temperature-dependent curve [15–17]. We find the same using NRG on C1-RWCs of length N_T (Fig. 2, circles). The reason is the neglect of the TBMs associated with sites $n > N_T$: Their contribution to the renormalization shift $\text{Re}[\mathcal{G}^{\text{bath}}(\omega = 0)]$ in Ω_r is missing. The approach developed above offers a straightforward cure: We simply compute $\chi(T)$ using C2-RWCs of length N_T , thus incorporating the energy shift induced by the remaining TBMs via

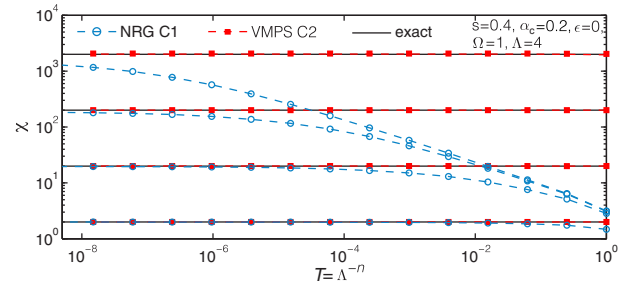


FIG. 2. DHO susceptibility $\chi(T)$ as function of temperature, computed by NRG on C1-RWCs (circles) and by VMPS on C2-RWCs (squares), for $\alpha = 0.1, 0.19, 0.199, \text{ and } 0.1999$ (from bottom to top). Solid lines show exact results.

the slow-mode shift for site N_T . Since the latter substantially affects the low-energy spectrum, these calculations require VMPS methods (see Secs. S-2 B and S-2 C of Ref. [19] for details). They yield T -independent χ values (Fig. 2, squares), in excellent agreement with the exact ones (Fig. 2, solid lines).

We remark that SWCs constructed using previous discretization schemes [24–26] either strongly over- or underestimate the critical coupling α_c , reflecting the presence of discretization artifacts. In contrast, our C2-RWCs yield α_c values that match the analytic results almost perfectly (see Sec. S-3 D of Ref. [19]). Thus, our RWC construction constitutes a general, new discretization scheme free of the discretization artifacts of previous schemes.

Spin-boson model. Next, we consider the SBM, which is not exactly solvable. In its Hamiltonian $\mathcal{H}_{\text{SBM}}^{\text{imp}} + \mathcal{H}^{\text{bath}}$,

$$\mathcal{H}_{\text{SBM}}^{\text{imp}} = -\frac{1}{2}\Delta\hat{\sigma}_x + \frac{1}{2}\hat{\sigma}_z[\epsilon + t_{\text{imp}}(b + b^\dagger)] \quad (7)$$

describes a spin- $\frac{1}{2}$ “impurity” ($\hat{\sigma}_i$ being Pauli matrices) linearly coupled to a bosonic bath, with $\Gamma^{\text{bath}}(\omega)$ again given by Eq. (6). ϵ and Δ denote the bias and the tunnel splitting of the impurity spin, respectively.

For the *sub-Ohmic* case ($0 < s < 1$), increasing α at zero temperature drives the SBM through a quantum phase transition (QPT) from a delocalized to a localized phase (with $\langle \hat{\sigma}_z \rangle_0 = 0$ or $\neq 0$, respectively). According to a quantum-to-classical correspondence (QCC) argument [15,16,27], this QPT belongs to the same universality class as that of a classical one-dimensional Ising chain with long-ranged interactions [28]. Thus, the critical exponents characterizing the QPT follow mean-field predictions for $s \leq 0.5$ and obey hyperscaling for $0.5 < s < 1$. The QCC predictions were confirmed numerically using Monte Carlo methods [29] or sparse polynomial bases [30].

In contrast, verifying the QCC predictions using NRG turned out to be challenging. Initial NRG studies [15] yielded non-mean-field exponents for $s < 0.5$, but were subsequently [16,17] found to be unreliable, due to two inherent limitations of NRG. The first was a too severe NRG truncation of Hilbert space in the localized phase; it was overcome in Ref. [6] by using a VMPS approach involving an optimized boson basis [31–33] on a SWC, which reproduced QCC predictions for critical exponents characterizing zero-temperature behavior. The second NRG limitation was the mass-flow problem:

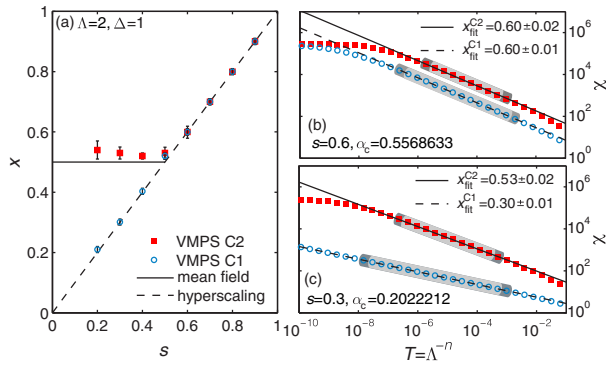


FIG. 3. (a) Critical exponent x for the sub-Ohmic SBM, as a function of s , computed by VMPS using RWCs of type C1 (circles) and C2 (squares). Examples of $\chi(T)$ curves used to extract these exponents are shown in (b) for $s = 0.3$ and (c) for $s = 0.6$. Error bars in (a) are derived by varying the fitting ranges, e.g., as indicated by dark and light shading in (b) and (c).

For exponents describing *finite*-temperature critical behavior at $\alpha = \alpha_c$, it causes NRG on SWCs to yield hyperscaling results not only for $0.5 < s < 1$ (correct) but also for $s < 0.5$ (incorrect). For example, consider the susceptibility $\chi(T) = \frac{d(\hat{\sigma}_z)_T}{d\epsilon} \Big|_{\epsilon=0}$, which scales as $\chi(T) \propto T^{-x}$ at the critical coupling α_c . The QCC predicts $x = 0.5$ for $s < 0.5$ and $x = s$ for $0.5 < s < 1$. In contrast, past NRG calculations yielded $x = s$ throughout the interval $0 < s < 1$ [16,17,24]. We recover the latter behavior if we compute $\chi(T)$ via VMPS calculations on length- N_T C1-RWCs [Fig. 3(a), circles]. In contrast, if we use length- N_T C2-RWCs instead, the results for x [Fig. 3(a), squares] agree well with QCC predictions, showing that the mass-flow problem has been cured.

Critical energy-level flow diagrams. The reason why the sub-Ohmic SBM shows qualitatively different critical behavior for $0.5 < s < 1$ and $s \leq 0.5$ is that the critical fixed point is interacting for the former but Gaussian for the latter [17]. To elucidate the difference, Fig. 4 shows energy-level flow diagrams, obtained by plotting the rescaled lowest-

lying energy eigenvalues of length- N Wilson chains, $\Lambda^N E_j$, as functions of N . For $s = 0.6$ (left column), having an interacting critical fixed point for which mass-flow effects are not relevant, the critical level flows for RWCs of type C1 and C2 are qualitatively similar [Figs. 4(a) and 4(b)], becoming stationary independent of N for large N , in a manner familiar from fermionic NRG.

In contrast, for $s = 0.4$ (right column), having a Gaussian fixed point for which mass-flow effects do matter, the critical C1 and C2 level flows are very different: Whereas the C1 flow becomes stationary [Fig. 4(c)] (an artifact of neglecting slow-mode shifts), the low-lying C2 levels all flow towards zero [Fig. 4(d)], causing the level spacing to decrease towards zero, too. This striking behavior, inaccessible when using SWCs, is characteristic of a Gaussian fixed point: It implies that the fixed-point excitation spectrum contains a zero-energy bosonic mode. Remarkably, our C2-RWCs yield a *quantitatively* correct description of the critical spectral flow for $0 < s < 0.5$: It follows a power law $\Lambda^n E_j \propto \epsilon_n^\kappa$ with $\kappa = (2s - 1)/3$, in perfect agreement with the prediction from controlled perturbative RG for a ϕ^4 -type theory with a dangerously irrelevant quartic coupling (see Sec. S-4 D of Ref. [19]).

Conclusions and outlook. Open Wilson chains are representations of quantum impurity models that achieve energy-scale separation while fully keeping track of the effects of bath modes, by iteratively replacing them by a sequence of separate baths at successively lower-energy scales, one for each chain site. Starting from such a fully open system, the effects of these baths can be included systematically. We have taken the first step in that direction, using the bath-induced energy shift for each site to define a renormalized Wilson chain. Remarkably, this simple scheme is sufficiently accurate to yield renormalized impurity properties free from the long-standing mass flow problem. The next step, namely, integrating out each site's bath more carefully, should lead to a description of dissipative effects on Wilson chains, as required for nonequilibrium situations. For example, the effect of bath F_n on the eigenstates of a length- n subchain could be treated using some simple approximation capable of mixing and broadening the eigenlevels (e.g., an equation-of-motion approach with a decoupling scheme). This is left for future work.

Finally, we note that our iterative construction of renormalized Wilson chains constitutes a well-controlled new discretization scheme that offers progress on two further fronts, unrelated to finite-size effects but relevant, e.g., when using NRG or DMRG as impurity solvers for dynamical mean-field theory [9–11,34], or to study multi-impurity models [35]. First, it avoids the discretization artifacts known to arise when conventional schemes [1,24–26] are used to treat strongly asymmetric bath spectra. Second, it can be generalized straightforwardly to treat multiflavor models having non-diagonal bath spectral functions (see Sec. S-1 B of Ref. [19]).

Acknowledgments. We thank Andrew Mitchell for a stimulating discussion on discretizing multiflavor impurity models. This research was supported by the DFG through the Excellence Cluster “Nanosystems Initiative Munich”, SFB/TR 12, SFB 631, SFB 1143 (M.V.), AN 275/8-1 (F.B.A.), and WE4819/2-1 (A.W.).

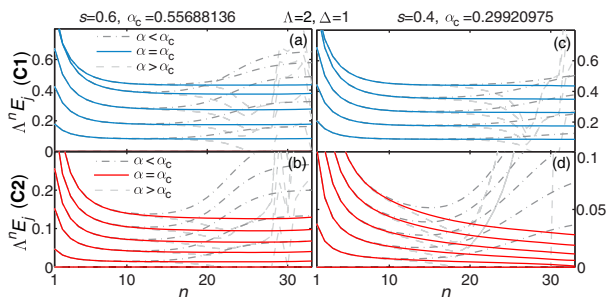


FIG. 4. Energy-level flow diagrams for the sub-Ohmic SBM with $s = 0.6$ (left column) and $s = 0.4$ (right column), computed by VMPS techniques [5,19] on C1-RWCs (top row) and C2-RWCs (bottom row). Dashed lines depict flow to delocalized ($\alpha < \alpha_c$) or localized fixed points ($\alpha > \alpha_c$), and solid lines depict critical flow ($\alpha = \alpha_c$). For the latter, the C2 flow in (d) is characteristic of a Gaussian fixed point.

- [1] K. G. Wilson, *Rev. Mod. Phys.* **47**, 773 (1975).
- [2] R. Bulla, T. A. Costi, and T. Pruschke, *Rev. Mod. Phys.* **80**, 395 (2008).
- [3] H. Saberi, A. Weichselbaum, and J. von Delft, *Phys. Rev. B* **78**, 035124 (2008).
- [4] A. Weichselbaum, F. Verstraete, U. Schollwöck, J. I. Cirac, and J. von Delft, *Phys. Rev. B* **80**, 165117 (2009).
- [5] I. Pizorn and F. Verstraete, *Phys. Rev. Lett.* **108**, 067202 (2012).
- [6] C. Guo, A. Weichselbaum, J. von Delft, and M. Vojta, *Phys. Rev. Lett.* **108**, 160401 (2012); B. Bruognolo, A. Weichselbaum, C. Guo, J. von Delft, I. Schneider, and M. Vojta, *Phys. Rev. B* **90**, 245130 (2014).
- [7] L. Borda, G. Zaránd, W. Hofstetter, B. I. Halperin, and J. von Delft, *Phys. Rev. Lett.* **90**, 026602 (2003).
- [8] A. V. Kretinin, H. Shtrikman, D. Goldhaber-Gordon, M. Hanl, A. Weichselbaum, J. von Delft, T. A. Costi, and D. Mahalu, *Phys. Rev. B* **84**, 245316 (2011).
- [9] R. Bulla, *Phys. Rev. Lett.* **83**, 136 (1999).
- [10] T. Pruschke and R. Bulla, *Eur. Phys. J. B* **44**, 217 (2005).
- [11] K. M. Stadler, Z. P. Yin, J. von Delft, G. Kotliar, and A. Weichselbaum, *Phys. Rev. Lett.* **115**, 136401 (2015).
- [12] A. Rosch, *Eur. Phys. J. B* **85**, 6 (2012).
- [13] F. B. Anders, *J. Phys.: Condens. Matter* **20**, 195216 (2008).
- [14] F. B. Anders and A. Schiller, *Phys. Rev. Lett.* **95**, 196801 (2005). H. E. Türeci, M. Hanl, M. Claassen, A. Weichselbaum, T. Hecht, B. Braunecker, A. Govorov, L. Glazman, A. İmamoğlu, and J. von Delft, *ibid.* **106**, 107402 (2011); C. Latta, F. Haupt, M. Hanl, A. Weichselbaum, M. Claassen, P. Fallahi, S. Faelst, L. Glazman, J. von Delft, H. E. Türeci, and A. İmamoğlu, *Nature (London)* **474**, 627 (2011).
- [15] M. Vojta, N.-H. Tong, and R. Bulla, *Phys. Rev. Lett.* **94**, 070604 (2005).
- [16] M. Vojta, N.-H. Tong, and R. Bulla, *Phys. Rev. Lett.* **102**, 249904(E) (2009).
- [17] M. Vojta, R. Bulla, F. Güttge, and F. Anders, *Phys. Rev. B* **81**, 075122 (2010).
- [18] G. Grosso and G. P. Parravicini, *Adv. Chem. Phys.* **62**, 81 (2007); M. Foulkes and R. Haydock, *J. Phys. C* **19**, 6573 (1986); E. R. Gagliano and C. A. Balseiro, *Phys. Rev. Lett.* **59**, 2999 (1987); Q. Si, M. J. Rozenberg, G. Kotliar, and A. E. Ruckenstein, *ibid.* **72**, 2761 (1994); K. A. Hallberg, *Phys. Rev. B* **52**, R9827(R) (1995).
- [19] See Supplemental Material at <http://link.aps.org/supplemental/10.1103/PhysRevB.95.121115>, which includes Refs. [36–42], for details about the OWC construction, numerical methods used, and additional numerical data.
- [20] If $\Gamma^{\text{bath}}(\omega)$ has power-law form $\propto \omega^s$, we can achieve this by taking the support of \mathcal{A}_n^S and \mathcal{A}_n^F to partition that of $-\frac{1}{\pi}\text{Im}\Sigma_n$ into low- and high-energy regimes [19].
- [21] This choice of $\delta\varepsilon_n^X$ aims to correctly describe low-energy properties, in order to solve the mass-flow problem. More generally, the $\delta\varepsilon_n^X$ may be viewed as fit parameters that optimize the truncated CFE representation of $\mathcal{G}^{\text{bath}}(\omega)$.
- [22] For the single-impurity Anderson model, this guarantees that the height of the zero-temperature Kondo resonance at $\omega = 0$, which is governed solely by $\text{Re}[\Sigma^{\text{bath}}(0)]$, is reproduced correctly, irrespective of the choice of Λ .
- [23] Chains that include neither fast nor slow shifts, $\delta\varepsilon_n^{F,S} = 0$, yield completely incorrect results; see Sec. S-3 of Ref. [19].
- [24] R. Bulla, N.-H. Tong, and M. Vojta, *Phys. Rev. Lett.* **91**, 170601 (2003); R. Bulla, H.-J. Lee, N.-H. Tong, and M. Vojta, *Phys. Rev. B* **71**, 045122 (2005).
- [25] V. L. Campo Jr. and L. N. Oliveira, *Phys. Rev. B* **72**, 104432 (2005).
- [26] R. Žitko and T. Pruschke, *Phys. Rev. B* **79**, 085106 (2009).
- [27] M. Vojta, *Phys. Rev. B* **85**, 115113 (2012).
- [28] M. E. Fisher, S.-k. Ma, and B. G. Nickel, *Phys. Rev. Lett.* **29**, 917 (1972); E. Luijten and H. W. J. Blöte, *Phys. Rev. B* **56**, 8945 (1997).
- [29] A. Winter, H. Rieger, M. Vojta, and R. Bulla, *Phys. Rev. Lett.* **102**, 030601 (2009).
- [30] A. Alvermann and H. Fehske, *Phys. Rev. Lett.* **102**, 150601 (2009).
- [31] C. Zhang, E. Jeckelmann, and S. R. White, *Phys. Rev. Lett.* **80**, 2661 (1998).
- [32] A. Weiße, H. Fehske, G. Wellein, and A. R. Bishop, *Phys. Rev. B* **62**, R747 (2000).
- [33] Y. Nishiyama, *Eur. Phys. J. B* **12**, 547 (1999).
- [34] F. A. Wolf, A. Go, I. P. McCulloch, A. J. Millis, and U. Schollwöck, *Phys. Rev. X* **5**, 041032 (2015).
- [35] A. K. Mitchell and R. Bulla, *Phys. Rev. B* **92**, 155101 (2015); A. K. Mitchell, P. G. Derry, and D. E. Logan, *ibid.* **91**, 235127 (2015).
- [36] A. Weichselbaum and J. von Delft, *Phys. Rev. Lett.* **99**, 076402 (2007).
- [37] L. Borda, *Phys. Rev. B* **75**, 041307 (2007); B. Lechtenberg and F. B. Anders, *ibid.* **90**, 045117 (2014).
- [38] S. R. White, *Phys. Rev. Lett.* **69**, 2863 (1992); *Phys. Rev. B* **48**, 10345 (1993); U. Schollwöck, *Rev. Mod. Phys.* **77**, 259 (2005).
- [39] U. Schollwöck, *Ann. Phys.* **326**, 96 (2011).
- [40] C. Brockt, F. Dorfner, L. Vidmar, F. Heidrich-Meisner, and E. Jeckelmann, *Phys. Rev. B* **92**, 241106 (2015); F. A. Y. N. Schröder and A. W. Chin, *ibid.* **93**, 075105 (2016); F. Dorfner and F. Heidrich-Meisner, *Phys. Rev. A* **93**, 063624 (2016).
- [41] N.-O. Linden, Master's thesis, LMU Munich, 2014.
- [42] H.-J. Lee, R. Bulla, and M. Vojta, *J. Phys.: Condens. Matter* **17**, 6935 (2005).

Open Wilson chains for quantum impurity models: Keeping track of all bath modes

Supplementary material

B. Bruognolo,^{1,2} N.-O. Linden,¹ F. Schwarz,¹ S.-S. B. Lee,¹ K. Stadler,¹
A. Weichselbaum,¹ M. Vojta,³ F. B. Anders,⁴ and J. von Delft¹

¹*Physics Department, Arnold Sommerfeld Center for Theoretical Physics and Center for NanoScience, Ludwig-Maximilians-Universität München, 80333 München, Germany*

²*Max-Planck-Institut für Quantenoptik, Hans-Kopfermann-Str. 1, D-85748 Garching, Germany*

³*Institut für Theoretische Physik, Technische Universität Dresden, 01062 Dresden, Germany*

⁴*Lehrstuhl für Theoretische Physik II, Technische Universität Dortmund, 44221 Dortmund, Germany*

The supplementary material presented below deals with four topics. Section S-1 offers a more detailed discussion of the construction of continued-fraction expansions and open Wilson chains. Section S-2 describes the numerical VMPS techniques used. Section S-3 is devoted to a detailed study of the dissipative harmonic oscillator, in order to benchmark our numerical methods against exact results. Section S-4 describes how the RG flow towards the Gaussian fixed point of the sub-ohmic spin-boson model for $0 < s \leq 0.5$ can be understood using scaling arguments.

S-1. DETAILED DISCUSSION OF CFE AND OWC CONSTRUCTION

Below we supply some technical details involved in the construction of (i) the continued-fraction expansion (CFE) and (ii) the open Wilson chain (OWC) presented in the main text. We begin in Subsection S-1 A with the case of a bath involving only a single flavor of excitations, as discussed in the main text. In Subsection S-1 B, we generalize the construction to a multi-flavor bath having a nondiagonal bath spectrum.

A. Single-flavor bath

(i) *Continued-fraction iteration step.*— We here give some details on the central step of the CFE, which takes a retarded correlator \mathcal{G}_n as input and produces as output a self-energy, split into low- and high-energy contributions.

The input correlator \mathcal{G}_n , being retarded, has the spectral representation $\mathcal{G}_n(\omega) = \int d\bar{\omega} \frac{\mathcal{A}_n(\bar{\omega})}{\omega - \bar{\omega} + i0^+}$, with a spectral function, $\mathcal{A}_n(\omega) = -\frac{1}{\pi} \text{Im} \mathcal{G}_n(\omega)$ that is normalized to unity, $\int d\omega \mathcal{A}_n(\omega) = 1$. If this correlator is represented in the form [Eq. (1)]

$$\mathcal{G}_n(\omega) = \frac{1}{\omega - \varepsilon_n - \Sigma_n(\omega)}, \quad (\text{S1})$$

with $\Sigma_n(\omega)$ analytic in the upper half-plane as required for a retarded self-energy, then the constant in the denominator must be equal to the average energy of the spectral function $\mathcal{A}_n(\omega)$, $\varepsilon_n = \int d\omega \omega \mathcal{A}_n(\omega)$. In the main

text this fact was used, but not explained. To understand its origin, invert Eq. (S1), multiply it by $\mathcal{G}_n(\omega)$, and integrate over frequency:

$$\begin{aligned} \int d\omega \Sigma_n(\omega) \mathcal{G}_n(\omega) &= \int d\omega \left[(\omega - \varepsilon_n) \mathcal{G}_n(\omega) - 1 \right] \\ &= \int d\omega \int d\bar{\omega} \left[\frac{\omega - \varepsilon_n}{\omega - \bar{\omega} + i0^+} - 1 \right] \mathcal{A}_n(\bar{\omega}) \\ &= \int d\bar{\omega} \int d\omega \left[\frac{\bar{\omega} - \varepsilon_n}{\omega - \bar{\omega} + i0^+} \right] \mathcal{A}_n(\bar{\omega}) \\ &= -i\pi \int d\bar{\omega} (\bar{\omega} - \varepsilon_n) \mathcal{A}_n(\bar{\omega}). \end{aligned} \quad (\text{S2})$$

Since both $\mathcal{G}_n(\omega)$ and $\Sigma_n(\omega)$ are by assumption retarded functions and hence analytic in the upper half-plane, the left-hand side of the first line yields zero, as can be seen by closing the integration contour in the upper half-plane. The second line follows from the right-hand side of the first using the spectral representation of \mathcal{G}_n , and the fact that \mathcal{A}_n is normalized to unity. Since the last line, being equal to the first, must equal zero too, it fixes ε_n to the value stated in above (again using the unit normalization of \mathcal{A}_n). Once ε_n has been fixed, the self-energy is fixed, too, by inverting Eq. (S1):

$$\Sigma_n(\omega) = \omega - \varepsilon_n - 1/\mathcal{G}_n(\omega). \quad (\text{S3})$$

To summarize: The fact that the retarded correlator $\mathcal{G}_n(\omega)$ is analytic implies the same for its self-energy $\Sigma_n(\omega)$; this uniquely fixes ε_n and thus also $\Sigma_n(\omega)$ itself, which in turn can be viewed as a correlator with its own self-energy, etc. Thus, the analyticity of $\mathcal{G}_n(\omega)$ guarantees that it is always possible to iteratively construct a CFE for it. The new twist added to this well-known fact in the present work is to zoom in to small energies by splitting the self-energy into slow and fast parts and using only the former as input for the next iteration step.

To explicitly implement this splitting, given by Eq. (2),

$$\Sigma_n(\omega) = \Sigma_n^S(\omega) + \Sigma_n^F(\omega), \quad \Sigma_n^X(\omega) = |t_n^X|^2 \mathcal{G}_n^X(\omega), \quad (\text{S4})$$

we proceed as follows. We split $\Gamma_n(\omega) = -\frac{1}{\pi} \text{Im} \Sigma_n(\omega)$, which may be viewed as the bath spectrum of iteration n , into slow and fast parts, $\Gamma_n = \Gamma_n^S + \Gamma_n^F$, with

$$\Gamma_n^X(\omega) = w_n^X(\omega) \Gamma_n(\omega). \quad (\text{S5})$$

Here the splitting functions $w_n^{S/F}(\omega)$ are defined on the support of Γ_n , take values in the interval $[0, 1]$, satisfy $w_n^S(\omega) + w_n^F(\omega) = 1$, and have weight predominantly at low/high energies. Then we write the split bath spectra as $\Gamma_n^X(\omega) = |t_n^X|^2 \mathcal{A}_n^X(\omega)$, with ‘‘couplings’’ t_n^X chosen as

$$|t_n^X|^2 = \int d\omega \Gamma_n^X(\omega), \quad (\text{S6})$$

to ensure that the new spectral functions $\mathcal{A}_n^X(\omega)$ are normalized to unity. Using them to define new retarded correlators via $\mathcal{G}_n^X(\omega) = \int d\bar{\omega} \frac{\mathcal{A}_n^X(\bar{\omega})}{\omega - \bar{\omega} + i0^+}$, we obtain the desired slow/fast splitting of the self-energy stated above.

Next we describe the choice of splitting functions $w_n^X(\omega)$ used to obtain the numerical results of the main text. Let $I_n^S = [\omega_{S_n}^-, \omega_{S_{n-1}}^+]$ denote the support of the slow spectral function \mathcal{A}_n^S . The bath spectrum for iteration n , $\Gamma_n(\omega) = -\frac{1}{\pi} \text{Im} \Sigma_n(\omega)$, has support on the same interval, say I_n , as the correlator $\mathcal{G}_n = \mathcal{G}_{n-1}^S$, i.e. $I_n = I_{n-1}^S$. To implement the splitting $\Gamma_n = \Gamma_n^S + \Gamma_n^F$, we partition this interval into disjoint slow and fast subranges, $I_n = I_n^S \cup I_n^F$, with $|\omega_{S_n}^\pm| \leq |\omega_{S_{n-1}}^\pm|$, and use corresponding step-form splitting functions:

$$w_n^X(\omega) = \begin{cases} 1 & \text{for } \omega \in I_n^X, \\ \text{otherwise.} & \end{cases} \quad (\text{S7})$$

To ensure energy-scale separation, I_n^S should be chosen such that

$$\max\{|\varepsilon_n|, |t_n^S|\} \leq \max\{|\varepsilon_{n-1}|, |t_{n-1}^S|\} / \Lambda \quad (\text{S8})$$

holds, with $\Lambda > 1$. If the bath spectrum $\Gamma^{\text{bath}}(\omega)$ has a flat or power-law form, a natural choice is $\omega_{S_n}^\pm = \omega_{S_{n-1}}^\pm / \Lambda$. This is the choice used for the numerical work in the main text. However, if $\Gamma^{\text{bath}}(\omega)$ has nontrivial structure, the choices for the subrange boundaries $\omega_{S_n}^\pm$ might have to be fine-tuned to ensure Eq. (S8) at each iteration. More generally, one might also explore using splitting functions $w_n^X(\omega)$ of smoother shape than those of Eq. (S7). The freedom of choice available for ensuring Eq. (S8) is one of the major strengths of the above strategy for generating a CFE.

(ii) *Construction of open Wilson chain.*— Here we provide some details on the construction of the OWC Hamiltonian of $\mathcal{H}_N^{\text{OWC}}$ of Eq. (3). It describes a chain with $N + 1$ sites, each coupled to a bath of its own, and site 0 coupled to the impurity (site -1) [Fig. 1(c)]. It is constructed such that the free ($t_{\text{imp}} = 0$) correlator of site 0 is given by a depth- N CFE, $\mathcal{G}_0 = \mathcal{G}^{\text{bath}}$.

We associate with each pair of correlators $\mathcal{G}_n^{S/F}$ from the CFE two mutually independent baths S_n and F_n . We regard \mathcal{G}_n^X as the free retarded correlator of a normalized bath operator $b_{X_n}^\dagger$, whose dynamics is generated by a bath Hamiltonian \mathcal{H}_n^X , chosen such that $\mathcal{G}_n^X(\omega) = \langle\langle b_{X_n} | b_{X_n}^\dagger \rangle\rangle_\omega$ has the form found via the CFE.

We start our OWC construction by associating bath S_{-1} with the original bath [Fig. 1(b)], setting $\mathcal{H}_{-1}^S =$

$\mathcal{H}^{\text{bath}}$, $b_{S_{-1}}^\dagger = b^\dagger$ and $\mathcal{G}_{-1}^S = \mathcal{G}^{\text{bath}}$, with impurity-bath coupling $t_{-1}^S = t_{\text{imp}}$. We then proceed iteratively, starting with $n = 0$. The central CFE iteration step of writing \mathcal{G}_{n-1}^S in the form of Eq. (1) corresponds, on the level of the Hamiltonian, to replacing the bath S_{n-1} by a new site n [Fig. 1(c)], with energy ε_n and normalized site operator f_n^\dagger , which is linearly coupled to two new baths, S_n and F_n , in such a way that its free ($t_{n-1}^S = 0$) site correlator \mathcal{G}_n equals \mathcal{G}_{n-1}^S [Eq. (1)]. To achieve this, we make the replacements $b_{S_{n-1}}^\dagger \rightarrow f_n^\dagger$ and

$$\mathcal{H}_{n-1}^S \rightarrow \varepsilon_n f_n^\dagger f_n + \sum_X (b_{X_n}^\dagger t_n^X f_n + \text{H.c.}) + \sum_X \mathcal{H}_n^X. \quad (\text{S9})$$

Then $\mathcal{G}_n = \langle\langle f_n | f_n^\dagger \rangle\rangle_\omega$ indeed matches Eq. (1), since the self-energy generated for it by the new baths, $\Sigma_n(\omega) = \sum_X |t_n^X|^2 \mathcal{G}_n^X(\omega)$, agrees with Eq. (2). Since $\mathcal{G}_n = \mathcal{G}_{n-1}^S$, f_n^\dagger and $b_{S_{n-1}}^\dagger$ have the same dynamics, i.e. the new site, bath S_n and bath F_n jointly have the same effect on site $n-1$ as the previous bath S_{n-1} . Now we iterate: we retain the fast bath F_n , but replace the slow bath S_n by a new site $n+1$ coupled to new slow and fast baths S_{n+1} and F_{n+1} , etc. After $N+1$ steps, the initial \mathcal{H} has been replaced by the OWC Hamiltonian $\mathcal{H}_N^{\text{OWC}}$ given in Eq. (3).

The above argument does not require the free Hamiltonians \mathcal{H}_n^X and bath operators $b_{X_n}^\dagger$ to be constructed explicitly. For concreteness we specify them nevertheless:

$$\mathcal{H}_n^X = \sum_q \varepsilon_{qn}^X b_{Xqn}^\dagger b_{Xqn}, \quad b_{Xn}^\dagger = \sum_q b_{Xqn}^\dagger \lambda_{qn}^X. \quad (\text{S10})$$

These involve a set of canonical annihilation and creation operators satisfying $[b_{Xqn}, b_{Xqn}^\dagger]_\pm = 1$ (+ for a fermionic anti-commutator, $-$ for a bosonic commutator). The bath operators b_{Xn} are normalized to satisfy $[b_{Xn}, b_{Xn}^\dagger]_\pm = 1$. The free dynamics of b_{Xn}^\dagger , generated by \mathcal{H}_n^X , is characterized by the free retarded correlator and spectral function

$$\mathcal{G}_n^X(\omega) = \sum_q \frac{|\lambda_{qn}^X|^2}{\omega - \varepsilon_{qn}^X + i0^+}, \quad (\text{S11a})$$

$$\mathcal{A}_n^X(\omega) = \sum_q |\lambda_{qn}^X|^2 \delta(\omega - \varepsilon_{qn}^X). \quad (\text{S11b})$$

The bath energies ε_{qn}^X and couplings λ_{qn}^X are assumed such that $\mathcal{G}_n^X(\omega)$ has the form obtained in the CFE.

B. Multi-flavor bath

Next we consider impurity models involving a multi-flavor bath with m_f flavors of excitations, labeled by an index $\nu = 1, \dots, m_f$. We assume that the impurity Hamiltonian $\mathcal{H}_{\text{imp}}[b_\nu^\dagger]$, describing the impurity degrees of freedom and their coupling to the bath, depends on the bath only through m_f bath operators b_ν^\dagger and their conjugates b_ν , not necessarily normalized or orthogonal,

with retarded correlator $\mathcal{G}_{\nu\nu'}^{\text{bath}}(\omega) = \langle\langle b_\nu; b_{\nu'}^\dagger \rangle\rangle_\omega$. We assume that the corresponding bath spectrum,

$$\Gamma_{\nu\nu'}^{\text{bath}}(\omega) = -[\mathcal{G}_{\nu\nu'}^{\text{bath}}(\omega) - \mathcal{G}_{\nu'\nu}^{\text{bath}*}(\omega)]/(2\pi i), \quad (\text{S12})$$

is a specified, Hermitian, positive definite *matrix* function (i.e. for any given ω , the eigenvalues of the matrix are real and non-negative). Together with the form of \mathcal{H}_{imp} , this matrix function fully determines the impurity dynamics. Models of this structure arise in studies of the Kondo compensation cloud [36], when considering multi-impurity situations [34], and in DMFT studies of multi-band lattice models, where $\Gamma_{\nu\nu'}^{\text{bath}}(\omega)$ is constructed iteratively from the impurity spectral function $\mathcal{A}_{\nu\nu'}^{\text{imp}}(\omega)$ computed at the previous DMFT iteration.

If $\Gamma_{\nu\nu'}^{\text{bath}}(\omega)$ can be diagonalized using a frequency-independent unitary transformation, the eigenvalues, say $\Gamma_\nu(\omega)$, constitute m_f hybridization functions that can be discretized independently, using either standard Wilsonian discretization or our RWC discretization scheme. Here we are interested in the more general case that diagonalizing the bath spectrum requires a frequency-dependent unitary transformation, $\Gamma_{\nu\nu'}^{\text{bath}}(\omega) = \sum_{\bar{\nu}} u_{\nu\bar{\nu}}^\dagger(\omega) \Gamma_{\bar{\nu}}(\omega) u_{\bar{\nu}\nu'}(\omega)$. This would be the case, for example, for DMFT studies of a fermionic lattice model with broken band degeneracy and spin-orbit coupling; the corresponding self-consistent impurity model is a multi-band Anderson model involving nondiagonal level-bath couplings, leading to a nondiagonal impurity spectral function.

To treat this situation in Wilsonian fashion, one could write the bath spectrum as $\Gamma_{\nu\nu'}^{\text{bath}}(\omega) = \int d\varepsilon_q \sum_{\bar{\nu}} v_{q\nu\bar{\nu}}^\dagger \delta(\omega - \varepsilon_q) v_{q\bar{\nu}\nu'}$, with bath-lead matrix elements $v_{q\nu\nu'} = \sqrt{\Gamma_\nu(\varepsilon_q)} u_{\nu\nu'}(\varepsilon_q)$, and discretize the integral logarithmically (with the implicit assumption that $\Gamma_\nu(\omega)$ and $v_{q\nu\nu'}(\omega)$ change sufficiently slowly with ω that within a discretization interval they may be replaced by constants). We note, though, that the neglect of truncated bath modes is potentially more problematic for multi- than single-flavor models, since $\Gamma_{\nu\nu'}^{\text{bath}}(\omega)$ will generically have matrix elements asymmetric in frequency.

Below we explain how multi-flavor models can alternatively be discretized using a generalization of our RWC construction. (We thank Andrew Mitchell for a stimulating discussion which led to this realization.) The overall strategy is completely analogous to the single-flavor case, but with a flavor index added to all creation and annihilation operators (e.g. $b_{X\nu\nu'}^\dagger$), and two flavor indices to all matrix elements (e.g. $t_{\nu\nu'}^X$) and correlators (e.g. $\mathcal{G}_{\nu\nu'}^X$). We will mostly use a compact notation that suppresses these indices and indicates their implicit presence by an underscore, e.g. b_{Xn}^\dagger , t_n^X , $\underline{\mathcal{G}}_n^X$, $(b_{Xn}^\dagger t_n^X)_{\nu\nu'} = b_{Xn\nu}^\dagger t_{n\nu\nu'}^X$, and $\underline{f}_n^\dagger \varepsilon_n \underline{f}_n = \sum_{\nu\nu'} f_{n\nu}^\dagger \varepsilon_{n\nu\nu'} f_{n\nu'}$, etc.

Extracting normalized modes from bath spectrum.— The CFE to be constructed below involves a sequence of bath spectra with matrix structure, generically denoted by $\underline{\Gamma}(\omega)$. Each is a Hermitian, positive definite matrix function, $\underline{\Gamma}(\omega) = \underline{\Gamma}^\dagger(\omega)$. We would like to express such a

function in terms of a Hermitian, positive definite matrix function $\underline{\mathcal{A}}(\omega)$ that is normalized as

$$\int d\omega \underline{\mathcal{A}}(\omega) = \underline{1}, \quad (\text{S13})$$

because such an $\underline{\mathcal{A}}(\omega)$ can be viewed as the spectral function of a set of *orthonormal* bath modes. To this end, we note that the frequency integral $\underline{w} = \int d\omega \underline{\Gamma}(\omega)$ yields a Hermitian, positive definite matrix. (Reason: If two matrices are Hermitian and positive definite, the same is true for their sum, and similarly for an integral of such matrix functions.) The matrix \underline{w} can thus be diagonalized in the form $\underline{w} = \underline{u}^\dagger \underline{d} \underline{u}$, with \underline{u} unitary and \underline{d} diagonal and positive. Then the matrix $\underline{t} = \underline{u}^\dagger \sqrt{\underline{d}} \underline{u}$ can be used to write the bath spectrum in the form

$$\underline{\Gamma}(\omega) = \underline{t}^\dagger \underline{\mathcal{A}}(\omega) \underline{t}, \quad (\text{S14})$$

where both \underline{t} and $\underline{\mathcal{A}}$ are Hermitian and positive definite, while $\underline{\mathcal{A}}$ by construction is normalized as in Eq. (S13). The first moment of $\underline{\mathcal{A}}$ yields a Hermitian matrix, too: $\underline{\varepsilon} = \int d\omega \omega \underline{\mathcal{A}}(\omega)$. In the chain to be constructed below, $\underline{\varepsilon}$ plays the role of an onsite Hamiltonian and \underline{t} that of a nearest-neighbor coupling. If desired, one may make another unitary transformation that diagonalizes either $\underline{\varepsilon}$ or \underline{t} , while leaving the normalization condition (S13) in tact.

Continued-fraction expansion.— As for the one-band case, we aim to iteratively represent $\underline{\mathcal{G}}^{\text{bath}}(\omega)$ in terms of a sequence of continued-fraction expansions that zoom in on low energies. These involve a sequence of Hermitian, positive definite functions, $\underline{\mathcal{A}}_n^X(\omega) = \underline{\mathcal{A}}_n^{X\dagger}(\omega)$. Each is normalized to unity [Eq. (S13)] and can be viewed as the spectral function of a retarded correlator $\underline{\mathcal{G}}_n^X(\omega)$,

$$\underline{\mathcal{A}}_n^X(\omega) = -[\underline{\mathcal{G}}_n^X(\omega) - \underline{\mathcal{G}}_n^{X\dagger}(\omega)]/(2\pi i), \quad (\text{S15})$$

which in turn can be expressed as

$$\underline{\mathcal{G}}_n^X(\omega) = \int d\bar{\omega} \frac{\underline{\mathcal{A}}_n^X(\bar{\omega})}{\omega - \bar{\omega} + i0^+}. \quad (\text{S16})$$

The multi-band CFE construction follows the one-band case, except that all correlators carry underscores to indicate their matrix structure. First we initialize the CFE by expressing the bath spectrum in terms of a normalized spectral function, $\underline{\Gamma}^{\text{bath}}(\omega) = t_{\text{imp}}^{S\dagger} \underline{\mathcal{A}}_{-1}^S(\omega) t_{\text{imp}}^S$ [cf. (S14)] and compute the corresponding retarded correlator $\underline{\mathcal{G}}_{-1}^S$ via Eq. (S16). Starting with iteration $n = 0$, we then iteratively use $\underline{\mathcal{G}}_{n-1}^S$ as input to define a new retarded correlator $\underline{\mathcal{G}}_n$ and its retarded self-energy $\underline{\Sigma}_n$,

$$\underline{\mathcal{G}}_n(\omega) = \underline{\mathcal{G}}_{n-1}^S(\omega) = 1/[\omega \underline{1} - \underline{\varepsilon}_n - \underline{\Sigma}_n(\omega)], \quad (\text{S17})$$

with $\underline{\varepsilon}_n = \int d\omega \omega \underline{\mathcal{A}}_n(\omega)$. Then we split this self-energy into low- and high-energy parts by writing it as

$$\underline{\Sigma}_n = \underline{\Sigma}_n^S + \underline{\Sigma}_n^F, \quad \underline{\Sigma}_n^X(\omega) = t_n^{X\dagger} \underline{\mathcal{G}}_n^X(\omega) t_n^X. \quad (\text{S18})$$

To be concrete, we achieve this splitting by proceeding as follows. We split $\underline{\Gamma}_n(\omega) = -[\underline{\Sigma}_n(\omega) - \underline{\Sigma}_n^\dagger]/(2\pi i)$, the bath spectrum of iteration n , into slow and fast parts, $\underline{\Gamma}_n = \underline{\Gamma}_n^S + \underline{\Gamma}_n^F$, with

$$\Gamma_{n,\nu\nu'}^X(\omega) = w_{n,\nu\nu'}^X(\omega)\Gamma_{n,\nu\nu'}(\omega) \quad (\text{S19})$$

(no index summation implied here), using symmetric, real matrix functions $\underline{w}_n^X(\omega)$. Their matrix elements $w_{n\nu\nu'}^{S/F}(\omega)$ are splitting functions that are defined on the support of $\underline{\Gamma}_n$, take values in $[0, 1]$, have weight predominantly at low/high energies, and satisfy $w_{n\nu\nu'}^S(\omega) + w_{n\nu\nu'}^F(\omega) = 1$. (The simplest choice would be $\underline{w}_n^X(\omega) = w_n^X(\omega)\mathbb{1}$, using the same pair of weighting functions for all matrix elements; but situations may arise where the additional freedom of making different choices for different matrix elements is useful.) Since the splitting functions are symmetric and non-negative, the split spectra $\underline{\Gamma}_n^X$ are Hermitian and positive definite matrix functions, too. We can thus express them in terms of normalized spectral functions [Eq. (S14)]:

$$\underline{\Gamma}_n^X(\omega) = t_n^{X\dagger} \underline{\mathcal{A}}_n^X(\omega) t_n^X. \quad (\text{S20})$$

Computing the corresponding retarded correlators $\underline{\mathcal{G}}_n^X$ [Eq. (S16)] we obtain the self-energy splitting stated in Eq. (S18). To ensure energy-scale separation, the weighting functions \underline{w}_n^X should be chosen such that

$$\max\{\|\underline{\varepsilon}_n\|, \|\underline{t}_n^S\|\} \leq \max\{\|\underline{\varepsilon}_{n-1}\|, \|\underline{t}_{n-1}^S\|\}/\Lambda \quad (\text{S21})$$

holds, with $\Lambda > 1$, where $\|\cdot\|$ denotes some matrix norm.

Iterating this procedure yields a sequence of CFEs for $\underline{\mathcal{G}}^{\text{bath}}$, in the same fashion as for the one-band case.

Chain representation.— The CFE data $(\underline{\varepsilon}_n, t_n^X, \underline{\mathcal{G}}_n^X)$ can now be used to represent the model in terms of a chain with $N + 1$ sites, each coupled to a bath of its own. The chain is constructed such that the free ($t_{-1}^S = 0$) correlator of the first site ($n = 0$) is given by a dept- N CFE. To this end, we associate each pair of correlators $\underline{\mathcal{G}}_n^{S/F}$ with two mutually independent baths S_n and F_n , and regard each $\underline{\mathcal{G}}_n^X$ as the free retarded correlator of a set of m_f normalized bath operators b_{Xn}^\dagger , whose free dynamics is generated by a bath Hamiltonian \mathcal{H}_n^X , such that $\underline{\mathcal{G}}_n^X(\omega) = \langle\langle b_{Xn} | b_{Xn}^\dagger \rangle\rangle_\omega$. These free bath Hamiltonians and bath operators have the form

$$\mathcal{H}_n^X = \sum_q b_{Xqn}^\dagger \underline{\varepsilon}_{qn}^X b_{Xqn}, \quad b_{Xn}^\dagger = \sum_q b_{Xqn}^\dagger \underline{\lambda}_{qn}^X, \quad (\text{S22})$$

where $\underline{\varepsilon}_{qn}^X$ and $\underline{\lambda}_{qn}^X$ are matrices w.r.t. to the flavor indices. $\underline{\varepsilon}_{qn}^X$ is diagonal and real, and $\underline{\lambda}_{qn}^X$ unitary, normalized such that $[b_{Xn}, b_{Xn}^\dagger]_\pm = \mathbb{1}$. The free bath correlators and spectral functions then have the explicit representations

$$\underline{\mathcal{G}}_n^X(\omega) = \sum_q \underline{\lambda}_{qn}^{X\dagger} [(\omega + i0^+) \mathbb{1} - \underline{\varepsilon}_{qn}^X]^{-1} \underline{\lambda}_{qn}^X, \quad (\text{S23a})$$

$$\underline{\mathcal{A}}_n^X(\omega) = \sum_q \underline{\lambda}_{qn}^{X\dagger} \delta(\omega \mathbb{1} - \underline{\varepsilon}_{qn}^X) \underline{\lambda}_{qn}^X. \quad (\text{S23b})$$

This representation for $\underline{\mathcal{A}}_n^X(\omega)$ shows explicitly that it is a Hermitian, positive definite matrix function.

The iterative OWC construction proceeds as for the single-flavor case, except that all operators, matrix elements and correlators now carry underscores to indicate implicit flavor indices. For example, the generalization of Eq. (S9) now involves the replacements $b_{S_{n-1}}^\dagger \rightarrow \underline{f}_n^\dagger$ and

$$\mathcal{H}_{n-1}^S \rightarrow \underline{f}_n^\dagger \underline{\varepsilon}_n \underline{f}_n + \sum_X (b_{Xn}^\dagger \underline{t}_n^X \underline{f}_n + \text{H.c.}) + \sum_X \mathcal{H}_n^X. \quad (\text{S24})$$

The final OWC Hamiltonian has the same form as Eq. (3) of the main text, suitably decorated with underscores, and with $\mathcal{H}^{\text{imp}}[\underline{J}_0^\dagger t_{\text{imp}}]$ as impurity Hamiltonian. Similarly, when moving on to a RWC, the energy shift equation (4) of the main text is decorated by underscores, i.e. we shift the onsite energy matrices $\underline{\varepsilon}_n$ by $\delta \underline{\varepsilon}_n^X$ shifts that should be chosen to optimize the truncated CFE representation of $\underline{\mathcal{G}}^{\text{bath}}$. We expect this step to be more important for multi- than single-flavor models, since $\underline{\Gamma}_n^X(\omega)$ will generically have matrix elements asymmetric in frequency. If one is interested mainly in correctly reproducing low-energy properties, one could choose $\delta \underline{\varepsilon}_n^X = \text{Re} \underline{\Sigma}_n^X(\omega = 0)$, as in the main text. Another option would be to view the $\delta \underline{\varepsilon}_n^X$ as fitting parameters, chosen to get the best possible agreement between the depth- n CFE for $\underline{\mathcal{G}}^{\text{bath}}(\omega)$ and its actual form.

S-2. NUMERICAL DETAILS

In this section, we elaborate on the details of the numerical methods employed in the main text. In Subsection S-2A we briefly review NRG and its limitations in the context of bosonic impurity models. In Subsection S-2B we discuss the VMPS techniques by which these limitations can be overcome. Finally, in Subsection S-2C we present a generalized VMPS scheme that simultaneously targets multiple low-energy states on the Wilson chain, which enables us to generate the well-controlled energy-level flow diagrams for the sub-Ohmic spin-boson model (SBM) shown in Fig. 4 of the main text.

A. Bosonic NRG

The numerical renormalization group (NRG) is one of the most powerful tools to numerically evaluate the properties of quantum impurity models [1]. Wilson's formulation of "standard NRG" involves two steps. First, the model is represented in terms of a Wilson chain, i.e. a semi-infinite tight-binding chain whose hopping matrix elements t_n decrease exponentially with n , ensuring energy-scale separation along the chain. In the main text and Sec. S-1, we have described in detail how this is achieved for an RWC; for details on setting up a SWC we refer to Refs. [24] and [2]. Second, the chain is diagonalized iteratively one site at a time, discarding high-energy

states at each step, to yield a set of so-called Wilson shells, where shell N contains the low-lying eigenstates of a finite chain whose last site is labelled N (a “length- N ” chain). These shells can be used to calculate both thermodynamic and dynamical quantities; in particular, we employed the full-density-matrix NRG scheme (fdm-NRG) to evaluate thermal averages of observables in this work [35].

Whereas NRG has been highly successful in the context of fermionic impurity models, its application to bosonic baths has been impeded by two numerical issues, (i) the mass-flow error and (ii) the local Hilbert space truncation. We elaborated on (i) in detail in the main text. We add that NRG cannot be completely cured from the mass flow using the C2-RWC construction, as discussed in more detail in Sec. S-3 below. This is related to the iterative nature of the NRG diagonalization procedure, which does not allow to incorporate any feedback of the slow-mode correction to earlier iterations, in contrast to the variational setup presented in Sec. S-2 B below. Problem (ii) is related to the fact that only a limited number of bosons can be included in an NRG calculation. NRG requires an *a priori* truncation of the infinite-dimensional local bosonic Hilbert space on each site n to a numerically feasible number of d_n bosonic states. For example, for the spin-boson model NRG is therefore not able to accurately deal with the fact that the oscillator displacement occurring in the localized phase grows exponentially along the Wilson chain, which implies that the number of bosons in the standard oscillator representation must increase exponentially, too [16].

In the context of the sub-Ohmic SBM, it has been thoroughly illustrated how the limitations of bosonic NRG can tamper with physical properties. Here, the interplay of these two numerical issues affected a number of critical exponents, causing them to follow hyperscaling instead of mean-field results for $0 < s < 0.5$ [15]. The internal consistency of these NRG results (which were later shown to be incorrect) was so striking that it initially led to the controversial conclusion, that the quantum-to-classical correspondence breaks down in case of the sub-Ohmic SBM. This subtle “conspiracy of errors” [27] implies that NRG is not fully equipped to deal with bosonic baths, since parts of the phase diagram and, in particular, the impurity quantum phase transition, may not be reliably accessible for the method.

B. VMPS with optimal boson basis

The intrinsic flaws of bosonic NRG can be completely dealt with by employing the strategy of the density matrix renormalization group (DMRG) to treat RWC Hamiltonians [4, 37]. To this end, we use the matrix-product-state (MPS) formulation of DMRG [38], which we refer to as variational matrix-product-state approach (VMPS) in the following [3, 4]. This method can overcome the issue of Hilbert space truncation by using a flex-

ible, shifted optimized boson basis (OBB) [31], as shown in [6, 39]. Moreover, the mass-flow problem can be successfully cured by performing the variational procedure on C2-RWCs, as demonstrated in the main text. We briefly elaborate on the main aspects of the VMPS approach and refer to [6] for technical details.

The goal of the VMPS approach is to efficiently represent the ground state of a Wilson chain with N bath sites in the formalism of matrix-product states [38]. A generic MPS of a bosonic impurity model has the form

$$|\psi\rangle = \sum_{\sigma, \mathbf{m}} A^{[\sigma]} A^{[m_0]} A^{[m_1]} \dots A^{[m_N]} |\sigma\rangle |\mathbf{m}\rangle, \quad (\text{S25})$$

where $|\sigma\rangle$ represents the local space of the impurity (e.g., a spin- $\frac{1}{2}$ degree of freedom) and $\mathbf{m} = |m_0\rangle \dots |m_N\rangle$ describes the local boson number eigenstates in a truncated Fock basis, i.e., $f_n^\dagger f_n |\mathbf{m}\rangle = m_n |\mathbf{m}\rangle$ with $m_n = 0, 1, \dots, d_n - 1$. Starting with a random MPS, the ground state is approximated by iteratively varying the tensors $A^{[\cdot]}$ to minimize the energy of the Wilson chain Hamiltonian, sweeping back and forth through the chain until a global energy minimum is reached with sufficient convergence.

One key advantage of VMPS over NRG is the ability to flexibly adapt the local bosonic state basis on each site of the Wilson chain during the optimization process. This concept of an adaptive boson basis enables us, for example, to determine the ground state also in the localized phase of the SBM faithfully, which is not possible in NRG calculations. Our OBB implementation includes two features: First, we introduce an additional basis transformation V with $V^\dagger V = \mathbb{1}$, which maps the local harmonic oscillator basis $|m_n\rangle$ onto a smaller effective basis $|\tilde{m}_n\rangle$ on each site n ,

$$|\tilde{m}_n\rangle = \sum_{m_n=0}^{d_n-1} V_{\tilde{m}_n, m_n} |m_n\rangle \quad (\tilde{m}_n = 0, \dots, \tilde{d}_n - 1). \quad (\text{S26})$$

V can be naturally embedded in the MPS structure and is optimized in an additional local update to determine the best set of local basis states $|\tilde{m}_n\rangle$ for the subsequent update steps [6].

Second, we explicitly incorporate any oscillator displacements occurring in strong-coupling phases when constructing the local boson basis sets. To this end, we shift the oscillator coordinate $\hat{x}_n = \frac{1}{\sqrt{2}}(f_n + f_n^\dagger)$ on each site n by its equilibrium value $\langle \hat{x}_n \rangle$ [30] employing an unitary transformation to the Hamiltonian of the system [6]. $\langle \hat{x}_n \rangle$ can be determined self-consistently in a variational setting. Using such a setup, the OBB is able to capture quantum fluctuations around the shifted coordinate $\hat{x}'_n = \hat{x}_n - \langle \hat{x}_n \rangle$.

In practice, the shifted OBB not only allows a significant increase of the size of the local basis sets from $d_n \approx \mathcal{O}(10^2)$ to $d_n \lesssim \mathcal{O}(10^4)$ by means of the basis transformation V . In addition, the shifted oscillator basis enables us to account for the exponentially growing oscillator displacements in a numerically quasi-exact

way, which would require a local dimension of up to $d_n^{\text{eff}} \approx (10^{10})$ in a nonshifted basis [6].

An additional advantage of the variational optimization over NRG is the fact that the former typically involves multiple sweeps along the chain, so that information from different parts of the Wilson chain (i.e., from different energy scales) is incorporated during the optimization process. This feedback mechanism is not needed for chains that have energy-scale separation. However, the latter is violated at the last site of a C2-RWC, where the slow-mode energy shift is large enough to affect the nature of the MPS not only on the last site but also on several preceding sites. In contrast to NRG, the VMPS approach is capable of feeding back this slow-mode information from low-energy scales to higher ones during the optimization sweeps, which is key to successfully avoid any mass-flow effects.

Even though the VMPS scheme described above only targets the ground state, it can be used to mimic finite-temperature averages on the Wilson chain, such as the thermal average $\langle a+a^\dagger \rangle_T$ or $\langle \hat{\sigma}_z \rangle_T$ needed to compute the local susceptibility $\chi(T)$ for the DHO or SBM, respectively. To this end, we compute the ground-state expectation value $\langle G|a+a^\dagger|G \rangle_{N_T}$ or $\langle G|\hat{\sigma}_z|G \rangle_{N_T}$ for a length- N_T C2-RWC, where N_T is chosen such that the chain's lowest energy scale matches the temperature, $T \sim \Lambda^{-N_T}$. This works because, for a length- N_T chain, the response of the ground state is calculated for a discrete spectrum whose low-energy excitations have characteristic spacing T . This is the strategy that was used for the VMPS calculations of $\chi(T)$ reported in the main text. A more detailed description of this strategy is given in Sec. S-3 below, devoted to a detailed study of the dissipative harmonic oscillator (DHO). There we compare several different strategies for computing thermal averages and benchmark their results against the exact solution for $\chi(T)$.

An important prerequisite for studying critical properties is a highly accurate determination of the critical coupling α_c . Numerically, it can be found in several ways. First, by determining the α -value at which the susceptibility $\chi(T=0)$ diverges; this was our method of choice in the context of the DHO. Second, by monitoring how the NRG or VMPS energy flow diagrams evolve with α . For the SBM there exist a third option, namely monitoring the behavior of the average boson occupation per site, $\langle m_n \rangle$: at the phase boundary it stays almost constant throughout the chain, but in the delocalized (localized) phase it decreases (increases) towards the end of the Wilson chain. We used the third scheme for the SBM, since it can be automated very easily. C2-chains sometimes required additional fine-tuning, since the slow-mode shift always increases the occupation numbers at the end of the chain.

We end this section with some technical notes. All VMPS ground-state calculations in this work for both DHO and SBM were performed using a 1-site update with fixed bond dimension $D = 60$, $d_n = 100$, and

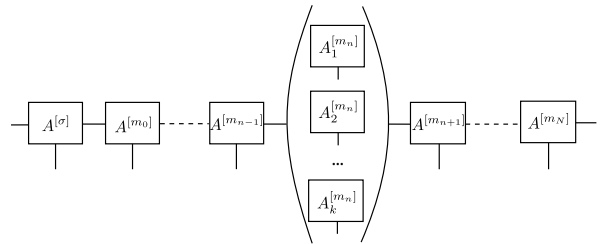


Figure S1. Illustration of mVMPS setup for variationally calculating the m lowest-energy excitation on a Wilson chain.

$\tilde{d}_n = 16$. Convergence was assumed if the change in the chain's ground-state energy dropped below the threshold $|\delta E_G| < 10^{-15}$, which for our longest chains corresponded to $\simeq 0.5$ of the hopping matrix element t_N to the last site. This typically took 10 to 50 sweeps. For the determination of the temperature-dependent susceptibility $\chi(T)$, we performed separate VMPS calculations for each value of T and used a five-point stencil to evaluate the numerical derivative with respect to ϵ . The convergence of the results with respect to all important numerical parameters was checked thoroughly.

C. Multilevel VMPS

The study of energy-level flow during the renormalization procedure is an important part of the NRG toolbox to characterize the fixed-point properties of an impurity model. However, in the presence of the mass-flow error, prominent for a bosonic bath with asymmetric bath spectrum, NRG does not correctly capture the physics of the critical fixed point and the resulting RG flow can no longer be considered reliable. On the other hand, we have already demonstrated that VMPS techniques are able to appropriately deal with mass flow; below we show that they can also be employed to properly access the energy-level flow at quantum critical points.

In its standard formulation, described above, VMPS only targets the ground state and does not have sufficient information about low-lying excited states on the Wilson chain to accurately describe the energy-level flow. In order to go beyond ground-state physics and properly capture the critical energy-level RG flow of multiple low-lying levels, we have implemented a multi-level VMPS (mVMPS) optimization scheme, in the spirit of Ref. [5], that simultaneously targets the lowest k energy eigenstates $|\psi_j\rangle$. A detailed description of our procedure may be found in Sec. 2.3.6 of [40]. Here we just outline the main idea.

Assuming canonical form of the MPS with the center shifted to site n , we define an array $\mathbf{A}^{[m_n]}$ consisting of k tensors $\{A_1^{[m_n]}, A_2^{[m_n]}, \dots, A_k^{[m_n]}\}$ (illustrated in Fig. S1).

For each tensor $A_j^{[m_n]}$, with $j = 1, \dots, k$, the state

$$|\psi_j\rangle = \sum_{\sigma, \mathbf{m}} A^{[\sigma]} A^{[m_0]} \dots A^{[m_{n-1}]} A_j^{[m_n]} A^{[m_{n+1}]} \dots A^{[m_N]} |\sigma\rangle |\mathbf{m}\rangle, \quad (\text{S27})$$

describes one of the k lowest-energy eigenstate of the specified Wilson chain Hamiltonian; the state corresponding to $j = 1$ targets the ground state. The optimization procedure then works as follows: we generate a local Krylov space on site n by subsequent application of the Hamiltonian on each of the k orthonormal states associated with the array $\mathbf{A}^{[m_n]}$. The resulting Hamiltonian \hat{H}_n has a block structure in the Krylov space, with nonzero elements in form of $k \times k$ blocks along the diagonal and the first off-diagonal. Next, we diagonalize the Hamiltonian in the Krylov subspace and construct from its eigenvectors an updated version of the array $\mathbf{A}^{[m_n]}$, each element being orthonormal to the others by construction. To move the orthonormal center of the MPS to the next site ($n + 1$), we form the reduced density matrix $\rho_{n,n+1}^{\text{red},j}$ of each component j by tracing out the rest of the chain and sum them up to form $\rho_{n,n+1}^{\text{red}}$. Similar to the original DMRG formulation, we then diagonalize $\rho_{n,n+1}^{\text{red}}$, keep only the D largest eigenvalues and use the resulting isometry to move the orthonormal center to site $n + 1$. We repeat the optimization procedure, sweeping multiple times through the entire chain. Convergence was assumed when the change in each energy level E_j dropped below the threshold $|\delta E_j| < 10^{-11}$, which for our longest multi-level chains corresponded to $\simeq 10^{-3}$ of the hopping matrix element t_N to the last site. In all mVMPS calculations we used bond dimensions of $D = 100$, $d_n = 40$.

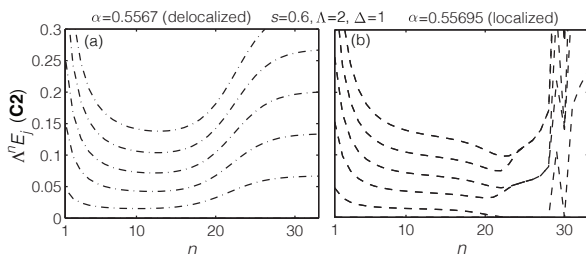


Figure S2. Energy-flow diagrams obtained with mVMPS for the SBM on a C2-RWC. (a) Flow to the delocalized fixed point, characterized by a unique ground state. (b) Flow to the localized fixed point, featuring a doubly degenerated ground-state level. Note that the flow gets distorted deep in the localized regime. This is a signature of the exponentially growing oscillator shifts which cannot be properly dealt with in the mVMPS setup.

To account for the mass flow in the energy-level flow of a length- N RWC system, we conduct a *separate* mVMPS calculation for *every* chain length $N' < N$. This ensures that the k excited states properly take into account the fast- and slow-mode correction at a particular energy scale, which is crucial for correctly describing the critical energy flow at a Gaussian fixed-point. Combining

the results for various lengths and rescaling each set of energies appropriately by a factor $\Lambda^{N'}$, we obtain the energy-flow diagrams in a variational setup.

In addition to the critical fixed-point flows shown in Fig. 3 of the main text, we here present the energy-flow to the stable fixed points in Fig. S2. Panel (a) displays the energy flow to the delocalized fixed point ($\alpha < \alpha_c$), which features a nondegenerate ground state. In contrast, the fixed point flow to the localized fixed point ($\alpha > \alpha_c$) in panel (b) clearly shows a doubly degenerated ground state before getting numerically distorted by the exponentially growing oscillator displacements.

The main goal of our mVMPS calculations is to study the *critical* energy-level flow for the SBM. Since at the critical point the truncation of the bosonic Hilbert space is not problematic, it was not necessary to incorporate the OBB scheme in our mVMPS setup. Doing so would become essential, however, when studying the effects of a local bias, $\epsilon \neq 0$, since then $\langle \hat{\sigma}_z \rangle \neq 0$. In particular, this would be needed if one wishes to compute the static susceptibility $\chi(T)$ using not just the VMPS ground-state expectation value for a length- N_T RWC (as described above), but a thermal average over a shell of low-lying VMPS eigenstates (as done in NRG). We have refrained from attempting such combined mVMPS+OBB computations of $\chi(T)$, since they are numerically expensive, and the ground-state-based scheme worked very well.

S-3. DISSIPATIVE HARMONIC OSCILLATOR

In this section, we perform a systematic study of the properties of RWCs in the context of the exactly solvable DHO, which was briefly introduced in the main text. We compare the RWC and SWC setups in detail with respect to the following issues: iteration details, static susceptibility, and critical coupling α_c .

A. Iteration details

We introduced two types of RWCs in the main text: C1 chains, which include only the fast shifts ($\delta \epsilon_N^S = 0$), and C2 chains, which contain both slow- and fast-mode shift in Eq. (4). For completeness, we also discuss a third type of RWC to be called C0 chains, which by definition include no energy shifts, i.e. $\delta \epsilon_n^{S/F} = 0$ in Eq. (4).

We have explored two versions of the RWC iteration scheme, that differ only in the choice of the frequencies $\omega_{S_n}^+$ that define the intervals $I_n^S = [0, \omega_{S_n}^+]$. For version 1, we chose $\omega_{S_n}^+$ in such a manner that the resulting hopping matrix elements t_n^S of the OWC agree with those used by Bulla, Tong and Vojta (BTV), [24] to be called t_n^{BTV} [Eq. (13) of Ref. 24], with relative error below 10^{-3} . (The error could be further reduced, if desired, by using a finer

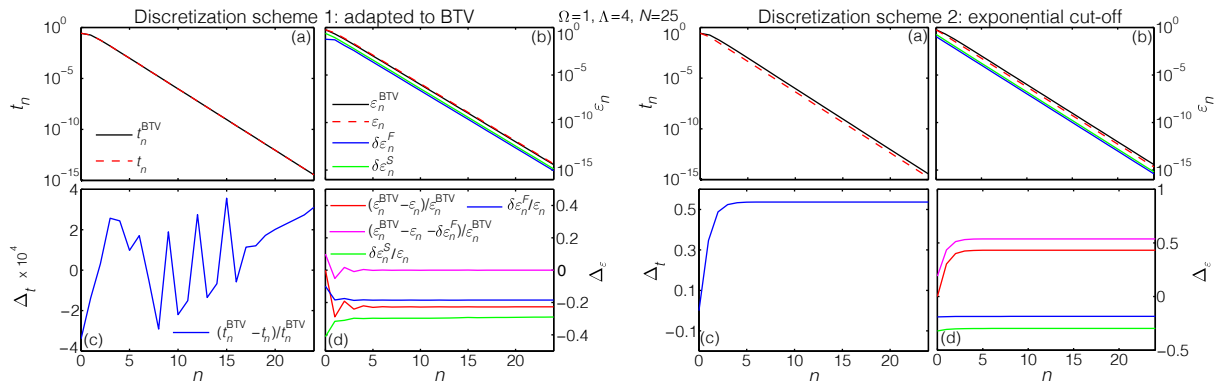


Figure S3. Iteration details: chain parameters. (a-d) Comparison of the Wilson chain parameters t_n and ε_n for $\alpha = 0.199$, obtained using the standard discretization scheme of BTV [24] for $\Lambda = 4$, or using two versions of the RWC-approach described above: for version 1 (left two columns), $\omega_{S,n}^+$ was fine-tuned to ensure that $t_n = t_n^{\text{BTV}}$; for version 2 (right two columns), we simply chose $\omega_{S,n}^+ = \omega_{S,n-1}^+/\Lambda$. (a) t_n^{BTV} used by BTV (black) and our t_n^S (red dashed). (b) The onsite energies $\varepsilon_n^{\text{BTV}}$ (black), our C0 onsite energies ε_n (red dashed), and the shifts $|\delta\varepsilon_n^F|$ (blue) and $|\delta\varepsilon_n^S|$ (green). Evidently, they all scale the same way with n . (c) Relative difference $\Delta_t = (t_n^{\text{BTV}} - t_n^S)/t_n^{\text{BTV}}$ in hopping elements. The noisy structure seen for version 1 (left, note the amplification factor of 10^4) reflects the ω -discretization grid used to represent the bath correlators $\mathcal{G}_n^X(\omega)$ during the OWC construction. (d) Relative differences Δ_ε of various onsite energies: $\Delta_\varepsilon^{\text{C0}} = (\varepsilon_n^{\text{BTV}} - \varepsilon_n)/\varepsilon_n^{\text{BTV}}$ (red); $\Delta_\varepsilon^{\text{C1}} = (\varepsilon_n^{\text{BTV}} - \varepsilon_n - \delta\varepsilon_n^F)/\varepsilon_n^{\text{BTV}}$ (purple); $\Delta_\varepsilon^F = \delta\varepsilon_n^F/\varepsilon_n$ (blue); and $\Delta_\varepsilon^S = \delta\varepsilon_n^S/\varepsilon_n$ (green). For version 1 (left), the relative difference between BTV and C0 energies (no shifts) is quite significant throughout ($\Delta_\varepsilon^{\text{C0}} \simeq 0.2$). The relative difference between BTV and C1 energies (only fast shifts) is significant for early iterations, but becomes small ($\Delta_\varepsilon^{\text{C1}} \lesssim 10^{-3}$) once the iteration scheme reaches self-similarity. For version 2 (right), both $\Delta_\varepsilon^{\text{C0}}$ and $\Delta_\varepsilon^{\text{C1}}$ differ significantly from 0. Both the fast and last slow mode shifts are comparable in magnitude to the bare OWC energies, $\mathcal{O}(\Delta_\varepsilon^{F/S}) = 1$.

frequency grid for representing $\Gamma_n(\omega)$, and more accurately fine-tuning the numerical integration routine used to evaluate the integral that yields t_n^S .) For version 2, we used a plain exponential discretization, $\omega_{S,n}^+ = \omega_{B,n}^+/\Lambda$.

A comparison of the resulting t_n^S , the bare onsite energies ε_n and the shifts $\delta\varepsilon_n^{F/S}$, is shown in Fig. S3. It has two take-home messages: First, all these quantities scale the same way with n and are comparable in magnitude [Figs. S3(a,b)]. In particular, the fast and slow shifts $\delta\varepsilon_n^{F/S}$ are comparable to the bare OWC energies ε_n . Second [Figs. S3(d)], our RWT energies, both $\varepsilon_n + \delta\varepsilon_n^F$ and $\varepsilon_n + \delta\varepsilon_n^F + \delta\varepsilon_n^S$, are in general different from the SWC onsite energies $\varepsilon_n^{\text{BTV}}$ obtained by BTV using standard Wilsonian discretization and tridiagonalization, the relative difference being $\mathcal{O}(1)$. For version 1, however, we note that the relative difference between $\varepsilon_n + \delta\varepsilon_n^F$ and $\varepsilon_n^{\text{BTV}}$ becomes negligible for after a few iterations, but for early ones the difference remains.

Note that we also explored a third discretization scheme similar to version 1, with the difference that we fixed the truncation energies $\omega_{S,n}^+$ such that the resulting hoppings agree with those resulting from the improved logarithmic discretization recently proposed by Zitko and Pruschke (ZP) [26]. This leads to results qualitatively similar to those of version 1, therefore we refrained from including them in the discussion above.

The results in the main text were obtained using version 2. This discretization scheme is particularly appealing due to its accuracy and simplicity. It is more ac-

curate than standard Wilsonian discretization, since by construction it reproduces the hybridization function correctly. The discretization scheme of ZP was devised to achieve this, too, but our scheme turns out to be more accurate, due to its inclusion of TBMs (compare green and red symbols in Fig. S5 below). Our discretization scheme is also simpler to implement than that of ZP, since their chain parameters are found by solving a differential equation, whereas our chain parameters (fixed fully by the energies $\tilde{\varepsilon}_n$ and couplings t_n^S) are found purely by numerical integrations. The accuracy of the latter can be easily controlled by distributing the grid points logarithmically and, in particular, increasing the resolution around the cut-off frequencies $\omega_{S,n}^+$. Note that our discretization scheme offers great flexibility, as one can easily relax the logarithmic discretization in favour of a linear or mixed one (log-linear or linear-log) if high- or low-energy properties need to be taken into account more carefully [4]. (The resulting chain would then have to be treated purely with VMPS methods.)

In addition, we have also examined the retarded self-energies Σ_n^S generated in different iterations n and checked to what extent our chain parameters reproduce the original bath correlator $\mathcal{G}^{\text{bath}}$ [Fig. S4]. (In this context, the two discretization schemes yield qualitatively similar results, so that Fig. S4 only displays version 2.) The main conclusion drawn from the real and imaginary part of Σ_n^S [Figs. S4(a,b)] for the power-law coupling spectrum Γ^{bath} considered here is that the iteration

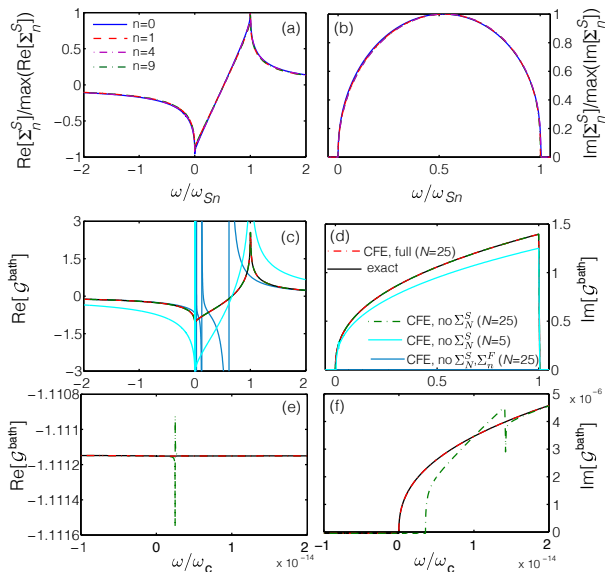


Figure S4. Iteration details: self-energies. (a) $\text{Re}[\Sigma_n^S(\omega)]$ and (b) $\text{Im}[\Sigma_n^S(\omega)]$, plotted vs. $\omega/\omega_{S_n}^+$ for $n = 0, 1, 4, 9$ (different colors), showing that the spectral functions and self-energies have a self-similar structure. (c-f) Various CFE representations of $\mathcal{G}^{\text{bath}} = \mathcal{G}_0$. (c) $\text{Re}[\mathcal{G}^{\text{bath}}(\omega)]$ and (d) $\text{Im}[\mathcal{G}^{\text{bath}}(\omega)]$ vs. ω/ω_c , calculated directly from $\Gamma^{\text{bath}}(\omega)$ (solid black), or from a CFE while including both $\Sigma_n^F(\omega)$ and $\Sigma_N^S(\omega)$ with $N=25$ (dashed red), only Σ_n^F with $N=5$ (cyan) or $N=25$ (dashed green), or neither of the two with $N=25$ (blue). In the latter case, the absence of any imaginary parts in the CFE causes $\text{Im}[\mathcal{G}^{\text{bath}}(\omega)]$ to vanish and $\text{Re}[\mathcal{G}^{\text{bath}}(\omega)]$ to have divergences. Behavior of (e) $\text{Re}[\mathcal{G}^{\text{bath}}(\omega)]$ and (f) $\text{Im}[\mathcal{G}^{\text{bath}}(\omega)]$ for $\omega \rightarrow 0$ with the same color code as in (c,d). The missing slow-mode term in the CFE using only $\Sigma_n^F(\omega)$ (green) causes discrepancies for both the imaginary and the real part only in the vicinity of $\omega = 0$ illustrating that the effect of slow-mode shifts becomes noticeable only at the lowest energy scale of a Wilson chain, associated with its last site.

scheme has a self-similar structure, in that the shape of $\text{Re}[\Sigma_n^S(\omega)]$ and $\text{Im}[\Sigma_n^S(\omega)]$ vs. ω/ω_{S_n} does not change with n . Moreover, the continued fraction expansion of $\mathcal{G}^{\text{bath}}$ [Figs. S4(c-f)] fully reproduces the original function (black) if both the fast- and last mode contributions $\Sigma_n^{F/S}(\omega)$ are included (dashed red), but if these are neglected (dashed green, cyan, blue), the low-frequency behavior changes significantly.

B. Various averaging schemes

For the VMPS calculations of $\chi(T)$ reported in the main text, we mimicked thermal averages by ground-state expectation values of C2-RWCs of length N_T . However, we have also explored several other averaging

schemes. For the sake of completeness, we briefly describe them here, and in the next section compare their results for the susceptibility of the DHO.

For a RWC of specified length N , we have explored the following ways of calculating ground-state expectation values or thermal averages, distinguished by combinations of the following labels: W stands for *Wilsonian* NRG with energy-based truncation; V for *variational* MPS; G for a ground-state expectation value; and T for a thermal average. For Wilsonian NRG calculations, we denote the eigenstates and -energies of Wilson shell n by $|s\rangle_n^W$ and E_{sn}^W , and by $|G\rangle_n^W$ and E_{Gn}^W for that shell's ground state. For VMPS calculations, we variationally minimize the ground-state expectation value of a length- N RWC in the space of all MPS having specified matrix dimensions. Call the resulting ground state $|G\rangle_N^V$, with energy E_{GN}^V .

We write $\langle \hat{O} \rangle_N^{GZ} = \langle G | \hat{O} | G \rangle_N^Z$ for a ground-state expectation value of type $Z = W$ or V . We write N_T for the length of a RWC whose smallest excitation energies are comparable to the temperature,

$$\max\{|\tilde{\epsilon}_{N_T}|, |t_{N_T}^S|\} \simeq T, \quad (\text{S28})$$

and $\langle \hat{O} \rangle_{N_T}^{\text{TW}}$ for a thermal average over all Wilson shell states $|s\rangle_{N_T}^W$. We will call this TW-averaging. Thermal averages can also be mimicked using a single state associated with a length- N_T chain, e.g. $\langle \hat{O} \rangle_{N_T}^{GZ} = \langle G | \hat{O} | G \rangle_{N_T}^Z$ (GW- or GV-averaging), because, by the choice of N_T , the characteristic energy spacing for low-energy excitations above such a state is of order T . GW-, TW- and GV-averaging require calculating a separate length- N_T chain for every temperature.

C. Susceptibility

In this section, we compare the various types of RWCs discussed above (C0,C1,C2) and the various averaging schemes by using them to calculate the static susceptibility of the DHO. It is defined by

$$\chi(T) = \lim_{\epsilon \rightarrow 0} \frac{d\langle a + a^\dagger \rangle_T}{d\epsilon}, \quad (\text{S29})$$

where $\langle \dots \rangle_T$ denotes a thermal expectation value. Its form is easily found analytically [17],

$$\chi_{\text{exact}}(T) = \frac{1}{\Omega + \text{Re}(\mathcal{G}^{\text{bath}}(\omega = 0))}, \quad (\text{S30})$$

which, importantly, is independent of temperature.

Alternatively, the static susceptibility can also be calculated via the dynamical correlation function

$$C(\omega) = \frac{1}{2\pi} \int_{-\infty}^{\infty} e^{i\omega t} C(t) dt, \quad (\text{S31})$$

where $C(t) = \frac{1}{2} \langle [(a + a^\dagger)(t), (a + a^\dagger)] \rangle_T$. The integral

$$\chi_{\text{dyn}}(T) = 4 \int_0^{\infty} \frac{C(\omega)}{\omega} d\omega \quad (\text{S32})$$

can analytically be shown to equal the static susceptibility, $\chi(T) = \chi_{\text{dyn}}(T)$, yielding an important consistency check for numerical calculations. Our Wilsonian NRG calculations passed this check for all three types of RWC introduced above (C0, C1, C2), where $\chi(T)$ was calculated by evaluating $\langle \dots \rangle_T$ in Eq. (S29) using a Wilson-shell thermal average $\langle \dots \rangle_{N_T}^{\text{TW}}$, and $\chi_{\text{dyn}}(T)$ was calculated using fdm-NRG [35]. This illustrates the internal consistency of Wilsonian NRG for a given RWC. However, none of these calculations reproduce the exact result (S30). In contrast, the latter *is* reproduced correctly when calculating χ using VMPS on chain type C2, as we now discuss in detail.

Fig. S5 shows $\chi(T)$ for three types of RWC, C0 (blue), C1 (green), and C2 (red), calculated in four different ways, involving either a CFE (solid lines), or a thermal average over Wilson shell N_T (TW, triangles), or two types of expectation values w.r.t. states associated with site N_T (GW, GV), as detailed in the figure caption. We observe the following salient features.

First, all four methods yield mutually consistent results both for C0 and for C1, but not for C2 (all orange data lie on a line, as do all blue data, but not all red data). Thus the methods differ mainly in their treatment of slow last modes, which are absent in C0 and C1, but present in C2.

Second, for C0 (orange), which has the structure of a *standard* Wilson chain without any TBM information included, $\chi_{\text{C0}}(T)$ differs from the exact result, χ_{exact} (dashed black line) in two important ways: instead of being T -independent, $\chi_{\text{C0}}(T)$ increases with decreasing T , eventually saturating toward a constant value, $\chi_{\text{C0}}(0)$; and this constant value disagrees from χ_{exact} . The reason for these failings was identified clearly by VBGA [17]: the neglect of TBMs causes $\text{Re}[\mathcal{G}^{\text{bath}}(0)]$ to be represented incorrectly [as is also clearly visible in Fig. S4(c)]. VBGA called the missing contribution to $\text{Re}[\mathcal{G}^{\text{bath}}(0)]$ a “mass-flow” error (since near a quantum phase transition, it implies an artificial scale-dependent shift of the order-parameter mass).

Third, for C1 (blue), which includes fast but not last slow modes, the T -dependence of $\chi_{\text{C1}}(T)$ persists, but its asymptotic low-temperature value agrees with the exact one, $\chi_{\text{C1}}(0) = \chi_{\text{exact}}$. Thus, including fast modes is essential to get the asymptotic value right. Indeed, if they are omitted but the slow mode correction included, one obtains curves (not shown) whose $T \rightarrow 0$ limits corresponds to those of C0 curves rather than the exact result.

Fourth, for C2 (red), which includes fast and last slow modes, two methods fully reproduce the T -independent result $\chi_{\text{C2}}(T) = \chi_{\text{exact}}$: CFE and GV. Their common feature is that both succeed in fully incorporating the slow-mode contributions to $\text{Re}[\mathcal{G}^{\text{bath}}(0)]$. For the CFE this is guaranteed by construction. For GV-averaging using $|G\rangle_{N_T}^{\text{V}}$, it reflects the ability of the variational MPS scheme to correctly deal with the large energy shift $\delta\varepsilon_{N_T}^{\text{S}}$ at the end of the length- N_T RWC.

Fifth, the other two methods fail to yield a T -independent result even for C2, since, being based on Wilsonian NRG, they fail to properly deal with the last slow shift. TW- and GW-averaging involve, respectively, a thermal average or ground-state expectation value for Wilson shell N_T ; but the slow shift $\delta\varepsilon_{N_T}^{\text{S}}$ on the last site is so large that upon adding it to the chain, some feedback to earlier sites becomes necessary. Since Wilsonian NRG does not allow for such feedback, while a variational MPS approach does (through back and forth optimization sweeps along the chain), TW- and GW-averaging fail, whereas GV-averaging does not. We also note that GW does better (yielding a weaker T -dependence) than TW. Presumably the reason is that the thermal average used by the latter incorporates information from higher-lying Wilson states $|s\rangle_{N_T}^{\text{W}}$, for which the $\omega = 0$ focus of the static approximation works less well than for the shell’s ground state $|G\rangle_{N_T}^{\text{W}}$.

The upshot of the above analysis is that GV-averaging fully meets the challenge of correctly computing $\chi(T)$ for the DHO. Therefore, GV-averaging was the scheme used for the VMPS calculation of $\chi(T)$ reported in Figs. 2 and 3 of the main text.

D. Critical coupling α_c

We now turn our attention a small but very important detail illustrating the power of RWCs to minimize discretization artefacts: the determination of the critical coupling α_c . Its analytical value for the parameters used here is $\alpha_c = 0.2$. Numerically, we determined α_c by monitoring the divergence of the susceptibility, as described at the end of Sec. S-2C.

On a SWC with $\Lambda = 4$, the analytical value is either largely overestimated when using the BTV discretization scheme ($\alpha_c^{\text{BTV}} \approx 0.228$), or underestimated when using the improved ZP discretization ($\alpha_c^{\text{ZP}} \approx 0.1984$); the deviations are due to the missing information of the TBMs in the Wilson chain setup. In Fig. S5, computed for $\alpha = 0.199$, this causes the low-temperature limit of the susceptibilities χ^{BTV} and χ^{ZP} to lie far below or above the analytical value χ_{exact} , respectively. (In fact, χ^{ZP} diverges in that figure because $\alpha = 0.199$ lies above the critical coupling α_c^{ZP} .)

In contrast, the critical coupling obtained for a C2-RWC matches almost perfectly with the analytic result. For our setup, we found $\alpha_c = 0.199998$. It is possible to systematically reduce the deviation from the analytical value of α_c even further by improving the resolution of the frequency grid used to represent $\mathcal{G}_n^X(\omega)$ while constructing a RWC. Once again, this illustrates the power of our RWC construction and points out how missing TBMs can introduce systematic “discretization” artefacts. Correspondingly, we expect that RWCs will turn out to be useful for reducing discretization artefacts also for other dynamic quantities such as local spectral functions.

As α is tuned ever closer to α_c , the VMPS scheme ex-

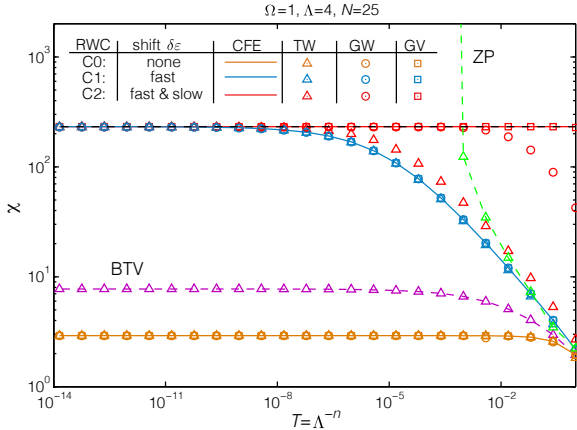


Figure S5. The static susceptibility $\chi(T)$ of the DHO as function of temperature, for $\alpha = 0.199$, $s = 0.4$. The black dashed line gives the exact result χ_{exact} expected from Eq. (S30), the purple and green symbols the results obtained with standard NRG using the discretization scheme of BTV and ZP, respectively. The other data are numerical results for three types of RWC, C0 (orange), C1 (blue), and C2 (red), obtained in four different ways. The first uses a CFE of length N_T to evaluate $\text{Re}[\mathcal{G}_0(0)]$ in Eq. (S30) (CFE, solid lines), while including both $\Sigma_n^S(\omega)$ and $\Sigma_n^F(\omega)$ for C2 (red), only $\Sigma_n^F(\omega)$ (blue), or neither of the two (orange). The second evaluates $\langle \dots \rangle_T$ in Eq. (S29) as thermal average over Wilson shell N_T (TW, triangles). The other two ways approximate $\langle \dots \rangle_T$ by an expectation value taken w.r.t. one of two different single states: the ground state $|G\rangle_{N_T}^W$ of Wilson shell N_T (GW, circles) and the variational ground state $|G\rangle_{N_T}^V$ of a length- N_T chain (GV, squares). In all cases, the derivative $d/d\epsilon$ in Eq. (S29) was evaluated numerically, using several ϵ -values chosen small enough (typically $\ll T$) to ensure that the calculated averages depend linearly on ϵ . TW-, GW- and GV-averages require a separate run for each combination of T and ϵ .

periences increasing convergence problems, resulting in increasing errors for $\chi(0)$. This is not surprising, because the effective potential of the DHO becomes ever shallower the nearer α approaches α_c , where the energy of one mode vanishes. That leads to very large zero-point fluctuations, and a very strong linear response to small values of ϵ . Increasing the VMPS bond dimension to keep more states during the calculation failed to significantly improve $\chi(0)$. We were able to ameliorate this convergence problem to some extent by implementing an optimized boson basis designed to incorporate large bosonic displacements. However, as a matter of principle, this problem will become unmanageable in the limit $\alpha \rightarrow \alpha_c$.

S-4. RG FLOW TOWARDS GAUSSIAN FIXED POINT

In this section, we connect the numerically obtained energy-level diagrams to analytical considerations and

show that the numerical results prove the existence of a Gaussian critical fixed point for the SBM with bath exponents $0 < s \leq 0.5$.

Using a Feynman path-integral representation, the spin-boson model (7) can be shown to be equivalent – in the scaling limit – to the following one-dimensional ϕ^4 theory:

$$\mathcal{S} = \int \frac{d\omega}{2\pi} (m_0 + |\omega|^s) |\phi(i\omega)|^2 + \int d\tau [u_0 \phi^4(\tau) + \bar{\epsilon} \phi(\tau)] \quad (\text{S33})$$

where $\bar{\epsilon}$ is a rescaled bias, and the $|\omega|^s$ term arises from integrating out the oscillator bath with bath exponent s ; this generates a bilinear coupling which is long-ranged in time. m_0 is the (bare) mass of the Ising order parameter ϕ ; an increase of m_0 corresponds to a decrease in the dissipation strength α . Finally, u_0 is the quartic self-interaction. By universality arguments, the same ϕ^4 theory also describes the phase transition of a classical Ising chain with $1/r^{s+1}$ interactions.

Power counting in Eq. (S33) yields the scaling dimensions at criticality:

$$\begin{aligned} \dim[\phi(\tau)] &= (1-s)/2, \\ \dim[u_0] &= 1 - 4\dim[\phi(\tau)] = 2s - 1, \end{aligned} \quad (\text{S34})$$

i.e., the system is above (below) its upper-critical dimension for $s < 0.5$ ($s > 0.5$).

In the following, we focus on the regime $0 < s \leq 0.5$ where the transition is controlled by a Gaussian fixed point. Although the quartic interaction u_0 is irrelevant at criticality, i.e., its fixed-point value is zero, it is required to stabilize the system and it influences observables in a nontrivial fashion, hence it is termed “dangerously irrelevant”. The scaling dimension (S34) implies that the leading-order behavior of the dimensionless renormalized quartic coupling u , defined as $u_0 = \mu^{1-2s} u$ with μ a renormalization energy scale, at criticality is given by

$$u \propto \epsilon_{\text{uv}}^{1-2s} \quad (\text{S35})$$

with logarithmic corrections present at $s=0.5$, where ϵ_{uv} is the running ultraviolet cutoff. From this we can expect that the many-body spectrum, i.e., the energy-level flow as described above, displays families of levels whose spacing goes to zero as the cutoff energy ϵ_{uv} goes to zero. This is in contrast to interacting critical fixed points, here realized for $0.5 < s < 1$ where the renormalized u reaches a finite fixed-point value: This causes the level spacings to approach constant values as $\epsilon_{\text{uv}} \rightarrow 0$ (see Ref. 41 for a detailed analysis of NRG fixed-point spectra at interacting critical points). Both behaviors are nicely borne out by our numerical results in Figs. 4 and S6.

While the effect of u on many observables can be calculated using (renormalized) perturbation theory, this does not apply to the level spectrum at criticality: For $u = 0$ the spectrum is degenerate (reflecting a bosonic zero mode), such that the effect of u is nonperturbative. This zero-mode physics in the presence of a quartic interaction is captured by the toy-model Hamiltonian for

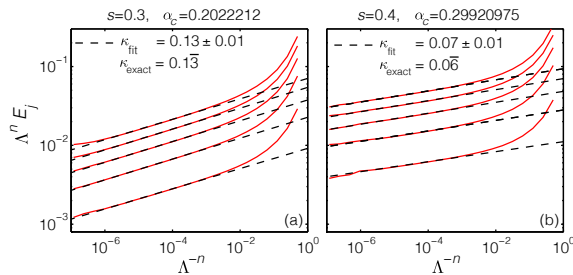


Figure S6. Energy-level flow diagram for the SBM on a C2-RWC obtained for (a) $s = 0.3$ and (b) $s = 0.4$ at the critical point. The dashed lines illustrate the power-law fits employed to extract the exponent κ characterizing the Gaussian fixed point. The numerical results are in excellent agreement with the analytical prediction $\kappa = (1 - 2s)/3$.

a quartic oscillator, $\mathcal{H}_4 = p^2/(2m) + ux^4$ in standard notation. Scaling considerations shows that the eigenenergies of this model obey the exact scaling $e_i \propto u^{1/3}$. Importantly, this toy model, if used with a renormalized

u , describes *renormalized* energy levels.

Let us now connect the behavior of these renormalized energy levels with those generated by NRG. To this end, we note that in NRG the Wilsonian scale $\varepsilon_n \propto \Lambda^{-n}$, which is an infrared cutoff, controls the RG flow in a way analogous to that of the running UV cutoff ε_{uv} in a perturbative RG scheme, as both schemes are designed to describe the renormalized physics at the scale ε_{uv} . Indeed, in an NRG calculation the ultraviolet cutoff at a fixed point is a multiple of the infrared cutoff ε_n . Combining the energy scaling of \mathcal{H}_4 with Eq. (S35), we conclude that the low-lying renormalized energy levels obtained from mVMPS, $\Lambda^n E_j$, scale with the Wilsonian energy scale $\varepsilon_n \propto \Lambda^{-n}$ as

$$\Lambda^n E_j \propto (\Lambda^{-n})^\kappa \text{ with } \kappa = (1 - 2s)/3, \quad (\text{S36})$$

characterizing the approach to a Gaussian fixed point. Fig. S6 shows a log-log plot of the energy-level flow for two values of s , together with a power-law fit. We obtain $\kappa = 0.13 \pm 0.01$ for $s = 0.3$ and $\kappa = 0.07 \pm 0.01$ for $s = 0.4$, in excellent agreement with the analytical prediction, which yields $0.4/3 = 0.13$ and $0.2/3 = 0.06$, respectively.

3 Overview of computed physical quantities

In this Chapter we give an overview of important physical quantities that we computed within this thesis. The following list is not meant to be complete. We rather concentrate on presenting computational particularities and details, which are of special use to NRG+DMFT practitioners. We omit any flavour indices in the following and set $k_B = h = e = 1$ within this thesis, if not included explicitly in the formulas.

3.1 Local orbital and spin susceptibilities and Kondo scales

The major physical quantities to unveil SOS in the 3HHM are the local orbital and spin susceptibility, as well as the corresponding orbital and spin Kondo scale.

Real-frequency local orbital and spin susceptibility. The dynamical real-frequency orbital and spin susceptibility for the impurity site are defined as

$$\chi_{\text{orb}}(\omega) = \frac{1}{8} \sum_a \langle \hat{T}^a \parallel \hat{T}^a \rangle_\omega \quad (3.1)$$

and

$$\chi_{\text{sp}}(\omega) = \frac{1}{3} \sum_\alpha \langle \hat{S}^\alpha \parallel \hat{S}^\alpha \rangle_\omega, \quad (3.2)$$

respectively [Wei12a, HW14], where $\hat{T}^a = \sum_{mm'\sigma} \hat{d}_{m\sigma}^\dagger \frac{1}{2} \tau_{mm'}^a \hat{d}_{m'\sigma}$ are the impurity orbital operators with the SU(3) Gell-Mann matrices, τ^a , normalized as $\text{Tr}[\tau^a \tau^b] = 2\delta_{ab}$, and \hat{S}^α are the impurity spin operators, defined in Sec. 1.2.1. Their imaginary parts are given as $\chi''(\omega) \equiv -\frac{1}{\pi} \text{Im} \chi(\omega)$. The (seemingly unnecessary) average in Eq. (3.1) and Eq. (3.2) is convenient in a calculation that exploits non-abelian symmetries, since it does not pick an arbitrary but fixed individual orbital operator \hat{T}^a [Wei12a].

Orbital and spin Kondo scale. The orbital and spin Kondo scale, T_K^{orb} and T_K^{sp} , below which Kondo screening of the local orbital and spin degrees of freedom set in, are specified as the peak positions of χ''_{orb} and χ''_{sp} , respectively. We remark that these scales are only defined up to a constant factor. Further, our definition of T_K does not guarantee strict universal scaling of physical quantities away from the scaling limit where the bandwidth is by far the largest energy scale in the system (for details and an altered definition of T_K that allows strict universal scaling of dynamical or thermal quantities for a given fixed Hamiltonian, see Ref. [HW14]). Note that, in the 3HHM, pure FL behavior, $\chi''_{\text{orb,sp}} \propto \omega$, is reached below T_K^{sp} .

Imaginary-time local orbital and spin susceptibility. The imaginary-time impurity orbital-orbital and spin-spin correlators are obtained from the real-frequency orbital and spin susceptibility, Eq. (3.1) and Eq. (3.2), respectively,

$$\begin{aligned} \langle \hat{T}(\tau) \hat{T}(0) \rangle &\equiv \frac{1}{8} \langle \hat{\mathbf{T}}(\tau) \cdot \hat{\mathbf{T}}(0) \rangle = \int d\omega n_B(\omega) \chi''_{\text{orb}}(\omega) e^{\omega\tau}, \\ \langle \hat{S}(\tau) \hat{S}(0) \rangle &\equiv \frac{1}{3} \langle \hat{\mathbf{S}}(\tau) \cdot \hat{\mathbf{S}}(0) \rangle = \int d\omega n_B(\omega) \chi''_{\text{sp}}(\omega) e^{\omega\tau}, \end{aligned} \quad (3.3)$$

with the Bose-Einstein distribution $n_B(\omega) = 1/(e^{\beta\omega} - 1)$, $\beta = 1/k_B T$ and the imaginary time $\tau \in [0, \beta/2]$. We remark that we implemented the term $n_B(\omega) e^{\omega\tau}$ in the form $1/(e^{\omega(\beta-\tau)} - e^{-\omega\tau})$ for the numerical evaluation of the integral.

Static local orbital and spin susceptibility. The static local orbital and spin susceptibility is defined as $\chi_0^{\text{orb,sp}} \equiv \chi_{\text{orb,sp}}(\omega = 0)$ with $\chi_{\text{orb,sp}}(\omega)$ of Eq. (3.1) and Eq. (3.2), respectively.

For $T > 0$, a technical NRG-related subtlety has to be considered in the way in which one has to extract the zero-frequency limit from the dynamical susceptibility, $\chi(\omega, T)$ [HW14]. In principle, the static susceptibility is obtained as the Hilbert transform [Kramers-Kronig relation, Eq. (2.20)] of $\chi''(\omega)$, $\chi_0(T) = -\text{P} \int d\omega \frac{\chi''(\omega')}{\omega'}$. $\chi''(\omega)$, the output of fdmNRG, is a Lehman representation [cf. Eq. (2.18)] which contains a δ -function of the form $\delta(\omega - E_{ab})$ with $E_{ab} = E_b - E_a$. P denotes a principal value integral. The problem is, that, for finite-size systems such as Wilson chains, this integral skips all degenerate terms of $\chi''(\omega)$ with $E_a = E_b$. Thus, their contribution to $\chi_0(T)$ has to be dealt with separately. This is taken care of by the fdmNRG routine, which generates, besides $\chi''(\omega)$, also a direct output for the additional contribution to $\chi_0(T)$. The contribution of the $E_a = E_b$ terms is negligible at $T = 0$, where the Wilson chain is in effect very long. However they become increasingly important for finite temperatures, where the Wilson chain in effect becomes shorter (automatically so in case of fdmNRG).

3.2 Real-frequency self-energy

Self-energy trick. We apply the so-called ‘‘self-energy trick’’, introduced by Bulla *et al.* in Ref. [BHP98], in order to improve the resolution of the one-particle self-energy, $\Sigma(\omega)$, within NRG. There, the self-energy is derived as the ratio,

$$\Sigma(\omega) = \frac{F(\omega)}{G(\omega)}, \quad (3.4)$$

of the two-particle retarded Green’s function,

$$F(\omega) = \langle [\hat{d}, \hat{H}_{\text{int}}[\hat{d}^\dagger]] \parallel \hat{d}^\dagger \rangle_\omega, \quad (3.5)$$

and the one-particle correlator $G(\omega) \equiv G_{\text{imp}}(\omega)$ [cf. Eq. (2.5)]. $\hat{H}_{\text{int}}[\hat{d}^\dagger]$ is the onsite interaction term of the local impurity Hamiltonian \hat{H}_{imp} [cf. Eq. (1.3b)].

Eq. (3.4) has clear advantages over the commonly used Dyson equation,

$$\Sigma(\omega) = G_{\text{imp}}^0(\omega)^{-1} - G_{\text{imp}}(\omega)^{-1}, \quad (3.6)$$

the difference of the inverse of the exactly known noninteracting retarded impurity Green’s function, $G_{\text{imp}}^0(\omega) = [\omega - \varepsilon_d - \Delta(\omega)]^{-1}$, and the interacting retarded impurity Green’s function, $G_{\text{imp}}(\omega)$ of Eq. (2.5), computed with NRG. While Eq. (3.6) directly transfers systematic numerical errors from $G_{\text{imp}}(\omega)$ to $\Sigma(\omega)$, the self-energy trick, Eq. (3.4), partly cancels out systematic errors in $F(\omega)$ and $G(\omega)$ by taking their ratio in $\Sigma(\omega)$. In particular, discretization and broadening artefacts, like artificial oscillations or overbroadening of high-energy features, are systematically reduced.

Overshoot correction. Despite using the self-energy trick, the self-energy has controlled, yet finite accuracy $\delta \text{Im} \Sigma(\omega)$ relative to $\max(|\text{Im} \Sigma(\omega)|)$. Therefore it can happen at sufficiently

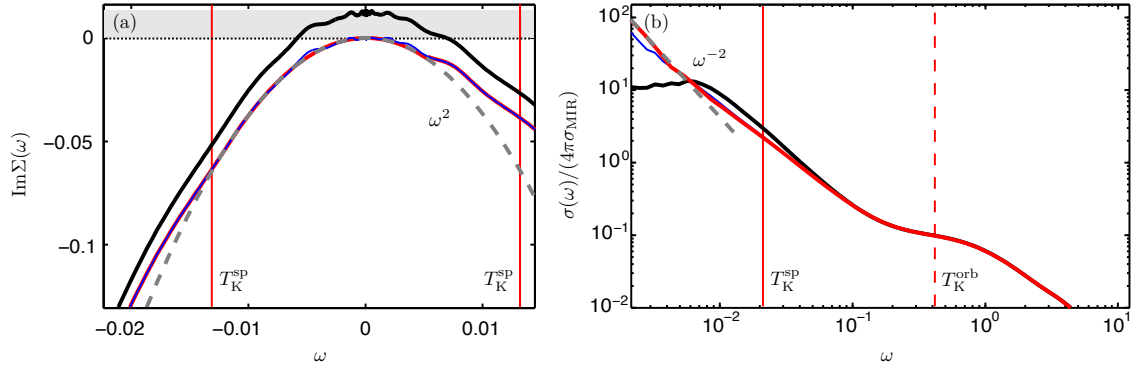


Figure 3.1 (a) The imaginary part of the self-energy, $\text{Im} \Sigma(\omega)$, and (b) the optical conductivity, $\sigma(\omega)$, for the 3HHM with $U = 7.5$, $J = 2$ at $n_d = 2$ and $T = 0$. $\sigma(\omega)$ is calculated with Eq. (3.15) using three different input functions for $\text{Im} \Sigma(\omega)$. The black curve is the original DMFT+NRG result of $\text{Im} \Sigma(\omega)$, the blue curve is the shifted result, $\text{Im} \Sigma_{\text{shift}}(\omega)$, and the red curve is an improved function (see text). The color scheme for $\sigma(\omega)$ in (b) follows the color scheme of (a). Dashed grey fits comply with FL behavior. Solid (dashed) vertical lines mark the spin (orbital) Kondo scale.

low temperatures that the self-energy “overshoots”, i.e. $\text{Im} \Sigma(\omega)$ can become slightly positive around the Fermi level, $\omega = 0$, which is unphysical.

During the DMFT self-consistency procedure this error needs to be fixed by hand by either “cutting” all positive values of $\text{Im} \Sigma(\omega)$, i.e. by setting them to zero, or by shifting $\text{Im} \Sigma(\omega)$ to $\text{Im} \Sigma_{\text{shift}}(\omega) = \text{Im} \Sigma(\omega) - \text{Im} \Sigma(\omega = 0)$. We found that both strategies lead to essentially the same converged DMFT results. This might be based on the fact that the overshooting of the self-energy is a systematic error: once a DMFT+NRG calculation is converged, the overshooting error in the output function $\text{Im} \Sigma(\omega)$ is reproduced in any further DMFT loop, although the cut or shifted version of $\text{Im} \Sigma(\omega)$ was used as input.

For the calculation of physical quantities, for which $\Sigma(\omega)$ serves as an input function, we use the shifted self-energy, based on $\text{Im} \Sigma_{\text{shift}}(\omega)$.

This procedure is demonstrated in Fig. 3.1 for the calculation of the optical conductivity, $\sigma(\omega)$, at $T = 0$ [cf. Sec. 3.6 and Eq. (3.15) for details of the calculation]. In Fig. 3.1(a) the original DMFT+NRG result, $\text{Im} \Sigma(\omega)$, is plotted in black, the shifted result, $\text{Im} \Sigma_{\text{shift}}(\omega)$, is plotted in blue. Whereas the black curve exceeds zero in the grey shaded area, the thin blue curve has its maximum at $\omega = 0$. Further it is purely negative and follows roughly FL behavior, $\text{Im} \Sigma(\omega) \propto \omega^2$, at low frequencies, as indicated by the dashed grey parabolic fit (cf. Sec. 3.9 for details about FL behavior). In addition, we build an improved function (red curve) to check the reliability of the optical conductivity calculation. It is a combination of the parabolic fit function at small ω and $\text{Im} \Sigma_{\text{shift}}(\omega)$ at larger ω . Thus, at low ω , exact FL behavior is incorporated and artificial oscillations are suppressed. In Fig. 3.1(b) we demonstrate, how these three choices for $\text{Im} \Sigma(\omega)$ affect the outcome of the optical conductivity, $\sigma(\omega)$. Clearly, $\sigma(\omega)$ differs at low frequencies. The black curve obviously misses the true FL behavior (Drude peak), $\sigma(\omega) \propto \omega^{-2}$, which is indicated by a grey dotted line in Fig. 3.1. It even exhibits an artificial maximum at approximately $\omega = 0.005$. In contrast, the blue curve keeps increasing with decreasing frequency, approaching but not fully reaching FL behavior. The red improved curve, which is based on the exact FL behavior in $\text{Im} \Sigma(\omega)$, displays the FL Drude peak at low frequencies, proofing the general quality of the calculation.

Within this thesis, unless specified otherwise, we mainly employ $\text{Im} \Sigma_{\text{shift}}(\omega)$ for an unbiased evaluation of our results, however, bearing in mind that these are, strictly speaking, only accurate up to a systematic error of $\text{Im} \Sigma(\omega = 0)$.

3.3 Real-frequency spectral function and local occupation

Spectral function. The local density of states (spectral function),

$$A(\omega) = -\frac{1}{\pi} \text{Im} G(\omega), \quad (3.7)$$

is defined as the imaginary part of the local interacting Green's function, $G(\omega)$, of Eq. (2.6) and fulfills the sum rule $\int d\omega A(\omega) = 1$. Within NRG, $A(\omega)$ can be directly obtained as the Lehman sum over discrete delta-peaks [cf. $A_{\text{raw}}(\omega)$, Eq. (2.19) of Sec. 2.2.4], which needs to be (log-Gaussian) broadened to obtain a smooth curve.

In order to reduce discretization artefacts, an improved version of $A(\omega)$ can be computed by inserting Eq. (2.5), i.e. $G_{\text{imp}}(\omega) = [\omega - \varepsilon_d - \Delta(\omega) - \Sigma(\omega)]^{-1}$, into Eq. (3.7), while using $\Sigma(\omega)$ obtained from the self-energy trick Eq. (3.4).

The full hybridization function for a flat band, $\Gamma(\omega) = \Gamma\Theta(|\omega| - D_{\text{NRG}})$, is calculated as

$$\Delta(\omega) = \frac{\Gamma}{\pi} \ln \left| \frac{\omega^+ + D_{\text{NRG}}}{\omega^+ - D_{\text{NRG}}} \right|. \quad (3.8)$$

Within DMFT+NRG, an improved version of $A(\omega)$ is obtained from Eq. (3.7) inserting the lattice Green's function, $G_{\text{latt}}(\omega)$ of Eq. (2.10) together with $\Sigma(\omega)$ of Eq. (3.4). The DMFT+NRG spectral functions shown in this thesis are always “improved” ones.

Local occupation. From the (improved) spectral function $A(\omega)$ we can directly obtain the filling (average occupation number), n_d , of the impurity (or equivalently, $\langle \hat{n}_i \rangle$, of a lattice site i),

$$n_d \equiv \langle \hat{n}_i \rangle = \int d\omega A(\omega) f(\omega), \quad (3.9)$$

where

$$f(\omega) = [e^{\omega/(k_B T)} + 1]^{-1} \quad (3.10)$$

is the Fermi-Dirac distribution function with the Fermi level at $\omega = 0$. When using $A_{\text{raw}}(\omega)$ of Eq. (2.19) the integral in Eq. (3.9) reduces to a simple sum, $n_d = \sum_j a_j f(\omega_j)$.

3.4 Matsubara Green's function and self-energy

Matsubara Green's function. The Matsubara correlator, $G(i\omega_n)$, associated with the retarded correlator, $G(\omega) = \langle \hat{d} \parallel \hat{d}^\dagger \rangle_\omega$ [cf. Eq. (2.5)], is the Hilbert transform of $A(\omega)$ [cf. Eq. (3.7)] and can be directly computed from NRG raw data as

$$G(i\omega_n) = \int d\omega \frac{A(\omega)}{i\omega_n - \omega} = \sum_j \frac{a_j}{i\omega_n - \omega_j}. \quad (3.11)$$

The expression $D(i\omega_0) = -\frac{1}{\pi} \text{Im} G(i\omega_0)$ with the first Matsubara frequency, ω_0 , is used within DMFT+QMC to estimate the density of states at the Fermi level (cf. Ref. [DSH⁺18] in Sec. 6.2).

Matsubara self-energy. The Matsubara self-energy is either obtained via the Hilbert transform

$$\Sigma(i\omega_n) = -\frac{1}{\pi} \int d\omega \frac{\text{Im} \Sigma(\omega)}{i\omega_n - \omega} \quad (3.12)$$

with $\Sigma(\omega)$ as defined in Eq. (3.4), or via the self-energy trick on the Matsubara axis,

$$\Sigma(i\omega_n) = \frac{F(i\omega_n)}{G(i\omega_n)}, \quad (3.13)$$

where $F(i\omega_n)$ is the Hilbert transform of $-1/\pi \text{Im} F(\omega)$ analogously to Eq. (3.11) [$F(\omega)$ is defined in Eq. (3.5)].

Note that results on the Matsubara axis obtained from Eq. (3.11) and Eq. (3.13) can be computed directly on the discrete data without the need for broadening.

3.5 ARPES structure factor and band dispersion relation

The structure factor or momentum-resolved spectral function, $A(\varepsilon_k, \omega)$, as experimentally accessible by angle-resolved photoemission spectroscopy (ARPES), is directly obtained from the self-energy $\Sigma(\omega)$ within DMFT [GKKR96]. For the Bethe lattice, we use the formula

$$A(\varepsilon_k, \omega) = -\frac{1}{\pi} \text{Im} [\omega + \mu - \varepsilon_k - \Sigma(\omega)]^{-1}. \quad (3.14)$$

The band dispersion relation can then be either defined as the maxima, $E^*(\omega)$, of $A(\varepsilon_k, \omega)$ for given ω , or as the maxima, $E(\varepsilon_k)$, of $A(\varepsilon_k, \omega)$ for given ε_k . Note that these definitions can lead to slightly different QP dispersions for the Bethe lattice (cf. Fig. 7.3, Fig. 7.7, and Fig. 7.8 in Chapter 7). $E(\varepsilon_k)$ is the solution to the equation $\omega + \mu - \varepsilon_k - \text{Re} \Sigma(\omega) = 0$, as used in Ref. [DSH⁺14]. For fixed ω , this trivially yields a single value for ε_k , but not necessarily a unique value for $E(\varepsilon_k) \equiv \omega$ for fixed ε_k (cf. the s-shaped QP band dispersions in Fig. S-4(a) of Ref. [SYvD⁺15] in Sec. 4.2, Fig. 11(b) of Ref. [SKWvD18] in Sec. 5.2, and Fig. 7.3, Fig. 7.7, Fig. 7.8 in Chapter 7).

3.6 Optical conductivity, kinetic energy, resistivity and the Mott-Ioffe-Regel (MIR) limit

Optical conductivity. The (real part of the) optical conductivity (per spinful band) is computed in linear response theory as in Ref. [DMiev⁺13],

$$\sigma(\omega) = \frac{2\pi e^2}{\hbar} \int d\omega' \frac{f(\omega') - f(\omega + \omega')}{\omega} \int d\varepsilon \Phi(\varepsilon) A(\varepsilon, \omega') A(\varepsilon, \omega + \omega'). \quad (3.15)$$

The transport velocity kernel,

$$\Phi(\varepsilon) = \frac{1}{V} \sum_{\mathbf{k}} \left(\frac{\partial \varepsilon_{\mathbf{k}}}{\partial k_x} \right)^2 \delta(\varepsilon - \varepsilon_{\mathbf{k}}) = \int \frac{d^d k}{(2\pi)^d} \left(\frac{\partial \varepsilon_{\mathbf{k}}}{\partial k_x} \right)^2 \delta(\varepsilon - \varepsilon_{\mathbf{k}}) \quad (3.16a)$$

$$\stackrel{\text{BETHE}}{=} \Phi(0) \left[1 - \left(\frac{\varepsilon}{D} \right)^2 \right]^{\frac{3}{2}}, \quad (3.16b)$$

contains the information about band velocities (here, given in x-direction),

$$v_{\mathbf{k}}^x = \left(\frac{\partial \varepsilon_{\mathbf{k}}}{\hbar \partial k_x} \right). \quad (3.17)$$

V is a normalization volume. Eq. (3.16b) is the transport velocity kernel for the Bethe lattice, Eq. (2.8). $A(\varepsilon, \omega)$ is the structure factor as defined in Eq. (3.14), $f(\omega)$ is the Fermi-Dirac distribution function of Eq. (3.10).

Kinetic energy. The kinetic energy, $K(\Omega)$, is the integral of the optical conductivity, $\sigma(\omega)$, up to a cutoff value Ω [SMP⁺12]:

$$\frac{K(\Omega)}{K(\infty)} = \frac{\int_0^\Omega d\omega \sigma(\omega)}{\int_0^\infty d\omega \sigma(\omega)}. \quad (3.18)$$

Within this thesis, $K(\Omega)$ is normalized to $K(\infty)$.

Resistivity. The temperature-dependent optical resistivity is given as the inverse of the optical conductivity evaluated at the Fermi level, $\omega = 0$,

$$\rho(T) = \frac{1}{\sigma(\omega = 0, T)}. \quad (3.19)$$

Mott-Ioffe-Regel (MIR) limit. In conventional metals $\rho(T)$ increases with temperature. This behavior can be explained in a QP picture: the mean-free path l of a QP gradually decreases because thermally-induced scattering events become more frequent. For phonon scattering at higher temperatures, i.e. above a small temperature below which electron-electron scattering is dominant, this leads to a linear growth of $\rho(T) \sim T$. However, this QP picture breaks down approximately when l becomes shorter than the interatomic spacing a , leading to the Mott-Ioffe-Regel (MIR) limit: $l_{\min} \approx a$ (other definitions include $k_{\text{F}} l_{\min} \approx 1$ or $k_{\text{F}} l_{\min} \approx 2\pi$) [IR60, Mot72, Gur81]. As a consequence, above a corresponding MIR temperature, T_{MIR} , the resistivity saturates in conventional metals, approaching a maximum value, ρ_{MIR} . While for most good metals, $l \gg a$ holds up to their melting temperatures, there is a vast number of metals for which the MIR resistivity saturation is observed [HTT04]. Interestingly, most strongly correlated metals, like cuprate HTSCs, heavy fermions, Hund metals (including iron-based HTSCs), and also several organic compounds, exceed the MIR limit and $\rho(T)$ does *not* saturate with increasing temperature. Due to this unconventional but common feature, which is generically assumed to be induced by some kind of NFL behavior, all these materials are collectively referred to as “bad metals” in the literature [EK95, HTT04].

Within this thesis, $\sigma(\omega)$ is measured in units of $\sigma_{\text{MIR}} = \frac{e^2 \Phi(0)}{\hbar D}$, the MIR limit value for a free electron gas derived in Ref. [DMicv⁺13] for a parabolic band in two dimensions, $\varepsilon(\mathbf{k}) = \frac{\hbar^2(k_x^2 + k_y^2)}{2m}$, using the criterion $k_{\text{FL}} l_{\min} = 1$. Accordingly, ρ is given in units of $\rho_{\text{MIR}} = 1/\sigma_{\text{MIR}}$.

3.7 Thermopower

The thermopower (Seebeck coefficient), $\alpha(T) = -\Delta\mathcal{V}/\Delta T$, is the ratio of an electrical field $-\Delta\mathcal{V}$ that is generated when a thermal gradient, ΔT is established in a material, measured under the condition that no electrical current flows [MG16]. We calculate $\alpha(T)$ with the Kubo formula of Ref. [MG16],

$$\alpha(T) = -\frac{k_B}{e} \frac{\int d\omega T(\omega) \beta \omega \left(-\frac{\partial f}{\partial \omega}\right)}{\int d\omega T(\omega) \left(-\frac{\partial f}{\partial \omega}\right)}, \quad (3.20)$$

with $\beta = 1/k_B T$. $f(\omega)$ is the Fermi-Dirac distribution function of Eq. (3.10) with its derivative

$$\frac{\partial f}{\partial \omega} = -\frac{\beta}{2} \frac{1}{1 + \cosh(\beta\omega)}. \quad (3.21)$$

The transport function, $T(\omega)$, (exemplified for transport in x-direction) reads

$$T(\omega) = \frac{2\pi e^2}{V} \sum_{\mathbf{k}} (v_{\mathbf{k}}^x)^2 A_{\mathbf{k}}(\omega)^2 = \frac{2\pi e^2}{\hbar^2} \int d\varepsilon \Phi(\varepsilon) A(\varepsilon, \omega)^2, \quad (3.22)$$

with $v_{\mathbf{k}}^x$ as defined in Eq. (3.17), $\Phi(\varepsilon)$ as in Eq. (3.16b) for the Bethe lattice, and $A(\varepsilon, \omega)$ as in Eq. (3.14).

In Ref. [MG16] it is pointed out that the following relations between the thermopower and the entropy, S , can be considered to interpret the temperature dependence of $\alpha(T)$. For a free electron gas of density, n , the direct relation, $\alpha = -S/ne$, holds at low temperatures and the Heikes formula, $\alpha_H = -1/e(\partial S/\partial n)_E = 1/e(\mu/T)_{\text{at}}$ at high-temperatures in the atomic limit. For multiorbital systems with integer filling, n_d , the latter relation can be expressed as [MG16],

$$\alpha_H = \frac{k_B}{2e} \log \frac{d_{n_d-1}}{d_{n_d+1}}, \quad (3.23)$$

which only depends on the degeneracies, d , of the atomic states with neighboring valences $n_d \pm 1$, but not on any other system parameter. Further, the Kelvin formula,

$$\alpha_K = -\frac{1}{e} \left(\frac{\partial S}{\partial n} \right)_T = \frac{1}{e} \left(\frac{\partial \mu}{\partial T} \right)_n, \quad (3.24)$$

is considered as an approximation to the thermopower.

3.8 Entropy

Within DMFT, where a lattice system is mapped self-consistently onto an impurity system, we can both calculate the impurity contribution to the entropy, as usually done within NRG [BCP08], and the lattice entropy. Importantly, these entropies differ (quantitatively but not qualitatively), as is discussed in detail in Sec. 7.3.

3.8.1 Impurity contribution to the entropy

The impurity contribution to the entropy, S_{imp} , is introduced in Eq. (48) and Eq. (53) of Ref. [BCP08] as the difference,

$$S_{\text{imp}}(T) = S_{\text{tot}}(T) - S_{\text{tot}}^{(0)}(T), \quad (3.25)$$

between the entropy of the total Wilson chain, S_{tot} , and the entropy of a reference system, $S_{\text{tot}}^{(0)}$, which is the bare conduction Hamiltonian without impurity. In practice, it is thus necessary to perform two independent NRG runs, one for the full Hamiltonian and one for the same Hamiltonian without impurity (e.g. by effectively removing it by setting ε_d to a very large number, we used $\varepsilon_d = 1000$).

3.8.2 Lattice entropy

In principle, two different approaches are available to calculate the lattice entropy within DMFT. One approach is based on the total internal energy, $\mathcal{E}_{\text{latt}}$, the other one on the free

energy, $\mathcal{F}_{\text{latt}}$, of the system. However, the latter approach leads to physically wrong results within our current implementation, as described below. The exact reason is still unknown and requires further investigation of both the derivation of the applied formulas and their numerical evaluation.

Lattice entropy from the total internal energy. In the first approach, the lattice entropy is obtained from the specific heat, $C(T) = \frac{\partial \mathcal{E}_{\text{latt}}}{\partial T}$, and the thermodynamic relation $T \frac{\partial S}{\partial T} = \frac{\partial \mathcal{E}}{\partial T}$ via integration,

$$S_{\text{latt}}(T) = S_{\text{latt}}(T_0) + \int_{T_0}^T dT' \frac{C(T')}{T'} \quad (3.26)$$

(following Eq. (238) of Ref. [GKKR96]). $S_{\text{latt}}(T_0)$ is a constant (in principle unknown) offset. In the case of a FL, however, $S_{\text{latt}}(T_0)$ can be determined exactly (with Eq. (3.42) in Sec. 3.9). For Hubbard-type models in the limit of large lattice coordination, the total internal energy is given by Eq. (7) of Ref. [Kot99], which we apply in the form,

$$\frac{\mathcal{E}_{\text{latt}}}{N_c} = \int d\omega f(\omega)(\omega + \mu)A(\omega) + 2t^2 \iint d\omega_1 d\omega_2 f(\omega_1) \frac{A(\omega_1)A(\omega_2)}{\omega_1 - \omega_2} \quad (3.27a)$$

$$= \int d\omega f(\omega)(\omega + \mu)A(\omega) - \frac{2t^2}{\pi} \int d\omega f(\omega) \text{Re} G(\omega) \text{Im} G(\omega), \quad (3.27b)$$

with the Fermi-Dirac distribution function, $f(\omega)$ [cf. Eq. (3.10)]. To reduce the double integration in Eq. (3.27a) to only one integral in Eq. (3.27b) we used the Kramers-Kronig relation, $\text{Re} G(\omega) = \frac{1}{\pi} P \int d\omega' \frac{\text{Im} G(\omega')}{\omega' - \omega} = P \int d\omega' \frac{A(\omega')}{\omega - \omega'}$.

Lattice entropy from the free energy. In the second approach, the lattice entropy is obtained as the derivative of the free energy. Following Eq. (46) of Ref. [GKKR96], the free energy of the lattice is composed of two parts, $\mathcal{F}_{\text{latt}} = \mathcal{F}_{\text{imp}} + \mathcal{F}_{\text{cor}}$: the impurity free energy, \mathcal{F}_{imp} , and a correction term for the lattice,

$$\mathcal{F}_{\text{cor}} = -T \sum_n \left[\ln G_{\text{latt}}(i\omega_n) - \int_{-D}^D d\varepsilon \rho_0(\varepsilon) \ln G^\varepsilon(i\omega_n) \right], \quad (3.28)$$

with the lattice Green's function $G_{\text{latt}}(i\omega_n) = \int d\varepsilon \rho_0(\varepsilon) G^\varepsilon(i\omega_n)$, the noninteracting density of states $\rho_0(\varepsilon)$, for which we use the Bethe lattice version, Eq. (2.8), and $G^\varepsilon(i\omega_n) = [i\omega_n + \mu - \Sigma(i\omega_n) - \varepsilon]^{-1}$. Note that the correction term Eq. (3.28) includes only local quantities within DMFT. For the lattice entropy we thus obtain the expression

$$S_{\text{latt}}(T) = -\frac{\partial \mathcal{F}_{\text{latt}}}{\partial T} = -\frac{\partial \mathcal{F}_{\text{imp}}}{\partial T} - \frac{\partial \mathcal{F}_{\text{cor}}}{\partial T} = S_{\text{imp}} + S_{\text{cor}}. \quad (3.29)$$

For S_{imp} we use Eq. (3.25). For S_{cor} we perform the partial derivative of the correction term Eq. (3.28). Often, S_{cor} is neglected in the literature, as it is supposed to be small, which is, however, not true in general, as explicated at the end of Sec. 3.9 and in Sec. 7.3.

We now turn to the explicit calculation of \mathcal{F}_{cor} . Eq. (3.28) is analytically continued in order to be able to directly use real-frequency NRG data. We apply the analytical continuation of the form

$$\frac{1}{\beta} \sum_n g(i\omega_n) = (-1) \oint \frac{dz}{2\pi i} f(z)g(z) \quad (3.30)$$

for a function $g(i\omega_n)$ with poles in the complex plane, fermionic Matsubara frequencies $\omega_n = 2\pi(n + \frac{1}{2})T$, and the Fermi-Dirac distribution function, $f(z)$ [cf. Eq. (3.10)]. A derivation is given in Ref. [BF11]. In Eq. (3.28), $g(i\omega_n) = \ln G(i\omega_n)$ has a branch cut at the real axes. So the contour integral leads to the expression

$$-T \sum_n \ln G(i\omega_n) = \oint \frac{dz}{2\pi i} f(z) \ln G(z) \quad (3.31a)$$

$$= \int \frac{d\omega}{2\pi i} f(\omega) [\ln G(\omega + i0^+) - \ln G(\omega - i0^+)]$$

$$= \int \frac{d\omega}{2\pi i} f(\omega) [\ln G^{\text{R}}(\omega) - \ln G^{\text{A}}(\omega)]$$

$$= \int \frac{d\omega}{2\pi i} f(\omega) \ln \left(\frac{G^{\text{R}}(\omega)}{G^{\text{A}}(\omega)} \right)$$

$$= \int \frac{d\omega}{\pi} f(\omega) \phi(\omega), \quad (3.31b)$$

where $\phi(\omega)$ is the phase of $G^{\text{R}}(\omega)$ and $G^{\text{R}} = G^{\text{A}*}$ are complex conjugates to each other. The real-frequency retarded Green's function, $G(\omega + i0^+) = G^{\text{R}}(\omega)$, is defined in the upper half plane whereas $G(\omega - i0^+) = G^{\text{A}}(\omega)$, the advanced Green's function, is defined in the lower half-plane. Overall, we therefore obtain for the correction term of the free energy Eq. (3.28),

$$\mathcal{F}_{\text{cor}} = \int \frac{d\omega}{\pi} f(\omega) \left[\phi(\omega) - \int_{-D}^D d\varepsilon \rho_0(\varepsilon) \phi^\varepsilon(\omega) \right] \quad (3.32a)$$

$$= \int \frac{d\omega}{\pi} f(\omega) [\Phi_1(\omega) - \Phi_2(\omega)], \quad (3.32b)$$

with

$$\Phi_1(\omega) \equiv \phi(\omega) = \arctan \left(\frac{\text{Im } G(\omega)}{\text{Re } G(\omega)} \right), \quad (3.33a)$$

$$\Phi_2(\omega) \equiv \int_{-D}^D d\varepsilon \rho_0(\varepsilon) \phi^\varepsilon(\omega), \text{ and} \quad (3.33b)$$

$$\phi^\varepsilon(\omega) = \arctan \left(\frac{\text{Im } \Sigma(\omega)}{\omega + \mu - \varepsilon - \text{Re } \Sigma(\omega)} \right), \quad (3.33c)$$

where, by construction, $\phi(\omega)$ and $\phi^\varepsilon(\omega)$ are only defined in the interval $[0, \pi]$, thus $\Phi_1(\omega)$ and $\Phi_2(\omega)$ have to be positive. The derivation of Eq. (3.33c) is completely analogous to Eq. (3.33a).

We illustrate the nontrivial calculation of S_{latt} in Fig. 3.2 for the particle-hole symmetric IHM of Eq. (1.1) with Coulomb interaction strength $U = 4$. Examples of original outcomes for $\Phi_1(\omega)$ and $\Phi_2(\omega)$ are plotted in Fig. 3.2(a,b) (cf. dashed blue and red curves, respectively). In order to fulfill that $\phi(\omega), \phi^\varepsilon(\omega) \in [0, \pi]$, we use $\phi(\omega) \bmod \pi$ and $\phi^\varepsilon(\omega) \bmod \pi$ in Eq. (3.33). This results in the “flipped” solid blue and solid red curves for $\Phi_1(\omega)$ and $\Phi_2(\omega)$, respectively. Their difference, $\Phi_1(\omega) - \Phi_2(\omega)$ (green curve) is multiplied by the Fermi-Dirac distribution function (dotted curve), leading to the orange curve. Integration thereof basically gives \mathcal{F}_{cor} [cf. blue curve in Fig. 3.2(d)]. This procedure is repeated for each data point of T . In Fig. 3.2(a) it is illustrated for $T = 0$, in Fig. 3.2(b) for $T = 0.5$. Corresponding spectral functions are shown in Fig. 3.2(c). The negative partial derivative of \mathcal{F}_{cor} results in S_{cor} [cf. blue curve in Fig. 3.2(d)], which shows a pronounced maximum at 0.08. We note that this behavior is qualitatively similar to the negative derivative of $A(\omega = 0)$ (cf. orange curve).

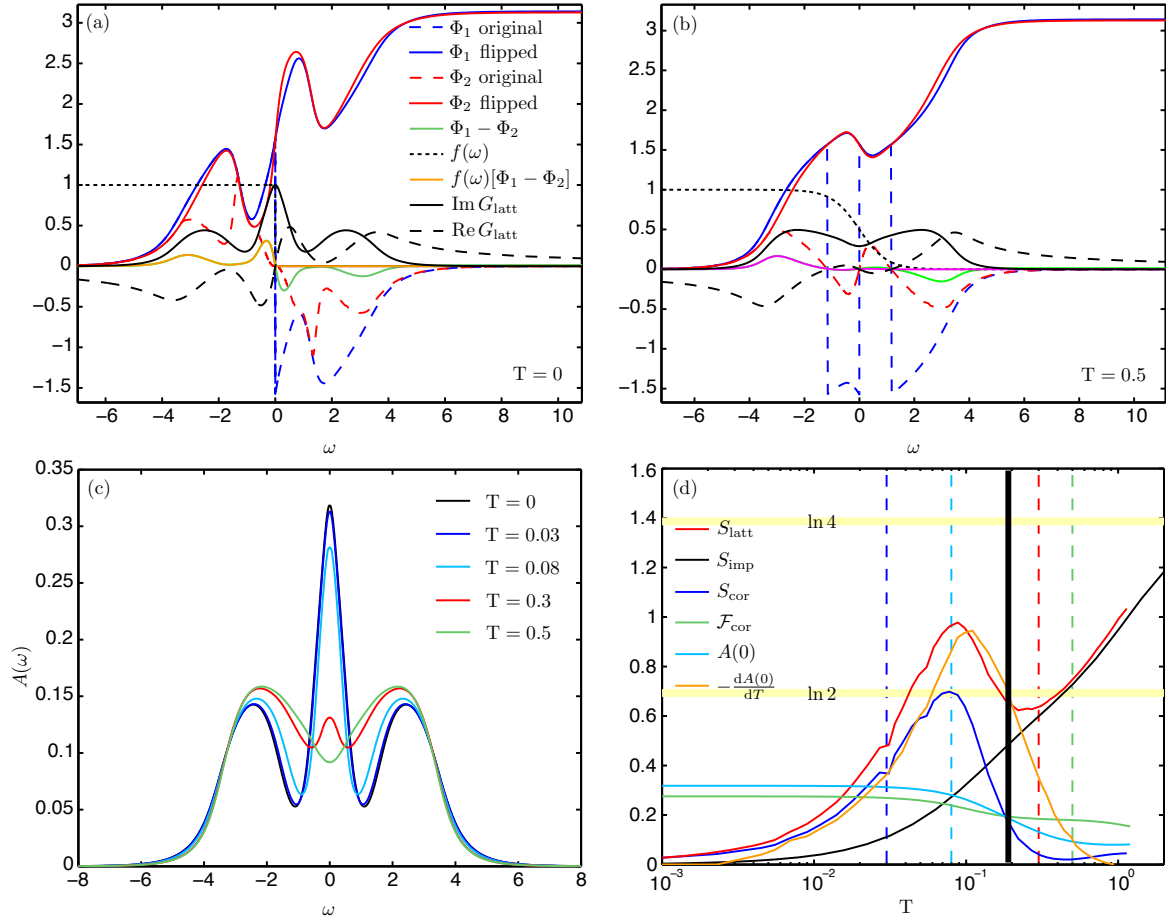


Figure 3.2 We illustrate the computation of $S_{\text{latt}}(T)$ for the 1HM with $U = 4$ and $\mu = -\frac{U}{2}$. (a,b) The calculation of \mathcal{F}_{cor} , Eq. (3.32), is divided into several steps. We plotted intermediate results for (a) $T = 0$ and (b) $T = 0.5$. (c) We also show spectral functions for several temperatures. These temperatures are marked by vertical dashed lines in (d) using the color code of (c). (d) The final result, S_{latt} , as well as its components S_{imp} and S_{cor} are plotted as functions of temperature. Further, $\mathcal{F}_{\text{cor}}(T)$, the spectral function $A(0, T)$ at zero frequency and its negative derivative are shown. In principle, a plateau at $\ln(2)$ is expected for $S_{\text{latt}}(T)$ and $S_{\text{imp}}(T)$ in the local moment regime for two spin degrees of freedom, $\ln(4)$ should be approached in the free orbital regime as charge fluctuations are included there. However, here, the plateau at $\ln(2)$ is replaced by a transition through $\ln(2)$ above the Kondo temperature T_K (vertical black line) for S_{imp} , because T_K is too near to the bare bandwidth of the model. $S_{\text{latt}}(T)$ exhibits an unphysical negative slope below about $\ln(2)$ (see text for details).

Interestingly, $S_{\text{cor}}(T)$ approaches zero as soon as the QPP of $A(\omega)$ has vanished. S_{imp} is obtained via Eq. (3.25) and plotted in black. Together, this leads to S_{latt} (cf. red curve). However, our final result exhibits a pronounced maximum with a negative slope above about 0.1, which would imply an unphysical negative specific heat. This flaw is generically found for various values of U , and also for the 3HHM. We are not aware of any published results using this approach. Hence, it is left for future investigations to reveal if this unphysical behavior is due to a failure of Eq. (3.28) and Eq. (3.29) or due to a computational subtlety.

3.9 Physical quantities in Landau's Fermi-liquid (FL) theory

Fermi-liquid theory is one of the most successful effective theories to tackle the many-body problem of metals. It was developed by L. D. Landau in the late 1950s and has been extended further, ever since. Its central idea is to describe a complicated system of interacting particles as a gas of noninteracting effective quasiparticles (QPs) which are characterized by renormalized parameters (such as an effective mass m^*). Its derivation is based on perturbation theory for which the adiabatic continuity principle holds, i.e. interactions enter on a perturbative level and are treated adiabatically. As a consequence, there is a one-to-one correspondence between the excitations of an interacting system and the low-energy excitations of a free Fermi gas (they are adiabatically connected), and occupation and quantum numbers are retained in the effective single QP picture of FL theory. The QPs follow Fermi statistics. However, they are neutral: they can be thought of electrons that are “dressed” (surrounded) by a screening cloud of charges which strongly confines, i.e. screens the effect of Coulomb interactions. Further, the QPs are only approximate eigenstates of the Hamiltonian. Eventually, FL theory allows a semi-classical description of transport in terms of scattering processes of QPs in a Fermi gas, similar to kinetic gas theory. This explains the success of free electron transport models. Yet, the FL QP picture is only applicable on time scales shorter than the (finite) QP lifetime, τ .

In the following, we present the FL form of the one-particle retarded lattice Green's function in momentum space and the corresponding spectral function within DMFT, and give an overview of FL features for various physical quantities used in this thesis. We remark that this section is based on Chapter 14 of Ref. [BF11] and Sec. 5.2 of Ref. [Sta13].

FL form of the one-particle Green's and spectral function within DMFT. By a linear expansion of the lattice Green's function in momentum space, Eq. (2.4), in $\mathbf{k} - \mathbf{k}_F$ and ω we obtain the retarded QP Green's function,

$$\tilde{G}_{\mathbf{k}}(\omega) = \frac{Z}{\omega - \tilde{\varepsilon}_{\mathbf{k}} + i\frac{1}{\tau(\omega)}}, \quad (3.34)$$

with the QP weight,

$$Z = \frac{1}{1 - \partial_{\omega} \text{Re} \Sigma(\omega)|_{\omega=0}}, \quad (3.35)$$

the inverse QP lifetime,

$$\tau^{-1}(\omega) = -Z \text{Im} \Sigma(\omega), \quad (3.36)$$

for small ω , and the effective energy,

$$\tilde{\varepsilon}_{\mathbf{k}} = Z(\mathbf{k} - \mathbf{k}_F) \partial_{\mathbf{k}} \varepsilon_{\mathbf{k}}|_{\mathbf{k}=\mathbf{k}_F}. \quad (3.37)$$

\mathbf{k}_F is the Fermi wave vector (Fermi surface) determined by the equation (cf. Sec. 3.10.2),

$$\varepsilon_{\mathbf{k}_F} - \mu_{\text{eff}} = 0, \quad (3.38)$$

with the renormalized (effective) chemical potential,

$$\mu_{\text{eff}} = \mu - \text{Re} \Sigma(\omega = 0). \quad (3.39)$$

The spectral function, $A_{\mathbf{k}}(\omega)$, then splits into two parts, a coherent FL part, $A_{\mathbf{k}}^{\text{FL}}(\omega) = -1/\pi \text{Im} \tilde{G}_{\mathbf{k}}(\omega)$, of spectral weight Z and an incoherent part, $A_{\mathbf{k}}^{\text{ic}}(\omega)$, of spectral weight $1 - Z$, which was neglected in the first order expansion:

$$A_{\mathbf{k}}(\omega) = A_{\mathbf{k}}^{\text{FL}}(\omega) + A_{\mathbf{k}}^{\text{ic}}(\omega) = \frac{1}{\pi} \frac{Z \frac{1}{\tau(\omega)}}{(\omega - \tilde{\varepsilon}_{\mathbf{k}})^2 + \left(\frac{1}{\tau(\omega)}\right)^2} + A_{\mathbf{k}}^{\text{ic}}(\omega). \quad (3.40)$$

For \mathbf{k} close to \mathbf{k}_F and very small ω , $A_{\mathbf{k}}^{\text{FL}}(\omega)$ describes a Lorentzian shaped coherent QP peak of width $\tau^{-1}(\omega)$ centered at the position $\tilde{\varepsilon}_{\mathbf{k}}$. Since the one-particle spectral function always integrates to $1 = Z + \text{incoherent contribution}$, this, indeed, justifies the terminology of $Z \leq 1$ as the ‘‘QP weight’’.

Overview of FL features of physical quantities. Below, we give an overview of FL features of physical quantities which we employed in this thesis to identify the FL regime in the 3HHM. For Hubbard-type models it was shown [MH89] that these features are retained at high dimensions, which is important in the DMFT context. The following list is neither meant to be exhaustive, nor does it contain detailed derivations.

- An essential quantity in this thesis is the QP weight, Z , defined in Eq. (3.35). $Z \in [0, 1]$ reflects the weight of the QP peak of the spectral function, and is, within DMFT, equal to the mass renormalization of the QPs,

$$Z = \frac{m}{m^*}, \quad (3.41)$$

with the free electron mass, m , and the effective QP mass, m^* . This relation can be derived by reformulating Eq. (3.37) to $\tilde{\varepsilon}_{\mathbf{k}} = (\mathbf{k} - \mathbf{k}_F)\mathbf{k}_F/m^*$ in analogy to the dispersion relation of free electrons, $\varepsilon_{\mathbf{k}} = \mathbf{k}^2/(2m)$.

Importantly, Z^{-1} thus measures the strength of electronic correlations (the electronic mass enhancement) of a correlated system. Strongly correlated systems, i.e. systems with heavy electron mass, are characterized by a small QP weight, Z [cf. Fig. 1.1]. In a MIT, Z is used to identify the metallic phase ($Z > 0$) and the insulating phase ($Z = 0$). We remark that very close to the MIT and for large temperatures exceeding τ^{-1} , the FL picture breaks down and Z only serves as a heuristic indicator of the behavior of the correlated system.

- Within DMFT, the renormalized chemical potential is constant in the FL regime, $\mu_{\text{eff}} = \text{const.}$
- The real part of the self-energy, $\text{Re} \Sigma(\omega)$, exhibits a linear-frequency FL behavior at $T = 0$.
- For small ω and T , the imaginary part of the self-energy, which is associated with the transport scattering rate, obeys the FL relation, $\text{Im} \Sigma \propto \omega^2 + (\pi T)^2$. The same relation

then holds for the inverse lifetime, τ^{-1} . We note that the latter is also referred to as coherence scale, $\Gamma^* = \tau^{-1}$.

For small ω and T , the scattering rate goes to zero, the lifetime becomes very large, and a free-electron-like spectral peak is reproduced, $A_{\mathbf{k}}^{\text{FL}}(\omega) \approx Z\delta(\omega - \tilde{\epsilon}_{\mathbf{k}})$, i.e. the behavior of a free particle with renormalized mass is approached, justifying the FL picture.

- The Matsubara self-energy follows the FL relation, $\text{Im}\Sigma(i\omega_n) \propto \omega_n$.
- The imaginary part of the orbital and spin susceptibility shows linear FL behavior, $\chi''_{\text{orb,sp}} \propto \omega$, at $T = 0$. The real part is Lorentzian shaped close to the Fermi level, i.e. it has a maximum with negative curvature of the form $\chi' = \chi'(0) - a\omega^2$. The temperature dependence of the static orbital and spin susceptibility is characterized by Pauli behavior in the FL regime, $\chi_0^{\text{orb,sp}}(T) = \text{const.}$
- The spectral function, $A(\omega)$, is Lorentzian shaped at $T = 0$.
- The optical conductivity, $\sigma(\omega)$, has a Lorentzian-shaped Drude peak and decays as ω^{-2} at $T = 0$.
- For the optical resistivity the FL relation, $\rho(T) \propto T^2$, holds.
- The thermopower exhibits linear FL behavior with temperature, $\alpha(T) \propto T$.
- Both the impurity contribution to the entropy and the lattice entropy (cf. Sec. 3.8) scale linearly in temperature in the FL regime,

$$S(T) = \gamma T \quad (3.42a)$$

$$\text{with } \gamma = \frac{2N_c\pi^2}{3\mathcal{Z}}. \quad (3.42b)$$

For the lattice entropy, the mass renormalization is given by Eq. (3.35), i.e. $\mathcal{Z} \equiv Z$, which is derived from the lattice Green's function. In contrast, for the impurity contribution to the entropy, the mass renormalization is given by $\mathcal{Z} \equiv Z_{\text{imp}}$, which has to be derived from the impurity Green's function, Eq. (2.5), instead, as shown in the following.

Similar to the derivation of Z above, we perform a first order expansion of Eq. (2.5) in ω , leading to $G_{\text{imp}}(\omega) = \frac{Z_{\text{imp}}}{\omega - \tilde{\epsilon}_d - iZ_{\text{imp}}\text{Im}\Delta(\omega)}$ with $\tilde{\epsilon}_d = Z_{\text{imp}}[\text{Re}\Delta(0) - \mu_{\text{eff}}]$ and

$$Z_{\text{imp}} = \frac{1}{1 - \partial_{\omega}[\text{Re}\Delta(\omega) + \text{Re}\Sigma(\omega)]|_{\omega=0}} = \frac{1}{Z^{-1} - \partial_{\omega}\text{Re}\Delta(\omega)|_{\omega=0}}, \quad (3.43)$$

where the self-consistency condition, Eq. (2.7), in the form $\Delta(\omega) = t^2G(\omega)$, can be used in case of DMFT when using a Bethe lattice.

Obviously, Z and Z_{imp} differ in the FL regime. This implies that, in general, the impurity contribution to the entropy and the lattice entropy of a system differ as well (cf. Sec. 7.3).

3.10 Benchmarks

A convenient way to check the accuracy of numerical results is to perform benchmarks with analytically known relations. A stringent test for NRG impurity model calculations with a flat conduction band is the Friedel sum rule, while DMFT results have to obey the Luttinger theorem and the Hartree-Fock limit for the Matsubara self-energy.

3.10.1 Friedel sum rule for NRG

In the case of a flat hybridization function, $\Gamma(\omega) = \Gamma\Theta(|\omega| - D_{\text{NRG}})$, and for $T = 0$, the impurity spectral function is pinned by the Friedel sum rule to

$$\pi\Gamma A(\omega = 0) = \sin^2(\delta) \quad (3.44)$$

with the scattering phase shift $\delta = \frac{\pi n_d}{2N_c}$, where $2N_c$ is the total number of spin \times orbital flavors. An equivalent form of the Friedel sum rule reads

$$\frac{n_d}{2N_c} = \frac{1}{2} - \frac{1}{\pi} \arctan\left(\frac{\varepsilon_d + \text{Re}\Sigma(\omega=0)}{\Gamma}\right). \quad (3.45)$$

A derivation is given in Sec. 5.2 of Ref. [Hew93].

The Friedel sum rule is a stringent test for the accuracy of our NRG results. Within this thesis, Eq. (3.45) is fulfilled within about 2%, Eq. (3.44) within less than 1%, because $A(\omega = 0)$ can be directly obtained from discrete NRG data. For instance, for the particle-hole symmetric spectral functions in Ref. [SMvDW16] (cf. Sec. 2.3.2), $A(\omega = 0)$ was calculated very accurately from the sum, $A(\omega = 0) = -\sum_j a_j \partial f(\omega)/\partial \omega|_{\omega=\omega_j}$, using the derivative of the Fermi-Dirac distribution function, Eq. (3.21), for convenience, at some artificial temperature $T_{\text{aux}} \ll T$.

We note that the Friedel sum rule is replaced by Luttinger pinning within DMFT, which is described in the subsequent section.

3.10.2 Luttinger theorem and Luttinger pinning for DMFT

Luttinger theorem. The Luttinger theorem [MH89, GKKR96] states that, in the limit of high dimension and at $T = 0$, the Fermi surface of a Hubbard-type system is *not* renormalized by interactions. The Fermi surface of a noninteracting system is defined as the solution to the equation, $\varepsilon_{\mathbf{k}_F} = \mu_0(n_0)$, with the noninteracting Fermi energy, μ_0 , which is fixed by the particle number, $n_0 = 2N_c \int_{-\infty}^{\mu_0} d\varepsilon \rho_0(\varepsilon)$. ρ_0 is the noninteracting density of states. From the condition that the number of particles in the noninteracting system has to be equal to the number of quasiparticles, n_d , in the interacting system,

$$n_0 = 2N_c \int_{-\infty}^{\mu_0} d\varepsilon \rho_0(\varepsilon) \stackrel{!}{=} 2N_c \int_{-\infty}^0 d\omega A(\omega) = n_d, \quad (3.46)$$

with the total number of spin \times orbital flavors, $2N_c$, the Luttinger theorem follows in the form

$$\mu_0 \stackrel{!}{=} \mu - \text{Re}\Sigma(\omega = 0) \equiv \mu_{\text{eff}}, \quad (3.47)$$

using the definition of μ_{eff} in Eq. (3.39). A detailed derivation of Eq. (3.47) is given in Ref. [MH89]. It is based on the central DMFT assumption, $\Sigma_{\mathbf{k}}(\omega) = \Sigma(\omega)$, which holds in infinite dimensions.

In order to check the accuracy of our DMFT+NRG results, we compute $n_0(\mu_{\text{eff}})$ and compare it to n_d . For the Bethe lattice, Eq. (2.8), n_0 can be evaluated explicitly, $n_0 = \frac{2N_c}{\pi} \left[\frac{\mu_{\text{eff}}}{2t} \cos\left(\arcsin \frac{\mu_{\text{eff}}}{2t}\right) + \arcsin \frac{\mu_{\text{eff}}}{2t} + \frac{\pi}{2} \right]$. We use $\mu_{\text{eff}} = \mu - \text{Re}\Sigma(i\omega_0)$ to compute n_0 in practice, since $\Sigma(i\omega_n)$ is less error-prone (cf. Sec. 3.4), and, for $T = 0$, we have $\text{Re}\Sigma(\omega = 0) = \text{Re}\Sigma(i\omega_0)$ with the first Matsubara frequency $\omega_0 = 0$.

Luttinger pinning. For a FL system, the Luttinger theorem implies ‘‘Luttinger pinning’’,

$$A(\omega = 0) = \rho_0(\mu_{\text{eff}}), \quad (3.48)$$

i.e. the correlated spectral function at the Fermi level, $A(\omega = 0)$, is pinned to its noninteracting value $\rho_0(\mu_{\text{eff}})$. The density of states at the Fermi surface is thus not renormalized.

Eq. (3.48) can be simply derived by expanding $\text{Re } \Sigma(\omega)$ of the lattice Green's function in momentum space, Eq. (2.4), in first order in ω , leading to

$$G_{\mathbf{k}}(\omega) \approx \frac{1}{\frac{\omega}{Z} + \mu_{\text{eff}} - \varepsilon_{\mathbf{k}} - i \text{Im } \Sigma(\omega)}. \quad (3.49)$$

We then calculate the corresponding spectral function in momentum space,

$$A_{\mathbf{k}}(\omega) = -\frac{1}{\pi} \text{Im } G_{\mathbf{k}}(\omega) = \frac{1}{\pi} \frac{\text{Im } \Sigma(\omega)}{\left(\frac{\omega}{Z} + \mu_{\text{eff}} - \varepsilon_{\mathbf{k}}\right)^2 + (\text{Im } \Sigma(\omega))^2} \quad (3.50)$$

and use Eq. (2.3) and Eq. (3.7) to obtain the local spectral function,

$$A(\omega) = \int d\varepsilon \rho_0(\varepsilon) A_{\mathbf{k}}(\omega), \quad (3.51)$$

for which we take the limit $\omega \rightarrow 0$,

$$A(\omega = 0) = \int d\varepsilon \rho_0(\varepsilon) \delta(\varepsilon - \mu_{\text{eff}}) = \rho_0(\mu_{\text{eff}}). \quad (3.52)$$

The results in this thesis fulfill Luttinger pinning at zero frequency within 1%.

3.10.3 Hartree-Fock limit of Matsubara self-energy for DMFT

The high-temperature (i.e. high-frequency) limit of the real part of the Matsubara self-energy within DMFT is estimated using the first moment (Hartree-Fock value) of the model. For the 3HHM this leads to

$$\lim_{\omega_n \rightarrow \infty} \text{Re } \Sigma(i\omega_n) = (5U - 6J) \frac{n_d}{6},$$

which is fulfilled within less than 0.01% for our results.

4 Spin-orbital separation (SOS)

4.1 Overview

In this Chapter we present our article “Dynamical Mean-Field Theory Plus Numerical Renormalization-Group Study of Spin-Orbital Separation in a Three-Band Hund Metal” [SYvD⁺15], which lies at the heart of this thesis. It touches two important issues in the field of strongly correlated electron systems. First, it addresses the need for real-frequency impurity solvers of multi-band models in DMFT and presents a state-of-the-art implementation of NRG as such a promising tool. Second, it provides a deeper understanding of a new class of strongly correlated electron systems, the Hund metals. Our major result is that these systems are characterized by spin-orbital separation (SOS).

NRG as multi-band impurity solver. The quality of DMFT results depends crucially on that of the impurity solver used to self-consistently solve its underlying quantum impurity model. For multi-band models, continuous-time QMC methods are often favored among impurity solvers in terms of versatility and performance. However, obtaining real-frequency spectra requires analytic continuation of imaginary (Matsubara) frequency QMC data, which is notoriously difficult. Furthermore, sign problems and extensive numerical costs at low temperatures limit their use in many cases. For instance, it is hard or even impossible to reach the true ground state in the normal phase of Hund metals. Thus, there is a continued need for *real*-frequency impurity solvers suitable for *multi*-band DMFT applications, which work at arbitrary temperatures.

In this article, we demonstrate that fdmNRG [WvD07, Wei12a, Wei12b] (cf. Sec. 2.2.4) is such a tool, offering unprecedented real-frequency spectral resolution at arbitrarily low energies and temperatures. As mentioned before, NRG is the gold standard for impurity models since many decades and was frequently used as impurity solver for DMFT – however, only for models with at most two bands. Recent technical progress has now made three-band calculations feasible due to various algorithmic NRG advances by us and others (cf. Sec. 2.2.4 for details). Most importantly, this includes the generic implementation of non-abelian symmetries that goes beyond the well-exploited SU(2) symmetry, and significant improvements in the representation of the shape of bath hybridization functions. This paper is the first to harness the combined power of all these technical advances in the context of multi-band DMFT+NRG. It can be regarded as a proof of concept of a technical breakthrough opening the door to the rich physics of lattice models with three- (or even more-) bands, and as the base for a number of subsequent publications employing the fdmNRG as impurity solver for DMFT [LvDW17, DSH⁺18, SKWvD18, LvDW18, KLK⁺19].

Spin-orbital separation in the 3HHM. In this paper, we illustrate the capabilities of our new methodology studying the simplest model of the normal state of a Hund metal, the 3HHM on a Bethe lattice at 1/3 filling, with DMFT+NRG. Note that the definition of U in the 3HHM is slightly altered compared to Eq. (1.2). We use standard not interleaved NRG in the present article. We thus exploit all abelian and non-abelian symmetries of the model (cf. Sec. 1.2.1). We study both the self-consistent solution of the 3HHM, i.e. Eq. (1.2), and

also, for comparison, the corresponding pure impurity model without self-consistency, i.e. the 3AHM defined in Eq. (1.3).

In a thorough benchmark with a state-of-the-art continuous-time QMC solver [Hau07a, Hau07b], developed by K. Haule, we explicitly demonstrate the high accuracy of our DMFT+NRG results. The benchmark results are kindly provided by Z. Yin, one of the authors of this article. Remarkably, the agreement is excellent, also at large frequencies, and Luttinger pinning (cf. Sec. 3.10.2) at zero frequency is fulfilled within 1%. Moreover, at $T = 0.002$, our NRG solver has overall a nearly 2 orders of magnitude better numerical efficiency than CTQMC. And while NRG is able to access arbitrarily low temperatures at same DMFT convergence and without much additional computational effort per DMFT iteration, the numerical costs of CTQMC grow exponentially with decreasing temperature.

Notably, the 3HHM has never before been analyzed using a non-perturbative real-frequency method. We therefore settle several outstanding issues, that could not be thoroughly mapped out by DMFT+QMC, and yield further insights. Specifically, we reach the following conclusions:

1. *We prove that the ground state of the 3HHM is a FL.* Amongst others, we make use of the renormalization group flows of NRG, which clearly reveal the relevant physics at all energy scales. We explicitly check that the ground state excitation spectrum can be interpreted in a FL picture, i.e. in terms of noninteracting single-particle excitations (cf. Sec. 4.B).

The existence of a FL ground state was a subject of controversy in the literature – also because DMFT+QMC calculations could not reach sufficiently low temperatures to fully reveal the FL phase. For instance, Refs. [HK09, MAM⁺11, YHK12] argued for a FL, whereas Ref. [WGTM08] argued for a NFL ground state. In somewhat different but related models, Ref. [OC12] argued for a NFL ground state, but Ref. [AT13] against.

2. *As a central result of this article and this thesis we unambiguously establish spin-orbital separation* by computing real-frequency spin and orbital susceptibilities: orbital screening occurs at much higher energies than spin screening, $T_K^{\text{orb}} \gg T_K^{\text{sp}}$ (with the orbital and spin Kondo scales as defined in Sec. 3.1). This leads to a very small coherence scale below which a FL is formed and a broad incoherent regime with screened orbital degrees of freedom coupled to slowly fluctuating large spins.

Importantly, T_K^{orb} and T_K^{sp} are, in principle, two independent scales, that can be varied individually with J and n_d (but not with U , as revealed in Ref. [SKW⁺D18] in Sec. 5.2). We show that SOS is absent for $J = 0$, while $T_K^{\text{orb}}/T_K^{\text{sp}}$ grows when J is increased from 0 to 1. Further, SOS is absent for $n_d \leq 1$ in the 3HHM and in the 2HHM (and 2AHM) with only two bands (cf. Sec. 4.A). Clearly, Hund metal physics requires at least three bands and a filling of more than one electron or hole.

However, we remark that T_K^{orb} and T_K^{sp} are not fully independent in the 3HHM: the maximal size of the incoherent regime is inherently limited. If one performs a Schrieffer-Wolff transformation (as done in Ref. [AK15]) to obtain a generalized multi-orbital Kondo model, the latter contains three different impurity-lead coupling constants, corresponding to effective exchange-type interactions in the spin-spin, orbital-orbital, and spin/orbital-spin/orbital sectors, respectively. Within the context of the 3HHM (and 3AHM), these three coupling constants are not independent. One can only vary them independently in the generalized Kondo model, offering a flexible route to tune the ratio $T_K^{\text{orb}}/T_K^{\text{sp}}$ in order to study the nature of the NFL fixed point, as done in Ref. [WSL⁺19].

Note that we do not claim to be the first to notice the possibility of SOS – but we do claim to be the first to study it carefully with non-perturbative theoretical tools sufficiently powerful to uncover its behavior in detail on the real-frequency axis. For instance, the fact that orbital fluctuations are quenched at a larger scale than spin fluctuations in the AHM at occupancy one away from half-filling has already been anticipated in a remarkable pioneering paper by I. Okada and K. Yosida in 1973 [OY73]. Okada and Yosida performed a Schrieffer-Wolff transformation and analyzed the resulting generalized Kondo-type model using a strong-coupling approach based on a rather simple variational wave-function (Fermi sea plus one extra electron or one extra hole). Though they were able to deduce on qualitative grounds that $T_K^{\text{orb}} > T_K^{\text{sp}}$, they were not able to give explicit expressions for T_K^{orb} and T_K^{sp} [cf. their statement after their Eq. (7.10)], nor to study the physics of the intermediate region. Much more recently, C. Aron and one of the authors, G. Kotliar, analyzed the same model using weak-coupling methods (poor man’s scaling RG) and presented perturbative, i.e. weak-coupling estimates of the T_K^{orb} and T_K^{sp} scales [AK15] (see discussion above and Sec. 1.2.1). However, such a poor man’s scaling approach, too, is unable to access the intermediate region where SOS takes place, because it would require sending $T_K^{\text{orb}} \rightarrow \infty$. To study this intermediate regime explicitly, a method is required that is not limited to either the strong-coupling or a weak-coupling regime (in contrast to Ref. [OY73] or Ref. [AK15]), but that can access all energy scales equally reliably. The NRG approach used here is such a method.

3. *We reveal a strong particle-hole asymmetry in the SOS regime with a shoulder-like structure in the spectral function, $A(\omega)$, and in $\text{Im} \Sigma(\omega)$, both occurring at negative frequencies only. Interestingly, for the parameters studied in this article ($J = 1$), the asymmetric structure of $\text{Im} \Sigma(\omega)$ leads to an apparent fractional power law for the imaginary Matsubara self-energy, $\text{Im} \Sigma(i\omega_n)$, confirming the results of previous DMFT+QMC studies [WGTM08, YHK12]. However, we show, as a genuinely new result, that this apparent fractional power law on the imaginary axis does not imply a generic fractional power law in the self-energy on the real axis, as conjectured in Ref. [YHK12]. Instead, we find this to be true only for positive frequencies (for $J = 1$) due to the strong breaking of particle-hole symmetry for a filling of $n_d = 2$. A more detailed discussion of the generality of these apparent power laws is given in Sec. 5.A. Obviously, the interpretation of imaginary-frequency data can sometimes be misleading. Since the self-energy can be probed experimentally in tunnelling and ARPES spectroscopy, this result has direct physical implications.*
4. *We show that SOS leads to a coherence-incoherence crossover with increasing temperature. This coherence-incoherence crossover was first observed in DFT+DMFT+QMC studies of iron pnictides [HK09] and further investigated in iron-chalcogenide and rutenate superconductors [MAM⁺11, YHK12]. In this article, we explicitly demonstrate that the coherence-incoherence crossover is connected to a Hund’s coupling-induced spectral weight transfer from very low to higher energies in $A(\omega)$. A detailed study of the temperature dependence of $A(\omega)$ and other physical quantities is given in Chapter 6 and Chapter 7.*
5. *The $T = 0$ spectral properties are not driven by DMFT self-consistency, since we find similar behavior also for a pure impurity model. Thus, Hund physics, i.e. SOS, is essentially impurity physics.*

To summarize, our paper describes an important technical advance (DMFT+NRG for a three-band model), which has enabled us to gain numerous new physical insights (listed above)

about a new class of correlated materials, the Hund metals. In particular, DMFT+NRG unlocks access to previously inaccessible subtle spectral features of such systems, like SOS, which are manifestly different from those of Mott-Hubbard systems. Our predictions can be tested in materials with weak orbital differentiation, such as Ba 122, hence our theory has falsifiable predictions.

We remark that this article investigates the 3HHM only for a limited set of parameters. An extensive study of the full phase diagram of the 3HHM at $T = 0$ is provided in Chapter 5, where we show that the parameters used here in Ref. [SYvD⁺15] lie rather close to the border of the Mott boundary. In Chapter 5 we give a clear picture of the Mott transition in the presence of zero and finite J , we establish SOS as a generic Hund's-coupling-induced phenomenon in the metallic regime and study its dependence on U , J and n_d . We investigate in detail the origin of strong correlations in Hund metals, i.e. Hundness versus Mottness. As a result, we establish a deeper understanding of SOS as a new screening route towards strong correlations in Hund metals.

Dynamical Mean-Field Theory Plus Numerical Renormalization-Group Study of Spin-Orbital Separation in a Three-Band Hund Metal

by

K. M. Stadler,¹ Z. P. Yin,² J. von Delft,¹ G. Kotliar,² and A. Weichselbaum¹

¹ Physics Department, Arnold Sommerfeld Center for Theoretical Physics and Center for
NanoScience, Ludwig-Maximilians-Universität München, 80333 München, Germany

²Department of Physics and Astronomy, Rutgers University, Piscataway, New Jersey 08854,
USA

reprinted on pages [90–94](#)

with permission from

Phys. Rev. Lett. **115**, 136401 (2015),

DOI: [10.1103/PhysRevLett.115.136401](https://doi.org/10.1103/PhysRevLett.115.136401).

© 2015 American Physical Society

Supplemental Material reprinted on pages [95–98](#).

Dynamical Mean-Field Theory Plus Numerical Renormalization-Group Study of Spin-Orbital Separation in a Three-Band Hund Metal

K. M. Stadler,¹ Z. P. Yin,² J. von Delft,^{1,*} G. Kotliar,² and A. Weichselbaum¹

¹*Physics Department, Arnold Sommerfeld Center for Theoretical Physics and Center for NanoScience, Ludwig-Maximilians-Universität München, 80333 München, Germany*

²*Department of Physics and Astronomy, Rutgers University, Piscataway, New Jersey 08854, USA*

(Received 21 April 2015; published 22 September 2015)

We show that the numerical renormalization group is a viable multi-band impurity solver for dynamical mean-field theory (DMFT), offering unprecedented real-frequency spectral resolution at arbitrarily low energies and temperatures. We use it to obtain a numerically exact DMFT solution to the Hund metal problem for a three-band model on a Bethe lattice at $1/3$ filling. The ground state is a Fermi liquid. The one-particle spectral function undergoes a coherence-incoherence crossover with increasing temperature, with spectral weight being transferred from low to high energies. Further, it exhibits a strong particle-hole asymmetry. In the incoherent regime, the self-energy displays approximate power-law behavior for positive frequencies only. The spin and orbital spectral functions show “spin-orbital separation”: spin screening occurs at much lower energies than orbital screening. The renormalization group flows clearly reveal the relevant physics at all energy scales.

DOI: 10.1103/PhysRevLett.115.136401

PACS numbers: 71.27.+a, 71.10.Fd, 75.20.Hr

Introduction.—A widely-used method for dealing with interactions in strongly-correlated electron systems and electronic structure calculations is dynamical mean-field theory (DMFT) [1,2]. It treats the interplay between a given lattice site (the “impurity”) and the rest of the lattice (the “bath”) as a quantum impurity model with a self-consistently determined hybridization function. Since DMFT’s performance depends on that of the method used to solve this impurity model, much effort has been invested over the years to develop ever more powerful impurity solvers. For multi-band models, continuous-time quantum Monte Carlo (CTQMC) methods appear to be the current favorites in terms of versatility and performance [3]. However, they are not without limitations: sign problems can occur, low-temperature calculations are costly, and obtaining real-frequency spectra requires analytic continuation of imaginary (Matsubara) frequency QMC data, which is notoriously difficult. Thus, there is a continued need for *real-frequency* impurity solvers suitable for *multi-band* DMFT applications.

In this Letter, we show that the numerical renormalization group (NRG) [4–6] is such a tool, offering unprecedented real-frequency spectral resolution at low energies. NRG is the gold standard for impurity models, with numerous previous DMFT applications (e.g., [7–13]) but, so far, was limited to models with at most two bands. However, recent technical progress [14–16] has now made three-band calculations feasible [17–19].

We illustrate the potential of DMFT + NRG by studying the minimal model [20–22] of a three-band “Hund metal” [23,24], which has both a Hubbard interaction U and a ferromagnetic Hund coupling J , with $U(1)_{\text{ch}} \times \text{SU}(2)_{\text{sp}} \times \text{SU}(3)_{\text{orb}}$ symmetry for its charge (ch), spin (sp), and orbital (orb) degrees of freedom. Hund metals

are multi-orbital materials with broad bands which are correlated via the Hund- J rather than the Hubbard- U interaction. Examples are iron pnictide and chalcogenide high-temperature superconductors [23,25], ruthenates [26,27], and other 4d transition metal oxides [21,28].

Early DMFT studies using CTQMC [3] as impurity solver suggest that consequences of the Hund’s rule coupling include (i) Fermi-liquid behavior at low energies [23] and (ii) a coherence-incoherence crossover with increasing temperature [23], relevant for various material systems [27,29]. The incoherent regime is characterized by (iii) a fractional power law for the imaginary part of the Matsubara self-energy [20,26,30], and (iv) the coexistence of fast quantum mechanical orbital fluctuations and slow spin fluctuations [20]. However, since CTQMC can not reach truly low temperatures, (i) could not be conclusively established yet, and a more detailed understanding of (ii)–(iv) is difficult to achieve based on imaginary-frequency data alone. Our real-frequency DMFT + NRG results definitively settle these issues and yield further insights. For the parameters used in our study, we find (i) a Fermi-liquid ground state; a real-frequency one-particle spectral function showing (ii) a coherence-incoherence crossover (driven by Hund J , not Hubbard U) with significant transfer of spectral weight from low to high energies, and (iii) strong particle-hole asymmetry, which leads to the above-mentioned apparent fractional power laws; (iv) two-stage screening, where spin screening occurs at much lower energies than orbital screening (“spin-orbital separation”); and (v) zero-temperature spectral properties that are similar with or without DMFT self-consistency, in contrast to Mott-Hubbard systems, where the DMFT self-consistency opens a gap in the quasiparticle spectrum at large interaction strength.

Model.—Our three-band model has the Hamiltonian

$$\hat{H} = \sum_i (-\mu \hat{N}_i + \hat{H}_{\text{int}}[\hat{d}_{i\nu}^\dagger]) + \sum_{\langle ij \rangle \nu} t \hat{d}_{i\nu}^\dagger \hat{d}_{j\nu}, \quad (1a)$$

$$\hat{H}_{\text{int}}[\hat{d}_{i\nu}^\dagger] = \frac{3}{4} J \hat{N}_i + \frac{1}{2} \left(U - \frac{1}{2} J \right) \hat{N}_i (\hat{N}_i - 1) - J \hat{\mathbf{S}}_i^2. \quad (1b)$$

Here, $\hat{d}_{i\nu}^\dagger$ creates an electron on site i of flavor (fl) ν , with composite index $\nu = (m\sigma)$ labeling its spin ($\sigma = \uparrow, \downarrow$) and orbital ($m = 1, 2, 3$). $\hat{N}_i = \sum_\nu \hat{d}_{i\nu}^\dagger \hat{d}_{i\nu}$ is the total number operator for site i and $\hat{\mathbf{S}}_i$ its total spin, with components $\hat{S}_i^\alpha = \sum_{m\sigma\sigma'} \hat{d}_{i m \sigma}^\dagger \frac{1}{2} \sigma_{\sigma\sigma'}^\alpha \hat{d}_{i m \sigma'}$, where σ^α are Pauli matrices. We study a Bethe lattice with nearest-neighbor hopping amplitude t , used as energy unit ($t = 1$). On-site interactions are described by \hat{H}_{int} [20]. The on-site Coulomb interaction U penalizes double occupancy. The ferromagnetic coupling $J > 0$ accounts for Hund's first rule by favoring a large spin per site. We choose the chemical potential μ such that the filling per lattice site is one below half-filling, $\langle \hat{N}_i \rangle \approx 2$, conducive to an intricate interplay of spin and orbital degrees of freedom.

Methods.—We use single-site DMFT to map the lattice model onto a three-band Anderson-Hund model (AHM) of the form $\hat{H}_{\text{AHM}} = \varepsilon_d \hat{N} + \hat{H}_{\text{int}}[\hat{d}_\nu^\dagger] + \hat{H}_{\text{bath+hyb}}$. Here, \hat{d}_ν^\dagger creates a local (“impurity”) electron of flavor ν with energy $\varepsilon_d = -\mu$, experiencing local interactions \hat{H}_{int} , with total number and spin operators \hat{N} and $\hat{\mathbf{S}}$ defined analogously to \hat{N}_i and $\hat{\mathbf{S}}_i$. The local site, on average, hosts two electrons ($n_d = \langle \hat{N} \rangle \approx 2$), forming a spin triplet and orbital triplet (the one hole relative to half-filling can be in one of three orbital levels). The local electrons hybridize with a three-band spinful bath,

$$H_{\text{bath+hyb}} = \sum_{k\nu} (\varepsilon_k c_{k\nu}^\dagger \hat{c}_{k\nu} + V_k [\hat{d}_\nu^\dagger \hat{c}_{k\nu} + \hat{c}_{k\nu}^\dagger \hat{d}_\nu]), \quad (2)$$

with a hybridization function $\Gamma(\varepsilon) = \pi \sum_k |V_k|^2 \delta(\varepsilon - \varepsilon_k)$ that fully characterizes the impurity-bath interplay. In DMFT, $\Gamma(\varepsilon)$ has the role of the effective Weiss mean-field and is determined self-consistently [1,2,31]. We studied both the self-consistent AHM (SCAHM) and also, for comparison, the pure impurity AHM (IAHM), without self-consistency, using a flat density of states with half-bandwidth D , $\Gamma(\varepsilon) \equiv \Gamma \Theta(D - |\varepsilon|)$.

We use full-density-matrix NRG [42] exploiting non-Abelian symmetries [15], both to solve the IAHM and for each SCAHM iteration (for NRG details, see [31]). The key idea of NRG, due to Wilson [4], is to discretize the bath's continuous spectrum logarithmically, map the model onto a semi-infinite “Wilson” chain with exponentially decaying hopping amplitudes, and exploit this energy-scale separation to iteratively diagonalize the model while discarding high-energy states. This allows one to zoom in on low-energy properties, at the expense of having only coarse-grained resolution at high energies. Nevertheless, NRG results are also accurate for spectral integrals even if

these include large energies, since they can be evaluated using discrete, unbroadened NRG data.

Matsubara benchmark.—We illustrate this by benchmarking NRG versus CTQMC [31], which treats the bath as a continuum and has no bath discretization issues. We used both methods to compute the self-energy $\Sigma(i\omega_n)$ of the Matsubara correlator $G(i\omega_n)$ associated with the retarded local correlator $G^R(\omega) = \langle d_\nu \| d_\nu^\dagger \rangle_\omega$. In NRG, its spectral function is expressed in terms of discrete data, $A(\omega) = -(1/\pi) \text{Im} G^R(\omega) \stackrel{\text{NRG}}{\approx} \sum_s a_s \delta(\omega - \xi_s)$, hence, $G(i\omega_n) = \int d\omega A(\omega)/(i\omega_n - \omega) \stackrel{\text{NRG}}{\approx} \sum_s a_s/(i\omega_n - \xi_s)$. Figure 1 compares NRG and CTQMC results for $\Sigma(i\omega_n)$ at $T = 0.002$. The agreement is excellent, also, at large frequencies [with relative deviations of $\lesssim 2.5\%$ for $\text{Im}\Sigma(i\omega_n)$ and $\lesssim 0.5\%$ for $\text{Re}\Sigma(i\omega_n)$]. However, the numerical costs differ vastly ($\approx 10^2$ versus 10^4 CPU hours) [31], since the chosen temperature is challengingly low for CTQMC, whereas NRG can access any temperature. Luttinger pinning at zero frequency [1,43] is fulfilled within 1% for both methods [31]. $\text{Im}\Sigma(i\omega_n)$ displays fractional power-law behavior for intermediate frequencies ($0.05 \lesssim \omega_n \lesssim 0.5$), as found in [20,26], and Fermi-liquid behavior ($\propto \omega_n$) for very low frequencies, as found in [23,27], but not in [26].

Coherence-incoherence crossover.—We now turn to real-frequency properties [Fig. 2]. At zero temperature, the local spectral function $A(\omega)$ of the SCAHM shows a well-defined low-energy quasiparticle peak and $-\text{Im}\Sigma^R(\omega)$ a dip reaching down to zero [insets of Figs. 2(a) and 2(b)]. This indicates that strong Kondo-type screening correlations exist between bath and local spin and orbital degrees of freedom. At higher energies, $A(\omega)$ also shows incoherent, rather flat particle-hole asymmetric side peaks, that reflect charge fluctuation.

With increasing temperature, a coherence-incoherence crossover occurs: the quasiparticle peak first weakens and then gives way to a pseudogap [Fig. 2(a)]; concurrently, the dip in $-\text{Im}\Sigma^R(\omega)$ is first smeared out into a broader minimum, which then changes into a maximum [Fig. 2(b)].

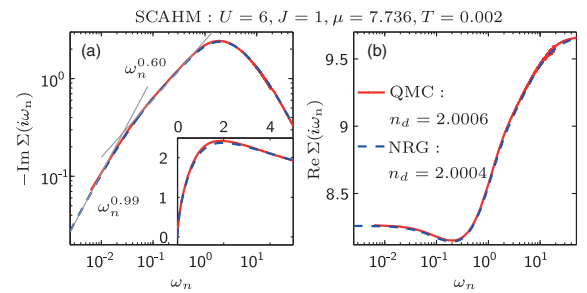


FIG. 1 (color online). Benchmark comparison of NRG and CTQMC for the three-band SCAHM. (a) Imaginary and (b) real part of the self-consistently converged self-energy as a function of Matsubara frequencies. Grey lines in (a) are power-law fits to low and intermediate-frequency data, respectively. The inset of (a) shows $\text{Im}\Sigma(i\omega_n)$ on a linear scale.

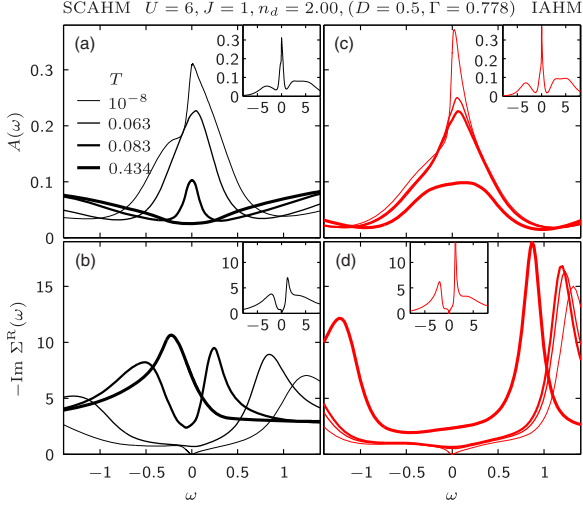


FIG. 2 (color online). (a) The local spectral function $A(\omega)$ and (b) the imaginary part of the retarded self-energy, $\text{Im}\Sigma^R(\omega)$, for the SCAHM, plotted versus frequency for four temperatures. Insets show a larger frequency range for $T = 10^{-8}$. (c)–(d) Same as in (a) and (b), but for an IAHM.

During this process, quasiparticle weight is transferred from low to high energies, in a way reminiscent of recent photoemission measurements [44–46] (see Fig. S-4 in [31]). Note that the spectral weight near $\omega \simeq 0$ remains nonzero at all temperatures, implying that metallic behavior persists for the parameters studied here. The evolution of these features to those of the Mott transition that occurs for larger values of U is left for future investigation.

Since the SCAHM is based on an impurity model, it is instructive to study a corresponding IAHM, with parameters tuned to yield a similar spectral function at $T = 0$ [Figs. 2(c) and 2(d)]. Likewise, it features a large low-energy (Kondo) peak that weakens with increasing temperature, though no pseudogap occurs. This shows that the $T = 0$ spectral properties of the SCAHM are governed by the impurity physics of the IAHM. The transfer of spectral weight with increasing T is driven by Hund J for both IAHM and SCAHM (see Fig. S-2 of [31]), and for the latter, it is amplified by DMFT self-consistency [compare Figs. 2(a) and 2(b)].

Particle-hole asymmetry.—Next, we exploit the power of NRG to zoom in to arbitrarily low energy scales: In Figs. 3(a) and 3(b), we replot, on a logarithmic scale, the data [black (red) for SCAHM (IAHM)] from Figs. 2(a)–2(d) for $A(\omega)$ and $\text{Im}\Sigma^R(\omega)$ at $T = 10^{-8}$. For comparison, the right column of Fig. 3 again shows results for the IAHM, but using parameters that yield smaller crossover scales (defined below), to better separate the low-energy features associated with spin and orbital screening from high-energy features associated with charge fluctuations. Note, again, the striking qualitative similarity between the SCAHM (black) and IAHM (red or blue) spectra – clearly, for $T = 0$, DMFT self-consistency plays no major role.

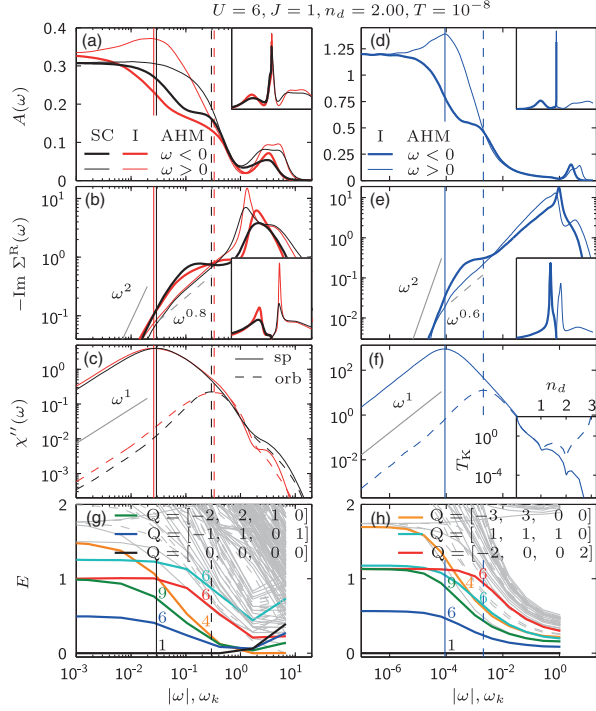


FIG. 3 (color online). (a)–(f) Spin-orbital separation in real-frequency, ground state correlators. The left column uses the same parameters and color code as Fig. 2 for the SCAHM (black) and IAHM with $(\Gamma, D) = (0.778, 0.5)$ (red). For comparison, the right column shows IAHM results with $(\Gamma, D) = (0.200, 1.0)$ (blue), yielding smaller crossover scales. (a) and (d) The local spectral functions, (b) and (e) the local self-energy, and (c) and (f) the spin and orbital susceptibilities, χ''_{sp} (solid) and χ''_{orb} (dashed). We use a logarithmic frequency scale, with thick (thin) lines for $\omega < 0$ ($\omega > 0$). Insets show data on a linear scale. In all panels, solid (dashed) vertical lines mark the spin (orbital) Kondo scale, T_K^{sp} (T_K^{orb}). Grey guide-to-the-eye lines indicate Fermi-liquid power laws (solid) or apparent fractional power laws (dashed). Inset to (f): Kondo scales T_K^{sp} (solid) and T_K^{orb} (dashed) for the IAHM, plotted as a function of n_d . (g) and (h) show NRG eigenlevel flow diagrams for the SCAHM and IAHM of panels (a)–(c) and (d)–(f), respectively: the rescaled energies of the lowest-lying eigenmultiplets of a Wilson chain of (even) length k are plotted versus its characteristic level spacing $\omega_k \propto \Lambda^{-k/2}$ (see text). Numbers above lines give multiplet degeneracies, Q their symmetry labels.

With decreasing temperature, the quasiparticle peaks in Figs. 2(a) and 2(c) show an increasing particle-hole asymmetry (which is not surprisingly away from half-filling), which at $T = 0$ is very pronounced: in Figs. 3(a) and 3(d), for $A(\omega)$, the thick ($\omega < 0$) lines show a shoulderlike structure for intermediate frequencies (between the vertical solid and dashed lines), while the thin ($\omega > 0$) lines do not; and in Figs. 3(b) and 3(e), for $\text{Im}\Sigma^R(\omega)$, the thick lines show a plateaulike structure, whereas the thin lines show approximate $\sim \omega^\alpha$ power-law behavior (with nonuniversal α). For the Matsubara self-energy obtained via the Hilbert transform

$\Sigma(i\omega_n) = -(1/\pi) \int d\omega \text{Im}\Sigma^R(\omega)/(i\omega_n - \omega)$, the asymmetric contributions from the power law and shoulder in $\text{Im}\Sigma^R(\omega \geq 0)$ conspire in such a way that $\text{Im}\Sigma(i\omega_n)$ shows an apparent fractional power law, but $\text{Re}\Sigma(i\omega_n)$ does not [Figs. 1(a) and 1(b)]. Conversely, this example illustrates that care is due when drawing real-frequency conclusions from imaginary-frequency power laws: if one is present only for $\text{Im}\Sigma(i\omega_n)$, but not for $\text{Re}\Sigma(i\omega_n)$ (as in [20,26]), then $\text{Im}\Sigma^R(\omega)$ need not show pure power-law behavior.

Spin-orbital separation.—Next, we elucidate the screening of local spin and orbital degrees of freedom by the bath of conduction electrons. To this end, Figs. 3(c) and 3(f), respectively, show the imaginary part (χ'') of the dynamical susceptibilities of the spin and orbital operators for the impurity site, $\chi_{\text{sp}}'' = \frac{1}{3} \sum_{\alpha} \langle \hat{S}^{\alpha} \| \hat{S}^{\alpha} \rangle_{\omega}$ and $\chi_{\text{orb}}'' = \frac{1}{8} \sum_{\alpha} \langle \hat{T}^{\alpha} \| \hat{T}^{\alpha} \rangle_{\omega}$, with orbital operators $\hat{T}^a = \sum_{mm'\sigma} \hat{d}_{m\sigma}^{\dagger} \frac{1}{2} \tau_{mm'}^a \hat{d}_{m'\sigma}$, where τ^a are the SU(3) Gell-Mann matrices, normalized as $\text{Tr}[\tau^a \tau^b] = 2\delta_{ab}$. Both χ_{sp}'' and χ_{orb}'' exhibit a peak with (nearly) power-law flanks, characteristic of Kondo screening of the local spin and orbital degrees of freedom. Strikingly, for both SCAHM and IAHM the peak for χ_{sp}'' occurs at a much lower energy and is much higher than for χ_{orb}'' . We take the peak positions to define the spin and orbital Kondo scales, T_{K}^{sp} and $T_{\text{K}}^{\text{orb}}$ (vertical solid and dashed lines). T_{K}^{sp} acts as the coherence scale below which Fermi-liquid behavior [$\text{Im}\Sigma^R(\omega) \propto \omega^2$, $\chi_{\text{sp,orb}}'' \propto \omega$, see Figs. 3(b)–3(f), grey lines] sets in. The $\text{SU}(2)_{\text{sp}}$ and $\text{SU}(3)_{\text{orb}}$ crossover scales differ strongly, $T_{\text{K}}^{\text{sp}} \ll T_{\text{K}}^{\text{orb}}$, because the Kondo temperature for an $\text{SU}(N)$ Kondo model scales as $\ln T_{\text{K}} \sim -1/N$ [47]. This implies two-stage screening, with spin screening occurring at significantly lower energies than orbital screening. This “spin-orbital separation”, featuring a very small coherence scale and an intermediate regime with screened orbital degrees of freedom coupled to slowly fluctuating, large spins, was first anticipated in Ref. [47] and, more recently, discussed qualitatively in Refs. [21,22]. Its explicit demonstration here is a central result of this Letter.

The inset of Fig. 3(f) depicts T_{K}^{sp} and $T_{\text{K}}^{\text{orb}}$ for the IAHM as a function of the filling n_d . For $n_d \approx 1$, where the bare impurity’s ground state has $\text{SU}(6)$ symmetry also for $J \neq 0$, $T_{\text{K}}^{\text{sp}} \approx T_{\text{K}}^{\text{orb}} \approx T_{\text{K}}^{\text{SU}(6)}$. As n_d increases from 1 to 2, T_{K}^{sp} and $T_{\text{K}}^{\text{orb}}$ split apart if $J \neq 0$, indicating that spin-orbital separation sets in. (See, also, Ref. [31], Fig. S-3.) As n_d continues to increase towards 3, T_{K}^{sp} drops below the lowest relevant energy scale and $T_{\text{K}}^{\text{orb}}$ becomes very large ($\gtrsim D$), reflecting the fact that, for half-filling, the orbitals form an orbital singlet from the outset. In this sense, $n_d \approx 2$ is special: there, conditions are optimal for the Hund coupling to align two spins in different orbitals without forming an orbital singlet.

RG flow.—In RG terms, the two-stage screening discussed above is associated with the RG flow between three fixed points, describing high, intermediate, and low-energy excitations. Their effective fixed point Hamiltonians have

ground state multiplets whose spin \times orbital structure is triplet \times triplet, triplet \times singlet, and singlet \times singlet, implying an impurity contribution to the ground state entropy of $\ln(9)$, $\ln(3)$, and $\ln(1)$, respectively (see Fig. S-5 in [31]). The RG flow between these fixed points can be visualized via NRG eigenlevel flow diagrams [Figs. 3(g) and 3(h)]. Technically, they show how the lowest-lying rescaled eigenlevels of a length- k Wilson chain evolve with k , where “rescaled” means given in units of $\omega_k \propto \Lambda^{-k/2}$ (as defined in [6]), where $\Lambda > 1$ is a discretization parameter [31]. Conceptually, these levels represent the finite-size spectrum of the impurity + bath put in a spherical box of radius $R_k \propto \Lambda^{k/2}$, centered on the impurity [4,48]: as k increases, the finite-size level spacing $\omega_k \propto 1/R_k$ decreases exponentially. The corresponding flow of the finite-size spectrum is stationary (k independent) while ω_k lies within an energy regime governed by one of the fixed points but changes when ω_k traverses a crossover between two fixed points.

Figures 3(g) and 3(h) show this RG flow for the SCAHM and the IAHM, revealing similar behavior for both [49]. We label multiplets by their $\text{U}(1)_{\text{ch}} \times \text{SU}(2)_{\text{sp}} \times \text{SU}(3)_{\text{orb}}$ symmetry labels, $Q = [q, 2S, q_1 q_2]$; here q denotes particle number relative to half-filling, S spin, and $(q_1 q_2)$ an $\text{SU}(3)$ irreducible representation, identified by a Young diagram with $q_1 + q_2$ (q_2) boxes in its first (second) row. The flow of the lowest-lying levels reveals two crossover scales, $T_{\text{K}}^{\text{orb}}$ and T_{K}^{sp} (whose spacing, though, is too small for the level flow in between to become stationary [50]). As ω_k drops below $T_{\text{K}}^{\text{orb}}$, orbital screening sets in, favoring orbital singlets [$(q_1 q_2) = (00)$], hence, other multiplets rise in energy. Similarly, as ω_k drops below T_{K}^{sp} , spin screening sets in, favoring spin singlets and pushing up multiplets with $S \neq 0$. For $\omega_k \ll T_{\text{K}}^{\text{sp}}$, the ground state is a spin and orbital singlet [$Q = (0, 0, 00)$]. We have checked that its excitation spectrum can be interpreted in terms of noninteracting single-particle excitations, thus confirming its Fermi-liquid nature.

Conclusions.—We have demonstrated the potential of DMFT + NRG as a real-frequency method to treat multi-orbital systems, with no need for analytic continuation. Applied to the simplest model of a three-band Hund metal, it revealed subtle spectral features which are manifestly different from those of Mott-Hubbard systems, and which can be probed in photoemission and STM spectroscopies.

Our work is a first step towards using LDA + DMFT + NRG to calculate ac and dc transport properties in strongly correlated materials. Such applications will typically involve less orbital symmetries than the model studied here, but could be treated using the recent “interleaved” NRG approach of [16]. The latter yields results of comparable accuracy and efficiency as when symmetries can be exploited [51].

A key advantage of NRG is its ability to iteratively uncover the system’s RG flow from high to low energies, revealing the relevant physics at each energy scale. In the context of Mott-Hubbard systems, RG ideas have been very fruitful even in very approximate implementations [52–54].

For the present Hund metal, the numerically exact RG flow achieved via DMFT + NRG revealed a clear, simple picture of the crossover from the incoherent to the coherent Fermi-liquid regime: two-stage screening of first orbital, then spin degrees of freedom. Using DMFT + NRG to gain this type of RG understanding of real material properties would be a worthwhile goal for future research.

We acknowledge fruitful discussions with C. Aron, A. Georges, K. Haule, A. Mitchell, and G. Zaránd. K. M. S., A. W., and J. v. D. were supported by DFG (Grants No. SFB-TR12, No. SFB631, the Nanosystems Initiative Munich, Grant No. WE4819/1-1, and No. WE4819/2-1), Z. P. Y. and G. K. by NSF Grant No. DMR1308141.

*Corresponding author.
vondelft@lmu.de

- [1] A. Georges, G. Kotliar, W. Krauth, and M. J. Rozenberg, *Rev. Mod. Phys.* **68**, 13 (1996).
- [2] G. Kotliar, S. Y. Savrasov, K. Haule, V. S. Oudovenko, O. Parcollet, and C. A. Marianetti, *Rev. Mod. Phys.* **78**, 865 (2006).
- [3] E. Gull, A. J. Millis, A. I. Lichtenstein, A. N. Rubtsov, M. Troyer, and P. Werner, *Rev. Mod. Phys.* **83**, 349 (2011).
- [4] K. G. Wilson, *Rev. Mod. Phys.* **47**, 773 (1975).
- [5] R. Bulla, T. A. Costi, and T. Pruschke, *Rev. Mod. Phys.* **80**, 395 (2008).
- [6] A. Weichselbaum, *Phys. Rev. B* **86**, 245124 (2012).
- [7] O. Sakai and Y. Kuramoto, *Solid State Commun.* **89**, 307 (1994).
- [8] R. Bulla, A. C. Hewson, and T. Pruschke, *J. Phys. Condens. Matter* **10**, 8365 (1998).
- [9] R. Bulla, *Phys. Rev. Lett.* **83**, 136 (1999).
- [10] R. Bulla, T. A. Costi, and D. Vollhardt, *Phys. Rev. B* **64**, 045103 (2001).
- [11] T. Pruschke and R. Bulla, *Eur. Phys. J. B* **44**, 217 (2005).
- [12] X. Deng, J. Mravlje, and R. Žitko, M. Ferrero, G. Kotliar, and A. Georges, *Phys. Rev. Lett.* **110**, 086401 (2013).
- [13] Ž. Osolin, T. Pruschke, and R. Žitko, *Phys. Rev. B* **91**, 075105 (2015).
- [14] A. I. Tóth, C. P. Moca, O. Legeza, and G. Zaránd, *Phys. Rev. B* **78**, 245109 (2008).
- [15] A. Weichselbaum, *Ann. Phys. (Amsterdam)* **327**, 2972 (2012).
- [16] A. K. Mitchell, M. R. Galpin, S. Wilson-Fletcher, D. E. Logan, and R. Bulla, *Phys. Rev. B* **89**, 121105 (2014).
- [17] C. P. Moca, A. Alex, J. von Delft, and G. Zaránd, *Phys. Rev. B* **86**, 195128 (2012).
- [18] M. Hanl, A. Weichselbaum, T. A. Costi, F. Mallet, L. Saminadayar, C. Bäuerle, and J. von Delft, *Phys. Rev. B* **88**, 075146 (2013).
- [19] M. Hanl, A. Weichselbaum, J. von Delft, and M. Kiselev, *Phys. Rev. B* **89**, 195131 (2014).
- [20] Z. P. Yin, K. Haule, and G. Kotliar, *Phys. Rev. B* **86**, 195141 (2012).
- [21] A. Georges, L. de Medici, and J. Mravlje, *Annu. Rev. Condens. Matter Phys.* **4**, 137 (2013).
- [22] C. Aron and G. Kotliar, *Phys. Rev. B* **91**, 041110 (2015).
- [23] K. Haule and G. Kotliar, *New J. Phys.* **11**, 025021 (2009).
- [24] Z. P. Yin, K. Haule, and G. Kotliar, *Nat. Mater.* **10**, 932 (2011).
- [25] Z. P. Yin, K. Haule, and G. Kotliar, *Nat. Phys.* **7**, 294 (2011).
- [26] P. Werner, E. Gull, M. Troyer, and A. J. Millis, *Phys. Rev. Lett.* **101**, 166405 (2008).
- [27] J. Mravlje, M. Aichhorn, T. Miyake, K. Haule, G. Kotliar, and A. Georges, *Phys. Rev. Lett.* **106**, 096401 (2011).
- [28] L. de Medici, J. Mravlje, and A. Georges, *Phys. Rev. Lett.* **107**, 256401 (2011).
- [29] F. Hardy, A. E. Böhmer, D. Aoki, P. Burger, T. Wolf, P. Schweiss, R. Heid, P. Adelman, Y. X. Yao, G. Kotliar, J. Schmalian, and C. Meingast, *Phys. Rev. Lett.* **111**, 027002 (2013).
- [30] S. Akhanjee and A. M. Tsvelik, *Phys. Rev. B* **87**, 195137 (2013).
- [31] See Supplemental Material at <http://link.aps.org/supplemental/10.1103/PhysRevLett.115.136401>, which includes Refs. [32–41], for details about the methods used and additional numerical data.
- [32] A. Weichselbaum, F. Verstraete, U. Schollwöck, J. I. Cirac, and J. von Delft, *Phys. Rev. B* **80**, 165117 (2009).
- [33] F. B. Anders and A. Schiller, *Phys. Rev. Lett.* **95**, 196801 (2005).
- [34] R. Peters, T. Pruschke, and F. B. Anders, *Phys. Rev. B* **74**, 245114 (2006).
- [35] R. Žitko, *Comput. Phys. Commun.* **180**, 1271 (2009).
- [36] R. Žitko and T. Pruschke, *Phys. Rev. B* **79**, 085106 (2009).
- [37] K. Stadler, A. Weichselbaum, and J. von Delft (to be published).
- [38] A. Weichselbaum, *Phys. Rev. B* **84**, 125130 (2011).
- [39] W. C. Oliveira and L. N. Oliveira, *Phys. Rev. B* **49**, 11986 (1994).
- [40] P. Werner, A. Comanac, L. de Medici, M. Troyer, and A. J. Millis, *Phys. Rev. Lett.* **97**, 076405 (2006).
- [41] K. Haule, *Phys. Rev. B* **75**, 155113 (2007).
- [42] A. Weichselbaum and J. von Delft, *Phys. Rev. Lett.* **99**, 076402 (2007).
- [43] E. Müller-Hartmann, *Z. Phys. B* **76**, 211 (1989).
- [44] M. Yi, D. H. Lu, R. Yu, S. C. Riggs, J.-H. Chu, B. Lv, Z. K. Liu, M. Lu, Y.-T. Cui, M. Hashimoto, S.-K. Mo, Z. Hussain, C. W. Chu, I. R. Fisher, Q. Si, and Z.-X. Shen, *Phys. Rev. Lett.* **110**, 067003 (2013).
- [45] H. Miao, L.-M. Wang, P. Richard, S.-F. Wu, J. Ma, T. Qian, L.-Y. Xing, X.-C. Wang, C.-Q. Jin, C.-P. Chou, Z. Wang, W. Ku, and H. Ding, *Phys. Rev. B* **89**, 220503 (2014).
- [46] M. Yi *et al.*, *Nat. Commun.* **6**, 7777 (2015).
- [47] I. Okada and K. Yosida, *Prog. Theor. Phys.* **49**, 1483 (1973).
- [48] J. von Delft, G. Zaránd, and M. Fabrizio, *Phys. Rev. Lett.* **81**, 196 (1998).
- [49] Details differ for $\omega_k \gtrsim T_K^{\text{orb}}$, because the SCAHM crossover scales on the left are larger than on the right [50].
- [50] To more clearly reveal the intermediate regime, one could study the Kondo-type model associated with our AHM, derived by [22]. By tuning its bare parameters independently, arbitrarily large ratios of $T_K^{\text{sp}}/T_K^{\text{orb}}$ can be achieved.
- [51] K. M. Stadler, A. K. Mitchell, J. von Delft, and A. Weichselbaum (to be published).
- [52] G. Moeller, Q. Si, G. Kotliar, M. Rozenberg, and D. S. Fisher, *Phys. Rev. Lett.* **74**, 2082 (1995).
- [53] D. S. Fisher, G. Kotliar, and G. Moeller, *Phys. Rev. B* **52**, 17112 (1995).
- [54] K. Held, R. Peters, and A. Toschi, *Phys. Rev. Lett.* **110**, 246402 (2013).

Dynamical Mean-Field Theory Plus Numerical Renormalization-Group Study of Spin-Orbital Separation in a Three-Band Hund Metal

Supplementary Material

K. M. Stadler,¹ Z. P. Yin,² J. von Delft,¹ G. Kotliar,² and A. Weichselbaum¹

¹*Physics Department, Arnold Sommerfeld Center for Theoretical Physics and Center for NanoScience, Ludwig-Maximilians-Universität München, 80333 München, Germany*

²*Department of Physics and Astronomy, Rutgers University, Piscataway, NJ 08854, USA*

(Dated: submitted April 21 2015)

The citations occurring in the supplementary material below refer to references given in the main text.

Computational details

Recent NRG progress.— While Wilson’s NRG [4, 5] has been tremendously successful in the past, significant further progress was achieved in recent years, triggered by the realizations that it (i) can be formulated in MPS language [6, 32], and (ii) that the discarded states can be used to construct a complete many-body basis of approximate energy eigenstates [33]. It has become possible (iii) to reliably calculate finite-temperature spectral functions in sum-rule conserving fashion [34, 42]; (iv) to treat a bath with nontrivial hybridization function by suitably optimizing its representation in terms of discrete bath states [35–37]; to treat multi-band models, either (v) by exploiting non-Abelian symmetries [14, 15] if the bands couple symmetrically to the impurity [17–19], as here, or (vi) by using an “interleaved” discretization scheme [16, 51]; and (vii) to greatly increase numerical efficiency by optimizing MPS bond dimensions and to ensure accuracy by checking the discarded weight [38]. Taken together, these advances make NRG a highly competitive real-frequency impurity solver for DMFT.

Details of our NRG implementation.— Wilson’s NRG approach is based on logarithmically coarse-graining the continuous bath in energy space into intervals of exponentially decreasing widths in order to resolve even the lowest relevant energy scale of the impurity system. To accurately represent the frequency-dependent hybridization function of the DMFT self-consistency condition in terms of a set of discrete states, we use a numerically stable implementation [37] of the discretization scheme of Ref. [36].

The model is then mapped onto a semi-infinite “Wilson” chain with exponentially decaying hopping amplitudes. This energy-scale separation is exploited to iteratively diagonalize the model by adding one site at a time, while discarding high-energy states. The accuracy of this truncation procedure can be checked by estimating the discarded weight $\delta\rho_{\text{disc}}$ [38], a quantitative convergence criterion inspired by DMRG, after each

run. Empirically, an NRG run is well-converged when $\delta\rho_{\text{disc}} < 10^{-12}$.

We exploit all available non-Abelian symmetries of the AHM studied here, namely $U(1)_{\text{ch}} \times SU(2)_{\text{sp}} \times SU(3)_{\text{orb}}$, by using the QSpace approach developed by A. Weichselbaum [15]. QSpace is a tensor library that is able to treat Abelian and non-Abelian symmetries on a generic level. In the presence of symmetries, the state space can be organized into symmetry multiplets, and tensors “factorize” into two parts, acting in the reduced multiplet space and the Clebsch Gordon coefficient space, respectively, vastly reducing numerical cost.

We use full-density-matrix NRG [6, 42] to calculate high-quality, sum-rule-conserving spectral functions at arbitrary temperature. Both for the IAHM and when implementing the DMFT self-consistency loop for the SCAHM (as described below) we smoothen the discrete spectral data provided by fdmNRG using the log-Gaussian smoothening approach of Ref. [42]. To improve the resolution of the smoothened spectral data we calculate the self-energy in every iteration from the ratio of two correlation functions [8].

NRG-related computational parameters.— The performance of NRG is further governed by the following computational parameters: the dimensionless logarithmic discretization parameter Λ ; the truncation energy E_{trunc} in rescaled units (as defined in Ref. 6), up to which all eigenmultiplets are kept, unless their number exceeds $N_{\text{keep}}^{\text{max}}$, the maximal number of kept multiplets per iteration; the number N_z of z -shifts for z -averaging [36, 39]; and the log-Gaussian broadening parameter σ for smooth spectral data [42].

We used $\Lambda = 4$ and $\sigma = 0.5$ throughout. We checked that the choice $\Lambda = 3$ and $\sigma = 0.5$, which is computationally somewhat more demanding, yields qualitatively similar results, as illustrated in Fig. S-1.

For the IAHM and the last DMFT iteration of the SCAHM, we used $N_z = 2$ and $E_{\text{trunc}} = 9$, and for impurity spectral functions and self-energies kept $N_{\text{keep}}^{\text{max}} = 5000$ multiplets at maximum, yielding discarded weights of $\delta\rho_{\text{disc}} < 10^{-13}$, unless specified otherwise. For the susceptibilities χ_{sp} and χ_{orb} we employed a smaller value for $N_{\text{keep}}^{\text{max}} = 1500$ (because the operators involved are numer-

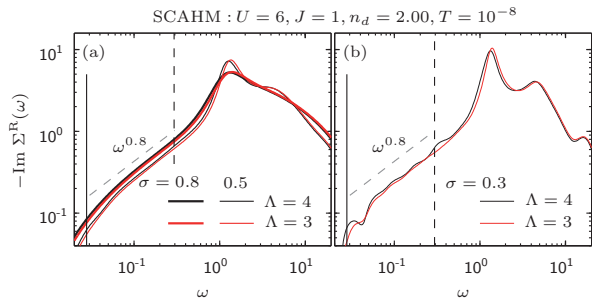


Figure S-1. Analysis of discretization and broadening issues: SCAHM results for $-\text{Im}\Sigma^R(\omega)$, for two choices of the NRG discretization parameter (black: $\Lambda = 4$; red: $\Lambda = 3$) and three choices of the broadening factor (fat lines in panel (a): $\sigma = 0.8$; thin lines in panel (a): $\sigma = 0.5$; thin lines in panel (b): $\sigma = 0.3$). Panel (a) shows that curves calculated using $\Lambda = 3$ or 4 , but broadened in the same way, essentially coincide (compare thin red and black lines, or thick red and black lines). As expected, reducing the broadening yields curves whose features (e.g. shoulders, kinks and peaks) are somewhat more clearly resolved (compare fat and thin curves), but the qualitative behavior does not change. In particular, in the rather narrow intermediate frequency regime where the curves show approximate fractional power law behavior, running parallel to the guides-to-the-eye dashed straight line, their slopes, and hence the corresponding exponents, are essentially equal (within the error bars arising from the narrowness of the frequency range used to extract the slopes). Panel (b) shows that if σ is reduced even more, to $\sigma = 0.3$, discretization artefacts arise, which are naturally stronger for $\Lambda = 4$ than for $\Lambda = 3$.

ically rather costly); this yielded values for T_K^{sp} and T_K^{orb} that are converged to better than 10% and consistent with the crossover scales derived from NRG eigenlevel flow diagrams. For earlier DMFT iterations, we used $N_z = 1$, $E_{\text{trunc}} = 7$ and $N_{\text{keep}}^{\text{max}} = 2500$, to lower numerical costs.

DMFT self-consistency loop.— In single-site DMFT a quantum lattice model is treated in a quantum mean-field fashion [1]. Spatial correlations are frozen out by dropping the momentum-dependence of the lattice self-energy, whereas temporal quantum fluctuations are retained. The lattice dynamics is then fully captured by the local retarded lattice Green’s function, $G_{\text{latt}}^R(\omega)$, given in terms of the purely local but still frequency dependent self-energy, $\Sigma^R(\omega)$, – or equivalently by the retarded Green’s function of an impurity model $G_{\text{imp}}^R(\omega)$ with equal local interactions (equal $\Sigma^R(\omega)$) and effective hybridization $\Gamma(\omega)$. This equivalence, $G_{\text{latt}}^R(\omega) = G_{\text{imp}}^R(\omega) \equiv G(\omega)$, imposes a self-consistency condition, that simplifies to $\Gamma(\omega) = -t^2 \text{Im} G_{\text{imp}}^R(\omega)$ for a Bethe lattice, and fully maps the quantum lattice problem onto an effective quantum impurity problem by iteratively

determining $\Gamma(\omega)$ [1]. In each iteration of the DMFT self-consistent mapping, we solve the quantum impurity model with NRG.

Computational costs.— Our CTQMC solver, developed by K. Haule, is based on an expansion in the hybridization function [40]. Its implementation is described in [41]. For the benchmark calculations shown in Fig. 1 of the main paper, our CTQMC solver was run in parallel using 2500 cores with $2 \cdot 10^8$ Monte Carlo steps in each core. To achieve DMFT self-consistency for $T = 0.002$, it needed less than 10 iterations of about 1.5 hours each. Our NRG code, developed by A. Weichselbaum [6, 15] and run on 8 cores in parallel with 128 GB memory in total, achieved DMFT self-consistency after 7 iterations, starting from a flat hybridization. The NRG run for the last DMFT iteration took 10 hours; for earlier iterations, run times were smaller. Overall, this results in nearly 2 orders of magnitude better numerical efficiency than CTQMC. Moreover, NRG is able to access arbitrarily low temperatures at same DMFT convergence and without much additional computational effort per DMFT iteration, whereas for CTQMC the numerical costs grow exponentially with decreasing temperature. For example, when temperature is further lowered to $T = 0.001$ within CTQMC, about 20 DMFT iterations with 6 hours each are needed to also converge the first few Matsubara frequencies, while the overall self-energy and Green’s function do not change much after a few iterations.

In the present context, the computational cost of solving the impurity problem by NRG does not significantly depend on either U or J . However, the choice of U does affect the number of DMFT iterations needed to reach self-consistency. This number increases significantly when U becomes so large that the system approaches a Mott transition. The latter falls beyond the scope of the present paper and is left for future investigation.

Supplementary results for physical quantities

Effect of turning on Hund coupling J .— Figs. S-2 and S-3 illustrate how turning on Hund coupling J from 0 to 1 at fixed $U = 6$ (as in main paper) affects the quasiparticle peak shown in Figs. 2(a,c), and the spin and orbital susceptibilities shown in Figs. 3(c,f), respectively. As discussed in the corresponding figure captions, Fig. S-2 clearly shows that the T -induced suppression of the quasi-particle peak is due to Hund physics, not Mott physics or thermal broadening; and Fig. S-3 shows that changing J from 0 to 1 reduces T_K^{sp} significantly, but T_K^{orb} only very slightly.

Structure factor $A(\omega, \varepsilon_k)$.— The coherence-incoherence crossover can be probed experimentally using angle-resolved photoemission spectroscopy

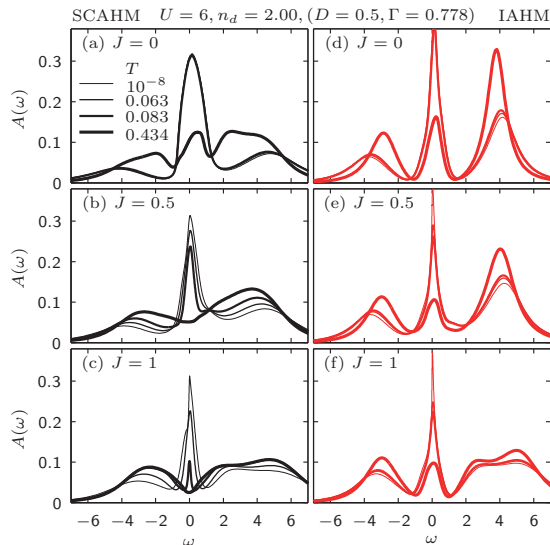


Figure S-2. The local spectral function $A(\omega)$ of the SCAHM (left column) and the IAHM (right column) for three values of Hund coupling J at fixed $U = 6$, for the four temperatures shown in Figs. 2(a,c) of the main text. Increasing J from 0 through 0.5 to 1 causes a significant reduction of the width of the quasi-particle peak at $T = 0$, and also of the coherence scale beyond which the quasi-particle peak begins to be suppressed with increasing T . Indeed, for $J = 0$ the quasi-particle peak is almost T -independent for the lowest three temperatures [the corresponding curves in panels (a,d) coincide almost completely], showing broadening only for very large T ; but for finite J , its suppression starts at much lower T , indicating that the coherence scale has been reduced. This clearly illustrates that the suppression of the quasi-particle peak is due to Hund physics, not Mott physics or thermal broadening, as discussed in the main text. For the SCAHM, this suppression is amplified through DMFT self-consistency, the more so the larger J [compare peak-heights in panels (b,c) with (e,f)].

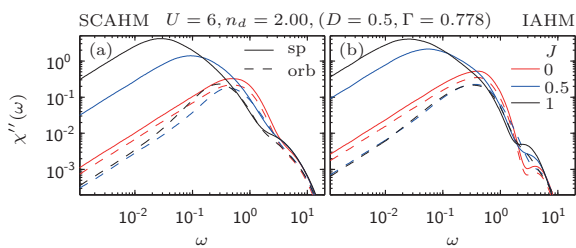


Figure S-3. The importance of Hund J for spin-orbital separation in real-frequency ground state susceptibilities for (a) the SCAHM and (b) the IAHM. We show χ''_{sp} (solid) and χ''_{orb} (dashed) for $U = 6$ (as in Figs. 3(c,f) of the main text), but now for three values of Hund coupling. As J is increased from $J = 0$ (red) to 0.5 (blue) to 1 (black), the peak position of χ''_{sp} (i.e. T_{K}^{sp}) shifts to significantly lower values, but that of χ''_{orb} (i.e. $T_{\text{K}}^{\text{orb}}$) shifts only very slightly. This is the hallmark of spin-orbital separation.

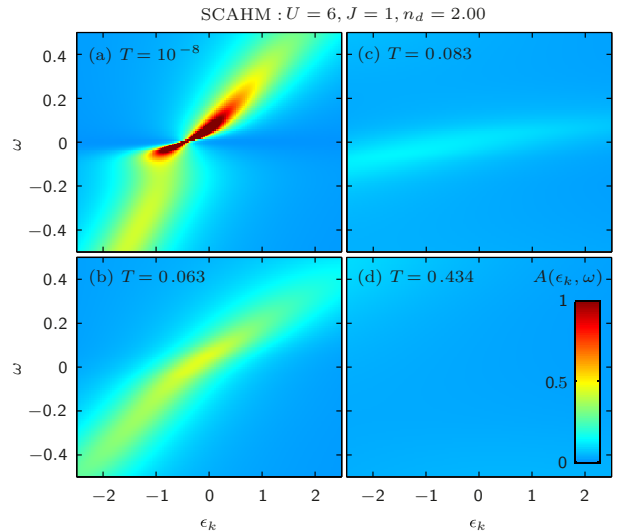


Figure S-4. (Color online) The spectral function $A(\varepsilon_k, \omega)$ of the SCAHM, calculated from the local spectral function $A(\omega)$ of Fig. 2(a), for the same four temperatures used there.

(ARPES) to measure the structure factor $A(\omega, k)$. Fig. S-4 shows our predictions for the temperature dependence of a related quantity, $A(\omega, \varepsilon_k)$, calculated from the local spectral function $A(\omega)$ using the standard DMFT protocol [1]:

$$A(\omega, \varepsilon_k) = -\frac{1}{\pi} \text{Im}[\omega + \mu - \varepsilon_k - \Sigma(\omega)]^{-1} \quad (1)$$

The temperature-induced suppression of the quasi-particle peak in $A(\omega)$ (Fig. 2, main text) is directly reflected in $A(\omega, \varepsilon_k)$ of Fig. S-4: at low temperatures it displays a *strong, dispersive peak* (ω_{peak} shifts with ε_k), *that weakens with increasing T* , eventually disappearing altogether. This type of behavior is characteristic of the physics of Hund metals. It does not occur for $J = 0$, since then the quasi-particle peak in $A(\omega)$ is essentially independent of T , as shown in Fig. S-2(a).

The behavior of $A(\varepsilon_k, \omega)$ shown in Fig. S-4 is qualitatively reminiscent of that observed in several recent ARPES studies of Hund metal systems: examples of a dispersing peak that disappears with increasing temperature, yet *not* due to thermal broadening, can be found in Fig. 3(a-c) of Ref. 44, Figs. 3(a-e) of Ref. 45, and Fig. 3 of Ref. 46.

It should be emphasized, though, that since our model is $SU(3)$ symmetric by construction, all three bands behave the same way, whereas the material systems of Ref. 44–46 all exhibit orbital selectivity. To be specific: Ref. 44 reports the observation of a temperature-induced crossover to an orbital-selective Mott phase in $A_x\text{Fe}_{2-y}\text{Se}_2$ ($A=\text{K,Rb}$) superconductors: with increasing temperature the system evolves into a state in which

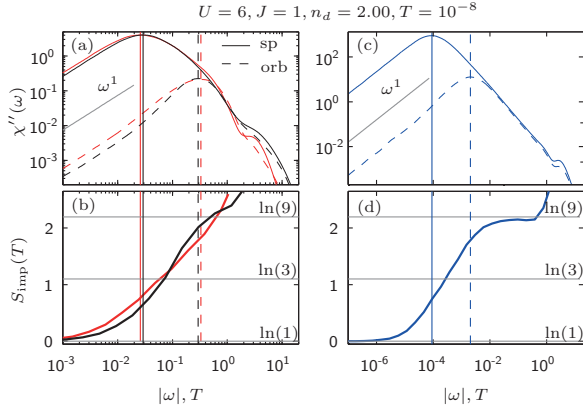


Figure S-5. (Color online) (a,c) Same panels as Fig. 3 (c,f) of main paper, showing the spin and orbital susceptibilities as functions of ω . (b,d) Impurity contribution to the entropy as function of T , (b) for the SCAHM (black) and IAHM with $(\Gamma, D) = (0.778, 0.5)$ (red) and (d) the IAHM with $(\Gamma, D) = (0.200, 1.0)$ (blue).

the d_{xy} bands have depleted spectral weight, while the d_{xz}/d_{yz} bands remain metallic. Similar behavior is found in Ref. 45 for $\text{Li}(\text{Fe}_{1-x}\text{Co}_x)\text{As}$, and in Ref. 46 for iron chalcogenide superconductors (FeCh). A detailed theory of such systems would therefore have to be based on a 3-band model *without* $\text{SU}(3)$ symmetry, which would go well beyond the scope of this paper and is left for the future. Nevertheless, it is remarkable that already the minimal Hund metal model studied here yields the qualitative feature of a dispersive excitation [peak in $A(\omega, \varepsilon_k)$] that disappears with increasing temperature, but not due to thermal broadening, and while remaining in a metallic state. In that sense Hundness by itself (not Mottness) might be the driving force in these materials.

Ground state impurity entropy.— In addition to the RG flow in Fig. 3(g,h) of the main paper, we also calculated the impurity contribution to the ground state entropy, $S_{\text{imp}}(T)$ [Fig. S-5]. From the three effective fixed point Hamiltonians associated with two-stage screening of orbital and spin degrees of freedom, a ground state impurity entropy of $\ln(1)$, $\ln(3)$ and $\ln(9)$ is expected for the low, intermediate and high-energy fixed point regimes, respectively. Below T_{K}^{sp} the Fermi-liquid spin-singlet \times orbital-singlet ground state structure is directly reflected in a ground state impurity entropy of $\ln(1)$ [Fig. S-5 (b,d)]. As the temperature traverses the intermediate regime between T_{K}^{sp} and $T_{\text{K}}^{\text{orb}}$, the entropy increases through the value $\ln(3)$ associated with a spin triplet and orbital singlet. However, no plateau is seen at $\ln(3)$, because the energy spacing between T_{K}^{sp} and $T_{\text{K}}^{\text{orb}}$ is too small for the corresponding RG flow to become stationary there [cf. Fig. 3 (g,h) of main paper]. Thus, S_{imp} shows a gradual transition from $\ln(1)$ to $\ln(9)$ above $T_{\text{K}}^{\text{orb}}$ in the free orbital regime, with triplet \times triplet structure

[Fig. S-5 (b,d)]. At the energy scale of the bare hopping or bandwidth, charge fluctuations set in, leading to a further enhancement of the entropy.

4.A Results for a two-band Hund metal

We complement the three-band study of the previous section with results for two bands to emphasize that the pure presence of finite J is not sufficient to evoke SOS.

Fig. 4.1 clearly shows that SOS is absent in the 2HHM and the 2AHM for $n_d = N_c - 1 = 1$ and $J = 1$: the orbital (dashed vertical lines) and spin (solid vertical lines) Kondo scales essentially coincide, $T_K^{\text{orb}} \approx T_K^{\text{sp}}$. (The small discrepancy of a factor $T_K^{\text{orb}}/T_K^{\text{sp}} \approx 1.5$ for the 2HHM is induced by the presence of charge fluctuations at higher energies.) Below T_K^{sp} , FL behavior is found [cf. solid grey guide-to-the-eye lines in Fig. 4.1(b-f)]. As a consequence, the QP peak of $A(\omega)$ in Fig. 4.1(a,d) has no substructure, there is no plateau in $\text{Im} \Sigma(\omega)$ [cf. Fig. 4.1(b,e)], $\chi''_{\text{orb}}(\omega) \approx \chi''_{\text{sp}}(\omega)$ in Fig. 4.1(c,f), and multiplets that are degenerate in the FL regime only split slightly at higher energies in the NRG flow diagram due to the different influence of charge fluctuations in the presence of Hund's coupling, but SOS splitting is absent [cf. the green $S = 1$ and the red $S = 0$ curves in Fig. 4.1(g,h)]. Note that $Q = [q, 2S, 2C]$ are the $U(1)_{\text{ch}} \times SU(2)_{\text{sp}} \times SU(2)_{\text{orb}}$ multiplet symmetry labels for $N_c = 2$, where q denotes particle number relative to half-filling, S the spin, and C the $SU(2)$ isospin (channel) quantum number.

The inset of Fig. 4.1(f) reveals the evolution of T_K^{orb} and T_K^{sp} with the filling n_d in the 2AHM. While for $n_d \leq 1$, we find $T_K^{\text{orb}} = T_K^{\text{sp}}$, an apparent SOS regime with $T_K^{\text{orb}} \gg T_K^{\text{sp}}$ opens for $1 < n_d < 2$. As n_d continues to increase towards 2, T_K^{sp} drops below the lowest relevant energy scale and T_K^{orb} becomes very large ($\gtrsim D$), reflecting the fact that for half-filling the orbitals form an orbital singlet from the outset. A similar observation holds for the inset of Fig. 3(f) of Ref. [SYvD⁺15] with $N_c = 3$. In Ref. [SKWvD18] (cf. Sec. 5.2) we thoroughly elucidate these observations for $N_c = 3$. It might be worthwhile to also study the regime, $1 < n_d < 2$, of the 2HHM in more detail to unveil its similarities and differences as compared to the 3HHM.

To summarize, we again emphasize that, in essence, SOS is a solid-state manifestation of Hund's first rule, the alignment of spins in different orbitals, which requires a filling of $1 < n_d < N_c$ electrons (or $N_c < n_d < 2N_c - 1$ holes) on average to show any effect.

4.B Unveiling the FL phase from NRG eigenenergy spectra

As remarked in Ref. [SYvD⁺15] (cf. Sec. 4.2) the ground state excitation spectrum of the 3AHM and the 3HHM (at $n_d = 2$) can be interpreted in terms of noninteracting single-particle excitations, thus confirming its FL nature (cf. Sec. 3.9). In the following, we explain this procedure for the 3AHM, the 3HHM, and the 2AHM for $n_d = N_c - 1$.

For each model, we plotted in Fig. 4.2 the rescaled energy spectrum which corresponds to an even NRG iteration in the converged ground state fixed point of its NRG flow diagram, respectively (see figure caption for details). The left column reveals the particle number, q , of each multiplet excitation (grey lines), the right column the spin quantum number, $2S$. Numbers on the grey lines give the full state space degeneracy for each multiplet. In the case of a FL ground state, we should be able to model the spectrum of a given Hamiltonian by constructing (all) possible combinations of particle and hole excitations from the ground state.

We start with the 3AHM in Fig. 4.2(a,b) and exemplify the procedure for the five lowest-lying multiplets. Here, $6 = 3 \times 2$ (orb \times sp) flavors imply 6 possible electronic states per given energy in a noninteracting QP picture. The ground state, for which all states below the Fermi energy are filled, lies at zero energy and is specified by the quantum numbers, $q = 0$ and $S = 0$ with degeneracy 1. This ground state can be excited by adding one hole (with spin up or down) to the system. The resulting hole excitation has quantum numbers,

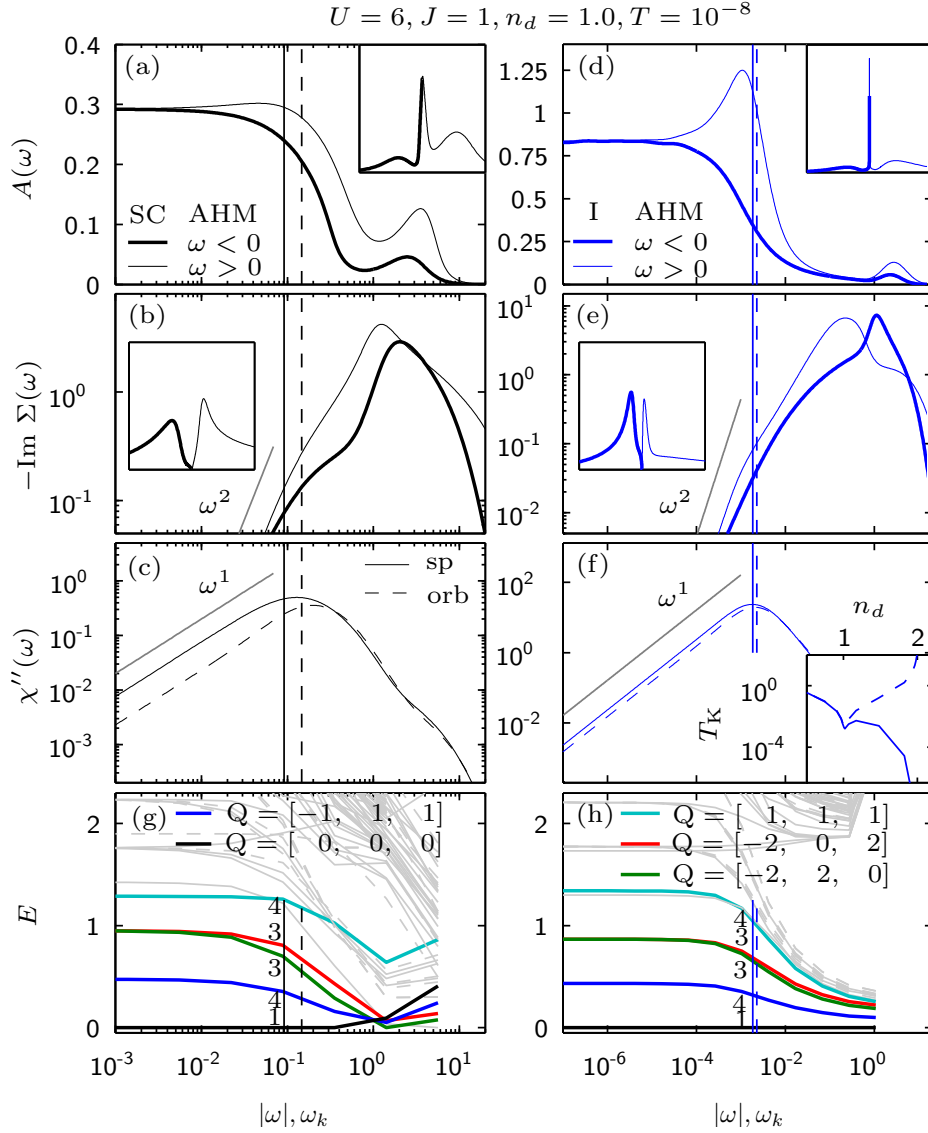


Figure 4.1 (a-f) Absence of SOS ($T_K^{\text{orb}} \approx T_K^{\text{sp}}$) in real-frequency ground-state correlators for (left column) the two-channel SCAHM (2HHM) and (right column) the two-channel IAHM (2AHM) with $n_d = 1$. Panels are analogous to Fig. 3 of Ref. [SYvD⁺15] in Sec. 4.2. (a,d) The local spectral functions, (b,e) the local self-energy, and (c,f) the spin and orbital susceptibilities, χ''_{sp} (solid) and χ''_{orb} (dashed). We use a logarithmic frequency scale, with thick (thin) lines for $\omega < 0$ ($\omega > 0$). Insets show data on a linear scale. In all panels, solid (dashed) vertical lines mark the spin (orbital) Kondo scale, T_K^{sp} (T_K^{orb}). Grey guide-to-the-eye lines indicate FL power laws (solid). Inset to (f): Kondo scales T_K^{sp} (solid) and T_K^{orb} (dashed) for the IAHM, plotted as function of n_d . (g) and (h) show NRG eigenlevel flow diagrams for the SCAHM and IAHM of panels (a-c) and (d-f), respectively: the rescaled energies of the lowest-lying eigenmultiplets of a Wilson chain of (even) length k are plotted versus its characteristic level spacing $\omega_k \propto \Lambda^{-k/2}$. For each multiplet, the number close to the line gives its full state space degeneracy, Q its symmetry labels.

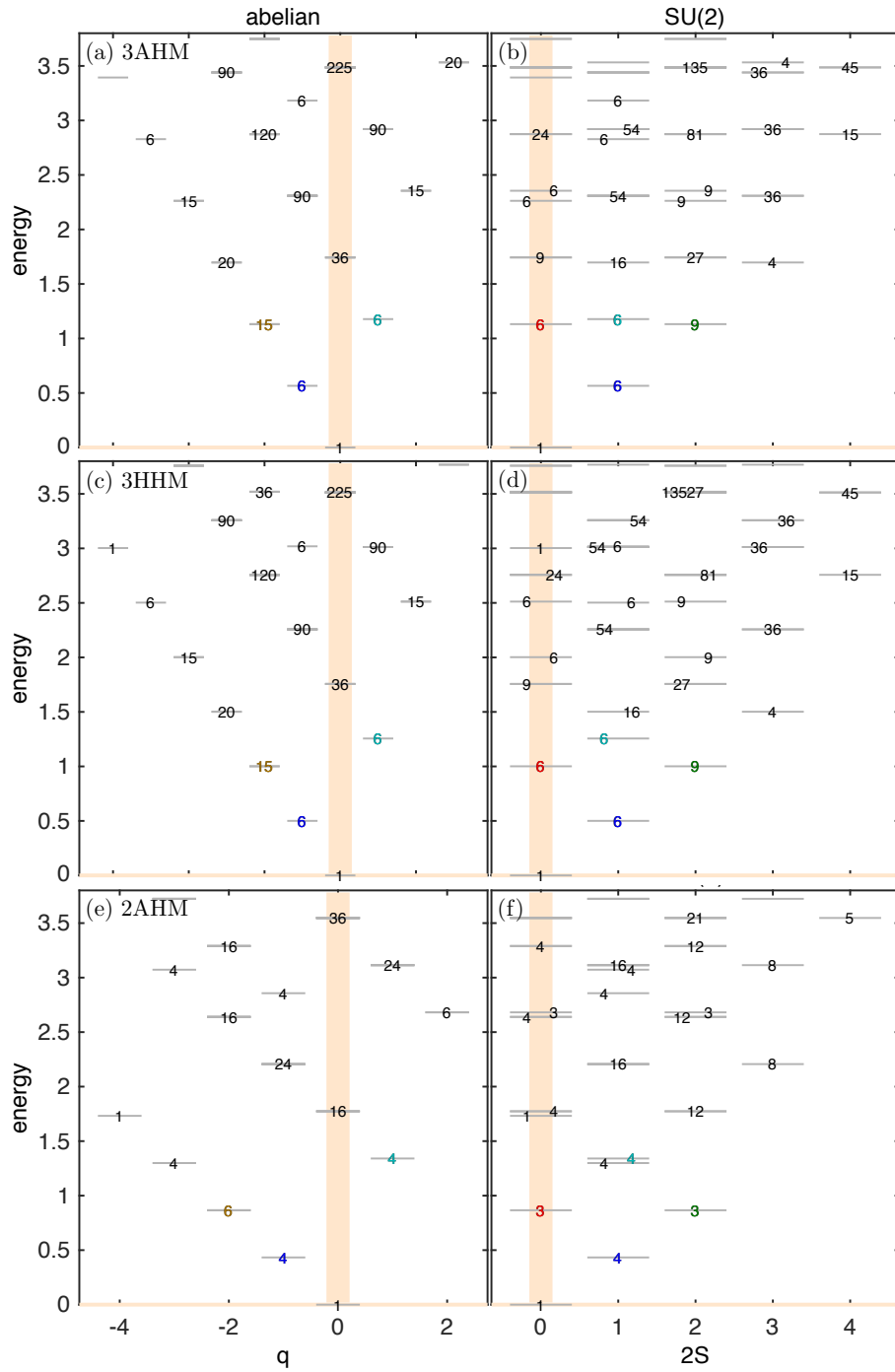


Figure 4.2 The rescaled energies of the lowest-lying eigenmultiplets (grey lines) are plotted versus (a,c,e) the particle number, q , and (b,d,f) the spin quantum number, $2S$, for an even NRG iteration (as this has a unique ground state) in the low-energy FL fixed-point regime of (a,b) the 3AHM, (c,d) the 3HHM, and (e,f) the 2AHM at $n_d = N_c - 1$. (a,b) corresponds to the NRG flow diagram in Fig. 3(h) and (c,d) to Fig. 3(g) of Ref. [SYvD⁺15], (e,f) corresponds to Fig. 4.1. Each multiplet is labeled by its full state space degeneracy. Colored labels indicate colored multiplets of the respective NRG flow diagram.

$q = -1$ and $2S = 1$ with a degeneracy of $\binom{6}{1} = 6$, because the hole can be in one of six possible states. In Fig. 4.2(a,b), we find the hole excitation at energy $E_h = 0.57$ (cf. the dark blue number). The excitation of one electron also yields 6 degenerate states with $q = 1$ and $S = 1$, but at energy $E_p = 1.18 \approx 2E_h$ in the spectrum [cf. the bright blue number in Fig. 4.2(a,b)]. The difference between the lowest particle and hole excitation energies originates from the particle-hole asymmetry of the model and determines the phase shift in the 3HHM, $\phi \equiv \frac{E_h}{E_h + E_p} = \frac{0.57}{0.57 + 1.18} \approx \frac{1}{3} \simeq \frac{n_d}{2N_c}$, which is equal to the filling ratio according to Friedel sum rule, Eq. (3.44). The excitation of two holes, each of energy E_h , has a degeneracy of $\binom{6}{2} = 15$ with $q = 2$ [cf. the brown number in Fig. 4.2(a)]. The two holes form either a 6-fold degenerate spin singlet with $S = 0$ [cf. the red number in Fig. 4.2(b)] or combine to a 9-fold degenerate spin triplet with $S = 1$ [cf. the green number in Fig. 4.2(b)]. For $S = 0$, the spin singlet has 6-fold degeneracy in the orbital sector only (two holes are distributed in three orbitals, leading to $\binom{3+2-1}{2} = 6$ possible states). For $S = 1$, the spin triplet is 3-fold degenerate in the spin sector and can occupy the three orbitals in $\binom{3}{2} = 3$ different ways, resulting in a $3 \cdot 3 = 9$ -fold degeneracy. After having analyzed the five lowest-lying multiplets, the FL character of the ground state in the 3AHM becomes already obvious. We remark that with increasing energy, the NRG multiplet eigenenergies deviate more and more from the true single-particle picture. The level spacing is widened exponentially due to the basic concept of energy scale separation within NRG.

The spectrum of the 3HHM in Fig. 4.2(c,d) can be interpreted in the same way as in the 3AHM above. However, the phase shift $\phi \equiv \frac{E_h}{E_h + E_p} = 0.29$ is not equal to the filling ratio $\frac{n_d}{2N_c} = \frac{1}{3}$, since the Friedel sum rule does not hold within DMFT.

For the 2AHM, we can analogously reproduce the energy spectrum of Fig. 4.2(e,f) in terms of noninteracting QP excitations. The only difference to the 3AHM is the number of flavors. The 2AHM has only 4×4 (orb \times sp) flavors and thus 4 possible states per given energy, changing the degeneracies of the multiplets. Further, the phase shift is $\phi \equiv \frac{E_h}{E_h + E_p} \approx \frac{1}{4} \simeq \frac{n_d}{2N_c}$, in accordance with Friedel sum rule.

As a result of the analysis of NRG eigenenergy spectra in this section, we unambiguously confirmed the FL ground state in the 3AHM, the 3HHM, and the 2AHM for $n_d = N_c - 1$.

5 Hundness versus Mottness: on the origin of strong correlations in Hund metals

5.1 Overview

In this Chapter we turn to a very central but controversially debated issue about Hund metals: what is the origin of strong correlations in these systems? Is it Mottness, i.e. the blocking of charge fluctuations close to a MIT induced by Coulomb interaction, as known from Mott-Hubbard systems? Or is it Hundness, a new route towards strong correlations induced by Hund’s rule coupling?

This fundamental question is thoroughly studied in our article entitled “Hundness versus Mottness in a three-band Hubbard-Hund model: On the origin of strong correlations in Hund metals” [SKWvD18], which we present in the next section. We remark that parts of this article were reused in the introduction to this thesis. We complement our insights of Ref. [SYvD⁺15] by providing an exhaustive real-frequency DMFT+NRG analysis of the full phase diagram of the 3HHM on a Bethe lattice at $T = 0$, in which Hund metals are represented at sizeable J and moderate U close to a filling of $n_d = 2$ (cf. Fig. 1.1). In this Hund-metal regime strong correlations are manifested in a low QP weight, Z , even rather far from the MIT at $n_d = 2$ and $n_d = 3$ (cf. Sec. 1.2.3). In particular, we carefully explore the MIT in the presence of zero and finite J and the effect of J , U , and n_d on the energy scales and the nature of SOS. Based on this, we clarify the differences between a Hund- and a Mott-correlated metal at $T = 0$.

Motivated by previous model studies, we examine three different scenarios that can, in principle, induce strong correlation effects in the Hund-metal regime of the phase diagram:

- (i) Hundness: the solid-state manifestation of Hund’s first rule is the key player to induce strong correlations;
- (ii) Mottness at $n_d = 2$: the interaction-induced MIT at one charge away from half-filling triggers strong correlations;
- (iii) Mottness at $n_d = 3$: the half-filled Mott insulator emanates strong correlations.

We study these scenarios by scanning the parameter space of the phase diagram in two orthogonal directions: we either vary n_d for different parameter sets of U and J , or we vary U and J for fixed $n_d = 2$. In the following, we elaborate on the backgrounds of (i)-(iii) and give an overview of our main insights:

- (i) The importance of Hund’s rule to promote a highly incoherent metallic state together with a large mass enhancement is emphasized by various authors, for instance in Refs. [WGTM08, HK09, MAM⁺11, dMMG11, YHK12, GMM13, AK15, MG16]. In particular, Z. P. Yin, K. Haule, and G. Kotliar [HK09, YHK12] suggested that the incoherent regime is controlled by the Hund’s-rule-induced coexistence of fast quantum mechanical orbital fluctuations and slow spin fluctuations, while P. Werner *et al.* [WGTM08] established an interpretation in terms of Hund’s-rule-induced frozen local moments (cf. Sec. 1.2.4).

We show as the main result of this article that in the Hund-metal regime, far from any MIT, indeed, Hundness and not Motttness, i.e. the localization of large spins rather than charges, is the key player to induce strong correlations. More precisely, a complex, intertwined, two-stage SOS screening process correlates the electrons in Hund metals (cf. also Ref. [SYvD⁺15] in the previous Chapter 4). Close to $n_d = 2$, orbital and spin degrees of freedom are, on the one hand, separated but, on the other hand, still coupled within this screening process: below T_K^{orb} , the orbital degrees of freedom form an orbital singlet through the formation of a large Hund's-coupling induced effective 3/2 spin – including a bath spin degree of freedom; and below T_K^{sp} , the latter is fully screened by the three bath channels of the 3HHM. Accordingly, the spectral function, $A(\omega)$, exhibits a two-tier QPP: a sharp central SU(2) Kondo resonance on top of a wide SU(3) Kondo resonance, clearly visible as a shoulder at negative frequencies. Interestingly, the SOS regime is characterized by apparent fractional power laws, as discussed in more detail in Sec. 5.A.

This screening process supports the interpretation of Z. P. Yin, K. Haule, and G. Kotliar [HK09, YHK12]. However, we also clarify that the two terminologies, “spin-freezing” and “spin-orbital separation”, ultimately describe the same physics of the Hund-metal regime.

- (ii) The findings in Refs. [dMMG11, GMM13], in particular the Janus-faced behavior of the MIT (cf. Sec. 1.2.4), motivated us to study scenarios (i) and (ii), i.e. to map out the MIT in the 3HHM at $n_d = 2$ based on real-frequency spectral data. For increasing $0 \leq J \lesssim 1$, we confirm that the physics of the MIT is governed by the gradual J -induced splitting of local multiplets within each charge sector, changing the nature of the actual ground state, and exponentially decreasing the Kondo scales. For sizeable $J > 1$, this splitting is completed and we observe a qualitative change in the emerging physics of the 3HHM. In this regime, we disentangle the Janus-faced behavior of the MIT by replacing U with the bare gap between the lowest atomic excitations of the Hubbard bands, $\Delta_b = U - 2J$, as an unambiguous measure of Motttness. We reveal that, for fixed J , both T_K^{orb} and T_K^{sp} decrease linearly with increasing Δ_b , but with a much larger slope in the case of T_K^{orb} . The ratio $T_K^{\text{orb}}/T_K^{\text{sp}}$ is universal (constant) as a function of Δ_b and rather large for $J \gtrsim 1$. For fixed Δ_b , $T_K^{\text{orb}}/T_K^{\text{sp}}$ saturates with increasing J . We further show that the QP weight is proportional to the spin Kondo scale, $Z \propto T_K^{\text{sp}}$. Importantly, this finding holds generically in the whole metallic regime due to its FL ground state. Thus, T_K^{sp} governs the strength of correlations, whereas T_K^{orb} governs the MIT (together with the Hubbard side bands). In sum, the low Z far from the MIT can then be directly explained by the SOS-reduced T_K^{sp} , thus by Hundness.

Based on these insights we develop a description of multi-band Hund-correlated and Mott-correlated metals in the presence of sizeable J , as relevant for instance for Sr_2RuO_4 and V_2O_3 [DSH⁺18]. Hund-correlated metals are far from the MIT and characterized by a very broad incoherent SOS regime: T_K^{orb} is comparable in magnitude to bare atomic energy scales of the system and T_K^{sp} is strongly reduced. In contrast, in Mott-correlated metals, close to the MIT, both T_K^{orb} and T_K^{sp} are strongly reduced, the SOS regime is vanishingly small, and the QPP well separated from the Hubbard bands. *Thus, Hund metals are dominated by the SOS Kondo-type screening process, while Mott-correlated metals are governed by the localization of charges, invoked by the DMFT self-consistency.*

- (iii) Based on the interpretation of cuprates as doped half-filled Mott-insulators and the research of Refs. [IL10, FB15, dMC17, dM17] we also study the scenario “Motttness at $n_d = 3$ ”. We explore the evolution of the Hubbard bands and the SOS for $2 < n_d \leq 3$.

In principle, SOS is a generic Hund's-coupling-induced feature for $1 < n_d < 3$ and sizeable J . However, we find that, close to the MIT at $n_d = 3$, the nature of both the Hubbard bands and the SOS change strongly. There, the orbital degrees of freedom get blocked by the formation of a $3/2$ *impurity* spin. In the SOS screening process, the orbital and spin dynamics thus get decoupled. *To summarize, we argue that Mottness at $n_d = 3$ does not mediate strong correlation effects in the Hund-metal regime.*

Further, we show that, at least for the parameters studied in our article, the electronic compressibility, $\kappa_{\text{el}} = \frac{\partial n_d}{\partial \mu}$, remains positive close to the MIT at $n_d = 3$, in contrast to findings of Ref. [dM17], which suggests genuine Hund's induced FL instabilities in terms of a negative compressibility (cf. Sec. 1.2.4). In Sec. 5.B we elaborate on this issue in more detail.

To summarize, in this article, we shed light on the origin and nature of strong correlations in Hund metals. We thoroughly corroborate that SOS is a new screening route towards heavy masses with relevance for Hund metals. Accordingly, Hundness is the origin of low Z in the Hund-metal regime of the 3HHM at $T = 0$, whereas close to the MIT at $n_d = 2$ and $n_d = 3$ typical Mott physics dominates. Hund-correlated systems are thus characterized by a large incoherent energy regime with itinerant orbitals coupled to quasi-free spins. This leads to interesting implications for the nature of electronic transport. In the next two Chapters we will unveil the signatures of Hund- and Mott-correlated systems in the temperature dependence of various physical quantities for the 3HHM.

Hundness versus Motttness in a three-band Hubbard-Hund model: On the origin of strong correlations in Hund metals

by

K. M. Stadler,¹ G. Kotliar,² A. Weichselbaum,^{3,1} and J. von Delft¹

¹Physics Department, Arnold Sommerfeld Center for Theoretical Physics and Center for NanoScience, Ludwig-Maximilians-Universität München, 80333 München, Germany

²Department of Physics and Astronomy, Rutgers University, Piscataway, NJ 08854, USA

³Condensed Matter Physics and Materials Science Department, Brookhaven National Laboratory, Upton, NY 11973, USA

reprinted on pages [107–151](#).

arXiv preprint: [arXiv:1808.09936](#) [cond-mat.str-el]

accepted by Ann. Phys. (NY)

Hundness versus Mottness in a three-band Hubbard-Hund model: On the origin of strong correlations in Hund metals [☆]

K. M. Stadler^{a,*}, G. Kotliar^b, A. Weichselbaum^{a,c}, J. von Delft^a

^a*Physics Department, Arnold Sommerfeld Center for Theoretical Physics and Center for NanoScience,
Ludwig-Maximilians-Universität München, 80333 München, Germany*

^b*Department of Physics and Astronomy, Rutgers University, Piscataway, NJ 08854, USA*

^c*Condensed Matter Physics and Materials Science Department, Brookhaven National Laboratory, Upton, New York 11973,
USA*

Abstract

Hund metals are multi-orbital systems with moderate Coulomb interaction, U , among charges and sizeable Hund's rule coupling, $J (< U)$, that aligns the spins in different orbitals. They show strong correlation effects, like very low Fermi-liquid coherence scales and intriguing incoherent transport regimes, resulting in bad-metallic behavior. But to what extent are these strong correlations governed by Mottness, i.e. the blocking of charge fluctuations close to a Mott insulator transition (MIT) induced by U , or by Hundness, a new route towards strong correlations induced by J ? To answer this question, we study the full phase diagram of a degenerate three-band Hubbard-Hund model on a Bethe lattice at zero temperature using single-site dynamical mean-field theory and the numerical renormalization group as efficient real-frequency multi-band impurity solver. Hund metal behavior occurs in this minimal model for a filling close to $n_d = 2$, moderate U and sizeable J , the “Hund-metal regime”. In particular, strong correlations manifest themselves there by an unusually low quasiparticle weight. Generalizing previous results on this model, we show that “spin-orbital separation” (SOS) is a generic Hund's-coupling-induced feature in the whole metallic regime of the phase diagram for $1 < n_d < 3$ and sizeable J . There orbital screening always occurs at much higher energies than spin screening below which Fermi-liquid behavior sets in. The low quasiparticle weight can then be directly explained in terms of the Hund's-coupling-reduced Fermi-liquid scale. We carefully analyze the effect of J (Hundness), and the effect of the MIT at $n_d = 2$ and $n_d = 3$ (Mottness) on the energy scales and the nature of SOS. *In the Hund-metal regime, far from any MIT, Hundness – the localization of large spins – is shown to be the key player to induce strong correlations.* There, physical properties are governed by a broad incoherent energy regime of SOS where intriguing Hund metal physics occurs: large, almost unscreened spins are *coupled* to screened orbital degrees of freedom. With increasing proximity to an MIT correlations are further enhanced and the Fermi-liquid scale is further reduced. However, in the Hund-metal regime, this effect of Mottness is minor. In contrast, very close to the MIT at $n_d = 2$, the incoherent spin-orbital separation regime is strongly downscaled and becomes negligibly small, whereas Mottness – the localization of charges – becomes dominant in inducing strong correlations. Close to the MIT at $n_d = 3$, the SOS regime widens up because the orbital degrees of freedom get blocked by the formation of an $S=3/2$ impurity spin, but its nature changes: the orbital and spin dynamics get decoupled. Our results confirm Hundness as a distinct mechanism towards strong correlations in the normal state of Hund metals, leading to various interesting implications for the nature of electronic transport.

Keywords: Hundness, Hund metal, multi-orbital model, Mott-insulator transition, numerical renormalization group, dynamical mean-field theory

PACS: 71.10.Fd, 71.27.+a, 71.30.+h, 75.20.Hr

1. Introduction and Motivation

1.1. Bad-metal superconductors

Iron-based high-temperature superconductors [1, 2] (HTSCs) are “bad metals”. On the one hand, in their superconducting state (with critical temperatures up to 56K [3–5]), they are perfect conductors with dissipationless supercurrents; on the other hand, in their normal state they conduct surprisingly badly. But which fundamental physical mechanism causes this bad-metallic behavior? Interestingly, this bad-metallic behavior is not found in conventional BCS-like superconductors, but it is reminiscent of the unconventional normal state of (doped) cuprate HTSCs. These are known to be strongly correlated and the conventional superconducting mechanism based on electron-phonon coupling is most likely not strong enough to generate their high critical temperatures.

There is firm evidence that strong correlation effects play a key role in iron-based HTSCs, as well. In their paramagnetic phase, these materials exhibit anomalous and bad transport properties that are characterized by very low Fermi-liquid (FL) coherence scales [6–9]. Above the FL scale puzzling non-Fermi-liquid (NFL) behavior [6–17] occurs in a large intermediate (paramagnetic) energy window, typically at or slightly below room temperature, together with poorly screened, large fluctuating local moments, as observed in observed in X-ray emission spectroscopy measurements [18–20]. At higher temperatures, the resistivity reaches unusually large values that exceed the Mott-Ioffe-Regel limit [6, 9]. In accordance, various experiments revealed particularly large mass enhancements [8, 9, 16, 17, 21–28].

1.2. Hundness versus Mottness in multi-orbital bad metals

Since the “standard model” of a Fermi liquid in condensed matter theory breaks down in the presence of strong correlations, both the superconducting and the bad-metal normal state are still poorly understood in the iron-based HTSCs. In particular, one widely but controversially debated fundamental question pertains to the origin of strong correlations: is it “Hundness” or “Mottness”?

Cuprate HTSCs are widely considered as doped charge-transfer Mott insulators [29, 30]. Strong correlations arise here due to Mottness: the proximity to a Mott-insulator transition (MIT), i.e. a transition at a critical interaction strength U_c from an (increasingly correlated) metal to an insulator, which is driven by a large Coulomb repulsion, U . In theoretical descriptions, the original multi-band electronic structure of cuprates is usually reduced to a low-energy effective (two-dimensional) one-band Hubbard model, such that U acts only between electrons in one orbital per lattice site and the MIT occurs at half-filling for undoped cuprates.

In contrast, doped *and* undoped iron-based HTSCs are (bad) metallic materials with an effective *multi*-band description that allows for an additional type of interaction: Hund’s rule coupling, J (Hundness), which favors the alignment of spins in different orbitals on the same (iron) atom and consequently correlates the electron hopping in terms of a non-trivial interplay of orbital and spin degrees of freedom [6, 7, 31]. In iron-based HTSCs and other multi-band materials, the strong correlation effects may thus be caused by either Hundness, or Mottness, or a combination of both.

Therefore, the following question has been raised [7, 32]: what is the role of “Hundness versus Mottness” as origin of strong correlations in multi-orbital bad metals? Here we address this question from a fundamental model-based point of view: we investigate the zero-temperature properties of a toy model, the degenerate three-band Hubbard-Hund model Hamiltonian (3HHM) [7, 31, 33], using single-site dynamical mean-field theory (DMFT) and a highly-efficient multi-band numerical renormalization group (NRG) impurity solver

*K.M.S., A.W., and J.v.D. acknowledge support from the excellence initiative NIM; A.W. was also supported by WE4819/1-1 and WE4819/2-1 until 12/2017 and by US DOE under contract number DE-SC0012704 since. G.K. was supported by National Science Foundation grant DMR-1733071. Author contributions: K.M.S. and G.K. proposed this project; K.M.S. performed the DMFT+NRG calculations; A.W. developed the NRG code and assisted K.M.S. in the initial stages of the DMFT+NRG computation. K.M.S. drafted the manuscript with the help of G.K., A.W and J.v.D.

*Corresponding author.

Email addresses: Katharina.M.Stadler@physik.uni-muenchen.de (K. M. Stadler), kotliar@physics.rutgers.edu (G. Kotliar), weichselbaum@bnl.gov (A. Weichselbaum), vondelft@lmu.de (J. von Delft)

[33–36] to tackle the correlated many-body problem. A central theme of our work is spin-orbital separation (SOS). It was first revealed and argued to be related to anomalous power law behavior for the Matsubara self-energy in Ref. [7], further analyzed using perturbative scaling arguments in Ref. [31], and conclusively established by a detailed DMFT+NRG analysis in Ref. [33]. (For a complementary study, where we focussed on finite-temperature properties not addressed in this paper, see Ref. [37].)

We next summarize the state of research on multi-band models motivating and providing the basis for this article.

2. Scope and Aim

2.1. Hund metals

For a long time strong electronic correlations in materials have exclusively been associated with the proximity to a MIT evoked by U , i.e. to the suppression of charge fluctuations. The MIT was extensively studied in one-band systems [38–41], including the cuprate HTSCs. But a MIT also occurs at any integer filling of multi-orbital materials. Examples are various 3d (and 4d) transition metal oxides with the prototypical Mott material V_2O_3 [37, 42–45].

Soon after the discovery of the iron pnictides [1, 2], it was realized that the special multi-orbital character of these HTSCs (and many other strongly correlated materials) allows for a new mechanism towards heavy effective masses: Hundness [6]. This new class of materials was dubbed “Hund metals” [46, 47] and includes multi-orbital materials like iron pnictides and chalcogenides [6, 7, 14, 15, 46–50], as well as various transition metal oxides of the 3d and 4d series, such as ruthenates [7, 47, 51–55]. Hund metals are characterized by rather broad bands leading to sizeable Hund’s coupling strengths compared to only moderate Coulomb interactions, which are strongly screened in these materials due to the large spatial extension of the correlated orbitals [52, 56].

Interestingly, bad-metal behavior can be found in essentially all these Hund metals. Although the importance of Hund’s coupling in realistic materials is increasingly being appreciated there is still an ongoing debate whether Hundness or Mottness is the key player in renormalizing the electron masses of Hund metals. This debate is strongly driven by the fact that, indeed, striking analogies in the (doping-temperature) phase diagrams of cuprate and iron-based HTSCs hint towards a common framework. For instance, in both cases superconductivity emerges in the vicinity of an incoherent metallic regime with NFL properties and unconventional spin dynamics. So, ultimately, understanding the normal state of Hund metals might lead to deeper insights into the superconducting mechanism in HTSCs.

2.2. Hund models

A very basic approach to address the issue of “Hundness versus Mottness” in Hund metals is to study the paramagnetic phase diagram of Hubbard-Kanamori-like model Hamiltonians (for a review, see Ref. [47]). These take into account two spin and *multiple* (N_c) orbital degrees of freedom, a Coulomb interaction, U , and, most importantly, a finite ferromagnetic Hund’s coupling, J . Hund-metal physics is then captured by these models for a filling, n_d , close to one charge away from half-filling: $n_d \approx N_c \pm 1$. This is motivated by the particle-hole asymmetry of real Hund materials. For instance, the average occupancy of the five Fe 3d orbitals is $d6$ for the undoped stoichiometric parent compounds of almost all iron-based HTSC families [50]. Small to moderate crystal field splittings, as well as hole or electron doping lead to variations in the occupancy, such that the electron densities can range between 5.5 and 6.3 electrons per iron atom [46, 50]. Assuming a fully filled e_g duplet, this leaves $n_d \sim 2$ electrons for three active t_{2g} orbitals. Similarly, ruthenates have an average filling of approximately four electrons in t_{2g} -orbitals.

Here we study the minimal model [7, 31] with relevance for Hund metals, the 3HHM, presented in Sec. 2.6. It involves three degenerate orbitals. We thus fully neglect any material-specific details like crystal-field splitting or realistic band structures, although undoubtedly present in real materials. Our aim in this study is to focus attention on the most generic aspects of Hundness and Mottness in the maximally simple context of full orbital degeneracy, in order to reveal which many-body effects can be understood on this simple model level and which ones require full information of the electronic structure. Since Hund’s

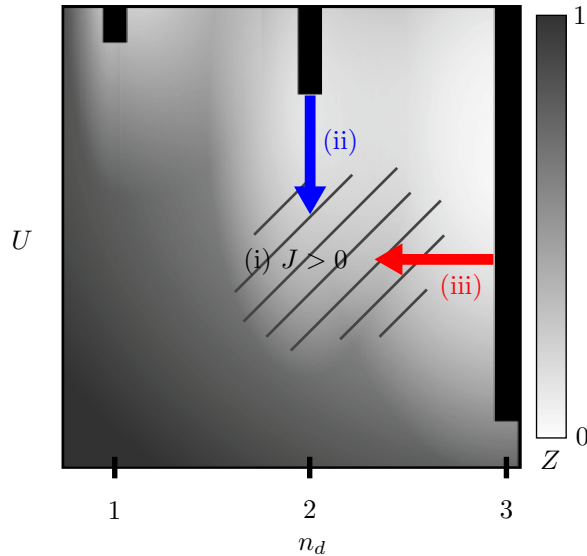


Figure 1: Schematic sketch of the n_d - U phase diagram for the 3HHM at finite J . We only show half of the phase diagram, as it is symmetric with respect to half-filling. The shading reflects the quasiparticle (QP) weight Z . Darker regions (large Z) indicate good metallic, lighter regions (small Z) bad-metallic behavior. The black bars mark Mott insulating phases. At all integer fillings, a MIT occurs above a (different) critical interaction strength, U_c . Interestingly, an extended light region exists also at moderate $U \ll U_c^{(2)}$ around $n_d = 2$ (and reaches to $n_d = 3$). In this “Hund-metal regime” (hatched area), where most Hund metals can be placed [53], strong electronic correlations might either be induced by Hundness, (i) the presence of sizeable J , or Mottness, (ii) the influence of the MIT at $n_d = 2$ (blue arrow), and (iii) the influence of the MIT at $n_d = 3$ (red arrow), or a combination of these scenarios.

rule coupling is only effective for a site occupation that is larger than one electron (and smaller than one hole), we simulate fillings $1 < n_d < 3$ with particular emphasis on $n_d = 2$. (By the particle-hole symmetry of the model with respect to half-filling, this also describes the fillings $3 < n_d < 5$.)

2.3. Phase diagram and bad-metal regime

Our work is motivated by the results of various single-site dynamical mean-field theory (DMFT) [47, 51, 53, 57] and slave-boson [32, 50, 58] studies of degenerate three-band Hubbard-Kanamori-type models that reproduced basic Hund metal physics: in the n_d - U phase diagram at finite J , they found strongly correlated, bad-metallic behavior in an extended region around a filling of $n_d = 2$, which we dub “Hund-metal regime” (hatched area in Fig. 1 at moderate $U \ll U_c^{(2)}$). Naturally, bad-metallic behavior (light regions in Fig. 1) occurs close to the MIT at $n_d = 2$, but interestingly, it also ranges down to rather small Coulomb interaction strengths $U \ll U_c^{(2)}$, provided that Hund’s coupling J is sizable (in a sense defined at the end of Sec. 2.6.1). Most Hund metals can be placed there, around one charge away from half-filling and at moderate U . Further, the bad-metallic regime (light area) also reaches out to the insulating state at half-filling, $n_d = 3$, where the MIT develops already at a very low critical interaction strength, $U_c^{(3)}$.

Bad-metal behavior manifests itself by a small quasiparticle (QP) weight Z . Based on a coherent FL QP picture, Z quantifies the weight of the coherent quasiparticle peak (QPP) of the local spectral function (correlated density of states). Within DMFT and slave-boson methods, the inverse QP weight is equivalent to the electronic mass enhancement, $Z^{-1} = m^*/m$, and thus serves as measure for strong electronic correlations. For Hund models with $N_c > 3$ bands, equivalent regions of low Z (hatched area) were revealed around all integer fillings $1 < n_d < N_c$ [32, 47, 58], but they are most prominent at $n_d = N_c \pm 1$ (see supplement of Ref. [32]).

We note that in the presence of crystal-field splitting Z and the filling can acquire an orbital dependence: various simulations [7, 11, 12, 32, 46, 48, 59–67] and measurements [8, 9, 17, 27, 28] suggest the occurrence of

orbital differentiation and even orbital selective Mott phases (OSMP), depending on the type and strength of the splitting [64, 67]. In the phase diagram, both effects seem to intensify with increasing J , increasing U , and decreasing distance to half-filling. A thorough understanding of the physics of degenerate multi-orbital models is a prerequisite for exploring these effects of orbital selectivity. However, pronounced orbital differentiation is considered to be relevant only for some Hund metals, e.g. for ruthenates. In contrast, for iron-pnictides, it might be less important. In the class of the iron-based HTSCs, only iron chalcogenides are expected to be at the verge of an orbital-selective MIT [46, 61]. Interestingly, many materials with large orbital differentiation are either no superconductors or exhibit only low transition temperatures: indeed, large orbital differentiation is argued to be harmful for superconductivity [46].

2.4. The Hund-metal problem

In principle, three scenarios seem possible to induce strong correlation effects and to lead to the bad-metallic behavior (low Z) in the Hund-metal regime (hatched area in Fig. 1) of a 3HHM also sufficiently far way from any Mott insulating state (black bars in Fig. 1):

- (i) Hundness: sizeable J is the key player to induce strong correlations with considerable electronic mass enhancements.
- (ii) Mottness at $n_d = 2$: the interaction-induced MIT at one charge away from half-filling, $n_d = 2$, triggers the strong correlations (blue arrow in Fig. 1).
- (iii) Mottness at $n_d = 3$: the strong correlations are emanated by the half-filled Mott insulator (red arrow in Fig. 1).

Scenario (i) suggests a new route towards strong correlations: Hundness. Sizeable Hund’s rule coupling, J , leads to the formation of high-spin states and to the suppression of Z . It goes back to Ref. [6] and is supported in various publications [7, 15, 33, 37, 46, 47, 52, 53, 55, 68].

Scenario (ii) is not much discussed in the literature, as $U_c^{(N_c-1)}$ is large while U has moderate values for Hund metals.

Scenario (iii) is motivated by the cuprate picture of doped half-filled Mott-insulators and advocated by several authors [12, 32, 50, 58]. In this scenario the existence of finite J would have a subordinate role in correlating the electrons by lowering $U_{c1}^{(3)}$.

Although all the model calculations cited above confirmed that strong correlation effects dominate the Hund-metal regime of the phase diagram their origin and nature have been under debate even for this toy model until today, either based on different physical interpretations or just on inconsistent terminology. In particular, scenarios (i)-(iii) have been discussed in the context of (D1) the existence of a spin-freezing phase [51], (D2) the “Janus-faced” influence of Hund’s rule coupling [47, 53, 57], and (D3) various proximity effects of the half-filled MIT [32, 50, 58], such as Hund’s-coupling-induced Fermi-liquid instabilities [58]. In this work we will elucidate the role of another very fundamental effect: (D4) spin-orbital separation (SOS) [7, 31, 33]. We will show that the phenomena (D1), (D2), and (D3) are directly connected to (D4). Based on this insight, we will study scenarios (i)-(iii) by revisiting (D1)-(D3) from the perspective of SOS in Sec. 2.7.

(D1) Spin-freezing phase

The so-called spin-freezing phase characterizes the Hund-metal regime in terms of a spin-spin correlation function with an unusually slow (imaginary-time) decay, which does not approach zero but a constant at finite temperature. In this picture, scattering off Hund’s-coupling-induced large composite and very long-lived (or even frozen, static) magnetic moments leads to the incoherent transport behavior.

The spin-freezing scenario was introduced in 2008 in a first (finite-temperature) DMFT study [51] of the n_d - U phase diagram of a degenerate three-band Hubbard-Kanamori model using a Quantum Monte Carlo (QMC) impurity solver. Later it was extended to (realistic) five-band calculations for iron-pnictides [11, 12, 14, 19] (demonstrating the importance of Hund’s rule coupling and electronic correlations for the formation of local moments in the paramagnetic phase [19]) and to models with crystal-field-splitting [66]

and spin-orbit coupling [69]. In 2015 it led to the proposal of a fluctuating-moment-induced spin-triplet superconducting mechanism for strontium ruthenates and uranium compounds [70].

The transition into the Hund-metal regime was first interpreted as a quantum phase transition from a paramagnetic metallic FL phase (at small n_d and/or small U) to an incoherent metallic NFL phase with frozen local moments (at larger n_d and/or larger U) [51]. Since 2011, the existence of a FL ground state (with fully screened local moments) has been anticipated in the Hund-metal regime and has led to the picture of a spin-freezing crossover at finite temperatures – although the complete decay of the imaginary-time spin-spin correlation function to zero has not been explicitly demonstrated until recently [71], because, in general, QMC solvers do not have access to low enough temperatures [14, 53]. However, a new QMC technique using (super) state-sampling [71] was able to show the FL ground state in the spin freezing-phase for fillings up to $n_d = 2.63$.

Spin-freezing has been assumed to originate, in principle, from (i) Hundness. However, similar to Z , the spin-freezing phenomenon is considered to be strongly doping dependent and is very pronounced in the vicinity of the half-filled Mott insulator [51, 70]. Interestingly, the crossover towards spin-freezing near $n_d = N_c - 1$ is characterized by a steep drop of Z as a function of n_d . A detailed quantitative analysis if and how the spin-freezing phenomenon is connected to Z , induced by (i) Hundness and/or influenced by Mottness of kind (ii) or (iii) has not yet been performed. One reason for this is that the mass enhancement could only be computed in an approximate manner because the QMC solver did not reach the FL regime [70]. Further, data was only available on the imaginary Matsubara frequency axis.

(D2) Janus-faced influence of Hund’s rule coupling

The “Janus-faced” influence of Hund’s rule coupling was a major result of a first more detailed DMFT+QMC study of the phase diagram of the degenerate three-band Hubbard-Kanamori model [47, 53, 57] (including a realistic classification of various 3d and 4d transition metal oxides via their mass enhancements). A detailed exploration in terms of the QP weight, Z , revealed that Hund’s coupling induces apparent conflicting tendencies at $n_d = 2$. On the one hand, increasing J promotes metallicity by shifting the critical interaction strength, $U_c^{(2)}$, of the MIT at $n_d = 2$ to higher values. On the other hand, at moderate U , increasing J reduces Z , supporting scenario (i) that Hund’s-coupling-induced strong correlations lead to bad-metallic behavior far from a Mott phase. Together, this Janus-faced behavior results in an interesting MIT for sizeable J upon increasing U that is qualitatively different from the MIT of one-band and multi-band Hubbard models without Hund’s coupling: starting from a weakly correlated metal at small U , the system first evolves into a strongly correlated metal which is stable for an extended range of U values and characterized by very small Z , before it eventually reaches the Mott insulating phase at large $U_c^{(2)}$.

The degenerate three-band study of Refs. [53, 57] was followed by similar analyses for up to five bands, both with [32, 47, 58] and without [58, 60, 63, 72] orbital degeneracy, revealing qualitatively similar behavior as in the three-band case. For degenerate models, Janus-faced behavior emerges for any integer filling away from single and half-filling.

But even for the degenerate three-band model the origin of the Janus-faced behavior has not been fully revealed. Obviously both the QPP itself and the opening of the insulating Mott gap are affected at the same time by changing J . Previous studies [47, 50, 53, 57] quantified these changes by performing a Hubbard-I-type analysis for the gap dependence and by calculating Z to characterize the QPP. However, without access to (reliable) real-frequency spectral data, the Hubbard-I predictions could never be explicitly verified and the physical origin of the low Z could only be speculated about. A connection to the low coherence scale in Hund metals was assumed but never proven, and the nature of the incoherent regime remained unclear. Although considered, a clear connection between spin-freezing and the Janus-faced behavior has not yet been demonstrated. Moreover, we note that the value of Z can have an error of up to 10% in these DMFT+QMC simulations (see supplement of Ref. [53]), also strongly affecting the values of U_c .

We therefore conclude that both scenarios (i) and (ii) should be revisited. In particular, the Janus-faced behavior has to be disentangled by identifying a measure for Mottness (ii) which does not change with J , in order to study the pure effect of Hundness (i), and to analyze the difference in nature between strongly correlated Hund metals at moderate U and strongly-correlated systems close to the MIT. Scenario (iii) will

be considered in the context of (D3).

(D3) *Proximity to the half-filled MIT*

At half-filling, $n_d = 3$, $U_c^{(3)}$ is strongly reduced. The region of low Z in Fig. 1 directly starts at the border of the MIT at $n_d = 3$ and extends, even at moderate U , from there to $n_d = 2$ with Z slightly increasing when passing from $n_d = 3$ to $n_d = 2$. Such a filling-dependence is observed in simulations and experiments of iron-based superconductors: their correlations are enhanced with hole-doping (i.e. approaching half-filling) [19, 27, 65, 73, 74]. Furthermore, also the spin-freezing phenomenon [51] is strongly doping dependent: the spin freezing phase occurs in the vicinity of the half-filled MIT.

Motivated by this behavior it has been argued in Refs. [32, 50, 58] that the suppression of Z around $n_d = 2$ at moderate U is connected to the MIT at half-filling, $n_d = 3$. In particular, the effect of suppressing intra-orbital double occupancy by J has been regarded as a direct link to the MIT at $n_d = 3$ [32]. However, it has been noted that in contrast to the one-band Hubbard model, the reduction of Z in Hund metals does not imply the general suppression of charge fluctuations (far from the MIT, as shown in Ref. [37]) and Z is thus not a good measure for the latter: the origin of low Z and its filling dependence is subtle. Again, DMFT+NRG real frequency data can help to further investigate this issue by complementing the slave-boson approaches of Refs. [32, 50] and quantitatively revealing the connection between spin-freezing and Z .

We note that for non-degenerate models, low Z is argued to be induced by the ‘‘proximity to a half-filled MIT’’, as well, but here, the half-filled MIT denotes an orbital selective Mott transition: when an orbital is individually half-filled it can become insulating, independently of the other orbitals [65]. This orbital decoupling effect is enhanced by Hund’s coupling, but will not be discussed further in this work.

In a slave-boson study [58] of degenerate and non-degenerate multi-band Hund models, a zone of negative compressibility, $\kappa_{\text{el}} = \frac{\partial n_d}{\partial \mu} < 0$, is observed at zero temperature for nonzero J in the n_d - U phase diagram, above $U \geq U_c$, reaching (depending on N_c) from half-filling towards $n_d = N_c + 1$. The transition from $\kappa_{\text{el}} > 0$ to $\kappa_{\text{el}} < 0$ is realized through a divergence of the compressibility, which occurs in the phase diagram together with a strong reduction in Z . In the absence of symmetry breaking in the model, this divergence is interpreted as a genuine thermodynamic Hund’s-coupling-induced instability towards a phase separation. The enhancement of κ_{el} has even been argued to be directly connected to the enhanced critical T_c of HTCS [57–59, 64]. This strong statement of a negative compressibility is solely the result of slave-boson approaches (rotationally invariant form of the Kotliar-Ruckenstein slave-bosons for the full Hubbard-Kanamori model involving two bands, and slave-spin mean-field approximation for the Hubbard-Kanamori model without spin flip and pair hopping term involving up to five bands). It has so far not been validated by another (zero-temperature) method.

In order to investigate if the suppression of Z in the Hund-metal regime is mediated by the MIT at half-filling and to check if a negative compressibility is a generic Hund’s-coupling-induced effect (i.e. independent of details of the model and the method), we will also study scenario (iii), the effect of the MIT at $n_d = 3$ on Z and κ_{el} .

(D4) *Spin-orbital separation (SOS)*

Besides the phenomena (D1), (D2), and (D3), also a Hund’s-coupling-induced coherence-incoherence crossover with increasing temperature has been discussed as a new and generic normal state property of Hund metals in the literature [6, 7]. Further an incoherent frequency regime with anomalous power-law exponents in the Matsubara self-energy was revealed for $1.5 \lesssim n_d \lesssim 2.5$, which is most pronounced at $n_d = 2$ [7, 51]. The incoherent temperature and frequency regime was proposed to be induced by two degrees of freedom that behave in different ways: the orbital degrees of freedom are quenched and fluctuate very rapidly while the spin degrees of freedom are unquenched and fluctuate albeit slowly (accordingly the local spin susceptibility has Curie-Weiss form and a large static value) [7, 37]. An analytic RG analysis in the Kondo regime [31] provided a simple understanding of the origin of the incoherent regime and established how the Kondo scales depend on the representations of the spin and orbital operators.

However, still, several issues needed to be clarified: in particular, the DMFT+QMC calculations could not reach sufficiently low temperatures to fully reveal the FL phase. To settle this issue, zero- (and finite-)

temperature, real-frequency DMFT+NRG calculations were performed in 2015 in Ref. [33] for the 3HHM of Eq.(1) at $n_d = 2$. These calculations clearly confirmed that, at zero temperature, finite Hund’s coupling leads to SOS [see Fig. 13(a)] – a two-stage screening process, in which orbital screening occurs at much higher energies than spin screening – thus strongly reducing the coherence scale below which a FL ground state is formed. Importantly, at intermediate energies above the coherence scale, a broad incoherent regime opens up involving screened, delocalized orbitals which are non-trivially coupled to almost unscreened, large, localized spins. The incoherent frequency regime is strongly particle-hole asymmetric and displays approximate power-law behavior in the self-energy for positive real frequencies only, leading to apparent fractional power laws on the imaginary Matsubara axis. SOS also occurs in pure impurity calculations without DMFT self-consistency. With increasing temperature, SOS in frequency space translates to a coherence-incoherence crossover for temperature-dependent quantities. Only recently, this two-stage crossover was confirmed in realistic DFT+DMFT+QMC simulations of the temperature dependence of the thermopower, entropy [55] and the local spin and orbital susceptibilities [37] for Sr_2RuO_4 . SOS is thus considered to be relevant not only for degenerated toy models but also for realistic Hund materials featuring tetragonal crystal-field splitting of the t_{2g} orbitals.

However, in Ref. [33] SOS was studied only at $n_d = 2$ for a small set of parameters U and J , which (as will be shown in Fig. 6) lie at the border of the coexistence region of the phase diagram, thus close to the MIT. Therefore many open questions remained: Is SOS a generic phenomenon of Hund metals? Where does it occur in the phase diagram and how is it influenced by J and the proximity to the MIT at $n_d = 2$ and $n_d = 3$? How is it connected to the phenomena of (D1)-(D3) and how to the low Z in the Hund-metal regime? And most importantly, what is the origin of SOS, scenario (i), (ii), or (iii), or a combination of these?

2.5. Aim of this paper

The aim of this work is to identify the origin of strong correlations in the Hund-metal regime of the 3HHM, based on real-frequency data, and to develop from this a global, unified and consistent scenario for strong correlation effects in Hund metals. For this we study scenarios (i)-(iii), i.e. “Hundness versus Mottness”, by scanning the full phase diagram of the 3HHM at zero temperature, using DMFT+NRG. In DMFT the lattice model (the 3HHM) is mapped self-consistently onto a quantum impurity model [the Anderson-Hund model (AHM) of Eq. (A.1)], which we solve with NRG, a powerful *real-frequency* multi-band impurity solver. NRG is well suited for the investigation of Hund and Mott physics as it both reveals the spectral properties of Hund metals down to its very low coherence scales and still captures the main features of the Hubbard side bands. We thus provide, for the first time, detailed and *unbiased* real-frequency spectral data in a large parameter space of the phase diagram instead of only measuring the strength of strong correlations by analyzing the behavior of Z , as done in previous studies [32, 47, 53, 57]. This allows us to reveal the origin of those correlations and the physical nature of the incoherent regime in Hund metals.

The paper is structured as follows. In Sec. 2.6 we give a detailed description of our model and discuss its local multiplet level structure at $n_d = 2$ (in particular its dependency on J) and at $n_d = 3$. The DMFT+NRG method is introduced in Appendix A. In Sec. 2.7 we present our main insights: we will show that the low Z in the Hund-metal regime results directly from the suppression of the coherence scale due to SOS. SOS therefore forms the basis of our main study and scenarios (i)-(iii) will be investigated from that perspective. In particular, we follow a three-fold approach in Sec. 2.7. We revisit (D1) the spin-freezing phase in Sec. 3, (D2) the Janus-faced influence of Hund’s rule coupling in Sec. 4, and the influence of (D3) the MIT at half-filling in Sec. 5, and explain these aspects step by step within the SOS framework.

2.6. Model and Methods

For our 3HHM we use the Hamiltonian of Refs. [7, 31, 33, 37] in the form

$$\hat{H}_{\text{HHM}} = \sum_i \left(-\mu \hat{n}_i + \hat{H}_{\text{int}}[\hat{d}_{i\nu}^\dagger] \right) + \sum_{\langle ij \rangle \nu} t \hat{d}_{i\nu}^\dagger \hat{d}_{j\nu}, \quad (1a)$$

$$\begin{aligned} \hat{H}_{\text{int}}[\hat{d}_{i\nu}^\dagger] &= U \sum_{\langle m \rangle} \hat{n}_{im\uparrow}^\dagger \hat{n}_{im\downarrow} + (U - J) \sum_{m \neq m'} \hat{n}_{im\uparrow}^\dagger \hat{n}_{im'\downarrow} + (U - 2J) \sum_{m < m', \sigma} \hat{n}_{im\sigma}^\dagger \hat{n}_{im'\sigma} \\ &- J \sum_{m \neq m'} \hat{d}_{im\uparrow}^\dagger \hat{d}_{im\downarrow} \hat{d}_{im'\downarrow}^\dagger \hat{d}_{im'\uparrow} \end{aligned} \quad (1b)$$

$$= \frac{1}{2} \underbrace{\left(U - \frac{3}{2}J \right)}_{\equiv \bar{U}} \hat{n}_i (\hat{n}_i - 1) - J \hat{\mathbf{S}}_i^2 + \frac{3}{4} J \hat{n}_i. \quad (1c)$$

This is a minimal version of the generalized Kanamori Hamiltonian of Ref. [47], with $U(1)_{\text{ch}} \times \text{SU}(2)_{\text{sp}} \times \text{SU}(3)_{\text{orb}}$ symmetry for its charge (ch), spin (sp) and orbital (orb) degrees of freedom. $\hat{d}_{i\nu}^\dagger$ creates an electron on site i of flavor (fl) $\nu = (m\sigma)$, which is composed of a spin ($\sigma = \uparrow, \downarrow$) and an orbital ($m = 1, 2, 3$) index. $\hat{n}_{i\nu} \equiv \hat{d}_{i\nu}^\dagger \hat{d}_{i\nu}$ counts the electrons of flavor ν on site i . $\hat{n}_i \equiv \sum_\nu \hat{n}_{i\nu}$ is the total number operator for site i with $n_d \equiv \langle \hat{n}_i \rangle$, and $\hat{\mathbf{S}}_i$ its total spin, with components $\hat{S}_i^\alpha = \sum_{m\sigma\sigma'} \hat{d}_{im\sigma}^\dagger \frac{1}{2} \sigma_{\sigma\sigma'}^\alpha \hat{d}_{im\sigma'}$, where σ^α are Pauli matrices. We study a Bethe lattice with degenerate bands, each of bandwidth $W = 4t$, i.e we assume negligible crystal field splitting and a uniform hopping amplitude t restricted to nearest-neighbor hopping between the same kind of orbital and spin degrees of freedom. Both the chemical potential μ and the hopping amplitude t are then equal for all flavors, leading to a locally $\text{SU}(6)_{\text{fl}}$ symmetric kinetic term in Eq. (1a). $t = 1$ serves as energy unit.

The onsite interaction term, \hat{H}_{int} , incorporates Hund's rule and Mott physics in its most basic form and reduces the symmetry to $\text{SU}(2)_{\text{sp}} \times \text{SU}(3)_{\text{orb}}$ for $J > 0$. It was first introduced by Dworin and Narath in a generalization of the Anderson impurity model to study magnetic impurities [75]. The first three terms of Eq. (1b) are density-density interactions. U is the intraorbital Coulomb interaction between electrons with opposite spins in the same orbital, $U - J < U$ the interorbital Coulomb interaction between electrons with opposite spins in different orbitals, and $U - 2J$ the Coulomb interaction between electrons with parallel spins in different orbitals, where the interorbital Coulomb interaction is further reduced by the ferromagnetic coupling J due to Hund's first rule that favors the alignment of spins. The last term of Eq. (1b) is a spin exchange term.

The generalized Kanamori Hamiltonian of Ref. [47] involves some additional terms not present in Eq. (1), which reduce the $\text{SU}(3)_{\text{orb}}$ symmetry in the orbital sector to $\text{SO}(3)_{\text{orb}}$. However, these additional terms do not affect the low-energy physics, since they are irrelevant in a renormalization group sense [76].

Eq. (1c) is a more compact notation of Eq. (1b) and summarizes the two main aspects of our model. The first term is known to trigger Mott physics, whereby U penalizes double occupancy of orbitals. The second term directly reflects Hund's first rule: it favors a large spin per site for $J > 0$. Note that the third term only shifts the chemical potential, μ .

We choose μ such that we obtain a total filling per lattice site, $n_d = \langle \hat{n}_i \rangle$, of $1 \leq n_d \leq 3$. For $n_d > 1$, Hund's first rule reduces the atomic ground state degeneracy and thus strongly influences the physics of the system. The orbital and spin degrees of freedom of electrons can show very distinct behavior and conspire in a highly non-trivial way, leading to striking new phenomena like spin-orbital separation [33]. In contrast, at half-filling, $n_d = 3$, a fundamentally different ground state emerges: a large spin state is formed and orbital degrees of freedom are fully blocked [47].

We treat the 3HHM of Eq. (1) with single-site DMFT and use full-density-matrix (fdm)NRG [34] as real-frequency impurity solver. For methodological details and further definitions of physical quantities used in the main paper, see Appendix A.

2.6.1. Multiplet structure at filling $n_d = 2$

The physical behavior of the system depends in a crucial manner on the multiplet structure of the local Hamiltonian, and can change in dramatic ways when parameters are tuned such that level crossings occur [77]. This section is therefore devoted to a detailed discussion of this multiplet structure.

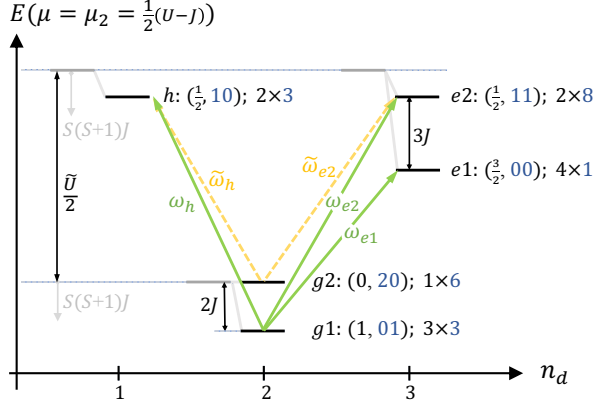


Figure 2: Local multiplet structure of a single 3HHM site at filling $n_d = 2$ using $\mu = \mu_2$, with $\tilde{U} \equiv U - \frac{3}{2}J$ as specified in Eq. (2). The energies for $J = 0$ are indicated by the thick grey levels, which are split when turning on J as indicated. The individual multiplets are given labels g for “ground state”, h for hole-like, and e for electron (particle) like, which are specific to the current filling, here $n_d = 2$. Each multiplet is followed by its symmetry labels (S, q) and the combined multiplet dimension of spin times $SU(3)$, with the $SU(2)$ spin S and $SU(3)$ representation $q \equiv (q_1, q_2) \equiv (q_1 q_2)$. The grey downward arrows indicate a lowering of the energy levels by the Hund’s term $-J\hat{S}_i^2$. The shown multiplet structure is complete for $n_d = 1, 2, 3$. Together with the vacuum state at $n_d = 0$ and the symmetry relative to half-filling, this yields a total number of states (relative to $n_d = 0, 6$ and $1, 5$ and $2, 4$ and 3) of $2 \cdot (1 \times 1) + 2 \cdot (2 \times 3) + 2 \cdot (1 \times 6 + 3 \times 3) + 1 \cdot (2 \times 8 + 4 \times 1) = 64 = 4^3$, i.e. the complete state space of three spinful fermionic levels. Note that 1-particle excitations from $g2$ (yellow lines) cannot reach the $S = \frac{3}{2}$ multiplet $e1$.

The local Hamiltonian of a single site i is given by $\hat{H}_{\text{loc}}^{(i)} \equiv \hat{H}_{\text{int}}[d_{i\nu}^\dagger] - \mu \hat{n}_i$. With focus on the specific filling $n_d = 2$, this Hamiltonian can be written as

$$\hat{H}_{\text{loc}}^{(i)} = \frac{\tilde{U}}{2}(\hat{n}_i - 2)^2 - J\hat{S}_i^2 - \underbrace{(\mu - \mu_2)}_{\equiv \delta\mu_2} \hat{n}_i - 2\tilde{U}. \quad (2)$$

with $\mu_2 \equiv \frac{3}{2}(U - J)$. Here the Coulomb interaction in the first term on the r.h.s. has been written such that for $\mu = \mu_2$, i.e. $\delta\mu = 0$ and small J , this Hamiltonian clearly favors the desired filling of $n_d = 2$. By writing the local states space in terms of symmetry multiplets, the above Hamiltonian reduces to one-dimensional multiplet blocks and hence already becomes diagonal. The symmetry labels of $SU(3)$ follow the Dynkin convention where the irreducible representation $q = (q_1, q_2) \equiv (q_1 q_2)$ corresponds to a Young diagram with $q_1 + q_2$ (q_2) boxes in its first (second) row.

For the case $\mu = \mu_2$, the multiplet structure of the local Hamiltonian in Eq. (2) is sketched in Fig. 2. There the two low-energy multiplets at $n_d = 2$ are labeled by $g1$ and $g2$, also referred to as the g -levels. The actual ground state multiplet $g1$ is in triplet configuration across two out of the three orbitals. The singlet configuration $g2$, split off by an energy $2J$, also includes the pair singlets within a single orbital. This therefore results in a total of $d_{g2} = 6$ symmetric states described by the single irreducible multiplet $q = (20)$. By removing an electron, this leads to the hole-like level, denoted by h . It contains just one electron, $n_d = 1$, which can be in any spin and orbital, hence $S = \frac{1}{2}$ and the defining representation $q = (10)$. Conversely, by adding a particle to the g -multiplets, one obtains half-filling $n_d = 3$. This allows states with one particle per orbital, resulting in one $S = \frac{3}{2}$ multiplet, labeled $e1$ with $(S, q) = (\frac{3}{2}, 00)$, and two $S = \frac{1}{2}$ multiplets. By symmetry, the latter ones need to be grouped with the six $S = \frac{1}{2}$ multiplets with a double and a singly occupied orbital into the single $SU(3)$ multiplet $q = (11)$ with 8 states total, forming the single multiplet $e2$.

In what follows, we now slightly alter the chemical potential towards finite $\delta\mu_2$ in Eq. (2), using the specific choice $\delta\mu_2 = -\frac{3J}{2}$. This raises the e -levels in Fig. 2 and lowers the h -level by equal amounts relative to the g -levels at $n_d = 2$, to the extent that level h and $e1$ become aligned, i.e. degenerate. This simplified setting is the reason for our choice of $\delta\mu_2$.

The resulting excitation energies from the ground state multiplet $g1$ can be simply determined from

Fig. 2 while also accounting for the plain shift due to $\delta\mu_2$ in Eq. (2),

$$\begin{aligned}
\circ & \quad \omega_{e1}^{(2)} \equiv +(E_{e1} - E_{g1}) = \frac{U}{2} - J, \\
+ & \quad \omega_{e2}^{(2)} \equiv +(E_{e2} - E_{g1}) = \frac{U}{2} + 2J, \\
\triangle & \quad \omega_h^{(2)} \equiv -(E_h - E_{g1}) = -\omega_{e1}^{(2)},
\end{aligned} \tag{3a}$$

where we added the superscript (2) to these transition frequencies for later reference to emphasize the current setting of having $n_d = 2$ (this filling is implicit for the g -, e -, and h -multiplet labels in the present discussion, for readability). The signs in Eqs. (3a) are taken in consistency with the definition of the spectral function $A(\omega)$, and is thus opposite for particle- and hole-like excitations. The symbols to the left will be used in Sec. 4 and Sec. 5 to mark the positions of the multiplet excitation energies in the spectral function $A(\omega)$.

Similarly, also the transition energies w.r.t. level $g2$ are simply derived from Fig. 2,

$$\begin{aligned}
+ & \quad \tilde{\omega}_{e2}^{(2)} \equiv +(E_{e2} - E_{g2}) = \omega_{e2}^{(2)} - 2J = \frac{U}{2}, \\
\triangle & \quad \tilde{\omega}_h^{(2)} \equiv -(E_h - E_{g2}) = \omega_h^{(2)} + 2J = -(\frac{U}{2} - 3J),
\end{aligned} \tag{3b}$$

where we note that the transition $\tilde{\omega}_{e1}^{(2)} = -\tilde{\omega}_h^{(2)}$ is forbidden for 1-particle spin-half excitation processes.

The above picture of well-separated ground-state multiplets breaks down entirely, once $\omega_{e1}^{(2)}$ in Eqs. (3a) becomes negative, i.e. levels h and $e1$ cross $g1$ as the new ground state. Hence we will mostly constrain our discussion to the regime $J/U < 0.5$. This regime, nevertheless, already reaches up to extraordinarily large Hund's coupling from a materials point of view where one typically encounters $J/U \lesssim 0.2$ [47].

For $J \ll U$, the g -levels are typically considered well-separated from the e - and h -levels. However, this picture already breaks down earlier, namely once the degenerate $e1$ - and h -levels pass across $g2$. According to the excitation energies in Eqs. (3b), this occurs at $\tilde{\omega}_h^{(2)} = 0$ which defines the crossover energy scale $J^* \equiv \frac{U}{6}$. The regime $J \gtrsim J^*$ quantifies what we mean by *sizeable* Hund's coupling in the 3HHM at $n_d = 2$. There for $J \gtrsim J^*$, we expect a qualitative change in the emerging physics of the 3HHM.

2.6.2. Multiplet structure at filling $n_d = 3$

We now focus on the filling $n_d = 3$ with the Hamiltonian

$$\hat{H}_{\text{loc}}^{(i)} = \frac{\tilde{U}}{2}(\hat{n}_i - 3)^2 - J\hat{S}_i^2 - \underbrace{(\mu - \mu_3)}_{\equiv \delta\mu_3} \hat{n}_i - \frac{9}{2}\tilde{U} \tag{4}$$

and $\mu_3 \equiv \frac{5}{2}U - 3J$. By construction, $\mu = \mu_3$, i.e. $\delta\mu_3 = 0$ directly leads to a particle-hole symmetric excitation spectrum, and therefore to exact half-filling at $n_d = 3$. The multiplets in Fig. 2 are shifted relative to each other for different n_d such that $n_d = 3$ becomes the new ground state symmetry sector with the lowest energy excitations in $n_d = 2$ and 4 split off symmetrically by $\tilde{U}/2$ at $J = 0$. Hence the g - and e -multiplets in the previous discussion for $n_d = 2$ as in Fig. 2 acquire the new respective labels h and g here at $n_d = 3$.

In the following we only focus on the case of sizeable J , and there, for simplicity, only on the lowest levels h , g , and e at $n_d = 2, 3, 4$, respectively. The level g has maximal spin $S = 3/2$ linked with an orbital singlet configuration $q = (00)$ [level $e1$ in Fig. 2]. The lowest hole level h at $n_d = 2$ has $(S, q) = (1, 01)$ [i.e. level $g1$ in Fig. 2]. The lowest particle level e at $n_d = 4$ is given by $(S, q) = (1, 10)$, i.e. the particle-hole transformed level h .

The excitation energies from the ground state multiplet g at $\mu = \mu_3$ can be simply determined from Eq. (4), analogous to Eq. (3a),

$$\begin{aligned}
* & \quad \omega_e^{(3)} \equiv +(E_e - E_g) = \frac{U}{2} + J, \\
\diamond & \quad \omega_h^{(3)} \equiv -(E_h - E_g) = -\omega_e^{(3)},
\end{aligned} \tag{5}$$

where the reference point of a filling of $n_d = 3$ is implied, yet also explicitly indicated with the superscript in the transition frequencies. We will refer to them in Sec. 5.

2.7. Overview of Results

In the following three sections we present our real-frequency-based DMFT+NRG results for the 3HHM. In Sec. 3 we reveal the connection between SOS and spin-freezing. We argue that while both terminologies describe in principle the same Hund physics, the latter term has the drawback that it was proposed based on QMC results that did not account for a Fermi-liquid ground state. In Sec. 4 we study the U - J -phase diagram at $n_d = 2$ and systematically disentangle the Janus-faced effects of (i) Hundness and (ii) Mottness. Thereby we quantitatively explain the existence of the low QP weight, Z , by SOS, which is revealed to occur in the whole metallic regime, but at different scales. We explain the difference between Hund- and Mott-correlated systems. In particular, we show that sizeable J leads to low Z also far away from the MIT at $n_d = 2$ and opens up a *large* incoherent frequency regime where intriguing Hund-correlated physics occurs: large, almost unscreened spins are coupled to screened orbital degrees of freedom. In Sec. 5, we study the doping-dependence of Z and the compressibility, κ_{el} . We demonstrate that, in principle, SOS also occurs and determines the low Z behavior at intermediate fillings, $1 < n_d < 3$. We give evidence that SOS is generically based on a two-stage screening process involving the formation and the full screening of effective $3/2$ spins. The details of this process, however, vary with filling. κ_{el} is shown to be positive at finite J for all fillings and values of U , that we have studied. Thus we assume that no Hund's-coupling-induced instabilities emerge in the system.

Overall, we scan the parameter space of the phase diagram in two orthogonal directions (indicated by the arrows in Fig. 1): we either vary n_d (along the horizontal direction of the red arrow) for different parameter sets of U and J as in Sec. 3 and Sec. 5, or we vary U (along the vertical direction of the blue arrow) and J for fixed $n_d = 2$ as in Sec. 4.

To summarize, we will develop a global picture of spin-orbital separation that strongly supports (i) Hundness as a new mechanism towards strong correlations in the normal state of Hund metals.

3. Spin-freezing and spin-orbital separation - two terminologies for the same Hund physics

To set the scene, we first revisit SOS [33] and explain its connection to the spin-freezing theory introduced in 2008 in a finite-temperature DMFT+QMC study [51] of the n_d - U phase diagram of a degenerate three-band Hund model.

3.1. Spin-orbital separation at $n_d = 2$ revisited

We calculate the dynamical real-frequency spin and orbital susceptibilities

$$\chi_{\text{sp}} = \frac{1}{3} \sum_{\alpha} \langle \hat{S}^{\alpha} \| \hat{S}^{\alpha} \rangle_{\omega}, \quad (6a)$$

$$\chi_{\text{orb}} = \frac{1}{8} \sum_a \langle \hat{T}^a \| \hat{T}^a \rangle_{\omega}, \quad (6b)$$

respectively, where $\hat{T}^a = \sum_{mm'\sigma} \hat{d}_{m\sigma}^{\dagger} \frac{1}{2} \tau_{mm'}^a \hat{d}_{m'\sigma}$ are the impurity orbital operators with the SU(3) Gell-Mann matrices, τ^a , normalized as $\text{Tr}[\tau^a \tau^b] = 2\delta_{ab}$.

Fig. 3(a) depicts the zero-temperature results of the imaginary parts, $\chi''(\omega) \equiv -\frac{1}{\pi} \text{Im} \chi(\omega)$, of the dynamical impurity orbital (dashed curve) and spin (solid curve) susceptibilities for $U = 5$, $J = 1$ and a filling of $n_d = 2$. The filled circle and the open square mark the orbital and spin Kondo scales, $T_{\text{K}}^{\text{orb}}$ and T_{K}^{sp} , which are defined as the peak positions of χ''_{orb} and χ''_{sp} , respectively. Clearly, these two energy scales are very distinct: in Fig. 3(a) we revisit the central result of our DMFT+NRG study of the 3CAHM – *spin-orbital separation* [see Fig. (3c) in Ref. [33] and also Fig. 13]. *Orbital screening sets in at much higher energies than spin screening, $T_{\text{K}}^{\text{orb}} \gg T_{\text{K}}^{\text{sp}}$, opening a non-trivial intermediate NFL regime exhibiting “Hund metal physics”: slowly fluctuating (not frozen), Hund's-coupling-induced large spins are coupled to screened orbital degrees of freedom.* The existence of large, composite spins which are only poorly screened, manifests itself in an enhancement of χ''_{sp} with decreasing frequencies. Interestingly, the fluctuations of these spins influence the physics of the screened orbitals, leading to an intriguing interplay of spin and orbital degrees of freedom:

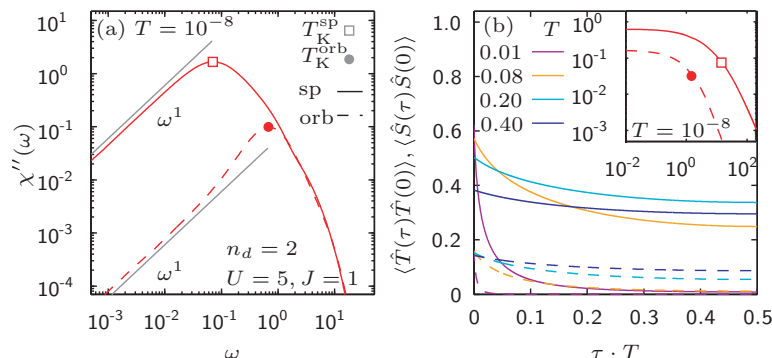


Figure 3: (a) The imaginary part of the dynamical real-frequency orbital χ''_{orb} (dashed) and spin χ''_{sp} (solid) susceptibility for $U = 5$, $J = 1$, $n_d = 2$ and $T = 0$. The orbital Kondo scale $T_{\text{K}}^{\text{orb}}$ (filled circle) and the spin Kondo scale T_{K}^{sp} (open square) are defined as the peak positions of χ''_{orb} and χ''_{sp} , respectively, and show SOS, i.e. $T_{\text{K}}^{\text{orb}} \gg T_{\text{K}}^{\text{sp}}$. Grey guide-to-the-eye lines indicate Fermi-liquid power laws. (b) The imaginary-time impurity orbital-orbital $\langle \hat{T}(\tau)\hat{T}(0) \rangle$ (dashed) and spin-spin $\langle \hat{S}(\tau)\hat{S}(0) \rangle$ (solid) correlator plotted as a function of the rescaled imaginary time $\tau \cdot T$ for the same parameters as in (a), but at different temperatures. The solid yellow and blue curves show spin-freezing: $\langle \hat{S}(\tau)\hat{S}(0) \rangle$ approach large constant values at times $\tau = 1/(2T)$. The inset shows the zero-temperature results of $\langle \hat{T}(\tau)\hat{T}(0) \rangle$ (dashed) and $\langle \hat{S}(\tau)\hat{S}(0) \rangle$ (solid) calculated from (a) the real-frequency susceptibilities. Both approach zero in the FL regime at very large imaginary times. The open square mark $1/T_{\text{K}}^{\text{orb}}$ and $1/T_{\text{K}}^{\text{sp}}$, respectively.

below $T_{\text{K}}^{\text{orb}}$, χ''_{orb} decreases as the frequency is lowered, indicating the screening of the orbital degrees of freedom. However, for $\omega > T_{\text{K}}^{\text{sp}}$, χ''_{orb} does not follow FL scaling, as the orbital degrees of freedom still “feel” the slowly fluctuating, large local moments. Below the very small, Hund’s-coupling-reduced coherence scale, $T_{\text{K}}^{\text{sp}} \approx 0.072$, both the spin and orbital degrees of freedom get fully screened and FL behavior is restored [$\chi''_{\text{orb}}(\omega) \propto \omega$ and $\chi''_{\text{sp}}(\omega) \propto \omega$, see Fig. 3(a), grey lines].

From the real-frequency orbital and spin susceptibility we also calculate the imaginary-time impurity orbital-orbital and spin-spin correlators,

$$\begin{aligned} \langle \hat{T}(\tau)\hat{T}(0) \rangle &\equiv \frac{1}{8} \langle \hat{\mathbf{T}}(\tau) \cdot \hat{\mathbf{T}}(0) \rangle = \int d\omega n_B(\omega) \chi''_{\text{orb}}(\omega) e^{\omega\tau}, \\ \langle \hat{S}(\tau)\hat{S}(0) \rangle &\equiv \frac{1}{3} \langle \hat{\mathbf{S}}(\tau) \cdot \hat{\mathbf{S}}(0) \rangle = \int d\omega n_B(\omega) \chi''_{\text{sp}}(\omega) e^{\omega\tau}, \end{aligned} \quad (7)$$

respectively, with the Bose-Einstein distribution $n_B(\omega) = 1/(e^{\beta\omega} - 1)$. In the inset of Fig. 3(b) we plot both correlators for zero temperature and the same parameters as in Fig. 3(a). In accordance with the real-frequency susceptibilities, the orbital-orbital correlator (dashed curve) is much smaller than the spin-spin correlator (solid curve). The latter approaches zero rather slowly, thus, the FL regime is only reached at very long imaginary times, $\tau > 100$.

3.2. Spin-freezing at $n_d = 2$

In order to understand the connection of SOS and the spin-freezing phenomenon that was based on *finite*-temperature DMFT+QMC [51] data, we have performed similar calculations at higher temperatures [see Fig. 3(b)]. For temperatures well below the FL coherence scale, $T < T_{\text{K}}^{\text{sp}}$, $\langle \hat{S}(\tau)\hat{S}(0) \rangle$ decays to zero on the scale $\tau = 1/(2T)$ (solid purple curve). For $T_{\text{K}}^{\text{orb}} \geq T \geq T_{\text{K}}^{\text{sp}}$, in contrast, $\langle \hat{S}(\tau)\hat{S}(0) \rangle$ approaches a large constant value at times $\tau \approx 1/(2T)$ (solid yellow and blue curves). This finite-temperature finding – a spin-spin correlation function which does not decay to zero at long times – was called “spin freezing” in Ref. [51] and interpreted as the existence of *frozen* local moments leading to an incoherent metallic state.

As exemplified in Fig. 3 (a,b) and further demonstrated in this work, spin freezing was a phenomenological interpretation of the spin-spin correlator based on a QMC solver that didn’t reach low enough temperatures

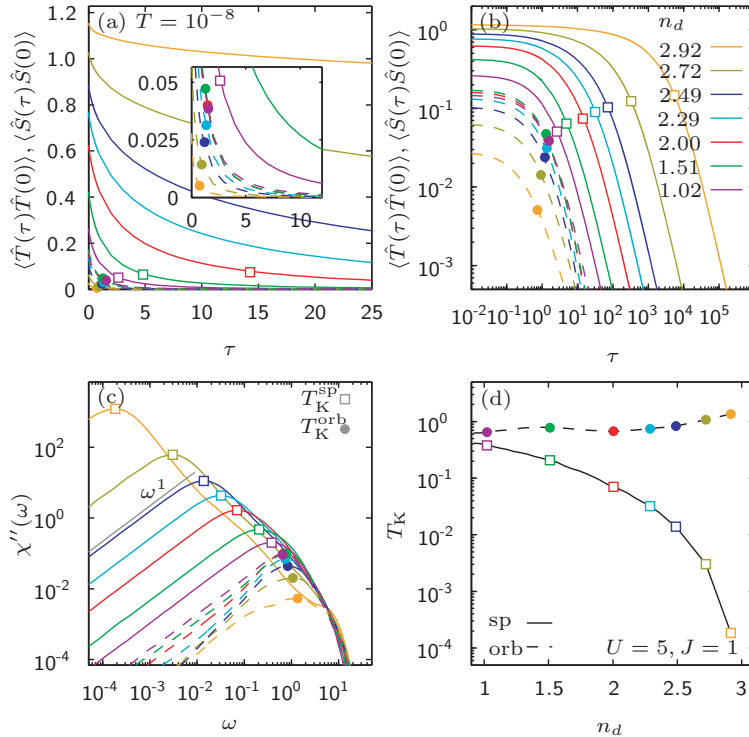


Figure 4: (a,b) The imaginary-time impurity orbital-orbital $\langle \hat{T}(\tau)\hat{T}(0) \rangle$ (dashed) and spin-spin $\langle \hat{S}(\tau)\hat{S}(0) \rangle$ (solid) correlators calculated from (c) the real-frequency susceptibilities for $U = 5, J = 1$, and $T = 0$ at various fillings n_d . The filled circles and the open squares mark $1/T_{\text{K}}^{\text{orb}}$ and $1/T_{\text{K}}^{\text{sp}}$, respectively. The inset in (a) shows a zoom to better resolve the orbital-orbital correlators. (a) For short imaginary times, the curves for $\langle \hat{S}(\tau)\hat{S}(0) \rangle$ seem to remain constant, a phenomenon which was interpreted as spin-freezing in Ref. [51]. (b) In contrast, for large imaginary times, they clearly show FL behavior. (c) The imaginary parts of the dynamical real-frequency orbital χ''_{orb} (dashed) and spin χ''_{sp} (solid) susceptibilities. The orbital Kondo scales $T_{\text{K}}^{\text{orb}}$ and the spin Kondo scales T_{K}^{sp} are marked as filled circles and open squares, respectively. (d) The orbital Kondo scales $T_{\text{K}}^{\text{orb}}$ (dashed line with filled circles) and spin Kondo scales T_{K}^{sp} (solid line with open squares) plotted versus the filling n_d . SOS is revealed for all $1 < n_d < 3$.

(or equivalently long enough times) to reveal the FL ground state for many parameters in the phase space. However, *the spins are not frozen, they fluctuate slowly above T_{K}^{sp} and get fully screened in the FL regime below T_{K}^{sp} .*

Moreover, a detailed analysis of $\langle \hat{T}(\tau)\hat{T}(0) \rangle$ at $n_d = 2$ in Fig. 3(b) shows that the orbital-orbital correlators (dashed yellow and dashed light and dark blue curves) do not fully decay to zero in the incoherent temperature regime $T > T_{\text{K}}^{\text{sp}}$, but remain finite, as well (as opposed to the statement in Ref. [51]). This finding supports the interpretation obtained from the real-frequency orbital susceptibility and further revises the spin-freezing picture: *the orbital degrees of freedom are screened below $T < T_{\text{K}}^{\text{orb}}$, but they are not fully decoupled from the spin dynamics.*

3.3. Spin-freezing for varying n_d

Originally, without access to the FL ground state, it was argued that the Hund-metal regime of the phase diagram in Fig. 1 is a spin-freezing NFL phase and that a quantum phase transition connects a paramagnetic FL phase (at small n_d and small U) and a paramagnetic NFL phase featuring frozen local moments (at larger n_d and larger U) [51].

In Fig. 4 we revisit this transition with our NRG solver at $T = 0$. We calculate the imaginary-time orbital-orbital and spin-spin correlators for intermediate $U = 5$, $J = 1$ and vary n_d from 1.02 to 2.92. Indeed, at short times, $\tau \lesssim 25$, our DMFT+NRG results in Fig. 4(a) seem to confirm this FL-to-NFL transition. For $n_d < 2$, $\langle \hat{S}(\tau)\hat{S}(0) \rangle$ decays to zero (solid purple and green curves) while at larger n_d it grows and remains finite (solid red to yellow curves), seemingly indicating frozen local moments.

However, in contrast to QMC solvers, we have direct access to exponentially long times (low temperatures) and can explicitly reveal the existence of a FL ground state for any given filling. In Fig. 4(b) we confirm that for sufficiently long times, $\tau \gg 1/T_K^{\text{sp}}$, $\langle \hat{S}(\tau)\hat{S}(0) \rangle$ approaches zero for all fillings, $1 < n_d < 3$ (solid curves). Equivalently, all real-frequency spin susceptibilities exhibit FL behavior below T_K^{sp} [$\chi''_{\text{sp}}(\omega) \propto \omega$, see Fig. 4(c), grey line]. Clearly, the NFL regime is not governed by the proximity to a quantum critical point.

The general existence of a FL ground state for all fillings was later conjectured [14, 53, 70] and only recently demonstrated [71] based on DMFT+QMC Hund-model studies, and spin freezing was reinterpreted as the existence of long-lived magnetic moments. Instead of a quantum phase transition, a “spin-freezing crossover” from a FL to a NFL state at finite temperatures was suggested [70] (which is called “coherence-incoherence crossover” by others [6, 7, 33]). The present work demonstrates directly and completely that *the time-dependence of orbital-orbital and spin-spin correlation functions reveal FL behavior in the long-time limit for all fillings $1 < n_d < 3$.*

3.4. Spin-orbital separation for varying n_d

Interestingly, we observe in Fig. 4 that *SOS*, i.e. $T_K^{\text{orb}} \gg T_K^{\text{sp}}$, occurs at all fillings $1 < n_d < 3$ (in Ref. [33], it was only explicitly revealed at $n_d = 2$). T_K^{sp} is found to be strongly doping dependent [see Fig. 4(c,d), open squares]. It decreases very fast with increasing filling $n_d \rightarrow 3$, such that the decay of $\langle \hat{S}(\tau)\hat{S}(0) \rangle$ with imaginary time becomes very weak and is therefore almost invisible on short time scales [Fig. 4(a), e.g. solid, yellow curve]. In contrast, T_K^{orb} is almost independent of the filling [see Fig. 4(c,d), filled circles]. It even increases slightly from $n_d = 2$ to $n_d = 3$. In summary, this leads to an intermediate regime of SOS that expands with larger $n_d \rightarrow 3$, mainly towards smaller energies [Fig. 4(d)].

Based on these insights we conclude that SOS is a generic feature in the whole Hund-metal regime, evolving with n_d in the following way. With increasing n_d , larger local moments form in the intermediate SOS regime and lead to the increase of the maximum of χ''_{sp} (or equivalently $\langle \hat{S}(\tau)\hat{S}(0) \rangle$) [see solid curves Fig. 4(a-c)]. At the same time, T_K^{sp} is lowered, because, heuristically, it is more difficult to screen these larger spins. In contrast, the height of χ''_{orb} (or equivalently $\langle \hat{T}(\tau)\hat{T}(0) \rangle$) decreases with increasing $n_d \rightarrow 3$ [see dashed curves in Fig. 4(a-c) and inset of (a)]. This reflects the reduction of the phase space for orbital fluctuations due to the formation of large spins composed of electrons in different orbitals. Consequently, the interplay of spin and orbital degrees of freedom is diminished for n_d close to 3.

This first crude analysis of our results with varying n_d will be refined in Sec. 5. There, we will show in more detail how it is connected to the SOS scenario introduced above for $n_d = 2$.

3.5. The connection between spin-freezing and spin-orbital separation

In sum, we argue that *the two terminologies, “spin-freezing” and “spin-orbital separation”, ultimately describe the same physics of the Hund-metal regime.* The large spins that appear as “frozen” at short imaginary times (which are accessible for QMC) were revealed by our real-frequency finite and zero-temperature DMFT+NRG approach as long-lived, slowly fluctuating, large local moments in the incoherent regime, that get fully screened at long imaginary times to form a FL ground state. In this picture, the intermediate energy regime of Hund metals with its incoherent transport properties is governed by scattering off (almost) free, large and long-lived magnetic moments that are non-trivially coupled to (almost) screened orbital degrees of freedom. A local spin susceptibility showing Pauli behavior at low and (quasi) Curie-Weiss behaviour at intermediate temperatures in Refs. [37, 78] supports this viewpoint.

We note that various DMFT+QMC findings on spin-freezing, such as spin-freezing in (realistic) five-band calculations for iron-pnictides [11, 12, 14, 19], spin-freezing in models with crystal-field-splitting [66], and spin-orbit coupling [69] eventually demonstrate the importance of SOS. In 2015, a fluctuating-moment-induced s-wave spin-triplet superconducting mechanism was proposed for Hund metals, where equal-spin

electrons are paired in different local orbitals. It was shown to be connected to the emergence of local magnetic moments in the NFL regime [70]. In 2016, it was even conjectured that the relevant model for cuprates, the single-orbital Hubbard model on the square lattice, can be mapped onto an effective multi-orbital problem with strong ferromagnetic Hund’s coupling, suggesting that spin-freezing (or equivalently SOS) is the universal mechanism which controls the properties of unconventional superconductors [79].

The insights gained above are relevant for a wide range of fillings n_d and interaction strengths U and J , as will be further demonstrated in Sec. 4 and Sec. 5. In these sections we will also clearly show that, indeed, SOS causes the numerically observed bad-metallic behavior in the 3HHM. SOS therefore constitutes the framework for our main study of Hund metals.

4. Janus-faced influence of Hund’s rule coupling: Hundness versus Motttness at $n_d = 2$

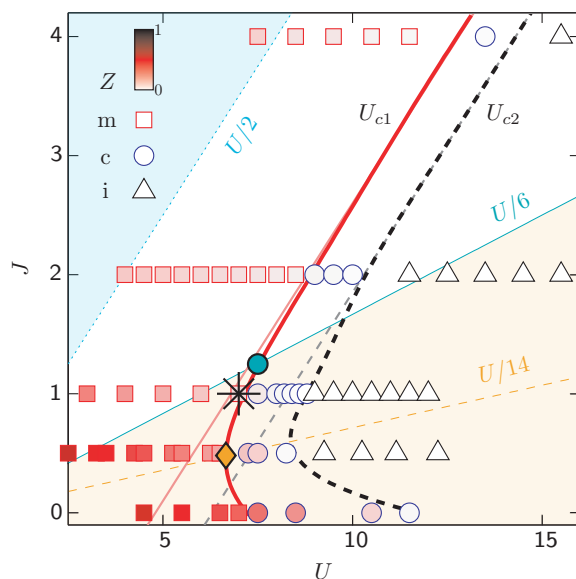


Figure 5: The zero-temperature phase diagram of the 3HHM at $n_d = 2$ reveals three phases in the J - U -plane: a metallic phase (squares), a coexistence region (circles), and an insulating phase (triangles), separated by two non-monotonic phase transition lines, U_{c1} (solid red curve) and U_{c2} (dashed black curve), obtained when initiating the DMFT self-consistency with an insulating and metallic seed, respectively. The color intensity of the symbols in the metallic and the coexistence region indicates the value of $Z \in [0, 1]$: the lower Z the more faded is the red color. Based on the discussion of the multiplet structure in Fig. 2, we added guides at $J = U/2$ [$\omega_{e1} = \omega_h = 0$] and $J = U/6$ [$\tilde{\omega}_h = 0$] and shaded the areas separated by these. The crossing point of U_{c1} with the $U/6$ (cyan circle) occurs at $(U, J) \approx (7.5, 1.25)$. We also added a guide $U/14$ (see text), whose crossing point with U_{c1} (orange diamond) occurs very close to the minimum of U_{c1} at $(U, J) \approx (6.66, 0.48)$. The black star marks the parameters for which SOS has first been revealed in Ref. [33]. [Note that Ref. [33] used a slightly different definition of the Coulomb energy which, while keeping the definition of J the same, corresponds to $U = 7$ here.]

In this section we derive SOS as a consistent explanation for the extended bad-metallic behavior (low Z) in the phase diagram at $n_d = 2$ that reaches from a high critical $U_c^{(2)}$ down to an unusually low U , i.e. we explain the Janus-faced behavior. By introducing clear measures for (i) Hundness and (ii) Motttness we are able to show that sizeable J , thus (i), leads to low Z also far away from the MIT at $n_d = 2$ and opens up a large incoherent SOS regime with intriguing Hund-correlated physics.

In this section, all results are calculated at $T = 0$. Further, we note that we will neglect the superscript (2) in $U_c^{(2)}$ because we will mainly refer to the filling, $n_d = 2$, in the following. The few exceptions where we refer to other fillings will be clear from the context.

4.1. U - J phase diagram

As an overview, Fig. 5 presents the full U - J phase diagram for $n_d = 2$ at $T = 0$. We find a metallic (squares), coexistence (circles) and insulating (triangles) region, which are separated by two distinct Mott transition lines, U_{c1} (solid red line) and U_{c2} (black dashed line), respectively. We note that, so far, only U_{c2} has been studied in the context of three-band Hund models in the literature, because it can be simply derived from the QP weight Z . The black star in Fig. 5 marks the parameters of the main result in Fig. 3 of Ref. [33], for which SOS was revealed. It lies at the border of the coexistence region close to U_{c1} , raising the question how stable this feature is at lower U .

In Landau's Fermi-liquid theory, the quasiparticle weight

$$Z = (1 - \partial_\omega \text{Re} \Sigma(\omega)|_{\omega=0})^{-1} = \frac{m}{m^*}$$

is obtained from the frequency-dependent self-energy $\Sigma(\omega)$, which is directly accessible in NRG, and measures the inverse mass enhancement within single-site DMFT. Landau's Fermi-liquid theory is based on a one-to-one correspondence between long-lived, coherent but renormalized Landau QPs and the low-energy excitations of a free Fermi gas. $Z \in [0, 1]$ reflects the weight of the Lorentzian-shaped coherent QPP of the momentum-dependent local spectral function in a first order expansion, while the additional incoherent part has weight $1 - Z$. In Fig. 5 the value of Z is indicated by the color intensity of the red squares and blue triangles in the conducting regime $U < U_{c2}$.

Similar to the case of the one-band Hubbard model, the MIT shows hysteresis at low temperatures in the multi-band case. Starting with an "insulating seed" (iS) [i.e. a real-frequency local spectral function $A(\omega)$, with an insulating Mott gap, Δ , around the Fermi level], the MIT transition occurs at a lower critical interaction strength, U_{c1} , at which Δ closes with decreasing U . Starting with a "metallic seed" (mS) [i.e. a metallic input spectral function with finite weight at $\omega = 0$] leads, in contrast, to a larger critical value, U_{c2} , above which the QP resonance is lost (accordingly $Z = 0$) and a stable gap is formed with increasing U . Therefore Z can be used to quantitatively track the MIT at U_{c2} when initiating the DMFT loop with a mS. The coexistence region between U_{c1} and U_{c2} is characterized by two solutions, a metallic solution for mS and an insulating solution for iS. This is typical for DMFT. As mean-field approach with an iterative solution scheme it can have more than one stable fixed point, depending on the initialization. Fig. 5 demonstrates that the coexistence region is broad at $J = 0$, reaching from moderate to large values of U ; for finite but small J , it strongly narrows, shifting to lower U values; and at $J > 1$, it eventually approaches a fixed width while shifting linearly with J to ever larger U values [80, 81]. It is known that for $J = 0$ both U_{c1} and U_{c2} grow as a function of N_c at all fillings of multi-orbital models [80]. In contrast, for given N_c , the effect of a finite J on U_{c1} and U_{c2} is strongly filling dependent [47, 53]. At half-filling U_{c1} and U_{c2} is strongly reduced, as finite J increases correlations by forming large $S = N_c/2$ spin states that block the orbitals. For one electron/hole, U_{c1} and U_{c2} increases with J , as J reduces the effective Coulomb interaction in the system. At all intermediate fillings $1 < n_d < N_c$, the special non-monotonic dependence of U_{c1} and U_{c2} on J occurs, which has been mentioned by several previous studies (especially for U_{c2}) [32, 47, 50, 53].

This non-monotonic behavior can be understood to a great extent from the local multiplet structure of the underlying local Hamiltonian. For $n_d = 2$, the relation of the local multiplet structure in Fig. 2 with the phase diagram is discussed in Fig. 5 (bright blue, white and orange regimes). As pointed out with Eqs. (3) in Sec. 2.6.1, we expect a strong qualitative change in the physics of the 3HHM once $\tilde{\omega}_h$ turns negative. For the local multiplet structure, this occurs at the sizeable Hund's coupling $J \geq U/6$. Accordingly, in the 3HHM, one can distinguish two regimes in the U - J phase diagram of Fig. 5, by relating the U_{c1} phase boundary with the reference line $J = U/6$, for which a single crossing point exists at $(U, J) \approx (7.5, 1.25)$ [cyan circle in Fig. 5]. Therefore, for the *sizeable* Hund's coupling

$$J > J_{c1}^* \cong 1.25, \quad (8)$$

which we define as the "Hund regime" in the 3HHM, the high-lying h - and $e1$ -multiplets have crossed below the $g2$ -level. In this regime, a qualitatively different behavior occurs all the way up to U_{c1} as compared to standard Mott physics. Specifically, Z is low in the entire "Hund regime" [see color shading of symbols in

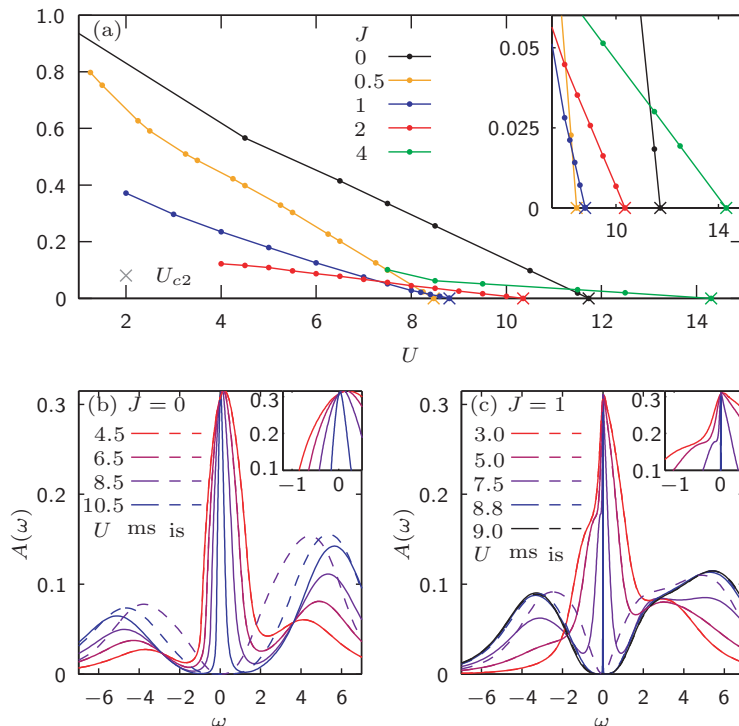


Figure 6: (a) The QP weight, Z , of the 3HHM at $n_d = 2$, plotted as a function of U , shows Janus-faced behavior when J is increased: on the one hand, at small to moderate U , Z decreases (metallicity worsens), on the other hand, U_{c2} (marked by crosses) increases (metallicity improves). Each dot on the curves represents a DMFT+NRG data point. The inset is a zoom of the U_{c2} -behavior. (b,c) The local spectral function, $A(\omega)$, shows a MIT with growing U for (b) $J = 0$ and (c) $J = 1$. Solid (dashed) lines are DMFT results for a metallic (insulating) seed. The insets zoom into the QP. For $J = 1$, the QP in $A(\omega)$ shows a shoulder characteristic of SOS.

Fig. 5]. In contrast, for $J < J_{c1}^*$, which we refer to as “good-metal regime”, Z reaches up to much larger values [squares are colored in intensive red in Fig. 5]. More generally, one may already expect the crossover to the Hund regime to set in earlier. For example, considering the approaching h -level at $\tilde{\omega}_h \sim 2\delta\omega_g$ with $\delta\omega_g \equiv \omega_{g2} - \omega_{g1} = 2J$, this results in $J = U/14$ [also indicated by an orange dashed line in Fig. 5]. Its crossing point with U_{c1} occurs around $(U, J) \approx (6.66, 0.48)$ [orange diamond in Fig. 5] which turns out to be in close proximity to the point where the non-monotonic behavior of U_{c1} versus J reaches a minimum, i.e. turns around at $U_{c1}^{\min} \simeq 6.66$. In summary, we see that as the Hund’s coupling exceeds the moderate value of $J \gtrsim J_{c1}^* \sim 1$, the 3HHM is dominated by Hund physics: sizeable J leads to a qualitative change in the local multiplet structure and thus to a strong change in the physics of the 3HHM, affecting both the phase boundaries, U_{c1} and U_{c2} , and the regime far from the MIT at much lower U , where Z is low.

The scaling of U_{c1} and U_{c2} for large J , eventually, is linked to a further stark change in the local multiplet structure, namely when the h - and e -levels actually become the new local ground states having $\omega_{e1} < 0$. Allowing for a shift by kinetic energy this suggests $U_{c1} \simeq 2J + \text{const}$. This scaling is approximated by thin solid red and dashed grey lines in Fig. 6(a), respectively, and will be further corroborated in Fig. 8(c).

4.2. Janus-faced behavior of Z

In Fig. 6(a) we plot Z versus U for various values of $J \in [0, 4]$. In general, Z is finite in the metallic phase (with an upper limit of $Z = 1$ for the non-interacting case) and zero in the insulating phase. U_{c2} is defined by the transition point between both phases [marked by \times in Fig. 6(a)]. We note, however, that near

the MIT Landau's Fermi-liquid theory might break down as a valid physical description of the excitations and Z only remains as a heuristic indicator of the MIT. For all J , we observe in Fig. 6(a) that Z decreases with increasing U in the metallic phase, thus strong correlation effects increase with increasing proximity to U_{c2} , as known from the half-filled one-band Hubbard MIT. However, the strength of correlations strongly differs for different values of J . For small J , Z is still large at small to moderate U , while for large J , Z is generally small [compare e.g. black and yellow curve to red or green curve in Fig. 6(a)]. Moreover, J induces competing effects. While Z strongly decreases with J at moderate U [see e.g. black to red curve at $U = 6$ in Fig. 6(a)], U_c increases with J (for $J \geq 0.5$, after a slight decrease for very small J) [see inset in Fig. 6(a)]. We thus observe Janus-faced behavior in our data similar to Ref. [53]: on the one hand J promotes bad metallicity by a loss of coherence, on the other hand it promotes metallicity by increasing U_{c2} . In sum, this Janus-faced behavior leads to a strongly reduced Z for sizeable J in a large interval of U (including the Hund-metal regime at $n_d = 2$) [as seen e.g. for the red or green curve in Fig. 6(a)]. We will clarify its physical origin and nature in the following by disentangling the opposing Janus-faced effects.

4.3. Real-frequency study of MIT at zero and finite J

For each data point in our U - J phase diagram, NRG yields a set of detailed frequency-dependent information of the system, in contrast to previous QMC or slave-boson studies. This is useful, because Z only measures the strength but not the type, Hundness or Mottness, of strong correlations.

Much additional information about the MIT can be gained from the real-frequency local spectral function, $A(\omega)$, defined in Eq. (A.6). For example, the dual character of strongly correlated electrons is directly reflected in the shape of $A(\omega)$. In Fig. 6(b,c) we track the MIT in $A(\omega)$, i.e. how this dual character changes with U , for $J = 0$ and $J = 1$, respectively. The metallic, delocalized behavior of electrons in the solid is characterized by a finite spectral weight at the Fermi level in form of a well-defined QPP [see e.g. solid and dashed red curves in Fig. 6(b,c)]. Local Kondo-type screening processes of the ground state multiplet dominate the low-energy physics of the self-consistent impurity model and lead in the 3HHM to a Fermi-liquid ground state with coherent QP excitations in the whole metallic phase, as will be discussed in detail later. The localized behavior of the electrons is manifest at high energies in terms of local (atomic) multiplet excitations which are broadened by the solid-state environment and form the Hubbard side bands (see discussion of Fig. 7). At small to moderate U , these incoherent high-energy bands are close to the Fermi level and even overlap, and the QPP is broad. With increasing U , the Hubbard side bands move to larger $|\omega|$ and the QPP narrows [compare red versus blue curves in Fig. 6(b,c)]. Above U_{c1} or U_{c2} (depending on the seed) the DMFT self-consistency opens a Mott gap in $A(\omega)$ around the Fermi level, the QPP vanishes and $A(\omega)$ then consists solely of the high-energy bands [see e.g. black curve in Fig. 6(c)]. Heuristically, this decrease of the QPP width with increasing U is tracked by the QP weight, Z , as the peak height is pinned to a fixed value at zero frequency (Luttinger pinning [82, 83]) for all $U < U_c$.

As part of the MIT, we also directly observe the coexistence region $U_{c1} < U < U_{c2}$ in Fig. 6(b,c). While the purely metallic and the purely insulating phase have only one solution of the DMFT self-consistency, independent of the seed, we find two differing solutions in the coexistence region, an insulating for iS and a metallic one for mS, respectively [see dashed versus solid purple and blue curves in Fig. 6(b,c)]. We note that NRG is perfectly suited for pinpointing U_{c1} and U_{c2} via $A(\omega)$, as its energy resolution is exponentially refined around the Fermi level, capturing the QPP down to its smallest width. Thus the iterative DMFT procedure does not break down before its solution becomes thermodynamically unstable. However, the broadening of discrete spectral data in NRG might minimally shift additional spectral weight to the Fermi level, thus artificially but only slightly shifting the coexistence region to larger U values.

At first glance, the MITs for $J = 0$ and $J = 1$ seem to behave overall similarly with changing U . However, we find striking differences between the spectra in Fig. 6(b) and Fig. 6(c), corresponding to the black and blue lines in Fig. 6(a), respectively.

As discussed above, Z is much lower for the $J = 1$ MIT than for the $J = 0$ MIT. Accordingly, we observe qualitative differences in the shape of the QPP. For finite J , in Fig. 6(c), the QPP has a shoulder at negative frequencies and a slight kink at positive frequencies. The shoulder (and the kink) drastically narrow the top of the QPP while the bottom remains broad. These features are present for all values of U , but they are more pronounced for smaller U , for which the overall width of the QPP is broader [see inset of Fig. 6(c)].

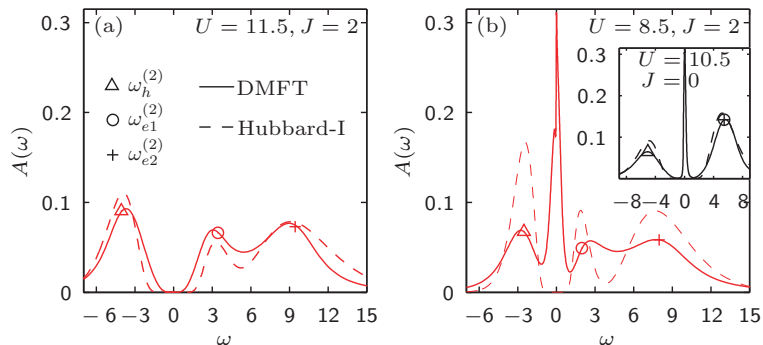


Figure 7: (a) Insulating and (b) metallic local spectral function, $A(\omega)$, for $J = 2$, obtained from DMFT+NRG (solid) and via Hubbard-I approximation (dashed). The symbols, as specified in the legend, correspond to the local multiplet excitations listed in Eqs. (3a). The inset in (b) shows results for $J = 0$. Here, the symbols correspond additionally to the transition frequencies in Eqs. (3b), i.e. triangles and pluses also correspond to $\tilde{\omega}_h$ and $\tilde{\omega}_{e2}$. In order to directly compare the Hubbard-I approximation with the log-Gaussian broadened DMFT+NRG results, we convoluted the Hubbard-I spectral function with a log-Gaussian broadening Kernel of width $\alpha = 0.4$, as defined in Ref. [34].

At $J = 0$, however, these features are absent [see Fig. 6(b) and its inset]. From Ref. [33] we know that the shoulder emerges due to SOS, which only occurs for finite $J > 0$. Fig. 6(c,d) thus give a first hint that *there is a direct connection between the Janus-faced low Z and SOS*.

Further, we find differences in the shape of the Hubbard side bands. For $J = 0$ there are two bumps in Fig. 6(b). The lower Hubbard band at negative frequencies is less pronounced than the upper Hubbard band at positive frequencies. With growing U , the distance between these Hubbard bands increases, reminiscent of the single-band Hubbard model. For $J = 1$ there are in principle two Hubbard side bands, as well, in Fig. 6(c), however the band at positive frequencies consists of two bumps, so that, at large U , we observe *three* peaks altogether. For small U , the negative frequency and the lower positive frequency peaks are hidden in the QPP [red curve in Fig. 6(c)] and only one positive-frequency bump is visible. But with growing $U \geq 4$ the lower peak is shifted to lower frequencies and the two-peak structure at positive frequencies clearly develops [see purple, blue and black curves in Fig. 6(c)].

4.4. Peak structure of Hubbard bands: Hubbard-I analysis

The peak structure of the Hubbard bands (at zero temperature) can be fully understood in terms of a Hubbard-I approximation of the lattice Green’s function, i.e. from its local multiplet excitations, as demonstrated in Fig. 7. (This was stated in previous studies but never demonstrated explicitly, due to the lack of reliable real-frequency data [47, 50, 53]. So far, a similar real-frequency analysis was only carried out for a three-band Hund model at $n_d = 1$ using Fork Tensor Product States as real-time DMFT solver [84]).

To obtain the local multiplet excitations spectrum of the underlying atomic problem, i.e. in the “atomic limit”, $t = 0$, we diagonalize the local Hamiltonian as discussed in Sec. 2.6.1 with Eq. (2) and schematically depicted in Fig. 2.

The positions of the peaks in the Hubbard bands shown in Fig. 7 are well captured by the discrete multiplet excitations indicated by the symbols provided with Eqs. (3). Thus *the structure of the incoherent side-bands can be understood from atomic physics*. In order to explicitly demonstrate this, i.e. to reproduce the form of the Hubbard bands, we use the Hubbard-I approximation around the atomic limit to disperse the atomic eigenstates by embedding them in a lattice environment. In this approximation the lattice self-energy is replaced in Eq. (A.5) by the purely atomic self-energy corresponding to the limit $t = 0$ in Eq. (1): $\Sigma(\omega) = \Sigma_{\text{atom}}(\omega)$. The atomic self-energy is given by $\Sigma_{\text{atom}}(\omega) = \omega + \mu - G_{\text{atom}}^{-1}(\omega)$ in terms of the atomic Green’s function, $G_{\text{atom}}(\omega) = \sum_M p_M / (\omega - \omega_M + i0^+)$, summing over the atomic multiplet excitation poles with p_M the probability for a one-particle excitation from the ground state into the excited state M .

The resulting Hubbard-I spectral functions are plotted with dashed lines in Fig. 7. The insulating DMFT spectral function for $U = 11.5$ and $J = 2$ is reproduced very well [Fig. 7(a)]. The structures of the Hubbard bands in the metallic states for $U = 8.5$ and $J = 2$ [Fig. 7(b)] and for $U = 10.5$ and $J = 0$ [inset of Fig. 7 (b)] are still matched reasonably well, but the QPP is not captured at all within the Hubbard-I approximation because finite-lifetime effects are not contained in the purely real atomic self-energy. For smaller U in the metallic regime, thus for a broader QPP in the spectral functions, the deviations between the DMFT and the Hubbard-I results therefore naturally increase.

The atomic excitation energies listed in Eqs. (3) fully explain the qualitatively different structure of the corresponding Hubbard bands: while two bumps are well-separated and pronounced at $J = 0$ (with a larger peak at positive frequency due to the higher degeneracy of the corresponding atomic excitation), the three-peaked Hubbard bands form a broad incoherent background for sizeable J , because J shifts the inner side-peaks at $\omega_{e1} = -\omega_h = \frac{U}{2} - J$ towards the Fermi level, while the peak at $\omega_{e2} = \frac{U}{2} + 2J$ is shifted to higher frequencies. This difference was also recently revealed for two archetypal correlated materials, the Mott material V_2O_3 and the Hund material Sr_2RuO_4 [37]. We note that additional structures at the low-energy edges of the Hubbard bands with doublon-holon origin [85] are principally expected, but presumably a higher resolution using adaptive broadening [86] and/or extensive z -averaging [87] would be needed to resolve them.

4.5. The “bare gap” as a measure of Mottness

In a next step we use the atomic excitation spectra for sizeable $J \gtrsim J_{c1}^*$ to derive a measure of Mottness. Following Refs. [47, 50, 53, 57], we define the “bare gap”, $\Delta_b \equiv \omega_{e1} - \omega_h = U - 2J$, as the distance between the lowest atomic excitations at positive and negative frequencies. [Incidentally, Δ_b is equal to the atomic interaction of the energetically most favored atomic configuration in line three of Eq. (1b)]. Up to an offset, Δ_b measures the distance to the MIT. In this sense it is similar to the true Mott insulating gap Δ which closes at the MIT. Here $\Delta = \omega^+ - \omega^-$ is defined from the criterion that $A(\omega) < 10^{-3}$ holds for $\omega^- < \omega < \omega^+$.

In the inset of Fig. 8(a) we plot Δ versus U (for iS) for various values of J and derive U_{c1} from the closure of the Mott insulating gap, $\Delta(U_{c1}) = 0$ (marked by crosses) using a well-suited linear extrapolation to the data points. Obviously, U_{c1} strongly depends on J (as seen already in Fig. 6). However, when Δ is plotted versus Δ_b [see Fig. 8(a)] the different lines lie ever closer to each other at large J and the critical value of the bare gap, $\Delta_b^{c1} \equiv U_{c1} - 2J$, approaches a constant value, $W_1 = 4.8$. This is also demonstrated in Fig. 8(b). For large $J \gg J_{c1}^*$, the critical interaction Δ_b^{c1} (solid red line) is J -independent. Consequently, Δ_b serves as measure for Mottness, in the sense that $W_1 - \Delta_b$ quantifies the distance to the MIT at U_{c1} (Δ_b^{c1}). Thus, the larger Δ_b , the closer the system is to the MIT and the stronger the influence of Mottness. We demonstrate that this idea also works for an mS: for $J > J_{c1}^*$, $\Delta_b^{c2} = U_{c2} - 2J$ approaches a constant value $W_1 = 6.3$ [see dashed black line in Fig. 8(b) and \times -signs in Fig. 8(c)]. We thus switch from U to $\Delta_b(J, U)$ as independent parameter in the following to quantify Mottness. However, we note that for $J < J_{c1}^*$, Δ_b^{c1} and Δ_b^{c2} do still depend on J , thus Δ_b breaks down as a simple measure for Mottness for small J in the above sense.

The reason for the $\Delta_b^{c,i}$ with $i = 1, 2$ becoming a constant for large J can again be roughly understood by simply looking at the local multiplet structure, where for $J > U/2$ the excited levels h and $e1$ actually pass across $g1$ (see discussion at end of Sec. 2.6.1). Therefore one may expect a qualitative change of behavior at $\Delta_b = U - 2J \sim \text{const}$, as already mentioned in Sec. 4.1.

The finite offset for Δ_b^{c1} can be explained with the Hubbard criterion [88] for the breakdown of the Mott insulating state, which uses $\Delta = \Delta_b - \tilde{W}(J) \equiv 0$ to conclude that $\Delta_b^{c1} \equiv \tilde{W}(J)$: the system becomes metallic when the effective kinetic energy in the system, $\tilde{W}(J)$, is large enough to overcome the energy cost of hopping, given by the energy scale of the bare gap Δ_b . $\tilde{W}(J)$ sets the scale for the dispersion of the Hubbard bands and can be regarded as the effective bandwidth of the system. As shown in Fig. 8(b), $\tilde{W}(J)$ has a large value $\tilde{W}(0) = 7.3$ at $J = 0$ and decreases with increasing but small J , approaching a constant $W_1 = 4.8$ for sizeable $J > J_{c1}^*$. From Fig. 2 we know that at the SU(6) symmetric point $J = 0$ the atomic excitation spectrum becomes more degenerate: $g2$ becomes degenerate with $g1$, and thus also a true ground state; furthermore, all three excited levels h , $e1$, and $e2$ become degenerate. Accordingly, the widths

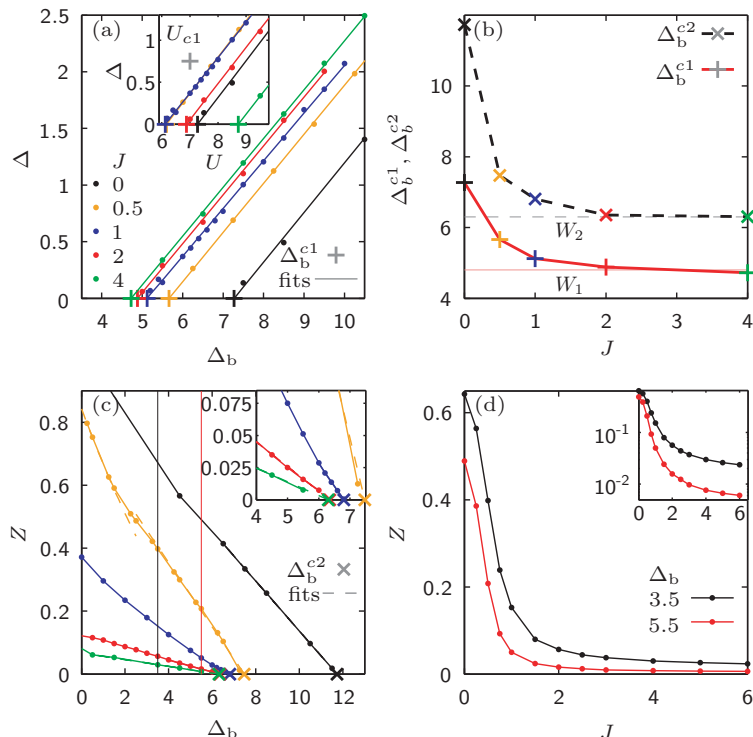


Figure 8: (a) Mott insulating gap, Δ , as a function of the bare gap, $\Delta_b = U - 2J$, for several values of J . Each dot on the curves represents a DMFT+NRG data point using iS. The lines are linear fits from which the critical Δ_b^{c1} values (pluses) are defined as $\Delta(\Delta_b^{c1}) = 0$. The inset shows the same data as a function of U . (b) Δ_b^{c1} and Δ_b^{c2} as functions of J : both first decrease roughly exponentially at small $J < J_{c1}^*$ [see also Sec. 4.7] and then approach fixed values, $W_1 = 4.8$ (thin solid red line) and $W_2 = 6.3$ (thin dashed grey line), respectively, at large $J > J_{c1}^*$. (c) Z is plotted as a function of Δ_b to disentangle the Janus-faced behavior of Fig. 6(a): the slope of Z decreases with increasing J , while $\Delta_b^{c2} = W_2$ is J -independent for sizeable $J > J_{c1}^*$ (and grows with decreasing J for $J < J_{c1}^*$). Thus Z is small far away from the MIT due to Hundness rather than Mottness. The dashed yellow lines are quadratic and linear fits to the $J = 0.5$ behavior of Z at small U and larger U , respectively. The inset is a zoom of the Δ_b^{c2} -behavior. (d) Z is plotted as a function of J , for two fixed values of Δ_b , indicated by the thin black and red lines in (c). Inset: same data in a semilog-plot of Z , revealing its roughly exponential decrease with increasing J for $J < J_{c1}^*$, whereas Z is very small but rather constant for $J > J_{c1}^*$.

of the Hubbard bands, i.e. $\tilde{W}(J)$, are larger at small J , because more hopping processes are allowed than for $J > J_{c1}^*$. In contrast, sizeable J favors high-spin states, reducing the atomic ground state degeneracy by quenching its orbital fluctuations and blocking many excitations. We note that a similar analysis was performed in Refs. [47, 50].

As in Ref. [47], we conclude that the non-monotonic behavior of U_{c1} can be summarized as follows: with growing J , U_{c1} decreases at small J due the reduction of the kinetic energy by orbital blocking, whereas it increases again at large J , due to the reduction of Δ_b by reducing the energy cost for the double occupancy of *different* orbitals. The turnaround occurs around $J \sim 1$, i.e. when J is on the order of the lattice hopping, $t = 1$. At the same time, as we point out at the end of Sec. 2.6.1, the non-monotonic behavior in U_{c1} can also be directly linked to a qualitative change in the underlying multiplet structure: the turn-around of U_{c1} coincides with the point in the parameter regime where the ‘excited’ levels h and $e1$ pass across the ‘low-energy’ level $g2$ in the metallic regime $J > U_{c1}/6$. This occurs when $J \gtrsim 1$. The behavior of U_{c2} , which is similar to U_{c1} , will be revisited and explained in Sec. 4.8 in the context of SOS.

4.6. Hundness as origin of strong correlations

In contrast to previous studies, we now use Δ_b as a measure for Mottness in Fig. 8(c,d) to disentangle the Janus-faced effects of J in Z and to analyze the “pure” effect of Hundness for strong correlations.

Fig. 8(c) shows Z versus Δ_b for various values of J . We observe that, as visible for $J = 0.5$, the reduction in Z with Δ_b first follows a quadratic behavior for small $\Delta_b < 4J$ (which coincides with $U < 6J$) followed, as visible for all values of J , by a linear behavior for moderate Δ_b up to Δ_b^{c2} (for $J = 0.5$ this behavior is illustrated by fits, shown as the upper and lower dashed yellow lines, respectively). For $J > J_{c1}^*$, Δ_b^{c2} is J -independent [see inset of Fig. 8(c)], and $W_2 - \Delta_b$ again measures the distance to the MIT.

For fixed Δ_b , we observe in Fig. 8(c) that increasing J reduces Z , with the decay in Z significantly slowed down for $J > J_{c1}^*$ (see inset).

The data along the thin red and black vertical lines is further summarized in Fig. 8(d). Note that the curve for $\Delta_b = 5.5$ already proceeds midway in between U_{c1} and U_{c2} in the coexistence region in Fig. 5 for large J (e.g., see intercept at $J = 0$ for their linear extrapolation), whereas $\Delta_b = 3.5$ is still in the metallic phase.

Interestingly, for fixed Δ_b , the overall suppression of Z with increasing J is more pronounced for smaller Δ_b , where the values of Z are still very large for small J , but strongly reduced for large J [compare e.g. the Z values following the thin vertical lines for $\Delta_b = 3.5$ and $\Delta_b = 5.5$ in Fig. 8(c) or compare black and red curve in Fig. 8(d)]. This behavior can be inferred from the important insight that increasing J reduces the *slope* of Z when plotted as a function of Δ_b (or U) in Fig. 8(c) for *all* $J > 0$, while Δ_b^{c2} is first reduced and then approaches a fixed value. As another major result of this work we thus summarize: *for sizeable J , Z is strongly lowered also far from the MIT, at small Δ_b , because Hundness promotes the reduction of the slope of Z .* The latter effect holds for *any* nonzero J [yellow, blue, red and green curve in Fig. 8(b)], even independently of the fact whether Δ_b is a valid measure of Mottness (green and red curve) or not (yellow curve). Therefore, *Hundness, i.e. scenario (ii), is the origin of strong correlations in the Hund-metal regime far from the MIT at $n_d = 2$.*

In the next section, we focus also on small $J < J_{c1}^*$. As seen in Fig. 8(d), in this regime, Z is reduced roughly exponentially with increasing J (see also inset). However, here, we cannot fully disentangle the Janus-faced behavior of Z using Δ_b .

4.7. Spin-orbital separation in the U - J phase diagram

In order to better understand the strong reduction of Z at small J and to reveal the physical nature causing the low Z for $J > J_{c1}^*$, we now systematically analyze the underlying DMFT+NRG real-frequency spectral data in the metallic (and coexistence) region of the U - J phase diagram. In particular, we consider $\chi''_{\text{orb}}(\omega)$ and $\chi''_{\text{sp}}(\omega)$, the imaginary parts of the dynamical impurity orbital and spin susceptibilities, defined in Eqs. (6), the local spectral function $A(\omega)$, and the imaginary part of the self-energy, $\text{Im}\Sigma(\omega)$, defined in Eqs. (A.4). Similar to Ref. [33], we plot $\chi''_{\text{orb}}(\omega)$ and $\chi''_{\text{sp}}(\omega)$ in Fig. 9(a) and Fig. 10(a) to deduce T_K^{orb} and T_K^{sp} from their respective maxima. $A(\omega)$ is plotted in Fig. 9(b-d) and Fig. 10(b-d), and $\text{Im}\Sigma(\omega)$ in Fig. 9(e,f) and Fig. 10(e,f). In Fig. 9 $\Delta_b = 3.5$ is fixed and J is varied, while in Fig. 10 $J = 2$ is fixed and U (Δ_b) is varied [the latter is similar to Fig. 6(c), there for $J = 1$].

SOS, i.e. $T_K^{\text{orb}} \gg T_K^{\text{sp}}$, occurs in the whole metallic regime for nonzero J , as seen in Fig. 9(a) and Fig. 10(a). It is a generic consequence of finite Hund’s coupling in particle-hole asymmetric *multi-band* systems, as anticipated early on [89]. Since T_K^{sp} is finite, the ground state is a FL [see thin grey $|\omega|^1$ -guide-to-the-eye lines in Fig. 9(a) and Fig. 10(a)] for all values of U and J at $n_d = 2$, independently of the proximity to the MIT. This strongly contradicts the spin-freezing phase scenario proposed in Ref. [51], but confirms the expectations of Refs. [6, 7, 14, 53].

For fixed Δ_b , the SOS regime opens up with increasing J [the maxima of $\chi''_{\text{sp}}(\omega)$ are shifted to smaller $|\omega|$ in Fig. 9(a)]. This effect is accompanied by the formation of a shoulder at $\omega < 0$, and a weak kink at $\omega > 0$ in $A(\omega)$, which narrow the top of the QPP [see Fig. 9(b-d)], and reveal a strong particle-hole asymmetry in the system. Accordingly, the imaginary part of the self-energy, $\text{Im}\Sigma(\omega)$, develops a pronounced shoulder (bump) in the SOS regime at $\omega < 0$ [Fig. 9(e)], and a kink at $\omega > 0$ [Fig. 9(e)], as well. Note that the kink is only visible for $J > 1$, while at smaller J , $\text{Im}\Sigma(\omega)$ seems to follow apparent power-laws (as indicated by the

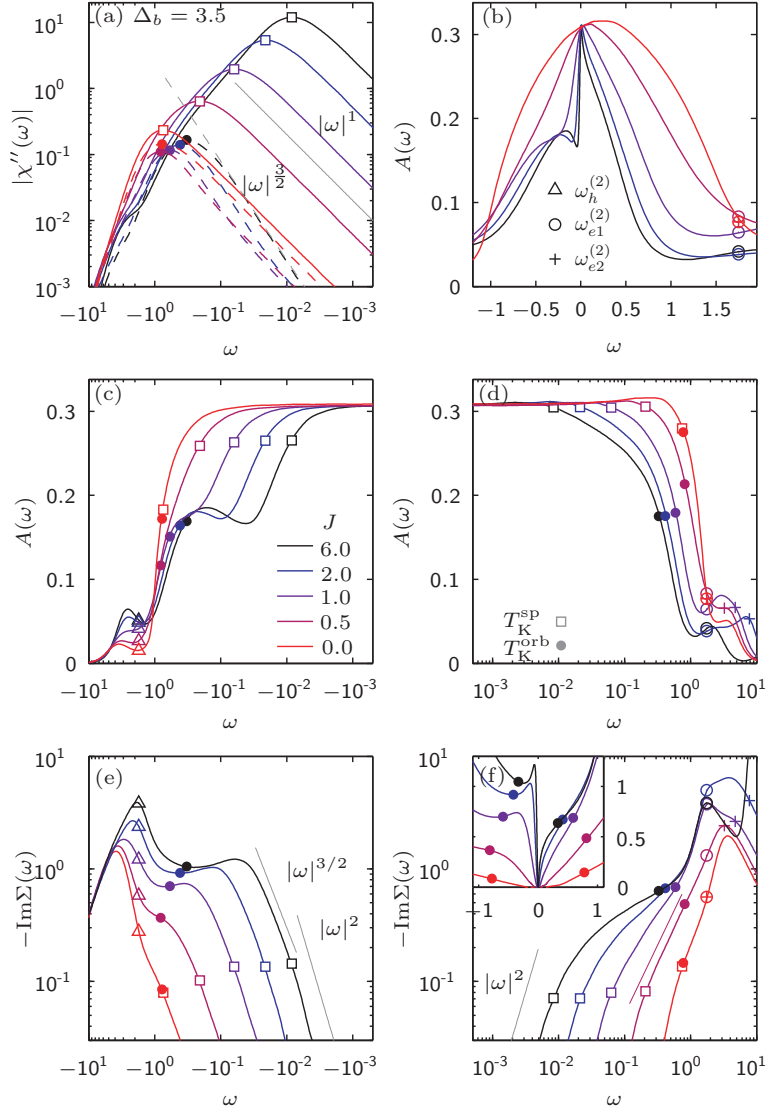


Figure 9: (a) The imaginary parts of the dynamical impurity orbital and spin susceptibilities, $|\chi''_{\text{orb}}(\omega)|$ (dashed) and $|\chi''_{\text{sp}}(\omega)|$ (solid), (b-d) the local spectral function $A(\omega)$, and (e,f) the imaginary part of the self-energy, $\text{Im}\Sigma(\omega)$, for fixed $\Delta_b = 3.5$ and various choices of J . (a) T_K^{orb} (filled circles) and T_K^{sp} (open squares) are defined from the maxima of $\chi''_{\text{orb}}(\omega)$ and $\chi''_{\text{sp}}(\omega)$, respectively. With increasing $J > 0$, an SOS regime clearly develops, $T_K^{\text{orb}} > |\omega| > T_K^{\text{sp}}$, with complex NFL behavior. $\chi''_{\text{orb}}(\omega)$ follows an apparent $|\omega|^{3/2}$ power law in the SOS regime (dashed grey guide-to-the-eye line), which we believe is just a cross-over behavior (see discussion in Sec. 5.5). Below T_K^{sp} , the expected $|\omega|^{-1}$ FL power-law behavior sets in, indicated by a solid grey guide-to-the-eye line. (b,c,d) With increasing J a $SU(6)$ Kondo resonance in $A(\omega)$ splits into a $SU(3)$ Kondo peak (shoulder for $\omega < 0$ and kink for $\omega > 0$) and a sharp $SU(2)$ Kondo QPP, reflecting two-stage screening of orbital and spin degrees of freedom due to SOS. These features are shown on (b) linear and (c,d) logarithmic frequency scales for (c) negative and (d) positive frequencies. (e,f) $\text{Im}\Sigma(\omega)$ is plotted versus (e) negative and (f) positive frequencies. Solid grey guide-to-the-eye lines indicate $|\omega|^{-2}$ FL power-law behavior and apparent $|\omega|^{3/2}$ behavior at $\omega < 0$, the magenta guide-to-the-eye line in (f) shows an apparent fractional-power law at $\omega > 0$ for $J = 0.5$. The latter fractional power laws presumably originate just from a cross-over behavior. The symbols, as specified in the legend in (b), correspond to the local multiplet excitations listed in Eqs. (3a). For $J = 0$, triangles and pluses also correspond to the transition frequencies in Eqs. (3b), i.e to $\tilde{\omega}_h$ and $\tilde{\omega}_{e2}$.

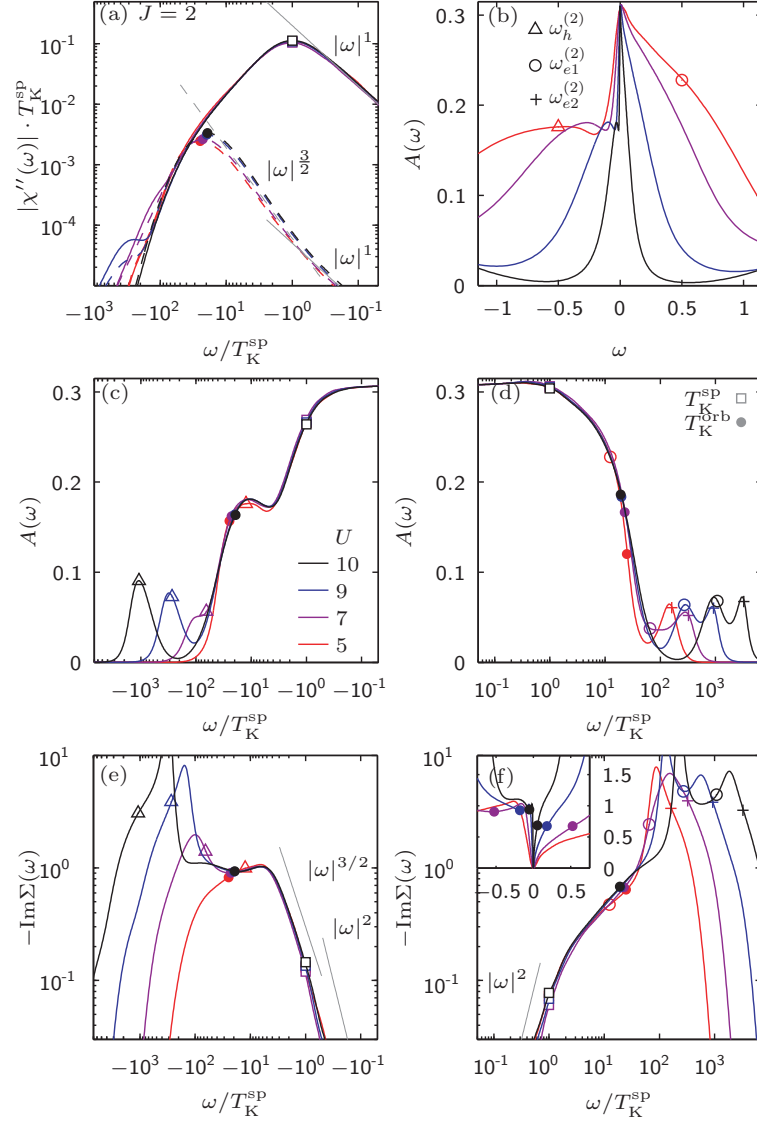


Figure 10: Similar data as in Fig. 9, but for fixed $J=2$ and various choices of U (Δ_b), plotted as a function of ω/T_K^{SP} on a logarithmic frequency scale in (a,c,d,e,f), and in (b) as a function of ω on a linear frequency scale. All curves are identical for $|\omega/T_K^{\text{SP}}| < T_K^{\text{orb}}/T_K^{\text{SP}} \approx 20$ while, nevertheless, the low-energy physics moves to smaller energies with increasing U on a linear scale (panel b). (c-f) Thus, “QP Hund features” in $A(\omega/T_K^{\text{SP}})$ and $\text{Im}\Sigma(\omega/T_K^{\text{SP}})$ are independent of U in both the rescaled SOS regime, and the rescaled FL regime for $|\omega| < T_K^{\text{SP}}$ (narrow, sharp peak in $A(\omega T_K^{\text{SP}})$). The symbols, as specified in the legend in (b), correspond to the local multiplet excitations listed in Eqs. (3a).

magenta guide-to-the-eye line for $J = 0.5$ in Fig. 9(f) and observed in Fig. 3(b,e) of Ref. [33]). For $J = 0$, the QPP is formed by one broad $SU(6)$ Kondo resonance. With increasing J , this Kondo resonance is split into a narrow $SU(2)$ spin Kondo resonance on top of a wider $SU(3)$ orbital Kondo resonance (e.g., the shoulder), corresponding to spin and orbital screening, respectively [see Fig. 13(a) for a schematic sketch]. The orbital features become strongly particle-hole asymmetric with increasing J , with lesser effects on the spin resonance. Thus, SOS is manifest in a two-tier QPP with a wide base and a narrow “needle” of (half-) width T_K^{orb} and T_K^{sp} , respectively. We see from the behavior of T_K^{orb} in Fig. 9(a) that the “full” width of the QPP is rather stable with increasing J (at least for negative frequencies). In contrast, the width of the needle strongly reduces with J [compare e.g. red and black curves in Fig. 9(b-d)].

We note that the orbital and spin screening in the 3HHM are non-trivial screening processes that differ from standard $SU(N)$ Kondo-type screening processes. The Kondo model corresponding to the 3HHM with specific representations of the impurity spin and orbital operators has been worked out in Refs. [31, 90], e.g. resulting in a ferromagnetic bare spin coupling. In particular, a complex, protracted RG flow has been revealed where orbital and spin degrees of freedom are *not* decoupled, leading to a subtle spin-orbital Kondo effect (see also Fig. 13): first, at higher energies, the intermediate-coupling NFL fixed point of an underlying effective 2 (spin)-channel $SU(3)$ Coqblin-Schrieffer model is reached, where the ferromagnetic spin coupling is quenched. Then, at much lower energies, the spin coupling renormalizes to an anti-ferromagnetic value and the RG flow results in a strong-coupling FL fixed point. For $J = 0$, the Kondo model reduces to the single-channel antiferromagnetic $SU(3 \times 2)$ Coqblin-Schrieffer model. Therefore, when for $J > 0$, we refer to a $SU(3)$ orbital and a $SU(2)$ spin Kondo resonance, or, for $J = 0$, to a $SU(6)$ Kondo resonance, we have this non-trivial spin-orbital Kondo effect in mind.

Fig. 10 shows similar data as in Fig. 9, but now for a fixed J and different values of U (Δ_b), plotted as a function of ω/T_K^{sp} in (a,c,d,e,f) and ω in (b). Here, U affects T_K^{orb} and T_K^{sp} in the same way: their ratio, $T_K^{\text{orb}}/T_K^{\text{sp}} \approx 20$, is essentially independent of U , such that the curves in Fig. 10(a) lie on top of each other for $|\omega| < T_K^{\text{orb}}$ (see also the discussion of Fig. 12, and the expressions for the orbital and spin Kondo scales derived in Ref. [31]). As a consequence, the shapes of the QPPs in $A(\omega)$ and the self-energies $\text{Im} \Sigma(\omega)$ are scale invariant for $|\omega| \leq T_K^{\text{orb}}$, too, when plotting both quantities as a function of ω/T_K^{sp} [see Fig. 10(c,d) and (e,f), respectively], reminiscent of the universal behavior in the single-band Hubbard model. The reason for this is that the ratio $T_K^{\text{orb}}/T_K^{\text{sp}}$ is constant in the underlying Kondo model [31] of the 3HHM (for a fixed $n_d = 2$ corresponding to a certain spin and orbital operator representation). This universal behavior of the Kondo scales is not changed by the DMFT self-consistency: the SOS is characteristic of impurity physics, i.e. it also emerges in the impurity AHM in the absence of an MIT [33]. The DMFT self-consistency just adjusts the overall width of the QPP, by affecting the value of T_K^{orb} , but not its internal structure, governed by $T_K^{\text{orb}}/T_K^{\text{sp}}$. In Fig. 10(b), on a linear frequency scale, the SOS features are more pronounced for larger T_K^{orb} , i.e. smaller U , when compared to bare energy scales in the system.

We summarize the effect of spin-orbital separation at $n_d = 2$ in Fig. 11. There we show the structure factor $A(\epsilon_k, \omega)$, as experimentally accessible by angle-resolved photoemission spectroscopy (ARPES), for $J = 0$ [panel (a)] and $J = 2$ [panel (b)]. Within DMFT, $A(\epsilon_k, \omega)$ is directly obtained from the self-energy $\Sigma(\omega)$: $A(\epsilon_k, \omega) = -\frac{1}{\pi} \text{Im} [\omega + \mu - \epsilon_k - \Sigma(\omega)]^{-1}$. The QP dispersion (white curve) is defined as the solution to the equation $\omega + \mu - \epsilon_k - \text{Re} \Sigma(\omega) = 0$ [91]. For fixed ω , this trivially yields a single value for ϵ_k , but not necessarily a unique value for ω for fixed ϵ_k . Considering the latter solution(s), $E(\epsilon_k)$, for given ϵ_k , then for $J = 0$, E shifts linearly with ϵ_k , i.e. the band corresponding to the QPP is fully characterized by a linear FL dispersion relation with constant slope $\frac{\partial E}{\partial \epsilon_k} \sim \frac{1}{m_{j=0}^*} \sim Z \sim T_K^{\text{sp}}$, in the whole frequency regime plotted in Fig. 11(a). In contrast, for $J = 2$, T_K^{sp} is reduced by more than one order of magnitude compared to $J = 0$. Thus $\frac{\partial E}{\partial \epsilon_k} \sim \frac{1}{m_{j=2}^*}$ is constant only in a very small energy regime [as indicated by the black dashed line in the inset of Fig. 11(b)]. Further, this slope is much smaller than for $J = 0$, indicating a strong reduction of the effective mass, m^* , for finite J (due to Hund’s-coupling-induced strong correlations). Interestingly, when entering the SOS regime for frequencies $|\omega|$ above the FL regime, the slope becomes steeper: the spin degrees of freedom become unscreened, the QPs thus “undressed” and the effective mass smaller. For $\omega > 0$, this change in the slope is manifest in a slight kink, followed by a rather constant behavior of $\frac{\partial E}{\partial \epsilon_k}$. For $\omega < 0$, the shoulder (bump), observed in $A(\omega)$ and $\text{Im} \Sigma(\omega)$, leads to a somewhat artificial s-shaped dispersion, E ,

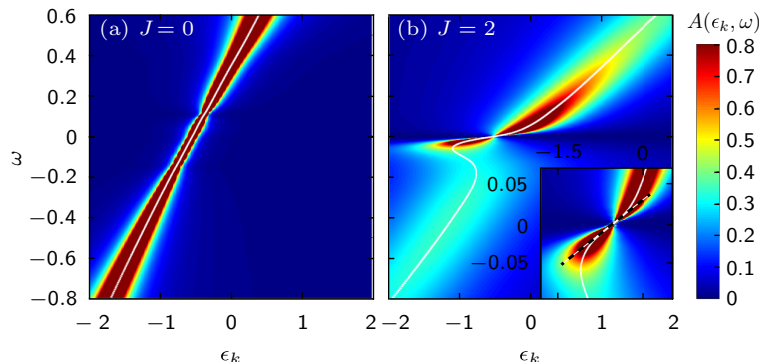


Figure 11: The structure factor, $A(\epsilon_k, \omega)$, at $\Delta_b = 3.5$ and $T = 0$ for (a) $J = 0$ and (b) $J = 2$. The white curves show the QP dispersion, E (see text for a definition). The inset in (b) zooms into the FL regime at $J = 2$. FL behavior is indicated by the black dashed guide-to-the-eye line.

including a divergence in the slope and negative effective masses (due to the Bethe lattice). In this regime, three maxima are observed in $A(\epsilon_k, \omega)$ at fixed ϵ_k . All these SOS features of $A(\epsilon_k, \omega)$ are completely absent for $J = 0$.

4.8. Spin-orbital separation as origin of low Z

We are now ready to reveal the connection of SOS and Z . We corroborate and summarize our findings of the previous Sec. 4.7 by directly analyzing the behavior of T_K^{orb} and T_K^{sp} as functions of Δ_b and J . Importantly, we expect, as pointed out earlier [see Luttinger pinning [82, 83], here with $A(\omega = 0) = 1/\pi$], that the width of the Kondo resonance scales linearly with the QP weight Z . As we will demonstrate below, in the Hund regime of J , this holds for the spin Kondo scale, i.e. $Z \propto T_K^{\text{sp}}$ for $J > J_{c1}^*$.

We replot the data of Fig. 8(c,d) in Fig. 12, but now with focus on T_K^{orb} and T_K^{sp} instead of Z on a linear [Fig. 12(a,c)] and a semi-logarithmic [Fig. 12(b,d)] scale. For reference, we also replot our Z data, but rescale it by a factor $a(J) \equiv T_K^{\text{sp}}/Z$ [indicated by the dotted grey curve in Fig. 12(c)], which is essentially the same for all values of Δ_b . Fig. 12(a,b) show that for fixed J , T_K^{sp} and Z have the same dependence on Δ_b , i.e. $T_K^{\text{sp}} = a(J)Z$, with a proportionality factor, $a(J) \simeq 0.36$, for $J > J_{c1}^*$ and increasing values of $a(J) > 0.36$ for decreasing $J < J_{c1}^*$ [see $a(J)$ in Fig. 12(c)]. Analogously, for fixed Δ_b and varying but sizeable $J > J_{c1}^*$ in Fig. 12(c,d), we find that $T_K^{\text{sp}} \approx 0.36 Z$.

We thus conclude, as a major result of this work, that *the reduction of Z in the Hund-metal regime of Fig. 1 at $n_d = 2$ is directly linked to the reduction of T_K^{sp} due to SOS*, and that all insights gained for Z hold for T_K^{sp} , and vice versa, specifically so for sizeable J . Based on the knowledge that the 3HHM at $n_d = 2$ has a FL ground state, it is of course expected that Z is a measure of the coherence scale using Landau's FL theory (see Luttinger theorem above), as e.g. also pointed out in Refs. [47, 50, 53]. In this work, we have now demonstrated *quantitatively* that and how Z and T_K^{sp} are connected. Additionally, we have conclusively identified the origin of low Z and the physical mechanism causing the bad-metallic transport – spin-orbital separation.

Fig. 12(a,b) demonstrate again the important insight that SOS is absent for $J = 0$ for all values of Δ_b (U): $T_K^{\text{orb}} = T_K^{\text{sp}}$ (black filled big circles and black open squares lie approximately on top of each other; the small difference is due to the fact that $|\chi''_{\text{orb}}(\omega)|$ was obtained from a calculation with different NRG parameters, i.e. stronger truncation due to numerical cost; we checked that using the same (stronger) truncation leads to exactly $T_K^{\text{orb}} = T_K^{\text{sp}}$. But also here, $T_K^{\text{sp}} = a(J)Z$ with $a(J) > 1$ [see dotted grey line in Fig. 12(c)] due to the FL ground state. In contrast, for nonzero J , SOS with $T_K^{\text{orb}} \gg T_K^{\text{sp}}$ occurs: with increasing J , T_K^{orb} is only moderately reduced, while T_K^{sp} and thus Z are strongly reduced (at fixed Δ_b). More importantly, *the slope of the linear function $T_K^{\text{sp}}(\Delta_b)$ and thus $Z(\Delta_b)$ is strongly reduced with increasing J* [solid lines in Fig. 12(a)], *while the slope of the linear function $T_K^{\text{orb}}(\Delta_b)$ is approximately J -independent* [dashed lines in

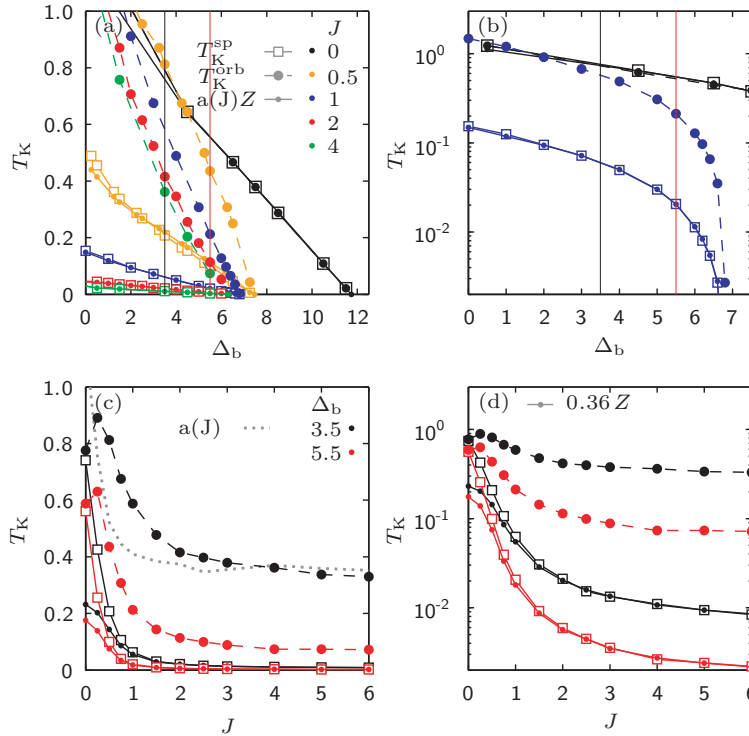


Figure 12: The orbital Kondo scale, T_K^{orb} (dashed curves with big filled circles), the spin Kondo scale, T_K^{sp} (solid curves with open squares), and the rescaled QP weight, $a(J)Z$ (dotted grey curve), plotted as a function of Δ_b for various values of J using (a) linear scale and (b) logarithmic scales for the y-axis. Both T_K^{orb} and T_K^{sp} decrease linearly with Δ_b , with a larger slope for T_K^{orb} if $J > 0$. The slope of T_K^{sp} strongly decreases with J , whereas the slope of T_K^{orb} is rather J -independent. SOS, $T_K^{\text{orb}} \gg T_K^{\text{sp}}$, occurs for all $\Delta_b \leq \Delta_b^{c2}$ at $J > 0$, but is more prominent at smaller Δ_b . (c,d) Same quantities as in (a,b) now plotted as a function of J for two values of Δ_b [indicated by vertical lines in (a)]. When J is turned on, both T_K^{orb} and T_K^{sp} decrease strongly, but differently, opening up the SOS regime at small $J < J_{c1}^*$, and saturating at $J > J_{c1}^*$.

Fig. 12(a)]. Far away from the MIT, at small to moderate Δ_b , this leads to a broad SOS regime which is extended from very low up to very large energy scales (comparable to the bare atomic excitations). When approaching the MIT with increasing Δ_b , both T_K^{orb} and T_K^{sp} decrease linearly, but with different slopes: the SOS regime shrinks and is shifted to lower energies [compare values of T_K^{orb} and T_K^{sp} at $\Delta_b = 3.5$ (black vertical line) and $\Delta_b = 5.5$ (red vertical line) for a fixed $J > 0$ in Fig. 12(a); see also the black ($\Delta_b = 3.5$) and red ($\Delta_b = 5.5$) curves in Fig. 12(c): for $J > J_{c1}^*$, the distance between dashed and solid line is smaller for larger $\Delta_b = 5.5$]. During this process the ratio $T_K^{\text{orb}}/T_K^{\text{sp}}$ first remains constant, as can be observed on a semi-logarithmic scale in Fig. 12(b) (blue curves). Very close to the MIT both T_K^{orb} and T_K^{sp} (and thus also Z) vanish together. Clearly, the DMFT self-consistency affects the QPP as a whole and finally destroys the QPP – including its internal structure – at the MIT.

We now also discuss in more detail the behavior of the Kondo scales and Z for fixed Δ_b and varying J [see Fig. 12(c,d)]. At small J , spin-orbital separation is turned on. The broad $SU(6)$ Kondo QPP with large $T_K^{\text{orb}} = T_K^{\text{sp}}$ splits very abruptly with increasing J into a $SU(3)$ and a $SU(2)$ Kondo resonance, reducing, after a slight decrease of T_K^{orb} , both T_K^{sp} and T_K^{orb} . As T_K^{sp} is affected much stronger, the ratio $T_K^{\text{orb}}/T_K^{\text{sp}}$ grows with increasing J , eventually saturating for sizeable $J > J_{c1}^*$. In the latter large- J regime, we observe that both T_K^{orb} and T_K^{sp} (Z) are only slightly reduced with increasing J [as already observed in Fig. 8(d) for Z], and $a(J) \approx 0.36$ is J -independent, i.e. SOS is fully developed and quite stable for sizeable J , and thus Z is low. Therefore, the main reason for lowering T_K^{sp} and Z upon turning on J can be heuristically ascribed to the

following effect: the ground state multiplet degeneracy is lifted by blocking orbital fluctuations through the selection of high-spin multiplets, as discussed in Sec. 2.6.1. The resulting orbital degeneracy is still much larger than the spin degeneracy. Consequently, local Kondo-type screening of orbital degrees of freedom occurs at much higher scales than spin screening. T_K^{orb} is only moderately whereas T_K^{sp} and thus Z are strongly lowered. As mentioned before, a quantitative analysis for a corresponding Kondo model is given in Refs. [31, 90]. As the degeneracy of the FL ground state changes when J is turned on, the factor $a(J)$ is strongly reduced, as well, in the small- J regime [see grey dotted curve in Fig. 12(c)]. The reduction of Z with increasing J is thus less severe than the reduction of T_K^{sp} (compare solid lines with small dots to solid lines with open squares).

Since $Z \propto T_K^{\text{sp}}$, also the behavior of $\Delta_b^{c2}(U_{c2})$ is determined by SOS. For $J \ll J_{c1}^*$, T_K^{sp} and thus $\Delta_b^{c2}(U_{c2})$ first decrease with increasing J [see Fig. 12(c) and Fig. 8(b), respectively]. For $J > J_{c1}^*$, T_K^{sp} plotted as a function of Δ_b essentially saturates, accordingly also Δ_b^{c2} saturates [see black dashed curves in Fig. 6(a) and Fig. 8(b)]. This explains why U_{c2} behaves non-monotonously, similar to U_{c1} , and shows that the bare gap, Δ_b , can be used as a measure of Mottness at sizeable J both for a mS and an iS.

Let us summarize the main conclusion of Sec. 4. *The main effect to induce strong correlations in the Hund metal regime of the 3HHM at $n_d = 2$ is Hundness rather than Mottness, i.e. the very abrupt turning-on of spin-orbital separation in the presence of nonzero (sizeable) J , independently of the value of Δ_b , thus also far from the MIT.* The MIT itself, which is purely induced by the DMFT self-consistency, is an additional but subleading effect in the system, that only further lowers the spin and orbital Kondo scales with increasing U . The formation of J -induced large spins is, in principle, a local process occurring on individual lattice sites. In contrast, the formation of a charge gap is a highly non-local process that needs to self-consistently incorporate the whole lattice dynamics (via a gapped hybridization function). As a consequence of Hundness, the nature of the incoherent transport is governed by “Hund metal physics” in the SOS regime at $n_d = 2$: large slowly fluctuating spins are non-trivially coupled to screened orbitals (see definition in Sec. 3.1).

But when SOS is a generic effect in the metallic regime of the 3HHM (and presumably of all particle-hole asymmetric degenerate multi-band Hund models), in which sense do Hund- and Mott-correlated systems then differ in nature?

4.9. Hund- versus Mott-correlated bad metals

Indeed, for the 3HHM at fixed and sizeable J , the features occurring for instance in $A(\omega)$, differ, in principle, only quantitatively when U is varied: the Kondo scales shift as a function of U , but the qualitative structure of the QPP does not change. However, we argue that the ratio of the bare atomic scales and the Kondo scales (in particular T_K^{orb}), or phrased differently, the ratio of the characteristic energy scale of the Hubbard bands and the overall width of the QPP, sets the framework for a meaningful characterization of Mott- and Hund-correlated systems: this ratio is much larger in Mott than in Hund systems (see Fig. 13), leading to qualitative different signatures, as demonstrated for temperature-dependent quantities in Ref. [37].

Hund metals (characterized by moderate U , but sizeable J) are by definition far from the MIT. Their lowest bare atomic excitation scales, ω_h and ω_{e1} are small [see discussion following Eqs. (3b)]. The Hubbard bands still overlap for moderate values of U and form a broad incoherent background in a range estimated by $\omega_{e2} - \omega_h$, having $\omega_h < 0 < \omega_{e1} < \omega_{e2}$. While T_K^{sp} and thus Z are considerably reduced, T_K^{orb} is comparable to the bare atomic excitation scales. This implies a ratio of order one between T_K^{orb} and the bare atomic excitation scales [see Fig. 13(b)]. As a consequence, the incoherent SOS window, $T_K^{\text{sp}} < |\omega| < T_K^{\text{orb}}$, is broad and “Hund metal physics” is relevant in a large energy window in Hund metals. For instance, the temperature-dependent local spin susceptibility of a Hund metal shows Curie-like behavior in the incoherent regime revealing large localized spins [37]. The low Z of Hund metals thus implies spin localization but no charge localization. Impurity physics dominates.

Multi-band Mott systems (characterized by U being large compared to J) are by definition close to the MIT. Their lowest bare atomic excitation scales, ω_h and ω_{e1} are large, thus the Hubbard bands are pronounced and well separated. Both Kondo scales are small and thus the QPP narrow. Together this implies that the bare atomic scales are much larger than T_K^{orb} [see Fig. 13(c)]. Further, the incoherent SOS window, $T_K^{\text{sp}} < |\omega| < T_K^{\text{orb}}$, is very small and “Hund metal physics” is almost not observable. Similar to

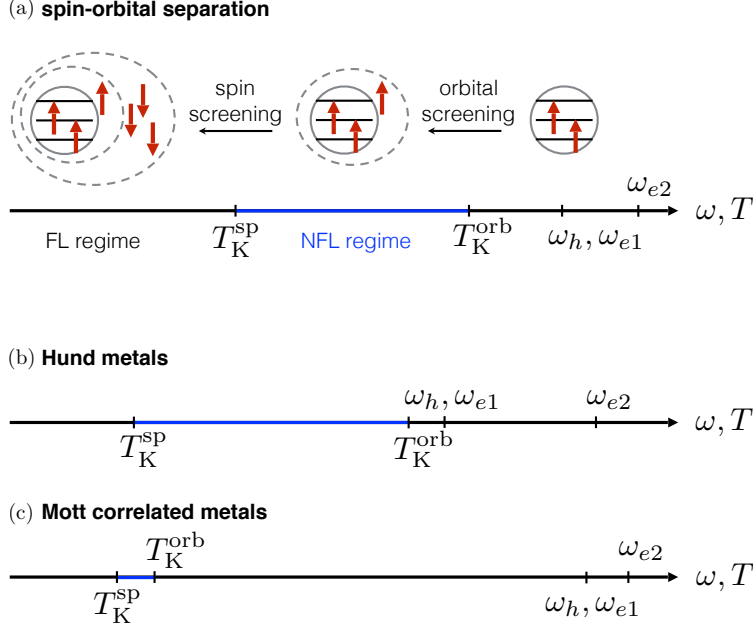


Figure 13: (a) Schematic depiction of the two-stage screening process of SOS at filling $n_d = 2$. First the orbital degrees of freedom are screened below the orbital Kondo scale, T_K^{orb} , by the formation of a large, effective, Hund’s-coupling induced $3/2$ -spin including a bath spin degree of freedom. Then, at a lower spin Kondo scale, T_K^{sp} , this effective $3/2$ -spin is fully screened by the three bath channels of the 3HHM (see also the discussion for Fig. 16 in Sec. 5.5). Incoherent NFL behavior is found for $T_K^{\text{sp}} < |\omega|, T < T_K^{\text{orb}}$, and FL behavior at energies below T_K^{sp} . (b) In Hund metals, bare atomic excitation scales, ω_h and ω_{e1} , and the overall width of the QPP, T_K^{orb} , are comparable in magnitude, while T_K^{sp} and thus Z are much smaller, opening a large relevant NFL regime in the system. (c) In Mott-correlated metals, we find $T_K^{\text{sp}} \sim T_K^{\text{orb}} \ll \omega_h, \omega_{e1}$, such that Z is reduced while SOS is not important.

one-band Mott systems, Z is low because charge fluctuations are suppressed. In sum, typical Mott physics, i.e. the DMFT self-consistency, dominates.

Finally, we note that the physics of Hund metals also strongly differs from that of generic one-band (or multi-band) Hubbard models (with $J = 0$) which are far from the MIT. First, the latter are weakly correlated, whereas a Hund system is strongly correlated, despite being far away from the MIT. Second, SOS and thus incoherent “Hund metal physics” only occurs for particle-hole asymmetric *multi*-orbital systems with at least three-bands, fillings of $1 < n_d < 2N_c - 1$ with $n_d \neq N_c$, and, most importantly, *nonzero* J .

5. Proximity to the half-filled MIT: Hundness versus Mottness at $2 < n_d < 3$

We now study the doping-dependence of the QP weight, Z , and of the electronic compressibility, $\kappa_{\text{el}} \equiv \frac{\partial n_d}{\partial \mu}$. In particular, we demonstrate that SOS also occurs for $2 < n_d < 3$, and that it determines the low Z -behavior there, as well. In particular, we focus on the question how Mottness of type (iii), i.e. the MIT at $n_d = 3$, affects SOS and whether (i) Hundness or (iii) Mottness is the key player to induce strong correlations in the Hund-metal regime for $n_d \gtrsim 2$. Further, we will show that, for all parameters studied, no Hund’s-coupling-induced Fermi-liquid instabilities (negative compressibilities) occur near the half-filled MIT of the 3HHM, in contrast to suggestions in Ref. [58].

5.1. MIT at $n_d = 3$

As mentioned before, at half-filling $n_d = 3$, $U_{e2}^{(3)}$ is much smaller than at other fillings. This is now explicitly demonstrated in Fig. 14(a), where we plotted $A(\omega)$ at $n_d = 3$, and $J = 1$ for various values of U ,

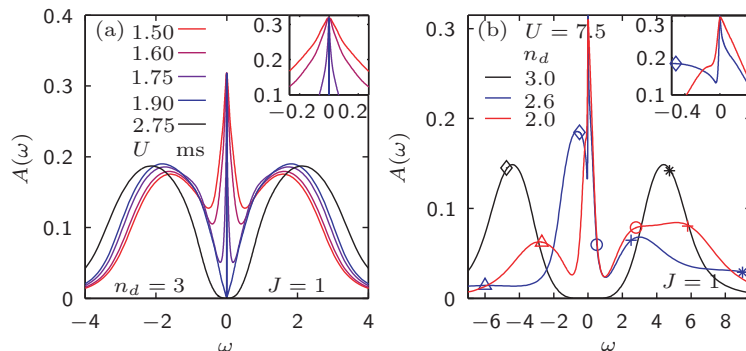


Figure 14: The zero-temperature local spectral function, $A(\omega)$, (a) for $n_d = 3$, $J = 1$ and various values of U , revealing an MIT with very small $2 < U_{c2}^{(3)} < 2.25$, and (b) for $U = 7.5$, $J = 1$ and varying n_d , revealing how the structure of the Hubbard side bands changes with filling. The five different markers represent the energy of the atomic multiplet excitations at given n_d [for $n_d = 2$, see Eqs. (3); for $n_d = 3$, see (5) for details and an assignment of the markers; for $n_d = 2.6$, the excitation energies are adapted to $\mu(n_d)$]. The insets in (a,b) zoom into the QPP.

revealing the MIT at $n_d = 3$. Starting from an mS and using $J = 1$, we deduce from our real-frequency data the extrapolated value $U_{c2}^{(3)} \sim 2.1 \pm 0.1$ at $n_d = 3$, which is strongly lowered compared to $U_{c2}^{(2)} = 8.8$ at $n_d = 2$. While the region of low Z around $n_d = 2$ reaches down to moderate values of U far below $U_{c2}^{(2)}$, i.e. far away from the MIT at $n_d = 2$ in Fig. 1, these U values are still larger than $U_{c2}^{(3)}$. Therefore, Refs. [32, 50] have argued that the MIT at $n_d = 3$ might be the reason for the low Z at moderate $U \ll U_{c2}^{(2)}$ (even at $n_d = 2$) – a statement that will be investigated in this section.

Further, we observe that also the structure of the Hubbard bands at $n_d = 3$ differs completely from those at $n_d = 2$ [compare red and black curves in Fig. 14(b)]. Specifically, in contrast to the $n_d = 2$ results of Sec. 4, the spectral functions of Fig. 14(a) are particle-hole symmetric and the QPP has no shoulder, only slight kinks (see inset). In a pictorial language, in the case of $n_d = 3$ for larger J , the only local multiplet is the $3/2$ spin, with a singlet orbital character. Hence orbital Kondo physics is absent (or quenched up to energies on the order of the local multiplet excitations, i.e. the Hubbard bands). Therefore SOS features, as revealed for $n_d = 2$, are absent at half-filling.

5.2. Peak structure of Hubbard bands at $2 \leq n_d \leq 3$

At integer filling $n_d = 2$ [red curve in Fig. 14(b)] $A(\omega)$ consists of three peaks away from $\omega = 0$, while at $n_d = 3$ it has only two pronounced peaks [black curve in Fig. 14(b)] that are particle-hole symmetric with respect to $\omega = 0$. The peak positions at finite frequency can be understood simply from the underlying atomic multiplet transition energies listed in Eqs. (3) for $n_d = 2$ and Eqs. (5) for $n_d = 3$, assuming sizeable J .

In order to study scenarios (i) and (iii) at intermediate fillings, $2 < n_d < 3$, we start by investigating the structure of the Hubbard side bands for a filling, $n_d = 2.6$ [blue curve in Fig. 14(b)]. We find that they are composed of all five types of atomic multiplet excitations from both the $n_d = 2$ and $n_d = 3$ ground states (5 peaks altogether) with their excitation energies adapted to $\mu(n_d = 2.6)$. Overall, at intermediate fillings, $n_d = 2 \rightarrow 3$, we find a smooth crossover in the structure of the Hubbard bands between their shape at $n_d = 2$ and $n_d = 3$, respectively, caused by the smooth level transformation of eigenstates in the spectrum of the local Hamiltonian with changing $\mu(n_d)$, interchanging the ground state and varying the probability of one-particle multiplet excitations. In contrast, the shape of the Kondo resonances at $\omega = 0$ change drastically when moving from $n_d = 2$ to $n_d = 3$.

5.3. Spin-orbital separation at $2 < n_d < 3$ as the origin of low Z

Next we gain insights from the structure of the QPP with varying n_d . Similar to Fig. 4, we study the filling dependence of T_K^{orb} (dashed curves) and T_K^{SP} (solid curves) in Fig. 15(a) and its inset, now for three

different values of U . With increasing n_d (decreasing distance to half-filling, $3 - n_d$), we observe an increasing separation of both Kondo scales, i.e. an increasing ratio of $T_K^{\text{orb}}/T_K^{\text{sp}}$, for all values of U . Thus SOS emerges for all fillings $1 < n_d < 3$ in the metallic phase (as already indicated in Sec. 3 and the inset of Fig. 3(f) in Ref. [33]). We will show, however, that the “nature” of SOS changes with n_d . We remark that the behavior of T_K^{sp} plotted versus n_d in the inset of Fig. 15(a) corroborates earlier results of Ref. [7].

We begin by considering $n_d = 1$. We note that, in the absence of charge fluctuations, i.e. for the pure Kondo limit of the AHM, and if the energy scale of charge fluctuations is much larger than the Kondo scales in the 3HHM (or AHM), the Hund’s coupling J just becomes an energy offset and hence irrelevant, such that the SU(6) symmetry remains intact. Therefore it holds at $n_d = 1$ that $T_K^{\text{orb}} = T_K^{\text{sp}}$ independent of J (as demonstrated for the impurity AHM in the inset of Fig. 3(f) in Ref. [33] and for a Kanamori model in Fig. 6 of Ref. [76]). In the presence of charge fluctuations at higher energies, it still holds $T_K^{\text{orb}} \approx T_K^{\text{sp}}$. For example, in Fig. 15(a) for the self-consistent 3HHM, T_K^{orb} is shifted by about a factor of 2 towards larger values compared to T_K^{sp} , especially for lower values of U which encourages larger charge fluctuations (see e.g. black curves). For n_d near 1, the Kondo scales are large in energy and comparable to the bare atomic multiplet excitations scales. Thus, signatures of the QP and of bare atomic physics merge in χ''_{orb} and χ''_{sp} [see Fig. 16(d)]. As both quantities are affected differently by the charge fluctuations due to Hund’s coupling, their maxima, T_K^{orb} and T_K^{sp} , become shifted in energy with respect to each other.

As the local occupation increases towards $n_d = 2$, SOS is turned on, i.e. the impurity’s ground state SU(6) symmetry is split, and T_K^{sp} decreases by more than a factor of 2 for $U = 2.25$ (solid black curve), of 5 for $U = 5$ (solid blue curve) and of 10 for $U = 7.5$ (solid red curve). At the same time, T_K^{orb} first slightly increases, reaching a maximum at around $n_d = 1.5$, and then (slightly) decreases again. For the largest $U = 7.5$, this leads to a reduction of T_K^{orb} by a factor of about 4 (dashed red curve; see also inset). There at $n_d = 2$, a strong minimum develops in T_K^{orb} and a shoulder in T_K^{sp} , respectively, with increasing U (red curves) due to the growing influence of the MIT at $n_d = 2$, lowering both Kondo scales (as explained in Sec. 4). For $n_d \rightarrow 3$, similar to the behavior in the inset of Fig. 3(f) in Ref. [33] for the impurity AHM, T_K^{sp} drops below the lowest relevant energy scale. On the contrary, T_K^{orb} grows up to energy scales comparable to the bare atomic scales in the system. This shows that orbital fluctuations are suppressed right away together with charge fluctuations. Hence no orbital Kondo physics can develop. What is left at half-filling, is a large spin $S = 3/2$ on the impurity that needs to be screened dynamically.

Figure 15(a) also shows Z (dotted curves) as a function of n_d . We find that, similar to the case of $n_d = 2$ in Sec. 4, Z essentially follows the behavior of T_K^{sp} for $2 \leq n_d < 3$ with $T_K^{\text{sp}}/Z \approx 0.4$, reflecting the fact that the ground state is a FL. Throughout this regime, *the small values of Z can be understood, via their proportionality to T_K^{sp} , to be a direct consequence of SOS, which ensures that $T_K^{\text{sp}} \ll T_K^{\text{orb}}$* . For $n_d \rightarrow 1$ the ratio T_K^{sp}/Z changes, due to strong changes in the ground state degeneracy [see deviations between dotted and solid curves for $n_d < 2$ in the inset of Fig. 15(a)], reminiscent of the behavior of Z for small J in Fig. 12(c).

We remark that from the behavior of $T_K^{\text{sp}}(n_d)$ we cannot deduce any indication for a relation between the physics at $n_d = 2$ and the physics at $n_d = 3$. On the contrary, we see markedly different physical behavior for $n_d = 3$ as compared to $n_d = 2$, e.g. with the absence of Kondo physics in the orbital sector, and in this sense the absence of SOS for $n_d = 3$. Further, the Hund-metal regime, (hatched area in Fig. 1) is special in that there we have not only SOS with $T_K^{\text{sp}} \ll T_K^{\text{orb}}$, but in addition also a dynamically generated, fairly small value of T_K^{orb} . Thus, conditions there are optimal for the Hund’s coupling to align spins in different orbitals without forming an orbital singlet from the outset, allowing for a non-trivial interplay between both spin and orbital degrees of freedom, which induces SOS. We thus argue that *the MIT at $n_d = 3$ does not trigger the low Z around $n_d = 2$* .

5.4. Spin-orbital separation at $2 \leq n_d < 3$: QPP structure

Next we study the qualitative change in the structure of the low-energy quasi-particle peak due to SOS with filling in more detail. In Fig. 15 (b,c,d) we plotted $A(\omega)$ with focus on the QPP, and in Fig. 15 (e,f) $\text{Im} \Sigma(\omega)$ for $U = 5$, $J = 1$ and various fillings, $1 \leq n_d < 3$.

In Fig. 15 (b), for $n_d > 2$, $A(\omega)$ is shown on a linear frequency scale and we marked the multiplet excitations of Sec. 2.6.1 and Sec. 2.6.2 [with the excitation energies adapted to $\mu(n_d)$], as some of these (diamonds

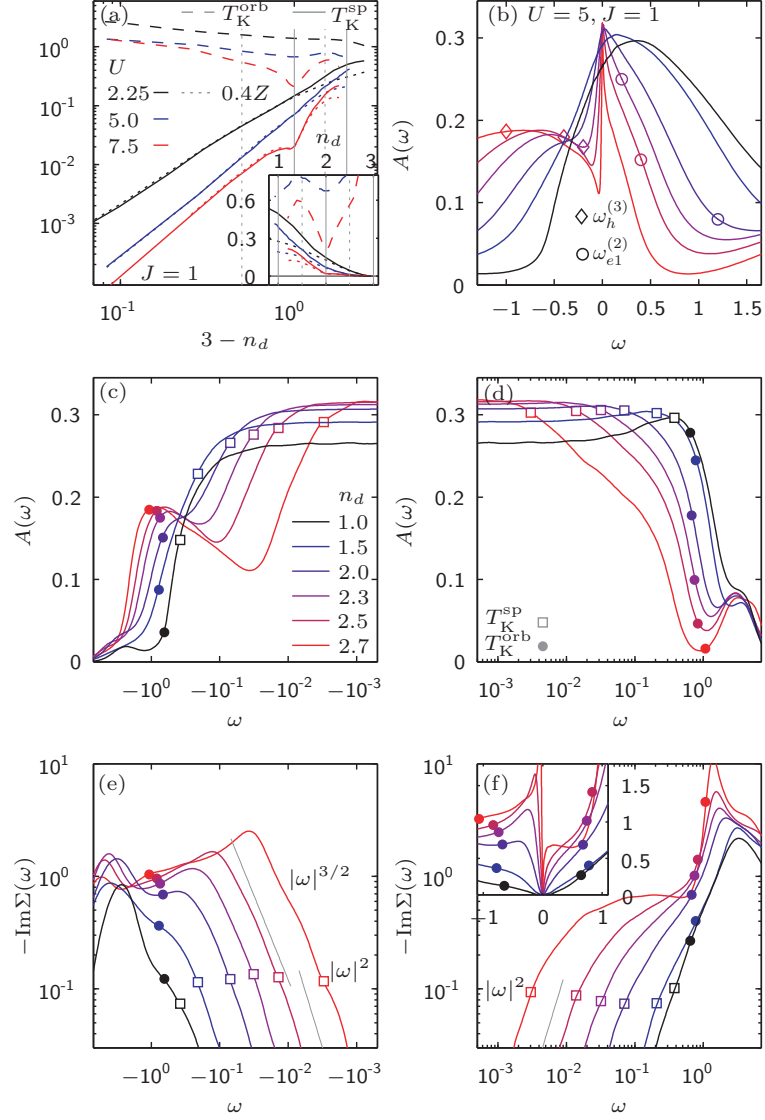


Figure 15: (a) The orbital and spin Kondo scales, T_K^{orb} (dashed) and T_K^{sp} (solid), on a log-log plot versus the distance to half-filling, $3 - n_d$, reveal the filling-dependence of SOS. The low QP weight Z (dotted curves) essentially follows the behavior of T_K^{sp} for $2 \leq n_d < 3$, and is thus determined by SOS. The inset shows the same data plotted versus n_d on a linear scale. (b-d) The local spectral function $A(\omega)$ for $U = 5, J = 1$ and various choices of n_d , shown on (b) linear and (c,d) logarithmic frequency scales for (c) negative and (d) positive frequencies. The symbols in (b) indicate atomic multiplet excitations at given n_d [for $n_d = 2$, see Eqs. (3); for $n_d = 3$, see (5) for details and an assignment of the markers; for $2 < n_d < 3$, the excitation energies are adapted to $\mu(n_d)$]. For $n_d \rightarrow 3$, the $\omega_h^{(3)}$ excitations (diamonds) gain weight and replace the SOS shoulder in $A(\omega)$, which is clearly present as a pure QP-like feature at $n_d = 2$. (e,f) The imaginary part of the self-energy, $\text{Im}\Sigma(\omega)$, plotted versus (e) negative and (f) positive frequencies. Solid grey guide-to-the-eye lines indicate $|\omega|^2$ FL power-law behavior and apparent $|\omega|^{3/2}$ behavior at $\omega < 0$. The latter fractional power-law presumably originates just from a cross-over behavior.

and circles) are rather low in energy and therefore might influence the shape of the QPP. Complementary to this, in Fig. 15 (c,d), $A(\omega)$ [and in Fig. 15 (e,f) $\text{Im}\Sigma(\omega)$] is shown on a logarithmic frequency scale and T_K^{orb} and T_K^{sp} are marked by open squares and filled circles, respectively [see legend in (d)]. Clearly, with increasing n_d , the SOS regime opens up: while there is no substructure in the QPP in $A(\omega)$ for $n_d \lesssim 1.5$ [black and blue curve in Fig. 15 (b,c,d)], a pronounced shoulder develops with increasing $n_d \gtrsim 2$ for $\omega < 0$ and a kink for $\omega > 0$. Accordingly, a shoulder (kink) emerges in $\text{Im}\Sigma(\omega)$ for $n_d > 1.5$ at $\omega < 0$ ($\omega > 0$) which develops to a pronounced bump (plateau) for $n_d > 2.5$ [see Fig. 15 (e,f)]. In a sense, the behavior of the SOS features with increasing $1 < n_d < 3$ seems reminiscent of their behavior with increasing J . We note however that the character of the shoulder in $A(\omega)$ changes for n_d well beyond 2: the shoulder gradually transforms into a Hubbard side band at the atomic hole excitation $\omega_h^{(3)}$ for $\omega < 0$ [diamonds in magenta and red curve in Fig. 15 (b); see also inset of Fig. 14]. In contrast, the QPP substructure narrows significantly, e.g. for $\omega > 0$, giving rise to a single albeit still strongly asymmetric Kondo peak at $n_d = 2.7$. A true QP-like shoulder only occurs for fillings $n_d \lesssim 2.5$, which we have checked in pure impurity AHM calculations, where the Kondo scales can be tuned to lower values and QP-like and atomic-like features are well separated.

5.5. Spin-orbital separation at $2 \leq n_d < 3$: NRG flow diagrams

The nature of SOS is best revealed by the RG flows accessible to NRG via finite-size level spectra, aka. energy flow diagrams [see Fig. 16(a-c)]. Technically, they show how the lowest-lying rescaled eigenlevels of a length- l Wilson chain [92, 93] evolve with l , where “rescaled” means given in units of $\omega_l \propto \Lambda^{-l/2}$ (in the convention of Ref. [35], where $\Lambda > 1$ is the NRG discretization parameter; see supplement of Ref. [33]). Conceptually, these levels represent the finite-size spectrum of the impurity+bath put in a spherical box of radius $R_l \propto \Lambda^{l/2}$, centered on the impurity [92, 94]: as l increases, the finite-size level spacing $\omega_l \propto 1/R_l$ decreases exponentially. The corresponding flow of the finite-size spectrum is stationary (l -independent) while ω_l lies within an energy regime governed by one of the fixed points, but changes when ω_l traverses a crossover between two fixed points. As the rescaled ground state energy of a Wilson chain differs for even and odd numbers l of sites due to fermionic parity, the RG flow of the system is separated into an “even” and “odd” NRG flow diagram, both reflecting the same physics of the system. In Fig. 16(a-c), we purely concentrate on the even flow, since this permits the energetically favored global (Kondo) singlet ground state as $l \rightarrow \infty$. We fully exploited the symmetries $U(1)_{\text{ch}} \times \text{SU}(2)_{\text{sp}} \times \text{SU}(3)_{\text{orb}}$ of the 3HHM in our NRG. Hence each line represents a multiplet and the color of each line specifies a well-defined symmetry sector $(Q, S, q_1 q_2)$, where the total charge Q is measured relative to half-filling, S is the total $\text{SU}(2)$ spin multiplet sector, and $q \equiv (q_1 q_2)$ is the $\text{SU}(3)$ orbital label.

The multiplets with significant spin or orbital character behave qualitatively differently in the flow diagrams in Figs. 16(a-c) at finite J at the crossover scales T_K^{sp} and T_K^{orb} (vertical dashed lines). The energy range in between defines the SOS regime. We emphasize that *the SOS regime is an entirely new intermediate phase, which is absent for $J = 0$ [see inset in Fig. 16(a)], and opens up right at the Kondo scale in the NRG flow diagram when turning on J , while the energy flow at large energies and the FL fixed point towards $\omega_l \rightarrow 0$ remains exactly the same.* At $n_d = 2$, the spacing between T_K^{orb} and T_K^{sp} , though, only spans about an order of magnitude which is too small for the level flow to display a stationary intermediate fixed point.

Above T_K^{orb} the spectra correspond to the high energy physics of the Hubbard bands. Below T_K^{sp} the excitation spectra reach a FL-fixed point with qualitatively identical multiplet eigenlevel structures for all values of n_d , U , and J : they can be interpreted in terms of non-interacting single-particle excitations [see also the $|\omega|^1$ -scaling of χ''_{orb} and χ''_{sp} in Fig. 16(d)].

We now focus on Fig. 16(a) for $n_d = 2$, $U = 5$ and sizeable $J = 1$ (similar to Fig. 3(g) in Ref. [33]). As ω_l drops below T_K^{orb} , orbital screening sets in, favoring orbital singlets $q = (00)$ [black and orange curves], hence other multiplets rise in energy. For the same charge Q , large-spin multiplets lie lower in energy (green curve lies below red one for $Q = -2$, and orange below bright blue for $Q = -3$). As ω_l drops below T_K^{sp} , spin screening sets in, favoring spin singlets and pushing up multiplets with $S \neq 0$. Now, multiplets with same particle number but different spins become degenerate (compare again green and red curves for $Q = -2$, and orange and bright blue curves for $Q = -3$).

Interestingly, with increasing n_d , where the spin-orbital regime becomes wider, a new flow behavior slowly emerges at energies entering from (just above) T_K^{orb} : the multiplet with large spin $S = 3/2$ and singlet

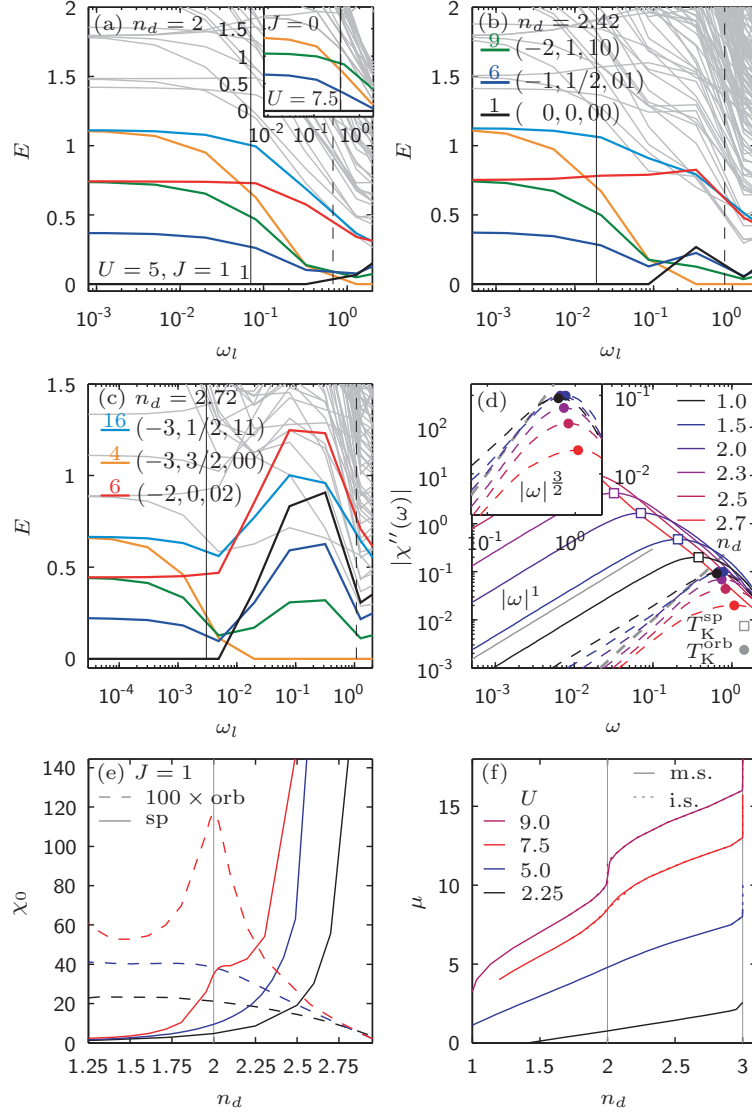


Figure 16: (a-c) Even NRG flow diagrams for different fillings, (a) $n_d = 2$, (b) $n_d = 2.42$, and (c) $n_d = 2.7$. The data represents rescaled energies of the lowest-lying eigenmultiplets of a Wilson chain of length l plotted versus the characteristic level spacing $\omega_l \propto \Lambda^{-l/2}$ (see text). NRG parameters: $\Lambda = 4$, $E_{\text{trunc}} = 9$, thus keeping up to $D^* \lesssim 5,000 U(1)_{\text{charge}} \times SU(2)_{\text{sp}} \times SU(3)_{\text{orb}}$ multiplets (corresponding to about $D = 155,000$ states) [35, 36]. The color specifies the symmetry sectors $(Q, S, q_1 q_2)$ (see text) as given in the legend. Numbers above lines in the legend give multiplet degeneracies. Solid (dashed) vertical lines mark the spin (orbital) Kondo scale, T_K^{sp} (T_K^{orb}), respectively, where the range $T_K^{\text{sp}} < |\omega| < T_K^{\text{orb}}$ represents the SOS regime. The inset of (a) shows, for comparison, the NRG flow for $J = 0$ at $U = 7.5$. (d) The imaginary parts of the dynamical impurity orbital and spin susceptibilities, $|\chi''_{orb}(\omega)|$ (dashed) and $|\chi''_{sp}(\omega)|$ (solid) for $U = 5$, $J = 1$ and various choices of n_d . T_K^{sp} (filled circles) and T_K^{orb} (open squares) are defined from the maxima of $\chi''_{orb}(\omega)$ and $\chi''_{sp}(\omega)$, respectively. $\chi''_{orb}(\omega)$ follows an apparent $|\omega|^{3/2}$ power law in the SOS regime (dashed grey guide-to-the-eye line) for fillings $2 \lesssim n_d \lesssim 2.5$, which is likely just a cross-over behavior as seen from the flows in (a,b). Below T_K^{sp} , the $|\omega|^1$ FL power-law behavior sets in, indicated by a solid grey guide-to-the-eye line. The inset is a zoom of $\chi''_{orb}(\omega)$, revealing different “slopes” of $\chi''_{orb}(\omega)$ in the SOS regime for different n_d . (e) The static local orbital and spin susceptibilities, χ_0^{orb} (dashed) and χ_0^{sp} (solid) are plotted as a function of n_d for three different values of U and $J = 1$. (f) The chemical potentials, μ , are plotted as functions of the filling n_d , for $J = 1$ and various values of U to study the behavior of the electronic compressibility κ_{el} .

orbital character $q = (00)$ [orange curve Figs. 16(a-c)], which is still outside the SOS regime at $n_d = 2$ [Fig. 16(a)], moves into the SOS regime at $n_d = 2.42$ [Fig. 16(b)], and takes over the ‘SOS regime’ at $n_d = 2.72$ [Fig. 16(c)]. At the same time, the T_K^{orb} moved upward and merges with the bare atomic energy scales. At T_K^{sp} , finally, a FL develops: the large spin $S = 3/2$ is screened and moves upward, crossing multiple lines. The new ground state at energies below T_K^{sp} is the Kondo spin singlet (black line).

Note that the crossing of the large spin state (orange line) starts just above T_K^{orb} at $n_d = 2$, and has moved all the way down to T_K^{sp} at $n_d = 2.72$. In particular, we also emphasize that the shoulder in $A(\omega)$ for $n_d = 2$ in Fig. 15(c) emerges precisely around this crossing region. Therefore this qualitative change in the energy flow diagram is responsible that *the intermediate SOS regime strongly changes its character as the filling is increased towards $n_d = 3$* . At $n_d = 3$ the SOS becomes trivial in the sense that the orbital blocking is immediately present due to the given filling.

Importantly, the structure of the flow below the crossing region, i.e the transition behavior with decreasing ω_l from the NFL into the FL fixed point is the same for all fillings $2 \leq n_d < 3$. It is therefore natural to assume that also in the SOS regime at $n_d = 2$, the physics is governed by an underlying NFL fixed point (i.e. a fixed point that would show up for a larger SOS region as observed in a new analysis [90] of the Kondo limit of the 3HHM), which also enforces the reversion of the lowest few multiplets compared to the FL fixed point and has a $S = 3/2$ and $(q_1 q_2) = (00)$ multiplet as ground state.

From the NRG flow analysis we deduce the following generic screening mechanism of SOS, which is visualized in Fig. 13(a) for $n_d = 2$.

SOS is a two-stage screening process. First the orbital degrees of freedom are quenched below the orbital Kondo scale, T_K^{orb} . In a Kondo-screening language, described in the following for $n_d = 2$, we have $S = 1$ in the spin sector, while in the orbital sector, we have the fundamental representation $q = (10)$ with dimension 3 [green lines in Figs. 16(a-c)], coupled to the 3 channels, leading to full orbital screening. As a result of this screening process *the impurity binds one electron from the bath to form an orbital singlet*. This electron has a spin $1/2$, which combines with the local spin 1 – due to ferromagnetic Hund’s coupling – to a spin $3/2$. *Then, at a lower spin Kondo scale, T_K^{sp} , this effective $3/2$ spin is fully screened by the three bath channels of the 3HHM.* The formation of the orbital singlet causes the orbital susceptibility to reach a maximum. The resulting free spin enhances the spin susceptibility as the frequency decreases [see Fig. 9(a), Fig. 10(a) and also Fig. 16(d)]. Since a bath electron with a specific orbital degree of freedom is included in the orbital screening process, *spin and orbital degrees of freedom are still coupled, leading to a highly intertwined NFL in the SOS regime at $n_d = 2$* . The same screening process occurs, in principle, for $2 \leq n_d < 3$ as well, but the details vary with filling. For n_d approaching 3, the $3/2$ spin is increasingly composed purely from the impurity spin, which facilitates the formation of the orbital singlet [T_K^{orb} grows in Fig. 15(a)], but is harder to be screened [T_K^{sp} decreases in Fig. 15(a)]. Thus the contribution of the bath electron in the screening process becomes less important, and the dynamics of the spin and orbital degrees of freedom get more and more decoupled. For $n_d = 3$, the orbital singlet is directly and locally formed from the impurity $3/2$ spin without any involvement from bath degrees of freedom. Accordingly, in a weak coupling analysis [31] of the 3HHM, it is emphasized that the spin Kondo scale depends *explicitly* on the representations of the spin and the orbital isospin, which is unusual and only occurs for complex Kondo models in which spins and orbitals are coupled.

5.6. Spin-orbital separation at $2 \leq n_d < 3$: susceptibilities

In Fig. 16(d), we analyze the behavior of the imaginary parts of the dynamical impurity orbital and spin susceptibilities χ''_{orb} and χ''_{sp} , for various fillings n_d at $U = 5$, $J = 1$, and in Fig. 16(e) the behavior of the static local orbital and spin susceptibilities $\chi_0 \equiv \chi(0)$ for various U at fixed $J = 1$. As already seen in Fig. 4(c), with increasing filling between $1 \leq n_d < 3$ in Fig. 16(d), the maxima of χ''_{sp} (T_K^{sp} , marked by open squares) increase in height and decrease in $|\omega|$, and accordingly χ_0^{sp} [solid curves in Fig. 16(e)] grows with n_d for all values of U . For $n_d \leq 2$, the enhancement of χ_0^{sp} is small and just part of an upward trend if $U \ll U_{c2}^{(2)}$ (black and blue curves), but develops into a shoulder if U is close to the MIT at $n_d = 2$ (red curve). For $n_d > 2$, χ_0^{sp} increases very strongly with growing n_d , almost diverging. In contrast, with increasing filling, $n_d \leq 2$, the maxima of χ''_{orb} almost coincide [see filled circles in Fig. 16(d)], and χ_0^{orb} is approximately

constant for $U \leq 5$ [see dashed black and blue curves in Fig. 16(e)]. Only for $U = 7.5$ much closer to $U_{c2}^{(2)}$, χ_0^{orb} first decreases and then strongly increases near the MIT at $n_d = 2$, indicating the presence of strong orbital fluctuations. With increasing filling, $n_d > 2$, the height of the maxima of χ_{orb}'' declines [see filled circles in Fig. 16(d)] and χ_0^{orb} drops to zero when approaching $n_d = 3$, for all values of U [see dashed curves in Fig. 16(e)], reflecting the absence of orbital fluctuations at this point. We remark that the occurrence of a maximum in χ_0^{orb} has also been shown in DMFT+QMC calculations [7].

In Fig. 16(d), $|\omega|^1$ -FL-scaling is clearly observed in χ_{orb}'' and χ_{sp}'' below T_K^{sp} for all values of n_d , as indicated by the solid grey guide-to-the-eye line. Within the SOS regime $T_K^{\text{sp}} < \omega < T_K^{\text{orb}}$, χ_{orb}'' shows NFL behavior (no $|\omega|^1$ -scaling) [see also inset of Fig. 16(d)]. With increasing $n_d > 1$ and widening SOS regime, the “slope” of χ_{orb}'' (on a log-log plot) becomes steeper than in the FL regime, i.e. an approximate power-law would have a power larger than 1. For $2 \lesssim n_d \lesssim 2.5$, χ_{orb}'' reaches an approximate power of $\frac{3}{2}$. This, however, is presumably not a pure power law, since the SOS regime is not wide enough, i.e. the RG flows of Fig. 16(a-c) are yet far from reaching a stationary fixed point in the SOS regime. For $n_d > 2.5$, however, the slope is again lowered to almost 1.

Based on these observation and the RG flows we argue that intriguing NFL behavior with relevance for Hund metals occurs mainly in the filling regime of approximately $1.5 \lesssim n_d \lesssim 2.5$. Only there, a complex two-stage screening process couples the dynamics of spin and orbital degrees of freedom by the formation of a large, effective Hund’s-coupling induced $3/2$ spin including a bath spin degree of freedom. Although fully screened, the orbital degrees of freedom still “feel” the slowly fluctuating, large local moments, which is reflected in the fact that, in the SOS regime in Fig. 16(d), the “slope” of χ_{orb}'' is increased compared to FL scaling.

To summarize, *we argue that the suppression of Z in the Hund metal regime around $n_d \gtrsim 2$ at moderate $U \ll U_{c2}^{(2)}$ is mainly caused by SOS*, and thus by the presence of a sizeable Hund’s coupling in the system. It is not triggered by Mottness (iii), the proximity to the MIT at half-filling, $n_d = 3$. Of course, as also known from the MIT in the one-band Hubbard model, Z is *further* lowered by the proximity to the MIT at $n_d = 3$, but this effect is strong only close to $n_d = 3$ and is subleading in the Hund-metal regime. Further, the physics close to $n_d = 3$ is dominated by fully blocked orbital degrees of freedom while for Hund metals the orbital degrees of freedom play a subtle role in the nature of the NFL physics.

We remark that our insights might be relevant to better understand the physics of iron pnictides with hole and electron doping [14, 19]. For instance, for BaFe2As2 (with a nominal $d6$ occupation in the parent compound) correlations are enhanced upon approaching half filling with hole-doping, achieved by replacing Ba with K, and reduced upon electron doping, achieved by replacing Fe with Co [65].

5.7. Filling dependence of the compressibility, κ_{el}

We finish this section with a discussion of the compressibility in Fig. 16(f). We plot μ versus n_d to access the zero-temperature behavior of the electronic compressibility, $\kappa_{\text{el}} = \frac{\partial n_d}{\partial \mu}$, for finite $J = 1$ and for several values of U , varying from slightly above $U_{c2}^{(3)}$ to slightly above $U_{c2}^{(2)}$. Solid (dashed) lines are the results for a mS (iS), respectively. Normally, κ_{el} has finite, positive values for metals and vanishes for insulators. We would like to investigate whether κ_{el} remains positive throughout, or becomes negative for n_d close to the MIT at $n_d = 2$ or close to the MIT at $n_d = 3$. The latter scenario, a zone of Hund’s-coupling-induced negative compressibility in the n_d - U phase diagram, has been observed in a slave-boson study [58] of degenerate and non-degenerate multi-band Hund models, for nonzero J and $U \geq U_c$ at $T = 0$. The divergence of κ_{el} , when κ_{el} changes sign, has been assumed to be connected to the enhanced critical T_c of HTCS. However, for the 3HHM, for all parameters studied in Fig. 16(f), μ clearly increases monotonically with n_d . Hence the slope, κ_{el} , is positive for all non-integer fillings, also close to the insulating phase at $n_d = 2$ and $n_d = 3$, where n_d is fixed and thus incompressible for varying μ , i.e. $\kappa_{\text{el}} = 0$. We summarize that, for our study, *no negative (or divergent) compressibility has been observed for the 3HHM*. We note, though, that in principle a compressibility divergence can occur very close to a MIT in certain situations [41].

6. Conclusion

In this work, we studied the full phase diagram of the 3HHM at zero temperature with real-frequency DMFT+NRG data. Our main goal was to reveal the origin of the bad-metallic behavior (characterized by a low quasiparticle weight Z) in the Hund-metal regime (hatched area in Fig. 1) and to establish a global picture of SOS.

As a main result we demonstrated that, for nonzero J and for fillings $1 < n_d < 3$, SOS is a generic feature in the *whole* metallic (and coexistence) phase of the 3HHM, independently of U : turning on J opens up a new incoherent energy regime, $T_K^{\text{orb}} > |\omega|, T > T_K^{\text{sp}}$, in the system. Interestingly, for fillings around $n_d = 2$ (i.e approximately in the regime $1.5 \lesssim n_d \lesssim 2.5$) the SOS is special, as has been pointed out in Ref. [7]. There, orbital and spin degrees of freedom are *coupled* and thus behave very distinctly: orbital degrees of freedom are (mostly) quenched below T_K^{orb} and fluctuate rapidly, whereas spin degrees of freedom are unquenched, form large local moments, and fluctuate extremely slowly. Below, the strongly reduced spin Kondo scale, T_K^{sp} , both orbital *and* spin degrees of freedoms are fully screened and FL behavior sets in.

We confirm in detail that the suppression of T_K^{sp} with increasing J can be explained from a qualitative change in the underlying local multiplet spectrum, involving a reduction in the atomic ground state degeneracy. Z is explicitly shown to be proportional to T_K^{sp} , and thus small due to SOS.

In agreement with the analysis in the Kondo regime of the 3HHM [31], we argue that SOS is a non-trivial two-stage screening process, in which orbital and spin degrees of freedom are explicitly coupled: below T_K^{orb} , the orbital degrees of freedom form an orbital singlet through the formation of a large, effective, Hund's-coupling induced $3/2$ spin – *including* a bath spin degree of freedom; and below T_K^{sp} , the latter is fully screened by the three bath channels of the 3HHM.

In the real-frequency spectral function, SOS results in a "two-tier" QPP peak with a narrow needle (width $\propto T_K^{\text{sp}}$) on top of a wide base (width $\propto T_K^{\text{orb}}$).

Based on the SOS analysis we conclude, as major result of this work, that in the Hund-metal regime, at sizeable J , moderate U well below $U_c^{(2)}$ and fillings close to $n_d = 2$, i.e far from any MIT, Hundness, i.e scenario (i), is the origin of bad-metallic behavior and governs the physics of Hund metals. This constitutes a new route towards strong correlations very distinct from Mottness: while in the latter case charges are localized in close proximity to an MIT, Hundness implies the localization of spins but not the localization of charges. For Hund-correlated metals, T_K^{orb} is comparable in magnitude to bare atomic energy scales of the system, while T_K^{sp} (and thus Z) is strongly reduced, leading to low FL coherence scales and to a broad incoherent SOS regime. Hundness is thus physics governed by the QP needle being narrow, while the QP base remains wide. Importantly, this regime is characterized by the non-trivial interplay of orbital and spin degrees of freedom, induced by the special two-stage SOS screening process, which essentially dominates the normal-state incoherence of Hund metals. We remark that Mottness of type (ii) does affect the SOS when the distance to the MIT is decreased at fixed $n_d = 2$, by further lowering T_K^{orb} and T_K^{sp} , while their ratio remains constant. Whereas T_K^{orb} governs the Mott transition (which requires the full QPP to disappear), T_K^{sp} , being proportional to Z , governs the strength of correlations.

Mott-correlated metals, close to the MIT at $n_d \approx 2$, are dominated by Mottness, while the SOS regime is strongly downscaled and becomes negligible.

Close to the MIT at $n_d = 3$, the SOS regime widens up because the orbital degrees of freedom get blocked by the formation of a $3/2$ impurity spin, but its nature changes: the orbital and spin dynamics get decoupled. Thus, Mottness of type (iii) does not mediate the low Z in the Hund-metal regime.

In sum, our DMFT+NRG results corroborate the physical picture of Hund metals established in Refs. [6, 7, 31, 47] and enabled the quantitative analysis of the real-frequency properties of their unusual incoherent SOS regime. We showed that the spin-freezing phenomenon [51] and the Janus-faced influence of Hund's rule coupling can be consistently explained in the framework of SOS. We also explicitly demonstrated that no Hund's-coupling-induced FL instabilities (negative compressibilities) [58] occurs in our study of the 3HHM phase diagram.

Appendix A. Methods

We treat the 3HHM of Eq. (1) with single-site DMFT and use full-density-matrix (fdm)NRG [34] as real-frequency impurity solver.

Appendix A.1. Single-site Dynamical Mean-Field Theory

Single-site DMFT is a widely-used non perturbative many-body approach to strongly correlated systems [82]. Its basic idea is to approximate the full non local self-energy of the correlated lattice model by the purely local, but still frequency-dependent self-energy, $\Sigma(\omega)$, of the corresponding self-consistently determined quantum impurity model. In our case, we iteratively map the lattice 3HHM of Eq. (1) onto a three-band Anderson-Hund model (AHM) of the form

$$\hat{H}_{\text{AHM}} = \hat{H}_{\text{imp}} + \hat{H}_{\text{bath+hyb}}, \quad (\text{A.1a})$$

$$\hat{H}_{\text{imp}} = \varepsilon_d \hat{N} + \hat{H}_{\text{int}}[\hat{d}_\nu^\dagger] \quad (\text{A.1b})$$

with the same local interaction term, \hat{H}_{int} , as in Eq. (1b). Within this mapping process, the hybridization function $\Gamma(\varepsilon) = \pi \sum_k |V_k|^2 \delta(\varepsilon - \varepsilon_k)$ is determined self-consistently and eventually fully characterizes the interplay of the impurity and the non-interacting three-band spinful bath,

$$H_{\text{bath+hyb}} = \sum_{k\nu} \left(\varepsilon_k c_{k\nu}^\dagger \hat{c}_{k\nu} + V_k [\hat{d}_\nu^\dagger \hat{c}_{k\nu} + \hat{c}_{k\nu}^\dagger \hat{d}_\nu] \right). \quad (\text{A.2})$$

Here \hat{d}_ν^\dagger creates a local (“impurity”) electron of flavor ν with energy $\varepsilon_d = -\mu$. The total spin operator $\hat{\mathbf{S}}$ (and $\hat{\mathbf{S}}_i$, respectively) are lattice sums over $(\hat{n}_i - N_c)$, i.e. charge relative to half-filling. The average local site occupation number $n_d \equiv \langle \hat{n}_i \rangle$ is a measure of the lattice filling per site.

The lattice dynamics is fully captured by the local retarded lattice Green’s function, $G_{\text{latt}}(\omega)$, which is – after the self-consistent mapping – equal to the retarded impurity Green’s function, $G_{\text{imp}}(\omega) = \langle \hat{d}_\nu | \hat{d}_\nu^\dagger \rangle_\omega$, imposing the self-consistency condition: $G_{\text{latt}}(\omega) = G_{\text{imp}}(\omega) \equiv G(\omega)$. Note that we consistently drop the flavor index ν for all correlation functions as they are identical by symmetry for all spins and orbitals.

In this work, we study Hund metals only on the Bethe lattice, i.e. we use the semi-elliptic density of states that occurs in this limit of infinite lattice coordination and neglect realistic band-structure effects, to investigate the pure correlation effects of multi-orbital Mott and Hund physics. The self-consistency condition can then be simplified to,

$$\Gamma(\omega) = -t^2 \text{Im} G(\omega). \quad (\text{A.3})$$

The approximation of a purely local self-energy in single-site DMFT is strictly valid only in the artificial limit of infinite lattice coordination number. However, if interactions act only locally in a lattice system with finite coordination number, as in the case of Hund’s rule coupling which is adopted from local atomic physics, single-site DMFT is assumed to be an appropriate method to reproduce the correct physics. This assumption is supported by recent cluster-DMFT calculations for Hund metals [95]. Further, single-site DMFT is in general able to capture basic strong correlations effects of finite dimensional systems (like the MIT) due to its non-perturbative character: through the energy-dependence of the local self-energy both the itinerant and localized nature of electrons, and thus both weak and strong correlations, can be handled on equal footing.

This is considered to be of utmost importance for the description of iron-based HTSCs and other Hund metals, as very likely, neither pure atomic physics nor pure band theory does apply. In these bad-metallic multi-orbital systems, the existence and interplay of itinerant, but strongly renormalized electrons *and* strongly, but not fully localized large spin moments have to be analyzed without any method-induced bias – even far from any Mott insulating state [19, 46, 49, 96].

Appendix A.2. Numerical Renormalization Group

In each step of the DMFT self-consistency loop, we solve the quantum-impurity problem Eq. (A.3) with fdmNRG, a powerful impurity solver that offers numerically exact real-frequency spectral resolution at arbitrarily low energies and temperatures for multi-band impurity models [34, 36, 97] and lattice models in the DMFT context [33, 85, 98].

NRG [36, 92, 93] has a longstanding and successful history as the standard tool to deal with impurity models. Its basic idea goes back to Wilson’s fundamental insight [92] to introduce a logarithmic discretization of the noninteracting bath Eq. (A.2) of an impurity model Hamiltonian and map the discretized bath onto a 1D semi-infinite, tight-binding chain, a “Wilson chain”, with the interacting impurity site coupled to one end. The hopping matrix elements then decay exponentially down the Wilson chain and introduce an energy-scale separation that allows for an iterative RG solution scheme based on successive diagonalization and truncation of high-energy states. The size of the Fock state space can thus be kept fixed with increasing chain length while still obtaining an exponentially increased resolution of the low-energy part of the spectrum. The resolution at high energies is, however, more coarse-grained. Nevertheless, our approach captures all essential high-energy features [34].

In recent years, significant progress has been made in developing NRG into an efficient high-quality multi-band DMFT impurity solver [33, 85, 97, 98]. Our fdmNRG solver is implemented based on the QSpace tensor library [36] applied to matrix product states (MPS) [35, 99] as generated in NRG. In the QSpace tensor library, Abelian and non-Abelian symmetries are implemented on a generic level: the state space is organized into symmetry multiplets, and tensors “factorize” into two parts, acting in the reduced multiplet space and the Clebsch Gordon coefficient space, respectively. Diagonalization of the NRG Hamiltonian at each iteration step can then be done in multiplet space rather than state space, significantly reducing the matrix sizes and hence computational cost. NRG calculations with three and even more *degenerate* bands [36, 90, 97] became feasible, also in the DMFT context [33, 98]. For solving our 3HHM in Eq. (1), we explicitly exploit its $U(1)_{\text{ch}} \times SU(2)_{\text{sp}} \times SU(3)_{\text{orb}}$ symmetries. We note that also models with three (or even more) *non-degenerate* bands are within the reach of NRG, using iNRG, the “interleaved” version of NRG [97]. It is thus also possible to study orbital differentiation with DMFT+iNRG, as will be demonstrated elsewhere [67].

The fdmNRG solver is established on a complete basis set [100, 101], constructed from the discarded states of all NRG iterations. Spectral functions for the discretized model are given from the Lehmann representation as a sum of poles, and can be calculated accurately directly on the real-frequency axis in sum-rule conserving fashion [102] at zero or arbitrary finite temperature. Continuous spectra are obtained by broadening the discrete data with a standard log-gaussian Kernel of frequency-dependent width [34, 93].

To improve the resolution of spectral data, we “z-average” over the results obtained from several, differing NRG runs, for which the logarithmic discretization of the bath has been uniformly shifted with respect to each other [87, 103]. We note that, within DMFT, the NRG discretization scheme (originally developed for the flat hybridization function $\Gamma(\varepsilon) = \Gamma\Theta(D - |\varepsilon|)$ of quantum impurity models with half-bandwidth $D=1$) has to be adapted to optimally discretize the frequency-dependent hybridization functions that emerge in every step of the self-consistency loop. Here, we use a numerically stable implementation [104] of the scheme in Refs. [87, 105] to accurately represent the nontrivial continuous baths in terms of discrete bath states.

Within the DMFT+NRG approach, the resolution of spectral data can be further improved by applying the so-called self-energy trick [106]. In every step of the iterative mapping, the self-energy is calculated as the ratio of two NRG correlation functions [106]

$$\Sigma(\omega) = \frac{F(\omega)}{G(\omega)}, \quad (\text{A.4})$$

where $F(\omega) = \langle [\hat{d}_\nu, \hat{H}_{\text{int}}[\hat{d}_\nu^\dagger]] | \hat{d}_\nu^\dagger \rangle_\omega$. The imaginary parts of both correlators, $F(\omega)$ and $G(\omega)$, are fdmNRG spectral functions while the real-parts are obtained from their Kramers-Kronig transformations, respectively. Instead of using the raw NRG result $G(\omega)$ for the self-consistency condition Eq. (A.3), an improved version of the (lattice) Green’s function is calculated via the simple analytic form

$$G_{\text{impr}}(\omega) = \frac{1}{2t^2} \left(\xi - \sqrt{\xi^2 - 4t^2} \right) \quad (\text{A.5})$$

with $\xi = \omega + \mu - \Sigma(\omega)$, valid only for the Bethe lattice. In this work we only refer to the improved Green's function and therefore drop the index from now on: $G(\omega) \equiv G_{\text{impr}}(\omega)$.

From the improved Green's function, we have direct access to the real-frequency spectral function, also called local density of states:

$$A(\omega) = -\frac{1}{\pi} \text{Im} G^R(\omega). \quad (\text{A.6})$$

All computational parameters and further details of our DMFT+NRG calculations are listed in the Supplementary material of Ref. [33].

In Ref. [33] we have already demonstrated that DMFT+NRG is perfectly suited for the investigation of the 3HHM. The exponentially enhanced resolution around the Fermi level resolves spectral features down to the lowest relevant energy scale of the system. In contrast to QMC solvers, the NRG solver thus reaches the strongly reduced FL ground state in a $T = 0^+$ simulation of the model. At the same time atomic-like features which constitute the Hubbard side bands are well reproduced, e.g. as shown in Sec. 4 and Sec. 5. The access to real-frequency quantities helps us to understand the nature of the incoherent regime together with NRG eigenlevel renormalization group (RG) flow diagrams that reveal the relevant physics at all energy scales.

References

- [1] Y. Kamihara, H. Hiramatsu, M. Hirano, R. Kawamura, H. Yanagi, T. Kamiya, H. Hosono, Iron-Based Layered Superconductor: LaOFeP, *Journal of the American Chemical Society* 128 (31) (2006) 10012–10013, URL <https://doi.org/10.1021/ja063355c>.
- [2] Y. Kamihara, T. Watanabe, M. Hirano, H. Hosono, Iron-Based Layered Superconductor La[O_{1-x}F_x]FeAs ($x = 0.05 - 0.12$) with $T_c = 26\text{K}$, *Journal of the American Chemical Society* 130 (11) (2008) 3296–3297, URL <https://doi.org/10.1021/ja800073m>.
- [3] Z.-A. Ren, G.-C. Che, X.-L. Dong, J. Yang, W. Lu, W. Yi, X.-L. Shen, Z.-C. Li, L.-L. Sun, F. Zhou, Z.-X. Zhao, Superconductivity and phase diagram in iron-based arsenic-oxides ReFeAsO_{1- δ} (Re = rare-earth metal) without fluorine doping, *EPL (Europhysics Letters)* 83 (1) (2008) 17002, URL <http://stacks.iop.org/0295-5075/83/i=1/a=17002>.
- [4] Z. A. Ren, J. Yang, W. Lu, W. Yi, G. C. Che, X. L. Dong, L. L. Sun, Z. X. Zhao, Superconductivity at 52 K in iron based F doped layered quaternary compound Pr[O_{1-x}F_x]FeAs, *Materials Research Innovations* 12 (3) (2008) 105–106, URL <https://doi.org/10.1179/143307508X333686>.
- [5] G. Wu, Y. L. Xie, H. Chen, M. Zhong, R. H. Liu, B. C. Shi, Q. J. Li, X. F. Wang, T. Wu, Y. J. Yan, J. J. Ying, X. H. Chen, Superconductivity at 56K in samarium-doped SrFeAsF, *Journal of Physics: Condensed Matter* 21 (14) (2009) 142203, URL <http://stacks.iop.org/0953-8984/21/i=14/a=142203>.
- [6] K. Haule, G. Kotliar, Coherence-incoherence crossover in the normal state of iron oxypnictides and importance of Hund's rule coupling, *New J. Phys.* 11 (2009) 025021, URL <http://iopscience.iop.org/1367-2630/11/2/025021>.
- [7] Z. P. Yin, K. Haule, G. Kotliar, Fractional power-law behavior and its origin in iron-chalcogenide and ruthenate superconductors: Insights from first-principles calculations, *Phys. Rev. B* 86 (2012) 195141, URL <http://link.aps.org/doi/10.1103/PhysRevB.86.195141>.
- [8] M. Yi, D. H. Lu, R. Yu, S. C. Riggs, J.-H. Chu, B. Lv, Z. K. Liu, M. Lu, Y.-T. Cui, M. Hashimoto, S.-K. Mo, Z. Hussain, C. W. Chu, I. R. Fisher, Q. Si, Z.-X. Shen, Observation of Temperature-Induced Crossover to an Orbital-Selective Mott Phase in A_xFe_{2-y}Se₂ (A=K, Rb) Superconductors, *Phys. Rev. Lett.* 110 (2013) 067003, URL <https://link.aps.org/doi/10.1103/PhysRevLett.110.067003>.
- [9] F. Hardy, A. E. Böhmer, D. Aoki, P. Burger, T. Wolf, P. Schweiss, R. Heid, P. Adelman, Y. X. Yao, G. Kotliar, J. Schmalian, C. Meingast, Evidence of Strong Correlations and Coherence-Incoherence Crossover in the Iron Pnictide Superconductor KFe₂As₂, *Phys. Rev. Lett.* 111 (2013) 027002, URL <https://link.aps.org/doi/10.1103/PhysRevLett.111.027002>.
- [10] K. Haule, J. H. Shim, G. Kotliar, Correlated Electronic Structure of LaO_{1-x}F_xFeAs, *Phys. Rev. Lett.* 100 (2008) 226402, URL <https://link.aps.org/doi/10.1103/PhysRevLett.100.226402>.
- [11] A. Liebsch, H. Ishida, Correlation-induced spin freezing transition in FeSe: A dynamical mean field study, *Phys. Rev. B* 82 (2010) 155106, URL <https://link.aps.org/doi/10.1103/PhysRevB.82.155106>.
- [12] H. Ishida, A. Liebsch, Fermi-liquid, non-Fermi-liquid, and Mott phases in iron pnictides and cuprates, *Phys. Rev. B* 81 (2010) 054513, URL <https://link.aps.org/doi/10.1103/PhysRevB.81.054513>.
- [13] M. Aichhorn, S. Biermann, T. Miyake, A. Georges, M. Imada, Theoretical evidence for strong correlations and incoherent metallic state in FeSe, *Phys. Rev. B* 82 (2010) 064504, URL <https://link.aps.org/doi/10.1103/PhysRevB.82.064504>.
- [14] P. Werner, M. Casula, T. Miyake, F. Aryasetiawan, A. J. Millis, S. Biermann, Satellites and large doping and temperature dependence of electronic properties in hole-doped BaFe₂As₂, *Nature Physics* 8 (2012) 331 – 337, URL <http://dx.doi.org/10.1038/nphys2250>.
- [15] A. A. Schafgans, S. J. Moon, B. C. Pursley, A. D. LaForge, M. M. Qazilbash, A. S. Sefat, D. Mandrus, K. Haule, G. Kotliar, D. N. Basov, Electronic Correlations and Unconventional Spectral Weight Transfer in the High-Temperature

- Pnictide $\text{BaFe}_{2-x}\text{Co}_x\text{As}_2$ Superconductor Using Infrared Spectroscopy, *Phys. Rev. Lett.* 108 (2012) 147002, URL <https://link.aps.org/doi/10.1103/PhysRevLett.108.147002>.
- [16] J. Fink, A. Charnukha, E. D. L. Rienks, Z. H. Liu, S. Thirupathaiah, I. Avigo, F. Roth, H. S. Jeevan, P. Gegenwart, M. Roslova, I. Morozov, S. Wurmehl, U. Bovensiepen, S. Borisenko, M. Vojta, B. Büchner, Non-Fermi-liquid scattering rates and anomalous band dispersion in ferropnictides, *Phys. Rev. B* 92 (2015) 201106, URL <https://link.aps.org/doi/10.1103/PhysRevB.92.201106>.
- [17] M. Yi, Z.-K. Liu, Y. Zhang, R. Yu, J. X. Zhu, J. J. Lee, R. G. Moore, F. T. Schmitt, W. Li, S. C. Riggs, J. H. Chu, B. Lv, J. Hu, M. Hashimoto, S. K. Mo, Z. Hussain, Z. Q. Mao, C. W. Chu, I. R. Fisher, Q. Si, Z. X. Shen, D. H. Lu, Observation of universal strong orbital-dependent correlation effects in iron chalcogenides, *Nature Communications* 6 (2015) 7777, URL <http://dx.doi.org/10.1038/ncomms8777>.
- [18] H. Gretarsson, A. Lupascu, J. Kim, D. Casa, T. Gog, W. Wu, S. R. Julian, Z. J. Xu, J. S. Wen, G. D. Gu, R. H. Yuan, Z. G. Chen, N.-L. Wang, S. Khim, K. H. Kim, M. Ishikado, I. Jarrige, S. Shamoto, J.-H. Chu, I. R. Fisher, Y.-J. Kim, Revealing the dual nature of magnetism in iron pnictides and iron chalcogenides using x-ray emission spectroscopy, *Phys. Rev. B* 84 (2011) 100509, URL <https://link.aps.org/doi/10.1103/PhysRevB.84.100509>.
- [19] J. Pellicciari, Y. Huang, K. Ishii, C. Zhang, P. Dai, G. F. Chen, L. Xing, X. Wang, C. Jin, H. Ding, P. Werner, T. Schmitt, Magnetic moment evolution and spin freezing in doped BaFe_2As_2 , *Scientific Reports* 7 (2017) 8003, URL <https://doi.org/10.1038/s41598-017-07286-6>.
- [20] S. Lafuerza, H. Gretarsson, F. Hardy, T. Wolf, C. Meingast, G. Giovannetti, M. Capone, A. S. Sefat, Y.-J. Kim, P. Glatzel, L. de' Medici, Evidence of Mott physics in iron pnictides from x-ray spectroscopy, *Phys. Rev. B* 96 (2017) 045133, URL <https://link.aps.org/doi/10.1103/PhysRevB.96.045133>.
- [21] M. M. Qazilbash, J. J. Hamlin, R. E. Baumbach, L. Zhang, D. J. Singh, M. B. Maple, D. N. Basov, Electronic correlations in the iron pnictides, *Nature Physics* 5 (2009) 647–650, URL <http://dx.doi.org/10.1038/nphys1343>.
- [22] T. Terashima, M. Kimata, N. Kurita, H. Satsukawa, A. Harada, K. Hazama, M. Imai, A. Sato, K. Kihou, C.-H. Lee, H. Kito, H. Eisaki, A. Iyo, T. Saito, H. Fukazawa, Y. Kohori, H. Harima, S. Uji, Fermi Surface and Mass Enhancement in KFe_2As_2 from de Haas–van Alphen Effect Measurements, *Journal of the Physical Society of Japan* 79 (5) (2010) 053702, URL <https://doi.org/10.1143/JPSJ.79.053702>.
- [23] T. Terashima, M. Kimata, H. Satsukawa, A. Harada, K. Hazama, M. Imai, A. Sato, S. Uji, K. Kihou, C.-H. Lee, H. Kito, H. Eisaki, A. Iyo, H. Fukazawa, Y. Kohori, H. Harima, De Haas–van Alphen oscillations in KFe_2As_2 , *Physica C: Superconductivity and its Applications* 470 (2010) S351 – S352, ISSN 0921-4534, URL <http://www.sciencedirect.com/science/article/pii/S0921453409007163>.
- [24] A. Tamai, A. Y. Ganin, E. Rozbicki, J. Bacsá, W. Meevasana, P. D. C. King, M. Caffio, R. Schaub, S. Margadonna, K. Prassides, M. J. Rosseinsky, F. Baumberger, Strong Electron Correlations in the Normal State of the Iron-Based $\text{FeSe}_{0.42}\text{Te}_{0.58}$ Superconductor Observed by Angle-Resolved Photoemission Spectroscopy, *Phys. Rev. Lett.* 104 (2010) 097002, URL <https://link.aps.org/doi/10.1103/PhysRevLett.104.097002>.
- [25] A. Yamasaki, Y. Matsui, S. Imada, K. Takase, H. Azuma, T. Muro, Y. Kato, A. Higashiya, A. Sekiyama, S. Suga, M. Yabashi, K. Tamasaku, T. Ishikawa, K. Terashima, H. Kobori, A. Sugimura, N. Umeiyama, H. Sato, Y. Hara, N. Miyagawa, S. I. Ikeda, Electron correlation in the FeSe superconductor studied by bulk-sensitive photoemission spectroscopy, *Phys. Rev. B* 82 (2010) 184511, URL <https://link.aps.org/doi/10.1103/PhysRevB.82.184511>.
- [26] S. V. Borisenko, V. B. Zabolotnyy, D. V. Evtushinsky, T. K. Kim, I. V. Morozov, A. N. Yaresko, A. A. Kordyuk, G. Behr, A. Vasiliev, R. Follath, B. Büchner, Superconductivity without Nesting in LiFeAs , *Phys. Rev. Lett.* 105 (2010) 067002, URL <https://link.aps.org/doi/10.1103/PhysRevLett.105.067002>.
- [27] T. Terashima, N. Kurita, M. Kimata, M. Tomita, S. Tsuchiya, M. Imai, A. Sato, K. Kihou, C.-H. Lee, H. Kito, H. Eisaki, A. Iyo, T. Saito, H. Fukazawa, Y. Kohori, H. Harima, S. Uji, Fermi surface in KFe_2As_2 determined via de Haas–van Alphen oscillation measurements, *Phys. Rev. B* 87 (2013) 224512, URL <https://link.aps.org/doi/10.1103/PhysRevB.87.224512>.
- [28] T. Yoshida, S.-i. Ideta, I. Nishi, A. Fujimori, M. Yi, R. Moore, S.-K. Mo, D. Lu, Z.-X. Shen, Z. Hussain, K. Kihou, C. H. Lee, A. Iyo, H. Eisaki, H. Harima, Orbital character and electron correlation effects on two- and three-dimensional Fermi surfaces in KFe_2As_2 revealed by angle-resolved photoemission spectroscopy, *Frontiers in Physics* 2 (2014) 17, URL <https://www.frontiersin.org/article/10.3389/fphy.2014.00017>.
- [29] J. Orenstein, A. J. Millis, Advances in the Physics of High-Temperature Superconductivity, *Science* 288 (5465) (2000) 468–474, ISSN 0036-8075, URL <http://science.sciencemag.org/content/288/5465/468>.
- [30] P. A. Lee, N. Nagaosa, X.-G. Wen, Doping a Mott insulator: Physics of high-temperature superconductivity, *Rev. Mod. Phys.* 78 (2006) 17–85, URL <https://link.aps.org/doi/10.1103/RevModPhys.78.17>.
- [31] C. Aron, G. Kotliar, Analytic theory of Hund's metals: A renormalization group perspective, *Phys. Rev. B* 91 (2015) 041110, URL <https://link.aps.org/doi/10.1103/PhysRevB.91.041110>.
- [32] L. Fanfarillo, E. Bascones, Electronic correlations in Hund metals, *Phys. Rev. B* 92 (2015) 075136, URL <https://link.aps.org/doi/10.1103/PhysRevB.92.075136>.
- [33] K. M. Stadler, Z. P. Yin, J. von Delft, G. Kotliar, A. Weichselbaum, Dynamical Mean-Field Theory Plus Numerical Renormalization-Group Study of Spin-Orbital Separation in a Three-Band Hund Metal, *Phys. Rev. Lett.* 115 (2015) 136401, URL <https://link.aps.org/doi/10.1103/PhysRevLett.115.136401>.
- [34] A. Weichselbaum, J. von Delft, Sum-Rule Conserving Spectral Functions from the Numerical Renormalization Group, *Phys. Rev. Lett.* 99 (7) 076402, URL <http://link.aps.org/abstract/PRL/v99/e076402>.
- [35] A. Weichselbaum, Tensor networks and the numerical renormalization group, *Phys. Rev. B* 86 (2012) 245124, URL <https://link.aps.org/doi/10.1103/PhysRevB.86.245124>.
- [36] A. Weichselbaum, Non-abelian symmetries in tensor networks: A quantum symmetry space approach, *Annals of Physics*

- 327 (2012) 2972–3047, URL <http://www.sciencedirect.com/science/article/pii/S0003491612001121>.
- [37] X. Deng, K. M. Stadler, K. Haule, A. Weichselbaum, J. von Delft, G. Kotliar, Signatures of Mottness and Hundness in archetypal correlated metals, arXiv:1708.05752 [cond-mat.str-el] URL <https://arxiv.org/abs/1708.05752v2>.
- [38] N. F. MOTT, Metal-Insulator Transition, *Rev. Mod. Phys.* 40 (1968) 677–683, URL <https://link.aps.org/doi/10.1103/RevModPhys.40.677>.
- [39] M. J. Rozenberg, G. Kotliar, H. Kajueter, G. A. Thomas, D. H. Rapkine, J. M. Honig, P. Metcalf, Optical Conductivity in Mott-Hubbard Systems, *Phys. Rev. Lett.* 75 (1995) 105–108, URL <https://link.aps.org/doi/10.1103/PhysRevLett.75.105>.
- [40] G. Kotliar, Landau theory of the Mott transition in the fully frustrated Hubbard model in infinite dimensions, *Eur. Phys. J. B* 11 (1) (1999) 27–39, URL <https://doi.org/10.1007/s100510050914>.
- [41] G. Kotliar, S. Murthy, M. J. Rozenberg, Compressibility Divergence and the Finite Temperature Mott Transition, *Phys. Rev. Lett.* 89 (2002) 046401, URL <https://link.aps.org/doi/10.1103/PhysRevLett.89.046401>.
- [42] D. B. McWhan, T. M. Rice, J. P. Remeika, Mott Transition in Cr-Doped V_2O_3 , *Phys. Rev. Lett.* 23 (1969) 1384–1387, URL <https://link.aps.org/doi/10.1103/PhysRevLett.23.1384>.
- [43] D. B. McWhan, A. Menth, J. P. Remeika, W. F. Brinkman, T. M. Rice, Metal-Insulator Transitions in Pure and Doped V_2O_3 , *Phys. Rev. B* 7 (1973) 1920–1931, URL <https://link.aps.org/doi/10.1103/PhysRevB.7.1920>.
- [44] D. B. McWhan, J. P. Remeika, J. P. Maita, H. Okinaka, K. Kosuge, S. Kachi, Heat Capacity of Vanadium Oxides at Low Temperature, *Phys. Rev. B* 7 (1973) 326–332, URL <https://link.aps.org/doi/10.1103/PhysRevB.7.326>.
- [45] P. Hansmann, A. Toschi, G. Sangiovanni, T. Saha-Dasgupta, S. Lupi, M. Marsi, K. Held, Mott-Hubbard transition in V_2O_3 revisited, *physica status solidi (b)* 250 (7) (2013) 1251–1264, URL <https://onlinelibrary.wiley.com/doi/abs/10.1002/pssb.201248476>.
- [46] Z. P. Yin, K. Haule, G. Kotliar, Kinetic frustration and the nature of the magnetic and paramagnetic states in iron pnictides and iron chalcogenides, *Nature Mat.* 10 (2011) 932 – 935.
- [47] A. Georges, L. de Medici, J. Mravlje, Strong Correlations from Hund’s Coupling, *Annual Rev. of Cond. Mat. Phys.* 4 (1) (2013) 137–178, URL <https://doi.org/10.1146/annurev-conmatphys-020911-125045>.
- [48] N. Lanatà, H. U. R. Strand, G. Giovannetti, B. Hellsing, L. de’ Medici, M. Capone, Orbital selectivity in Hund’s metals: The iron chalcogenides, *Phys. Rev. B* 87 (2013) 045122, URL <https://link.aps.org/doi/10.1103/PhysRevB.87.045122>.
- [49] E. Bascones, B. Valenzuela, M. J. Calderón, Magnetic interactions in iron superconductors: A review, *Comptes Rendus Physique* 17 (1) (2016) 36 – 59, ISSN 1631-0705, URL <http://www.sciencedirect.com/science/article/pii/S1631070515000924>.
- [50] L. de’ Medici, M. Capone, Modeling Many-Body Physics with Slave-Spin Mean-Field: Mott and Hund’s Physics in Fe-Superconductors, Springer International Publishing, Cham, ISBN 978-3-319-56117-2, 115–185, URL https://doi.org/10.1007/978-3-319-56117-2_4, 2017.
- [51] P. Werner, E. Gull, M. Troyer, A. J. Millis, Spin freezing transition and non-Fermi-liquid self-energy in a three-orbital model, *Phys. Rev. Lett* 101 (2008) 166405, URL <http://journals.aps.org/prl/abstract/10.1103/PhysRevLett.101.166405>.
- [52] J. Mravlje, M. Aichhorn, T. Miyake, K. Haule, G. Kotliar, A. Georges, Coherence-Incoherence Crossover and the Mass-Renormalization Puzzles in Sr_2RuO_4 , *Phys. Rev. Lett.* 106 (2011) 096401, URL <http://journals.aps.org/prl/abstract/10.1103/PhysRevLett.106.096401>.
- [53] L. de’ Medici, J. Mravlje, A. Georges, Janus-Faced Influence of Hund’s Rule Coupling in Strongly Correlated Materials, *Phys. Rev. Lett.* 107 (2011) 256401, URL <https://link.aps.org/doi/10.1103/PhysRevLett.107.256401>.
- [54] D. Stricker, J. Mravlje, C. Berthod, R. Fittipaldi, A. Vecchione, A. Georges, D. van der Marel, Optical Response of Sr_2RuO_4 Reveals Universal Fermi-Liquid Scaling and Quasiparticles Beyond Landau Theory, *Phys. Rev. Lett.* 113 (2014) 087404, URL <https://link.aps.org/doi/10.1103/PhysRevLett.113.087404>.
- [55] J. Mravlje, A. Georges, Thermopower and Entropy: Lessons from Sr_2RuO_4 , *Phys. Rev. Lett.* 117 (2016) 036401, URL <https://link.aps.org/doi/10.1103/PhysRevLett.117.036401>.
- [56] T. Kroll, S. Bonhommeau, T. Kachel, H. A. Dürr, J. Werner, G. Behr, A. Koitzsch, R. Hübel, S. Leger, R. Schönfelder, A. K. Ariffin, R. Manzke, F. M. F. de Groot, J. Fink, H. Eschrig, B. Büchner, M. Knupfer, Electronic structure of $LaFeAsO_{1-x}F_x$ from x-ray absorption spectroscopy, *Phys. Rev. B* 78 (2008) 220502, URL <https://link.aps.org/doi/10.1103/PhysRevB.78.220502>.
- [57] L. de’ Medici, Hund’s coupling and its key role in tuning multiorbital correlations, *Phys. Rev. B* 83 (2011) 205112, URL <https://link.aps.org/doi/10.1103/PhysRevB.83.205112>.
- [58] L. de’ Medici, Hund’s Induced Fermi-Liquid Instabilities and Enhanced Quasiparticle Interactions, *Phys. Rev. Lett.* 118 (2017) 167003, URL <https://link.aps.org/doi/10.1103/PhysRevLett.118.167003>.
- [59] L. de’ Medici, S. R. Hassan, M. Capone, X. Dai, Orbital-Selective Mott Transition out of Band Degeneracy Lifting, *Phys. Rev. Lett.* 102 (2009) 126401, URL <https://link.aps.org/doi/10.1103/PhysRevLett.102.126401>.
- [60] R. Yu, Q. Si, U(1) slave-spin theory and its application to Mott transition in a multiorbital model for iron pnictides, *Phys. Rev. B* 86 (2012) 085104, URL <https://link.aps.org/doi/10.1103/PhysRevB.86.085104>.
- [61] R. Yu, Q. Si, Orbital-Selective Mott Phase in Multiorbital Models for Alkaline Iron Selenides $K_{1-x}Fe_{2-y}Se_2$, *Phys. Rev. Lett.* 110 (2013) 146402, URL <https://link.aps.org/doi/10.1103/PhysRevLett.110.146402>.
- [62] T. Misawa, K. Nakamura, M. Imada, Ab Initio Evidence for Strong Correlation Associated with Mott Proximity in Iron-Based Superconductors, *Phys. Rev. Lett.* 108 (2012) 177007, URL <https://link.aps.org/doi/10.1103/PhysRevLett.108.177007>.
- [63] E. Bascones, B. Valenzuela, M. J. Calderón, Orbital differentiation and the role of orbital ordering in the magnetic state of Fe superconductors, *Phys. Rev. B* 86 (2012) 174508, URL <https://link.aps.org/doi/10.1103/PhysRevB.86.174508>.

- [64] L. Huang, L. Du, X. Dai, Complete phase diagram for three-band Hubbard model with orbital degeneracy lifted by crystal field splitting, *Phys. Rev. B* 86 (2012) 035150, URL <https://link.aps.org/doi/10.1103/PhysRevB.86.035150>.
- [65] L. de' Medici, G. Giovannetti, M. Capone, Selective Mott Physics as a Key to Iron Superconductors, *Phys. Rev. Lett.* 112 (2014) 177001, URL <https://link.aps.org/doi/10.1103/PhysRevLett.112.177001>.
- [66] S. Hoshino, P. Werner, Electronic orders in multiorbital Hubbard models with lifted orbital degeneracy, *Phys. Rev. B* 93 (2016) 155161, URL <https://link.aps.org/doi/10.1103/PhysRevB.93.155161>.
- [67] F. Kugler, S.-S. Lee, G. Kotliar, J. von Delft, A. Weichselbaum, to be published .
- [68] Z. P. Yin, K. Haule, G. Kotliar, Magnetism and charge dynamics in iron pnictides, *Nature Physics* 7 (2011) 294–297, URL http://www.nature.com/nphys/journal/v7/n4/abs/nphys1923.html?lang=en?WT.ec_id=NPHYS-201104.
- [69] A. J. Kim, H. O. Jeschke, P. Werner, R. Valentí, J Freezing and Hund's Rules in Spin-Orbit-Coupled Multiorbital Hubbard Models, *Phys. Rev. Lett.* 118 (2017) 086401, URL <https://link.aps.org/doi/10.1103/PhysRevLett.118.086401>.
- [70] S. Hoshino, P. Werner, Superconductivity from Emerging Magnetic Moments, *Phys. Rev. Lett.* 115 (2015) 247001, URL <https://link.aps.org/doi/10.1103/PhysRevLett.115.247001>.
- [71] A. Kowalski, A. Hausoel, M. Wallerberger, P. Gunacker, G. Sangiovanni, State- and superstate-sampling in hybridization-expansion continuous-time quantum Monte Carlo, arXiv:1807.00361 [cond-mat.str-el] URL <https://arxiv.org/abs/1807.00361>.
- [72] E. Bascones, M. J. Calderón, B. Valenzuela, Low Magnetization and Anisotropy in the Antiferromagnetic State of Undoped Iron Pnictides, *Phys. Rev. Lett.* 104 (2010) 227201, URL <https://link.aps.org/doi/10.1103/PhysRevLett.104.227201>.
- [73] T. Sudayama, Y. Wakisaka, T. Mizokawa, S. Ibusa, R. Morinaga, T. J. Sato, M. Arita, H. Namatame, M. Taniguchi, N. L. Saini, Doping-Dependent and Orbital-Dependent Band Renormalization in $\text{Ba}(\text{Fe}_{1-x}\text{Co}_x)_2\text{As}_2$ Superconductors, *Journal of the Physical Society of Japan* 80 (11) (2011) 113707, URL <https://doi.org/10.1143/JPSJ.80.113707>.
- [74] F. Hardy, A. E. Böhrer, L. de' Medici, M. Capone, G. Giovannetti, R. Eder, L. Wang, M. He, T. Wolf, P. Schweiss, R. Heid, A. Herbig, P. Adelmann, R. A. Fisher, C. Meingast, Strong correlations, strong coupling, and s-wave superconductivity in hole-doped BaFe_2As_2 single crystals, *Phys. Rev. B* 94 (2016) 205113, URL <https://link.aps.org/doi/10.1103/PhysRevB.94.205113>.
- [75] L. Dworin, A. Narath, Orbital Paramagnetism of Localized Nonmagnetic Impurities in Metals, *Phys. Rev. Lett.* 25 (1970) 1287–1291, URL <https://link.aps.org/doi/10.1103/PhysRevLett.25.1287>.
- [76] A. Horvat, R. Žitko, J. Mravlje, Low-energy physics of three-orbital impurity model with Kanamori interaction, *Phys. Rev. B* 94 (2016) 165140, URL <https://link.aps.org/doi/10.1103/PhysRevB.94.165140>.
- [77] M. Aichhorn, L. Pourovskii, V. Vildosola, M. Ferrero, O. Parcollet, T. Miyake, A. Georges, S. Biermann, Dynamical mean-field theory within an augmented plane-wave framework: Assessing electronic correlations in the iron pnictide LaFeAsO , *Phys. Rev. B* 80 (2009) 085101, URL <https://link.aps.org/doi/10.1103/PhysRevB.80.085101>.
- [78] K. Stadler, A. Weichselbaum, G. Kotliar, J. von Delft, Temperature-dependence of Hund metal physics, to be published .
- [79] P. Werner, S. Hoshino, H. Shinaoka, Spin-freezing perspective on cuprates, *Phys. Rev. B* 94 (2016) 245134, URL <https://link.aps.org/doi/10.1103/PhysRevB.94.245134>.
- [80] S. Florens, A. Georges, G. Kotliar, O. Parcollet, Mott transition at large orbital degeneracy: Dynamical mean-field theory, *Phys. Rev. B* 66 (2002) 205102, URL <https://link.aps.org/doi/10.1103/PhysRevB.66.205102>.
- [81] K. Inaba, A. Koga, Phase diagrams of the two-orbital Hubbard model with different bandwidths, *Phys. Rev. B* 73 (2006) 155106, URL <https://link.aps.org/doi/10.1103/PhysRevB.73.155106>.
- [82] A. Georges, G. Kotliar, W. Krauth, M. J. Rozenberg, Dynamical mean-field theory of strongly correlated fermion systems and the limit of infinite dimensions, *Rev. Mod. Phys.* 68 (1) (1996) 13.
- [83] E. Müller-Hartmann, The Hubbard model at high dimension: some exact results and weak coupling theory, *Z. Phys. B* 76 (1989) 211, URL <http://link.springer.com/article/10.1007/2F01312686#page-1>.
- [84] D. Bauernfeind, M. Zingl, R. Triebl, M. Aichhorn, H. G. Evertz, Fork Tensor-Product States: Efficient Multiorbital Real-Time DMFT Solver, *Phys. Rev. X* 7 (2017) 031013, URL <https://link.aps.org/doi/10.1103/PhysRevX.7.031013>.
- [85] S.-S. B. Lee, J. von Delft, A. Weichselbaum, Doublon-Holon Origin of the Subpeaks at the Hubbard Band Edges, *Phys. Rev. Lett.* 119 (2017) 236402, URL <https://link.aps.org/doi/10.1103/PhysRevLett.119.236402>.
- [86] S.-S. B. Lee, A. Weichselbaum, Adaptive broadening to improve spectral resolution in the numerical renormalization group, *Phys. Rev. B* 94 (2016) 235127, URL <https://link.aps.org/doi/10.1103/PhysRevB.94.235127>.
- [87] R. Žitko, T. Pruschke, Energy resolution and discretization artifacts in the numerical renormalization group, *Phys. Rev. B* 79 (8) 085106, URL <http://link.aps.org/abstract/PRE/v79/e085106>.
- [88] J. Hubbard, Electron correlations in narrow energy bands, *Proceedings of the Royal Society of London A: Mathematical, Physical and Engineering Sciences* 276 (1365) (1963) 238–257, ISSN 0080-4630, URL <http://rspa.royalsocietypublishing.org/content/276/1365/238>.
- [89] I. Okada, K. Yosida, Singlet Ground State of the Localized d-Electrons Coupled with Conduction Electrons in Metals, *Progress of Theoretical Physics* 49 (5) (1973) 1483–1502, URL <http://dx.doi.org/10.1143/PTP.49.1483>.
- [90] E. Walter, K. Stadler, G. Kotliar, A. Weichselbaum, J. von Delft, to be published .
- [91] X. Deng, A. Sternbach, K. Haule, D. N. Basov, G. Kotliar, Shining Light on Transition-Metal Oxides: Unveiling the Hidden Fermi Liquid, *Phys. Rev. Lett.* 113 (2014) 246404, URL <https://link.aps.org/doi/10.1103/PhysRevLett.113.246404>.
- [92] K. G. Wilson, The renormalization group: Critical phenomena and the Kondo problem, *Rev. Mod. Phys.* 47 (4) (1975) 773–840.
- [93] R. Bulla, T. A. Costi, T. Pruschke, Numerical renormalization group method for quantum impurity systems, *Reviews of*

- Modern Physics 80 (2) 395, URL <http://link.aps.org/abstract/RMP/v80/p395>.
- [94] J. von Delft, G. Zaránd, M. Fabrizio, Finite-Size Bosonization of 2-Channel Kondo Model: A Bridge between Numerical Renormalization Group and Conformal Field Theory, Phys. Rev. Lett. 81 (1) (1998) 196–199.
- [95] P. Sémon, K. Haule, G. Kotliar, Validity of the local approximation in iron pnictides and chalcogenides, Phys. Rev. B 95 (2017) 195115, URL <https://link.aps.org/doi/10.1103/PhysRevB.95.195115>.
- [96] N. Mannella, The magnetic moment enigma in Fe-based high temperature superconductors, Journal of Physics: Condensed Matter 26 (47) (2014) 473202, URL <http://stacks.iop.org/0953-8984/26/i=47/a=473202>.
- [97] K. M. Stadler, A. K. Mitchell, J. von Delft, A. Weichselbaum, Interleaved numerical renormalization group as an efficient multiband impurity solver, Phys. Rev. B 93 (2016) 235101, URL <https://link.aps.org/doi/10.1103/PhysRevB.93.235101>.
- [98] S.-S. B. Lee, J. von Delft, A. Weichselbaum, Filling-driven Mott transition in SU(N) Hubbard models, Phys. Rev. B 97 (2018) 165143, URL <https://link.aps.org/doi/10.1103/PhysRevB.97.165143>.
- [99] U. Schollwöck, The density-matrix renormalization group in the age of matrix product states, Annals of Physics 326 (1) (2011) 96 – 192, ISSN 0003-4916, URL <http://www.sciencedirect.com/science/article/pii/S0003491610001752>, january 2011 Special Issue.
- [100] F. B. Anders, A. Schiller, Real-Time Dynamics in Quantum-Impurity Systems: A Time-Dependent Numerical Renormalization-Group Approach, Phys. Rev. Lett. 95 (19) 196801, URL <http://link.aps.org/abstract/PRL/v95/e196801>.
- [101] F. B. Anders, A. Schiller, Spin precession and real-time dynamics in the Kondo model: Time-dependent numerical renormalization-group study, Phys. Rev. B 74 (2006) 245113, URL <https://link.aps.org/doi/10.1103/PhysRevB.74.245113>.
- [102] R. Peters, T. Pruschke, F. B. Anders, Numerical renormalization group approach to Green’s functions for quantum impurity models, Phys. Rev. B 74 (24) 245114, URL <http://link.aps.org/abstract/PRB/v74/e245114>.
- [103] W. C. Oliveira, L. N. Oliveira, Generalized numerical renormalization-group method to calculate the thermodynamical properties of impurities in metals, Phys. Rev. B 49 (1994) 11986–11994, URL <http://link.aps.org/doi/10.1103/PhysRevB.49.11986>.
- [104] S.-S. Lee, K. Stadler, J. von Delft, A. Weichselbaum, to be published .
- [105] R. Žitko, Adaptive logarithmic discretization for numerical renormalization group methods, Computer Physics Communications 180 (2009) 1271, URL <http://www.sciencedirect.com/science/article/pii/S0010465509000630>.
- [106] R. Bulla, A. C. Hewson, T. Pruschke, Numerical renormalization group calculations for the self-energy of the impurity Anderson model, J. Phys.: Condens. Matter 10 (1998) 8365, URL <http://iopscience.iop.org/0953-8984/10/37/021>.

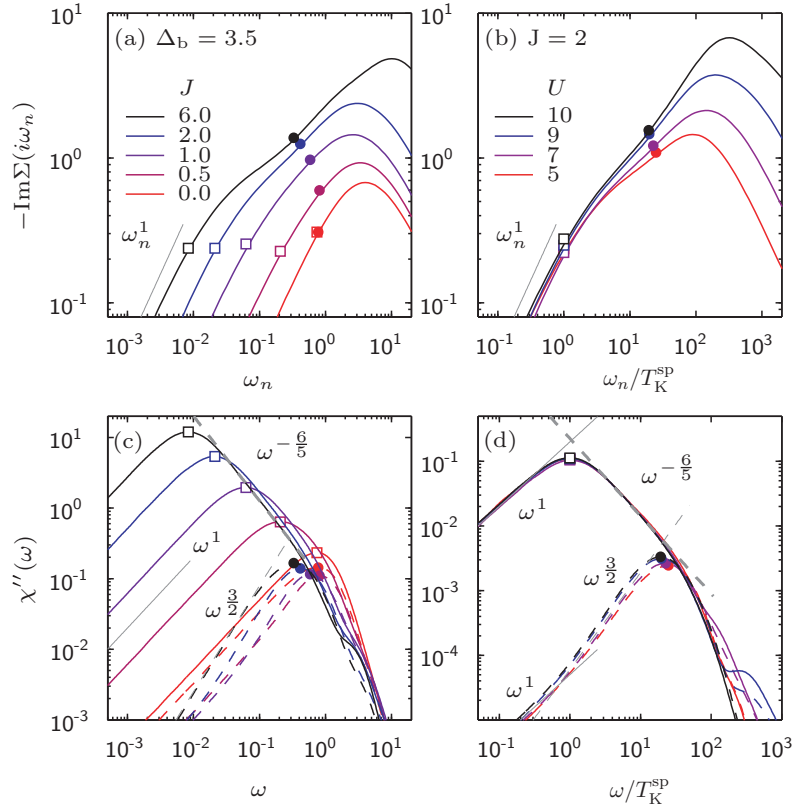


Figure 5.1 (a,b) Imaginary part of the Matsubara self-energy, $\text{Im} \Sigma(i\omega_n)$, and (c,d) imaginary part of the orbital (dashed) and spin (solid) susceptibility, $\chi''(\omega)$, plotted versus (a,b) ω and (c,d) ω/T_K^{SP} for (a,c) various values of J at fixed $\Delta_b = 3.5$ and for (b,d) various values of U at fixed J . Solid thin grey guide-to-the-eye lines indicate FL behavior, dashed thin and thick grey guide-to-the-eye lines demonstrate fractional power-law behavior in the SOS regime for the orbital and spin susceptibility, respectively.

5.A Power-law behavior

We complement the $T = 0$ study of Ref. [SYvD⁺15] (cf. Sec. 4.2) and Ref. [SKWvD18] (cf. Sec. 5.2) with a discussion of the apparent fractional power-law behavior, which emerges for various physical quantities in the SOS frequency regime of the 3HHM at $n_d = 2$.

The search for fractional power-law behavior in the 3HHM is motivated by work of P. Werner *et al.* [WGTM08] and Z. Yin *et al.* [YHK12]. They revealed unusual fractional power laws for the Matsubara self-energy and argued that these might be related to the experimentally observed power laws in the optical conductivity of chalcogenides and ruthenades. In Ref. [SYvD⁺15] we confirmed the existence of a power law in $\text{Im} \Sigma(i\omega_n)$ for $U = 7$ and $J = 1$, while $\text{Im} \Sigma(\omega)$ was shown to be highly particle-hole asymmetric. In Ref. [SKWvD18] we analyzed that, in the SOS regime for $\omega < 0$, $\text{Im} \Sigma(\omega)$ seems to feature a power law, $|\omega|^{3/2}$, followed by a shoulder [cf. Fig. 9(e) and Fig. 10(e) of Ref. [SKWvD18] in Sec. 5.2]. For $\omega > 0$, results for $J \lesssim 1$ exhibit apparent power laws while, for $J > 1$, two regimes with different frequency dependencies emerge, which are separated by a kink [cf. Fig. 9(f) and Fig. 10(f) of Ref. [SKWvD18] in Sec. 5.2].

In Fig. 5.1(a) [Fig. 5.1(b)] we present results for $\text{Im} \Sigma(i\omega_n)$ for the same parameters as used in Fig. 9 (Fig. 10) of Ref. [SKWvD18] in Sec. 5.2. Interestingly, we find that also $\text{Im} \Sigma(i\omega_n)$ follows an apparent power law, if any, only for $J \lesssim 1$ in the incoherent region

(as observed in Fig. 1 of Ref. [SYvD⁺15]), but features rather two regimes with different ω_n dependencies (or a crossover behavior) for $J > 1$.

We now turn to the orbital and spin susceptibility. In Fig. 9(a) and Fig. 10(a) of Ref. [SKWvD18] (cf. Sec. 5.2) we pointed out that the imaginary part of the orbital susceptibility follows an apparent power law $\chi''_{\text{orb}}(\omega) \propto \omega^{3/2}$ in the SOS regime. In the following, we also analyze the behavior of $\chi''_{\text{sp}}(\omega)$. We thus replotted Fig. 9(a) and Fig. 10(a) of Ref. [SKWvD18] in Fig. 5.1(c) and (d), respectively. Interestingly, we find a universal power law, $\chi''_{\text{sp}}(\omega) \propto \omega^{-6/5}$, in the SOS regime, which is clearly visible for $J > 1$ (cf. thick grey dashed guide-to-the-eye lines).

This fractional power-law behavior in the spin excitation, emerging from incomplete screening in the SOS regime (fully screened, i.e. itinerant, orbital degrees of freedom are coupled to quasi-atomic-like spins), was only recently shown in Ref. [LCMK18, WAC19] to be connected to a Hund-metal description of superconductivity with an electronic (spin fluctuation) pairing mechanism. Based on an Eliashberg framework (γ model with a power-law frequency dependence) superconductivity in iron-based HTSCs was argued to be mediated by a bosonic propagator with a power-law exponent $\gamma \approx 1.2$, which is equal to the power-law exponent of the spin susceptibility, $\chi''_{\text{sp}}(\omega)$, in the 3HHM. Remarkably, $\gamma = 1.2$ was recently confirmed experimentally for two types of iron-based HTSCs [MBY⁺18]. In this picture, pairing in a Hund metal is mediated by local spin fluctuations interacting with electronic quasiparticles, which fits to the nature of the incoherent SOS regime. It would thus be valid for superconducting transition temperatures larger than the FL scale in Hund metals.

As a final remark of this discussion about power-law behavior in the 3HHM, we note that, from the perspective of NRG flow diagrams, the existence of power-laws in the SOS regime of the 3HHM is puzzling at first glance, because, at $n_d = 2$, the NRG flow does not reach a stationary intermediate fixed point but shows a crossover behavior (presumably between an underlying but not visible NFL fixed point at high energies and the FL fixed point at low energies) [cf. Fig. 16(a-c) of Ref. [SKWvD18] in Sec. 5.2]. However, in a new analysis of the Kondo limit of the 3HHM, Ref. [WSL⁺19], the existence of universal power laws in this crossover regime was clearly derived. Further, it is unambiguously demonstrated that the crossover regime connects a NFL intermediate fixed point, which is stationary in the Kondo model, with the low-energy FL fixed point. And strikingly, the same power-law exponent of 1.2 is found there, $\chi''_{\text{sp}}(\omega) \propto \omega^{-1.2}$, stressing the importance of the crossover regime for understanding the NFL physics of Hund metals.

5.B The search for a negative compressibility

In Sec. 5.7 of Ref. [SKWvD18] (cf. Sec. 5.2) we studied the compressibility, $\kappa_{\text{el}} = \frac{\partial n_d}{\partial \mu}$, in order to find out, if the 3HHM is also characterized by a region of negative compressibility at $T = 0$, as stated in Ref. [dM17]. There, two different versions of the Hubbard-Kanamori model were investigated with slightly different methods. The full Hubbard-Kanamori model was tackled with a rotationally invariant slave-boson method (but only for two bands). The Hubbard-Kanamori model without spin-flip and pair-hopping terms was solved with a slave-spin mean-field method (for up to five bands). While for the latter large regions with $\kappa_{\text{el}} < 0$ were found (for $U \geq U_{c2}$ and n_d close to 3), which widen with growing J/U , the full model exhibits much smaller regions with $\kappa_{\text{el}} < 0$, which first grow quickly with J/U , but then shrink again, and eventually disappear for large J/U . This suggests that the regions of $\kappa_{\text{el}} < 0$ in the 3HHM, if existing, might be small and hard to find. Certainly, the choice $J/U = 1/2.25 \approx 0.44$, as used in Fig. 16(f) of Ref. [SKWvD18], is large compared to the values studied for the full Hubbard-Kanamori in Ref. [dM17], and might therefore not

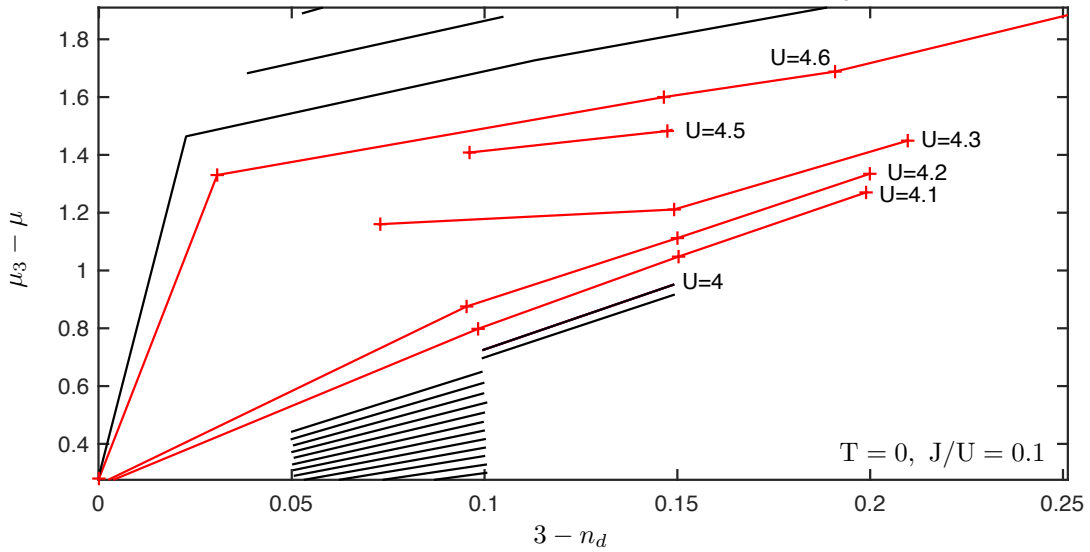


Figure 5.2 The chemical potential, $\mu_3 - \mu$, plotted versus the filling, $3 - n_d$. μ_3 is defined in Sec. 2.6.2. of Ref. [SKWvD18] (cf. Sec. 5.2). The red curves mark results for U close to $U \geq U_{c2}$ with $U_{c2} \approx 4.1$. The curves for $4.2 < U < 4.6$ seem to develop a very flat slope, κ_{el}^{-1} , for $n_d > 3 - 0.15$.

reveal a region of $\kappa_{el} < 0$ in the 3HHM. We thus concentrate now on a much smaller ratio, $J/U = 0.1$, as also used in Ref. [dM17].

In Fig. 5.2 we plotted $\mu_3 - \mu$ versus $3 - n_d$ for different values of U . Since the data points are rather sparse, these are preliminary results. The red curves mark results for U close to $U \geq U_{c2}$ with $U_{c2} \approx 4.1$. Similar to Fig. 1 and Fig. S2 of Ref. [dM17], the slope, κ_{el}^{-1} , is large for $U \lesssim U_{c2}$ and, interestingly, strongly changes its behavior in a small region, $U \geq U_{c2}$, close to $n_d = 3$. However, in contrast to Ref. [dM17], the slope only becomes very small (i.e. κ_{el} indeed becomes very large) in this region, but not negative for the available data (cf. curves for $4.3 \leq U \leq 4.6$ and $3 - n_d \lesssim 0.15$). It would be worthwhile to calculate more data points in this region, which is however quite cumbersome, because convergence slows down exponentially close to the insulating phase at $n_d = 3$. Further, similar calculations at smaller (and larger) J/U are needed for a thorough understanding.

At this stage, it is hard to ultimately judge the existence of a negative compressibility in the 3HHM. On the one hand, we have not yet found any parameters for which $\kappa_{el} < 0$, on the other hand, we have strong indications for a region with almost diverging κ_{el} for $J/U = 0.1$. As a final remark we point out that for $J/U = 0.1$ and n_d close to 3, a physical connection to the SOS screening process in the Hund-metal regime is not very likely.

6 Signatures of Mottness and Hundness in archetypal correlated metals

6.1 Overview

The major goal of this Chapter is to identify “smoking gun” properties to identify two distinct routes of screening from the atomic degrees of freedom towards emerging quasiparticles, guided by either Mott or Hund physics. So far, clear-cut criteria for experimentally distinguishing strongly correlated Hund metals from strongly correlated metals of Mott type are few – even ten years after the introduction of the novel concept of Hund metals [HK09, YHK12], and, although, Hund metals are much more common than metals of Mott type (in the sense that Mott physics requires adjusting parameters to be close to a MIT, while Hund physics happens in a large parameter regime far from an MIT). Motivated by these facts, we contribute to a precise classification of those phenomena, to be regarded as a decisive fingerprint of the Hund metal’s nature, in our article “Signatures of Mottness and Hundness in archetypal correlated metals” [SKWvD18], which we present in the following.

In Ref. [SKWvD18] we follow a twofold strategy, namely an inductive and a deductive approach: we unveil signatures of Mottness and Hundness in two well-studied archetypal strongly correlated materials, the Mott-correlated material, V_2O_3 , and the Hund metal, Sr_2RuO_4 , with the ab-initio method DFT+DMFT+(continuous-time)QMC, and also deduce their generality from the simplified 3HHM Hamiltonian using DMFT+NRG. While the author of this thesis, who is also one of the two first authors of this article, carried out the DMFT+NRG calculations, the other first author, X. Deng, performed the realistic material simulations.

From the perspective of an atomic picture, both V_2O_3 and Sr_2RuO_4 are characterized by three non-degenerate t_{2g} shells occupied by two holes or electrons, respectively. We argue that they have different effective U values, hence different distances to the Mott boundary and thus differ in the nature of their correlations. While such a statement is hard to be proved generically from material simulations only, we also perform model calculations, where we are able to independently vary and control U and J and know the phase diagram [SKWvD18]. We provide caricatures of both archetypal materials, for which we can unambiguously disentangle the origin of strong correlations. We use the 3HHM with sizeable J and three degenerate bands hosting two electrons, and place our prototypical Mott-correlated model system close to the Mott boundary of the phase diagram and our prototypical Hund system far from it. We also contrast the differences of the Hund system to a weakly correlated Mott system with $J = 0$, which is far from the Mott boundary, and to a strongly correlated Mott system without Hund’s coupling, to illustrate the unique nature of Hund metals.

In particular, we analyze the local spectra [the local density of states, $A(\omega)$, and ARPES spectra, $A(\epsilon_k, \omega)$] and the local susceptibilities describing the charge, spin and orbital degrees of freedom. Importantly, we observe qualitatively the same Mott and Hund signatures in the archetypal materials, V_2O_3 and Sr_2RuO_4 , and the corresponding Hund and Mott model systems. We thus prove that our new insights can be clearly viewed as characteristic of the general phenomenology of Mott and Hund physics, independently of material-dependent

details, such as the band structure or crystal fields, and that they are therefore applicable to various strongly correlated materials.

The most important signatures of Hund systems as opposed to strongly and weakly correlated Mott systems are summarized as follows:

- Local spectra and charge susceptibility.

The QPP persists up to highest temperatures (a signature of “resilient quasiparticles”) in Hund systems, exhibiting large charge fluctuations, whereas a pseudogap develops with increasing temperature in all Mott systems at a characteristic energy scale T_M (which is much lower than bare excitations scales), suppressing charge fluctuations. This can be explained by the well-known fact that the Hubbard bands overlap far from the Mott boundary, while they are well separated close to it. Further, Hund metals can be distinguished from weakly correlated Mott systems in terms of their enhanced effective mass (though being far away from the Mott boundary), as readily apparent from ARPES data.

- Local static spin and orbital susceptibilities.

We introduce the concept of onset scales for orbital and spin screening, $T_{\text{orb}}^{\text{onset}}$ and $T_{\text{sp}}^{\text{onset}}$, via the deviation of the respective susceptibilities from Curie behavior with decreasing temperature, indicative of free local moments. *In Hund metals, we find that $T_{\text{orb}}^{\text{onset}} \gg T_{\text{sp}}^{\text{onset}}$ with $T_{\text{orb}}^{\text{onset}}$ as high as the atomic excitation scales of the Hubbard bands. In contrast, in Mott systems, spin and orbital screening occurs simultaneously below a much lower scale, $T_{\text{sp}}^{\text{onset}} \approx T_{\text{orb}}^{\text{onset}} = T_M$, together with the formation of the QPP. Also in weakly correlated Mott system with $J = 0$, there is no separation of the onset scales of orbital and spin screening. We remark that the completion scales for orbital and spin screening (where Pauli behavior sets in with decreasing temperature) are also separated in the presence of finite J in both Hund and Mott systems, while they are equal for $J = 0$.*

Overall, *Hund metals show a qualitatively novel and distinct screening route compared to other strongly and weakly correlated systems: orbital screening occurs at much larger temperatures than spin screening.* Thus Hund metals are uniquely characterized by a large temperature regime of SOS reaching from temperatures as high as atomic excitation scales down to the very low FL scale, where both orbital and spin degrees of freedom are fully screened.

Admittedly, the defining signatures distinguishing Hund- and Mott-correlated metals for V_2O_3 and Sr_2RuO_4 are found in ranges of temperatures well above those (below room temperature) where this distinction was born (for instance in iron pnictides [HK09, HBA⁺13]). Indeed, experimental measurements at high temperature that can be directly compared to our findings are few, as far as we are aware of, but not none. An indirect evidence of the pseudogap opening in V_2O_3 was found in the optic measurements of Ref. [BPN⁺08]. Nevertheless, further measurements can in principle be carried out to high temperatures (note that the melting points of V_2O_3 and Sr_2RuO_4 are around 2000K), and our predictions are verifiable even though high temperature transport measurements are not easy. Further, our findings in the spectral evolution and the novel screening scales are general, as supported by the simplified model Hamiltonian study. They are not restricted to the two canonical materials and have broader implications. To connect our findings to experiments, it would be a viable route to exploit Hund and Mott systems with lower characteristic energy scales. In these systems, the signatures that we have identified would be easier to probe experimentally and can be used to gain insights on the underlying nature of correlations. Candidates could be organic/molecular conductors, where the interaction is typically small. For example, the Mott scale, T_M , is a few tens of Kelvin in κ -(BEDT-TTF)₂Cu[N(CN)₂]₂Br_xCl_{1-x} (cf. the schematic phase diagram in Ref. [YDS⁺11]).

We remark that this project was initiated by X. Deng and G. Kotliar, and carried out by X. Deng and the author of this thesis together with K. Haule, G. Kotliar, A. Weichselbaum, and J. von Delft. The author of this thesis strongly revised and finalized this article together with G. Kotliar, A. Weichselbaum, and J. von Delft.

Based on the insights of this article, we further investigate the issue “Hundness versus Motttness” in terms of a more detailed and broad 3HHM model study of the temperature dependence of a number of physical quantities in the next Chapter.

Signatures of Mottness and Hundness in archetypal correlated metals

by

Xiaoyu Deng,^{1,*} Katharina M. Stadler,^{2,*} Kristjan Haule,¹ Andreas Weichselbaum,^{3,2} Jan von Delft,² and Gabriel Kotliar^{1,3}

*These authors contributed equally to this work.

¹Department of Physics and Astronomy, Rutgers University, Piscataway, New Jersey 08854, USA

²Physics Department, Arnold Sommerfeld Center for Theoretical Physics and Center for NanoScience, Ludwig-Maximilians-Universität München, 80333 München, Germany

³ Condensed Matter Physics and Materials Science Department, Brookhaven National Laboratory, Upton, New York 11973, USA

reprinted on pages [159–169](#).

arXiv preprint: [arXiv:1708.05752](https://arxiv.org/abs/1708.05752) [cond-mat.str-el]

submitted to Nat. Commun.

Supplemental Material reprinted on pages [170–173](#).

Signatures of Mottness and Hundness in archetypal correlated metals

Xiaoyu Deng,^{1,*} Katharina M. Stadler,^{2,*} Kristjan Haule,¹
Andreas Weichselbaum,^{3,2} Jan von Delft,² and Gabriel Kotliar^{1,3}

¹*Department of Physics and Astronomy, Rutgers University, Piscataway, New Jersey 08854, USA*

²*Physics Department, Arnold Sommerfeld Center for Theoretical Physics and Center for NanoScience, Ludwig-Maximilians-Universität München, 80333 München, Germany*

³*Condensed Matter Physics and Materials Science Department, Brookhaven National Laboratory, Upton, New York 11973, USA*

(Dated: January 16, 2019)

Physical properties of multi-orbital materials depend not only on the strength of the effective interactions among the valence electrons but also on their type. Strong correlations are caused by either Mott physics that captures the Coulomb repulsion among charges, or Hund physics that aligns the spins in different orbitals. We identify four energy scales marking the onset and the completion of screening in orbital and spin channels. The differences in these scales, which are manifest in the temperature dependence of the local spectrum and of the charge, spin and orbital susceptibilities, provide clear signatures distinguishing Mott and Hund physics. We illustrate these concepts with realistic studies of two archetypal strongly correlated materials, and corroborate the generality of our conclusions with a model Hamiltonian study.

The excitation spectra and transport properties of transition metal oxides at high energy and/or high temperature are well described in terms of dressed atomic excitations with their characteristic multiplet structure. At very low energy scales, by contrast, metallic systems are well described in terms of strongly renormalized Landau quasiparticles forming dispersive bands. Describing the evolution of the excitation spectrum as a function of energy scale is a fundamental problem in the theory of strongly correlated materials. Starting with the Fermi liquid quasiparticles at the lowest energy scales, and raising the temperature, one can view this evolution as their gradual undressing. Conversely, starting from the high energy end, one can understand the evolution of the excitation spectrum as the screening of the orbital and spin excitations of atomic states, which gradually bind to give rise to quasiparticles. Here we consider the temperature dependence of this screening process for correlated multi-orbital systems with strong on-site atomic-like interactions, involving both a Coulomb repulsion U and Hund's coupling J . The former differentiates between different charge configurations without preference for a given spin or orbital configuration, whereas the latter favors the highest spin state.

It is well known that strong correlation effects can arise due to proximate Mott insulating states in which strong on-site Coulomb repulsion slows down charge fluctuations or even blocks the charge motion and localizes the electrons [1, 2]. However, many materials far away from the Mott insulating state, notably the 3d iron-based superconductors [3, 4] and ruthenates [5, 6], display strong correlation effects as a result of strong Hund coupling rather than the Hubbard U . These so-called ‘‘Hund metals’’ [3–14] were proposed to be a new type of strongly correlated electron system, characterized by spin-orbital separation [9–11].

The existence of different origins of correlations, Coulomb U or Hund J , poses an important question: what are the defining signatures distinguishing Mott and Hund metals? The goal of this work is to answer this question, by pointing out that Hund and Mott metals differ strikingly in the temperature dependencies of their local correlated spectra and the local susceptibilities describing the charge, spin and orbital degrees of freedom. These differences reflect two distinct screening routes for how quasiparticles emerge from the atomic degrees of freedom, with spin-orbital separation involved for Hund metals, but not for Mott metals.

We provide evidence of the two distinct screening routes by investigating (i) two realistic materials and (ii) a model Hamiltonian. For (i) we consider two archetypal materials with non-degenerate orbitals, the Mott system V_2O_3 [15–17] and the Hund metal Sr_2RuO_4 [18]. We compute their properties using density functional theory plus dynamical mean-field theory (DFT+DMFT) [19–21], which has been successfully used to describe the available experimental measurements for V_2O_3 [22–28] and Sr_2RuO_4 [5, 29–31]. For (ii) we study a 3-band Hubbard-Hund model (3HHM) with three degenerate bands hosting two electrons. This 3HHM is the simplest model capable of capturing both Hund and Mott physics and the crossover between them as function of increasing U [9, 10]. Whereas Ref. [10] focused on $T = 0$, here we focus on temperature dependence. We study the 3HHM using DMFT and the numerical renormalization group (DMFT+NRG). We accurately determine the location of the Mott transition at zero temperature and show that provided that J is sizeable, the temperature dependence of physical properties for large U near the Mott transition line qualitatively resembles that of V_2O_3 , while for small U far from the transition it

* These authors contributed equally to this work. Correspondence: xiaoyu.deng@gmail.com.

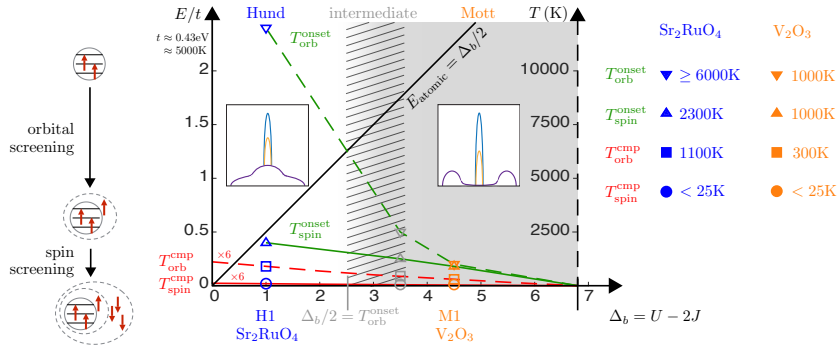


FIG. 1. Schematic sketch of the behavior of four characteristic temperature scales, $T_{\text{orb}}^{\text{onset}}$ (green dashed), $T_{\text{spin}}^{\text{onset}}$ (green solid), $T_{\text{orb}}^{\text{comp}}$ (red dashed), $T_{\text{spin}}^{\text{comp}}$ (red solid), marking the onset and the completion of screening of orbital and spin degrees of freedom, respectively, as functions of the bare gap, $\Delta_b = U - 2J$, between the upper and lower Hubbard side band. Open symbols on the left give the values of these scales as obtained from DMFT+NRG calculations for our 3-band Hubbard-Hund model, with $J = 1$ and $U = 3$ (green), $U = 5.5$ (grey) and $U = 6.5$ (yellow). On the right, closed symbols give corresponding values obtained from DFT+DMFT calculations for the materials Sr_2RuO_4 (green) and V_2O_3 (yellow). Left: cartoon of two-stage screening for three local levels with $J \neq 0$, containing two electrons with total spin $S = 1$: with decreasing temperature, first orbital screening of the hole occurs, whereby a delocalized spin $1/2$ combines with the local spin 1 to yield an orbital singlet with spin $3/2$; then spin screening occurs, yielding an orbital and spin singlet [10]. The energy scales characterizing the two screening stages lie far apart for Hund systems, but close together for Mott systems. Insets: cartoons of the local density of states, $A(\omega)$, for a Hund system (left) and a Mott system close to the Mott transition (right), summarizing the essential differences in the evolution of the quasiparticle peak with decreasing temperature (purple to yellow to blue).

resembles that of Sr_2RuO_4 . Therefore, our 3HHM results elucidate the physical origin of the differences between these materials. Indeed, we argue that our findings are applicable to general multi-orbital materials and characteristic of the general phenomenology of Mott and Hund physics, independent of material-dependent details, such as the initial band structure.

Overview of results

We start with an overview of our most important observations. We first identify four temperature scales, characterizing the onset and completion of screening of the orbital and spin degrees of freedom as the temperature is lowered. The scales for the onset of screening, $T_{\text{orb}}^{\text{onset}}$ and $T_{\text{spin}}^{\text{onset}}$, are defined as the temperatures at which the static local orbital and spin susceptibilities, χ_{orb} and χ_{spin} , first show deviations from the Curie behavior, $\chi \propto 1/T$, shown by free local moments. The scales for the completion of screening, $T_{\text{orb}}^{\text{comp}}$ and $T_{\text{spin}}^{\text{comp}}$, mark the transition of these susceptibilities to Pauli behavior, saturating to constants at very low temperatures. For orientation, Fig. 1 summarizes the behavior of these scales with increasing Coulomb interaction at fixed Hund's coupling, as will be elaborated throughout the text below. The most striking observation is that increasing U pushes the onset scales $T_{\text{orb}}^{\text{onset}}$ and $T_{\text{spin}}^{\text{onset}}$ closer together until they essentially coincide. As a consequence, the Hund regime (small U) and the Mott regime (large U , close to the Mott transition), though adiabatically connected via a crossover regime, show dramatic differences for the temperature dependence of physical quantities (discussed below). The trends shown in the figure were extracted from our analysis of the 3HHM, but they match those found for V_2O_3 and Sr_2RuO_4 (see legend on the right), and we expect them to be generic for multi-orbital Mott and/or Hund systems.

Mott systems. Coulomb interactions are strong in Mott systems, so that there is a large separation between the upper and lower Hubbard bands associated with atomic excitations, resulting in a significant gap or pseudogap. It is well established that, in the context of a metal-insulator transition, a metallic state is induced by the formation of a quasiparticle resonance from either the center of the gap or the edges of the Hubbard bands. Vice versa, starting from a correlated metal of Mott-type, a gap (or pseudogap) between incoherent spectra is restored when the coherence resonance is destroyed. The transition from insulator to metal can be induced by doping or tuning the ratio of the interaction versus the bandwidth [2], but it also occurs when the coherence resonance emerges by decreasing temperature. For example, in a model study of a doped single-band Mott insulator at infinite dimensions, the spectra at high temperature exhibit a two-peak structure reminiscent of a Mott gap, from which a coherence resonance emerges as “resilient quasiparticles” appear [45].

Here we propose that the presence of a gap/pseudogap regime in the local density of states (LDOS) at temperatures so high that the coherence resonance is destroyed is a fingerprint of Mott physics in general situations. We show that, at high temperatures, the LDOS of a multi-orbital Mott system exhibits two incoherent peaks above and below

the Fermi energy, reflecting atomic particle- and hole-like excitations, with a pseudogap in between, signifying the proximity to charge localization. When the temperature is lowered, a clear and sharp quasiparticle resonance suddenly emerges near the Fermi energy (for a cartoon depiction, see Fig. 1, right inset), signifying the appearance of mobile charge carriers. This occurs at a well-defined temperature scale, T_M , well below the lowest atomic excitation energy, E_{atomic} , involved in the incoherent two-peak structure. This Mott behavior is also reflected in the temperature dependence of various local susceptibilities. With decreasing temperature the static local charge susceptibility and local charge fluctuations first remain small and rather constant while the local spin and orbital susceptibilities exhibit Curie behavior, indicative of unscreened local moments. Once the temperature drops below T_M , the appearance of mobile carriers causes the local charge susceptibility and charge fluctuations to increase, and the spin and orbital susceptibilities to deviate from pure Curie behavior, reflecting the onset of screening. For Mott systems, this onset thus occurs simultaneously for orbital and spin degrees of freedom, $T_{\text{spin}}^{\text{onset}} = T_{\text{orb}}^{\text{onset}} = T_M$.

Hund systems. The above signatures of Mott physics are in stark contrast to the behavior of Hund systems. These typically have much smaller values of U , and hence E_{atomic} . Consequently, the Hubbard side bands effectively overlap, so that the LDOS features a single incoherent peak even at temperatures as high as E_{atomic} or beyond. This broad peak evolves into a coherent quasiparticle peak as the temperature is lowered (for a cartoon depiction, see Fig. 1, left inset). Due to the absence of a pseudogap at large temperatures, the local charge susceptibility is large already at high temperatures and increases continuously, but only slightly, with decreasing temperature. Strikingly, the local orbital and spin susceptibilities show deviations from Curie-like behavior already at much higher temperatures than those in Mott systems. Moreover, orbital screening starts well before spin screening, $T_{\text{orb}}^{\text{onset}} \gg T_{\text{spin}}^{\text{onset}}$. Thus, Hund metals exhibit spin-orbital separation, featuring a broad temperature window, from $T_{\text{orb}}^{\text{onset}}$ down to $T_{\text{spin}}^{\text{onset}}$, involving screened, delocalized orbitals coupled to unscreened, localized spins. Importantly, $T_{\text{orb}}^{\text{onset}}$ can be much larger than E_{atomic} in Hund metals, which is why no pseudogap appears even up to temperatures well above E_{atomic} (it would appear only for $T \gtrsim T_{\text{orb}}^{\text{onset}}$, since it requires the breakdown of both spin *and* orbital screening). The fact that $T_{\text{spin}}^{\text{onset}}$ and E_{atomic} are both $\ll T_{\text{orb}}^{\text{onset}}$ is a crucial difference relative to Mott systems. There $T_{\text{spin}}^{\text{onset}} \simeq T_{\text{orb}}^{\text{onset}} \ll E_{\text{atomic}}$, so that the breakdown of spin and orbital screening, and the concomitant emergence of a pseudogap, *is* possible at temperatures well below E_{atomic} .

In principle, both multi-orbital Mott and Hund materials exhibit spin-orbital separation in the *completion* of screening: χ_{orb} crosses over to Pauli behavior at a larger temperature scale than χ_{spin} , i.e. $T_{\text{orb}}^{\text{cmp}} \gg T_{\text{spin}}^{\text{cmp}}$. Since Fermi-liquid behavior occurs below $T_{\text{spin}}^{\text{cmp}}$, this scale can be identified with the Fermi-liquid scale $T_{\text{FL}} \equiv T_{\text{spin}}^{\text{cmp}}$. However, spin-orbital separation in the completion of screening is much more pronounced for the Hund material.

Two archetypical materials: V_2O_3 and Sr_2RuO_4

Established facts. We begin our discussion of the two example materials by summarizing some of their well-established properties. V_2O_3 , a paramagnetic metal at ambient conditions, is proximate to an isostructural Mott transition (that can be induced by slightly Cr-doping), and a temperature-driven magnetic transition [15–17]. It exhibits Fermi-liquid behavior at low temperature when antiferromagnetism is quenched by doping or pressure [15–17]. Sr_2RuO_4 , on the other hand, is a paramagnetic metal far away from a Mott insulating state [33]. As temperature decreases it shows Fermi-liquid behavior and eventually becomes superconducting at very low temperature [18]. Despite the very different distances to a Mott insulating state, both materials have large specific heat coefficients in their Fermi-liquid states [15–18]. In both materials the observed Fermi-liquid scales are extremely low (around 25K [15–17, 34]), much smaller than the bare band energy or interaction parameters (order of eV). Pronounced quasiparticle peaks are observed in both materials using photoemission spectroscopy [35–38], and large values of mass renormalization are seen in Sr_2RuO_4 in various measurements [39–41]. Notably, the local physics on V/Ru sites are similar, with nominally two electrons/holes in three t_{2g} orbitals. Due to the crystal field of the surrounding oxygen, the t_{2g} orbitals of V are split into e_g^π orbitals with two-fold degeneracy and an energetically higher-lying a_{1g} orbital, while those of Ru are split into xz/yz orbitals with two-fold degeneracy and an energetically lower-lying xy orbital. Two electrons (holes) in three orbitals favor a spin-triplet $S = 1$ atomic state because of Hund’s coupling in both V_2O_3 [22, 42–44] and Sr_2RuO_4 [5].

Local spectra.

We compute the spectra of the relevant correlated orbitals in V_2O_3 and Sr_2RuO_4 up to high temperature with DFT+DMFT. We have not taken into account the effects of the temperature-dependent changes in lattice parameters, which have been shown to be very important in materials near the Mott transition such as V_2O_3 [32]. Nevertheless, the LDA+DMFT calculations here bring a degree of realism, such as band structure and crystal field effects, which is not present in the 3HHM calculations discussed further below. We focus first on the density of states at the Fermi level, estimated via $D(i\omega_0) = -\frac{1}{\pi}\text{Im}G(i\omega_0)$ (ω_0 is the first Matsubara frequency, G the computed local Green’s function). Fig. 2(a) depicts the temperature dependence of $D(i\omega_0)$ for e_g^π and a_{1g} orbitals in V_2O_3 . The results show that both orbitals share a characteristic temperature, $T_M = 1000\text{K}$: $D(i\omega_0)$ is fairly flat at temperatures above T_M , which implies approximately “rigid”, i.e. temperature-independent, spectra. Below T_M , $D(i\omega_0)$ gradually acquires

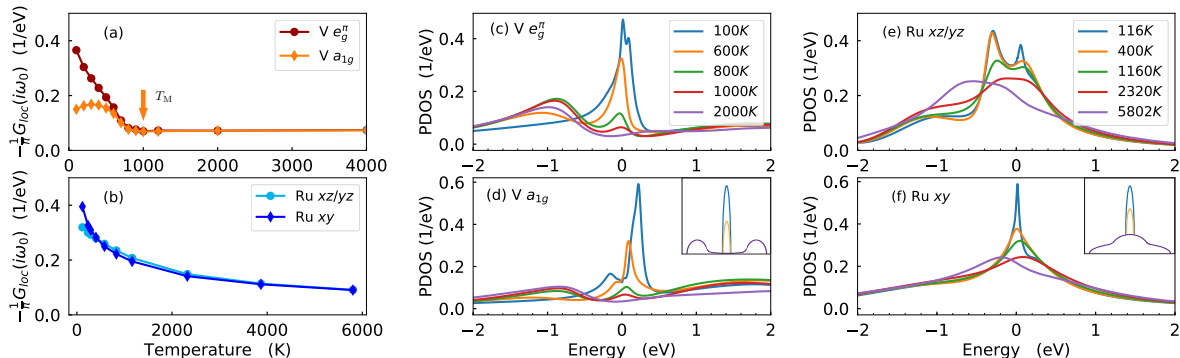


FIG. 2. The local spectra of the correlated orbitals in V_2O_3 [panels (a,c,d)] and Sr_2RuO_4 [panels (b,e,f)] exhibit different behaviors in their temperature dependence. (a,b) The density of states at the Fermi level, estimated by $D(i\omega_0) = -\frac{1}{\pi}\text{Im}G(i\omega_0)$. (c-f) The correlated real-frequency spectra (PDOS), $D(\omega) = -\frac{1}{\pi}\text{Im}G(\omega)$. $D(i\omega_0)$ shows a suppression at a characteristic temperature $T_M = 1000\text{K}$ (indicated by the purple arrow) in V_2O_3 (a), while it evolves smoothly in Sr_2RuO_4 (b). As temperature decreases, in V_2O_3 the coherence resonance of both e_g^π and a_{1g} orbitals emerges from the pseudogap regime with low density of states between two incoherent peaks (c,d), while in Sr_2RuO_4 the coherence resonance of both $d_{xz/yz}$ and d_{xy} orbitals emerges from a single broad incoherent peak with large finite density of states at the Fermi level (e,f). The insets in (d,f), repeated from Fig. 1, are cartoons of the temperature dependence of the Mott and Hund PDOS.

a larger magnitude in both orbitals as temperature is lowered, signaling the formation of a quasiparticle resonance. We note that it increases monotonically with decreasing temperature in the e_g^π orbitals, but in the a_{1g} orbital it first increases and then decreases a little. Thus at low temperature the density of states at the Fermi level has a dominant e_g^π character. We emphasize that the evolution of $D(i\omega_0)$ is smooth and a first-order MIT is not involved. By contrast, in Sr_2RuO_4 the temperature dependence of the densities of states, $D(i\omega_0)$, of $d_{xz/yz}$ and d_{xy} orbitals is very different, as depicted in Fig. 2(b). For both orbitals, $D(i\omega_0)$ increases as temperature is decreased, with gradually increasing slope, showing no flat regime even at extremely high temperatures, where their values are already larger than those for V_2O_3 above T_M . In contrast to the case of V_2O_3 , a quasiparticle resonance is present even at the highest temperatures studied and, thus, no characteristic temperature is found for its onset, as discussed in the next paragraph.

We also study the correlated real-frequency projected density of states (PDOS), $D(\omega) = -\frac{1}{\pi}\text{Im}G(\omega)$, for the different orbitals. These are obtained by analytically continuing the computed Matsubara self-energy and then computing the local Green's function. The results for V_2O_3 are depicted in Fig. 2(c,d). At very high temperatures, we observe a typical Mott feature: a pseudogap exists at the Fermi level, between two broad humps in the incoherent spectra, with maxima near -1eV and 2eV . With decreasing temperature spectral weight is transferred from the high-energy humps into the pseudogap and a quasiparticle peak emerges similarly in both orbitals at the Fermi level on top of the pseudogap. The characteristic temperature for the onset of the formation of the coherence resonance is roughly consistent with $T_M = 1000\text{K}$ determined above. As temperature decreases further, the magnitude of the coherence peak in both orbitals increases gradually, and at very low temperature both orbitals show a coherence resonance with a pronounced, thin cusp. In the e_g^π orbitals the resonance is peaked at the Fermi level while the a_{1g} quasiparticle peak slightly moves away from the Fermi level when the temperature is lowered, thus reducing the density of states at the Fermi level. The resulting temperature evolution of the zero-frequency density of states in both orbitals is consistent with the $D(i\omega_0)$ discussed above, including the non-monotonic behavior of the a_{1g} orbital in Fig. 2(a). For Sr_2RuO_4 the slow increase of the density of states at the Fermi level, $D(i\omega_0)$, with decreasing temperature becomes clear from the PDOS, shown in Fig. 2(e,f). The correlated high-temperature local spectra are characterized by a single broad feature (no side-humps), which shifts its position slightly towards the Fermi level with decreasing temperature, while its shape remains almost unchanged. This is very different from the spectra in V_2O_3 , which at high temperatures show a pseudogap between two broad side peaks. When the temperature is decreased further, a sharp narrow peak gradually develops in both orbitals from the broad, incoherent feature. In this process only a small fraction of spectral weight is transferred from higher frequencies to a 1eV range around the Fermi level. At low temperature, the spectra of both $d_{xz/yz}$ and d_{xy} orbitals are similar to their corresponding DFT values with a renormalized bandwidth and show a pronounced, thin cusp as in the case of V_2O_3 .

The different temperature dependences of the local spectra of V_2O_3 and Sr_2RuO_4 can be viewed as fingerprints distinguishing Mott from Hund systems, respectively. With decreasing temperature the quasiparticle resonance of

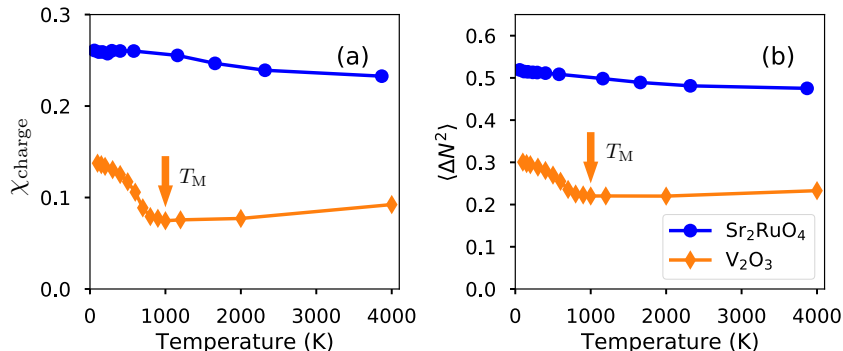


FIG. 3. (a) The static local charge susceptibility χ_{charge} , and (b) local charge fluctuation $\langle \Delta N^2 \rangle$, computed for V₂O₃ (diamonds) and Sr₂RuO₄ (circles). In the Hund system Sr₂RuO₄ both χ_{charge} and $\langle \Delta N^2 \rangle$ are large and only weakly dependent on temperature. By contrast, in the Mott system V₂O₃ they are much smaller and strongly temperature-dependent. The purple arrows indicate that in V₂O₃ the minima of the local charge susceptibility and fluctuation occur at the same temperature scale, T_M , as that marking the emergence of the quasiparticle peak in the local PDOS.

V₂O₃ emerges from a high-temperature pseudogap regime with very low density of states between incoherent spectra [see purple curve in the cartoon in inset of Fig. 2(d)]. This is consistent with the widely held belief that Mott physics governs V₂O₃. It is described by a single characteristic temperature scale, T_M , which indicates the onset of formation of the quasiparticle resonance. By contrast, for Sr₂RuO₄ the quasiparticle resonance develops with decreasing temperature from a single incoherent peak that has a large value at the Fermi level already at very high temperature [see purple curve in the cartoon in inset of Fig. 2(f)]. The demonstration of these two distinct routes towards forming the coherent Fermi-liquid at low temperature is one of the main results of this work.

Susceptibilities. We next consider the static local charge susceptibility, $\chi_{\text{charge}} = \int_0^\beta \langle N_d(\tau) N_d(0) \rangle d\tau - \beta \langle N_d \rangle^2$, and the local charge fluctuations, $\langle \Delta N^2 \rangle = \langle N_d^2 \rangle - \langle N_d \rangle^2$, shown in Figs. 3(a) and 3(b), respectively. (N_d is the total occupancy of t_{2g} orbitals.) For both materials, the behavior of χ_{charge} mimics that of $\langle \Delta N^2 \rangle$, hence we focus on the latter below. $\langle \Delta N^2 \rangle$ is much smaller, with a much stronger temperature dependence, in V₂O₃ than in Sr₂RuO₄. For V₂O₃, $\langle \Delta N^2 \rangle$ initially remains small and almost constant with decreasing temperature, signifying the suppression of charge fluctuations in the pseudogap regime. It then increases rather abruptly, signifying the onset of charge delocalization, at the same temperature, $T_M = 1000$ K (purple arrow in Fig. 3(a)), as that where the quasiparticle peak begins to emerge. By contrast, for Sr₂RuO₄ $\langle \Delta N^2 \rangle$ exhibits only a weak temperature dependence, persisting up to the highest temperature studied but changing by less than 10% over this range.

We have also computed the static local spin and orbital susceptibilities, defined as $\chi_{\text{spin}} = \int_0^\beta \langle S_z(\tau) S_z(0) \rangle d\tau$ and $\chi_{\text{orb}} = \int_0^\beta \langle \Delta N_{\text{orb}}(\tau) \Delta N_{\text{orb}} \rangle - \beta \langle \Delta N_{\text{orb}} \rangle^2$, where S_z is the total spin momentum in the t_{2g} orbitals, $\Delta N_{\text{orb}} = N_a/2 - N_b$ is the occupancy difference per orbital, and (a, b) denotes (e_g^{π}, a_{1g}) in V₂O₃ and $(xz/yz, xy)$ in Sr₂RuO₄, respectively. The results are depicted in Fig. 4. In V₂O₃, both the spin and orbital susceptibilities exhibit Curie behavior, i.e. $T\chi_{\text{spin}}$ and $T\chi_{\text{orb}}$ are approximately constant at high temperature (Fig. 4(a)). Notably, with decreasing temperature deviations from the Curie behavior set in at the same characteristic temperature, $T_M = 1000$ K, as that determined above from the local PDOS evolution. Thus, spin and orbital degrees of freedom start to be screened simultaneously with the formation of a coherence resonance in the prototype Mott system V₂O₃, $T_{\text{orb}}^{\text{onset}} = T_{\text{spin}}^{\text{onset}} = T_M$. By contrast, in the Hund material Sr₂RuO₄, Curie-like behavior in the spin susceptibility is seen only at very high temperatures. With decreasing temperature, it ceases already at around $T_{\text{spin}}^{\text{onset}} \simeq 2300$ K (Fig. 4(c)), a scale much higher than that in V₂O₃. For the orbital susceptibility the situation is even more extreme: it does not show Curie behavior even at the highest temperature studied ($T_{\text{orb}}^{\text{onset}} \geq 6000$ K). This is evidence of spin-orbital separation in Sr₂RuO₄: the screening of the orbital degrees of freedom starts at much higher temperature than that of the spin degrees of freedom, $T_{\text{orb}}^{\text{onset}} \gg T_{\text{spin}}^{\text{onset}}$. Hence the onset of deviations from Curie-like behavior in the spin/orbital susceptibility, i.e. the onset of screening of spin/orbital degrees of freedom, is very different in V₂O₃ and Sr₂RuO₄. These differences constitute another set of fingerprints distinguishing Mott from Hund systems. It will be further analyzed below in the context of our 3HHM calculations.

Next we discuss the completion of orbital and spin screening, characterized by the temperature scales, $T_{\text{orb}}^{\text{cmp}}$ and $T_{\text{spin}}^{\text{cmp}}$, below which the corresponding susceptibilities become constant. In both materials, χ_{orb} seems to become essentially constant at low temperatures, with the orbital screening completion scale in V₂O₃, $T_{\text{orb}}^{\text{cmp}} \simeq 300$ K (Fig. 4(b)),

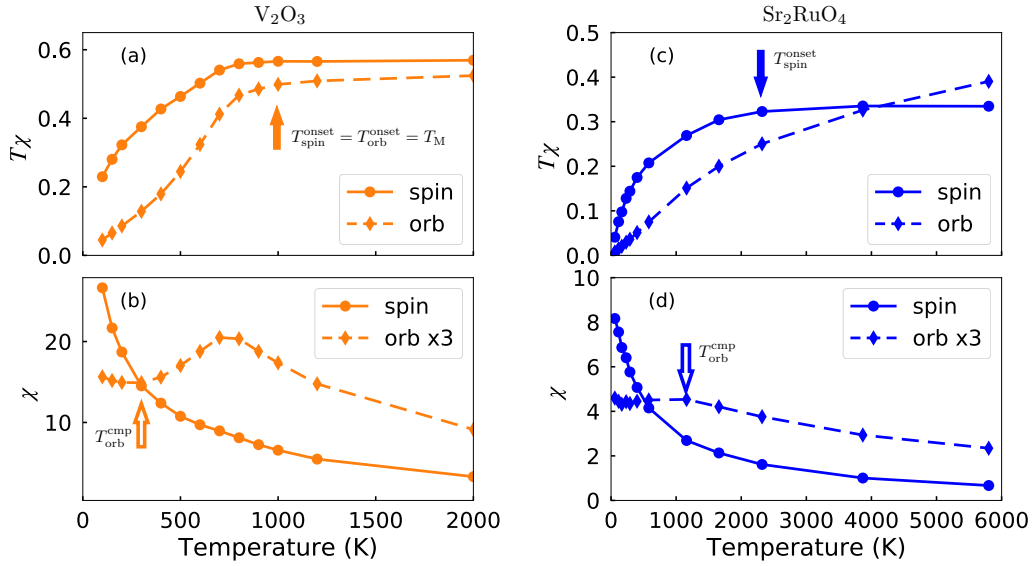


FIG. 4. The static local orbital and spin susceptibilities χ_{orb} and χ_{spin} of V_2O_3 (a,b) and Sr_2RuO_4 (c,d), plotted as functions of temperature, with $T\chi$ and χ shown in the upper and lower panels, respectively. The Curie law holds above 1000K (indicated by open purple arrow) in the spin and orbital susceptibility of V_2O_3 (a). In Sr_2RuO_4 the spin susceptibility follows Curie-like behavior above 2300K (indicated by open cyan arrow), while the orbital susceptibility does not follow a Curie law in the temperature range studied (c). The spin susceptibility of both materials (b,d) does not saturate at the lowest accessible temperature, indicating an even lower Fermi-liquid scale. The orbital susceptibility has only weak temperature dependence below 300K in V_2O_3 (b) and below 1100K in Sr_2RuO_4 (d) (indicated by filled blue arrows).

being much smaller than in Sr_2RuO_4 , $T_{\text{orb}}^{\text{cmp}} \simeq 1100\text{K}$ (Fig. 4(d)). By contrast, in both materials the spin susceptibility increases with decreasing temperature, and is not fully screened even at the lowest temperature studied. This is consistent with the experimental observations that in both materials T_{FL} is as low as about 25K, and T_{FL} provides an estimation for $T_{\text{spin}}^{\text{cmp}}$ at which the spin degrees of freedom are fully screened. In summary, we clearly deduce spin-orbital separation in the completion of screening, $T_{\text{orb}}^{\text{cmp}} \gg T_{\text{spin}}^{\text{cmp}}$, for the Hund metal Sr_2RuO_4 , while this effect is less pronounced in the Mott material V_2O_3 , where χ_{orb} in addition shows a bump before it tends to saturate at lower temperatures.

In Hund metals the spin-orbital separation has been pointed out in numerical studies of the frequency dependence of the local self-energy and susceptibilities [9–11] and in an analytical estimate of the Kondo scales [13]. Here, our results reveal that it also occurs in the temperature domain. We note that our computed spin susceptibility of Sr_2RuO_4 is consistent with earlier results using a narrower temperature range [46].

Entropy. In both materials the entropy of the correlated atom reaches a plateau of $\ln(3 \times 3 = 9)$ at high temperatures as expected for a high spin ($S = 1$) state with large contribution from three active t_{2g} orbital degrees of freedom [8, 9]. Notably, in Mott systems, with decreasing temperature the plateau persists down to the temperature scale, T_{M} , until which both the spin and orbital degrees of freedom remain unquenched and the quasiparticle resonance has not yet formed in the pseudogap of the local correlated spectrum. These results are discussed in the supplement [47].

Three-band Hubbard-Hund model

Model Hamiltonian. We now turn to the 3HHM, described by the Hamiltonian

$$\hat{H} = \sum_i \left(-\mu \hat{N}_i + \hat{H}_{\text{int}}[\hat{d}_{i\nu}^\dagger] \right) + \sum_{\langle ij \rangle \nu} t \hat{d}_{i\nu}^\dagger \hat{d}_{j\nu}, \quad (1)$$

$$\hat{H}_{\text{int}}[\hat{d}_{i\nu}^\dagger] = \frac{1}{2} (U - \frac{3}{2}J) \hat{N}_i (\hat{N}_i - 1) - J \hat{\mathbf{S}}_i^2 + \frac{3}{4} J \hat{N}_i.$$

The on-site interaction term incorporates Mott and Hund physics through U and J respectively. $\hat{d}_{i\nu}^\dagger$ creates an electron on site i of flavor $\nu = (m\sigma)$, which is composed of a spin ($\sigma = \uparrow, \downarrow$) and orbital ($m = 1, 2, 3$) index. $\hat{n}_{i\nu} = \hat{d}_{i\nu}^\dagger \hat{d}_{i\nu}$ counts the electrons of flavor ν on site i . $\hat{N}_i = \sum_\nu \hat{n}_{i\nu}$ is the total number operator for site i and $\hat{\mathbf{S}}_i$ its total spin,

with components $\hat{S}_i^\alpha = \sum_{m\sigma\sigma'} \hat{d}_{im\sigma}^\dagger \frac{1}{2} \sigma_{\sigma\sigma'}^\alpha \hat{d}_{im\sigma'}$, where σ^α are Pauli matrices. We take a uniform hopping amplitude, $t = 1$, serving as energy unit in the 3HHM, and a Bethe lattice in the limit of large lattice coordination. The total width of each of the degenerate bands is $W = 4$. We choose the chemical potential μ such that the total filling per lattice site is $\langle N_i \rangle = 2$. The model is solved numerically exactly using DMFT+NRG [9, 10].

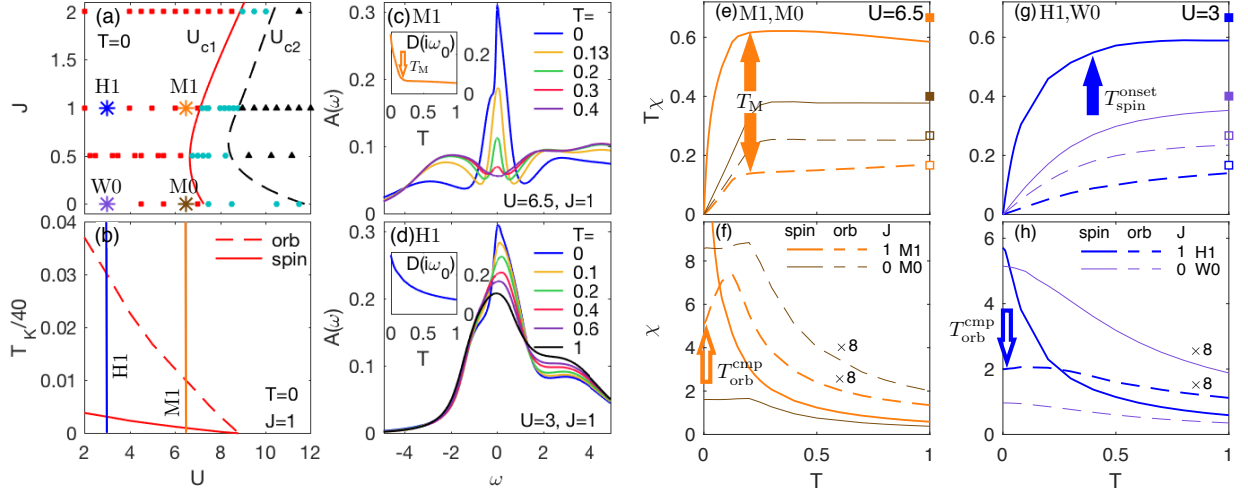


FIG. 5. Disentangling features of Mott and Hund physics in a DMFT+NRG study of the 3HHM (unit of energy: hopping amplitude $t = 1$). (a) The $T = 0$ phase diagram (cf. Fig. 5 of [10]) reveals three phases in the J - U -plane: a metallic phase (red squares), a coexistence region (blue circles), and an insulating phase (black triangles), separated by two phase transition lines U_{c1} (solid red curve), and U_{c2} (dashed black curve), respectively. In panels (c-h) we focus on four parameter combinations, indicated in (a) by colored asterisks: two Mott systems with $U = 6.5$ near the U_{c1} phase transition line, with $J = 1$ (M1) or $J = 0$ (M0); and two systems with $U = 3$ far from the transition and deep in the metallic state, a Hund system with $J = 1$ (H1) and a weakly correlated system with $J = 0$ (W0). (b) The Kondo temperatures, here shown for $J = 1$ (cf. Fig. 12 of [10]) are extracted from frequency-dependent susceptibilities at $T = 0$, as defined in [9]. T_K^{spin} (T_K^{orb}) corresponds to the screening of spin (orbital) degrees of freedom. Fermi liquid behavior sets in below the temperature scale $T_K^{\text{spin}}/40 \approx T_{\text{spin}}^{\text{cmp}}$. Orange and blue vertical lines mark the values of U used for M1 and H1, respectively. (c,d) The temperature dependence of the LDOS for M1 and H1, respectively. The energy scale of the lowest bare atomic excitations, $\pm E_{\text{atomic}} = \pm(\frac{1}{2}U - J)$, and thus the Hubbard bands, is much larger for M1 than H1. For M1 in (c) a pseudogap (a typical Mott feature) emerges when the temperature increases past a characteristic value, T_M , which lies far below the rather large scale $E_{\text{atomic}}^{\text{M1}} \simeq 2.25$. By contrast, for H1 in (d) a pronounced peak in the density of states still exists even at very high temperatures, $T > 0.5$, that exceed the rather small scale $E_{\text{atomic}}^{\text{H1}} \simeq 0.5$. The insets of (c,d) show the LDOS at the Fermi level, estimated by $D(i\omega_0) = -\frac{1}{\pi} \text{Im}G(i\omega_0)$, for M1 (orange) and H1 (blue). (f-h) The local spin and orbital susceptibilities are shown as functions of T for M1 (orange) and M0 (brown) in (e,f), and for H1 (blue) and W0 (purple) in (g,h), with $T\chi$ depicted in the upper panels (e,g) and χ in the lower panels (f,h). (e,g) For temperatures well above $T_{\text{orb}}^{\text{onset}}$ or $T_{\text{spin}}^{\text{onset}}$, respectively, $T\chi_{\text{orb}}$ and $T\chi_{\text{spin}}$ approach plateaus, indicative of a Curie law, as expected for unscreened spin or orbital degrees of freedom. The observed plateau heights are roughly comparable to the values expected [48] for free local moments with occupancy strictly equal to 2 and, for M1 and H1 (M0 and W0), spin equal to 1 (and 0), for which $T\chi_{\text{spin}}^{\text{free}} = \frac{1}{3} \langle \hat{S}^2 \rangle = 2/3$ ($2/5$) and $T\chi_{\text{orb}}^{\text{free}} = \frac{1}{8} \langle \hat{T}^2 \rangle = 1/6$ ($4/15$) indicated by filled and empty squares on the right vertical axes, respectively. (Deviations of the observed plateaus from these local moment values reflect admixtures of states with different occupancy or spin.) For M1 in (e), the Curie law ceases to hold for both χ_{orb} and χ_{spin} below about $T_M \simeq 0.2$ (orange arrow). For H1 in (g), χ_{spin} deviates from a Curie-like behavior below about $T \simeq 0.4$ (blue arrow), while χ_{orb} does not follow a Curie law in the temperature range displayed. For M0 in (e) and W0 in (g), deviations from Curie behavior set in at similar temperatures for χ_{spin} and χ_{orb} . Thus the onset of screening shows spin-orbital separation for H1, but not for M1 (due to its proximity to the Mott transition), and also not for M0 and W0 (since these have $J = 0$). (f,h) For both M1 and H1, χ_{spin} saturates at very low Fermi-liquid temperatures (not displayed here, but clearly deducible from the underlying zero-temperature NRG data [9, 10]). By contrast, χ_{orb} is approximately temperature independent below $T = 0.01$ (orange arrow) for M1 in (f) and below $T = 0.03$ (blue arrow) for H1 in (h). For M0 in (f) and W0 in (h), χ_{orb} and χ_{spin} become temperature independent at similar temperatures. Thus, the completion of screening shows tendencies of spin-orbital separation for M1 and H1 (since $J \neq 0$), but not for M0 and W0 (since $J = 0$). Moreover, $T_{\text{spin}}^{\text{cmp}}$ and hence T_{FL} is much smaller for $J \neq 0$ than for $J = 0$.

Phase diagram. The 3HHM enables the exploration of a broad region of parameters at arbitrary low temperatures. Fig. 5(a) illustrates the J - U phase diagram at $T = 0$. To illustrate the difference between large and small U , and non-zero and zero J , we will focus on four parameter combinations, denoted by M1, H1, M0 and W0, depicted by asterisks in Fig. 5(a), and defined in detail in the figure caption. The Mott system M1 ($U = 6.5$) and the Hund

system H1 ($U = 3$), both with $J = 1$, lie close to or far from the Mott transition and qualitatively mimic V_2O_3 and Sr_2RuO_4 respectively, considering their multi-orbital nature, sizable Hund's coupling and distances to the Mott transition. The Mott system M0 ($U = 6.5$) and the weakly correlated system W0 ($U = 3$), both with $J = 0$, illustrate the consequences of turning off Hund's coupling altogether.

Fig. 5 displays the LDOS, $A(\omega) = -(1/\pi)\text{Im}G(\omega)$, for M1 and H1 (c,d); the corresponding density of states at the Fermi level (insets of (c,d)), estimated by $D(i\omega_0) = -\frac{1}{\pi}\text{Im}G(i\omega_0)$; and the static local susceptibilities $T\chi$ (e,g) and $\chi \equiv \chi_d(\omega = 0)$ (f,h) for the spin (solid) and orbital (dashed) degrees of freedom of M1 (orange), M0 (brown), H1 (blue) and H0 (purple). The corresponding dynamical real-frequency spin and orbital susceptibilities are defined as $\chi_{d,\text{spin}}(\omega) = \frac{1}{3} \sum_{\alpha} \langle \hat{S}^{\alpha} \parallel \hat{S}^{\alpha} \rangle_{\omega}$ and $\chi_{d,\text{orb}}(\omega) = \frac{1}{8} \sum_a \langle \hat{T}^a \parallel \hat{T}^a \rangle_{\omega}$, respectively [48, 49], where $\hat{T}^a = \sum_{mm'\sigma} \hat{d}_{m\sigma}^{\dagger} \frac{1}{2} \tau_{mm'}^a \hat{d}_{m'\sigma}$ are the impurity orbital operators with the SU(3) Gell-Mann matrices, τ^a , normalized as $\text{Tr}[\tau^a \tau^b] = 2\delta_{ab}$. The qualitative similarities (especially of Fig. 5(c,d,g,f,h)) with those in Fig. 2 and Fig. 4 are obvious, in spite of the simplified band structure and the absence of crystal fields. Let us now discuss these in detail.

Mott system M1. The basic features of V_2O_3 are reproduced by M1, lying close to the phase transition line. At high temperatures we also observe a pseudogap in the incoherent spectra at the Fermi level, formed between two broad Hubbard sidebands, one at negative and one with minor substructure at positive frequencies, respectively (Fig. 5(c), red and purple curves). With decreasing temperature spectral weight is transferred from these high-energy humps into the pseudogap, building up a clear peak at about $T_M \simeq 0.2$, which evolves into a pronounced, sharp coherence resonance at very low temperature (Fig. 5(c), blue curve). This behavior is confirmed by $D(i\omega_0)$ (inset of Fig. 5(c)). $T\chi$ shows flat Curie behavior for both orbital and spin degrees of freedom in the pseudogapped phase at high temperatures. With decreasing temperature the orbitals and spins start to get screened simultaneously at the same energy scale, $T_{\text{orb}}^{\text{onset}} = T_{\text{spin}}^{\text{onset}} = T_M$, at which the resonance emerges in the pseudogap (Fig. 5(e)), analogously to the behavior in the Mott material V_2O_3 .

Hund system H1. For the Hund system H1 far from the phase transition line, the physical properties (LDOS, local spin- and orbital susceptibility) show the same qualitatively behavior as for Sr_2RuO_4 . At very high temperatures (above $T_{\text{spin}}^{\text{onset}} \simeq 0.4$, red, purple and black curves in Fig. 5(d)) the local spectral function has a large density of states near the Fermi energy, in contrast to the pseudogap present for M1. At these large temperatures the spin susceptibility shows Curie-like behavior, in that $T\chi_{\text{spin}}$ is essentially constant there, whereas $T\chi_{\text{orb}}$ decreases with decreasing temperature (Fig. 5(g)). This indicates that the spins are still large and (quasi-)free while the orbitals are already being screened, $T_{\text{spin}}^{\text{onset}} \ll T_{\text{orb}}^{\text{onset}}$. Below $T_{\text{spin}}^{\text{onset}}$ also the spin degrees of freedom get screened and a pronounced quasiparticle peak gradually develops, with a sharp cusp at low frequencies and very low temperatures (blue curve in Fig. 5(d)). In contrast to M1, $D(i\omega_0)$ for H1 is large already at high temperatures and increases continuously with decreasing temperature (inset of Fig. 5(d)).

Completion of screening. In principle, for both M1 and H1, i.e. both close to and far from the Mott transition, orbital screening is completed at a higher temperature than spin screening. Indeed, an approximately temperature-independent, Pauli-like susceptibility, is observed for χ_{orb} (dashed lines) below $T_{\text{orb}}^{\text{cmp}}$ (indicated by arrows in Figs. 5(f,h)), while χ_{spin} (solid lines) still increase with decreasing temperature, hence $T_{\text{orb}}^{\text{cmp}} \gg T_{\text{spin}}^{\text{cmp}}$. (This effect is more pronounced for H1, i.e. far from the Mott transition.) By contrast, the corresponding M0 and W0 curves in Figs. 5(f,h), having $J = 0$, show no spin-orbital separation for the completion of screening, i.e. $T_{\text{orb}}^{\text{cmp}} \simeq T_{\text{spin}}^{\text{cmp}}$, as described in more detail in the figure caption.

Discussion

The DMFT solution of the 3HHM with nonzero J enables us to understand the interplay between Mott and Hund physics and its materials manifestations from an impurity model perspective. Far from the transition, a picture in terms of a multi-orbital Kondo model in a broad-bandwidth metallic bath applies. Standard analysis of the logarithmic Kondo singularities showed that $T_{\text{spin}}^{\text{onset}} \ll T_{\text{orb}}^{\text{onset}}$ [13]. As we approach the Mott boundary, charge fluctuations are blocked, resulting in well-separated Hubbard bands. Here the onset of the Kondo resonance is not signaled by logarithmic singularities but instead it is driven by the DMFT-self-consistency condition [50]. In this regime the onsets of screening for spin and orbital degrees of freedom occur at the same scale, namely that where charge delocalization sets in. The spin-orbital separation in the completion of screening, which occurs at *low temperatures* in both Mott and Hund systems, can be understood from a zero-temperature analysis of the 3HHM. We define characteristic Kondo scales T_K^{orb} and T_K^{spin} , from the maximum in the zero-temperature, frequency-dependent local orbital and spin susceptibilities [9], respectively, and display them in Fig. 5(b) for $J = 1$ as a function of U . We find that $T_K^{\text{spin}} \ll T_K^{\text{orb}}$, so an intermediate region with free spins and quenched orbitals is a generic feature of multi-orbital systems with significant Hund's coupling as was surmised from earlier studies. For both the Hund and Mott system results we deduce that $T_K/40 \approx T^{\text{cmp}}$: spin-orbital separation in frequency space thus has a direct manifestation in the completion of screening as a function of temperature. Below the spin completion scale we have a Fermi liquid. As we approach the Mott boundary for increasing U the spin-orbital separation region shrinks, and all the energy scales are reduced, as shown in Fig. 5(b), elucidating the reduced $T_{\text{orb}}^{\text{cmp}}$ in the Mott system (and in V_2O_3) compared to the

Hund system (and Sr_2RuO_4).

Finally, we note that the systems M0 and W0, with $J = 0$, show no spin-orbit separation for the onset or completion of screening (see Figs. 5(e-l) and their discussion in the figure caption). Conversely, turning on J pushes the Fermi liquid scale $T_{\text{FL}} = T_{\text{spin}}^{\text{cmp}}$ strongly downward relative to $T_{\text{orb}}^{\text{onset}}$. This significantly reduces the quasiparticle weight $Z = m/m^*$ (which is proportional to T_{FL} [10]) and increases the strength of correlations. Hence the Hund system H1 is much more strongly correlated than W0, although U is the same for both. These differences leave clear fingerprints in photoemission spectra, where Z characterizes the slope of the quasiparticle dispersion. Moreover, the shape of the quasiparticle peak shows substructure indicative of spin-orbital separation for sizable J , but not for $J = 0$. For a detailed illustration of these points, see Ref. [47], Fig. S-2.

Conclusions

In conclusion, we revealed contrasting signatures of Mottness and Hundness in two archetypal materials, V_2O_3 and Sr_2RuO_4 , in the formation of the quasiparticle resonance in the local correlated spectra, and in the temperature dependence of the charge, spin, and orbital susceptibility as well as the impurity entropy. Mott and Hund physics manifest in the process in which the atomic degrees of freedom at high energies evolve towards low energies to form fermionic quasiparticles. We highlight the observation of four temperature scales that characterize the onset and the completion of screening of the spin and the orbital degrees of freedom. We find that a non-zero Hund's coupling leads to spin-orbital separation in the completion of screening at low temperatures, $T_{\text{orb}}^{\text{cmp}} \gg T_{\text{spin}}^{\text{cmp}}$, and this is more pronounced for Hund systems. However, Mott and Hund systems show contrasting behavior at intermediate to high energies, due to the very different relations of their overall quasiparticle peak width and their atomic excitation scales: $T_{\text{orb}}^{\text{onset}} \ll E_{\text{atomic}}$ for Mott systems vs. $E_{\text{atomic}} \lesssim T_{\text{orb}}^{\text{onset}}$ for Hund systems. In the Mott system V_2O_3 the strong Coulomb repulsion localizes the charge at high temperature, with decreasing temperature the onset of charge localization triggers the simultaneous onset of the screening of the spin and orbital degrees, accompanied by the formation of the coherence resonance at $T_{\text{M}} \equiv T_{\text{spin}}^{\text{onset}} = T_{\text{orb}}^{\text{onset}} \ll E_{\text{atomic}}$. In contrast, in Sr_2RuO_4 Coulomb repulsion is much weaker, so that no charge localization occurs even at very high temperatures. Therefore, charge fluctuations triggering the onset of screening are possible even at high temperatures, leading – due to the presence of sizeable Hund's coupling – to a clear separation in the energy scales at which this screening sets in for spin and orbital fluctuations, with $T_{\text{spin}}^{\text{onset}} \ll T_{\text{orb}}^{\text{onset}}$. All these findings are generic and do not depend on microscopic details. They only require a sizeable Hund's coupling, and are controlled by the distance to the Mott localization boundary. This is confirmed by a DMFT+NRG study of a model 3-band Hubbard-Hund Hamiltonian, thus establishing a general phenomenology of Mottness and Hundness in multi-orbital systems. Our results give not only new perspectives into the archetypal strongly correlated materials, V_2O_3 and Sr_2RuO_4 , but will be useful in interpreting experimental measurements on other correlated metals and in identifying the origin of their correlations.

Methods

The two prototype materials are investigated using the all-electron DMFT method as implemented in Ref. [51] based on the WIEN2k package [52] and the continuous-time quantum Monte-Carlo (CTQMC) impurity solver [53, 54]. We used projectors within a large (20eV) energy window, i.e. we used a high energy cutoff scale, to construct local orbitals, thus the oxygen orbitals hybridizing with the d orbitals were explicitly included. With such a large energy window the resulting d orbitals are very localized. In our two example materials these are the t_{2g} levels of Ru and V atoms, which we treated dynamically with DMFT, all other states were treated statically and no states were eliminated in the calculations. The nominal “double counting” scheme with the form $\Sigma_{DC} = U(n_{\text{imp}} - 1/2) - \frac{1}{2}J(n_{\text{imp}} - 1)$ was used where n_{imp} is the nominal occupancy of d orbitals. The onsite interactions in terms of Coulomb interaction U and Hund's coupling J were chosen to be $(U, J) = (6.0, 0.8)\text{eV}$ for V in V_2O_3 and $(U, J) = (4.5, 1.0)\text{eV}$ for Ru in Sr_2RuO_4 . The impurity entropy was computed by integrating the impurity internal energy up to high temperature, following Ref. [55]. Our DFT+DMFT setup was successful in describing the correlation effects in both materials [28, 31]. It captures the phase diagram of V_2O_3 which exhibits a Mott MIT and our computed electronic structure is consistent with experimental measurements [28]. The approach also describes the electronic structure of Sr_2RuO_4 and is in good agreement with the results of experimental measurements [31] and other DFT+DMFT calculations [5, 29, 30]. In addition our studies [28, 31] correctly characterize the transport and optical properties of both materials. These successes gave us confidence to extend our studies to even higher temperatures, and for quantities which have yet to be measured experimentally.

We solved the 3HHM using DMFT [19] in combination with an efficient multi-band impurity solver [9, 10], the full-density-matrix (fdm) NRG [56]. Our fdmNRG solver employs a complete basis set [57, 58], constructed from the discarded states of all NRG iterations. Spectral functions for the discretized model are given from the Lehmann representation as a sum of poles, and can be calculated accurately directly on the real axis in sum-rule conserving fashion [59] at zero or arbitrary finite temperature. Continuous spectra are obtained by broadening the discrete data with a standard log-gaussian Kernel of frequency-dependent [56, 60] width. Further, fdmNRG is implemented in the unified tensor representation of the QSpace approach [49] that allows us to exploit Abelian and non-Abelian

symmetries on a generic level [here $U(1)_{\text{charge}} \times SU(2)_{\text{spin}} \times SU(3)_{\text{orb}}$]. For further details of our DMFT+NRG calculations see the Supplementary material of [9].

Acknowledgments: Work by X.D. was supported by NSF DMR-1733071. Work by K.H. was supported by NSF DMR 1405303. Work by G.K. was supported by U.S. Department of energy, Office of Science, Basic Energy Sciences as a part of the Computational Materials Science Program. K.M.S., A.W., and J.v.D. acknowledge support from the excellence initiative NIM; A. W. was also supported by WE4819/1-1 and WE4819/2-1.

Author contributions: X.D., K.M.S. and G.K. proposed this project; X.D. performed the DFT+DMFT calculations and analyzed the results together with G.K. and K.H.; K.H. developed the DFT+DMFT code used and assisted the computation setup; K.M.S. performed the DMFT+NRG calculations; A.W. developed the NRG code and assisted K.M.S. in the initial stages of the DMFT+NRG computation. X.D. and K.M.S. drafted the manuscript with the help of G.K., K.H., A.W and J.v.D.

Data availability: The authors declare that the data supporting the findings of this study are available within the paper [and its supplementary information files].

-
- [1] van der Marel, D. & Sawatzky, G. A. Electron-electron interaction and localization in d and f transition metals. *Physical Review B* **37**, 10674–10684 (1988).
- [2] Imada, M., Fujimori, A. & Tokura, Y. Metal-insulator transitions. *Reviews of Modern Physics* **70**, 1039 (1998).
- [3] Haule, K. & Kotliar, G. Coherence-incoherence crossover in the normal state of iron oxypnictides and importance of Hund’s rule coupling. *New Journal of Physics* **11**, 025021 (2009).
- [4] Yin, Z. P., Haule, K. & Kotliar, G. Kinetic frustration and the nature of the magnetic and paramagnetic states in iron pnictides and iron chalcogenides. *Nature Materials* **10**, 932–935 (2011).
- [5] Mravlje, J. *et al.* Coherence-incoherence crossover and the mass-renormalization puzzles in Sr_2RuO_4 . *Physical Review Letters* **106**, 096401 (2011).
- [6] Werner, P. *et al.* Spin freezing transition and non-Fermi-liquid self-energy in a three-orbital model. *Physical Review Letters* **101**, 166405 (2008).
- [7] de’ Medici, L. Mravlje, J., & Georges, A. Janus-Faced Influence of Hund’s Rule Coupling in Strongly Correlated Materials. *Physical Review Letters* **107**, 256401 (2011).
- [8] Georges, A., de’Medici, L. & Mravlje, J. Strong correlations from Hund’s coupling. *Annual Review of Condensed Matter Physics* **4**, 137–178 (2013).
- [9] Stadler, K. M., Yin, Z. P., von Delft, J., Kotliar, G. & Weichselbaum, A. Dynamical mean-field theory plus numerical renormalization-group study of spin-orbital separation in a three-band Hund metal. *Physical Review Letters* **115**, 136401 (2015).
- [10] Stadler, K. M., Kotliar, G., Weichselbaum, A. & von Delft, J. Hundness versus Mottness in a three-band Hubbard-Hund model: on the origin of strong correlations in Hund metals. *arXiv:1808.09936 [cond-mat]* (2018).
- [11] Yin, Z. P., Haule, K. & Kotliar, G. Fractional power-law behavior and its origin in iron-chalcogenide and ruthenate superconductors: Insights from first-principles calculations. *Physical Review B* **86**, 195141 (2012).
- [12] Khajetoorians, A. A. *et al.* Tuning emergent magnetism in a Hund’s impurity. *Nature Nanotechnology* **10**, 958–964 (2015).
- [13] Aron, C. & Kotliar, G. Analytic theory of Hund’s metals: A renormalization group perspective. *Physical Review B* **91**, 041110 (2015).
- [14] Mravlje, J. & Georges, A. Thermopower and entropy: Lessons from Sr_2RuO_4 . *Physical Review Letters* **117**, 036401 (2016).
- [15] McWhan, D. B., Rice, T. M. & Remeika, J. P. Mott transition in Cr-doped V_2O_3 . *Physical Review Letters* **23**, 1384–1387 (1969).
- [16] McWhan, D. B., Menth, A., Remeika, J. P., Brinkman, W. F. & Rice, T. M. Metal-insulator transitions in pure and doped V_2O_3 . *Physical Review B* **7**, 1920–1931 (1973).
- [17] McWhan, D. B. *et al.* Heat capacity of vanadium oxides at low temperature. *Physical Review B* **7**, 326–332 (1973).
- [18] Maeno, Y. *et al.* Superconductivity in a layered perovskite without copper. *Nature* **372**, 532–534 (1994).
- [19] Georges, A., Kotliar, G., Krauth, W. & Rozenberg, M. J. Dynamical mean-field theory of strongly correlated fermion systems and the limit of infinite dimensions. *Reviews of Modern Physics* **68**, 13 (1996).
- [20] Kotliar, G. *et al.* Electronic structure calculations with dynamical mean-field theory. *Reviews of Modern Physics* **78**, 865–951 (2006).
- [21] Held, K. Electronic structure calculations using dynamical mean field theory. *Advances in Physics* **56**, 829–926 (2007).
- [22] Held, K., McMahan, A. & Scalettar, R. Cerium volume collapse: Results from the merger of dynamical mean-field theory and local density approximation. *Physical Review Letters* **87** (2001).
- [23] Laad, M. S., Craco, L. & Müller-Hartmann, E. Orbital-selective insulator-metal transition in V_2O_3 under external pressure. *Physical Review B* **73**, 045109 (2006).
- [24] Poteryaev, A. I. *et al.* Enhanced crystal-field splitting and orbital-selective coherence induced by strong correlations in V_2O_3 . *Physical Review B* **76**, 085127 (2007).
- [25] Hansmann, P. *et al.* Mott-Hubbard transition in V_2O_3 revisited. *physica status solidi (b)* **250**, 1251–1264 (2013).
- [26] Grieger, D. & Lechermann, F. Effect of Chromium doping on the correlated electronic structure of V_2O_3 . *Physical Review B* **90**, 115115 (2014).

- [27] Grieger, D. & Fabrizio, M. Low-temperature magnetic ordering and structural distortions in vanadium sesquioxide V_2O_3 . *Physical Review B* **92**, 075121 (2015).
- [28] Deng, X., Sternbach, A., Haule, K., Basov, D. N. & Kotliar, G. Shining light on transition-metal oxides: Unveiling the hidden fermi liquid. *Physical Review Letters* **113**, 246404 (2014).
- [29] Dang, H. T., Mravlje, J., Georges, A. & Millis, A. J. Band Structure and Terahertz Optical Conductivity of Transition Metal Oxides: Theory and Application to $CaRuO_3$. *Physical Review Letters* **115**, 107003 (2015).
- [30] Dang, H. T., Mravlje, J., Georges, A. & Millis, A. J. Electronic correlations, magnetism, and Hund's rule coupling in the ruthenium perovskites $SrRuO_3$ and $CaRuO_3$. *Physical Review B* **91**, 195149 (2015).
- [31] Deng, X., Haule, K. & Kotliar, G. Transport properties of metallic ruthenates: A DFT+DMFT investigation. *Physical Review Letters* **116**, 256401 (2016).
- [32] Baldassarre, L., Perucchi, A., Nicoletti, D., Toschi, A., Sangiovanni, G., Held, K., Capone, M., Ortolani, M., Malavasi, L., Marsi, M., Metcalf, P., Postorino, P. & Lupi, S. Quasiparticle evolution and pseudogap formation in V_2O_3 : An infrared spectroscopy study. *Physical Review B* **77**, 113107 (2008).
- [33] Carlo, J. P. *et al.* New magnetic phase diagram of $(Sr,Ca)_2RuO_4$. *Nature Materials* **11**, 323–328 (2012).
- [34] Hussey, N. E. *et al.* Normal-state magnetoresistance of Sr_2RuO_4 . *Physical Review B* **57**, 5505 (1998).
- [35] Yokoya, T. *et al.* Evidence for correlation effects in Sr_2RuO_4 from resonant and x-ray photoemission spectroscopy. *Physical Review B* **53**, 8151–8154 (1996).
- [36] Mo, S.-K. *et al.* Prominent quasiparticle peak in the photoemission spectrum of the metallic phase of V_2O_3 . *Physical Review Letters* **90**, 186403 (2003).
- [37] Rodolakis, F. *et al.* Quasiparticles at the mott transition in V_2O_3 : Wave vector dependence and surface attenuation. *Physical Review Letters* **102**, 066805 (2009).
- [38] Fujiwara, H. *et al.* Evidence for the constancy of U in the mott transition of V_2O_3 . *Physical Review B* **84**, 075117 (2011).
- [39] Bergemann, C., Mackenzie, A. P., Julian, S. R., Forsythe, D. & Ohmichi, E. Quasi-two-dimensional fermi liquid properties of the unconventional superconductor Sr_2RuO_4 . *Advances in Physics* **52**, 639–725 (2003).
- [40] Iwasawa, H. *et al.* High-energy anomaly in the band dispersion of the ruthenate superconductor. *Physical Review Letters* **109**, 066404 (2012).
- [41] Veenstra, C. N. *et al.* Determining the surface-to-bulk progression in the normal-state electronic structure of Sr_2RuO_4 by angle-resolved photoemission and density functional theory. *Physical Review Letters* **110**, 097004 (2013).
- [42] Mila, F. *et al.* Orbitally Degenerate Spin-1 Model for Insulating V_2O_3 . *Physical Review Letters* **85**, 1714–1717 (2000).
- [43] Park, J.-H. *et al.* Spin and orbital occupation and phase transitions in V_2O_3 . *Physical Review B* **61**, 11506–11509 (2000).
- [44] Di Matteo, S., Perkins, N. B. & Natoli, C. R. Spin-1 effective hamiltonian with three degenerate orbitals: An application to the case of V_2O_3 . *Physical Review B* **65**, 054413 (2002).
- [45] Deng, X. *et al.* How bad metals turn good: Spectroscopic signatures of resilient quasiparticles. *Physical Review Letters* **110**, 086401 (2013).
- [46] Mravlje, J. & Georges, A. Thermopower and Entropy: Lessons from Sr_2RuO_4 . *Physical Review Letters* **117**, 036401 (2016).
- [47] The impurity entropy of correlated atoms in V_2O_3 and Sr_2RuO_4 (Link to supplementary) (2018).
- [48] Hanl, M. and Weichselbaum, A. Local susceptibility and Kondo scaling in the presence of finite bandwidth. *Phys. Rev. B* **89**, 075130 (2014).
- [49] Weichselbaum, A. Non-abelian symmetries in tensor networks: A quantum symmetry space approach. *Annals of Physics* **327**, 2972–3047 (2012).
- [50] Fisher D. *et al.* Mid Gap States in The Doped Hubbard Model . *Physical Review B* **52**, 17112 (1995).
- [51] Haule, K., Yee, C.-H. & Kim, K. Dynamical mean-field theory within the full-potential methods: Electronic structure of $CeIrIn_5$, $CeCoIn_5$, and $CeRhIn_5$. *Physical Review B* **81**, 195107 (2010).
- [52] Blaha, P., Schwarz, K., Madsen, G. K. H., Kvasnicka, D. & Luitz, J. *WIEN2K, An Augmented Plane Wave + Local Orbitals Program for Calculating Crystal Properties* (Karlheinz Schwarz, Techn. Universität Wien, Austria, Wien, Austria, 2001).
- [53] Werner, P., Comanac, A., de' Medici, L., Troyer, M. & Millis, A. J. Continuous-time solver for quantum impurity models. *Physical Review Letters* **97**, 076405 (2006).
- [54] Haule, K. Quantum Monte Carlo impurity solver for cluster dynamical mean-field theory and electronic structure calculations with adjustable cluster base. *Physical Review B* **75**, 155113 (2007).
- [55] Haule, K. & Birol, T. Free energy from stationary implementation of the DFT+DMFT functional. *Physical Review Letters* **115**, 256402 (2015).
- [56] Weichselbaum, A. & von Delft, J. Sum-Rule Conserving Spectral Functions from the Numerical Renormalization Group. *Physical Review Letters* **99**, 076402 (2007).
- [57] Anders, F. B. & Schiller, A. Real-time dynamics in quantum-impurity systems: A time-dependent numerical renormalization-group approach. *Physical Review Letters* **95**, 196801 (2005).
- [58] Anders, F. B. & Schiller, A. Spin precession and real-time dynamics in the Kondo model: Time-dependent numerical renormalization-group study. *Physical Review B* **74**, 245113 (2006).
- [59] Peters, R., Pruschke, T. & Anders, F. B. Numerical renormalization group approach to Green's functions for quantum impurity models *Physical Review B* **74**, 245114 (2006).
- [60] Bulla, R., Costi, T. A. & Pruschke, T. Numerical renormalization group method for quantum impurity systems. *Reviews of Modern Physics* **80**, 395–450 (2008).

Signatures of Mottness and Hundness in archetypal correlated metals- Supplementary: the Temperature Evolution of Impurity Entropy in V_2O_3 and Sr_2RuO_4

Xiaoyu Deng,^{1,*} Katharina M. Stadler,^{2,*} Kristjan Haule,¹
Andreas Weichselbaum,^{3,2} Jan von Delft,² and Gabriel Kotliar^{1,3}

¹*Department of Physics and Astronomy, Rutgers University, Piscataway, New Jersey 08854, USA*

²*Physics Department, Arnold Sommerfeld Center for Theoretical Physics and Center for NanoScience,*

Ludwig-Maximilians-Universität München, 80333 München, Germany

³*Condensed Matter Physics and Materials Science Department,
Brookhaven National Laboratory, Upton, New York 11973, USA*

(Dated: January 15, 2019)

Entropy

We have computed the entropy of the correlated atom in both V_2O_3 and Sr_2RuO_4 up to high temperature within the DFT+DMFT framework. The results depicted in Fig. S-1. Notably in both systems, the impurity entropy initially shows a high-temperature plateau at high temperature. As the temperature decreases, the entropy decreases markedly below about $T_M = 1000K$ in V_2O_3 and below $T = 2000K$ in Sr_2RuO_4 . The value of the plateau is approximately $\ln(9)$ for both materials. This indicates that both spin and orbital degrees of freedom contribute significantly to the entropy in both materials and the most relevant atomic states likely have large spin $S = 1$ and large effective orbital angular momentum $L = 1$, as discussed in models [1, 2].

It is not surprising that in V_2O_3 the entropy plateau holds down to the same characteristic temperature $T_M = 1000K$, where the Curie behavior in the spin and orbital susceptibility ceases to exist, since the spin and orbital degrees of freedom remain free with decreasing temperature down to T_M . In Sr_2RuO_4 the entropy departs from the plateau at much larger temperature than in V_2O_3 and the characteristic temperature $T = 2000K$ is close to the temperature at which the Curie behavior ceases in the spin susceptibility T_{spin}^{onset} . We note that at this temperature the orbital degrees of freedom might already be close to fully delocalized although even the highest temperatures studied here are too low for the orbital susceptibility to exhibit a Curie behavior, as shown by the $T\chi_{orb}(0)$ [Main Text, Fig.3(c)]. This is supported by the observation that, at around $T = 2000K$, the slope of $T\chi_{orb}(0)$ increases significantly with decreasing temperature. Therefore, the entropy contribution due to orbital degrees of freedom is large. In addition, the large charge fluctuation in Sr_2RuO_4 may contribute to the entropy accumulation as well. As temperature decreases, the entropy decreases continuously and crosses a value $\ln(3)$ expected for an unscreened $S = 1$ atomic state. We note that the crossing occurs at a temperature when the orbital degrees of freedom are (almost) fully screened: in V_2O_3 at about 400K, and in Sr_2RuO_4 at about 750K (Fig. S-1). Indeed, both temperatures are roughly comparable to the screening scale T_{orb}^{cmp} in the corresponding materials. This is consistent with the observation that the orbital degrees of freedom are fully screened at much higher temperatures than the spin degrees of freedom in both materials. The spin degrees of freedom are responsible for the large entropy found in an extended temperature regime where the orbital degrees of freedom are frozen. Overall, these results suggest a strong correlation between the entropy accumulation and the unscreening of spin and orbital degrees of freedom.

Both V_2O_3 and Sr_2RuO_4 have a large entropy at the lowest temperature considered, which highlights the strong correlated nature of these two materials. Interestingly, the large values of entropy are found in experimental measurements. In V_2O_3 the entropy change across the transition from a metallic state to the antiferromagnetic state at $T = 150K$ is as large as $0.65k_B$ [4–6]. Assuming that the electronic entropy of the ordered state is zero [7], this value provides an estimation of the entropy in metallic V_2O_3 and fits very well in our computed impurity entropy (Fig. S-1). In Sr_2RuO_4 , as a first order approximation, the electronic entropy of Sr_2RuO_4 can be written as $S = \gamma T$ where γ is the specific heat coefficient in the Fermi-liquid regime. The approximated entropy matches our computed result at about 100K. These agreements suggest that the large entropy in both materials are mainly due to the local correlated electrons. In connection with the evolution of the local spectra, we see that in a large temperature range beyond the Fermi-liquid scale the large entropy is accompanied by a coherence resonance, a feature of "resilient quasiparticles" [8].

We remark that the large total orbital angular momentum $L = 1$ highlights the importance of the orbital degrees of freedom in the electronic structure. Its role has been emphasized in Sr_2RuO_4 [9, 10], however it is not much discussed in V_2O_3 . The large orbital angular momentum in V_2O_3 is a direct consequence of the fact that the a_{1g} orbital is partially filled and contributes to the atomic degrees of freedom [11–13]. It is therefore very unlikely that the a_{1g} is effectively excluded by a correlation-enhanced crystal field splitting, as suggested by several studies [15–18]. This is

* These authors contributed equally to this work. Correspondence: xiaoyu.deng@gmail.com.

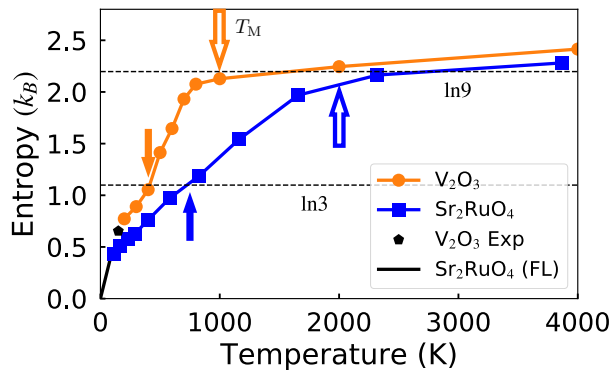


FIG. S-1. The impurity entropy per V/Ru atom computed with DFT+DMFT in V_2O_3 (orange) and Sr_2RuO_4 (blue). A plateau at about $\ln(9)$ is seen in both materials, starting approximately at 1000K in V_2O_3 and approximately at 2000K in Sr_2RuO_4 (open arrows). As temperature decreases, the entropy crosses $\ln(3)$ continuously, at about 400K in V_2O_3 and about 750K in Sr_2RuO_4 (filled arrows). The black pentagon denotes an estimation of the entropy in V_2O_3 from experimental measurements [4–6]. The black line indicates a Fermi-liquid approximation of the electronic entropy of Sr_2RuO_4 , $S = \gamma T$, taking the specific heat coefficient $\gamma = 38\text{mJ/molK}^2$ at low T [14].

consistent with the conclusion drawn in a recent angular-resolved photoemission spectroscopy measurement [19]. Our findings shed light on the nature of the Mott transition in V_2O_3 .

Photoemission spectra

To further elucidate the difference between Mott and Hund systems, Fig. S-2 shows local spectra (first row) and photoemission spectra (subsequent rows) obtained from model calculations for four parameter combinations (described in the figure caption). We will discuss (i) the difference between large and small U , (ii) the difference between finite and zero J , and (iii) how J affects the slope of the dispersion in the photoemission plots.

(i) For the large- U Mott systems M1 and M0 in the first and second columns, the local spectrum $A(\omega)$ (first row) shows well-defined Hubbard side bands. At low temperatures these are separated by a central quasiparticle peak, which is suppressed with increasing T , giving way to a pseudogap. Correspondingly, in the photoemission spectra (subsequent rows) the spectral weight at low frequencies decreases very strongly as the temperature is increased. By contrast, for the Hund system H1 and weak Mott system W0 in the third and fourth columns, both having moderate U , the local spectra (first row) show no well-separated Hubbard side bands, and with increasing temperature the central quasiparticle peak weakens somewhat but persists, so that no pseudogap develops. Correspondingly, the photoemission spectra retain significant low-frequency weight even at high temperatures (subsequent rows).

(ii) For the finite- J systems M1 and H1 in the first and third columns, the lowest-temperature quasiparticle peak features a rather sharp, asymmetric central peak with a shoulder on its left flank. This substructure reflects J -induced spin-orbital separation, $T_K^{\text{spin}} \ll T_K^{\text{orb}}$, leading to a sharp Kondo resonance in the spin sector together with a broader Kondo resonance in the orbital sector [2, 3]. Correspondingly, this substructure is absent for the $J = 0$ systems M0 and W0 in the second and fourth columns.

(iii) The strength of the local correlations can be gauged from the slope of the low-energy dispersion relation, governed by the quasiparticle weight, $Z = m/m^*$. This quantity is proportional to the weight of the spin Kondo resonance [3]. Since finite J strongly reduces the latter, the low-temperature dispersion (for given U) has much smaller slope for J finite than zero (compare first to second column, and third to fourth). The fairly small slope of the dispersion for H1 (third column) compared to W0 (fourth column) thus is a smoking gun difference between a true Hund system and a pure Mott system tuned far from the Mott transition – even though both have rather weak U , the former has strong correlations (induced by finite J), the latter does not.

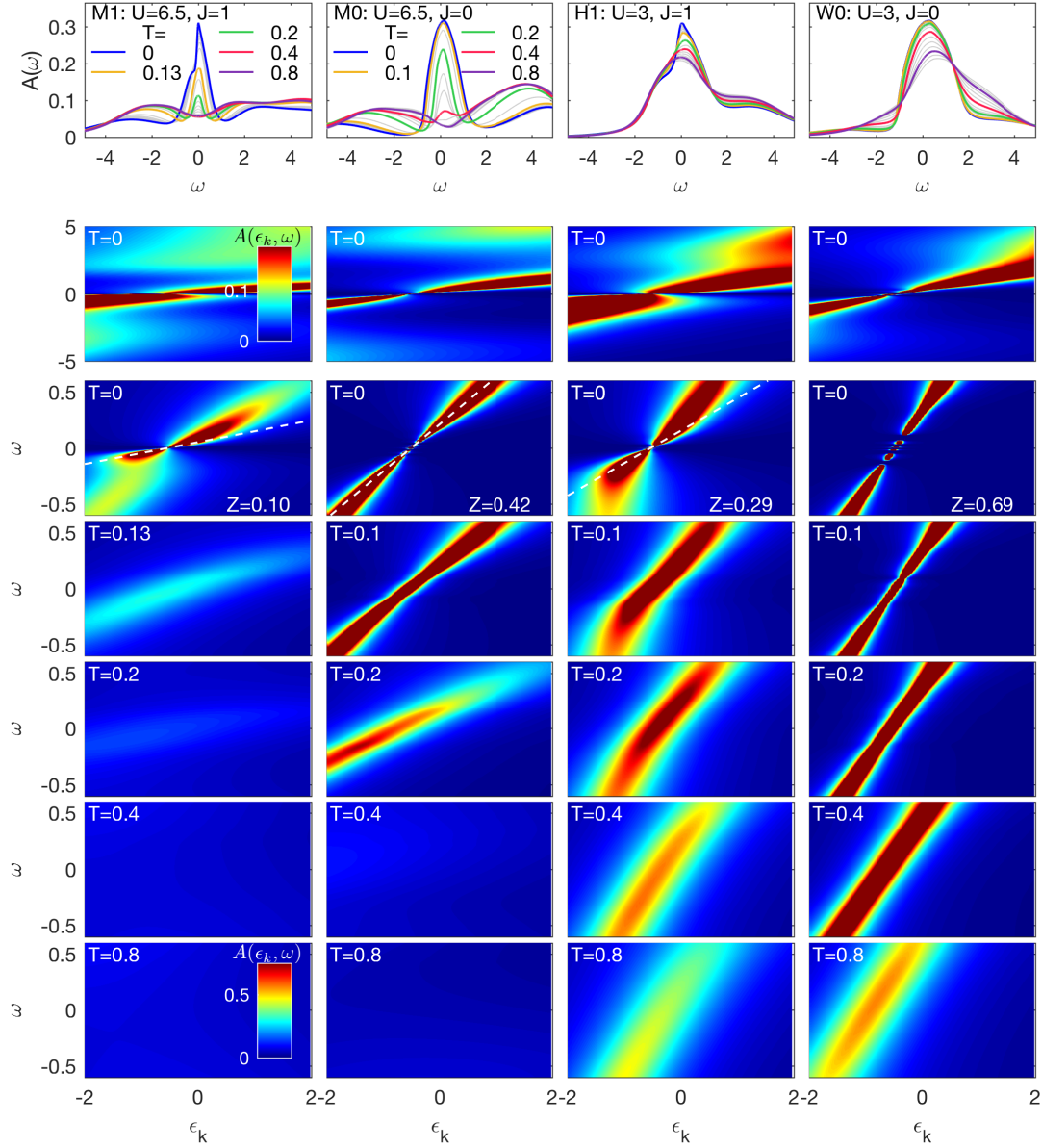


FIG. S-2. Spectral data obtained for the 3HHM for the four parameter combinations marked by asterisks in Fig. 5(a) of the main text: two Mott systems with $U = 6.5$ close to the Mott transition, having $J = 1$ (M1, first column) or $J = 0$ (M0, second column); and two systems with $U = 3$ far from the Mott transition, a Hund system with $J = 1$ (H1, third column) and a weakly correlated system with $J = 0$ (W0, fourth column). First row: local spectral functions $A(\omega)$ for various temperatures (the legend for M0 also applies to H1, W0). Second row: corresponding photoemission spectra $A(\epsilon_k, \omega) = -\frac{1}{\pi} \text{Im}[\omega + \mu - \epsilon_k - \Sigma(\omega)]^{-1}$, computed using the standard DMFT protocol [20], at $T = 0$. Subsequent rows: low-frequency zooms of photoemission spectra, for five different temperatures.

-
- [1] Georges, A., de'Medici, L. & Mravlje, J. Strong correlations from Hund's coupling. *Annual Review of Condensed Matter Physics* **4**, 137–178 (2013).
- [2] Stadler, K. M., Yin, Z. P., von Delft, J., Kotliar, G. & Weichselbaum, A. Dynamical mean-field theory plus numerical renormalization-group study of spin-orbital separation in a three-band Hund metal. *Physical Review Letters* **115**, 136401

- (2015).
- [3] Stadler, K. M., Kotliar, G., Weichselbaum, A. & von Delft, J. Hundness versus Mottness in a three-band Hubbard-Hund model: on the origin of strong correlations in Hund metals. *arXiv:1808.09936 [cond-mat]* (2018).
 - [4] McWhan, D. B., Rice, T. M. & Remeika, J. P. Mott transition in Cr-doped V_2O_3 . *Physical Review Letters* **23**, 1384–1387 (1969).
 - [5] McWhan, D. B., Menth, A., Remeika, J. P., Brinkman, W. F. & Rice, T. M. Metal-insulator transitions in pure and doped V_2O_3 . *Physical Review B* **7**, 1920–1931 (1973).
 - [6] McWhan, D. B. *et al.* Heat capacity of vanadium oxides at low temperature. *Physical Review B* **7**, 326–332 (1973).
 - [7] A small entropy in the antiferromagnetic phase of V_2O_3 is expected since the paramagnetic-antiferromagnetic transition is first-order and the atomic fluctuations are quenched by the long-range order. The estimated entropy is consistent with the estimation using the low temperature specific heat coefficient in the Fermi liquid state, as is done for Sr_2RuO_4 in the supplementary. The Fermi liquid state is reached by quenching the antiferromagnetism by doping or pressure and the corresponding specific heat coefficients in different samples are reported [4, 6].
 - [8] Deng, X. *et al.* How bad metals turn good: Spectroscopic signatures of resilient quasiparticles. *Physical Review Letters* **110**, 086401 (2013).
 - [9] Mravlje, J. *et al.* Coherence-incoherence crossover and the mass-renormalization puzzles in Sr_2RuO_4 . *Physical Review Letters* **106**, 096401 (2011).
 - [10] Mravlje, J. & Georges, A. Thermopower and Entropy: Lessons from Sr_2RuO_4 . *Physical Review Letters* **117**, 036401 (2016).
 - [11] Deng, X., Sternbach, A., Haule, K., Basov, D. N. & Kotliar, G. Shining light on transition-metal oxides: Unveiling the hidden fermi liquid. *Physical Review Letters* **113**, 246404 (2014).
 - [12] Held, K., McMahan, A. & Scalettar, R. Cerium volume collapse: Results from the merger of dynamical mean-field theory and local density approximation. *Physical Review Letters* **87** (2001).
 - [13] Leonov, I., Anisimov, V. I. & Vollhardt, D. Metal-insulator transition and lattice instability of paramagnetic V_2O_3 . *Physical Review B* **91**, 195115 (2015).
 - [14] Mackenzie, A. P. *et al.* Observation of quantum oscillations in the electrical resistivity of $SrRuO_3$. *Physical Review B* **58**, R13318–R13321 (1998).
 - [15] Poteryaev, A. I. *et al.* Enhanced crystal-field splitting and orbital-selective coherence induced by strong correlations in V_2O_3 . *Physical Review B* **76**, 085127 (2007).
 - [16] Hansmann, P. *et al.* Mott-Hubbard transition in V_2O_3 revisited. *physica status solidi (b)* **250**, 1251-1264 (2013).
 - [17] Grieger, D. & Lechermann, F. Effect of Chromium doping on the correlated electronic structure of V_2O_3 . *Physical Review B* **90**, 115115 (2014).
 - [18] Grieger, D. & Fabrizio, M. Low-temperature magnetic ordering and structural distortions in vanadium sesquioxide V_2O_3 . *Physical Review B* **92**, 075121 (2015).
 - [19] Lo Vecchio, I. *et al.* Fermi surface of metallic V_2O_3 from angle-resolved photoemission: Mid-level filling of e_g^π bands. *Physical Review Letters* **117**, 166401 (2016).
 - [20] Georges, A., Kotliar, G., Krauth, W. & Rozenberg, M. J. Dynamical mean-field theory of strongly correlated fermion systems and the limit of infinite dimensions. *Reviews of Modern Physics* **68**, 13 (1996).

7 SOS revisited: frequency and temperature dependence

Although the 3HHM is the most basic model to capture the physics of Hund metals, its emergent physical behavior is highly complex. Especially the interplay of two different types of degrees of freedom combined with the asymmetry of the model leads to puzzling phenomena, such as SOS (cf. Chapters 4 and 5) or the separation of onset scales for spin and orbital screening (cf. Chapter 6). Even after many years of research the 3HHM is still not fully understood.

In this Chapter we revisit the 3HHM. We study in detail the implications of particle-hole asymmetry for frequency-dependent quantities at $T = 0$ (in Sec. 7.1), the evolution of the QPP with increasing temperature (in Sec. 7.2), and investigate the temperature dependence of various quantities, such as static local susceptibilities, the QP weight, scattering rate, resistivity, thermopower or entropy (in Sec. 7.3). In particular, we are interested in the nature of the incoherent transport regime. Further, we reveal the different features that emerge for Hund-correlated and Mott-correlated systems, i.e. far from and close to the MIT phase boundary, respectively (cf. Fig. 5 of Ref. [SKWvD18] in Sec. 5.2 or Fig. 4 of Ref. [DSH+18] in Sec. 6.2).

Considering the fact that most materials are multi-orbital systems, this study is far from being merely academic. Even ten years after the introduction of the Hund-metal concept triggered by DMFT studies [HK09], there is still a great deal of confusion as to which features of materials should be assigned to Mottness and which ones to Hundness, and what can be understood in terms of simple models and what requires full details of electronic structure. We thus intend to contribute to a systematic identification of those phenomena, which can be regarded as a decisive fingerprint of the Hund’s metal nature, thereby aiding significantly the interpretation of present and future experimental results and guiding the corresponding theoretical analysis.

A first detailed temperature-dependent study of the implications of particle-hole asymmetry in Hubbard-type models was given in Ref. [DMicv+13] for a one-band hole-doped Mott insulator, i.e. for a model with only one type of degrees of freedom (spins). It was shown that a well-defined QPP of “resilient” quasiparticle excitations (RQPs) exists above the FL scale, T_{FL} , and that it dominates an intermediate incoherent transport regime up to T_{MIR} . Above this temperature the resistivity exceeds the MIR limit (cf. Sec. 3.6 for a definition) and the RQPs eventually disappear, or more specifically, the QPP merges with the lower Hubbard band. Interestingly, the RQPs are longer-lived for electron-like than for hole-like excitations, due to the particle-hole asymmetry in the model. This asymmetry further leads to different scales, ω^- and ω^+ , below which FL behavior is found at negative and positive frequencies at $T = 0$. Another remarkable feature is that the coherence scale, Γ^* (cf. Sec. 3.9), shows FL behavior for temperatures larger than T_{FL} , resulting in a so-called hidden FL [XHK13].

Having these results in mind, we now turn to the more complex 3HHM at $\frac{1}{3}$ filling. The following sections serve as summary with preliminary figures and discussions for an upcoming publication.

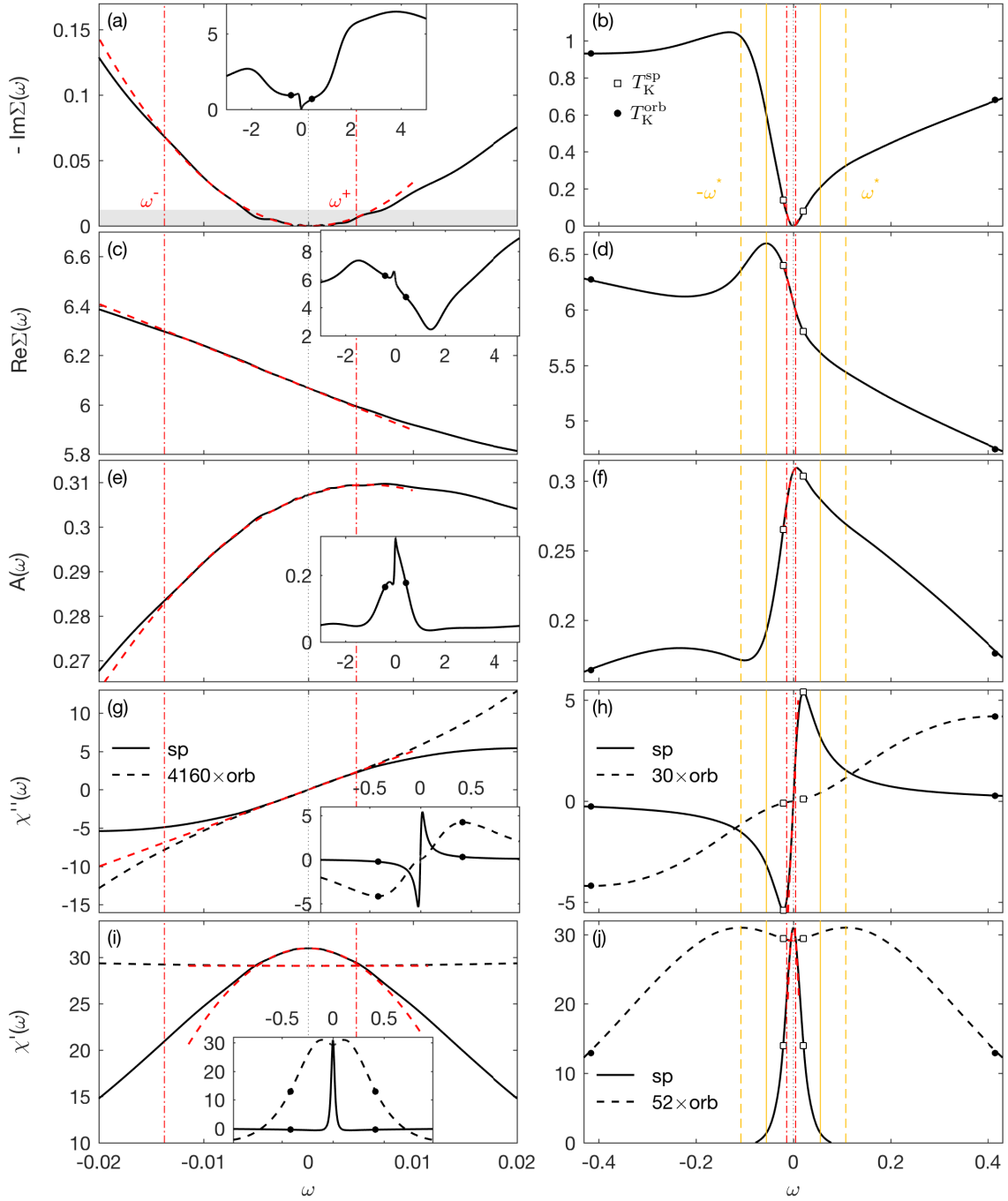


Figure 7.1 (a,b) The imaginary part, $\text{Im}\Sigma(\omega)$, and (c,d) the real part, $\text{Re}\Sigma(\omega)$, of the self-energy; (e,f) the local spectral function, $A(\omega)$; (g,h) the imaginary part, $\chi''(\omega)$, and (i,j) the real part, $\chi'(\omega)$, of the spin (solid) and orbital (dashed) susceptibility are plotted versus frequency for $\Delta_b = 3.5$, $J = 2$, and $T = 0$. Left panels are zooms into the FL regime, whereas their insets show the quantities on a large frequency range. The SOS regime is presented in the right panels. Dashed red lines reveal FL behavior for $\text{Im}\Sigma(\omega)$, $\text{Re}\Sigma(\omega)$, and $A(\omega)$ in the asymmetric range, $\omega^- < \omega < \omega^+$, with $\omega^+ = \frac{1}{3}\omega^-$ (indicated by vertical dash-dotted red lines) and for the orbital and spin susceptibility in the symmetric range, $|\omega| < \omega^+$. The vertical dashed yellow lines represent the energy scale, $|\omega^*|$, of the maximum of $\chi'_{\text{orb}}(\omega)$, which is approximately equal to the energy scale of the maximum of $-\text{Im}\Sigma(\omega)$ in (b). The vertical solid yellow lines denote the energy scale of the maximum of $\text{Re}\Sigma(\omega)$ at $\omega < 0$ in (b). For orientation these vertical dashed and solid yellow lines are repeated for $\omega > 0$. Filled dots and open squares mark the orbital and spin Kondo scales, respectively. The grey area in (a) indicates the systematic error of $\text{Im}\Sigma(\omega)$ (cf. Sec. 3.2 for details).

7.1 Asymmetry of frequency-dependent quantities at zero temperature

In Fig. 7.1 we revisit the self-energy, $\Sigma(\omega)$, defined in Eq. (3.4), the spectral function, $A(\omega)$, defined in Eq. (3.7), and the orbital and spin susceptibility, $\chi(\omega)$, defined in Eq. (3.1) and Eq. (3.2), respectively, at $T = 0$. We use $J = 2$ deep in the Hund regime (cf. Fig. 5 and Sec. 4.1 of Ref. [SKWvD18]) and a bare gap of $\Delta_b = U - 2J = 3.5$ (cf. Sec. 4.5 of Ref. [SKWvD18]). This choice yields a fully developed SOS regime. We start with a detailed investigation of the FL regime (cf. left panels of Fig. 7.1) and then concentrate on the SOS regime (cf. right panels of Fig. 7.1). Due to the universal behavior of the model with respect to Δ_b (respectively U) (cf. Fig. 10 of Ref. [SKWvD18]) the following findings are generic in the metallic regime of the 3HHM, but can occur on very different energy scales (depending on the value of Δ_b).

Asymmetry in the FL regime. The left panels of Fig. 7.1 zoom into the frequency regime below T_K^{sp} (which is marked by open squares in the right panels). Interestingly, similar to the results of Ref. [DMicv⁺13] we observe in Fig. 7.1(a,c,e) that FL behavior holds up to different frequency scales, ω^- and ω^+ , at $\omega < 0$ and $\omega > 0$, respectively. The FL behavior is indicated by the red dashed curves: a parabola for $-\text{Im} \Sigma(\omega)$ in panel (a), a linear fit for $\text{Re} \Sigma(\omega)$ in panel (c) and a parabola for $A(\omega)$ in panel (e) (cf. Sec. 3.9 for details on FL behavior). Clearly, the black DMFT+NRG results deviate earlier from the red FL curves on the positive frequency side, i.e. at a lower scale $\omega^+ = \frac{1}{3}\omega^-$. We point out that this ratio is equal to the filling ratio, $\frac{n_d}{2N_c}$, of the lattice. Furthermore, we find that the position of the maximum of $A(\omega)$ approximately coincides with ω^+ . In Fig. 7.1(g,i) we plotted the imaginary and the real part of the orbital and spin susceptibilities, respectively. In contrast to $\Sigma(\omega)$ and $A(\omega)$ these quantities are particle-hole symmetric. Both the imaginary parts of the orbital and spin susceptibilities, $\chi''(\omega)$, follow the red dashed linear FL fit only for $|\omega| \lesssim \omega^+$. Accordingly, the real part of the spin susceptibility, $\chi'_{\text{sp}}(\omega)$, also exhibits parabolic FL scaling in this regime, while the real part of the orbital susceptibility, $\chi'_{\text{orb}}(\omega)$, is constant. We recall that the existence of different frequency scales, ω^- and ω^+ , below which FL behavior occurs, was shown to give rise to a hidden FL [XHK13] and to RQPs above the FL regime [DMicv⁺13], scenarios that will be investigated in the next sections.

Asymmetry in the SOS regime. We now address the SOS regime, $T_K^{\text{orb}} > \omega > T_K^{\text{sp}}$, plotted in the right panels of Fig. 7.1. T_K^{orb} is marked by filled circles, T_K^{sp} by open squares. Already in Refs. [SYvD⁺15, SKWvD18] (cf. Chapters 4 and 5) we clearly revealed a strong particle-hole asymmetry of $\text{Im} \Sigma(\omega)$ and $A(\omega)$. These quantities were shown to exhibit a shoulder-like structure for $\omega < 0$ in the SOS regime, while a rather smooth behavior with a weak kink (for $J > 1$) was revealed for $\omega > 0$ [cf. Fig. 3(a-e) in Ref. [SYvD⁺15] of Sec. 4.2 and Figs. 9(c-f) and 10(c-f) in Ref. [SKWvD18] of Sec. 5.2]. These structures are again studied in detail in Fig. 7.1(b,d,f). The shoulder in $-\text{Im} \Sigma(\omega)$ at $\omega < 0$ has a small maximum (bump) which is marked by a dashed yellow vertical line, $-\omega^*$. This is followed by a strong reduction of the scattering rate with decreasing $|\omega|$ [cf. Fig. 7.1(b)]. Nevertheless, within the whole SOS regime, $-\text{Im} \Sigma(\omega)$ is smaller at $\omega > 0$ than at $\omega < 0$, with the consequence that electron-like excitations are more long-lived (cf. also the discussion in Sec. 7.2). The shoulder of $-\text{Im} \Sigma(\omega)$ at $\omega < 0$ implies a large but rather stable scattering rate for hole-like excitations over a broad range of energies. Note that $\text{Im} \Sigma(\omega)$ is only weakly frequency dependent at $\omega > 0$, as well. The shoulder-like structure in $-\text{Im} \Sigma(\omega < 0)$ directly translates to a sharp maximum in $\text{Re} \Sigma(\omega < 0)$. The position of this maximum is marked by a vertical solid yellow

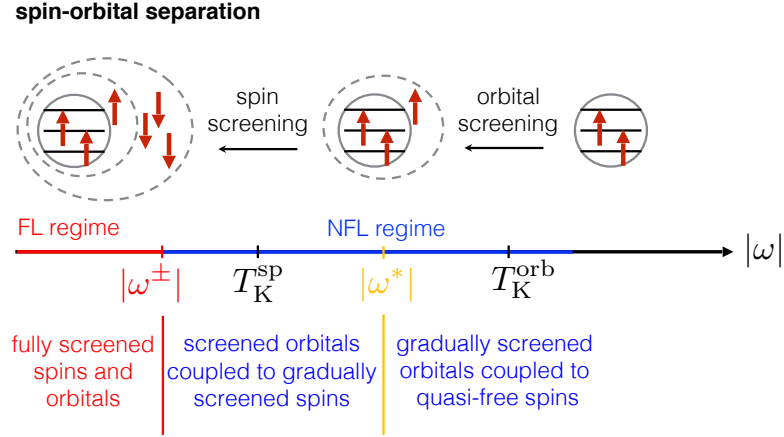


Figure 7.2 Refined schematic depiction of the two-stage screening process of SOS at filling $nd = 2$ (based on Fig. 13 of Ref. [SKWvD18]). First the orbital degrees of freedom start to be screened at the orbital Kondo scale, T_K^{orb} . This involves the formation of an orbital singlet by building a large effective Hund’s-coupling induced $3/2$ spin including a bath spin degree of freedom. $|\omega^*|$ marks the completion of orbital screening. Below $|\omega^*|$ the $3/2$ spin is gradually screened by the three effective channels of the 3HHM. Well below the spin Kondo scale, T_K^{sp} , full screening of both orbital and spin degrees of freedom is reached at the FL scale $|\omega^\pm|$, below which FL behavior occurs in frequency dependent quantities. Note that the scale $|\omega^*|$ is derived from $\chi'_{\text{orb}}(\omega)$, a particle-hole symmetric quantity, while in general the system is particle-hole asymmetric.

line in Fig. 7.1(d). Moreover, we observe a shoulder in $A(\omega)$ for $\omega < -\omega^*$ in Fig. 7.1(f). In Ref. [SYvD⁺15] and Ref. [SKWvD18] (cf. Sec. 4.2 and Sec. 5.2, respectively) this two-tier structure of the QPP was shown to be connected to a non-trivial intertwined spin-orbital Kondo screening process resulting in a narrow, “needle-formed” $SU(2)$ spin Kondo resonance on top of a broad $SU(3)$ orbital Kondo resonance (cf. Sec. 5.5 of Ref. [SKWvD18] for a detailed description).

Interestingly, we can identify the dashed yellow frequency scale, $\pm\omega^*$, with the maxima of $\chi'_{\text{orb}}(\omega)$ in Fig. 7.1(j). This finding helps us to interpret the SOS frequency structure and to establish a connection between different frequency regimes with the intertwined two-stage screening process of SOS (cf. Fig. 7.2, an adapted version of Fig. 13 in Ref. [SKWvD18]). First the orbital degrees of freedom are gradually screened, which is roughly marked by the orbital Kondo scale, T_K^{orb} . The orbital screening is accomplished by the formation of an orbital singlet. This implies the emergence of a large effective Hund’s-coupling-induced $3/2$ spin involving a bath spin degree of freedom. The scale $|\omega^*|$ marks the “completion” of this process, resulting in a maximum of $\chi'_{\text{orb}}(\omega)$. For frequencies below $|\omega^*|$ spin screening sets in: the large $3/2$ spin is screened by the three channels of the 3HHM. Since orbital and spin degrees are coupled in this process, $\chi'_{\text{orb}}(\omega)$ still decreases slightly with decreasing $|\omega|$, finally saturating at the FL scale, $|\omega^\pm|$, well below T_K^{sp} . The incoherent NFL frequency regime (cf. blue regime in Fig. 7.2) is divided by $|\omega^*|$ into two different parts. For $\omega < 0$, the shoulder in $\text{Im}\Sigma(\omega)$ and in $A(\omega)$ correspond to the high- $|\omega|$ NFL part that is characterized by gradually screened orbitals coupled to quasi-free spins, whereas the downturn (upturn) in $-\text{Im}\Sigma(\omega)$ ($A(\omega)$) governs the low- $|\omega|$ NFL part. For $\omega > 0$, $\text{Im}\Sigma(\omega)$ and $A(\omega)$ have a kink close to $|\omega^*|$. Above this kink the slope of both quantities is almost constant and much smaller than the slope for frequencies below the kink. We note however that, for $\omega > 0$, $|\omega^*|$ is just a rough orientation to describe the physics, as we expect in principle two differing scales for $\omega < 0$

and $\omega > 0$ due to the particle-hole asymmetry of the system, similar to the FL scales, ω^\pm . To summarize, we emphasize that the scattering rate is only weakly energy dependent in the NFL regime for $|\omega| \gtrsim |\omega^*|$ and we suggest that this scattering rate can be associated with gradually screened orbitals coupled to quasi-free spins.

We note that in contrast to the 3HHM, in a corresponding three-orbital Kondo model [YHK12, AK15, WSL⁺19] a stationary NFL fixed point is reached with fully screened orbitals, while the spin remains largely uncoupled and fluctuates strongly. In this case, we expect the heuristic crossover scale $|\omega^*|$ for the completion of orbital screening and the onset of spin screening to split into two scales.

Remarkably, the SOS structure of $\Sigma(\omega)$ was equivalently found in DFT+DMFT+QMC simulations of Sr_2RuO_4 [MAM⁺11, SMB⁺14, MG16] for the xy and xz band. In Ref. [SMB⁺14] it is argued that especially the shoulder in $\text{Im } \Sigma(\omega)$ leads to intriguing phenomena, like a waterfall structure in ARPES or excess spectral weight in the optical conductivity. Both phenomena are regarded as hints for the existence of RQPs well above the FL scale. Based on our results above we speculate that the NFL regime can indeed be described by a certain type of RQPs, which we dub ‘‘Hund quasiparticles’’ (HQPs). To corroborate this idea we investigate ARPES data and the optical conductivity for the 3HHM in the next section.

7.2 Temperature dependence: ARPES and the optical conductivity

ARPES at zero temperature. Fig. 7.3 shows the structure factor, $A(\epsilon_k, \omega)$, as experimentally accessible by angle-resolved photoemission spectroscopy (ARPES), together with $A(\omega)$, $\text{Re } \Sigma(\omega)$ and $\text{Im } \Sigma(\omega)$ for the same parameters as in Fig. 7.1. We are interested in how the SOS structure is reflected in the ARPES data at $T = 0$, in how it develops with increasing temperature, and if it can be interpreted as the signature of HQPs.

Fig. 7.3(a) is a zoom into the FL regime. The white (blue) curve shows the QP band dispersion, which is defined as the maxima, $E^*(\omega)$, of $A(\epsilon_k, \omega)$ for given ω (as the maxima, $E(\epsilon_k)$, of $A(\epsilon_k, \omega)$ for given ϵ_k) (cf. Sec. 3.5 for details about these definitions). In the FL regime below the thin dash-dotted red horizontal lines, ω^+ and ω^- , both definitions lead to the same low-energy FL dispersion relation (cf. thick dashed red line) of slope $Z = 0.06$ [with a Fermi surface crossing point $E^*(\omega = 0) = \mu_{\text{eff}}$]. Above ω^+ and below ω^- , i.e. in the SOS regime, the QP band starts to deviate from FL behavior. This is also visible in Fig. 7.3(c). For $\omega > 0$, E (and E^*) turns sharply upwards with increasing ϵ_k into a steep linear function. For $\omega < 0$, E develops into a s-shaped curve for decreasing ϵ_k . In contrast, E^* essentially keeps following the red FL line down to the bottom of the band at about $-\omega^*$. For $\omega < -\omega^*$, E^* approaches the steep linear behavior of $E(\epsilon_k)$. Note that the slope of E is slightly larger for negative than for positive frequencies in the SOS regime.

To summarize, we observe three regimes with different behavior of $A(\epsilon_k, \omega)$. At very low frequencies, the QP band can be described in terms of Landau QPs with heavy masses, $Z^{-1} = m^*/m$, which is reflected by the flat slope, Z , of the band dispersion. These Landau QPs are more stable on the negative frequency side. Above the FL regime, the band behavior changes strongly. In this crossover regime, we discover a kink at $\omega > 0$ and a jump (or s-shaped change) at around $-\omega^*$, signalling the transition to a new type of QP transport: for $|\omega| > |\omega^*|$ the band has a much steeper slope, i.e. a less severe mass enhancement. It might be described in terms of HQPs, i.e. in terms of gradually screened orbitals coupled to quasi-free large spins, which are characterized by a rather flat scattering rate (cf. the previous section).

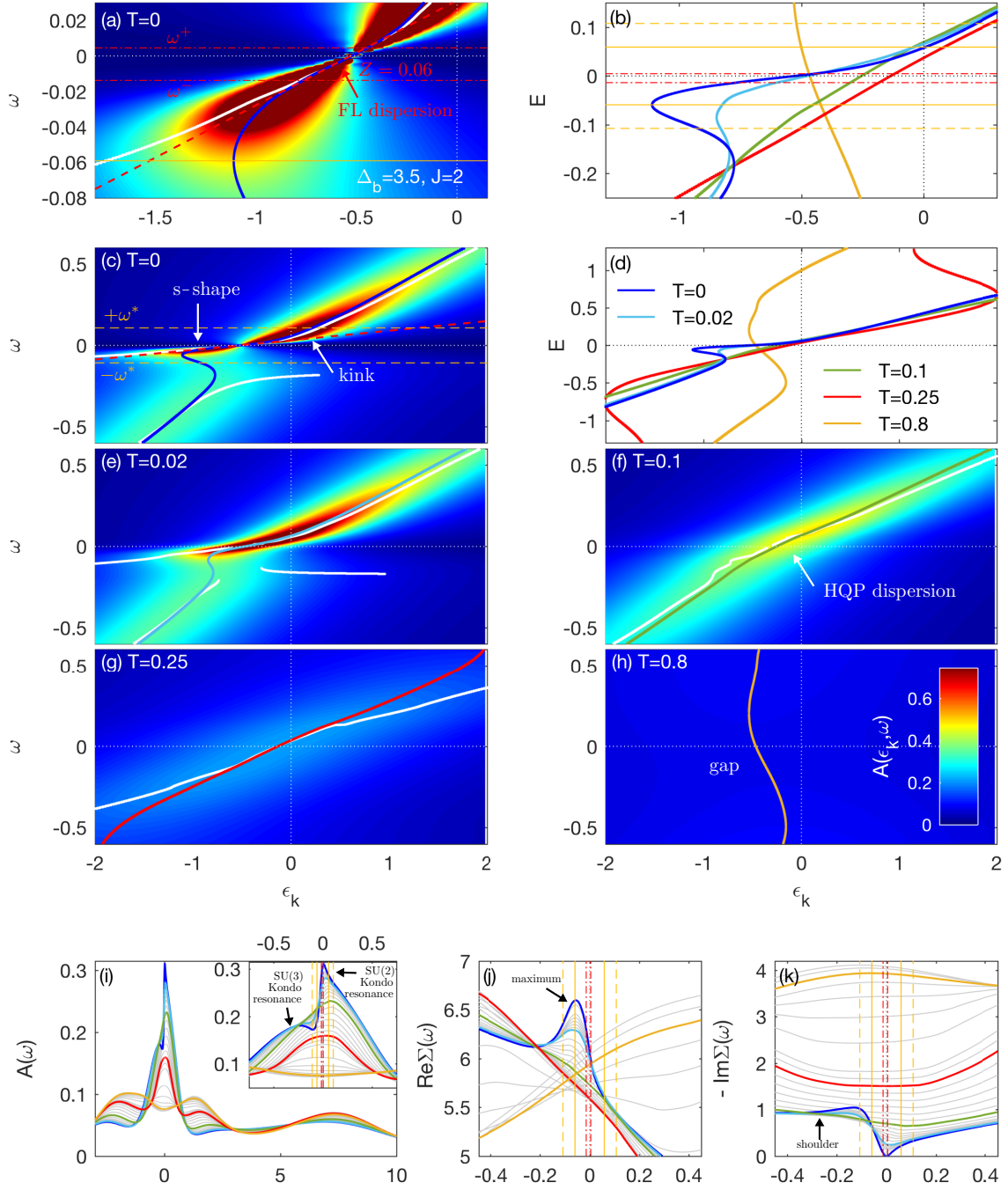


Figure 7.3 (a,c,e-h) The structure factor, $A(\epsilon_k, \omega)$, (b,d) the dispersion relation, $E(\epsilon_k)$, (i) the spectral function, $A(\omega)$, (j) the real part, $\text{Re}\Sigma(\omega)$, and (k) the imaginary part, $\text{Im}\Sigma(\omega)$, of the self-energy, all plotted for various temperatures for the same parameters, $\Delta_b = 3.5$ and $J = 2$, as in Fig. 7.1. (a,c,e-h) The colored curves highlight the dispersion relation, $E(\epsilon_k)$, the white curves show the alternative definition of the dispersion relation, $E^*(\omega)$, respectively. Panels (a,b) are zooms of panels (c,d). The FL regime, $\omega^- < \omega < \omega^+$, is marked by dash-dotted red (a,b) horizontal and (i-k) vertical lines. The thick dashed red line in panel (a) denotes FL behavior of the low-energy dispersion relation. Its slope, $Z = m/m^*$, reflects the strength of local correlations. The solid yellow (b) horizontal and (i-k) vertical lines denote the energy scale of the maximum in $\text{Re}\Sigma(\omega < 0)$ at $T = 0$ [cf. Fig. 7.1(d)]. The dashed yellow (a-c) horizontal and (i-k) vertical lines show $\pm\omega^*$.

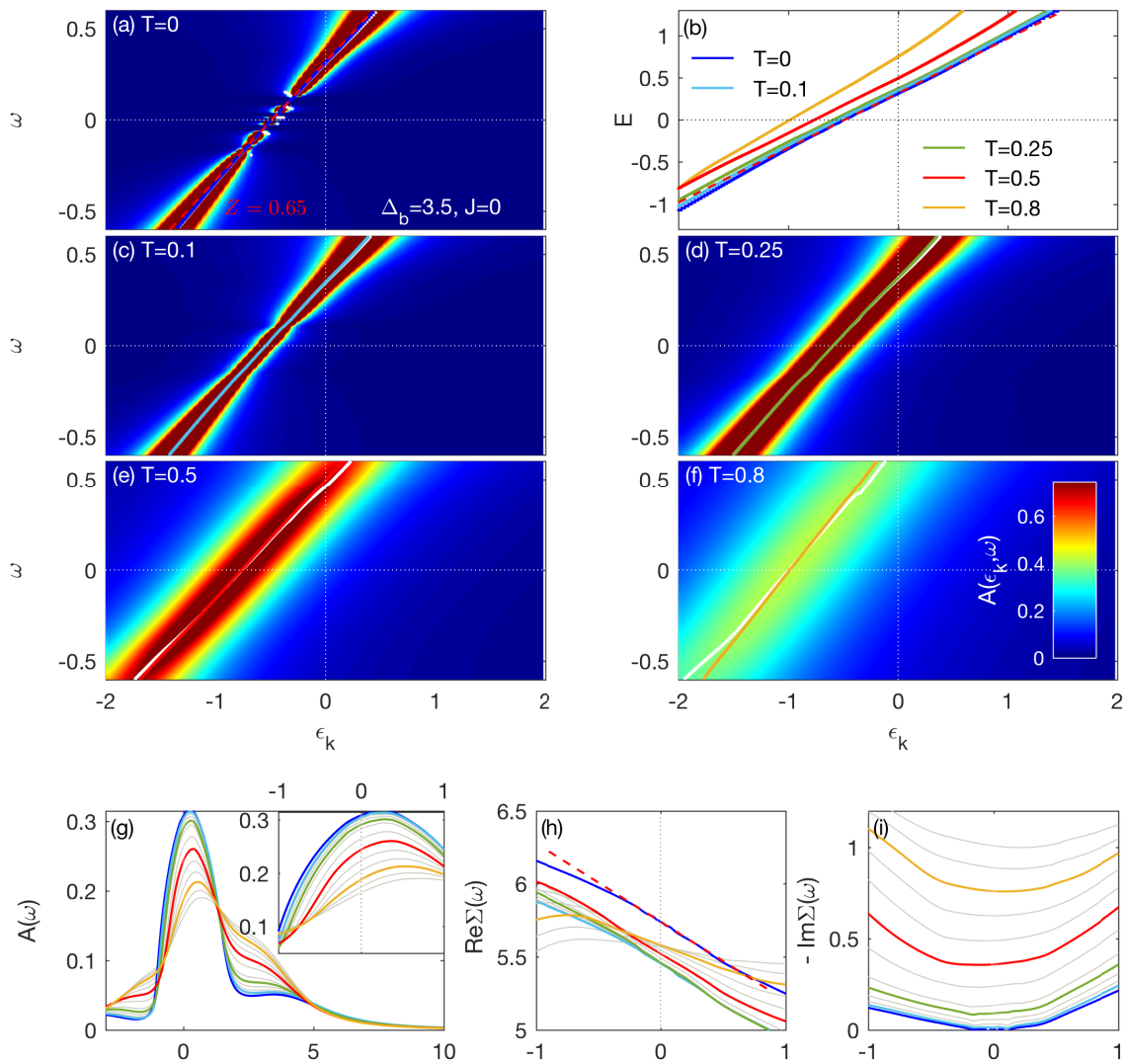


Figure 7.4 Same quantities as in Fig. 7.3 for $\Delta_b = 3.5$ and $J = 0$. (h) Note that the difference in $\text{Re}\Sigma(\omega = 0)$ between $T = 0$ and $T > 0$ arises from a 4% deviation of $n_d(T = 0)$ from $n_d = 2$. The FL scales are not shown and $\pm\omega^*$ does not exist for $J = 0$.

The steep slope of the HQP band (especially at negative frequencies) is reminiscent of the (inverted) waterfall structure discovered in ARPES spectra and realistic DFT+QMC studies of Sr_2RuO_4 [SMB⁺14]. We thus corroborate the idea of Ref. [SMB⁺14] that the waterfall structure is a signature of RQPs in Hund metals. Further, more subtle changes (kinks) at about 30meV were reported in ARPES data of Sr_2RuO_4 [MAM⁺11, SMB⁺14, TZR⁺18], which are likely caused by local electronic correlations [TZR⁺18], and therefore can be associated with the crossover from the FL to the NFL regime.

We remark that a waterfall structure was also found in ARPES plots for the hole-doped one-band Hubbard model in Ref. [DMicv⁺13].

ARPES at finite temperature. In order to verify the idea of robust HQPs governing the intermediate incoherent transport regime, we study the evolution of the QP band and its dispersion E with temperature in Fig. 7.3(c,e-h) and Fig. 7.3(b,d), respectively.

We find that first the s-shaped structure gradually dissolves with increasing temperature, whereas the steep linear behavior of the band in the SOS frequency regime at $\omega > 0$ and $\omega < 0$ remains unchanged [cf. bright blue curve in Fig. 7.3(b,d) and Fig. 7.3(e)]. At $T = 0.1$ the Landau QP band has fully disappeared and only a slight kink at the Fermi level separates the linear resilient HQP bands at $\omega > 0$ and $\omega < 0$ [cf. green curves in Fig. 7.3(b,d) and Fig. 7.3(f)]. For $\Delta_b = 3.5$, the HQP band flattens with increasing temperature and eventually completely vanishes above $T > 0.25$ [cf. red and yellow curves in Fig. 7.3(b,d) and Fig. 7.3(g,h)].

This evolution of the QP band with temperature is also reflected in $A(\omega)$, $\text{Re}\Sigma(\omega)$, and $\text{Im}\Sigma(\omega)$ [cf. Fig. 7.3(i-k)]. In the FL temperature regime a sharp SU(2) Kondo peak in $A(\omega)$, a pronounced maximum in $\text{Re}\Sigma(\omega)$, and a shoulder and dip in $\text{Im}\Sigma(\omega)$ are clearly visible (cf. blue curves). With increasing temperature there is a gradual crossover into the NFL regime. The height of the SU(2) Kondo resonance in $A(\omega)$ reduces and the two-tier structure of the QPP disperses by redistributing spectral weight from the SU(2) Kondo peak to the SU(3) Kondo resonance shoulder. However, the width of the broad SU(3) Kondo resonance is essentially unaffected by this redistribution. Accordingly, also the maximum in $\text{Re}\Sigma(\omega)$ and the dip and the shoulder in $\text{Im}\Sigma(\omega)$ get gradually smeared out. Notably, the minimum of $-\text{Im}\Sigma(\omega, T)$ is shifted to positive frequencies within this process. This hints towards long-lived electron-like excitations governing the incoherent transport of this crossover regime. Well above $T > 0.1$ the whole QPP in $A(\omega)$ becomes strongly reduced eventually reaching a pseudogap at high temperatures. $\text{Re}\Sigma(\omega)$ and $\text{Im}\Sigma(\omega)$ become strongly temperature dependent. The minimum in $-\text{Im}\Sigma(\omega)$ is shifted back towards $\omega \approx 0$. Finally, the pseudogap leads to a sign change of the slope of $\text{Re}\Sigma(\omega)$ and the curvature of $\text{Im}\Sigma(\omega)$. Note that the behavior of $\text{Re}\Sigma(\omega)$ directly determines the behavior of $A(\epsilon_k, \omega)$ [cf. Eq. (3.14)], which can be easily seen from the behavior of $E(\epsilon_k)$ in Fig. 7.3(b,d).

Again, the evolution of the QP band with temperature strongly hints towards the existence of different types of QPs. At very low T in the FL regime, the band is described by a low-frequency FL-like QP band with a rather flat dispersion. Correspondingly, $A(\omega)$ exhibits a sharp SU(2) Kondo resonance. In the NFL regime at higher temperatures, we find a much steeper (slightly particle-hole asymmetric) HQP band, and the two-tier QPP in $A(\omega)$ is reduced to a single broad resilient SU(3) Kondo resonance. However, here, for rather large $\Delta_b = 3.5$, this HQP band [SU(3) Kondo resonance in $A(\omega)$] quickly vanishes with increasing temperature and we additionally find a crossover to a pseudogap at $T \approx 0.2$.

Importantly, for $J = 0$ the SOS features are fully absent in $A(\epsilon_k, \omega)$, $A(\omega)$, $\text{Re}\Sigma(\omega)$, and $\text{Im}\Sigma(\omega)$ (cf. Fig. 7.4). The FL behavior holds for a rather large temperature regime (at least up to $T \approx 0.25$) and is characterized by a very stable large dispersion and thus a rather small mass enhancement. RQPs do not exist.

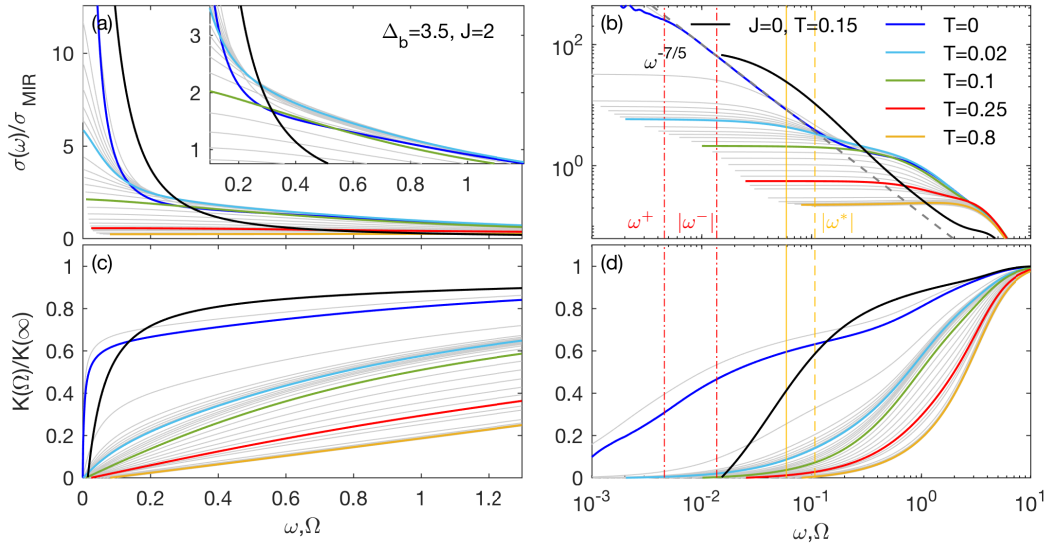


Figure 7.5 (a,b) The optical conductivity, $\sigma(\omega)$, and the kinetic energy, $K(\Omega)$, are plotted for various temperatures on (a,c) a linear and (b,d) a logarithmic frequency scale. We used the same parameters, $\Delta_b = 3.5$ and $J = 2$, as in Fig. 7.1 and Fig. 7.3. In addition, data for $\Delta_b = 3.5$ and $J = 0$ (at $T = 0.15$) is shown in black. (b,d) $|\omega^\pm|$, below which FL behavior should set in, is marked by vertical dash-dotted red lines. The vertical solid yellow lines denote the energy scale of the maximum in $\text{Re}\Sigma(\omega < 0)$ at $T = 0$ [cf. Fig. 7.1(d)]. The vertical dashed yellow lines show $|\omega^*|$.

Optical conductivity. We next study the optical conductivity, $\sigma(\omega)$ [cf. Eq. (3.15)], for the same parameters, $\Delta_b = 3.5$ and $J = 2$, as in the previous paragraph. $\sigma(\omega)$ is plotted on a linear and a logarithmic frequency scale in Fig. 7.5(a,b), respectively. In addition, we also show data for $\Delta_b = 3.5$ and $J = 0$ (at $T = 0.15$, which is still in the FL temperature regime). At $T = 0$ we expect a FL Drude peak. However, the data (blue curve) is not accurate enough to resolve the FL behavior at very low frequencies, $\omega < |\omega^\pm|$ (cf. discussion of Fig. 3.1 in Sec. 3.2). In the (low-frequency) NFL regime, $|\omega^\pm| \lesssim \omega \lesssim |\omega^*|$, we observe a power-law flank in $\sigma(\omega)$, $\propto \omega^{-\alpha}$, with $\alpha \approx 7/5$ at $T = 0$. Notably, for $\omega > |\omega^*|$ a broad NFL shoulder develops. With increasing temperature below $T \approx 0.1$ spectral weight is shifted from low frequencies into this shoulder, while the high-frequency part of $\sigma(\omega)$ remains unaffected. Note that the NFL shoulder is absent for $J = 0$ [cf. black curve in Fig. 7.5(a,b)]. At higher temperatures the NFL shoulder gradually decreases in height. The second shoulder at much higher frequencies is a Hubbard-band feature. It remains stable up to highest temperatures and is also present for $J = 0$. We suspect that the NFL shoulder at $\omega > |\omega^*|$ is an optical fingerprint of the HQP band [SU(3) Kondo resonance in $A(\omega)$] and can indeed be interpreted as Hund’s-coupling-induced excess spectral weight, caused by RQPs, as suggested in Ref. [SMB⁺14]. Further, our results (for $T \lesssim 0.1$) are reminiscent of recent optical conductivity measurements [YYW⁺17] for KFe_2As_2 .

In Fig. 7.5(c,d) the kinetic energy, $K(\Omega)$ [as defined in Eq. (3.18)], is plotted as a function of frequency, Ω , for various temperatures. In Ref. [SMP⁺12] an unusual spectral weight transfer from low to high energies was observed at low temperatures in $K(\Omega)$ for iron pnictides. This observation would correspond to line crossings of different $K(\Omega, T)$ curves for $J = 2$ in Fig. 7.5(c,d), which is yet not found in our data. We remark that this might be due to the rather large $\Delta_b = 3.5$ (cf. next paragraphs).

ARPES for Hund- and Mott-correlated metals. In Ref. [SKWvD18] (cf. Sec. 5.2) we showed that a Hund- and a Mott-correlated metal with finite J can be distinguished by

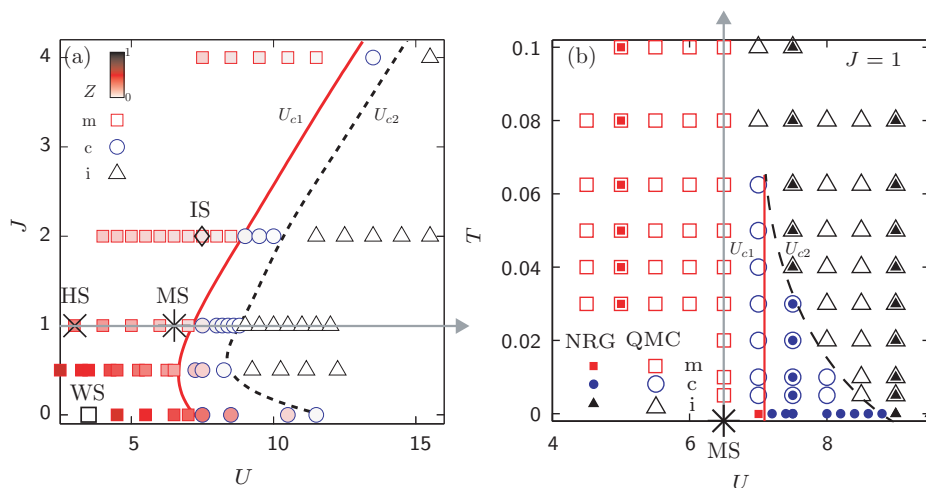


Figure 7.6 (a) The zero-temperature phase diagram of the 3HHM has three phases in the J - U -plane: a metallic phase (squares), a coexistence region (circles), and an insulating phase (triangles). These are separated by two phase transition lines U_{c1} (solid red curve) and U_{c2} (dashed black curve), respectively. The color intensity of the symbols in the metallic and the coexistence region indicates the value of $Z \in [0, 1]$: the lower Z the more faded is the red color. The phase diagram is adapted from Ref. [SKWvD18]. In this Chapter we present temperature-dependent results for a Hund system (HS) far away from the U_{c1} phase transition line deep in the metallic state (cross), a Mott system (MS) near the transition (asterisk), an intermediate system (IS) having both Hund and Mott features (open diamond), and a weakly correlated system (WS) with $J = 0$ far from U_{c1} (open square). (b) The T - U phase diagram of the 3HHM for $J = 1$ is characterized by a metallic phase (red squares), a coexistence phase (blue circles), and an insulating phase (black triangles) in accordance with (a). Big open symbols mark DMFT+QMC results kindly provided by Zhiping Yin. Small filled symbols mark our DMFT+NRG results, for which we have performed benchmarks with the DMFT+QMC results for $T > 0$ to check the accuracy of our finite-temperature data. $U_{c1}(T)$ (solid red curve) and $U_{c2}(T)$ (dashed black curve) are rough estimates only. The U_{c1} line for the DMFT+NRG data is slightly shifted to larger U values as compared with DMFT+QMC. We assume that this is caused by the fact that the Hubbard bands are slightly overbroadened in DMFT+NRG such that the closing of the insulating gap occurs already at slightly higher U .

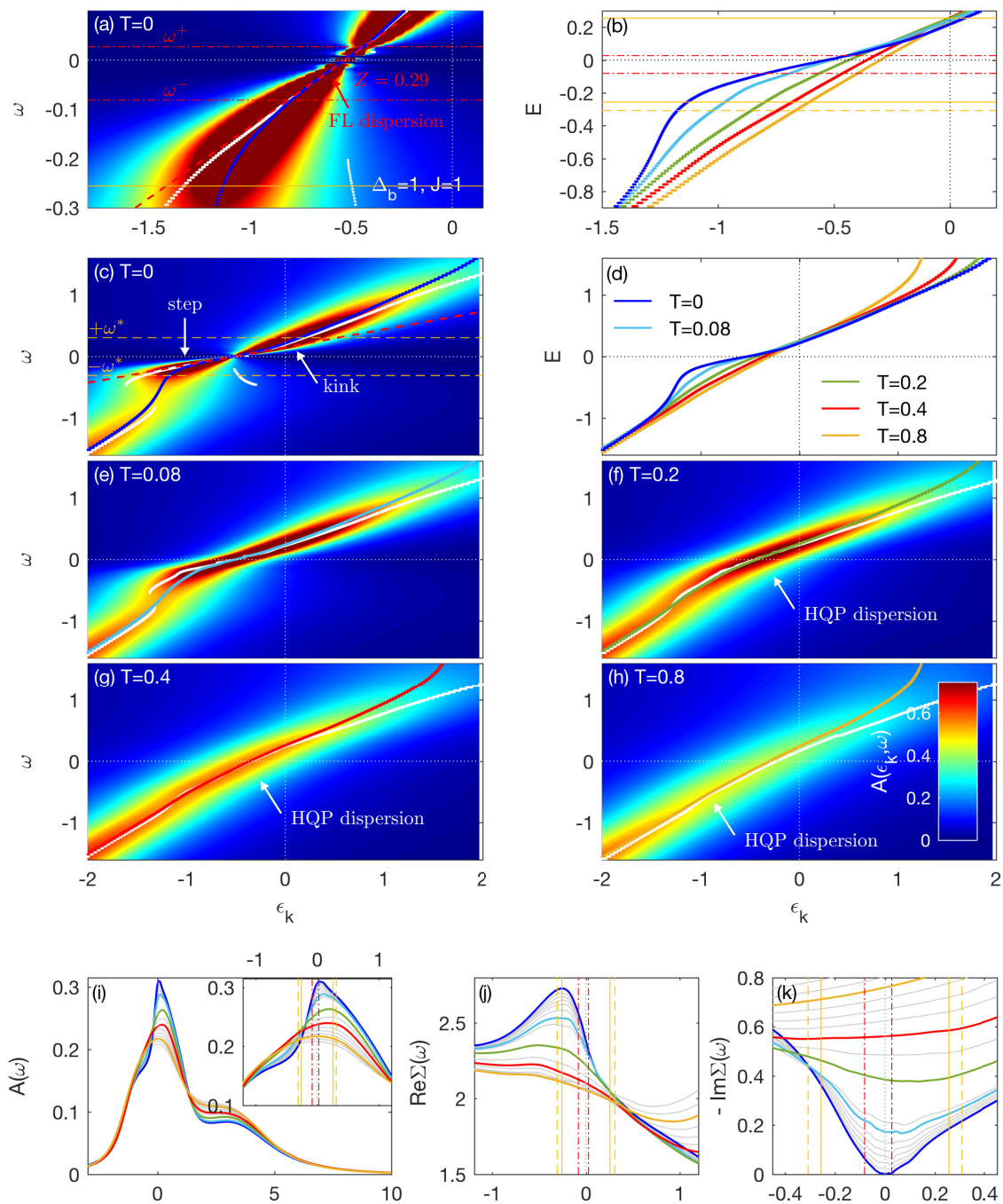


Figure 7.7 Same quantities as in Fig. 7.3 for a Hund system (HS) with parameters $\Delta_b = 1$ and $J = 1$.

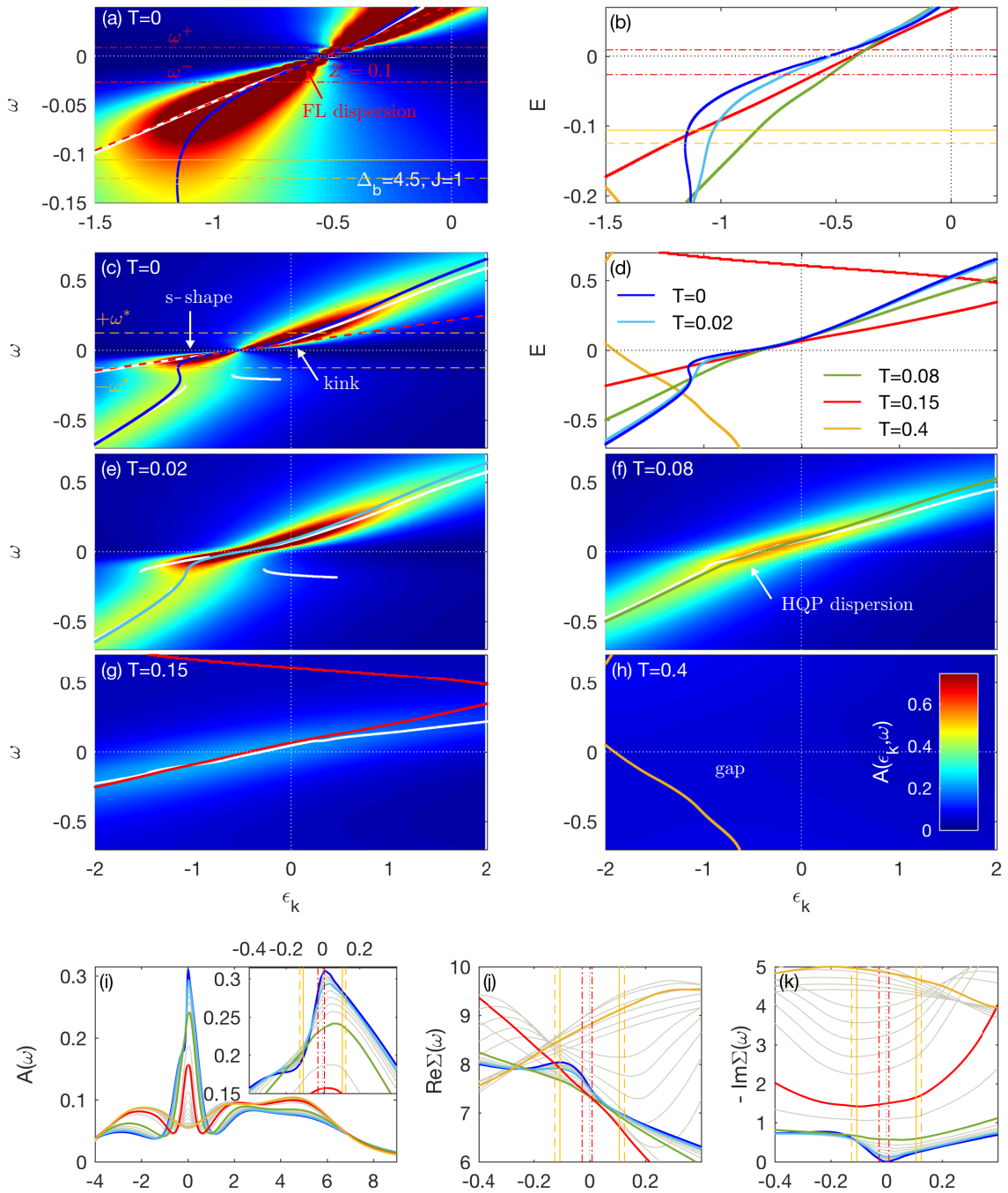


Figure 7.8 Same quantities as in Fig. 7.3 for a Mott system (MS) with parameters $\Delta_b = 4.5$ and $J = 1$.

the size and energy scale of the SOS regime at $T = 0$. While the SOS frequency regime is large in Hund systems, it becomes very small in Mott systems. We study in the following how this difference manifests itself in the temperature dependence of ARPES data.

To this end we, concentrate on a prototypical Hund system (HS) with $\Delta_b = 1$ and $J = 1$ in Fig. 7.7 and a prototypical Mott system (MS) with $\Delta_b = 4.5$ and $J = 1$ in Fig. 7.8, similar to Ref. [DSH⁺18] (cf. Sec. 6.2). While the HS is defined to be far away from the phase transition line of the MIT, the MS is put close to that boundary, as demonstrated in Fig. 7.6(a,b). We expect that these two systems show clear signatures of either Hundness or Mottness, respectively. We remark that, in contrast to the HS and MS, the system with $\Delta = 3.5$ and $J = 2$ (IS), discussed in the previous paragraphs, lies in an intermediate regime (but still rather close to the Mott boundary) [cf. diamond in Fig. 7.6(a)]. It is therefore dominated by both Hund and Mott features.

In the HS (cf. Fig. 7.7) we observe a rather large FL-frequency regime at $T = 0$ [cf. Fig. 7.7(a,c)]. The slope of the Landau QP band is small, $Z = 0.29$. The mass enhancement in the system is thus fairly large, $Z^{-1} = m^*/m = 3.45$. The transition to a more steep HQP-like band occurs at rather high frequencies $|\omega^*| \approx 0.31$ [cf. Fig. 7.7(c)]. With increasing temperature, SOS features like the s-shaped band at $\omega < 0$ and the kink at $\omega > 0$ dissolve very slowly, while the steeper HQP-like part of the band remains stable [cf. Fig. 7.7(d)]. For $T \gtrsim 0.2$ a very robust, almost temperature independent HQP band governs the incoherent transport regime. The slope of this band remains quite stable over a very broad range of frequencies (especially for $\omega < 0$) up to the highest temperature plotted [cf. Fig. 7.7(d)]. This robustness of the HQP band is reflected in the stable form of the QPP flank of $A(\omega)$ at negative frequencies [cf. Fig. 7.7(i)]. Interestingly, this flank is stabilized by the lower Hubbard band, which lies at $\omega_h = -0.5$ [SKWvD18], i.e. the SU(3) Kondo resonance and atomic excitations merge in the HS, resulting in a robust ARPES feature with mixed valence character at very high temperatures. We remark that, while the minimum of $-\text{Im} \Sigma(\omega, T)$ is shifted to positive frequencies with increasing temperature for $T < 0.4$, this minimum vanishes at higher temperatures and $-\text{Im} \Sigma(\omega, T)$ becomes an increasing function of frequency close to the Fermi level. This might again be caused by mixed valence physics, which becomes important at an energy scale around 0.5. Interestingly, very similar behavior of the minimum of $-\text{Im} \Sigma(\omega, T)$ is observed for the hole-doped one-band Hubbard model of Ref. [DMicv⁺13]. There, a well-defined QPP persists with increasing temperature above T_{FL} until it merges with the lower Hubbard band at high temperatures.

In the MS (cf. Fig. 7.8) we also find a FL frequency regime and the SOS features at $T = 0$ [cf. Fig. 7.8(a,c)]. However, these occur at much lower frequencies than in the HS (for instance, $|\omega^*| = 0.12$), as expected from the results in Ref. [SKWvD18]. Moreover, $Z = 0.1$ is smaller for larger Δ_b [SKWvD18]. With increasing temperature, the SOS features vanish very quickly (already below $T = 0.08$) in the MS [cf. Fig. 7.8(b,d)]. The emergent HQP band [cf. Fig. 7.8(f)] is very unstable with increasing temperature and already disappears at around $T = 0.15$ [cf. Fig. 7.8(d,g)]. Above $T \gtrsim 0.2$ a pseudogap has fully replaced the QPP [cf. Fig. 7.8(h,i)]. While for $T \lesssim 0.08$ the minimum of $-\text{Im} \Sigma(\omega, T)$ is shifted to positive frequencies, it is gradually shifted back towards negative frequencies with increasing temperature and finally turns over to a maximum in the presence of a pseudogap [cf. Fig. 7.8(k)].

To summarize, both the HS and the MS show SOS features in $A(\epsilon_k, \omega)$ at $T = 0$: (i) a rather flat low-frequency Landau QP band of slope Z ; (ii) a NFL crossover behavior (in form of s-shaped band or a step-like feature at $\omega < 0$ and a kink at $\omega > 0$); and (iii) an extended HQP band. The latter consists of an $\omega > 0$ and an $\omega < 0$ part, both of which exhibit linear dispersion relations with large slopes, where the slope for $\omega < 0$ is slightly larger than the slope for $\omega > 0$. However, these SOS features occur at very different energy scales in the HS and the MS [SKWvD18]: while in the HS they are extended over a broad frequency range up

to atomic energy scales, they are compressed and lie at very small frequency scales in the MS. Consequently, in the HS, these features govern the whole transport regime. In particular, very robust HQPs exist up to highest temperatures. In contrast, in the MS, SOS physics only survives at very low temperatures, whereas the behavior of $A(\epsilon_k, \omega)$ at higher temperatures is dominated by classical Mott physics, i.e. the DMFT self-consistency opens a (pseudo)gap and quickly destroys the HQPs.

7.3 Temperature dependence of various physical quantities

In this section we finally classify generic Hund-metal signatures in the temperature dependence of various physical quantities, interpret them based on the results of the previous sections, and stress the differences to multi-orbital Mott systems. In particular, we investigate the static local orbital and spin susceptibility, the quasiparticle weight, the local density of states and the scattering rate at the Fermi level, the coherence scale, the resistivity, the effective chemical potential, the thermopower, and the entropy in Fig. 7.9, Fig. 7.11, and Fig. 7.12. We again study the HS (yellow), the MS (black), the “intermediate” system (IS) with $\Delta_b = 3.5$ and $J = 2$ (red) – which is close to the Mott boundary but also shows signs of Hundness due to the large value of $J = 2$ – and a weakly correlated system (WS) with $\Delta_b = 3.5$ and $J = 0$ (blue) [cf. Fig. 7.6(a)].

Static local orbital and spin susceptibility, quasiparticle weight. We start with a detailed analysis of the static local orbital and spin susceptibility, $T\chi_0^{\text{orb,sp}}$ in Fig. 7.9(a,b,e,f) and $\chi_0^{\text{orb,sp}}$ in Fig. 7.9(c,d,g,h), to refine our findings of Ref. [DSH⁺18] in Sec. 6.2 (cf. Sec. 3.1 for computational details). We also plotted the quasiparticle weight, $Z(T)$, in Fig. 7.9(a,b,e,f) [and additionally in Fig. 7.11(a,b)]. In principle, $Z(T)$ is physically only rigorously defined in the FL regime. Nevertheless, for temperatures in the NFL regime, it is still computationally well-defined and we use it to interpret the physics on an heuristic level.

We begin with a discussion of the results for the HS in Fig. 7.9(a-d). As shown in Ref. [DSH⁺18], the HS exhibits much higher onset scales for orbital than for spin screening: $T_{\text{orb}}^{\text{onset}} \gg T_{\text{sp}}^{\text{onset}}$. $T\chi_0^{\text{orb}}$ decreases with decreasing temperature for all temperatures plotted [cf. dashed yellow curves in Fig. 7.9(a,b)], i.e. the onset for orbital screening, $T_{\text{orb}}^{\text{onset}} > 1$, is on the order of bare excitations scales. The onset of spin screening, $T_{\text{sp}}^{\text{onset}} \approx 0.25$, is signalled by the deviation from Curie-like (constant) behavior of $T\chi_0^{\text{sp}}$ with decreasing temperature, which we mark by the yellow triangle [cf. solid yellow curves in Fig. 7.9(a,b)]. Note that $T_{\text{sp}}^{\text{onset}} \approx 0.25$ is chosen slightly smaller compared to Ref. [SKWvD18] (where we chose $T_{\text{sp}}^{\text{onset}} \approx 0.4$). This choice is motivated by the ARPES data in Fig. 7.7. There the onset of spin screening is reflected in the formation of a flat low-frequency band in addition to the steep HQP band, resulting in a pronounced step-like feature at $T = 0$. In Fig. 7.7(d) the onset of the step formation is visible for $T \lesssim 0.2$. Furthermore, we motivate this choice in terms of the behavior of χ_0^{orb} . With $T_{\text{sp}}^{\text{onset}} \approx 0.25$, the onset scale of spin screening is equal to the temperature scale for the completion of orbital screening: χ_0^{orb} shows Pauli (constant) behavior for $T < T_{\text{sp}}^{\text{onset}} \approx T_{\text{orb}}^{\text{cmp}}$ [cf. dashed yellow curve in Fig. 7.9(c,d)]. When the temperature is further lowered, also χ_0^{sp} reaches Pauli behavior at $T_{\text{FL}} = T_{\text{sp}}^{\text{cmp}}$ (yellow cross). Then spin screening is completed and the system is a FL.

In Fig. 7.10(a) we summarize our observations in a schematic sketch. In a HS, the SOS screening process of Fig. 7.2 is directly reflected in the temperature dependence of physical quantities. For $T_{\text{orb}}^{\text{onset}} > T > T_{\text{sp}}^{\text{onset}}$, HQPs, i.e. gradually screened (quasi-itinerant) orbitals coupled to quasi-free spins, dominate the physics and lead to a robust HQP band in ARPES spectra and a Curie-like spin susceptibility. At very high temperatures mixed-valence physics

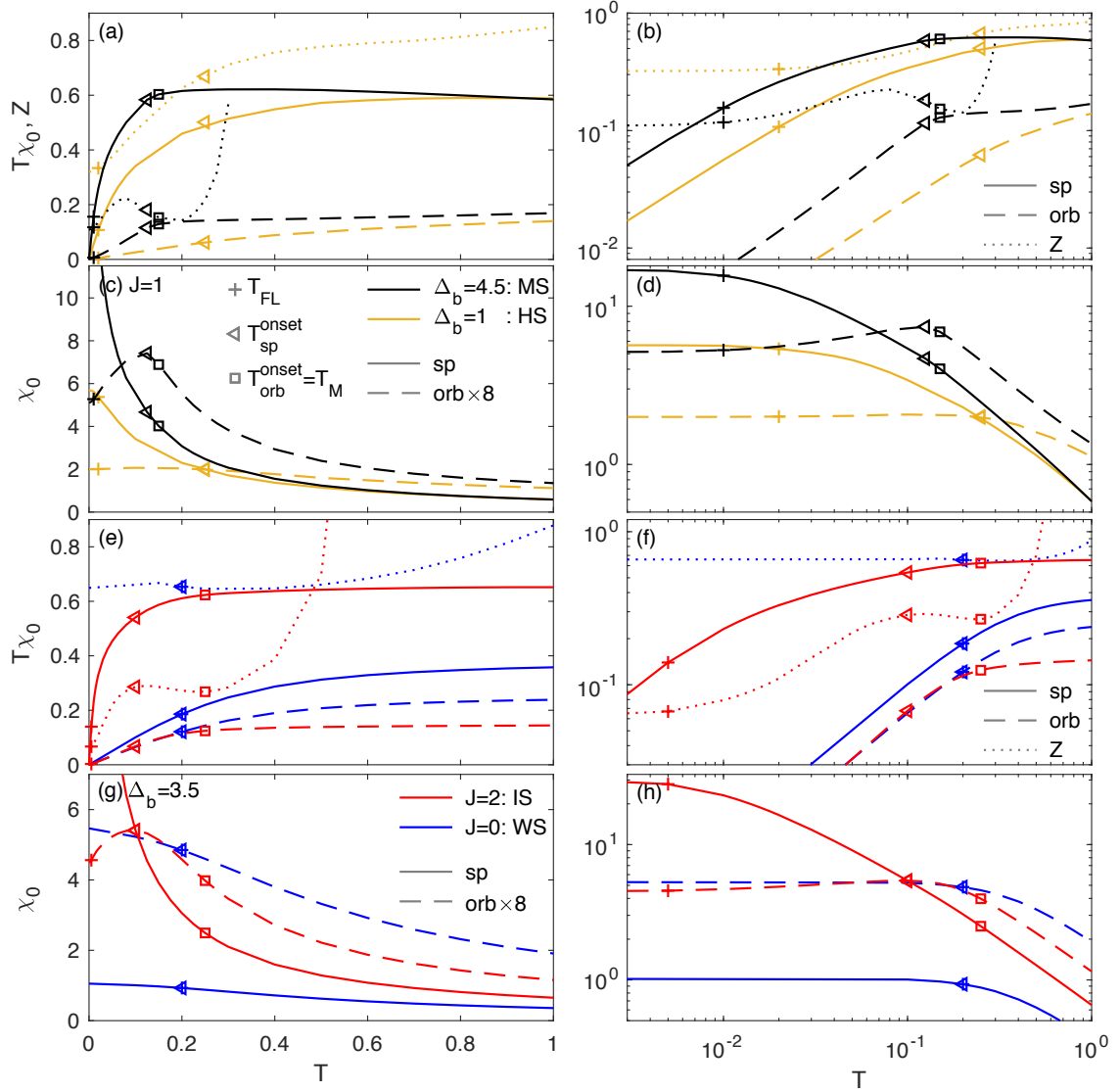


Figure 7.9 The static local orbital (dashed) and spin (solid) susceptibility, (a,b,e,f) $T\chi_0^{\text{orb,sp}}$ and (c,d,g,h) $\chi_0^{\text{orb,sp}}$, are plotted versus temperature for the MS (black), the HS (yellow), the IS (red), and the WS (blue). In addition, the quasiparticle weight ($Z(T)$), is shown in (a,b,e,f). The squares mark the onset of orbital screening, $T_{\text{orb}}^{\text{onset}}$, below which $T\chi_0^{\text{orb}}$ deviates from Curie behavior. Note that $Z(T)$ diverges for $T > T_{\text{orb}}^{\text{onset}}$. The triangles mark the maxima of χ_0^{orb} and also signal the onset of spin screening, $T_{\text{sp}}^{\text{onset}}$, below which $T\chi_0^{\text{sp}}$ deviates from Curie-like behavior. The crosses denote the FL scale, T_{FL} , below which FL behavior is found. In the MS, we observe that $T_{\text{sp}}^{\text{onset}} \approx T_{\text{orb}}^{\text{onset}} = T_M$. In the HS, we find $T_{\text{orb}}^{\text{onset}} \gg T_{\text{sp}}^{\text{onset}}$, as discussed in Ref. [DSH⁺18].

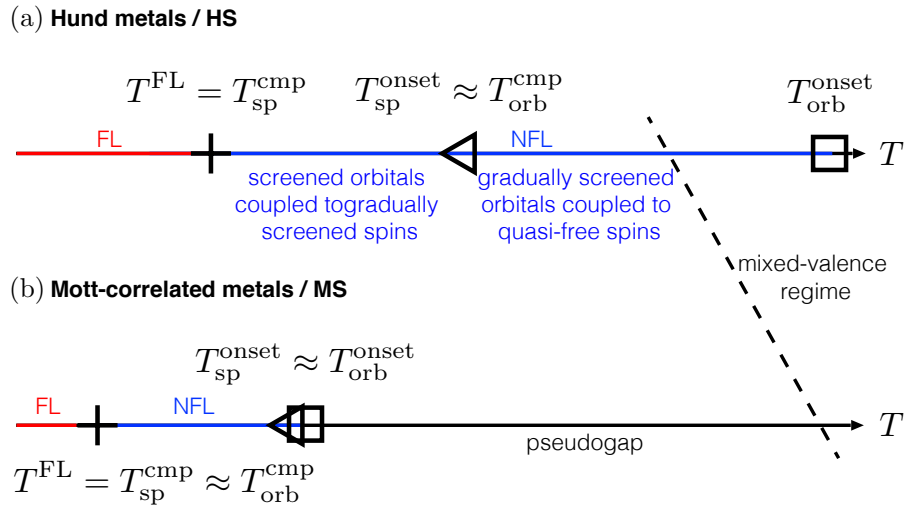


Figure 7.10 (a) Schematic sketch of different temperature regimes in a Hund metal. For $T > T_{\text{FL}}$, the HS is a NFL up to temperatures in the order of bare energy scales, where also mixed-valence physics becomes important. The NFL regime reflects the complex SOS screening process of Fig. 7.2. First orbitals get screened with decreasing temperature for $T_{\text{orb}}^{\text{onset}} > T > T_{\text{orb}}^{\text{cmp}}$. In this regime transport is governed by HQPs which are characterized by gradually screened orbitals coupled to quasi-free spins. Only when the orbital screening process is completed spins get screened below $T_{\text{sp}}^{\text{onset}} \approx T_{\text{orb}}^{\text{cmp}}$, i.e., in this regime, the HQPs get gradually dressed to form heavier Landau QPs. For $T < T_{\text{FL}} = T_{\text{sp}}^{\text{cmp}}$, the HS is a FL and both orbital and spin degrees of freedom are fully screened. (b) Schematic sketch of different temperature regimes in a multi-orbital Mott-correlated metal. In a MS, a pseudogap governs the physics in an extended temperature regime, $T > T_{\text{sp}}^{\text{onset}} \approx T_{\text{orb}}^{\text{onset}} = T_{\text{M}}$. For temperatures below T_{M} , both orbital and spin degrees of freedom get screened simultaneously with the onset of a Kondo resonance, which is driven by the DMFT-self-consistency condition. The NFL regime for $T_{\text{M}} > T > T_{\text{FL}}$ is followed by a FL regime for very small $T < T_{\text{FL}} = T_{\text{sp}}^{\text{cmp}} \approx T_{\text{orb}}^{\text{cmp}}$, where both orbital and spin degrees of freedom are fully screened.

might additionally come into play, because the lower (and a part of the upper) Hubbard band is merged at $\omega_h = -0.5$ (and $\omega_{e1} = +0.5$) into the QPP in the HS [cf. Fig. 7.7(i)]. Due to the special SOS screening process, the spins can only get screened as soon as the orbitals are fully screened at $T_{\text{orb}}^{\text{cmp}}$, thus $T_{\text{sp}}^{\text{onset}} \approx T_{\text{orb}}^{\text{cmp}}$. For $T_{\text{sp}}^{\text{onset}} > T > T_{\text{FL}}$ also the spins get gradually screened, eventually resulting in the full screening of both degrees of freedom and thus in a FL below T_{FL} . The spin screening is signalled by the formation of a step-like feature in ARPES spectra and by a Pauli-like orbital susceptibility.

This screening route is also reflected in $Z(T)$ [cf. dotted yellow curve in Fig. 7.9(a,b)]. For $T_{\text{orb}}^{\text{onset}} > T > T_{\text{sp}}^{\text{onset}}$, the existence of resilient HQPs leads to a plateau-like feature in $Z(T)$. With decreasing temperature, $T_{\text{sp}}^{\text{onset}} > T > T_{\text{FL}}$, $Z(T)$ decreases and approaches a second plateau in the FL regime $T < T_{\text{FL}}$. The reduction of $Z(T)$ shows that the HQPs are additionally “dressed” through spin screening, resulting in heavier Landau QPs.

The MS behaves very differently. As shown in Ref. [DSH⁺18], $T_{\text{M}} \equiv T_{\text{orb}}^{\text{onset}} \approx T_{\text{sp}}^{\text{onset}}$ [cf. black triangle and square in Fig. 7.9(a,b)]. For $T > T_{\text{M}} \approx 0.15$ both $T\chi_0^{\text{orb}}$ and $T\chi_0^{\text{sp}}$ exhibit a Curie plateau and the spectral function is characterized by a pseudogap. Both degrees of freedom get screened simultaneously with the onset of a Kondo resonance [cf. Fig. 7.8(g,i)], which is driven by the DMFT-self-consistency condition, in contrast to the Kondo screening in the HS. Interestingly, $T_{\text{sp}}^{\text{onset}}$ now corresponds to the position of a maximum in χ_0^{orb} [cf. black triangle and black dashed curve in Fig. 7.9(c,d)]: the orbital dynamics is strongly influenced by the spin screening and true Pauli behavior is only reached for $T < T_{\text{FL}}$ in the MS, thus $T_{\text{FL}} = T_{\text{sp}}^{\text{cmp}} \approx T_{\text{orb}}^{\text{cmp}}$. This behavior is summarized in Fig. 7.10(b). In the MS, Mott physics dominates and with increasing temperature essentially destroys SOS physics by opening a pseudogap already at low temperatures. Again, $Z(T)$ reflects these findings [cf. dotted black curve in Fig. 7.9(a,b)]. Similar to the HS, $Z(T)$ is small and constant for $T < T_{\text{FL}}$. But instead of a second HQP plateau as in the HS, $Z(T)$ has a maximum directly below T_{M} and diverges for $T > T_{\text{M}}$.

To corroborate our picture above, we similarly study the IS and the WS in Fig. 7.9(e-h). The IS is rather close to the Mott boundary [cf. diamond in Fig. 7.6(a)]. Thus, we observe Mott signatures at high temperatures: for $T > T_{\text{orb}}^{\text{onset}} \approx 0.25$, $T\chi_0^{\text{orb}}$ shows Curie behavior [cf. red square in Fig. 7.9(e,f)] and a pseudogap exists [cf. Fig. 7.3(g,i)]. However, due to the large $J = 2$, we find Hund signatures, as well, at intermediate and low temperatures: orbital and spin screening are slightly separated, $T_{\text{orb}}^{\text{onset}} > T_{\text{sp}}^{\text{onset}}$, and $Z(T)$ features a plateau for $T_{\text{orb}}^{\text{onset}} > T > T_{\text{sp}}^{\text{onset}}$. $T_{\text{sp}}^{\text{onset}}$ marks a maximum in χ_0^{orb} [cf. Fig. 7.9(g,h)], which is however less pronounced than in the MS. Full screening with Pauli behavior of both χ_0^{orb} and χ_0^{sp} is reached at $T < T_{\text{FL}}$. Due to the large Hund’s coupling T_{FL} (and accordingly $Z(T = 0)$ [SKWvD18]) is lowest in the IS compared to the HS, MS, and WS. In sum, the IS exhibits an intermediate system, showing a mixture of Hund and Mott features.

Finally, we concentrate on the WS, a system without Hund’s coupling, $J = 0$ (cf. also Fig. 7.4). In Fig. 7.9(e-h), χ_0^{orb} and χ_0^{sp} behave equally for the WS with $\chi_0^{\text{sp}}/\chi_0^{\text{orb}} = 1.5$. The FL regime is extended up to very high temperatures [$Z(T)$ is essentially constant in Fig. 7.9(e,f)]. Both Hund and Mott features are absent in the WS and the system is only weakly correlated with $Z(T = 0) = 0.65$.

In the next paragraphs we continue to compare the HS, MS, IS, and WS. In Fig. 7.11 we replotted Z , show the local density of states, $A(\omega = 0)$, and the imaginary part of the self-energy, $\text{Im}\Sigma(\omega = 0)$, at the Fermi level, and concentrate on the coherence scale, Γ^*/T (cf. definition in Sec. 3.9), and the resistivity, ρ , as defined in Sec. 3.6.

Local density of states and scattering rate at the Fermi level. Fig. 7.11(c,d) depicts $A(\omega = 0)$. For $T < T_{\text{FL}}$, $A(\omega = 0)$ is a constant function of temperature for all systems. For

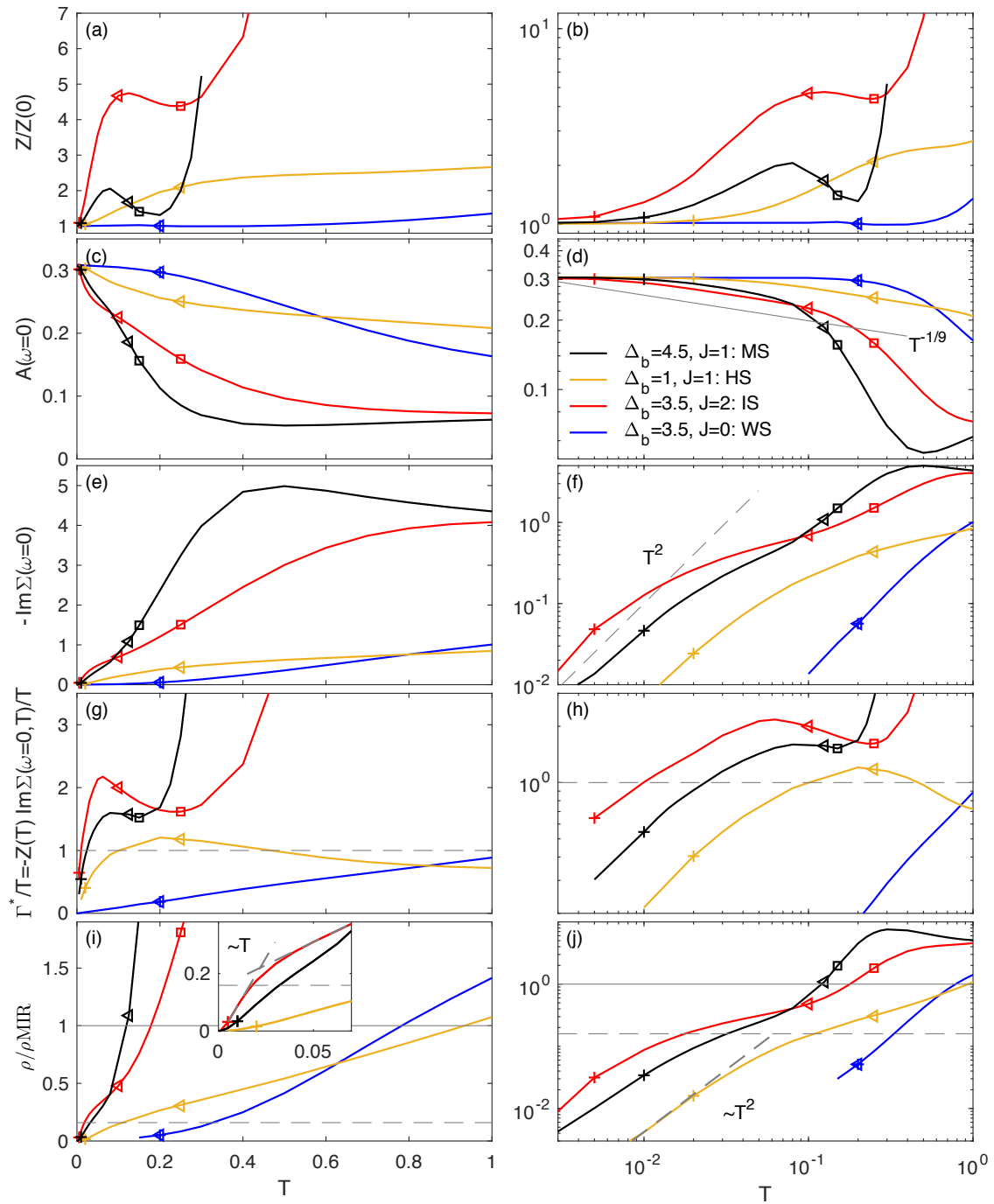


Figure 7.11 (a,b) The quasiparticle weight, $Z/Z(0)$, (c,d) the local density of states at the Fermi level, $A(\omega = 0)$, (e,f) the scattering rate at the Fermi level, $\text{Im} \Sigma(\omega = 0)$, (g,h) the coherence scale, Γ^*/T , and (i,j) the resistivity, ρ , are plotted as functions of temperature on (left panels) a linear and on (right panels) a logarithmic scale for the MS (black), the HS (yellow), the IS (red) and the WS (blue). Symbols are defined as in Fig. 7.9. (f,j) The dashed grey guide-to-the-eye lines indicate FL behavior. (g,h) The horizontal dashed grey lines mark $\Gamma^*/T^* = 1$. (i,j) The horizontal dashed (solid) grey lines mark the MIR limit defined via $k_{\text{F}}l_{\text{min}} \approx 2\pi$ ($k_{\text{F}}l_{\text{min}} \approx 1$).

$T_{\text{FL}} < T < T_{\text{sp}}^{\text{onset}}$, in the case of $J > 0$, we discover a power-law behavior: $A(\omega = 0) \propto T^{-1/9}$. In the HS, this power-law behavior persists up to the highest temperature plotted. In contrast, in the MS, the power law is not fully developed. Moreover, the MS is characterized by a strong decrease of $A(\omega = 0)$ with increasing $T > T_{\text{sp}}^{\text{onset}}$, reflecting the formation of a pseudogap. The IS behaves in a manner similar to the MS. However, T_{FL} is smaller, the power law is fully developed and the decay of $A(\omega = 0)$ is slower. In the WS the power law is absent and $A(\omega = 0)$ decays slightly for $T > T_{\text{FL}}$.

The scattering rate, $-\text{Im} \Sigma(\omega = 0)$, is plotted as a function of temperature in Fig. 7.11(e,f). For $T < T_{\text{FL}}$, $-\text{Im} \Sigma(\omega = 0)$ follows FL behavior [cf. dashed grey guide-to-the-eye line in Fig. 7.11(f)]. In the HS, for $T > T_{\text{FL}}$, the scattering rate is small and shows a crossover to a rather flat behavior in the NFL regime. In contrast, in the MS, the scattering rate increases massively for $T \gtrsim T_{\text{M}}$ [cf. Fig. 7.11(e)], saturating at high temperatures due to the presence of a pseudogap. The IS shows a mixture of both the Hund and the Mott behavior. $-\text{Im} \Sigma(\omega = 0)$ first flattens for $T_{\text{FL}} < T < T_{\text{sp}}^{\text{onset}}$, but then increases strongly for $T > T_{\text{sp}}^{\text{onset}}$, saturating as well at very high temperatures. Notably, $-\text{Im} \Sigma(\omega = 0)$ is larger for the IS than for the MS for $T < 0.1$, which is caused by the larger $J = 2$ in the IS. The scattering rate in the WS is small and FL-like. It keeps growing slowly with increasing temperature.

Coherence scale. In Fig. 7.11(g,h) we plot the coherence scale, Γ^*/T , with $\Gamma^*(T) = -Z(T)\text{Im} \Sigma(\omega = 0, T)$. The coherence temperature, T^* , is defined as $\Gamma^*/T^* \equiv 1$ (cf. intercepts with horizontal dashed grey line). Above T^* coherent Landau QPs become short-lived and the FL picture breaks down. The HS is characterized by a very broad maximum of Γ^*/T in the NFL regime around $T_{\text{sp}}^{\text{onset}}$. This behavior is reminiscent of DMFT results for Sr_2RuO_4 , where Γ^*/T keeps increasing in a crossover regime above $T^* \approx 100\text{K}$ and reaches a plateau above 350K [MAM⁺11]. In contrast, the MS shows only a small plateau in Γ^*/T around $T_{\text{sp}}^{\text{onset}}$ before it diverges [due to the divergence of $Z(T)$]. Again, the IS features a mixture of both the Hund and the Mott behavior. Γ^*/T first exhibits a maximum at $T_{\text{sp}}^{\text{onset}}$, but then diverges at $T_{\text{orb}}^{\text{onset}}$. In the WS, Γ^*/T is very small and grows continuously with increasing temperature. In Ref. [DMicv⁺13] the existence of asymmetric FL scales, ω^\pm , was shown to lead to a hidden FL ($\Gamma^* \propto T^2$ holds above T_{FL}). However, we cannot resolve a hidden FL in our data although it might exist.

Resistivity. The resistivity, $\rho(T)$, is shown in Fig. 7.11(i,j). In the FL regime, we find T^2 behavior (though this is hard to resolve very accurately). Equivalently to the findings for the hole-doped Mott insulator [DMicv⁺13], we observe that, for $T_{\text{FL}} < T < T_{\text{sp}}^{\text{onset}}$, $\rho(T)$ first increases approximately linearly with a negative intercept, then it shows a kneelike feature (kink), above which a linear increase with positive intercept sets in [cf. red curve in inset of Fig. 7.11(i)]. In the HS, $\rho(T)$ keeps increasing linearly up to the highest temperature plotted, and thus behaves qualitatively in the same way as the hole-doped Mott insulator in Ref. [DMicv⁺13]. This is an intriguing similarity considering that both systems are assumed to be governed by RQPs in their NFL regime. Moreover, our findings for the HS are reminiscent of the DFT+DMFT simulations [HK09] and measurements [HBA⁺13] of the resistivity in iron pnictides. In contrast to the HS, in the IS a second kink occurs at $T_{\text{sp}}^{\text{onset}}$, and $\rho(T)$ grows strongly with increasing temperature until it saturates above $T_{\text{orb}}^{\text{onset}}$ in the presence of a stable pseudogap. In the MS, we do not observe a kneelike feature but a kink at $T \approx 0.8$, above which $\rho(T)$ increases massively with growing temperature. The WS is again characterized by a large FL temperature regime, reaching up to very high temperatures. $\rho(T)$ is much smaller for the $J = 0$ than for finite J systems. We remark that for all systems $\rho(T)$ crosses the MIR limit defined via $k_{\text{F}}l_{\text{min}} \approx 2\pi$ roughly at T^* [cf. horizontal dashed grey line in Fig. 7.11(i,j)] and continues to grow above this limit. (The MIR limit defined as $k_{\text{F}}l_{\text{min}} \approx 1$

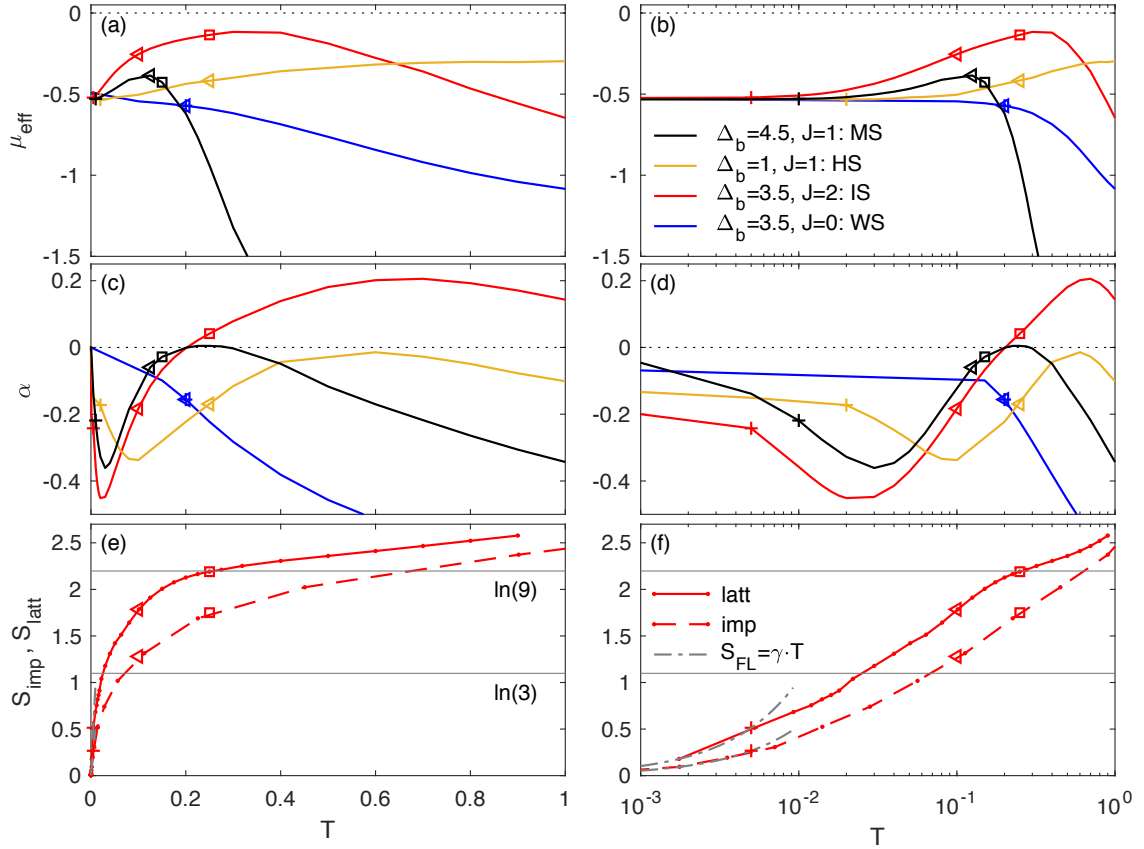


Figure 7.12 (a,b) The effective chemical potential, μ_{eff} , (c,d) the thermopower, α , and (e,f) the impurity contribution to the entropy (dashed), S_{imp} , and the lattice entropy (solid), S_{latt} , plotted as functions of temperature (left panels) on a linear and (right panels) on a logarithmic scale for the MS (black), the HS (yellow), the IS (red) and the WS (blue). Symbols are defined as in Fig. 7.9. (f) The grey dash-dotted curves indicate FL behavior for S_{imp} and S_{latt} , respectively.

is marked by the horizontal solid grey lines.) As expected, the MS crosses the MIR limit at a smaller temperature scale than the HS. Notably, the IS crosses the MIR limit at an even lower scale although Coulomb interactions are larger in the MS than in the IS. This strong correlation effect is due to Hundness, i.e. large J .

Effective chemical potential. We now turn to Fig. 7.12. We first study the evolution of the effective chemical potential, $\mu_{\text{eff}} = \mu - \text{Re} \Sigma(\omega = 0)$, [cf. Eq. (3.39)] in Fig. 7.12(a,b). For $T < T_{\text{FL}}$, μ_{eff} is constant and Luttinger pinning holds (cf. Sec. 3.10.2 for details). Interestingly, for all systems with finite J , μ_{eff} increases towards 0 with increasing temperature, $T_{\text{FL}} < T < T_{\text{sp}}^{\text{onset}}$, i.e. towards an effective half-filling of the system. In the HS, this trend is retained above $T_{\text{sp}}^{\text{onset}}$ until μ_{eff} approaches a plateau in the mixed-valence regime. This behavior fits to the SOS screening picture (cf. Fig. 7.2 and Fig. 7.10) where, above T_{FL} , spins are gradually unscreened to form an effective 3/2 spin, while the orbitals are still in an orbital singlet for $T < T_{\text{sp}}^{\text{onset}}$. For $T > T_{\text{sp}}^{\text{onset}}$, the orbitals start to get unscreened while large quasi-free spins persist. In the MS, μ_{eff} drastically reduces for $T > T_{\text{M}}$. In the IS, μ_{eff} first increases markedly almost up to 0 and then decreases for $T > T_{\text{orb}}^{\text{onset}}$ similarly to the MS. In contrast, for $J = 0$, the WS directly decreases above T_{FL} . Obviously, the substantial continuous increase of $\mu_{\text{eff}}(T)$ with increasing temperature towards half-filling, i.e. an inflating Fermi volume, is connected to the existence of a finite J in the 3HHM, while the

decrease of $\mu_{\text{eff}}(T)$ with increasing temperature is a Mott feature. We note, however, that in the hole-doped one-band Hubbard system of Ref. [DMicv⁺13], $\mu_{\text{eff}}(T)$ is an increasing function of temperature, as well.

Thermopower. In Fig. 7.12(c,d) we show the thermopower (Seebeck coefficient), $\alpha(T)$, as defined in Eq. (3.20) and compare the 3HHM results to the thermopower of Sr_2RuO_4 in Ref. [MG16]. In the FL regime, the thermopower of the 3HHM at $n_d = 2$ decreases electron-like, i.e. $\alpha(T) < 0$. Accordingly, in Sr_2RuO_4 (which would correspond to $n_d = 4$ in the 3HHM) a hole-like increase is observed. However, our data is not accurate and dense enough to unveil FL behavior, $\alpha(T) \propto T$. Similar to the (broad) maximum in $\alpha(T)$ of Sr_2RuO_4 around 300K – 500K, we observe a minimum in the crossover regime $T_{\text{FL}} < T < T_{\text{sp}}^{\text{onset}}$. In the HS, we further find a saturation (broad maximum) well above $T_{\text{sp}}^{\text{onset}}$. In the IS and the MS, a maximum occurs above $T_{\text{orb}}^{\text{onset}}$, as well. Overall, the behavior of $\alpha(T)$ is similar for all systems with finite J . However, the minimum is much more extended and lies at higher energies in the HS compared to the MS [cf. Fig. 7.12(c)]. In contrast, the WS with $J = 0$ does not exhibit any minimum (or maximum) in $\alpha(T)$. Here, the thermopower decreases in a FL-like fashion in an extended temperature range.

In sum, we conclude that the HS reflects the findings of Ref. [MG16]. Using $t \approx 5000\text{K}$ (a value which is estimated from a comparison of the model bandwidth with the realistic bandwidth of Sr_2RuO_4 [DSH⁺18]), the minimum of $\alpha(T)$ of the HS is indeed in the same temperature range (300K – 500K) as observed for Sr_2RuO_4 . We thus confirm the ideas of Ref. [MG16] that this unusual feature in $\alpha(T)$ can be associated with quenched orbitals and fluctuating spins as present in the two-stage SOS screening process. To be more precise, the minimum of $\alpha(T)$ in the 3HHM corresponds to the crossover regime, where the spins get gradually screened to form coherent Landau QPs. Thus, this minimum in $\alpha(T)$ is observed together with the formation of the step-like (s-shaped) ARPES feature [cf. Fig. 7.7].

Entropy. We conclude our study of Hund and Mott features in the 3HHM by calculating the lattice entropy and the impurity contribution to the entropy for the IS [cf. Fig. 7.12]. Similar calculations for the HS, the MS, and the WS will be carried in a future study. For the computation of the lattice entropy, $S_{\text{latt}}(T)$, we use Eq. (3.26). The impurity contribution to the entropy, $S_{\text{imp}}(T)$, is obtained with Eq. (3.25). Remarkably, we find that $S_{\text{latt}}(T)$ is larger than $S_{\text{imp}}(T)$ in the whole temperature range $0 < T < 1$, while both entropies behave qualitatively in the same way. The difference between $S_{\text{latt}}(T)$ and $S_{\text{imp}}(T)$ already arises in the FL regime, where the entropy is given as $S(T) = \gamma T$ with $\gamma = \frac{2N_c\pi^2}{3Z}$ (cf. Sec. 3.9). Within DMFT, $Z = Z$ of the lattice is smaller than $Z = Z_{\text{imp}}$ of the impurity calculation. Although this insight can be simply derived, we are not aware of any previous results that explicitly demonstrated this quantitative difference of the impurity and the lattice entropy. We intend to generically verify this observation by performing further calculations for the 3HHM and the one-band Hubbard model.

For the 3HHM, we observe the two-stage SOS screening process in both entropies. For $T > T_{\text{orb}}^{\text{onset}}$, the IS is characterized by a pseudogap and both the spin and orbital degrees of freedom are unscreened, resulting in $S_{\text{latt}} > \ln(9)$. (S_{latt} slightly exceeds $\ln(9)$ because of charge fluctuations being active.) S_{imp} crosses $\ln(9)$ at slightly higher temperatures. Note that $T_{\text{orb}}^{\text{onset}}$ is induced by the DMFT self-consistency and is thus a lattice-related quantity, which might explain why $S_{\text{latt}}(T_{\text{orb}}^{\text{onset}}) = \ln(9)$. For $T < T_{\text{orb}}^{\text{onset}}$, $S_{\text{latt}}(T)$ and $S_{\text{imp}}(T)$ decrease continuously with decreasing temperature, reflecting the screening of orbital degrees of freedom, while spin degrees of freedom are still quasi-free. We observe that $S_{\text{latt}}(T)$ crosses $\ln(3)$ below $T_{\text{sp}}^{\text{onset}}$, while $S_{\text{imp}}(T)$ crosses $\ln(3)$ at about $T_{\text{sp}}^{\text{onset}}$. The value $\ln(3)$ is associated

	$ \omega^\pm $	$ \omega^* $	
	FL regime	NFL regime	
		crossover regime	HQP regime
	fully screened orbitals and spins	HQP screening: screened orbitals coupled to gradually screened spins	HQP formation: gradually screened orbitals coupled to quasi-free spins
$A(\epsilon_k, \omega)$	flat FL band with slope Z	s-shaped (step-like) feature at $\omega < 0$, kink at $\omega > 0$	extended steep HQP band (waterfall structure)
$A(\omega)$	sharp SU(2) Kondo resonance	↔	shoulder at $\omega < 0$ = SU(3) Kondo resonance
$\Sigma(\omega)$	$\text{Im}\Sigma(\omega) \propto \omega^2$ $[\text{Re}\Sigma(\omega) - \text{Re}\Sigma(0)] \propto \omega$	pronounced maximum in $\text{Re}\Sigma(\omega)$ at $\omega < 0$	shoulder in $-\text{Im}\Sigma(\omega)$ at $\omega < 0$
$\sigma(\omega)$	Drude peak	power law	shoulder = excess spectral weight

Figure 7.13 Overview of important SOS features in the 3HHM for $n_d = 2$ at $T = 0$. Features are described as functions of decreasing frequency.

with a spin triplet and an orbital singlet. For $T < T_{\text{FL}}$ we find FL behavior for both S_{latt} and S_{imp} , indicated by the dash-dotted grey fits, respectively [cf. Fig. 7.7(f)].

Overall, we clearly observe that the two-stage SOS screening process is a continuous process: the entropy continuously decreases with decreasing temperature, i.e. no stable NFL fixed point is reached in the system (this was already pointed out in the Supplementary of Ref. [SYvD⁺15]). Instead, we are faced with an intriguing complex crossover behavior (cf. Sec. 5.A).

7.4 Summary of main insights

We conclude by giving an overview of our main insights about Hund and Mott physics in the 3HHM and again contrast the most important signatures identifying Hund- and Mott-correlated metals.

At $T = 0$, finite J induces an intertwined two-stage SOS screening process in the 3HHM at $n_d = 2$, which results in three different screening regimes: a FL regime, a NFL crossover regime and a NFL HQP regime. The SOS features (cf. Fig. 7.13 for an overview) that occur within these regimes are generic and are found for both the metallic HS and the metallic MS, since SOS physics is essentially impurity physics [SYvD⁺15]. However, there is an important difference. In the HS, the SOS features are extended over a broad frequency range. The HQP regime reaches up to bare excitation scales and merges with a mixed-valence regime. In contrast, in the MS, the SOS features lie at very low energies and are very narrow, thus rather unimportant. The QPP is well-separated from the Hubbard bands.

In the HS, the SOS screening process is also reflected in the temperature dependence. We identify essentially the same screening regimes as for $T = 0$. Our major finding is the existence of robust HQPs, governing the NFL transport regime. We point out that we reproduced several signatures in the HS that have been found for Sr_2RuO_4 . In the MS, SOS features persist only at very low temperatures and are destroyed at intermediate temperatures by the formation of a pseudogap through the DMFT self-consistency. Thus HQPs do not survive in the MS. Important temperature-dependent signatures for the HS and the MS are summarized in Fig. 7.14.

		T_{FL}	$T_{\text{sp}}^{\text{onset}} \approx T_{\text{orb}}^{\text{cmp}} \approx T_{\text{orb}}^{\text{onset}} = T_{\text{M}}$	$T_{\text{orb}}^{\text{onset}}$	T
		NFL regime (HS versus MS)			
		crossover regime		pseudogap regime	
		FL regime	HQP screening: screened orbitals coupled to gradually screened spins	HQP formation: gradually screened orbitals coupled to quasi-free spins	pseudogap: HQPs do not survive
		fully screened orbitals and spins	orbitals and spins get screened simultaneously		
$A(\epsilon_k, \omega)$		s-shaped (step-like) feature is formed, HQP band is unaffected	robust HQP band pseudogap		
$A(\omega, T)$		two-tier structure of QPP is formed	resilient SU(3) Kondo resonance (stabilized by Hubbard bands) pseudogap		
$\Sigma(\omega, T)$		mimimum of $-\text{Im}\Sigma(\omega, T)$ at $\omega > 0$ (long-lived electron-like excitations)	no minimum (or maximim) close to the Fermi level in mixed valence regime minimum is replaced by a maximum		
$\Sigma(\omega = 0, T)$		small	rather flat plateau in the presence of a pseudogap, then strong decrease		
$\chi_0^{\text{sp}}(T)$	Pauli behavior	$T\chi_0^{\text{sp}}$ decreases	Curie behavior Curie behavior		
$\chi_0^{\text{orb}}(T)$	Pauli behavior	Pauli behavior decreases	$T\chi_0^{\text{orb}}$ increases with T Curie behavior		
$Z(T)$	constant	increases with T	saturates diverges		
$\rho_0(T)$	T^2	slight decrease strong decrease	slight decrease plateau in the presence of a pseudogap, then strong decrease		
$\mu_{\text{eff}}(T)$	constant	decreases from near half-filling: strong Fermi volume change	plateau-like increases strongly		
$\alpha(T)$	electron-like increase	minimum	maximum		

Figure 7.14 Overview of important Hund and Mott features in the temperature-dependence of various physical quantities. Hund-related features are marked yellow, Mott-related features are marked grey. Common features are on white background. Note that the temperature scale is only schematic. For instance, T_{M} in the MS is smaller than $T_{\text{sp}}^{\text{onset}}$ in the HS. Features are described as functions of decreasing temperature.

8 Conclusion and outlook

Until very recently mainly two classes of strongly correlated material systems dominated the research: heavy fermion materials (as realized in intermetallics with partially filled $4f$ or $5f$ orbitals) and Mott-Hubbard systems (as realized in transition metal oxides). Motivated by the discovery of high-temperature superconductivity in iron pnictides, a completely new class of correlated systems was identified about ten years ago: the Hund metals. They are now the subject of intensive theoretical and experimental study, and can be regarded as a new and hot field of enormous interest to the condensed matter theory community. Understanding the normal state properties of Hund metals, such as the iron pnictides, is key for understanding high-temperature superconductivity.

In this thesis we have used DMFT+NRG to investigate the normal state properties of the degenerate three-band Hubbard-Hund model (3HHM) with focus on $1/3$ filling, a minimal model with relevance for Hund metals. Our study has been based on the following key questions: What is the origin of strong correlations in the normal phase of Hund metals, Mottness or Hundness? And what are the decisive fingerprints of a Hund metal as opposed to a Mott-correlated metal?

This dissertation has three essential take home messages, one concerning our method, one concerning the physics of Hund metals and one concerning the impact of this work:

1. **fdmNRG is a powerful and competitive *real-frequency multi-band* impurity solver for DMFT.**

Its state-of-the art implementation is based on the QSpace tensor library [Wei12a] applied to matrix product states (MPS) [Sch11, Wei12b]. In contrast to commonly used continuous-time QMC solvers, fdmNRG works reliable at zero and finite temperatures, revealing the ground state of a system, while also capturing its evolution with increasing temperature. Moreover, fdmNRG provides high-quality spectral data directly on the real-frequency axis with an exponentially enhanced resolution around the Fermi level. Thus, spectral features are resolved down to the lowest relevant energy scale of the system, and can be compared to experiments, like ARPES, straightaway, i.e. without analytical continuation from Matsubara data. The availability of numerically exact real-frequency data considerably facilitates the physical interpretation of DMFT results. Further, eigenlevel renormalization group flow diagrams unambiguously reveal the relevant physics at all energy scales. So far, the fact that computational costs for NRG increase exponentially with the number of particle flavors has strongly limited the use of NRG as impurity solver for DMFT. However, fdmNRG allows to exploit all abelian and non-abelian symmetries of a given model Hamiltonian, tremendously improving the numerical efficiency in the case of high-symmetry models.

We have demonstrated the merits of the standard fdmNRG implementation (sNRG) as impurity solver for single-site DMFT by studying the 3HHM at zero and finite temperatures.

By explicitly exploiting its non-abelian symmetries, we have been able to successfully apply DMFT+NRG for the first time to a model with more than two bands [SYvD⁺15].

With a focus on low-symmetry multi-band impurity models, for instance models with broken orbital symmetry, we have analyzed interleaved NRG (iNRG), a recently-proposed scheme of interleaving the Wilson chains for different fermion flavors [MGWF⁺14], which dramatically increases the numerical efficiency. In Ref. [SMvDW16] we have applied iNRG to the single impurity Anderson model, the two-channel Kondo model, and a three-channel Anderson-Hund model, and have revealed that, strikingly, the accuracy of iNRG is comparable to sNRG. We thus demonstrated that iNRG is a viable and technically simple alternative to sNRG for high-symmetry models and, importantly, can be used to solve a range of lower-symmetry multi-band problems that are inaccessible to sNRG. This discovery opens the door to new applications of DMFT+NRG using iNRG as an impurity solver, such as lattice models with crystal-field splitting, cluster DMFT or realistic material simulations.

2. “Spin-orbital separation” (SOS) is a new Kondo-type two-stage screening route towards heavy masses in multi-orbital Hund metals, which is induced by sizeable Hund’s rule coupling, J , instead of strong Coulomb repulsion, U , as in Mott-correlated systems.

In an extensive real-frequency DMFT+sNRG study of the 3HHM [SYvD⁺15, DSH⁺18, SKWvD18], we have analyzed the nature and origin of strong correlations in the Hund-metal regime of the phase diagram, i.e. close to a filling of $1/3$, at moderate U and sizeable J . Based on this, we have identified defining signatures of Hund metals as opposed to Mott-correlated metals.

In Ref. [SYvD⁺15], we have conclusively established the existence of SOS, a two-stage screening process, in which orbital degrees of freedom are screened at much higher energies than spin degrees of freedom: $T_K^{\text{orb}} \gg T_K^{\text{sp}}$. Thus, the spin Kondo scale, T_K^{sp} , is strongly lowered, dramatically reducing the quasiparticle weight, i.e. enhancing the effective electron mass in the system. Below T_K^{sp} , FL behavior is found. Above T_K^{sp} and below the orbital Kondo scale, T_K^{orb} , an incoherent NFL regime with intriguing anomalous behavior exists. Since SOS also occurs in pure impurity calculations without DMFT self-consistency, it is clearly induced by Hund’s first rule, which aligns spins in different orbitals, and not by the DMFT self-consistency condition.

We remark that signatures of SOS in the 3HHM had first been revealed and argued to be related to anomalous power law behavior for the Matsubara self-energy in Ref. [YHK12], and had further been analyzed using perturbative scaling arguments in Ref. [AK15]. In agreement with this analysis in the Kondo regime of the 3HHM, we argue in Ref. [SKWvD18] that SOS is a non-trivial Kondo-type screening process, in which orbital and spin degrees of freedom are explicitly coupled: below T_K^{orb} , the orbital degrees of freedom form an orbital singlet through the formation of a large effective Hund’s-coupling-induced $3/2$ spin – *including* a bath spin degree of freedom; and below T_K^{sp} , the latter is fully screened by the three bath channels of the 3HHM. Importantly, in the 3HHM, the ratio $T_K^{\text{orb}}/T_K^{\text{sp}}$ is bounded above. Thus, its NFL regime is rather narrow and can be regarded as a crossover regime from an underlying intermediate NFL fixed point to its low-energy FL fixed point, as visible in renormalization group flow diagrams. Indeed, a NRG study of the three-orbital Kondo model [WSL⁺19] revealed the nature of this NFL fixed point, by tuning T_K^{orb} and T_K^{sp} such that the SOS energy window is very wide. In a nutshell, the NFL regime is governed by screened orbitals coupled to atomic-like Hund’s-coupling-induced large spins.

At zero temperature, clear signatures of SOS include: (i) a low-frequency FL regime with a narrow “needle”-formed SU(2) Kondo peak in the local density of states, a low-frequency Landau QP band with a small slope given by Z in ARPES spectra, FL scaling of the self-energy, a Drude peak in the optical conductivity; (ii) a NFL crossover regime signalling the deviation from FL behavior characterized by a step-like feature in the dispersion at $\omega < 0$ and a kink at $\omega > 0$ [accordingly, $\text{Re}\Sigma(\omega < 0)$ exhibits a pronounced maximum]; and (iii) an intermediate-frequency “Hund quasiparticle” (HQP) NFL regime with a SU(3) Kondo resonance in the local density of states, also identifiable as excess spectral weight in the optical conductivity and as a resilient slightly particle-hole asymmetric steep “HQP band” in ARPES spectra (waterfall structure), which is extended over a large frequency range, where the scattering rate is only weakly energy dependent [e.g. there is a shoulder in $\text{Im}\Sigma(\omega < 0)$]. We remark that the particle-hole asymmetry of the 3HHM leads to two distinct FL scales in frequency space and to very different features in the SOS regime at negative and positive frequencies (e.g in ARPES spectra, but not in the particle-hole symmetric dynamical susceptibilities).

The incoherent SOS frequency regime shows apparent power-law behavior with different fractional exponents in the imaginary part of the orbital and spin susceptibility, the optical conductivity, and in a limited sense also in the imaginary part of the self-energy. The fractional exponent of the imaginary part of the spin susceptibility (-1.2) has only recently been discussed in the context of an Eliashberg-based superconducting theory [LCMK18, WAC19], suggesting that the pairing interaction between fermions in iron-based HTSCs is mediated by quasi-local spin excitations described by a bosonic propagator with exponent $\gamma \approx 1.2$. In this picture, resilient incoherent HQPs, i.e. quasi-itinerant orbital degrees of freedom coupled to atomic-like (almost unscreened) spins – which have been revealed and intensively discussed as a major result of this thesis – would be the key ingredient of high-temperature superconductivity: HQPs would be the fabric and its spin degrees of freedom (in terms of incoherent local spin fluctuations) the glue of high-temperature superconductivity in Hund metals.

In Ref. [SKWvD18], we have demonstrated that the origin of strong correlations in the Hund-metal regime of the 3HHM phase diagram is Hundness, i.e., there, the SOS screening process is the key player to induce heavy masses and strong correlation effects.

Based on our model study and corroborated by a realistic simulation of Sr_2RuO_4 [DSH⁺18], we suggest the following definition of a Hund metal. A Hund metal lies far from any MIT phase boundary. Strong correlations are induced by two stage SOS Kondo-type screening, which leads to the localization of spins rather than charges. The incoherent SOS regime is extended over a broad range of energies, reaching up to bare excitation scales. In the model, at high frequencies, the SU(3) Kondo resonance (shoulder) merges with the Hubbard bands. At very low temperatures, the local density of states exhibits a two-tier quasiparticle peak on top of a broad incoherent background. The SOS screening process also governs the temperature dependence of Hund metals, up to highest temperatures. Most importantly, we argue that the nature of the incoherent transport regime is governed by resilient HQPs, while the FL regime is described in terms of Landau QPs. In Ref. [DSH⁺18], we have identified two different temperature scales for the onset of orbital and spin screening in Hund metals, $T_{\text{orb}}^{\text{onset}}$ and $T_{\text{sp}}^{\text{onset}}$, respectively. For $T_{\text{orb}}^{\text{onset}} > T > T_{\text{sp}}^{\text{onset}}$, HQPs dominate the high temperature physics and lead to a Curie-like static spin susceptibility (while the static orbital susceptibility is a decreasing function of temperature) and a resilient QPP (without substructure) in the local density of states. In the model, we find a robust HQP band in ARPES spectra, an additional HQP plateau in $Z(T)$, a rather flat (electron-like) scattering rate, a linear resistivity exceeding the MIR limit, and an inflated Fermi volume. At very high temperatures, mixed-valence physics additionally comes into play. Due to the special SOS screening process, the spins

can only get screened as soon as the orbitals are fully screened at $T_{\text{orb}}^{\text{cmp}}$, thus $T_{\text{sp}}^{\text{onset}} \approx T_{\text{orb}}^{\text{cmp}}$. For $T_{\text{sp}}^{\text{onset}} > T > T_{\text{FL}}$ also the spins get gradually screened, eventually resulting in the full screening of both degrees of freedom and thus in a FL below T_{FL} . The spin screening is signalled by the formation of a step-like feature in ARPES spectra, while the completion of orbital screening is characterized by a Pauli-like orbital susceptibility. In this regime, the thermopower has a minimum, as observed in experiments for ruthenates [MG16].

In contrast, Mott-correlated metals (with $\sim 1/3$ filling such as V_2O_3 [DSH⁺18]) are close to the MIT phase boundary. Thus, at zero temperature, both $T_{\text{K}}^{\text{orb}}$ (and T_{K}^{sp}) are strongly reduced compared to bare excitation scales and the SOS regime is very small, i.e. a narrow QPP exists between well-separated pronounced Hubbard bands. With increasing temperature, SOS features (and HQPs) only survive at very low temperatures (and at very low frequencies), whereas the behavior at higher temperatures is fully governed by classical Mott physics (as known from the one-band Hubbard model): the DMFT self-consistency condition opens up a pseudogap in the local spectrum by localizing the charges. Conversely, with decreasing temperature, spin and orbital degrees of freedom get screened simultaneously at the temperature scale, $T_{\text{M}} = T_{\text{orb}}^{\text{onset}} \approx T_{\text{sp}}^{\text{onset}}$, with the onset of a Kondo resonance, driven by DMFT.

In sum, we shed light on two qualitatively different screening routes from the atomic degrees of freedom to the emerging heavy QPs in strongly correlated systems, driven by Hundness or Mottness, and corroborated that Hundness, i.e. SOS Kondo-type screening, dominates the anomalous physics of Hund metals in terms of resilient HQPs.

3. This dissertation has paved the way to a broad application of DMFT+NRG.

First of all, we point out that even the simplest three-band Hund model, studied here, is a huge playground in itself regarding the richness of its physics. The interplay of two different types of degrees of freedom together with the particle-hole asymmetry of the 3HHM still holds various puzzles to be solved. In particular, the intermediate filling regime between $1/3$ and half-filling has not been fully investigated yet and a temperature study might be worthwhile. But also the investigation of more complex models is now possible using iNRG as impurity solver. For instance, the fate of SOS in the presence of broken orbital symmetry should be analyzed in the 3HHM with crystal-field splitting. In this regard, also orbital differentiation and orbital-selective Mott physics is of great interest. Furthermore, DMFT+iNRG can be applied to study realistic models using DFT band structures.

Based on this dissertation, DMFT+NRG has panned out in our Munich theoretical solid state physics group, led by Prof. Jan von Delft, and many exciting projects have evolved. The fdmNRG solver has been advanced further by the implementation of an adaptive broadening scheme [LW16], increasing the resolution of spectral data at large frequencies. Additionally, also non-diagonal hybridization functions can be handled now. Current DMFT+NRG follow-up projects include the investigation of models with spin-orbit coupling (S.-S. Lee, Y. Wang, G. Del Bimbo), a study of orbital-selective Mott physics in a three-band Hund model with two degenerate bands and one band separated by crystal-field splitting (F. Kugler), realistic simulations of Sr_2RuO_4 [KLK⁺19] (F. Kugler), two-site cluster DMFT+NRG [Gle19] (A. Gleis), the calculation of two-particle correlators (four-point functions), such as the pair susceptibility to monitor superconductivity in multi-band Hund models (S.-S. Lee), but also a thorough NRG study of the three-orbital Kondo model [WSL⁺19] with relevance for Hund-metal physics (E. Walter). As a long-term goal, the development of a well-documented open-source DMFT+fdmNRG package would be highly desirable.

Last but not least, let us return to the picture of high-temperature superconductivity, that P. W. Anderson has drawn in Ref. [And07] for cuprates to point out the importance of strong electronic correlations: a mammoth (U) and an elephant (J) sit in a refrigerator together with a little mouse (bosonic glue). In this thesis, we have demonstrated the major role of the elephant in the normal state of Hund metals. However, we can just speculate about its role in the very controversially debated mechanism of high-temperature superconductivity in iron-based HTSCs – until someone eventually opens the door of this refrigerator.

List of Figures

- 1.1 Schematic sketch of the n_d - U phase diagram for the 3HHM at finite J . We only show half of the phase diagram, as it is symmetric with respect to half-filling. The shading reflects the quasiparticle weight Z . Darker regions (large Z) indicate good metallic, lighter regions (small Z) bad-metallic behavior. The black bars mark Mott insulating phases. At all integer fillings, a MIT occurs above a (different) critical interaction strength, U_c . Interestingly, an extended light region exists also at moderate $U \ll U_c^{(2)}$ around $n_d = 2$ (and reaches to $n_d = 3$). In this “Hund-metal regime” (hatched area), where most Hund metals can be placed [dMMG11], strong electronic correlations might either be induced by Hundness, (i) the presence of sizeable J , or Mottness, (ii) the influence of the MIT at $n_d = 2$ (blue arrow), and (iii) the influence of the MIT at $n_d = 3$ (red arrow), or a combination of these scenarios. This figure is taken from Ref. [SKWvD18]. 9
- 2.1 (a) Within DMFT an interacting lattice model is mapped self-consistently onto a quantum impurity model (here, illustrated for a one-band model). (b) DMFT self-consistency loop with NRG as impurity solver (black box). Solving the impurity model is computationally the most costly step of the iterative mapping process, which is indicated by a thick line in the triangle. (c) Caley tree for $z = 3$. The Caley tree for $z \rightarrow \infty$ is the Bethe lattice with semi-circular density of states. This figure is adapted from Ref. [Sta13]. 21
- 2.2 NRG in a nutshell. (a) Sketch of a self-consistently determined (one-band) quantum impurity model with the impurity (red) coupled (bright blue) to a non-interacting continuous bath (dark blue). (b) Within NRG the bath is discretized logarithmically with discretization parameter, $\Lambda > 1$. Each bath interval is represented by one bath state (blue circles). (c) The discretized model is mapped onto a one-dimensional semi-infinite “Wilson chain”, with the interacting impurity site coupled to one end, and nearest-neighbor hopping matrix elements, t_n , decaying logarithmically down the chain. (d) An iterative RG procedure is applied, in which the Wilson chain Hamiltonian is successively diagonalized. At each iteration, N , high energy eigenstates (grey) are discarded and low energy states (red) are kept. (e) The resulting eigenstates can be formulated in matrix-product-state (MPS) language. (f) full-density-matrix (fdm)NRG allows to compute highly accurate spectral functions, here exemplified for the symmetric 1HM, Eq. (1.1), with $U/D = 2$, $T = 0$, $\Lambda = 2$, and $N_z = 4$ ($D = 2t$). Raw spectral data, $A_{\text{raw}}/|\omega|$ is plotted in grey, the smoothed spectral function in blue, and an improved spectral function [cf. Sec. 3.3] in red. (g) Renormalization group flow diagram for the symmetric SIAM ($U = 0.8$, $\Gamma = 0.02$, $\Lambda = 2$, $D_{\text{NRG}} = 1$) plotted for even iterations. The red bar marks the spin Kondo scale $N(T_K)$. This figure is adapted from Ref. [Sta13]. 23

- 2.3 (a) Matsubara self-energy, $\text{Im } \Sigma(i\omega_n)$, plotted on a logarithmic imaginary-frequency scale for different temperatures for the 3HHM with $U = 6.5$, and $J = 2$. The inset shows the same data on a linear scale. (b) Corresponding spectral functions, $A(\omega)$, plotted versus linearly scaled *real* frequencies. . . . 28
- 3.1 (a) The imaginary part of the self-energy, $\text{Im } \Sigma(\omega)$, and (b) the optical conductivity, $\sigma(\omega)$, for the 3HHM with $U = 7.5$, $J = 2$ at $n_d = 2$ and $T = 0$. $\sigma(\omega)$ is calculated with Eq. (3.15) using three different input functions for $\text{Im } \Sigma(\omega)$. The black curve is the original DMFT+NRG result of $\text{Im } \Sigma(\omega)$, the blue curve is the shifted result, $\text{Im } \Sigma_{\text{shift}}(\omega)$, and the red curve is an improved function (see text). The color scheme for $\sigma(\omega)$ in (b) follows the color scheme of (a). Dashed grey fits comply with FL behavior. Solid (dashed) vertical lines mark the spin (orbital) Kondo scale. 71
- 3.2 We illustrate the computation of $S_{\text{latt}}(T)$ for the 1HM with $U = 4$ and $\mu = -\frac{U}{2}$. (a,b) The calculation of \mathcal{F}_{cor} , Eq. (3.32), is divided into several steps. We plotted intermediate results for (a) $T = 0$ and (b) $T = 0.5$. (c) We also show spectral functions for several temperatures. These temperatures are marked by vertical dashed lines in (d) using the color code of (c). (d) The final result, S_{latt} , as well as its components S_{imp} and S_{cor} are plotted as functions of temperature. Further, $\mathcal{F}_{\text{cor}}(T)$, the spectral function $A(0, T)$ at zero frequency and its negative derivative are shown. In principle, a plateau at $\ln(2)$ is expected for $S_{\text{latt}}(T)$ and $S_{\text{imp}}(T)$ in the local moment regime for two spin degrees of freedom, $\ln(4)$ should be approached in the free orbital regime as charge fluctuations are included there. However, here, the plateau at $\ln(2)$ is replaced by a transition through $\ln(2)$ above the Kondo temperature T_K (vertical black line) for S_{imp} , because T_K is too near to the bare bandwidth of the model. $S_{\text{latt}}(T)$ exhibits an unphysical negative slope below about $\ln(2)$ (see text for details). 78
- 4.1 (a-f) Absence of SOS ($T_K^{\text{orb}} \approx T_K^{\text{sp}}$) in real-frequency ground-state correlators for (left column) the two-channel SCAHM (2HHM) and (right column) the two-channel IAHM (2AHM) with $n_d = 1$. Panels are analogous to Fig. 3 of Ref. [SYvD⁺15] in Sec. 4.2. (a,d) The local spectral functions, (b,e) the local self-energy, and (c,f) the spin and orbital susceptibilities, χ_{sp}'' (solid) and χ_{orb}'' (dashed). We use a logarithmic frequency scale, with thick (thin) lines for $\omega < 0$ ($\omega > 0$). Insets show data on a linear scale. In all panels, solid (dashed) vertical lines mark the spin (orbital) Kondo scale, T_K^{sp} (T_K^{orb}). Grey guide-to-the eye lines indicate FL power laws (solid). Inset to (f): Kondo scales T_K^{sp} (solid) and T_K^{orb} (dashed) for the IAHM, plotted as function of n_d . (g) and (h) show NRG eigenlevel flow diagrams for the SCAHM and IAHM of panels (a-c) and (d-f), respectively: the rescaled energies of the lowest-lying eigenmultiplets of a Wilson chain of (even) length k are plotted versus its characteristic level spacing $\omega_k \propto \Lambda^{-k/2}$. For each multiplet, the number close to the line gives its full state space degeneracy, Q its symmetry labels. . . . 100

- 4.2 The rescaled energies of the lowest-lying eigenmultiplets (grey lines) are plotted versus (a,c,e) the particle number, q , and (b,d,f) the spin quantum number, $2S$, for an even NRG iteration (as this has a unique ground state) in the low-energy FL fixed-point regime of (a,b) the 3AHM, (c,d) the 3HHM, and (e,f) the 2AHM at $n_d = N_c - 1$. (a,b) corresponds to the NRG flow diagram in Fig. 3(h) and (c,d) to Fig. 3(g) of Ref. [SYvD⁺15], (e,f) corresponds to Fig. 4.1. Each multiplet is labeled by its full state space degeneracy. Colored labels indicate colored multiplets of the respective NRG flow diagram. 101
- 5.1 (a,b) Imaginary part of the Matsubara self-energy, $\text{Im} \Sigma(i\omega_n)$, and (c,d) imaginary part of the orbital (dashed) and spin (solid) susceptibility, $\chi''(\omega)$, plotted versus (a,b) ω and (c,d) ω/T_K^{SP} for (a,c) various values of J at fixed $\Delta_b = 3.5$ and for (b,d) various values of U at fixed J . Solid thin grey guide-to-the-eye lines indicate FL behavior, dashed thin and thick grey guide-to-the-eye lines demonstrate fractional power-law behavior in the SOS regime for the orbital and spin susceptibility, respectively. 152
- 5.2 The chemical potential, $\mu_3 - \mu$, plotted versus the filling, $3 - n_d$. μ_3 is defined in Sec. 2.6.2. of Ref. [SKWvD18] (cf. Sec. 5.2). The red curves mark results for U close to $U \geq U_{c2}$ with $U_{c2} \approx 4.1$. The curves for $4.2 < U < 4.6$ seem to develop a very flat slope, κ_{el}^{-1} , for $n_d > 3 - 0.15$ 154
- 7.1 (a,b) The imaginary part, $\text{Im} \Sigma(\omega)$, and (c,d) the real part, $\text{Re} \Sigma(\omega)$, of the self-energy; (e,f) the local spectral function, $A(\omega)$; (g,h) the imaginary part, $\chi''(\omega)$, and (i,j) the real part, $\chi'(\omega)$, of the spin (solid) and orbital (dashed) susceptibility are plotted versus frequency for $\Delta_b = 3.5$, $J = 2$, and $T = 0$. Left panels are zooms into the FL regime, whereas their insets show the quantities on a large frequency range. The SOS regime is presented in the right panels. Dashed red fits reveal FL behavior for $\text{Im} \Sigma(\omega)$, $\text{Re} \Sigma(\omega)$, and $A(\omega)$ in the asymmetric range, $\omega^- < \omega < \omega^+$, with $\omega^+ = \frac{1}{3}\omega^-$ (indicated by vertical dash-dotted red lines) and for the orbital and spin susceptibility in the symmetric range, $|\omega| < \omega^+$. The vertical dashed yellow lines represent the energy scale, $|\omega^*|$, of the maximum of $\chi'_{\text{orb}}(\omega)$, which is approximately equal to the energy scale of the maximum of $-\text{Im} \Sigma(\omega)$ in (b). The vertical solid yellow lines denote the energy scale of the maximum in $\text{Re} \Sigma(\omega)$ at $\omega < 0$ in (b). For orientation these vertical dashed and solid yellow lines are repeated for $\omega > 0$. Filled dots and open squares mark the orbital and spin Kondo scales, respectively. The grey area in (a) indicates the systematic error of $\text{Im} \Sigma(\omega)$ (cf. Sec. 3.2 for details). 176
- 7.2 Refined schematic depiction of the two-stage screening process of SOS at filling $n_d = 2$ (based on Fig. 13 of Ref. [SKWvD18]). First the orbital degrees of freedom start to be screened at the orbital Kondo scale, T_K^{orb} . This involves the formation of an orbital singlet by building a large effective Hund's-coupling induced 3/2 spin including a bath spin degree of freedom. $|\omega^*|$ marks the completion of orbital screening. Below $|\omega^*|$ the 3/2 spin is gradually screened by the three effective channels of the 3HHM. Well below the spin Kondo scale, T_K^{SP} , full screening of both orbital and spin degrees of freedom is reached at the FL scale $|\omega^\pm|$, below which FL behavior occurs in frequency dependent quantities. Note that the scale $|\omega^*|$ is derived from $\chi'_{\text{orb}}(\omega)$, a particle-hole symmetric quantity, while in general the system is particle-hole asymmetric. 178

- 7.3 (a,c,e-h) The structure factor, $A(\epsilon_k, \omega)$, (b,d) the dispersion relation, $E(\epsilon_k)$, (i) the spectral function, $A(\omega)$, (j) the real part, $\text{Re} \Sigma(\omega)$, and (k) the imaginary part, $\text{Im} \Sigma(\omega)$, of the self-energy, all plotted for various temperatures for the same parameters, $\Delta_b = 3.5$ and $J = 2$, as in Fig. 7.1. (a,c,e-h) The colored curves highlight the dispersion relation, $E(\epsilon_k)$, the white curves show the alternative definition of the dispersion relation, $E^*(\omega)$, respectively. Panels (a,b) are zooms of panels (c,d). The FL regime, $\omega^- < \omega < \omega^+$, is marked by dash-dotted red (a,b) horizontal and (i-k) vertical lines. The thick dashed red line in panel (a) denotes FL behavior of the low-energy dispersion relation. Its slope, $Z = m/m^*$, reflects the strength of local correlations. The solid yellow (b) horizontal and (i-k) vertical lines denote the energy scale of the maximum in $\text{Re} \Sigma(\omega < 0)$ at $T = 0$ [cf. Fig. 7.1(d)]. The dashed yellow (a-c) horizontal and (i-k) vertical lines show $\pm\omega^*$ 180
- 7.4 Same quantities as in Fig. 7.3 for $\Delta_b = 3.5$ and $J = 0$. (h) Note that the difference in $\text{Re} \Sigma(\omega = 0)$ between $T = 0$ and $T > 0$ arises from a 4% deviation of $n_d(T = 0)$ from $n_d = 2$. The FL scales are not shown and $\pm\omega^*$ does not exist for $J = 0$ 181
- 7.5 (a,b) The optical conductivity, $\sigma(\omega)$, and the kinetic energy, $K(\Omega)$, are plotted for various temperatures on (a,c) a linear and (b,d) a logarithmic frequency scale. We used the same parameters, $\Delta_b = 3.5$ and $J = 2$, as in Fig. 7.1 and Fig. 7.3. In addition, data for $\Delta_b = 3.5$ and $J = 0$ (at $T = 0.15$) is shown in black. (b,d) $|\omega^\pm|$, below which FL behavior should set in, is marked by vertical dash-dotted red lines. The vertical solid yellow lines denote the energy scale of the maximum in $\text{Re} \Sigma(\omega < 0)$ at $T = 0$ [cf. Fig. 7.1(d)]. The vertical dashed yellow lines show $|\omega^*|$ 183
- 7.6 (a) The zero-temperature phase diagram of the 3HHM has three phases in the J - U -plane: a metallic phase (squares), a coexistence region (circles), and an insulating phase (triangles). These are separated by two phase transition lines U_{c1} (solid red curve) and U_{c2} (dashed black curve), respectively. The color intensity of the symbols in the metallic and the coexistence region indicates the value of $Z \in [0, 1]$: the lower Z the more faded is the red color. The phase diagram is adapted from Ref. [SKWvD18]. In this Chapter we present temperature-dependent results for a Hund system (HS) far away from the U_{c1} phase transition line deep in the metallic state (cross), a Mott system (MS) near the transition (asterisk), an intermediate system (IS) having both Hund and Mott features (open diamond), and a weakly correlated system (WS) with $J = 0$ far from U_{c1} (open square). (b) The T - U phase diagram of the 3HHM for $J = 1$ is characterized by a metallic phase (red squares), a coexistence phase (blue circles), and an insulating phase (black triangles) in accordance with (a). Big open symbols mark DMFT+QMC results kindly provided by Zhiping Yin. Small filled symbols mark our DMFT+NRG results, for which we have performed benchmarks with the DMFT+QMC results for $T > 0$ to check the accuracy of our finite-temperature data. $U_{c1}(T)$ (solid red curve) and $U_{c2}(T)$ (dashed black curve) are rough estimates only. The U_{c1} line for the DMFT+NRG data is slightly shifted to larger U values as compared with DMFT+QMC. We assume that this is caused by the fact that the Hubbard bands are slightly overbroadened in DMFT+NRG such that the closing of the insulating gap occurs already at slightly higher U 184
- 7.7 Same quantities as in Fig. 7.3 for a Hund system (HS) with parameters $\Delta_b = 1$ and $J = 1$ 185

- 7.8 Same quantities as in Fig. 7.3 for a Mott system (MS) with parameters $\Delta_b = 4.5$ and $J = 1$ 186
- 7.9 The static local orbital (dashed) and spin (solid) susceptibility, (a,b,e,f) $T\chi_0^{\text{orb,sp}}$ and (c,d,g,h) $\chi_0^{\text{orb,sp}}$, are plotted versus temperature for the MS (black), the HS (yellow), the IS (red), and the WS (blue). In addition, the quasiparticle weight (dotted), $Z(T)$, is shown in (a,b,e,f). The squares mark the onset of orbital screening, $T_{\text{orb}}^{\text{onset}}$, below which $T\chi_0^{\text{orb}}$ deviates from Curie behavior. Note that $Z(T)$ diverges for $T > T_{\text{orb}}^{\text{onset}}$. The triangles mark the maxima of χ_0^{orb} and also signal the onset of spin screening, $T_{\text{sp}}^{\text{onset}}$, below which $T\chi_0^{\text{sp}}$ deviates from Curie-like behavior. The crosses denote the FL scale, T_{FL} , below which FL behavior is found. In the MS, we observe that $T_{\text{sp}}^{\text{onset}} \approx T_{\text{orb}}^{\text{onset}} = T_{\text{M}}$. In the HS, we find $T_{\text{orb}}^{\text{onset}} \gg T_{\text{sp}}^{\text{onset}}$, as discussed in Ref. [DSH⁺18]. 189
- 7.10 (a) Schematic sketch of different temperature regimes in a Hund metal. For $T > T_{\text{FL}}$, the HS is a NFL up to temperatures in the order of bare energy scales, where also mixed-valence physics becomes important. The NFL regime reflects the complex SOS screening process of Fig. 7.2. First orbitals get screened with decreasing temperature for $T_{\text{orb}}^{\text{onset}} > T > T_{\text{orb}}^{\text{cmp}}$. In this regime transport is governed by HQPs which are characterized by gradually screened orbitals coupled to quasi-free spins. Only when the orbital screening process is completed spins get screened below $T_{\text{sp}}^{\text{onset}} \approx T_{\text{orb}}^{\text{cmp}}$, i.e., in this regime, the HQPs get gradually dressed to form heavier Landau QPs. For $T < T_{\text{FL}} = T_{\text{sp}}^{\text{cmp}}$, the HS is a FL and both orbital and spin degrees of freedom are fully screened. (b) Schematic sketch of different temperature regimes in a multi-orbital Mott-correlated metal. In a MS, a pseudogap governs the physics in an extended temperature regime, $T > T_{\text{sp}}^{\text{onset}} \approx T_{\text{orb}}^{\text{onset}} = T_{\text{M}}$. For temperatures below T_{M} , both orbital and spin degrees of freedom get screened simultaneously with the onset of a Kondo resonance, which is driven by the DMFT-self-consistency condition. The NFL regime for $T_{\text{M}} > T > T_{\text{FL}}$ is followed by a FL regime for very small $T < T_{\text{FL}} = T_{\text{sp}}^{\text{cmp}} \approx T_{\text{orb}}^{\text{cmp}}$, where both orbital and spin degrees of freedom are fully screened. 190
- 7.11 (a,b) The quasiparticle weight, $Z/Z(0)$, (c,d) the local density of states at the Fermi level, $A(\omega = 0)$, (e,f) the scattering rate at the Fermi level, $\text{Im} \Sigma(\omega = 0)$, (g,h) the coherence scale, Γ^*/T , and (i,j) the resistivity, ρ , are plotted as functions of temperature on (left panels) a linear and on (right panels) a logarithmic scale for the MS (black), the HS (yellow), the IS (red) and the WS (blue). Symbols are defined as in Fig. 7.9. (f,j) The dashed grey guide-to-the-eye lines indicate FL behavior. (g,h) The horizontal dashed grey lines mark $\Gamma^*/T^* = 1$. (i,j) The horizontal dashed (solid) grey lines mark the MIR limit defined via $k_{\text{FLmin}} \approx 2\pi$ ($k_{\text{FLmin}} \approx 1$). 192
- 7.12 (a,b) The effective chemical potential, μ_{eff} , (c,d) the thermopower, α , and (e,f) the impurity contribution to the entropy (dashed), S_{imp} , and the lattice entropy (solid), S_{latt} , plotted as functions of temperature (left panels) on a linear and (right panels) on a logarithmic scale for the MS (black), the HS (yellow), the IS (red) and the WS (blue). Symbols are defined as in Fig. 7.9. (f) The grey dash-dotted curves indicate FL behavior for S_{imp} and S_{latt} , respectively. 194
- 7.13 Overview of important SOS features in the 3HHM for $n_d = 2$ at $T = 0$. Features are described as functions of decreasing frequency. 196

-
- 7.14 Overview of important Hund and Mott features in the temperature-dependence of various physical quantities. Hund-related features are marked yellow, Mott-related features are marked grey. Common features are on white background. Note that the temperature scale is only schematic. For instance, T_M in the MS is smaller than T_{sp}^{onset} in the HS. Features are described as functions of decreasing temperature. 197

Bibliography

- [ABM⁺10] Markus Aichhorn, Silke Biermann, Takashi Miyake, Antoine Georges, and Masatoshi Imada, *Theoretical evidence for strong correlations and incoherent metallic state in FeSe*, Phys. Rev. B **82** (2010), 064504. See page: [1](#)
- [AK15] Camille Aron and Gabriel Kotliar, *Analytic theory of Hund’s metals: A renormalization group perspective*, Phys. Rev. B **91** (2015), 041110. See pages: [5](#), [6](#), [8](#), [11](#), [14](#), [15](#), [86](#), [87](#), [103](#), [179](#), and [200](#)
- [And07] Philip W. Anderson, *Is there glue in cuprate superconductors?*, Science **316** (2007), no. 5832, 1705–1707. See pages: [1](#), [16](#), and [203](#)
- [APV⁺09] Markus Aichhorn, Leonid Pourovskii, Veronica Vildosola, Michel Ferrero, Olivier Parcollet, Takashi Miyake, Antoine Georges, and Silke Biermann, *Dynamical mean-field theory within an augmented plane-wave framework: Assessing electronic correlations in the iron pnictide LaFeAsO*, Phys. Rev. B **80** (2009), 085101. See page: [7](#)
- [AS05] Frithjof B. Anders and Avraham Schiller, *Real-time dynamics in quantum-impurity systems: A time-dependent numerical renormalization-group approach*, Phys. Rev. Lett. **95** (2005), no. 19, 196801. See page: [26](#)
- [AS06] ———, *Spin precession and real-time dynamics in the Kondo model: Time-dependent numerical renormalization-group study*, Phys. Rev. B **74** (2006), 245113. See page: [26](#)
- [AT13] S. Akhanejee and A. M. Tsvelik, *Analytically tractable model of bad metals*, Phys. Rev. B **87** (2013), 195137. See page: [86](#)
- [BCP08] R. Bulla, T. A. Costi, and Th. Pruschke, *Numerical renormalization group method for quantum impurity systems*, Rev. Mod. Phys. **80** (2008), 395–450. See pages: [9](#), [22](#), [27](#), and [75](#)
- [BCS57] J. Bardeen, L. N. Cooper, and J. R. Schrieffer, *Theory of superconductivity*, Phys. Rev. **108** (1957), 1175–1204. See page: [1](#)
- [BCV01] R. Bulla, T. A. Costi, and D. Vollhardt, *Finite-temperature numerical renormalization group study of the Mott transition*, Phys. Rev. B **64** (2001), 045103. See page: [9](#)
- [BCV10] E. Bascones, M. J. Calderón, and B. Valenzuela, *Low magnetization and anisotropy in the antiferromagnetic state of undoped iron pnictides*, Phys. Rev. Lett. **104** (2010), 227201. See page: [13](#)
- [BF11] H. Bruus and K. Flensberg, *Many-body quantum theory in condensed matter physics*, 8. ed., Oxford University Press, Oxford, 2011. See pages: [77](#) and [79](#)

- [BHP98] Ralf Bulla, Alex C. Hewson, and Thomas Pruschke, *Numerical renormalization group calculations for the self-energy of the impurity Anderson model*, J. Phys.: Condens. Matter **10** (1998), 8365. See pages: [9](#), [20](#), [22](#), [27](#), and [70](#)
- [BHZ97] R. Bulla, A. C. Hewson, and G.-M. Zhang, *Low-energy fixed points of the σ - τ and the $O(3)$ symmetric Anderson models*, Phys. Rev. B **56** (1997), 11721–11740. See page: [24](#)
- [BLS⁺17] B. Bruognolo, N.-O. Linden, F. Schwarz, S.-S. B. Lee, K. Stadler, A. Weichselbaum, M. Vojta, F. B. Anders, and J. von Delft, *Open Wilson chains for quantum impurity models: Keeping track of all bath modes*, Phys. Rev. B **95** (2017), 121115. See pages: [17](#) and [49](#)
- [BM86] J. G. Bednorz and K. A. Müller, *Possible high T_c superconductivity in the Ba-La-Cu-O system*, Zeitschrift für Physik B Condensed Matter **64** (1986), no. 2, 189–19. See page: [1](#)
- [BPN⁺08] L. Baldassarre, A. Perucchi, D. Nicoletti, A. Toschi, G. Sangiovanni, K. Held, M. Capone, M. Ortolani, L. Malavasi, M. Marsi, P. Metcalf, P. Postorino, and S. Lupi, *Quasiparticle evolution and pseudogap formation in V_2O_3 : An infrared spectroscopy study*, Phys. Rev. B **77** (2008), 113107. See page: [156](#)
- [Bul99] R. Bulla, *Zero temperature metal-insulator transition in the infinite-dimensional Hubbard model*, Phys. Rev. Lett. **83** (1999), 136–139. See pages: [9](#) and [22](#)
- [BVC12] E. Bascones, B. Valenzuela, and M. J. Calderón, *Orbital differentiation and the role of orbital ordering in the magnetic state of Fe superconductors*, Phys. Rev. B **86** (2012), 174508. See pages: [10](#) and [13](#)
- [BVC16] Elena Bascones, Belén Valenzuela, and Maria José Calderón, *Magnetic interactions in iron superconductors: A review*, Comptes Rendus Physique **17** (2016), no. 1, 36 – 59. See pages: [5](#) and [8](#)
- [BWG⁺14] Benedikt Bruognolo, Andreas Weichselbaum, Cheng Guo, Jan von Delft, Imke Schneider, and Matthias Vojta, *Two-bath spin-boson model: Phase diagram and critical properties*, Phys. Rev. B **90** (2014), 245130. See page: [49](#)
- [BWM⁺15] Karsten Balzer, F. Alexander Wolf, Ian P. McCulloch, Philipp Werner, and Martin Eckstein, *Nonthermal melting of Néel order in the Hubbard model*, Phys. Rev. X **5** (2015), 031039. See pages: [16](#) and [29](#)
- [BZE⁺10] S. V. Borisenko, V. B. Zabolotnyy, D. V. Evtushinsky, T. K. Kim, I. V. Morozov, A. N. Yaresko, A. A. Kordyuk, G. Behr, A. Vasiliev, R. Follath, and B. Büchner, *Superconductivity without nesting in LiFeAs*, Phys. Rev. Lett. **105** (2010), 067002. See page: [2](#)
- [BZT⁺17] Daniel Bauernfeind, Manuel Zingl, Robert Triebl, Markus Aichhorn, and Hans Gerd Evertz, *Fork tensor-product states: Efficient multiorbital real-time DMFT solver*, Phys. Rev. X **7** (2017), 031013. See page: [16](#)
- [CK94] Michel Caffarel and Werner Krauth, *Exact diagonalization approach to correlated fermions in infinite dimensions: Mott transition and superconductivity*, Phys. Rev. Lett. **72** (1994), 1545–1548. See page: [15](#)

- [dM11] Luca de' Medici, *Hund's coupling and its key role in tuning multiorbital correlations*, Phys. Rev. B **83** (2011), 205112. See pages: [10](#), [11](#), [12](#), [13](#), and [14](#)
- [dM17] ———, *Hund's induced Fermi-liquid instabilities and enhanced quasiparticle interactions*, Phys. Rev. Lett. **118** (2017), 167003. See pages: [10](#), [11](#), [13](#), [14](#), [104](#), [105](#), [153](#), and [154](#)
- [dMC17] Luca de' Medici and Massimo Capone, *Modeling many-body physics with slave-spin mean-field: Mott and Hund's physics in Fe-superconductors*, pp. 115–185, Springer International Publishing, Cham, 2017. See pages: [5](#), [6](#), [10](#), [11](#), [13](#), and [104](#)
- [dMGC14] Luca de' Medici, Gianluca Giovannetti, and Massimo Capone, *Selective Mott physics as a key to iron superconductors*, Phys. Rev. Lett. **112** (2014), 177001. See pages: [10](#) and [13](#)
- [dMHCD09] Luca de' Medici, S. R. Hassan, Massimo Capone, and Xi Dai, *Orbital-selective Mott transition out of band degeneracy lifting*, Phys. Rev. Lett. **102** (2009), 126401. See pages: [10](#) and [14](#)
- [DMicv⁺13] Xiaoyu Deng, Jernej Mravlje, Rok Žitko, Michel Ferrero, Gabriel Kotliar, and Antoine Georges, *How bad metals turn good: Spectroscopic signatures of resilient quasiparticles*, Phys. Rev. Lett. **110** (2013), 086401. See pages: [2](#), [9](#), [73](#), [74](#), [175](#), [177](#), [182](#), [187](#), [193](#), and [195](#)
- [dMMG11] Luca de' Medici, Jernej Mravlje, and Antoine Georges, *Janus-faced influence of Hund's rule coupling in strongly correlated materials*, Phys. Rev. Lett. **107** (2011), 256401. See pages: [3](#), [5](#), [9](#), [10](#), [11](#), [12](#), [13](#), [103](#), [104](#), and [205](#)
- [DN70] Lowell Dworin and Albert Narath, *Orbital paramagnetism of localized nonmagnetic impurities in metals*, Phys. Rev. Lett. **25** (1970), 1287–1291. See page: [6](#)
- [DSH⁺14] Xiaoyu Deng, Aaron Sternbach, Kristjan Haule, D. N. Basov, and Gabriel Kotliar, *Shining light on transition-metal oxides: Unveiling the hidden Fermi liquid*, Phys. Rev. Lett. **113** (2014), 246404. See page: [73](#)
- [DSH⁺18] Xiaoyu Deng, Katharina M. Stadler, Kristjan Haule, Andreas Weichselbaum, Jan von Delft, and Gabriel Kotliar, *Signatures of Mottness and Hundness in archetypal correlated metals*, arXiv:1708.05752 [cond-mat.str-el] (2018). See pages: [3](#), [5](#), [7](#), [11](#), [13](#), [17](#), [22](#), [26](#), [72](#), [85](#), [104](#), [175](#), [187](#), [188](#), [189](#), [191](#), [195](#), [200](#), [201](#), [202](#), and [209](#)
- [EK95] V. J. Emery and S. A. Kivelson, *Superconductivity in bad metals*, Phys. Rev. Lett. **74** (1995), 3253–3256. See pages: [2](#) and [74](#)
- [FB15] L. Fanfarillo and E. Bascones, *Electronic correlations in Hund metals*, Phys. Rev. B **92** (2015), 075136. See pages: [5](#), [10](#), [11](#), [13](#), and [104](#)
- [FC17] Rafael M Fernandes and Andrey V Chubukov, *Low-energy microscopic models for iron-based superconductors: a review*, Reports on Progress in Physics **80** (2017), no. 1, 014503. See page: [7](#)

- [FCR⁺15] J. Fink, A. Charnukha, E. D. L. Rienks, Z. H. Liu, S. Thirupathaiah, I. Avigo, F. Roth, H. S. Jeevan, P. Gegenwart, M. Roslova, I. Morozov, S. Wurmehl, U. Bovensiepen, S. Borisenko, M. Vojta, and B. Büchner, *Non-Fermi-liquid scattering rates and anomalous band dispersion in ferropnictides*, Phys. Rev. B **92** (2015), 201106. See pages: [1](#) and [2](#)
- [GK92] Antoine Georges and Gabriel Kotliar, *Hubbard model in infinite dimensions*, Phys. Rev. B **45** (1992), 6479–6483. See pages: [19](#) and [22](#)
- [GKKR96] Antoine Georges, Gabriel Kotliar, Werner Krauth, and Marcelo J. Rozenberg, *Dynamical mean-field theory of strongly correlated fermion systems and the limit of infinite dimensions*, Rev. Mod. Phys. **68** (1996), no. 1, 13. See pages: [8](#), [19](#), [22](#), [73](#), [76](#), and [82](#)
- [Gle19] Andreas Gleis, Master’s thesis, Ludwig-Maximilians-Universität München, (to be published) 2019. See pages: [16](#), [31](#), and [202](#)
- [GLK⁺11] H. Gretarsson, A. Lupascu, Jungho Kim, D. Casa, T. Gog, W. Wu, S. R. Julian, Z. J. Xu, J. S. Wen, G. D. Gu, R. H. Yuan, Z. G. Chen, N.-L. Wang, S. Khim, K. H. Kim, M. Ishikado, I. Jarrige, S. Shamoto, J.-H. Chu, I. R. Fisher, and Young-June Kim, *Revealing the dual nature of magnetism in iron pnictides and iron chalcogenides using x-ray emission spectroscopy*, Phys. Rev. B **84** (2011), 100509. See page: [2](#)
- [GML⁺11] Emanuel Gull, Andrew J. Millis, Alexander I. Lichtenstein, Alexey N. Rubtsov, Matthias Troyer, and Philipp Werner, *Continuous-time Monte Carlo methods for quantum impurity models*, Rev. Mod. Phys. **83** (2011), 349–404. See page: [15](#)
- [GMM13] Antoine Georges, Luca de’ Medici, and Jernej Mravlje, *Strong correlations from Hund’s coupling*, Annual Rev. of Cond. Mat. Phys. **4** (2013), no. 1, 137–178. See pages: [4](#), [5](#), [6](#), [7](#), [10](#), [11](#), [12](#), [13](#), [103](#), and [104](#)
- [Gur81] M. Gurvitch, *Ioffe-Regel criterion and resistivity of metals*, Phys. Rev. B **24** (1981), 7404–7407. See page: [74](#)
- [GWPT08] E. Gull, P. Werner, O. Parcollet, and M. Troyer, *Continuous-time auxiliary-field Monte Carlo for quantum impurity models*, EPL (Europhysics Letters) **82** (2008), no. 5, 57003. See page: [15](#)
- [GWvDV12] Cheng Guo, Andreas Weichselbaum, Jan von Delft, and Matthias Vojta, *Critical and strong-coupling phases in one- and two-bath spin-boson models*, Phys. Rev. Lett. **108** (2012), 160401. See page: [49](#)
- [Hau07a] Kristjan Haule, *DFT + embedded DMFT functional*, published online: <http://hauleweb.rutgers.edu/tutorials/index.html>, 2007. See page: [86](#)
- [Hau07b] Kristjan Haule, *Quantum monte carlo impurity solver for cluster dynamical mean-field theory and electronic structure calculations with adjustable cluster base*, Phys. Rev. B **75** (2007), 155113. See pages: [15](#) and [86](#)
- [Hav16] Maurits W. Haverkort, *Quany for core level spectroscopy - excitons, resonances and band excitations in time and frequency domain*, Journal of Physics: Conference Series **712** (2016), no. 1, 012001. See page: [16](#)

- [HBA⁺13] F. Hardy, A. E. Böhmer, D. Aoki, P. Burger, T. Wolf, P. Schweiss, R. Heid, P. Adelmann, Y. X. Yao, G. Kotliar, J. Schmalian, and C. Meingast, *Evidence of strong correlations and coherence-incoherence crossover in the iron pnictide superconductor KFe_2As_2* , Phys. Rev. Lett. **111** (2013), 027002. See pages: [1](#), [2](#), [4](#), [10](#), [15](#), [156](#), and [193](#)
- [HBdM⁺16] F. Hardy, A. E. Böhmer, L. de' Medici, M. Capone, G. Giovannetti, R. Eder, L. Wang, M. He, T. Wolf, P. Schweiss, R. Heid, A. Herbig, P. Adelmann, R. A. Fisher, and C. Meingast, *Strong correlations, strong coupling, and s-wave superconductivity in hole-doped $BaFe_2As_2$ single crystals*, Phys. Rev. B **94** (2016), 205113. See pages: [1](#), [2](#), [4](#), [10](#), [13](#), and [15](#)
- [HDD12] Li Huang, Liang Du, and Xi Dai, *Complete phase diagram for three-band Hubbard model with orbital degeneracy lifted by crystal field splitting*, Phys. Rev. B **86** (2012), 035150. See pages: [10](#) and [14](#)
- [Hew93] A. C. Hewson, *The Kondo problem to heavy fermions*, Cambridge University Press, 1993. See page: [82](#)
- [HicvM16] Alen Horvat, Rok Žitko, and Jernej Mravlje, *Low-energy physics of three-orbital impurity model with Kanamori interaction*, Phys. Rev. B **94** (2016), 165140. See page: [7](#)
- [HK09] Kristjan Haule and Gabriel Kotliar, *Coherence-incoherence crossover in the normal state of iron oxyprnctides and importance of Hund's rule coupling*, New J. Phys. **11** (2009), 025021. See pages: [1](#), [2](#), [4](#), [5](#), [11](#), [14](#), [86](#), [87](#), [103](#), [104](#), [155](#), [156](#), [175](#), and [193](#)
- [HL85] Mark S. Hybertsen and Steven G. Louie, *First-principles theory of quasiparticles: Calculation of band gaps in semiconductors and insulators*, Phys. Rev. Lett. **55** (1985), 1418–1421. See page: [7](#)
- [HSK08] K. Haule, J. H. Shim, and G. Kotliar, *Correlated electronic structure of $LaO_{1-x}F_xFeAs$* , Phys. Rev. Lett. **100** (2008), 226402. See pages: [1](#), [4](#), [5](#), and [14](#)
- [HTS⁺13] P. Hansmann, A. Toschi, G. Sangiovanni, T. Saha-Dasgupta, S. Lupi, M. Marsi, and K. Held, *Mott-Hubbard transition in V_2O_3 revisited*, physica status solidi (b) **250** (2013), no. 7, 1251–1264. See page: [3](#)
- [HTT04] N. E. Hussey, K. Takenaka, and H. Takagi, *Universality of the Mott-Ioffe-Regel limit in metals*, Philosophical Magazine **84** (2004), no. 27, 2847–2864. See pages: [2](#) and [74](#)
- [Hub63] J. Hubbard, *Electron correlations in narrow energy bands*, Proceedings of the Royal Society of London A: Mathematical, Physical and Engineering Sciences **276** (1963), no. 1365, 238–257. See page: [2](#)
- [Hun25] F. Hund, *Zur Deutung verwickelter Spektren, insbesondere der Elemente Scandium bis Nickel*, Zeitschrift für Physik **33** (1925), no. 1, 345–371. See page: [3](#)
- [HW14] Markus Hanl and Andreas Weichselbaum, *Local susceptibility and Kondo scaling in the presence of finite bandwidth*, Phys. Rev. B **89** (2014), 075130. See pages: [69](#) and [70](#)

- [HW15] Shintaro Hoshino and Philipp Werner, *Superconductivity from emerging magnetic moments*, Phys. Rev. Lett. **115** (2015), 247001. See page: [12](#)
- [HW16] ———, *Electronic orders in multiorbital Hubbard models with lifted orbital degeneracy*, Phys. Rev. B **93** (2016), 155161. See pages: [10](#) and [12](#)
- [icvHP⁺13] R. Žitko, D. Hansen, E. Perepelitsky, J. Mravlje, A. Georges, and B. S. Shastry, *Extremely correlated Fermi liquid theory meets dynamical mean-field theory: Analytical insights into the doping-driven Mott transition*, Phys. Rev. B **88** (2013), 235132. See page: [2](#)
- [IL10] Hiroshi Ishida and Ansgar Liebsch, *Fermi-liquid, non-Fermi-liquid, and Mott phases in iron pnictides and cuprates*, Phys. Rev. B **81** (2010), 054513. See pages: [1](#), [10](#), [11](#), [12](#), and [104](#)
- [IR60] A. F. Ioffe and A. R. Regel, *Non-crystalline, amorphous and liquid electronic semiconductors*, Prog. Semicond. **4** (1960), 237–291. See page: [74](#)
- [KBK⁺08] T. Kroll, S. Bonhommeau, T. Kachel, H. A. Dürr, J. Werner, G. Behr, A. Koitzsch, R. Hübel, S. Leger, R. Schönfelder, A. K. Ariffin, R. Manzke, F. M. F. de Groot, J. Fink, H. Eschrig, B. Büchner, and M. Knupfer, *Electronic structure of LaFeAsO_{1-x}F_x from x-ray absorption spectroscopy*, Phys. Rev. B **78** (2008), 220502. See page: [5](#)
- [KHH⁺06] Yoichi Kamihara, Hidenori Hiramatsu, Masahiro Hirano, Ryuto Kawamura, Hiroshi Yanagi, Toshio Kamiya, and Hideo Hosono, *Iron-based layered superconductor: LaOFeP*, Journal of the American Chemical Society **128** (2006), no. 31, 10012–10013. See page: [1](#)
- [KHSK12] Andrey Kutepov, Kristjan Haule, Sergey Y. Savrasov, and Gabriel Kotliar, *Electronic structure of Pu and Am metals by self-consistent relativistic GW method*, Phys. Rev. B **85** (2012), 155129. See page: [7](#)
- [KHW⁺18] A. Kowalski, A. Hausoel, M. Wallerberger, P. Gunacker, and G. Sangiovanni, *State- and superstate-sampling in hybridization-expansion continuous-time quantum Monte Carlo*, arXiv:1807.00361 [cond-mat.str-el] (2018). See page: [12](#)
- [KJWV17] Aaram J. Kim, Harald O. Jeschke, Philipp Werner, and Roser Valentí, *J freezing and Hund’s rules in spin-orbit-coupled multiorbital Hubbard models*, Phys. Rev. Lett. **118** (2017), 086401. See page: [12](#)
- [KLK⁺19] F. Kugler, S.-S. Lee, G. Kotliar, J. von Delft, and A. Weichselbaum, to be published (2019). See pages: [10](#), [16](#), [31](#), [85](#), and [202](#)
- [KMR02] G. Kotliar, Sahana Murthy, and M. J. Rozenberg, *Compressibility divergence and the finite temperature Mott transition*, Phys. Rev. Lett. **89** (2002), 046401. See page: [2](#)
- [KmWW80] H. R. Krishna-murthy, J. W. Wilkins, and K. G. Wilson, *Renormalization-group approach to the Anderson model of dilute magnetic alloys. I. Static properties for the symmetric case*, Phys. Rev. B **21** (1980), 1003–1043. See pages: [22](#) and [24](#)
- [Koh99] W. Kohn, *Nobel lecture: Electronic structure of matter—wave functions and density functionals*, Rev. Mod. Phys. **71** (1999), 1253–1266. See page: [7](#)

- [KOK17] A.L. Kutepov, V.S. Oudovenko, and G. Kotliar, *Linearized self-consistent quasiparticle GW method: Application to semiconductors and simple metals*, Computer Physics Communications **219** (2017), 407 – 414. See page: [7](#)
- [Kot99] G. Kotliar, *Landau theory of the Mott transition in the fully frustrated Hubbard model in infinite dimensions*, Eur. Phys. J. B **11** (1999), no. 1, 27–39. See pages: [2](#) and [76](#)
- [KS65] W. Kohn and L. J. Sham, *Self-consistent equations including exchange and correlation effects*, Phys. Rev. **140** (1965), A1133–A1138. See page: [7](#)
- [KWHH08] Yoichi Kamihara, Takumi Watanabe, Masahiro Hirano, and Hideo Hosono, *Iron-based layered superconductor $La[O_{1-x}F_x]FeAs$ ($x = 0.05 - 0.12$) with $T_c = 26K$* , Journal of the American Chemical Society **130** (2008), no. 11, 3296–3297. See page: [1](#)
- [LCMK18] Tsung-Han Lee, Andrey Chubukov, Hu Miao, and Gabriel Kotliar, *Pairing mechanism in Hund’s metal superconductors and the universality of the superconducting gap to critical temperature ratio*, Phys. Rev. Lett. **121** (2018), 187003. See pages: [153](#) and [201](#)
- [LGH⁺17] S. Lafuerza, H. Gretarsson, F. Hardy, T. Wolf, C. Meingast, G. Giovannetti, M. Capone, A. S. Sefat, Y.-J. Kim, P. Glatzel, and L. de’ Medici, *Evidence of Mott physics in iron pnictides from x-ray spectroscopy*, Phys. Rev. B **96** (2017), 045133. See page: [2](#)
- [LHGH14] Y. Lu, M. Höppner, O. Gunnarsson, and M. W. Haverkort, *Efficient real-frequency solver for dynamical mean-field theory*, Phys. Rev. B **90** (2014), 085102. See page: [16](#)
- [LI10] Ansgar Liebsch and Hiroshi Ishida, *Correlation-induced spin freezing transition in FeSe: A dynamical mean field study*, Phys. Rev. B **82** (2010), 155106. See pages: [1](#), [10](#), and [12](#)
- [LNW06] Patrick A. Lee, Naoto Nagaosa, and Xiao-Gang Wen, *Doping a Mott insulator: Physics of high-temperature superconductivity*, Rev. Mod. Phys. **78** (2006), 17–85. See page: [3](#)
- [LSG⁺13] Nicola Lanatà, Hugo U. R. Strand, Gianluca Giovannetti, Bo Hellsing, Luca de’ Medici, and Massimo Capone, *Orbital selectivity in Hund’s metals: The iron chalcogenides*, Phys. Rev. B **87** (2013), 045122. See pages: [5](#) and [10](#)
- [LvDW17] Seung-Sup B. Lee, Jan von Delft, and Andreas Weichselbaum, *Doublon-holon origin of the subpeaks at the Hubbard band edges*, Phys. Rev. Lett. **119** (2017), 236402. See pages: [16](#), [24](#), [27](#), and [85](#)
- [LvDW18] ———, *Filling-driven Mott transition in $SU(N)$ Hubbard models*, Phys. Rev. B **97** (2018), 165143. See pages: [16](#), [26](#), and [85](#)
- [LW16] Seung-Sup B. Lee and Andreas Weichselbaum, *Adaptive broadening to improve spectral resolution in the numerical renormalization group*, Phys. Rev. B **94** (2016), 235127. See pages: [24](#), [27](#), [28](#), and [202](#)

- [MAM⁺11] Jernej Mravlje, Markus Aichhorn, Takashi Miyake, Kristjan Haule, Gabriel Kotliar, and Antoine Georges, *Coherence-incoherence crossover and the mass-renormalization puzzles in Sr_2RuO_4* , Phys. Rev. Lett. **106** (2011), 096401. See pages: [5](#), [11](#), [14](#), [86](#), [87](#), [103](#), [179](#), [182](#), and [193](#)
- [Man14] Norman Mannella, *The magnetic moment enigma in Fe-based high temperature superconductors*, Journal of Physics: Condensed Matter **26** (2014), no. 47, 473202. See page: [8](#)
- [MBY⁺18] H. Miao, W. H. Brito, Z. P. Yin, R. D. Zhong, G. D. Gu, P. D. Johnson, M. P. M. Dean, S. Choi, G. Kotliar, W. Ku, X. C. Wang, C. Q. Jin, S.-F. Wu, T. Qian, and H. Ding, *Universal $2\Delta_{max}/k_B T_c$ scaling decoupled from the electronic coherence in iron-based superconductors*, Phys. Rev. B **98** (2018), 020502. See page: [153](#)
- [MG16] Jernej Mravlje and Antoine Georges, *Thermopower and entropy: Lessons from Sr_2RuO_4* , Phys. Rev. Lett. **117** (2016), 036401. See pages: [5](#), [11](#), [15](#), [74](#), [75](#), [103](#), [179](#), [195](#), and [202](#)
- [MGWF⁺14] Andrew K. Mitchell, Martin R. Galpin, Samuel Wilson-Fletcher, David E. Logan, and Ralf Bulla, *Generalized Wilson chain for solving multichannel quantum impurity problems*, Phys. Rev. B **89** (2014), 121105. See pages: [17](#), [19](#), [22](#), [28](#), [29](#), [30](#), and [200](#)
- [MH89] E. Müller-Hartmann, *The Hubbard model at high dimension: some exact results and weak coupling theory*, Z. Phys. B **76** (1989), 211. See pages: [80](#) and [82](#)
- [MJPH05] Thomas Maier, Mark Jarrell, Thomas Pruschke, and Matthias H. Hettler, *Quantum cluster theories*, Rev. Mod. Phys. **77** (2005), 1027–1080. See page: [8](#)
- [MMR⁺73] D. B. McWhan, A. Menth, J. P. Remeika, W. F. Brinkman, and T. M. Rice, *Metal-insulator transitions in pure and doped V_2O_3* , Phys. Rev. B **7** (1973), 1920–1931. See page: [3](#)
- [MNI12] Takahiro Misawa, Kazuma Nakamura, and Masatoshi Imada, *Ab initio evidence for strong correlation associated with Mott proximity in iron-based superconductors*, Phys. Rev. Lett. **108** (2012), 177007. See page: [10](#)
- [Mot49] N. F. Mott, *The basis of the electron theory of metals, with special reference to the transition metals*, Proceedings of the Physical Society. Section A **62** (1949), no. 7, 416. See page: [2](#)
- [Mot68] ———, *Metal-insulator transition*, Rev. Mod. Phys. **40** (1968), 677–683. See page: [2](#)
- [Mot72] ———, *Conduction in non-crystalline systems IX. the minimum metallic conductivity*, The Philosophical Magazine: A Journal of Theoretical Experimental and Applied Physics **26** (1972), no. 4, 1015–1026. See page: [74](#)
- [MRM⁺73] D. B. McWhan, J. P. Remeika, J. P. Maita, H. Okinaka, K. Kosuge, and S. Kachi, *Heat capacity of vanadium oxides at low temperature*, Phys. Rev. B **7** (1973), 326–332. See page: [3](#)
- [MRR69] D. B. McWhan, T. M. Rice, and J. P. Remeika, *Mott transition in Cr-doped V_2O_3* , Phys. Rev. Lett. **23** (1969), 1384–1387. See page: [3](#)

- [MV89] Walter Metzner and Dieter Vollhardt, *Correlated lattice fermions in $d = \infty$ dimensions*, Phys. Rev. Lett. **62** (1989), 324–327. See page: [19](#)
- [MWR⁺14] H. Miao, L.-M. Wang, P. Richard, S.-F. Wu, J. Ma, T. Qian, L.-Y. Xing, X.-C. Wang, C.-Q. Jin, C.-P. Chou, Z. Wang, W. Ku, and H. Ding, *Coexistence of orbital degeneracy lifting and superconductivity in iron-based superconductors*, Phys. Rev. B **89** (2014), 220503. See page: [15](#)
- [NnFH17] Y. Núñez Fernández and K. Hallberg, *Solving the multi-site and multi-orbital Dynamical Mean Field Theory using Density Matrix Renormalization*, arXiv:1711.08745 [cond-mat.str-el] (2017). See pages: [16](#) and [29](#)
- [NnFH18] ———, *Metal-insulator transition in the hybridized two-orbital Hubbard model revisited*, Journal of Physics: Conference Series **1041** (2018), no. 1, 012002. See pages: [16](#) and [29](#)
- [NnFKH18] Y. Núñez Fernández, G. Kotliar, and K. Hallberg, *Emergent low-energy bound states in the two-orbital Hubbard model*, Phys. Rev. B **97** (2018), 121113. See pages: [16](#) and [29](#)
- [NSA15] Yusuke Nomura, Shiro Sakai, and Ryotaro Arita, *Nonlocal correlations induced by Hund’s coupling: A cluster DMFT study*, Phys. Rev. B **91** (2015), 235107. See page: [9](#)
- [OC12] T. Tzen Ong and Piers Coleman, *Local quantum criticality of an iron-pnictide tetrahedron*, Phys. Rev. Lett. **108** (2012), 107201. See page: [86](#)
- [OM00] J. Orenstein and A. J. Millis, *Advances in the physics of high-temperature superconductivity*, Science **288** (2000), no. 5465, 468–474. See page: [3](#)
- [OO94] Wanda C. Oliveira and Luiz N. Oliveira, *Generalized numerical renormalization-group method to calculate the thermodynamical properties of impurities in metals*, Phys. Rev. B **49** (1994), 11986–11994. See pages: [25](#) and [27](#)
- [OPicv15] Žiga Osolin, Thomas Pruschke, and Rok Žitko, *Fine structure of spectra in the antiferromagnetic phase of the Kondo lattice model*, Phys. Rev. B **91** (2015), 075105. See page: [9](#)
- [OY73] Isamu Okada and Kei Yosida, *Singlet ground state of the localized d -electrons coupled with conduction electrons in metals*, Progress of Theoretical Physics **49** (1973), no. 5, 1483–1502. See pages: [14](#), [15](#), and [87](#)
- [PB05] Th. Pruschke and R. Bulla, *Hund’s coupling and the metal-insulator transition in the two-band Hubbard model*, The European Physical Journal B - Condensed Matter and Complex Systems **44** (2005), no. 2, 217–224. See pages: [9](#) and [22](#)
- [PHI⁺17] Jonathan Pelliciari, Yaobo Huang, Kenji Ishii, Chenglin Zhang, Pengcheng Dai, Gen Fu Chen, Lingyi Xing, Xiancheng Wang, Changqing Jin, Hong Ding, Philipp Werner, and Thorsten Schmitt, *Magnetic moment evolution and spin freezing in doped $BaFe_2As_2$* , Scientific Reports **7** (2017), 8003. See pages: [2](#), [8](#), [12](#), and [13](#)
- [PKP11] Robert Peters, Norio Kawakami, and Thomas Pruschke, *Orbital order, metal-insulator transition, and magnetoresistance effect in the two-orbital Hubbard model*, Phys. Rev. B **83** (2011), 125110. See page: [22](#)

- [PP10] Robert Peters and Thomas Pruschke, *Orbital and magnetic order in the two-orbital Hubbard model*, Phys. Rev. B **81** (2010), 035112. See page: [22](#)
- [PPA06] Robert Peters, Thomas Pruschke, and Frithjof B. Anders, *Numerical renormalization group approach to Green's functions for quantum impurity models*, Phys. Rev. B **74** (2006), no. 24, 245114. See page: [27](#)
- [QHB⁺09] M. M. Qazilbash, J. J. Hamlin, R. E. Baumbach, Lijun Zhang, D. J. Singh, M. B. Maple, and D. N. Basov, *Electronic correlations in the iron pnictides*, Nature Physics **5** (2009), 647–650. See page: [2](#)
- [RCD⁺08] Zhi-An Ren, Guang-Can Che, Xiao-Li Dong, Jie Yang, Wei Lu, Wei Yi, Xiao-Li Shen, Zheng-Cai Li, Li-Ling Sun, Fang Zhou, and Zhong-Xian Zhao, *Superconductivity and phase diagram in iron-based arsenic-oxides $ReFeAsO_{1-\delta}$ ($Re = \text{rare-earth metal}$) without fluorine doping*, EPL (Europhysics Letters) **83** (2008), no. 1, 17002. See page: [1](#)
- [RKK⁺95] M. J. Rozenberg, G. Kotliar, H. Kajueter, G. A. Thomas, D. H. Rapkine, J. M. Honig, and P. Metcalf, *Optical conductivity in Mott-Hubbard systems*, Phys. Rev. Lett. **75** (1995), 105–108. See page: [2](#)
- [RSL05] A. N. Rubtsov, V. V. Savkin, and A. I. Lichtenstein, *Continuous-time quantum Monte Carlo method for fermions*, Phys. Rev. B **72** (2005), 035122. See page: [15](#)
- [RYL⁺08] Z. A. Ren, J. Yang, W. Lu, W. Yi, G. C. Che, X. L. Dong, L. L. Sun, and Z. X. Zhao, *Superconductivity at 52 K in iron based F doped layered quaternary compound $Pr[O_{1-x}F_x]FeAs$* , Materials Research Innovations **12** (2008), no. 3, 105–106. See page: [1](#)
- [Sch11] Ulrich Schollwöck, *The density-matrix renormalization group in the age of matrix product states*, Annals of Physics **326** (2011), no. 1, 96 – 192, January 2011 Special Issue. See pages: [26](#) and [199](#)
- [SHK17] Patrick Sémon, Kristjan Haule, and Gabriel Kotliar, *Validity of the local approximation in iron pnictides and chalcogenides*, Phys. Rev. B **95** (2017), 195115. See page: [8](#)
- [SKWvD18] Katharina M. Stadler, Gabriel Kotliar, Andreas Weichselbaum, and Jan von Delft, *Hundness versus Mottness in a three-band Hubbard-Hund model: On the origin of strong correlations in Hund metals*, arXiv:1808.09936 [cond-mat.str-el] (2018). See pages: [1](#), [5](#), [7](#), [9](#), [10](#), [11](#), [17](#), [22](#), [24](#), [26](#), [73](#), [85](#), [86](#), [99](#), [103](#), [152](#), [153](#), [154](#), [155](#), [175](#), [177](#), [178](#), [183](#), [184](#), [187](#), [188](#), [191](#), [200](#), [201](#), [205](#), [207](#), and [208](#)
- [SMB⁺14] D. Stricker, J. Mravlje, C. Berthod, R. Fittipaldi, A. Vecchione, A. Georges, and D. van der Marel, *Optical response of Sr_2RuO_4 reveals universal Fermi-liquid scaling and quasiparticles beyond Landau theory*, Phys. Rev. Lett. **113** (2014), 087404. See pages: [5](#), [15](#), [179](#), [182](#), and [183](#)
- [SMP⁺12] A. A. Schafgans, S. J. Moon, B. C. Pursley, A. D. LaForge, M. M. Qazilbash, A. S. Sefat, D. Mandrus, K. Haule, G. Kotliar, and D. N. Basov, *Electronic correlations and unconventional spectral weight transfer in the high-temperature pnictide $BaFe_{2-x}Co_xAs_2$ superconductor using infrared spectroscopy*, Phys. Rev. Lett. **108** (2012), 147002. See pages: [1](#), [5](#), [11](#), [15](#), [74](#), and [183](#)

- [SMvDW16] K. M. Stadler, A. K. Mitchell, J. von Delft, and A. Weichselbaum, *Interleaved numerical renormalization group as an efficient multiband impurity solver*, Phys. Rev. B **93** (2016), 235101. See pages: [17](#), [19](#), [22](#), [28](#), [29](#), [82](#), and [200](#)
- [Sta13] Katharina M. Stadler, *Towards exploiting non-abelian symmetries in the dynamical mean-field theory using the numerical renormalization group*, Master's thesis, Ludwig-Maximilians-University Munich, 2013. See pages: [19](#), [21](#), [23](#), [79](#), and [205](#)
- [SWM⁺11] Takaaki Sudayama, Yuki Wakisaka, Takashi Mizokawa, Soshi Ibuka, Rei Morinaga, Taku J. Sato, Masashi Arita, Hirofumi Namatame, Masaki Taniguchi, and Naurang L. Saini, *Doping-dependent and orbital-dependent band renormalization in $Ba(Fe_{1-x}Co_x)_2As_2$ superconductors*, Journal of the Physical Society of Japan **80** (2011), no. 11, 113707. See page: [13](#)
- [SYvD⁺15] K. M. Stadler, Z. P. Yin, J. von Delft, G. Kotliar, and A. Weichselbaum, *Dynamical mean-field theory plus numerical renormalization-group study of spin-orbital separation in a three-band Hund metal*, Phys. Rev. Lett. **115** (2015), 136401. See pages: [5](#), [7](#), [8](#), [11](#), [14](#), [17](#), [22](#), [24](#), [26](#), [73](#), [85](#), [88](#), [99](#), [100](#), [101](#), [103](#), [104](#), [152](#), [153](#), [177](#), [178](#), [196](#), [200](#), [206](#), and [207](#)
- [TGR⁺10] A. Tamai, A. Y. Ganin, E. Rozbicki, J. Bacsá, W. Meevasana, P. D. C. King, M. Caffio, R. Schaub, S. Margadonna, K. Prassides, M. J. Rosseinsky, and F. Baumberger, *Strong electron correlations in the normal state of the iron-based $FeSe_{0.42}Te_{0.58}$ superconductor observed by angle-resolved photoemission spectroscopy*, Phys. Rev. Lett. **104** (2010), 097002. See page: [2](#)
- [TKK⁺10] Taichi Terashima, Motoi Kimata, Nobuyuki Kurita, Hidetaka Satsukawa, Atsushi Harada, Kaori Hazama, Motoharu Imai, Akira Sato, Kunihiro Kihou, Chul-Ho Lee, Hijiri Kito, Hiroshi Eisaki, Akira Iyo, Taku Saito, Hideto Fukazawa, Yoh Kohori, Hisatomo Harima, and Shinya Uji, *Fermi surface and mass enhancement in KFe_2As_2 from de Haas-van Alphen effect measurements*, Journal of the Physical Society of Japan **79** (2010), no. 5, 053702. See page: [2](#)
- [TKK⁺13] Taichi Terashima, Nobuyuki Kurita, Motoi Kimata, Megumi Tomita, Satoshi Tsuchiya, Motoharu Imai, Akira Sato, Kunihiro Kihou, Chul-Ho Lee, Hijiri Kito, Hiroshi Eisaki, Akira Iyo, Taku Saito, Hideto Fukazawa, Yoh Kohori, Hisatomo Harima, and Shinya Uji, *Fermi surface in KFe_2As_2 determined via de Haas-van Alphen oscillation measurements*, Phys. Rev. B **87** (2013), 224512. See pages: [2](#), [10](#), and [13](#)
- [TKS⁺10] Taichi Terashima, Motoi Kimata, Hidetaka Satsukawa, Atsushi Harada, Kaori Hazama, Motoharu Imai, Akira Sato, Shinya Uji, Kunihiro Kihou, Chul-Ho Lee, Hijiri Kito, Hiroshi Eisaki, Akira Iyo, Hideto Fukazawa, Yoh Kohori, and Hisatomo Harima, *De Haas-van Alphen oscillations in KFe_2As_2* , Physica C: Superconductivity and its Applications **470** (2010), S351 – S352. See page: [2](#)
- [TZR⁺18] A. Tamai, M. Zingl, E. Rozbicki, E. Cappelli, S. Ricco, A. de la Torre, S. McKeeown Walker, F. Y. Bruno, P.D.C. King, W. Meevasana, M. Shi, M. Radovic, N.C. Plumb, A.S. Gibbs, A.P. Mackenzie, C. Berthod, H. Strand, M. Kim, A. Georges, and F. Baumberger, *High-resolution photoemission on Sr_2RuO_4 reveals correlation-enhanced effective spin-orbit coupling and dominantly local self-energies*, arXiv:1812.06531 [cond-mat.str-el] (2018). See pages: [8](#) and [182](#)

- [vB04] U von Barth, *Basic Density-Functional Theory - an overview*, Physica Scripta **2004** (2004), no. T109, 9. See page: [7](#)
- [vDZF98] Jan von Delft, Gergely Zaránd, and Michele Fabrizio, *Finite-size bosonization of 2-channel Kondo model: A bridge between numerical renormalization group and conformal field theory*, Phys. Rev. Lett. **81** (1998), no. 1, 196–199. See page: [24](#)
- [vP09] Rok Žitko and Thomas Pruschke, *Energy resolution and discretization artifacts in the numerical renormalization group*, Phys. Rev. B **79** (2009), no. 8, 085106. See pages: [16](#), [22](#), [24](#), [25](#), [27](#), and [28](#)
- [Ž09] Rok Žitko, *Adaptive logarithmic discretization for numerical renormalization group methods*, Computer Physics Communications **180** (2009), 1271. See pages: [16](#), [22](#), [24](#), [25](#), and [28](#)
- [WAC19] Yi-Ming Wu, Artem Abanov, and Andrey V. Chubukov, *Pairing in quantum critical systems: Transition temperature, pairing gap, and their ratio*, Phys. Rev. B **99** (2019), 014502. See pages: [153](#) and [201](#)
- [WCdM⁺06] Philipp Werner, Armin Comanac, Luca de’ Medici, Matthias Troyer, and Andrew J. Millis, *Continuous-time solver for quantum impurity models*, Phys. Rev. Lett. **97** (2006), 076405. See page: [15](#)
- [WCM⁺12] Philipp Werner, Michele Casula, Takashi Miyake, Ferdi Aryasetiawan, Andrew J. Millis, and Silke Biermann, *Satellites and large doping and temperature dependence of electronic properties in hole-doped BaFe₂As₂*, Nature Physics **8** (2012), 331 – 337. See pages: [1](#), [5](#), and [12](#)
- [Wei11] A. Weichselbaum, *Discarded weight and entanglement spectra in the numerical renormalization group*, Phys. Rev. B **84** (2011), 125130. See pages: [26](#), [27](#), and [30](#)
- [Wei12a] ———, *Non-abelian symmetries in tensor networks: A quantum symmetry space approach*, Annals of Physics **327** (2012), 2972–3047. See pages: [5](#), [9](#), [22](#), [26](#), [28](#), [69](#), [85](#), and [199](#)
- [Wei12b] ———, *Tensor networks and the numerical renormalization group*, Phys. Rev. B **86** (2012), 245124. See pages: [5](#), [24](#), [26](#), [85](#), and [199](#)
- [WGM⁺15] F. Alexander Wolf, Ara Go, Ian P. McCulloch, Andrew J. Millis, and Ulrich Schollwöck, *Imaginary-time matrix product state impurity solver for dynamical mean-field theory*, Phys. Rev. X **5** (2015), 041032. See pages: [16](#) and [29](#)
- [WGTm08] Philipp Werner, Emanuel Gull, Matthias Troyer, and Andrew J. Millis, *Spin freezing transition and non-Fermi-liquid self-energy in a three-orbital model*, Phys. Rev. Lett **101** (2008), 166405. See pages: [5](#), [10](#), [11](#), [12](#), [13](#), [14](#), [86](#), [87](#), [103](#), and [152](#)
- [Wil75] Kenneth G. Wilson, *The renormalization group: Critical phenomena and the Kondo problem*, Rev. Mod. Phys. **47** (1975), no. 4, 773–840. See pages: [9](#), [22](#), [24](#), and [49](#)

- [WMPS14] F. Alexander Wolf, Ian P. McCulloch, Olivier Parcollet, and Ulrich Schollwöck, *Chebyshev matrix product state impurity solver for dynamical mean-field theory*, Phys. Rev. B **90** (2014), 115124. See pages: [16](#) and [29](#)
- [WMS14] F. Alexander Wolf, Ian P. McCulloch, and Ulrich Schollwöck, *Solving nonequilibrium dynamical mean-field theory using matrix product states*, Phys. Rev. B **90** (2014), 235131. See pages: [16](#) and [29](#)
- [WSL⁺19] E. Walter, K. Stadler, S.-S. B. Lee, J Wang, G. Kotliar, A. Weichselbaum, and J. von Delft, to be published (2019). See pages: [8](#), [24](#), [86](#), [153](#), [179](#), [200](#), and [202](#)
- [WvD07] Andreas Weichselbaum and Jan von Delft, *Sum-rule conserving spectral functions from the numerical renormalization group*, Phys. Rev. Lett. **99** (2007), no. 7, 076402. See pages: [5](#), [8](#), [9](#), [24](#), [26](#), [27](#), and [85](#)
- [WVS⁺09] A. Weichselbaum, F. Verstraete, U. Schollwöck, J. I. Cirac, and Jan von Delft, *Variational matrix-product-state approach to quantum impurity models*, Phys. Rev. B **80** (2009), 165117. See page: [26](#)
- [WXC⁺09] G Wu, Y L Xie, H Chen, M Zhong, R H Liu, B C Shi, Q J Li, X F Wang, T Wu, Y J Yan, J J Ying, and X H Chen, *Superconductivity at 56K in samarium-doped SrFeAsF*, Journal of Physics: Condensed Matter **21** (2009), no. 14, 142203. See page: [1](#)
- [XHK13] Wenhui Xu, Kristjan Haule, and Gabriel Kotliar, *Hidden Fermi Liquid, scattering rate saturation, and Nernst effect: A dynamical mean-field theory perspective*, Phys. Rev. Lett. **111** (2013), 036401. See pages: [175](#) and [177](#)
- [YDS⁺11] S. Yasin, M. Dumm, B. Salameh, P. Batail, C. Mezière, and M. Dressel, *Transport studies at the Mott transition of the two-dimensional organic metal κ -(BEDT-TTF)₂Cu[N(CN)₂]Br_xCl_{1-x}*, The European Physical Journal B **79** (2011), no. 4, 383–390. See page: [156](#)
- [YHK11a] Z. P. Yin, K. Haule, and G. Kotliar, *Kinetic frustration and the nature of the magnetic and paramagnetic states in iron pnictides and iron chalcogenides*, Nature Mat. **10** (2011), 932 – 935. See pages: [4](#), [5](#), [6](#), [8](#), [10](#), and [11](#)
- [YHK11b] ———, *Magnetism and charge dynamics in iron pnictides*, Nature Physics **7** (2011), 294–297. See pages: [5](#) and [11](#)
- [YHK12] ———, *Fractional power-law behavior and its origin in iron-chalcogenide and ruthenate superconductors: Insights from first-principles calculations*, Phys. Rev. B **86** (2012), 195141. See pages: [1](#), [5](#), [6](#), [8](#), [10](#), [11](#), [14](#), [86](#), [87](#), [103](#), [104](#), [152](#), [155](#), [179](#), and [200](#)
- [YIN⁺14] Tepei Yoshida, Shin-ichiro Ideta, Ichiro Nishi, Atsushi Fujimori, Ming Yi, Rob Moore, Sung-Kwan Mo, Donghui Lu, Zhi-Xun Shen, Zahid Hussain, Kunihiro Kihou, C. H Lee, Akira Iyo, Hiroshi Eisaki, and Hisatomo Harima, *Orbital character and electron correlation effects on two- and three-dimensional Fermi surfaces in KFe₂As₂ revealed by angle-resolved photoemission spectroscopy*, Frontiers in Physics **2** (2014), 17. See pages: [2](#) and [10](#)

- [YLY⁺13] M. Yi, D. H. Lu, R. Yu, S. C. Riggs, J.-H. Chu, B. Lv, Z. K. Liu, M. Lu, Y.-T. Cui, M. Hashimoto, S.-K. Mo, Z. Hussain, C. W. Chu, I. R. Fisher, Q. Si, and Z.-X. Shen, *Observation of temperature-induced crossover to an orbital-selective Mott phase in $A_x\text{Fe}_{2-y}\text{Se}_2$ ($A=K, Rb$) superconductors*, Phys. Rev. Lett. **110** (2013), 067003. See pages: [1](#), [2](#), and [10](#)
- [YLZ⁺15] M. Yi, Z-K Liu, Y. Zhang, R. Yu, J. X. Zhu, J. J. Lee, R. G. Moore, F. T. Schmitt, W. Li, S. C. Riggs, J. H. Chu, B. Lv, J. Hu, M. Hashimoto, S. K. Mo, Z. Hussain, Z. Q. Mao, C. W. Chu, I. R. Fisher, Q. Si, Z. X. Shen, and D. H. Lu, *Observation of universal strong orbital-dependent correlation effects in iron chalcogenides*, Nature Communications **6** (2015), 7777. See pages: [1](#), [2](#), and [10](#)
- [YMI⁺10] A. Yamasaki, Y. Matsui, S. Imada, K. Takase, H. Azuma, T. Muro, Y. Kato, A. Higashiya, A. Sekiyama, S. Suga, M. Yabashi, K. Tamasaku, T. Ishikawa, K. Terashima, H. Kobori, A. Sugimura, N. Umeyama, H. Sato, Y. Hara, N. Miyagawa, and S. I. Ikeda, *Electron correlation in the FeSe superconductor studied by bulk-sensitive photoemission spectroscopy*, Phys. Rev. B **82** (2010), 184511. See page: [2](#)
- [YS12] Rong Yu and Qimiao Si, *$U(1)$ slave-spin theory and its application to Mott transition in a multiorbital model for iron pnictides*, Phys. Rev. B **86** (2012), 085104. See pages: [10](#) and [13](#)
- [YS13] ———, *Orbital-selective Mott phase in multiorbital models for alkaline iron selenides $K_{1-x}\text{Fe}_{2-y}\text{Se}_2$* , Phys. Rev. Lett. **110** (2013), 146402. See page: [10](#)
- [YS17] ———, *Orbital-selective Mott phase in multiorbital models for iron pnictides and chalcogenides*, Phys. Rev. B **96** (2017), 125110. See page: [10](#)
- [YYW⁺17] Run Yang, Zhiping Yin, Yilin Wang, Yaomin Dai, Hu Miao, Bing Xu, Xianggang Qiu, and Christopher C. Homes, *Observation of an emergent coherent state in the iron-based superconductor $K\text{Fe}_2\text{As}_2$* , Phys. Rev. B **96** (2017), 201108. See pages: [4](#), [10](#), [15](#), and [183](#)